Investigation of the wingtip vortex behind an oscillating airfoil

David M. Birch
Department of Mechanical Engineering
McGill University, Montreal

September 2005

A thesis submitted to McGill University
in partial fulfillment of the requirements
of the degree of Doctor of Philosophy

Your file Votre référence
ISBN: 978-0-494-25101-0
Our file Notre référence
ISBN: 978-0-494-25101-0

Abstract

The near-field flow structure of the tip vortex generated by a NACA 0015 wing oscillating though the attached-flow, light-stall and deep-stall regimes was investigated at $Re_c = 1.86 \times 10^5$. Particular emphasis was placed on the effects of oscillation frequency and mean incidence upon the spatial and temporal evolution of the unsteady vortex structure. Phase-locked, ensemble-averaged cross-flow and axial velocity fields, vorticity distributions, and turbulence structures over a full cycle of oscillation were compared to static wing-tip vortex results, and the dynamic effects upon the vortex strength, size, trajectory and associated induced drag were examined. Through the attached-flow and light-stall oscillations, most vortex properties were qualitatively similar to the static cases, though a small degree of hysteresis between the pitch-up and pitch-down phases of motion was observed. The radial distributions of circulation within the inner region of the vortex were self-similar, and showed only small variations from the static case. When the wing was oscillated through the deep-stall regime, a dramatic decrease in tip vortex strength and concentration was observed at the end of the upstroke, as a result of the growth of the leading-edge vortex and subsequent catastrophic flow separation. The use of passive spoilers and active flaps to control the strength and trajectory of the tip vortex was also investigated.

Résumé

La structure de l'écoulement à champ proche du vortex d'extrême pointe produite par une aile NACA 0015 oscillant en régimes d'écoulement-attaché, décrochage-lèger et décrochage-extreme a été étudié au numéro $Re_c = 1.86 \times 10^5$. On a particulièrement porté attention aux effets de la fréquence d'oscillation et de l'incidence moyenne sur l'évolution spatiale et temporelle de la structure instable du vortex. Les champs de vitesse, les distributions de vorticité, et les structures de turbulence axiale obtenus à travers un cycle complet d'oscillation ont été comparés aux résultats statiques du vortex produit par une aile statique, et les effets dynamiques sur la puissance du vortex, la taille, la trajectoire et la trainée-induite associée ont été examinés. Pour les cas d' écoulement-attaché et dérochage-lèger, la plupart des propriétés du vortex étaient qualitativement semblables aux cas statiques, cependant un petit degré d'hystérésis fut remarqué. Les distributions radiales de la circulation dans la région intérieure du vortex étaient auto-semblable, et seulement des petites variations du cas statique ont paru. Quand l'aile a été assujetti aux oscillations de décrochage-profond, une diminution dramatique de puissance et de concentration maximale de vortex a été observée, en raison de la formation du vortex de décrochage-profond et de la séparation catastrophique de l'écoulement. L'utilisation des déporteurs passifs et d' ailerons actifs pour contrôler la puissance et la trajectoire du vortex a été également étudiée.

Acknowledgements

The author wishes to extend his gratitude to Professor Tim Lee for his guidance and support throughout the course of this work. Furthermore, the author wishes to thank his colleagues Peter Gerontakos and Maya El-Rayes, as well as the technical staff of the Department of Mechanical Engineering, including Georges Tewfik, Mario Iacobaccio, Mario Sglavo, Tony Micozzi and Nick DiPalma.

Table of contents

1 List of symbols

A	nondimensional constant
B	nondimensional constant
b	wing span
c	airfoil chord
C	nondimensional constant
C_D	coefficient of drag, $2D/\rho u_\infty^2 bc$
C_L	coefficient of lift, $= 2L/\rho u_\infty^2 bc$
$C_{D,3D}$	coefficient of drag of wing in three-dimensional configuration, $= 2D/\rho u_\infty^2 bc$
$C_{L,3D}$	coefficient of lift of wing in three-dimensional configuration, $= 2L/\rho u_\infty^2 bc$
d	radial scale of vortex axial profile
D	drag
D_i	induced drag
e	Correlation coefficient in Equation C3
E	transducer voltage output
K	nondimensional constant
L	lift
M	mach number
P	pressure
Q	effective cooling velocity
r	radial co-ordinate
Re_c	chord Reynolds number, $= u_\infty c/\nu$
S	wing area
s	integration path
t	time
u	streamwise velocity component
u_∞	free-stream velocity
u_{conv}	convection velocity
v	transverse velocity component
$v_\perp$	velocity component perpendicular to sensor wire

$v_{\parallel}$	velocity component parallel to sensor wire
v_r	radial velocity in cylindrical co-ordinate system
v_θ	tangential velocity in cylindrical co-ordinate system
w	spanwise velocity component
x	streamwise co-ordinate
y	transverse co-ordinate
z	spanwise or axial co-ordinate
$\Delta\alpha$	wing oscillation amplitude
Γ	vortex circulation
α	angle of attack
α_c	angle of attack, compensated for convection time lag
α_n	nondimensional constant in Equation 2
α_o	mean wing incidence
α_{ss}	static stall angle
β	yaw angle
ϕ	roll angle, also velocity potential function
κ	nondimensional frequency, $= \pi f c/u_\infty$
λ	oscillation wavelength, also length-scale of vortex, $= (c/2)C_{L,3D}$, in Equation 8
μ	rotor advance ratio, $= u_{tip} / u_\infty$
ν	kinematic viscosity
θ	cone angle, also angular co-ordinate
ρ	fluid density
σ	cross-flow velocity source term
σ_y	RMS amplitude of vortex core meandering along transverse axis
σ_z	RMS amplitude of vortex core meandering along spanwise axis
ω	circular frequency, $= 2\pi f$
ξ	parameter dependent upon vortex roll-up rate, $= (\Gamma/\pi)(b/\alpha_n)^{-1}$
ψ	stream function
ζ	vorticity

Subscripts:

o	outer vortex value (bounding 98% of total circulation)
c	core vortex value (bounded by $v_{\theta\ max}$)
max	maximum
min	minimum
θ	tangential value (polar co-ordinate system)
r	radial value (polar co-ordinate system)
a	axial value
∞	free-stream value

2 List of figures

3 List of tables

4 Introduction

The tip vortex generated by a finite wing continues to be of particular interest in aeronautical applications both because of its significant contribution toward overall aircraft drag at low speeds, and because of its hazardous effects on aircraft flight safety. These vortices can persist several tens or even several hundreds of chords downstream of the generating wing, and can pose a serious danger to closely spaced aircraft during take-off and landing operations, when altitude may not be sufficient to recover from the pitching and rolling motions induced by the vortices. Furthermore, the vortices produced by canards or strakes may adversely affect the flow around other lifting surfaces located downstream, and may result in undesirable performance or stability characteristics.

The wing tip vortex is formed as a direct consequence of lift generation. The production of lift is associated with a transverse pressure gradient which imposes an additional three-dimensional component of velocity upon the flow in the vicinity of the tip, resulting in a concentration of streamwise vorticity. The vortex is initially fed by the wing boundary layer vorticity, and in the near field (less than 3 chord lengths downstream), the tip vortex continues to grow and develop, rolling up additional shear layer vorticity into an ever-increasing, tightening spiral as it convects downstream. As the successive turns of the spiral draw together, the length scale of the vortex sheet decreases and the turns smooth together under the action of viscous and turbulent diffusion. As the vortex develops, the core region is rapidly stabilized by the near solid-body rotation, while in the vicinity of the location of maximum tangential velocity, where the shear stresses are significant, turbulent and viscous losses serve to decay and diffuse the vortex with time and downstream distance.

In rotorcraft applications, the blade tip vortex is a major source of noise and vibration. When a rotor blade encounters the low-pressure vortex trailing from the preceding blade, the result is a sudden, impulsive loading on the blade which can cause both local material deflection (leading to eventual vibration and fatigue damage) as well as an acoustic noise that can limit low-altitude helicopter operations in populated areas.

The flow around rotorcraft blades is fundamentally different from the flow around static wings because of the unsteady conditions. In order to induce net force imbalances on the rotor disk and produce rolling or pitching moments in response to the pilot control input, the pitch of the blades must be varied as a function of the angle subtended between the blade and the axis of the fuselage. The unsteady effects of these cyclic pitch oscillations energize the boundary layer over the blade during the upstroke and permit it to remain attached at instantaneous angles of attack much larger than the static stall angle, dramatically increasing the maximum section lift coefficient relative to a static wing. During the pitch-down phase of motion, the dynamic effects delay boundary layer re-attachment, introducing a significant degree of hysteresis in the lift curve between the pitch-up and pitch-down phases of motion. Furthermore, for oscillations with maximum angles of attack exceeding the static stall angle, a large, transient, spanwise leading-edge vortex (LEV) tends to form and convect rapidly downstream over the suction surface, resulting in a large increase in both lift and drag coefficient, as well as a very large negative moment coefficient.

The large increase in lift experienced by a wing oscillating with large amplitude is expected to lead to a similarly dramatic increase in the strength of the tip vortices relative to the static case, resulting in an increase in the noise, vibration and wear of which they can be the cause. Consequently, the control and mitigation of the blade tip vortices becomes very desirable. The degree of blade-vortex interaction varies with the flight conditions, and is most significant when a rotorcraft is descending with a low forward flight speed, such as during a landing approach (a maneuver which generally is performed at low altitude, which is incidentally when the noise could potentially be the most disruptive). On the other hand, during forward-flight cruise conditions, blade-vortex interaction effects may be negligible. Commonly used passive control techniques, including modification of the blade geometry, are effective but generally result in a reduction in the aerodynamic performance characteristics of the blade. Therefore, since vortex control may not be required during the bulk of the mission, an active control system would reduce the blade vortex interaction noise without a significant performance penalty.

In this study, the effects of sinusoidal pitch oscillations of a rectangular wing upon the near-field formation and growth of its wing tip vortex are characterized, and an active control technique utilizing an actuated short-span trailing-edge tab located near the wing tip is evaluated. It is theorized that a controlled tab deflection at phase angles at which a strong tip vortex is produced will sufficiently alter the boundary layer conditions in the vicinity of the tip to diffuse the vortex and limit its strength. Furthermore, for dynamic stall oscillations, the tab may be used to control the LEV in the tip region, as well as any interaction between the LEV and the tip vortex. Because there has yet to be, to the author's knowledge, a detailed characterization of the tip vortex produced by a wing oscillating through the present range of amplitudes, this study is expected to represent a significant contribution to the understanding of the phenomenon.

5 Literature review

5.1 The static wing-tip vortex

The study of the wing-tip vortices generated by lifting bodies can be divided into two distinct categories: the near-field, where the roll-up and merging of the layers of the vortex sheet is yet incomplete, and the far-field, where the majority of the circulation has already been entrained into the vortices and the vortices are quasisteady and homogenous. Theoretical and analytical studies of the initial roll-up of the tip vortex are very limited, both because of the complexity of the flow fields and the strong dependence on wing tip geometry. Also, since the development of the vortices can continue for several tens of wing chords and can be greatly influenced by free-stream turbulence and wall effects, experimental studies on the far-field of the vortex are for the most part limited to flight-tests and are very few in number.

Some of the earliest theoretical work on the initial roll-up of a tip vortex was carried out by Betz (1932), who analyzed the mechanism governing the roll-up of a tip vortex . Modeling a wing wake as a semi-infinite vortex sheet, Betz showed that the wake would roll up at the edges as a result of velocity auto-induction, as required by the Biot-Savart law. Though the Betz model is still applied in some situations because of its reasonable accuracy and relative simplicity, it was developed with the assumption that the flow is laminar and inviscid. Furthermore, because the vortex sheet was assumed semi-infinite, the Betz model tends to over-predict the vortex roll-up rate. Further downstream, once the roll-up process was complete, Betz required that the moment of inertia of the vorticity about its centroid be conserved, which, though yielding reasonable results, produces velocity singularities at the vortex centers. A similar solution for the far-field vortices was proposed by Spreiter and Sacks (1951), which required that the vorticity be concentrated in two Rankine vortices, and that the total kinetic energy of the flow be conserved during the roll-up process. While eliminating the velocity singularities at the vortex centers, the Spreiter-Sacks model greatly overpredicted the vortex radius and tended not to agree with experimental data as well as the Betz model (Widnall 1975).

Moore and Saffman (1973) considered laminar, inviscid flow in the near-field of a finite wing with a spanwise circulation distribution of the form

$$\Gamma(y) \equiv \oint_s \vec{v} \cdot \partial\vec{s} = 2\Gamma_{root}\left(\frac{b}{y}\right)^{n-1} \quad ; \qquad 0 < n < 1 \tag{1}$$

where Γ is the circulation around a path s, v is the velocity vector, y is the spanwise co-ordinate, b is the span, and n is an arbitrary parameter which allows for variability in the wing loading. Moore and Saffman had shown that the vortex sheet will tend to roll up into the spiral defined by the expression

$$r(\theta) = \left(\frac{\xi}{\theta}t\right)^{\frac{1}{1+n}} \qquad \text{where } \xi = \left(\frac{\Gamma_{root}}{\pi}\right)\left(\frac{b}{\alpha_n}\right)^{n-1} \tag{2}$$

where r is the radial distance from the vortex center, θ is the angular co-ordinate, t is time, α_n is a constant, and ξ is a parameter which depends on the wing loading and is a measure of the vortex roll-up rate. As θ becomes large, the spiral tightens and the successive turns smooth together, and the tangential velocity v_θ approaches ξ / r^n. While this model is more versatile and tends to be more accurate, it still requires that the flow is inviscid and that the wing boundary layer is laminar upon separation- two conditions which are not usually met in practical aeronautical applications.

Phillips (1981) developed a model of the initial roll-up of a turbulent wing-tip vortex generated by a wing with the circulation distribution given in Eq. (1). The vortex was then divided into four discrete regions: an inner core region (I), where the flow undergoes nearly solid-body rotation; an annular region in the vicinity of the radius of maximum tangential velocity (II) where the momentum effects are large relative to the viscous effects, and circulation increases logarithmically with radius (analogously to the logarithmic region of a turbulent boundary layer) independently of the wing loading parameter n; an outer core region (III), where the turbulent stresses decay proportionally to r^{-2}; and a roll-up region (IV) where the discrete turns of the turbulent vortex sheet have not yet merged into the homogenous vortex. Phillips presented a similarity solution to the turbulent Navier-Stokes equation expressed in terms of circulation,

$$\frac{1}{2\pi}\frac{\partial \Gamma}{\partial t} = \nu \frac{1}{2\pi r}\frac{\partial}{\partial r}\left[r^3 \frac{\partial}{\partial r}\left(\frac{\Gamma}{r^2}\right)\right] - \frac{1}{r}\frac{\partial}{\partial r}(r^2 \overline{v_r' v_\theta'}) \tag{3}$$

(where t is time, r is a radial co-ordinate, ν is the kinematic viscosity, and $v_r'v_\theta'$ is the cross-flow plane component of the Reynolds stress tensor) for each of the regions I, II and III, requiring the solutions to match at the interfaces between the regions. The limiting case of the laminar solution is used for the boundary and initial conditions. This solution required no restricting assumptions on the turbulent stresses, could be applied to wings with a variety of circulation distributions, and showed fairly good agreement with experimental results.

On the other hand, experimental investigations of the formation and early development of the tip vortex are more numerous. Francis and Katz (1988) conducted a flow-visualization study of the structure of the tip vortex in the near field ($0.48 < x/c < 1$) of a NACA 66 wing with a blunt tip at a chord Reynolds number Re_c ($= u_\infty c/\nu$, where u_∞ is the free-stream velocity, c is the airfoil chord, and ν is the fluid kinematic viscosity) = 0.1 to 5×10^6 and an angle of attack α up to 12°, and presented several empirical relationships describing the motion and growth of the vortex with both Re_c and α. A number of secondary vortex structures and shear layer eddies were observed to form and become entrained in the developing tip vortex.

Shekarriz *et al.* (1993) studied the tip vortex formed by a low-aspect ratio airfoil-like submarine sail at $0 < x/c < 6.7$ at $Re_c = 0.36 - 2.2 \times 10^5$ with $\alpha = 5°$ and $10°$ using the technique of particle-image velocimetry, and found that the tip vortex formed rapidly, attaining a maximum strength of 66% of the bound circulation (estimated from measurements of the lift coefficient) within one chord length of the trailing edge, after which it remained fairly constant up to nearly 7 chords downstream. Shekarriz *et al.* also observed significant secondary structures in the vortex, resulting in irregular fields of axial and tangential velocities in the cross-flow plane, and, because of the care taken in ensuring that no axial pressure gradient was present, concluded that the wake-like core axial velocities observed were most likely due to a momentum deficit resulting from the boundary layer of the wing being entrained into the tip vortex.

The nature of the axial or streamwise flow in the vicinity of the vortex core has been itself the subject of much study. Measurements of axial velocities have shown there to be in some cases an excess and in others a deficit of velocity relative to the free-stream, ranging from 50% to almost 180% of u_∞, depending on the specific parameters of the experiment. Some of the earliest work was done by Batchelor (1964), who presented a similarity solution of the Navier-Stokes equations for a laminar, viscous tip vortex far downstream of a lifting surface, and showed that the axial velocity is actually nonzero, as

$$v_\theta = v_{\theta\max}\left(1+\frac{0.5}{A_o}\right)\frac{r_c}{r}\left[1-e^{-Kr^2/r_c^2}\right] \tag{4}$$

$$u_a = u_c e^{-Kr^2/d^2} \tag{5}$$

(where v_θ is the tangential velocity, $v_{\theta max}$ is the maximum tangential velocity occurring at the core radius r_c, u_a is the axial velocity, u_c is the axial velocity at the vortex center, K = 1.25643 (Devenport *et. al. 1996*) and d is the radial scale of the axial profile). Batchelor also demonstrated that the radial pressure gradient balances the centrifugal force in the fluid, consequently the streamwise decrease in tangential velocities resulting from the viscous action results in a positive axial pressure gradient, decelerating the flow. Phillips and Graham (1984) experimentally studied the far-field interactions between axial and tangential velocities in a turbulent vortex by superimposing an axial jet or wake upon a vortex produced by a pair of wings in the absence of an axial pressure gradient at $Re_c = 7.4 \times 10^4$, with $45 < x/c < 109$ and $\alpha = 9°$. Results showed that an axial velocity excess or deficit at the vortex center increases the rate of turbulent diffusion of momentum by introducing additional turbulence into the vortex. Also, an axial velocity excess was shown to cause longitudinal stretching of the vortex, further increasing its rate of decay. When the jet flow rate was adjusted to yield a zero net momentum flux through the cross-flow plane, very little diffusion of the vortex was observed, suggesting that the axial velocities within the vortex core contribute significantly to the diffusion of vorticity in a turbulent trailing vortex. Anderson and Lawton (2003) showed that the vortex core axial velocities for a variety of wing tip geometries and loading conditions collapse onto one curve when normalized against circulation and vortex diameter, suggesting that the magnitude of the circulation rather than its distribution is the determining factor in producing core axial velocity excesses or deficits.

Green and Acosta (1991) studied the flow behind an elliptically-loaded NACA 66-209 wing with a rounded tip at $Re_c = 3 - 12 \times 10^5$, for $x/c = 2$ and 10, and $\alpha = 5°$ and 10° using nonintrusive, optical methods. The total circulation of the trailing vortices at the downstream planes was found to be within 3% of the bound circulation. Axial velocities were shown to be either in excess or deficit of u_∞, and near to the wing exhibited high-frequency fluctuations with a magnitude of up to $1.1u_\infty$ about a mean velocity excess of $1.62\ u_\infty$. The fluctuations decayed rapidly with distance downstream to a magnitude of about $0.18\ u_\infty$ about a mean of $1.12\ u_\infty$. The tangential velocity profiles only varied slightly with downstream distance, but fluctuations in tangential velocity decreased considerably. Green and Acosta observed two dominant frequencies within the spectral contents of the fluctuations which they measured; one higher-frequency component of large magnitude which was always present, and one low frequency component which occurred only under heavier loading conditions.

Broadband instabilities at normalized frequencies fc/u_∞ (where f is the frequency and c is the wing chord) of order 0.01 in wing-tip vortices have been commonly observed in experimental investigations (Westphal and Mehta (1989), McAlister and Takahashi

(1991), Rokhsaz *et al.* (2000)) and are often attributed to test facility free-stream turbulence or wind-tunnel wall interference effects. Devenport *et al.* (1996) conducted a detailed experimental investigation of a NACA 0012 wing with $4 < x/c < 30$ and $\alpha = 5°$ at $Re_c = 5.3 \times 10^5$ using a miniature four-sensor hot-wire probe, in which particular attention was given to the low-frequency spatial 'meandering' of the vortex. Since the meandering of the vortex line is random, the result would be to cause long time-averaged vorticity field measurements to approach a Gaussian distribution. By describing the instantaneous position of a given streamwise cross-section of a tip vortex using a probability density function and applying the results to Batchelor's analytical solution of the velocity profile as stated in Equations 4-5, Devenport *et al.* demonstrated that long time-averaged measurements lacking any correction for vortex meandering could result in errors in mean core radius and tangential velocity measurements as large as 64%; furthermore, the measured RMS values and those predicted by meandering alone corresponded to each other to within the measurement error, suggesting that the RMS values were dominated by the effects of meandering. A correction procedure was proposed to adjust the magnitudes of the measured mean and RMS velocities and vorticities to compensate for a Gaussian meandering by reconstructing the probability-density function and adjusting it to fit the measured data. The length scale of the vortex meandering, however, was shown to be very small, and the corrections for $r/c > 0.1$ were negligible. After applying the corrections described to their experimental results, Deventport *et. al.* reported a vortex core radius of 0.036 chords, a tangential velocity magnitude of 0.27 u_∞ and a core axial velocity of 0.84 u_∞. These corrected values were also shown to remain constant for $5 < x/c < 30$. Results showed that co-rotating secondary vortex structures within the developing tip vortex were rolled together with the main vortex, resulting in the formation of a stratified vortex core downstream. Furthermore, by normalizing the vortex turbulence data against wake measurements, the results collapsed for all cases, suggesting that the wake was the source of all the turbulence observed within the vortex rather than the vortex itself.

Chow *et al.* (1997) and Dacles-Mariani *et al.* (1995) compiled a large amount of detailed computational and experimental data around the tip and in the near-field region ($-1.14 < x/c < 0.68$) of a low aspect-ratio rectangular NACA 0012 wing with a rounded tip at $Re_c = 4.6 \times 10^6$ and $\alpha = 10°$. Experiments were carried out using a miniature seven-hole pressure probe and a triple-sensor hot-wire probe, and the flow fields were simulated using a 3-dimensional finite-difference Navier-Stokes solver and 1.5×10^6 grid points. Boundary conditions were taken from experimental measurements, and simulation results agreed with experiments to within 3%, suggesting a high level of confidence in the data. Core axial velocities and maximum tangential velocities were observed as high as 1.77 u_∞, and 1.0 u_∞, respectively, and peak RMS velocities were measured at 24%. The peak turbulence intensity in the vortex decreased significantly with increasing downstream distance as the turbulence contributed by the rolled-up wake was rapidly stabilized by the nearly solid-body rotation of the vortex core. Near the trailing edge, the peak turbulence intensity occurred in the vicinity of r_c, but shifted to a radius of approximately 1/3 r_c further downstream- an effect not attributable to vortex meandering, as the effects of meandering were experimentally determined to be negligible. Significantly, the measurements of the Reynolds stress fields showed that the turbulent stresses were not aligned with the mean strain rates, indicating that one of the conditions of application of standard isotropic eddy-viscosity turbulence models fails in the turbulent wing-tip vortex.

Ramaprian and Zheng (1997) studied the tip vortex generated by a NACA 0015 with a flat tip in the range of $0.16 < x/c < 3.33$, with $Re_c = 1.8 \times 10^5$ and $\alpha = 5°$ and $10°$, nonintrusively using three-component laser-doppler velocimetry with tracer particles injected directly into the tip vortex by means of holes in the tip of the wing. Axial velocities in this study were shown to be exclusively wake-like, with $u_{a,c} = 0.68\ u_\infty$ near the trailing edge, and then rapidly increasing to 0.74 u_∞ within one chord length. Cross-flow velocity fields were nearly axissymmetric at $x/c = 1$, and the maximum tangential velocity was to the order of 50% of u_∞. Peak values of axial velocity, tangential velocity and cross-flow vorticity remained fairly constant from $x/c = 1$ to $x/c = 3.33$. The vortices rapidly attained self-similarity, and Ramaprian and Zheng proposed an empirical third-order polynomial in r^2 to describe the radial distribution of circulation of the form

$$\frac{\Gamma}{\Gamma_c} = A_1\left(\frac{r}{r_c}\right)^2 + A_2\left(\frac{r}{r_c}\right)^4 + A_3\left(\frac{r}{r_c}\right)^6 \qquad 0 < \frac{r}{r_c} < 1.2 \qquad (6)$$

where A_1, A_2 and A_3 are constants.

Birch *et al.* (2003, 2004) measured the velocity and vorticity distributions of the tip vortex produced by a square-tipped NACA 0015 wing at $Re_c = 2.01 \times 10^5$ for $-0.5 < x/c < 2$ and $2° < \alpha < 18°$ using a miniature seven-hole pressure probe. For $x/c < 0$ (upstream of the trailing edge), the flow structure was dominated by the presence of secondary vortex structures which were subsequently rolled into the main vortex, which attained axissymmetry by $x/c = 0.5$. Between $x/c = 0.5$ and $x/c = 2$, the vortex strength and velocity distributions remained fairly constant, indicating that the rolling up of the wake was mostly complete a half-chord downstream of the trailing edge. Core axial velocities were observed to switch from being wake-like ($\approx 0.85\ u_\infty$ for $\alpha = 4°$) to jet-like ($\approx 1.15\ u_\infty$ for $\alpha = 14°$) as α increased, while the magnitudes of velocity excess or deficit decreased with distance downstream until axisymmetry was attained. Results also showed that the vortex diameter did not have a clear dependence on the wing loading. Regardless of α or x/c, the fully developed vortices were self-symmetric, and the circulation distributions agreed well with those arrived at analytically by Hoffman and Joubert (1963), namely,

$$\frac{\Gamma}{\Gamma_o} = A_i\left(\frac{r}{r_c}\right)^2 \qquad \frac{r}{r_c} < 0.4$$

$$\frac{\Gamma}{\Gamma_o} = A_o \log\left(\frac{r}{r_c}\right) + B_o \qquad 0.5 < \frac{r}{r_c} < 1.4 \tag{7}$$

where A_i, A_o and B_o are constants which, along with the inequalities describing the ranges of application, were determined experimentally. Results also agreed well with those of Ramaprian and Zheng (1997).

5.2 *Flow around a two-dimensional oscillating airfoil*

Two-dimensional airfoils undergoing sinusoidal oscillations in pitch have been the subject of a large number of experimental, computational and analytical studies. Particular attention has been given to the engineering prediction of performance characteristics, as well as to the characterization of the mechanisms of dynamic stall (associated with the abrupt loss of lift and increase in pitching moment experienced when the maximum angle of attack at exceeds α_{ss}, the static stall angle), because of their importance in determining both the rotorcraft flight envelopes and unsteady blade loads. Detailed reviews were provided by McCroskey (1982) and Carr (1987).

The nature of the flow around an oscillating airfoil can be classified into one of three basic categories, depending on the maximum amplitude of oscillation (McCroskey1982); these are illustrated in Figure 1. When the maximum instantaneous angle of attack of the wing is less than the static-stall angle, the flow remains attached to the wing throughout the cycle of oscillation. Dynamic boundary-layer improvement and time-lag effects result in a small amount of hysteresis in the load loops, with the instantaneous lift falling short of the static values during pitch up and exceeding the static values during pitch-down, for a given angle of attack. The boundary layer transition may occur within a laminar separation bubble, due to natural instabilities, or can be bypassed, depending on the flow parameters, oscillation parameters and the airfoil geometry. If the airfoil is oscillated beyond α_{ss}, a thin layer of flow reversal develops at the trailing edge and propagates upstream over the surface of the airfoil (points b-d in Figure 1), underneath the turbulent boundary layer. At the onset of dynamic stall, the flow separates from the airfoil, and the fluid in the leading edge region rolls into a leading-edge vortex (LEV) (point e) which subsequently grows and convects rapidly downstream over the suction surface of the airfoil (points f-g), resulting in a nonlinear increase in lift and negative pitching moment. If the maximum incidence only slightly exceeds α_{ss} (the light stall case), the LEV is fairly small and its influence on the airfoil pressure distributions is not significant. Dynamic stall occurs when the LEV convects beyond the trailing edge, resulting in an abrupt loss of lift. The strength of the LEV formed increases with the maximum instantaneous angle of attack, and in cases where the incidence greatly exceeds

α_{ss}, the low pressure associated with the LEV causes a dramatic increase in the maximum coefficient of lift C_{Lmax}, and as it convects over the suction surface, the pressure peak shifts toward the trailing edge, resulting in large negative pitching moments and negative aerodynamic damping of the airfoil section. Following dynamic stall, the flow remains separated until the beginning of the next upstroke, at which point the flow re-attaches from the leading edge.

Some early work on the nature and the mechanisms of dynamic stall were carried out by Johnson and Ham (1972), who studied a Joukowski airfoil both experimentally and analytically. As the airfoil was pitching up, boundary layer transition occurred in the vicinity of the leading edge by means of a laminar separation bubble; the laminar boundary layer separated near the leading edge, destabilized, and underwent transition to turbulence. The separated turbulent shear layer was then able to entrain sufficient momentum from the free-stream flow to overcome the adverse pressure gradient and re-attach to the surface as an attached turbulent boundary layer. Johnson and Ham concluded that the onset of dynamic stall was due to the bursting of the laminar separation bubble as the pressure gradient in the leading edge region became too adverse for the turbulent shear layer to re-attach. The authors were able to predict the stalling angle with reasonable accuracy by empirically incorporating the location of the transition point into the thin-airfoil equations. However, Johnson and Ham acknowledge that the flow fields are dominated by the LEV for very large angles (an inherently viscous phenomenon), and as such the inviscid thin-airfoil theory is not applicable.

A simple theoretical model of an oscillating airfoil was developed by McCroskey (1973), yielding the surface pressure distribution along the airfoil by additively combining the independent effects of thickness, camber and unsteady effects, and then neglecting higher order terms. This simplified, linear model yielded results which agreed reasonably well to both the nonlinear solution as well as to experiment, for small oscillations. McCroskey also presented an extension of his linear solution capable of predicting the dynamic stall angle, and compared the theoretically evaluated stall limits to the experimental results. The model reproduced the trends of the experimental data, but consistently underpredicted the dynamic stall angle. The author concluded that the dynamic stall overshoot was being influenced by unsteady viscous effects which could not be reproduced by the linearized model, and that as a result, the dynamic stall limits could not be evaluated based solely on the condition of the inviscid pressure gradients over the airfoil.

Martin *et al.* (1974) studied experimentally the mechanisms of dynamic stall on a NACA 0012 airfoil oscillating through the deep stall regime with $\alpha(t) = 15° + 14°\sin(\omega t)$, (where ω is the circular frequency, $= 2\pi f$, and f is the frequency of oscillation) and reduced frequencies κ ($= \pi fc/u_\infty$) of 0.05, 0.1 and 0.24 and Re_c ranging from 1 to 3×10^6. Results showed that the dynamic stall angle decreases with increasing Re_c, while the opposite trend was recorded previously for Re_c values an order of magnitude smaller, suggesting that the dynamic stall process is different in the two ranges of Re_c. Also, increasing κ resulted in an increase in the dynamic stall delay. The authors documented the existence of a short laminar separation bubble (less than 2% of the wing chord prior to stall) but the data was insufficient to conclude that stall was initiated by the bursting of the laminar separation bubble. However, a local surface velocity peak was observed in the leading edge region before the minimum pressure peak occurred at that location, suggesting that flow separation was initiated in the vicinity of the leading edge.

McCroskey and Philippe (1975) carried out a numerical and experimental investigation of a NACA 0012 airfoil (both with and without a leading edge modification) oscillating with mean angles between 0 and 15°, and with a peak-to-peak amplitude of 12°, with $5 \times 10^5 < Re_c < 2 \times 10^6$. In the numerical model, the location of the critical points were taken from McCroskey's linearized model (1973), and incorporated a turbulent boundary layer eddy-viscosity model, shown to be quasisteady in that the oscillation did not alter the physics of the turbulence (the authors noted, however, that at very large frequencies, both the eddy viscosity and kinetic energy models of turbulence tended to break down). The presence and effects of the laminar separation bubble were also incorporated into the numerical model. Experimental data was obtained from surface-mounted skin friction sensors and from hot-wire probes located near the airfoil surface. The numerical results agreed well with experiments in attached flow cases, but at larger angles of attack the numerical model did not reproduce well the effects of dynamic stall. Results of the model showed that the laminar boundary layer was negligibly affected by the dynamic effects (relative to the effects of the pressure gradient), but that the effect of the oscillation on the turbulent boundary layer was significant, and increased with the incidence. Also, according to the model developed, the laminar separation bubble did not burst prior to the onset of dynamic stall.

The role played by the laminar separation bubble in the mechanism of dynamic stall was further investigated by McCroskey, Carr and McAlister (1976), who used surface-mounted pressure transducers and skin friction gauges to measure the loads and detailed boundary layer characteristics of a NACA 0012 airfoil, oscillating such that $\alpha(t) = 15° + 10° \sin(\omega t)$ and $\kappa \leq 0.25$, at $Re_c = 2.5 \times 10^6$. For the typical case of $\kappa = 0.15$, results showed that the thin layer of flow reversal propagated upstream from the 90% chord location at $\alpha = 19°$ to the 30% chord location at $\alpha = 23.4°$ during the upstroke. The boundary layer thickened during this time, and developed eddies. At $\alpha = 23.4°$, the turbulent boundary layer abruptly broke down over the wing surface from the leading edge region to the 30% chord location. Since the laminar separation bubble never extended beyond the 0.7% chord location at the end of the upstroke, these results suggest that the bubble plays only a passive role in the dynamic stall process. Furthermore, by placing boundary layer trips over the geometric leading edge, the authors were able to cause the boundary layer to undergo transition without laminar separation. The trips promoted the breakdown of the turbulent boundary layer and caused the dynamic stall onset to become more irregular and difficult to define, but the overall characteristics of dynamic stall remained the same. Modified NACA 0012 airfoils, with reduced leading-edge radii, were also tested in order to evaluate the effects of elongated laminar separation bubbles on the dynamic stalling process and to determine if an elongated bubble would burst. In all cases tested, the dynamic stall process began with the breakdown of the boundary layer rather than bubble bursting, with the exception of one case in which a very long bubble was observed (extending up to to 5% of the wing chord, compared to 0.8% for the nominal NACA 0012). The authors also observed that the dynamic stall angle was a strong function of κ, as was the strength of the shed leading-edge vortex (and therefore the degree of load loop hysteresis). As κ increased, the dynamic effects stabilized the boundary layer, delaying separation. For the case of $\kappa = 0.25$, the flow remained attached until the end of the upstroke ($\alpha = 25°$) and the leading edge vortex began to form at the beginning of the downstroke (Figure 2).

McCroskey *et. al.* (1981) also investigated a number of other airfoil sections to evaluate the effects of overall airfoil geometry on the characteristics of dynamic stall. Models were fitted with surface-mounted pressure transducers and skin friction sensors, and were oscillated with $\alpha(t) = 10° + 10° \sin(\omega t)$, and $\kappa = 0.1$. Models were tested at a free-stream Mach number of 0.3 at standard atmospheric pressure, corresponding to $Re_c = 4.2 \times 10^6$. Results showed that the geometry affects the nature of the onset of stall and the chordwise progression of boundary layer separation, as can κ. The differences in the perfomance characteristics of the airfoil sections were significant when the maximum incidence was small and boundary layer effects dominated. However, as the maximum incidence increased, the large leading edge vortex shed by each of the sections began to dominate the flow and the differences that resulted from the earlier behaviour of the boundary layer were small.

Francis and Keese (1985) measured the surface pressure distributions around a NACA 0012 pitching at constant rate about an axis passing through the 31.7% chord location, with $7.7 \times 10^4 < Re_c < 1.7 \times 10^5$. Since the stalling mechanism for a pitching airfoil is similar to that of an oscillating airfoil, the results can be qualitatively applied. The authors showed that for large enough pitch rates, separation was delayed to incidences as high as 60° and lift was nearly tripled, demonstrating that the boundary layer improvement effects are a strong function of the surface velocity. Also, the study showed that as the pitch rate increased above a certain limit, further incremental increases result in only marginal increases in overshoot.

Using a combination of analytical and empirical treatments, Ericsson and Reding (1988) developed a theoretical model of the oscillating airfoil which was capable of predicting the dynamic performance characteristics of the airfoil through the light and deep stall regimes, given only the static data and the flow and oscillation parameters. The model divided the unsteady flow fields into a number of discrete quasi-steady and transient phenomena, and the individual contributions of each toward the time-dependant airfoil loads were evaluated. A reasonable approximation of the unsteady airfoil performance characteristics could then be computed by summing together these contributions. The important factors considered included (i) time-lag effects, which resulted from the finite time required for the airfoil to respond to changes in the flow field; (ii) accelerated flow effects, caused by the lag in the pressure gradient, and (iii) moving wall effects, which accounted for the delay of flow separation resulting from the unsteady boundary condition on the airfoil surface. Furthermore, the transient effects encountered after the onset of dynamic stall were modeled, including the moving separation point and suction peak generated by the passage of the leading edge vortex. The results of these predictive techniques were compared to a number of different published data, and agreed well. The authors later supplemented this study with an extension of their analysis into the full-scale, compressible flow regime (Ericsson and Reding 1988 b). The additional effects of the Mach and Reynolds numbers were shown to be significant, but once these effects were incorporated into the model, it was able to predict with reasonable accuracy both the stall flutter boundaries and shock-induced stall measured experimentally.

Panda and Zaman (1994) used a cross-wire probe to measure the flow fields behind a NACA 0012 airfoil oscillating such that $\alpha(t) = 15° + 10° \sin(\omega t)$, with $0.2 < \kappa < 1.6$ and $Re_c = 2.2 \times 10^4$ and 4.4×10^4. The authors observed a large trailing-edge vortex in addition to the leading-edge vortex, which formed as the leading-edge vortex was shed. The vorticity fields were computed from the velocity measurements, and the phase-locked circulatory component of lift (related to the bound vorticity) was then estimated based on the vorticity flux through a control volume containing the airfoil. The noncirculatory component of lift, related to the motion of the airfoil, was evaluated analytically and was shown to be small for low values of κ. The results were compared to force balance measurements and agreed well for small κ, but the linear decomposition of lift into circulatory and noncirculatory components was no longer possible as κ increased. The increase in the load loop hysteresis with increasing κ was attributed to the phase lag in the formation and shedding of the leading-edge vortex.

The flow field around a pitching NACA 0012 airfoil with $Re_c = 10^4$ and a free-stream Mach number $M_\infty = 0.2$ was numerically simulated to the second order by Choudhuri *et. al.* (1994). The laminar, compressible Navier-Stokes equations were solved using both a structured and an unstructured grid technique, and the results obtained from the two different computational methods agreed well with each other. The authors observed that the leading-edge vortex emerged as a result of the formation of two critical points (a rotation center and a saddle point) in the leading edge region. A counter-rotating secondary vortex and a co-rotating tertiary vortex were then formed, and the separation of the boundary layer and shedding of the leading-edge vortex was attributed to the interaction between the primary vortex with the secondary and tertiary structures.

Oshima and Ramaprian (1997) obtained the instantaneous flow fields around a pitching NACA 0015 airfoil with $Re_c = 5.4 \times 10^4$ and 1.5×10^5 using the technique of particle-image velocimetry, and compared the results to previous surface pressure measurements as well as to previously published numerical results. At the onset of dynamic stall, the shear layer over the wing destabilized and rolled into a number of discrete vortices. The leading-edge vortex was observed to be formed by the rolling up of the vorticity present in the shear layer upstream of the midchord, whereas the vorticity present from the midchord to the trailing edge was observed to roll into a separate shear layer vortex. The trailing edge flow reversal was also detected prior to the onset of dynamic stall, but the high level of freestream turbulence prevented the formation of the laminar separation bubble, thus altering the transition mechanism and precluding any conclusions regarding the processes involved in the onset of dynamic stall.

Lee and Basu (1998) used a closely-spaced array of surface-mounded thin-film sensors mounted on a NACA 0012 airfoil oscillating with $\alpha(t) = 0° + 7.5° \sin(\omega t)$ and $\alpha(t) = 7.5° + 7° \sin(\omega t)$, and with $\kappa = 0.053$ and 0.09, to observe the temporal and spatial progression of the critical boundary layer points (leading edge stagnation, laminar separation, turbulent re-attachment, transition , flow reversal), as well as the formation and shedding of the leading-edge vortex. The results were qualitatively validated using flow visualization techniques. The authors showed that laminar separation and transition were delayed during pitch-up and promoted during pitch-down, and that as a consequence of the dynamic effects, the boundary layer remained attached at angles of attack larger than α_{ss}. The authors also found that the dynamic stall process originated with the abrupt breakdown of the turbulent boundary layer rather than with the bursting of the laminar separation bubble.

Akbari and Price (2003) numerically simulated the laminar flow around a NACA 0012 airfoil oscillating such that, primarily, $\alpha(t) = 15° + 10° \sin(\omega t)$ with $Re_c = 1.0 \times 10^4$ and $0.15 < \kappa < 0.5$. The results showed a delay of stall and an increase in the airfoil loads relative to the static case. A primary leading-edge vortex was observed to form and shed, which may have been followed by one or more secondary vortices, depending on the oscillation and flow parameters. Increasing κ had the effect of delaying dynamic stall and increasing the maximum lift, as well as decreasing the negative moment damping. Both the Reynolds number and the chordwise location of the axis of oscillation were found to have only a minor effect on the load loops and dynamic stall angle.

Lee and Gerontakos (2004) continued the earlier study of Lee and Basu (1998) by supplementing the thin-film sensor measurements with both surface pressure measurements and hot-wire scans of the airfoil wake, and by increasing the maximum incidences well into the deep stall regime. These measurements were carried out using at $Re_c = 1.35 \times 10^5$ and $0.0125 < \kappa < 0.3$. For smaller incidences (within the static stall limit), the authors observed little hysteresis in the load loops. A laminar boundary layer was detected at low incidences, and at larger incidences (though still within the static stall limit) a shorter laminar separation bubble formed relative to the static case. The lift-vs.-incidence slope was slightly larger relative to the static case, and the lag in the motion of the boundary layer critical points was slightly increased with increasing κ. For the case of deep stall oscillations, with $\alpha(t) = 10° + 15° \sin(\omega t)$ and $\kappa = 0.1$, the trailing-edge flow reversal was first observed at $\alpha = 12.9°$ on the upstroke, and progressed to the 26% chord location at $\alpha = 21.6°$. The laminar separation bubble was observed to span from 3.4% to 9.5% of the chord during this range of motion. When $\alpha = 21.8°$, the boundary layer broke down catastrophically. The breakdown of the turbulent boundary layer disrupted the laminar separation bubble, resulting in the initiation of the roll-up of the leading-edge vortex, which grew and convected over the airfoil for $21.8° < \alpha < 24.7°$ on the upstroke, and after $\alpha = 24.7°$ (the incidence of maximum lift), the lift decreased dramatically and the flow progressed to a fully separated state. A secondary vortex was observed to form following the shedding of the leading edge vortex for values of κ larger than 0.1. The boundary layer remained fully separated until 14.1° on the downstroke, and reattachment progressed from the leading edge to the trailing edge from 14.1° to 1.1°.

5.3 *Oscillating wing tip vortex*

Unlike the large volume of work already done on the subject of both the static wing tip vortex and the oscillating two-dimensional airfoil, very few studies have been published in which the tip vortex generated by an oscillating finite wing was investigated. Because of its complex, three-dimensional, unsteady and possibly transient nature, the oscillating wing-tip vortex is equally challenging to simulate as it is to measure experimentally.

Freymuth *et. al.* (1986) carried out an early flow-visualization study of the tip vortex generated by a NACA 0015 wing in an accelerating flow with incidences up to 60° and a Reynolds number based on rate of acceleration $R = \rho(du/dt)^{1/2}c^{3/2}/\mu = 5200$. The results identified the complex nature of the unsteady tip vortex, and its interaction with the leading edge vortices formed.

Ramaprian and Zheng (1998) made extensive phase-locked measurements of a NACA 0015 wing with an aspect ratio of 2, oscillated such that $\alpha(t) = 10° + 5° \sin(\omega t)$ with $Re_c = 1.8 \times 10^5$ and $\kappa = 0.1$, using a laser-doppler velocimetry system capable of resolving the three components of velocity. Measurements were made in cross-flow planes situated in the range $0.16 < x/c < 2.66$. The vortex was observed to be more agitated and disorganized during the pitch-down phase of the motion as a result of the entrainment of the separated turbulent boundary layer from the suction side of the wing, causing the flow fields to exhibit significant hysteresis during a cycle of oscillation. At a typical streamwise location, the core axial velocities were generally observed to be wake-like in character with a minimum value at the vortex center of between 0.65 u_∞ and 0.76 u_∞. During the pitch-down phase of the motion, however, the axial velocity exceeded the free-stream values by 17%. Tangential velocities were observed to attain a maximum of 0.56 u_∞ and 0.70 u_∞ during pitch up and pitch down, respectively. Nondimensional axial vorticity (= $\zeta c/u_\infty$, where ζ is the clockwise vorticity) was observed to range from 10 to 36, and was generally greater during the pitch-down phase of motion. The circulation of the vortex was found to vary significantly during a cycle of motion, and was generally larger during pitch-down than during pitch-up for a given instantaneous angle of attack. Through most of the oscillation cycle, the inner regions of the unsteady tip vortices exhibited the same universal self-similar structure as the measured static tip vortices and the analytical result of Hoffman and Joubert shown in Equation 7. The vortex trajectory as a function of phase and of streamwise location was also documented. Spatial excursions as a result of the wing oscillation were significant in the transverse direction, but the spanwise location of the vortex center remained nearly stationary. Both the time-mean transverse and spanwise positions of the vortex center coincided fairly closely to the location of the static tip vortex in the near field, given by

$$\frac{y_c}{\lambda} = 0.09\left(\frac{x+1}{\lambda}\right)^{0.5} \qquad \text{for } 1 \le (x+1)/\lambda \le 10$$

$$\frac{z_c}{\lambda} = 0.09\left(\frac{x+1}{\lambda}\right)^{0.75} \qquad \text{for } 1 \le (x+1)/\lambda \le 10 \qquad (8)$$

where y_c is the transverse location of the vortex center, z_c is the spanwise location of the vortex center, x is the streamwise distance from the trailing edge, and λ is the length-scale of the vortex, defined by the authors as $(c/2)C_{L,3D}$.

Chang and Park (2000) used a triple hot-film probe to measure the phase-locked velocity fields behind a NACA 0012 wing with an aspect ratio of 4, oscillated such that $\alpha(t) = 15° + 15° \sin(\omega t)$, with $Re_c = 3.4 \times 10^5$ and $\kappa = 0.09$. Measurement planes were located at $x/c = 0.5$ and 1.5. A much steeper spatial velocity gradient was observed during the pitch-up phase of the motion relative to the pitch-down phase, indicative of the massive flow separation which occurred during pitch-down. A wake-like vortex core was observed throughout the oscillation cycle, which was attributed by the authors to the low Reynolds number. Peak tangential velocities were approximately 0.35 u_∞ and 0.45 u_∞ during pitch-up and pitch-down, respectively. The vortex strength exhibited the hysteresis characteristic of dynamic stall, but the magnitude of the abrupt decrease in tip vortex strength at the end of the pitch-up phase was small relative to the catastrophic loss of lift associated with dynamic stall for large amplitude pitch oscillations.

5.4 Unsteady tip vortex flow control

Because of their practical value in rotorcraft applications, a number of techniques to control the leading-edge vortex or the blade-tip vortex and mitigate or delay their adverse effects have been developed and documented. the use of passive stall control techniques, such as fixed flaps, blade twist or spoilers, cannot be modulated with the changing conditions of flight or blade azimuthal angle, resulting in a performance penalty. Active control techniques, including actuated control surfaces, variable geometry airfoil sections and mass removal or injection, often involve complex electromechanical systems to be installed in the constrained space and highly stressed environment of the rotor blade. A review of stall control techniques is provided by Lorber *et. al.* (2000).

The tip vortex generated by a rotor was studied numerically by Liu *et. al.* (2001), who compared the effectiveness of momentum injection to that of passive trailing-edge spoilers at diffusing the tip vortex. The spoilers modeled were short span elements fixed normal to the chord at the trailing edge, approximately spanning from the 85% to 95% radius locations. Momentum injection was achieved by means of tangential jets located in the trailing edge region, on the suction side of the wing. Jets located on the pressure side of the wing were also tested, but were shown to be only marginally effective. Both the spoiler and the momentum injection reduced the peak tangential velocity in the blade tip vortex by as much as 70%, but the momentum injection resulted in a significantly lower increase in blade drag and power requirements relative to the uncontrolled case.

Han and Leishman (2004) studied the tip vortex produced by a rotor blade model fitted with ducts passively channeling high pressure fluid from the vicinity of the leading-edge stagnation point to the blade tip in order to introduce high-energy, turbulent fluid into the laminar core of the developing tip vortex. The blade model was a rectangular NACA 2415 with a semiaspect ratio of 9.1. The rotor was operated in hover with a constant collective pitch of 4° and tip Mach and Reynolds numbers of 0.26 and 2.72×10^5, respectively. The technique of laser-Doppler velocimetry was used to measure the flow fields behind the rotating blade, together with flow visualization images. The results showed that the turbulent jets diffused the tip vortex, reducing the peak tangential velocities by as much as 60%, while increasing the rotor power requirements by 3%.

A number of studies have shown that the oscillating loads on a rotor blade can be effectively reduced using short-span control surfaces, or even entire blades, with actively controllable deflection angle time-histories (Chopra and McCloud, 1983; Hammond, 1983; Shaw *et. al.*, 1989). In general, the use of short-span control surfaces is preferable to active pitch control at the blade root, as the control surface generates a lower power penalty and is independent of the primary flight controls (Viswamurthy and Ganguli, 2004).

Viswamurthy and Ganguli (2004) studied the effects of multiple trailing-edge flaps upon the vibration of a rotating blade using a numerical model with a coupled blade aerodynamic and elastic response. The flaps were located outboard of the 80%-span station, and occupied 20% of the blade chord. Configurations of one, two, three and four independently actuated flaps were tested, and the deflection time-histories were selected to minimize the amplitude of the periodic component of the elastic deformation of the blade. Viswamurthy and Ganguli showed that while single-flap and multiple-flap configurations were similarly effective at reducing the deformation of the blades (yielding a maximum 72% reduction in blade deflection amplitude), multiple flap configurations required lower deflection angles to achieve the same effectiveness, and thus required less control input power and resulted in lower torque penalties. Furthermore, the authors showed that a lesser degree of vibration reduction (though still significant) could be achieved with much lower flap deflection amplitudes by simultaneously minimizing both required actuator power and vibration loading, and that even minimal control surface deflection resulted in reduced blade loads.

Spencer *et. al.* (2002) experimentally developed and tested a method of reducing the unsteady loads experienced by a rotating blade using a neurocontroller. Both an actuated 4.6%-radius trailing-edge flap located near the blade tip and an actuated, 10%-radius variable-twist blade tip were tested. Blade loads were recorded using strain gauges, and displacement transducers were used to record actuator deflection angles. The adaptive control system was capable of learning the blade response to control input and determining an optimal deflection time-history to reduce the amplitude of blade vibration. The system was able to reduce the vibratory loads by 73% using the trailing-edge flaps and by 98% using the variable-twist blade tip. However, while the neurocontroller was highly effective at attenuating the blade vibration for a variety of flight conditions, the interaction between the blades and the fluid, and the mechanism by which the loads were reduced, was not investigated.

For the case of a rigid wing model, oscillatory control surface input can also be used to destabilize a tip vortex. Haverkamp *et. al.* (2005) studied the effect of actuated outboard flaps upon the far-field development of the tip vortex flow structures generated by a static wing using three-component particle-image velocimetry. The model tested was a NACA 0012 rectangular wing with a chord of 5.3 cm and an aspect ratio of 7, towed through water with a constant incidence at $Re_c = 50\,000$. Flaps of various span ratios, chord ratios and geometries were tested. Results showed that flaps oscillated at specific frequencies tended to excite the instabilities in the trailing vortex system and lead to an accelerated breakdown of the vortex. The particular frequencies to which the vortex was most susceptible were determined by exhaustive testing. While the focus of this study was on the far-field reduction of induced rolling moments, a significant reduction in vortex strength was observed as near as one span downstream of the wing.

While it has been shown that the magnitude of the oscillating loads on a rotor blade can be effectively reduced using actuated surfaces with controllable deflection time-histories, the effect of these methods of control upon the formation, development and convection of the tip vortex and its subsequent impingement upon the following blade is still not well understood.

To summarize, a number of previous studies have shown that an airfoil undergoing oscillations in pitch will generate complex, time-dependant flow fields resulting in significant hysteresis in the dynamic loads experienced by the wing, relative to the static case. Yet, despite its importance to rotary-wing aircraft applications, the nature and development of the tip vortex produced by an oscillating wing are still not well understood. The purpose of the present study is to develop the more thorough characterization of the unsteady tip vortex necessary in order to implement a system of active unsteady tip vortex control.

6 Experimental procedure

6.1 *Flow facilities*

Quantitative flow measurement experiments were carried out in the J. A. Bombardier wind tunnel located in the Experimental Aerodynamics Laboratory of the McGill University Department of Mechanical Engineering (Figure 3). The flow facility is powered by a vibration-isolated, 2.5 m diameter,16-blade fan driven by a computer-controlled, variable-speed AC motor and equipped with an acoustic silencer. The test section measures $1.2 \times 0.9 \times 2.7$ m in the z, y and x directions, respectively, and is isolated from the downstream fan by a 9 m long diffuser section. The upstream flow is conditioned by a 3 m contraction section with a contraction ratio of approximately 10:1, as well as a 10 mm honeycomb and a series of 2 mm vorticity screens. The free-stream flow in the test section has a turbulence intensity of less than 0.08% at 35 m/s. Wing models were mounted horizontally from the side wall of the test section such that the wing tip was on the tunnel centerline.

Inside the test section, flow measurement probes were mounted on a computer-controlled, five degree-of-freedom traverse which was actuated by the data acquisition system, enabling full automation of the scanning process. The spatial resolution of the traverse was 20 μm in each of the x, y and z axes, and the total test section blockage from the traverse was approximately 4%. For load measurements, a force balance was mounted on a turntable, and the assembly was installed in the floor of the test section. The force balance sensor plate was supported by cantilever-type springs with the maximum deflection limited to 2 mm; deflections along each axis were measured independently using linear variable distance transformer (LVDT) displacement transducers with a resolution of 88 and 48 Newtons per Volt in the axes normal and parallel to the wing chord, respectively. The force balance response was linear to within 0.2% in the range of calibration used.

6.2 *The seven-hole pressure probe*

The seven-hole pressure probe system was used for measuring the time-average velocity vectors at the location of the probe tip, and consisted of three basic components: the probe sting assembly, the transducer array, and the signal conditioner unit.

The probe sting assembly was manufactured and assembled in the Experimental Aerodynamics Laboratory of McGill University's Department of Mechanical Engineering. The probe tip is approximately 2.8 mm in diameter, has seven 0.5-mm diameter holes drilled in close-packed configuration along its axis, and was precision-ground to a 30° cone angle at the tip. The probe shaft is 130 mm long and is fixed to the end of a 400 mm long, 12 mm diameter sting (Figure 4). The pressure taps in the probe tip are connected to the transducer array by means of 1.6 mm-diameter flexible tubing which is threaded through the probe sting.

The pressure transducer array is a series of seven Honeywell DRAL 501-DN differential pressure transducers with a full-scale range of 50 mm water head, fixed to a rigid sub-frame which ensured that all the transducer membranes were kept in the same plane. Care was taken to minimize the length of flexible tubing used in connecting the probe tip and the transducers. The transducer array was secured to the traversing mechanism downstream of the probe sting, behind an aerodynamic fairing. The common reference pressure for all of the transducers was the ambient atmospheric pressure measured from inside a damping unit.

The transducer array signal conditioner unit is a custom-built, seven-channel analogue signal differential amplifier that uses an external DC offset, and provides a fixed gain of 5:1. The total output sensitivity of the seven-hole pressure probe system is approximately 28 mV/Pa on all channels. No analogue filtering was required, because the flow fields measured with the seven-hole probe were always steady and because the length of tubing connecting the probe tip to the pressure transducers was sufficiently long to provide hydraulic damping of frequencies greater than approximately 5 Hz. The output from the signal conditioner unit was routed simultaneously to the data acquisition system and to an oscilloscope for monitoring. The probe was calibrated *in situ,* using the techniques of Wenger and Devenport (1999) and Treaster and Yocum (1979), and is described in detail in Appendix A.

6.3 *The triple-sensor hot-wire probe*

A triple-sensor hot-wire probe was used for measuring the three components of velocity as a function of time, allowing measurement of transient flow phenomena as well as the accurate determination of all of the Reynolds stresses. The triple wire system consisted of three major components: the probe and sting assembly, the constant-temperature anemometer (CTA) bridge unit and the signal conditioning unit. The probe used was the Auspex model AVEP-3-102 (Figure 5), which has an array of three hot-wire sensors with no common prong, oriented with a cone angle of 45° and roll angles of 0°, 120° and 240° relative to the axis of the sting. The sensors were 5 μm diameter nickel-chromium wires which were resistance-welded onto the probe prongs. The sensor wires were 0.7 mm long and occupied a measurement volume of about 3 mm^3. To verify the effects of probe interference, a typical static tip vortex flow field was measured using both the triple-sensor hot-wire probe and the much smaller and less intrusive seven-hole pressure probe. The fields agreed to within the experimental error, indicating that the triple-sensor hot-wire probe interfered with the flow to a similarly small degree.

The probe assembly was bonded to a 10 mm diameter hollow sting, through which the sensor leads were threaded. The sting terminated on the downstream end in a custom-machined miniature junction box which was fitted with three isolated, signal-grade gold-plated female BNC connectors (Amphenol model 31-10). The junction box was also designed to mechanically mate with the universal sensor mounting bracket on the traversing mechanism to ensure precise, repeatable positioning. The cables connecting the sting junction box and the CTA bridge unit were Pomona model 2249-Y-144, high-conductance BNC signal cables. Because of the length of the cables and the low levels of the sensor outputs, standard grade BNC cables were found to result in an unacceptably low signal-to-noise ratio.

The three CTA channels used were DANTEC model 56C17 anemometer bridges. Because the sensors themselves could not be separated from the sensor leads or the junction box, the bridges circuits could not be used to determine the sensor wire resistances, required to properly set the wire heating current. Instead, the resistance of the sensor wires were calculated based on resistance measurements taken of the sensor prongs, leads and connectors together before and after the sensor wires were installed. The signal conditioning unit is a custom-built, variable-gain analogue signal difference amplifier with a variable internal reference source, in series with a low-pass RC filter circuit with a filter frequency of 1 kHz. The sensor was calibrated *in situ,* using a high-efficiency technique and second-order interpolation; the probe calibration is described in detail in Appendix B.

6.4 *Data acquisition and reduction*

Data was collected using an 8-channel, 16-bit ComputerBoards model CIO-DAS1402/16 integrated data acquisition system driven by a Pentium II PC. For seven-hole probe measurements taken of the static wing tip vortex, the seven pressures were independently sampled at 300 Hz for 10 seconds. Since the pressure transducer calibration curves were linear to within less than 1%, only the mean voltages were recorded and later converted into velocities. For triple-sensor hot-wire probe measurements of the unsteady tip vortices, the anemometer bridge outputs were sampled simultaneously for 10 seconds at 500 Hz, together with a reference signal proportional to the wing incidence. Some longer scans were conducted to validate convergence, though higher sampling rates and longer sample times were precluded by the data storage capacity (each triple-sensor hot-wire scan generated up to 4×10^7 data points). For both the seven-hole pressure probe and the triple-sensor hot-wire probe, measurement grids consisted of a square array of measuring points with a spacing $\Delta y = \Delta z = 3.2$ mm. The size of the scan grid was adjusted depending on the size and motion of the vortex structures observed. A schematic of the instrumentation used is shown in Figure 6 (a).

The cross-flow vorticity was calculated from the filtered velocity measurements using centered finite-differences, so that

$$\zeta_{i,j} = -\left(\frac{\partial v}{\partial z} - \frac{\partial w}{\partial y}\right) \approx -\left(\frac{v_{j+1} - v_{j-1}}{2\Delta z} - \frac{w_{i+1} - w_{i-1}}{2\Delta y}\right) \tag{9}$$

where $i = 2, 3, ..., n$-1 and $j = 2, 3, ..., m$-1 and n and m are the number of measurement points in the spanwise and transverse directions. Forward and rearward biased finite-differences were used on the edges of the measurement grid, when $i = 1$ and n, and when $j = 1$ and m. The vortex total and core circulation were calculated by numerically applying Stokes' theorem, as

$$\Gamma_o = \sum\sum \zeta_{i,j} \times \Delta z \Delta y \qquad \Gamma_o(r_{i,j} + \Delta r) < 0.98 \times \Gamma_o(r_{i,j})$$

$$\Gamma_c = \sum\sum \zeta_{i,j} \times \Delta z \Delta y \qquad r_{i,j} < r_c$$

with

$$r_{i,j} = \sqrt{(z_j - z_c)^2 + (y_i - y_c)^2} \tag{10}$$

where the origin of the polar co-ordinate system is located on the vortex center, at (z_c, y_c), and the vortex core radius r_c is defined as the radius at which v_θ is maximum. Data fields were resampled at $\Delta y = \Delta z = 0.8$ mm using second-order interpolation for the purposes of calculating the circulation.

The induced drag of the wing was calculated from the cross-flow velocity measurements of the tip vortex using the method of Kuzunose (1997, 1998), as well as from the vorticity fields using the method of Maskell (1973). The induced drag calculations of Kuzunose and Maskell are based on the requirement that the drag on a wind tunnel model be equal to the streamwise component of the reaction force of the model upon a control volume containing the model. The control volume is bounded upstream by a plane S_∞ subjected only to the uniform free-stream flow, and downstream by the cross-flow measurement plane S, such that the only mass flux is through the surfaces S_∞ and S. The conservation of momentum then requires that the total drag on the model be

$$D = \iint_{S_\infty} \left(P_\infty + \rho_\infty u_\infty^2\right) dydz - \iint_{S} \left(P + \rho u^2\right) dydz \tag{11}$$

Since continuity requires that the mass flow through S_∞ and S be identical, Equation 11 can be re-expressed as

$$D = \iint_{S} \left[\rho u\left(u_\infty - u\right) + \left(P_\infty - P\right)\right] dydz \tag{12}$$

where the flow has been assumed incompressible. The combination of the integrals is possible since the projected area of S_∞ and S in the y-z plane can be identical. By assuming that the streamwise velocity gradients are small, Kuzunose solved for the induced drag as

$$D_i = \iint_{S_2} \frac{\rho_\infty}{2} \left(v^2 + w^2\right) dydz \tag{13}$$

which is a measure of the kinetic energy associated with the mean cross-flow velocity field, and is easily evaluated. In the near field of a wing tip vortex, however, the assumption that the streamwise gradients are small may not be valid. Maskell decomposed the cross-flow velocity vectors within S into a stream function $\psi(y,z)$ and a velocity potential function $\phi(y,z)$, implicitly defined by the relationships

$$v = \frac{\partial \psi}{\partial z} + \frac{\partial \phi}{\partial y} \tag{14}$$

$$w = -\frac{\partial \psi}{\partial y} + \frac{\partial \phi}{\partial z} \tag{15}$$

so that continuity is identically satisfied. The boundary condition that ψ and ϕ both be zero on the edges of the measurement surface is further imposed. A streamwise term σ, behaving as a source in the cross-flow plane, is defined such that

$$\sigma \equiv -\frac{\partial u}{\partial x} = \frac{\partial v}{\partial y} + \frac{\partial w}{\partial z} \tag{16}$$

as required by continuity. Maskell then obtained

$$D_i = \frac{\rho}{2} \iint_{S_\zeta} \psi \zeta \, dydz - \frac{\rho}{2} \iint_S \phi \sigma \, dydz \tag{17}$$

where ζ is the vorticity and the surface S_ζ is the region within S where the vorticity is nonzero. Unlike the Kuzunose calculation, this result is independent of the streamwise gradients. It can be shown analytically that for cases where the streamwise gradients vanish, the Maskell solution for induced drag identically equals the Kuzunose solution (Giles 1999).

The implicitly defined, coupled functions ψ and ϕ were determined from the experimental data by converting Equations 15 and 16 into centered finite-differences,

$$v_{i,j} = \frac{\psi_{i,j+1} - \psi_{i,j-1}}{2\Delta z} + \frac{\phi_{i+1,j} - \phi_{i-1,j}}{2\Delta y} \tag{18}$$

$$w_{i,j} = \frac{-\psi_{i+1,j} + \psi_{i-1,j}}{2\Delta y} + \frac{\phi_{i,j+1} - \phi_{i,j-1}}{2\Delta z} \tag{19}$$

Together with the boundary conditions specified, determining the values of ψ and ϕ at each of the $n \times m$ measurement points reduces to solving a linear system of equations of order $n^2 \times m^2$. Though more accurate than the Kuzunose method, the Maskell method is substantially more computationally intensive.

6.5 *Wing models*

The time-domain wing tip vortex flowfield measurements were taken behind a rectangular, square-tipped NACA 0015 wing with no twist, with a chord c of 20.3 cm and a semispan b of 49.5 cm, corresponding to an aspect ratio of 2.4. The model was CNC-machined from a solid block of aluminum, and then polished. Dimensional tolerances on the model were 500 μm in span, and 250 μm in both the chord and thickness. The trailing edge thickness was 1 mm. The model was equipped with a 25% c trailing-edge tab which spanned from the 87%-span location to the tip. Special care was taken to minimize the distortion of the airfoil profile by the presence of the tab and hinge, and the gap between the tab and the main body of the wing was less than 25 μm. The tab was actuated by means of a Futaba model S-3003 servomotor located at the wing root and driven by a custom-built controller which could actuate the tab in response to a signal in phase with the wing oscillation (Figure 6a). In addition, the wing model could be fitted with passive trailing-edge spoilers with a height h of 2.3% of the wing chord, over the same spanwise range as the tab on either the pressure or the suction side of the wing. A series of 2 mm-diameter holes were drilled into the wing suction and pressure surfaces 38% from the leading edge in the tip region at a 30° inclination from the wing tangent, in order to allow the injection of smoke into the tip vortex formation region for qualitative flow visualization purposes. Smoke was injected from a port located at the wing root, and the smoke pressure could be adjusted in order to minimize mass injection. When not in use, the smoke injection holes were blocked and carefully smoothed over. The wing was mounted on a steel shaft through its quarter-chord axis and held in the wind tunnel by a bearing mounted in a support which was rounded to minimize interference. An aluminum endplate 45 cm in diameter and 3 mm thick was installed at the wing root to isolate the wing from any disturbances emanating from the support or tunnel wall (Figure 6b)

The wing was oscillated by means of a four-bar mechanism mounted on the exterior of the wind tunnel. The mechanism allowed continuous adjustment of the wing mean incidence, and could provide a range of oscillation amplitudes from 6° to 14° in increments of 2°. The four-bar mechanism provided an output which was sinusoidal to within 2% (Figure 6c), and was powered by an Exlar model DXM340C servomotor driven by an Emerson model FX316/PCM1 programmable motion controller. The time-dependent incidence angle of the wing was recorded as a phase reference, and was monitored using a potentiometer mounted on the wing shaft. A custom-built analogue signal conditioner with a gain of 20 and a low-pass RC filter frequency of 0.1 kHz was used to ensure that the potentiometer signal was smooth and continuous, and resulted in an absolute phase error of less than 0.5%. The frequency of oscillation was monitored in real-time using a Hewlett-Packard model 3582A spectral analyzer, and was constant to within 0.01 Hz.

Dynamic lift and drag information for the two-dimensional airfoil sections were obtained using a second wing model. A rectangular, square-tipped NACA 0015 wing with no twist, with a chord of 25 cm and a span of 37 cm (corresponding to an aspect ratio of 1.5) could be mounted in the same oscillation mechanism as the model previously described. This larger model was fitted with 50 pressure taps located along the mid-span of both the pressure and suction sides, and had a 25% chord, full-span trailing edge flap which could be actuated using the same custom-built controller. The model was mounted between two end plates 35 cm in diameter and 3 mm thick. Pressure signals were recorded using a Honeywell DRAL 501 DN differential pressure transducer (with a range of 50 mm of water head) connected to the pressure taps via a ScaniValve solenoid switching valve. The length of tubing between the transducer and the pressure taps was minimized in order to maximize the frequency response of the system, as the compressibility effects within the 1.5 mm-diameter tubes had a damping effect on the measurements. The dynamic response of the pressure measurements was tested using the method described by Lee and Gerontakos (2004) and Lee and Basu (1998), and the time lag effects were negligible for frequencies of less than 3 Hz.

6.6 Experimental uncertainty

The maximum experimental uncertainty has been approximated as follows: mean velocity, 3.5%; velocity fluctuation, 3%; streamwise vorticity component, 8%; vortex outer and core radii, 4% (Birch *et. al.* 2004). These estimates include approximations of the errors due to signal noise (0.05%), and analogue signal conditioning (0.25%), which were additively combined to yield a worst-case approximation. The total data acquisition error was also verified experimentally by sampling calibration signals; the average error between the calibration signal and the sampled signal was less than the error approximated additively, so the latter was used. The upper bound of the sensor calibration error (3%) was approximated based on the response of the sensor to flows of large angularity, which minimize the sensitivity. The sensor repeatability (0.2%) was estimated by examining several typical velocity time traces obtained while measuring a steady, undisturbed free-stream velocity. Again, as a worst case, the upper bound of the total velocity error estimate was taken as the additive combination of all of the errors listed above. A more detailed description of the experimental uncertainty is presented in Appendix D.

A symmetric, Gaussian weighted spatial filter was applied to both steady time-mean and phase-locked ensemble-averaged velocity measurements in order to reduce the effective measurement error without altering the vorticity magnitudes. Because the velocity fields measured are expected to be smooth and continuous, the Gaussian spatial filtering technique resulted in an increase in the effective sample size at a given point, reducing the error in the velocity fluctuation measurement. The magnitude of the reduction was approximated by examining the effect of the spatial filter on the convergence of the velocity fluctuation calculation for a large-size, typical time-domain data set, and the filtered measurements were shown to converge to within 2%. The spatial filter had the effect of reducing the random velocity field error by as much as 50%, and improving the calculation of integrated field quantities by as much as 14%.

The upper bound of the vorticity error includes the incremental positional error of the traverse, and was estimated by applying the finite difference of Equation (9) to a typical but severe velocity gradient. The error in vortex radius was due to the spatial resolution of the scan.

The vortex meandering effect was also investigated using the correlation technique of Devenport *et. al.* (1996). Due in part to the low level of freestream turbulence in the flow facility used, the diffusive effects of the vortex meandering upon the measurements were determined to be small in the present experiments. Furthermore, the trajectory and development of a tip vortex can be significantly affected by the proximity of the wing tip to the wind tunnel walls. No wall corrections were applied to the present measurements. A more detailed analysis and discussion of the vortex meandering is included in Appendix C.

The experimental model and traverse, when installed in the wind tunnel test section, resulted in a total flow blockage ratio of less than 6.5%. Tests showed that the blockage did not significantly affect the test-section flow uniformity, and is expected to contribute negligibly to the overall uncertainty (Katz 1995).

7 Results and discussion

7.1 Static wing tip vortex

In order to develop an understanding of the nature of the tip vortex generated by an oscillating wing, a detailed characterization of the static wing tip vortex was carried out to serve as a basis of comparison. Measurements were made behind a NACA 0015 model at $Re_c = 1.85 \times 10^5$, for $2° < \alpha < 18°$, and $-0.5 < x/c < 1.5$, with particular attention being given to the evolution of the flow fields, vorticity distributions, critical vortex quantities and induced drag with increasing incidence and downstream distance. While the Reynolds and Mach numbers selected for this study were considerably lower than those of a full-scale helicopter blade tip environment (where velocities can exceed the local speed of sound), these results will nonetheless provide valuable insight into the nature of the three-dimensional unsteady flow fields.

7.1.1 Variation of static vortex characteristics with streamwise location

The near-field, the streamwise evolution of the tip vortex generated by a static wing at $\alpha = 10°$ is illustrated in Figures 7-8, which show the velocity vectors, together with contours of constant vorticity. The early emergence of organized, vortical structures in the vicinity of the wing tip is evident by the appearance of three-dimensional flow patterns and axial vorticity concentrations at the $x/c = -0.5$ station. The initial development of the wing tip vortex was characterized by the appearance of a number of secondary vortices which increased in size and strength over the wing ($-0.5 \leq x/c \leq -0.1$; Figure 8 a-c), as they were fed by the wing boundary layer vorticity and the highly vortical fluid originating from the region of flow separation directly outboard of the wing tip. The secondary vortices merged rapidly together into the growing primary tip vortex, and are nearly completely coalesced immediately downstream of the trailing edge ($x/c = 0.05$; Figure 8 d). The flow fields in the region $0.05 \leq x/c \leq 0.5$ were characterized by the continued development of the tip vortex, as the shear layer vorticity was rapidly entrained and the successive layers of fluid were merged together. The vortex radius increased, and peak vorticity and tangential velocity decreased as the vortex began to approach axisymmetry. By the $x/c = 0.5$ (Figures 7 g and 8 g) measuring station , the inner region began to show the characteristics of a fully-developed vortex; namely, a radially symmetric tangential velocity pattern, and evenly spaced circular isovorticity contours. The flow in the outer region of the vortex, however, was still dominated by the remnants of the shear layer vorticity, which was spiraling around the vortex. The size of the axisymmetric region increased with downstream distance ($0.5 \leq x/c \leq 2$; Figure 8 g-i) as the vortex continued to merge and develop, while the location of the vortex center shifted gradually upwards and inboard under the action of the induced velocity caused by the remaining wake vorticity.

Figure 9 shows contours of constant axial velocity at the same measurement stations along the wing and in the near wake. Over the wing ($-0.5 \leq x/c \leq -0.1$; Figure 9 a-c), the axial velocity fields were dominated by the wing boundary layers, though by $x/c = -0.25$, a small region of velocity deficit (i.e., $u/u_\infty < 1$), and another of velocity excess ($u/u_\infty > 1$) began to appear. As the vortex developed downstream, it continued to be characterized by islands of axial velocity excess and deficit, with the vortex center corresponding approximately to a jet-like region. The axial velocity fields are driven by two competing mechanisms; the first is the decelerating effect of the entrainment of low-momentum fluid from the wing boundary layer, and the second is the accelerating effect resulting from the positive axial gradient in tangential velocity. While developing, the vortex increases in strength as it rolls up additional vorticity from the feeding shear-layer. The resulting axial increase in the swirl velocity generates a region of reduced pressure around the vortex center, and a negative axial pressure gradient dP/dx arises as a consequence. Since the magnitude of the pressure gradient is also a function of radial distance from the vortex center, regions of axial velocity excess and deficit may exist simultaneously in the vortex. Downstream of the $x/c = 0.5$ measurement station (Figures 9 g - i), once the vortex was nearly fully-developed, the magnitudes of the axial velocity excesses and deficits began to decrease under both the action of turbulent diffusion and the decreasing spatial gradient of vortex strength.

The variation of v_θ/u_∞, u/u_∞, $\zeta c/u_\infty$ and u'/u_∞ (where u'/u_∞ is the normalized root-mean-square axial velocity) with radial distance along a line passing transversely through the vortex center is plotted in Figure 10. The tangential velocity is shown to vary nearly linearly near the vortex center (where it switches direction) and asymptotically vanish as the distance from the vortex center increases, properties which are characteristic of turbulent line vortices (Figure 10 a). While the vortex was developing ($x/c < 0.5$) and the region inside which the successive turns of the shear layer had merged was still small, the peak tangential velocity was greater on the pressure side of the vortex than on the suction side, and was located nearer to the vortex center by as much as 5% of the wing chord. Once the vortex had become nearly fully developed ($x/c \geq 0.5$) and the bulk of the shear layer vorticity had already been entrained into the vortex, the asymmetry in v_θ was reduced. The vorticity is similarly plotted across the vortex center in Figure 10 (b). The vortex center corresponds to the location of maximum vorticity, and the vorticity decayed rapidly with distance from the vortex center. For $x/c \leq 0.15$, a secondary peak occurred on the suction side of the wing, indicative of the yet incomplete merging of the outermost turn of feeding layer. As x/c increased, the vorticity distribution becoame rapidly more symmetric about the vortex center, and attained its minimum value further from the vortex center as a result of the diffusion of the vortex. Figure 10 (c) illustrates the development of the axial velocity across the vortex center with streamwise location. At all streamwise measurement stations, the islands of axial velocity excess and deficit were distinctly evident, and the axial velocity at the vortex center was at all locations jet-like. At $x/c = 0.05$ and 0.15, a strong velocity deficit occurred, with $u/u_\infty < 0.75$, at the same suction-side location as the secondary vorticity peak, consistent with the yet incomplete merging of the shear-layer. The magnitudes of the velocity variations decayed rapidly from $0.05 \leq x/c \leq 0.5$, but after the vortex had nearly completed its development, there was little change in the axial velocity profiles with increasing streamwise distance.

The streamwise evolution of some of the critical vortex properties is summarized in Figure 11. Over the wing, the growing tip vortex entrained a significant amount of vorticity from the wing boundary layer, resulting in a substantial increase in the value of the normalized vortex strength $\Gamma_o/u_\infty c$ (defined by Equation 10) in that region. From x/c = 0.05 to x/c = 0.15, there was a rapid increase in both the normalized vortex radius r_o/c and $\Gamma_o/u_\infty c$, as the vortex continued to entrain shear layer vorticity. The vortex radius decreased by more than 30% between x/c = 0.15 and x/c = 0.5 and then remained fairly constant at 14% of the wing chord, while $\Gamma_o/u_\infty c$ decreased only slightly before attaining a constant value of approximately 0.27 at x/c = 0.5. This marked decrease in r_o/c, together with the fairly stable value of $\Gamma_o/u_\infty c$, is indicative of a tightening of the spiraling shear layer in the early stages of vortex development for $0.15 \leq x/c \leq 0.5$. The normalized vortex core radius r_c/c and core strength $\Gamma_c/u_\infty c$ rapidly stabilize at approximately 0.06 and 0.17, respectively, and the lack of any significant variation in these values downstream of the x/c = 0.15 measurement station suggests that the bulk of the development downstream of this station is taking place in the outer region of the vortex. The maximum normalized vorticity is shown in Figure 11 (c). The vortex core vorticity remained fairly constant at an average magnitude of $\zeta c/u_\infty = 24$ from x/c = 0.05 to 2, indicating that variations in the vortex strength were a result of the evolution of the vorticity distributions rather than changes in the peak magnitude of the vorticity. It is also interesting to note that the ratio Γ_c/Γ_o had value of approximately 76% immediately downstream of the trailing edge, which was similar to the theoretical value of 71.5% for a fully developed laminar vortex.

The normalized peak tangential velocity increased rapidly over the wing, attaining a maximum value of $v_\theta/u_\infty = 0.61$ at the trailing edge, and subsequently decreased slowly and linearly with downstream distance (Figure 11 d) to a value of 0.50 at x/c = 2, as the vortex core entrained little additional vorticity from the shear layer and gradually began to decay. As v_θ increased with downstream distance, the resulting axial pressure gradient accelerated the normalized core axial velocity from $u_c/u_\infty = 0.62$ at x/c = 0.5 to u_c/u_∞ =

1.04 at the trailing edge. The core axial velocity remained an average 3% above u_∞ from the trailing edge to $x/c = 2$.

The induced drag coefficient C_{Di} ($=D_i / \frac{1}{2}\rho u_\infty^2 S$, where D_i is the induced drag and S is the wing area), calculated both by the method of Kuzunose (Equation 13) and the method of Maskell (Equation 17), are plotted in Figure 11 (e). The value of C_{Di} is a function of the wing loading only, and as such was expected to be independent of x/c; the calculated values downstream of $x/c = 0.5$ remained constant at approximately 0.014 (Equation 13) and 0.013 (Equation 17).

Figure 11 (f) shows the normalized vortex trajectory along the spanwise axis (z/c) and transverse axis (y/c). Over the wing, the primary vortex moved rapidly toward the pressure side of the wing, and then began to drift gradually back toward the suction side downstream of the trailing edge. Along the transverse axis, the vortex tended to move gradually inboard in the near field as it rolled up more of the vortex sheet .

The radial distribution of circulation is plotted in Figure 12 (a) for some representative streamwise locations from $x/c = 0.5$ to 2. The rapid increase in circulation with increasing r/c within and around the vortex core is followed by a steady decay of the growth rate as Γ approaches Γ_o. Since the vortex strength had already stabilized by the $x/c = 0.5$ measurement station, the curves were expected to asymptote to the same value of $\Gamma_o/u_\infty c$, to within the experimental uncertainty. The nearly symmetric, inner region of the steady wing tip vortex also exhibited strongly self-similar characteristics even before the vortex had attained a nearly fully-developed state. Figure 12 (b) shows some additional radial distributions of circulation, normalized against the core radius r_c and circulation Γ_c and plotted on a semilogarithmic scale. The curves were coincident for $r/r_c < 1.4$, with Γ/Γ_c varying proportionally to r^2 within $r/r_c \approx 0.4$, and proportionally to $\log(r/r_c)$ for $r/r_c > 0.5$. For values of $r/r_c > 1.4$, the divergence of the curves is indicative of the continuing development of the vortex and the entrainment of additional amounts of vorticity originating from the inboard side of the wing. The empirical constants of Hoffmann and Joubert's model (Equation 7) were also determined and are presented in Table 1. Additionally, for $r/r_c < 1.2$, the data was fitted to the third-order polynomial suggested by Ramaprian and Zheng (Equation 6), yielding the coefficients A_1, A_2 and A_3

equal to 1.756, -1.044 and 0.263, respectively. In all of the cases presented, the autocorrelation coefficient was greater than 99.8%.

7.1.2 Variation of static vortex characteristics with wing incidence

Selected cross-flow velocity vectors of the static tip vortex at the $x/c = 1$ measurement station and at selected incidences, together with the corresponding contours of constant normalized streamwise vorticity and axial velocity, are shown in Figure 13. The cross-flow velocity vectors (Figure 13 a) illustrate the growth and migration of the vortex with increasing incidence. The magnitude of the cross-flow velocity increased with the wing loading and the vortices became larger and more distinct.

Figure 13 (b) shows a composite plot of the contours of constant $\zeta c/u_\infty$ for values of α ranging from 2° to 19°. For angles of attack between 2° and α_{ss} ($\approx 15°$), the magnitude of $\zeta c/u_\infty$ increased and the isocontours became more closely spaced as the wing shear layer vorticity increased in magnitude. Also, the outermost region of the vortex becames more irregular with increasing incidence. As the trailing-edge separation point progressed upstream along the wing, a greater amount of disorganized, low-momentum fluid was convected downstream and entrained into the outer region of the vortex. For $\alpha > \alpha_{ss}$, the peak magnitudes decreased and the isocontours became less closely spaced and more irregular, as a result of the rapid decrease in the wing loading and the increase in the size of the region of flow separation. The axial velocity contours (Figure 13 c) were symmetric and wake-like for $\alpha \leq 6°$. As the incidence increased beyond 6°, the axial velocity field developed islands of wake-like flow while the core axial velocity deficit decreased, and at $\alpha \approx 12°$, the core axial velocity began to exceed the free-stream while the islands of wake-like flow persisted in the region around the vortex center.

The changes in the flow structure with increasing incidence are further illustrated in Figure 14, which shows v_θ/u_∞, u/u_∞, $\zeta c/u_\infty$ and u'/u_∞ plotted against radial distance along a transverse line through the vortex center, at the $x/c = 1$ measurement station. The tangential velocity varied almost linearly with radius within the vortex core (Figure 14 a), with the slope increasing with increasing α for $\alpha < \alpha_{ss}$, and remaining fairly insensitive to

α for $\alpha > \alpha_{ss}$. The peak tangential velocity was of greater magnitude and occurred at a smaller radial distance on the pressure side of the vortex, indicating that the vortex was not yet fully developed. The discrepancy between the peak tangential velocities on the pressure and suction sides of the vortex became significant for $\alpha > \alpha_{ss}$, with a circumferential variation of nearly 50%. After the static stall angle had been exceeded, the magnitude of v_θ on the suction side of the wing was significantly reduced and a local plateau occurs around r_c as a result of the entrainment of the low-momentum fluid from the separated wing wake into the vortex. The vorticity distributions across the vortex center, however, remained fairly symmetric even at wing incidences greater than α_{ss} (Figure 14 b). The peak vorticity, along with the size of the region of nonzero vorticity, increased with increasing α for $\alpha < \alpha_{ss}$. For $\alpha > \alpha_{ss}$, the peak vorticity gradually decreased with increasing α while the vortex size increased significantly, resulting from the diffusion of the vortex by the entrainment of the wing wake. The axial velocity across the vortex center was wake-like and symmetric for $\alpha \leq 7°$, with the maximum velocity deficit occurring at the vortex center. As α increased from 8° to 11°, the axial velocity distributions became more irregular as a result of the formation of islands of axial velocity deficit, while the peak deficit gradually moved from the location of the vortex center to the pressure side of the wing. At $\alpha = 12°$, a region of local axial velocity excess formed at the vortex center, and a second island of wake-like flow developed on the suction side of the vortex. The magnitude of the velocity excess at the vortex center increased with α for $\alpha < \alpha_{ss}$, while the velocity deficits remained fairly constant locally.

An overview of the variation of the critical vortex flow quantities with increasing wing incidence is provided by Figure 15. As the wing incidence was increased from 0° to α_{ss}, the magnitudes of $\Gamma_o/u_\infty c$ and $\Gamma_c/u_\infty c$ both increased linearly (with $\Gamma_c/\Gamma_o \approx 0.73$), and then decreased for $\alpha > \alpha_{ss}$ (Figure 15 a), as expected, reflecting the trend in C_L. Prior to stall, the vortex outer and core radii both increased linearly as well, though both r_o and r_c continued to increase for $\alpha > \alpha_{ss}$ (Figure 15 b). Since the peak magnitudes of both $\zeta c/u_\infty$ (Figure 15 c) and v_θ/u_∞ (Figure 15 d) followed trends similar to $\Gamma_o/u_\infty c$, the continued increase in vortex radius beyond static stall is indicative of the diffusion of the vortex resulting from the entrainment of the separated wake. Figure 15 (d) also shows the normalized core axial velocity, which increased gradually for $\alpha < \alpha_{ss}$ and became jet-like at $\alpha \approx 12°$. After stall, u_c/u_∞ dropped rapidly due to the decrease in the axial pressure gradient caused by the diffusion of the vortex. Figure 15 (e) shows the variation of induced drag with increasing α. The $C_{Di} \propto C_L^2$ relationship predicted by Prandtl's lifting-line theory is apparent for $\alpha < \alpha_{ss}$, with a constant of proportionality $1/K \approx 0.005$ (where $dC_L/d\alpha$ was determined from the force balance measurements). In the present low-Re, low aspect ratio study, lifting-line theory overpredicted the induced drag by an order of magnitude, yielding instead

$$1/K = \left(K_o + \frac{1}{\pi e AR} \right) = 0.081 \tag{20}$$

where e is the Oswald wing span efficiency factor, AR is the aspect ratio, and K_o is the pressure drag magnification factor, with a typical value of 0.007 (Naik and Ostowari, 1990). It is also interesting to note that the induced drag contributed to no more than 20% of the total drag, as determined from the force balance measurements. The vortex trajectory, plotted against α in Figure 15 (f) shows that increasing the wing lift for $\alpha < \alpha_{ss}$ had little effect on the spanwise position of the vortex, though the vortex was displaced downward together with the wing trailing edge. For $\alpha > \alpha_{ss,}$ the vortex was pulled inboard and further downward by the pressure gradient resulting from the large region of flow separation.

The radial distribution of circulation for the tip vortex generated at selected angles of attack is shown in Figure 16 (a). As α increased, $\Gamma_o/u_\infty c$ increased, along with the rate of increase of Γ with radius (i.e., $d\Gamma/dr$) and the radius at which the peak value was attained, as a result of the growth of the vortex and the concentration of the additional shear layer vorticity in the inner region of the vortex. Once α surpassed $\alpha_{ss,}$ $d\Gamma/dr$ decreased as the vortex became more diffuse, consistent with the fairly constant value of Γ_o and the continued increase in r_o observed for $\alpha > \alpha_{ss}$. The self-similarity of the vortex inner region ($r/r_c < 1.4$) is maintained throughout the range of α tested (Figure 16 b), even for the case of $\alpha > \alpha_{ss}$. For $r/r_c > 1.4$, the curves failed to collapse, again because the vortex merging and development was not yet complete at the $x/c = 1$ measurement station. The empirical constants which fit the curves of Γ/Γ_c vs. r/r_c to Equation 7 are listed in Table 2. For $r/r_c < 1.2$, the results for $4° < \alpha < \alpha_{ss}$ were also fitted to the third-order polynomial of Equation 6, and the resulting coefficients were $A_1 = 1.6489$, $A_2 = -0.9419$, and $A_3 = 0.2375$. The autocorrelation coefficients for the tabulated constants were at least 99.7% in all cases.

7.2 *Oscillating wing*

With the characteristics of the static wing tip vortex established as a basis for comparison, the tip vortex generated by a wing undergoing sinusoidal oscillations in pitch with reduced frequency κ between 0.09 and 0.18 (values typical of a full-scale helicopter rotor), was investigated at the same chord Reynolds number. Oscillations with maximum incidences less than α_{ss} and greater than α_{ss} were tested, and measurements were made in the near field at measurement planes situated in the range $0.5 \leq x/c \leq 2.5$.

7.2.1 Pitch oscillations within the static stall angle

Figure 17 shows a composite plot of the phase-locked, ensemble-averaged contours of constant $\zeta c/u_\infty$, u/u_∞ and u'/u_∞ at the $x/c = 1$ measurement station for the typical oscillation case $\alpha(t) = \alpha_o + \Delta\alpha \sin(2u_\infty \kappa t/c)$, with $\alpha_o = 8°$, $\Delta\alpha = 6°$, and $\kappa = 0.18$. Note that α_u indicates the wing angle of attack during the pitch-up phase of motion and α_d indicates the wing angle of attack during the pitch-down phase of motion. While the $\zeta c/u_\infty$ contours in Figure 17 (a) are not significantly different than those from the static wing, the contours during pitch-up are somewhat more symmetric and more evenly distributed than the static case, which can be attributed to the dynamic boundary layer improvement effects (Ericsson and Reding,1988; McCroskey, 1982). Remnants of the wing wake are still visible in the outermost contours shown. Once the pitch-down phase of the motion begins, no significant diffusion or enlargement of the vortex was observed, suggesting that no large-scale separation took place, and that throughout the cycle of oscillation, the flow remained mostly attached to the wing. Furthermore, no LEV was observed to form or shed in the present low-amplitude oscillation case.

The normalized axial velocity fields remained strongly wake-like (with velocity deficits as large as 55% u_∞) and symmetric around the vortex center for $3° \leq \alpha_u \leq \alpha_{max}$, but developed islands of wake- and jet-like flow at the beginning of the pitch-down phase of motion which were similar to those observed at larger α for the static case (Figure 17 b). During pitch-up, the vortex being generated and convected downstream was continually increasing in strength with time, so that along the vortex center dP/dx was positive and the flow was decelerated. When the wing began to pitch downwards, the vortex strength began decreasing with time, reversing the sign of the pressure gradient and causing jet-like axial velocities near the vortex center. The regions of $u/u_\infty < 1$ persisted as well during pitch-down, as the wing boundary layer continued to be rolled into the vortex, entraining additional low-momentum fluid.

Contours of the normalized root-mean-square (RMS) axial velocity u'/u_∞ are shown in Figure 17 (c). Within the inner region of the vortex, the u'/u_∞ fields were also fairly symmetric throughout the cycle of oscillation, with the successive turns of the spiraling wing shear layer still visible in the outer region. No significant change in the shape of the contours occurred between the pitch-up and pitch-down phases, suggesting that the pressure gradients and resulting acceleration of the flow did not have a significant stabilizing effect on the fluctuating velocities, despite the dramatic effect on the phase-locked mean axial velocities.

It is important to note that an effective phase lag exists between the flow fields at the measurement plane and the instantaneous value of α recorded simultaneously. If a tracer particle is released in the wing tip region at some $\alpha(t)$, it would convect downstream and arrive at the measurement station some Δt later; at that time, the instantaneous wing incidence would be $\alpha(t+\Delta t)$. For a given $\alpha(t)$, the value of $\alpha(t+\Delta t)$ will depend on κ and the streamwise location of the measurement station, so in order to directly compare developing tip vortices for different values of κ and x/c, it is necessary to compensate the measured instantaneous values of α for the convection time lag. In the present study, the convection time lag has been compensated where indicated using a method similar to that of Chang and Park (2000). If it is assumed that the streamwise distortion of the flow structures is small within the length-scales considered and the structures are convected downstream at a constant velocity u_{conv}, the convection time lag Δt can be directly calculated. Where Chang and park took the mean axial velocity in the vortex region as u_{conv}, the velocity excesses obtained in the present study rendered such a method inappropriate. Instead, a constant $u_{conv} = u_\infty$ was assumed as this is the effective upper bound and would therefore result in the smallest corrections, yielding the most conservative result. Table 3 shows some of the typical values of the compensated angles of attack used at various κ for the case of $x/c = 1$, together with values yielded by a number of other possible approximations for convection velocity.

Detailed cross-flow velocity vector fields, and $\zeta c/u_\infty$, u/u_∞ and u'/u_∞ contour plots for the case of $\kappa = 0.18$ at selected compensated angles of attack α_c are presented in Figure 18, and are compared to results at similar values of α_c for the case of $\kappa = 0.09$. For all values of κ, regardless of the phase of the motion, the cross-flow velocity vectors showed a high degree of radial symmetry around the vortex center, though with the magnitudes $(v^2 + w^2)^{1/2}$ larger toward the inboard side of the wing, on the suction side of the vortex. There was no evidence of an LEV or a post-stall region of massive flow separation. The vorticity contours showed little variation in general size and shape between the cases of $\kappa = 0.09$ and $\kappa = 0.18$ for the different values of α_c, but the shape, location, concentration and magnitude of the contours exhibited significant hysteresis between the pitch-up and pitch-down phases of motion, with the vortices more concentrated during pitch-down. The outermost vorticity contours during pitch-down also became more irregular and distributed, as the vorticity in the outer region of the vortex became more diffused. The most significant difference between the cases of $\kappa = 0.09$ and $\kappa = 0.18$ is visible in the u/u_∞ distributions. At $\alpha_{c,u} = 6°$ (Figure 18 a), there was little variation in the contours with increasing κ. Both the cases were very symmetric about the vortex center, and had maximum velocity deficits of approximately 75% u_∞. At $\alpha_{c,u} = 12°$ (Figure 18 b), when $\kappa = 0.09$, the axial velocity was entirely wake-like (with a minimum level of $\approx$85% u_∞), though it had broken up into several separate islands; however, when κ was increased to 0.18, the radial symmetry of the wake-like profile was maintained, and with a much lower minimum level ($\approx$55% u_∞). This difference in the u/u_∞ fields is consistent with the increase in the magnitude of the axial circulation gradient $d\Gamma_o/dx$ with increasing κ, and the corresponding increase in the magnitude of dP/dx. At $\alpha_{c,d} = 12°$ (Figure 18 c), islands of velocity excess began to appear for both values of κ, though slightly larger magnitudes were observed at the higher κ. At $\alpha_{c,d} = 6°$, the u/u_∞ contours showed very little variation with increasing κ. The contours of constant u'/u_∞ were generally of similar magnitude and shape for both $\kappa = 0.09$ and $\kappa = 0.18$. At $\alpha_{c,u} = 6°$ and $\alpha_{c,d} = 6°$, the u'/u_∞ contours were symmetric about the vortex center, but at $\alpha_{c,u} = 12°$ and $\alpha_{c,d} = 12°$, the peak RMS velocity occured in pockets around the vortex center at a radial distance $\approx r_o/c$, while the fluctuations in the vortex core were stabilized by the nearly solid-body rotation of the fluid (Chow *et. al.*,1997). Since the overall form of the u'/u_∞ contours was fairly insensitive to κ, the effect of $d\Gamma_o/dx$ upon the diffusion of turbulence was reasonably small.

Figure 19 shows the variation of v_θ/u_∞, $\zeta c/u_\infty$, u/u_∞ and u'/u_∞ with radial distance measured transversely from the vortex center, at $\alpha_{c,u} = 12°$ and $\alpha_{c,d} = 12°$ with $x/c = 1$, for the cases of $\kappa = 0.09$, 0.12 and 0.18. Similar to the static vortex, the v_θ/u_∞ distributions (Figure 19 a) were nearly linear within the inner region, and began to decay outside of r_c. The hysteresis between the pitch-up and pitch-down motions were evident, as the pressure- and suction- side peak values of v_θ/u_∞ were consistently higher during the pitch-down phase of motion, and the difference increased with κ. The slopes of the linear regions were also larger during pitch-down, indicative of a more concentrated vortex core. During the upstroke, the peak value of v_θ/u_∞ was larger on the suction side of the vortex and occurred closer to the vortex center than the pressure side peak. During the downstroke, however, a greater discrepancy between the pressure- and suction- side peaks was observed (in excess of 10% of u_∞), whereas the radial positions of the peaks were more symmetric about the center. In all cases, the maximum v_θ/u_∞ peak was smaller for the case of the dynamic vortex than for the static one. The distributions of $\zeta c/u_\infty$ (Figure 19 b) also exhibited a high degree of radial symmetry, decaying rapidly from a maximum at the vortex center, similar to the static case. The vorticity peaks were lower and decayed more slowly for a given κ during pitch-up than during pitch down, while the rate of decay with radial distance increased with κ during pitch-up and decreased with κ during pitch-down. The static $\zeta c/u_\infty$ distribution generally had a higher peak, and decayed more gradually than the dynamic cases.

The radial distributions of u/u_∞ (Figure 19 c) showed some significant differences between the pitch-up and pitch-down phases of wing motion. During pitch-up, u/u_∞ was generally wake-like, with the magnitude increasing and symmetry improving with κ. The velocity deficit recovered more quickly on the pressure side of the wing, whereas on the suction side, u/u_∞ increased more gradually and attained a maximum value somewhat smaller than unity. For the case of $\kappa = 0.18$, the radial distribution of u/u_∞ was sufficiently symmetric to qualitatively compare to Batchelor's laminar model (Equation 5), and the results agreed surprisingly well. During pitch-up, the islands of velocity excess and deficit were evident, though at the vortex center u/u_∞ was consistently greater than unity by an amount which increased with κ. Again, while u/u_∞ returned to a value close to unity on the pressure side of the vortex, it recovered to values generally lower on the suction side. While in some cases the u/u_∞ distributions were similar between the static and oscillating cases, the regions of velocity excess or deficit were significantly larger for the oscillating case. Figure 19 (d) shows the distributions of u'/u_∞, which had a maximum near the vortex center and decreased more rapidly on the pressure side of the wing than on the suction side, similar to u/u_∞. The values of u'/u_∞ were generally lower on pitch-up as a result of the dynamic boundary layer improvement effects, and the hysteresis increased with κ. The magnitude of the fluctuations tended to increase with κ, however at $\kappa = 0.18$, very large local values of $(1-u/u_\infty)^2$ deflated u'. A more meaningful comparison is shown in Figure 19 (e), where u' is shown scaled by u_c/u_∞.

Figure 20 shows the radial variation of circulation for the vortex at $\alpha_{c,u} = 12°$ and $\alpha_{c,d} = 12°$, at the $x/c = 1$ location, for $\kappa = 0.09 - 0.18$. As with the static case, $\Gamma/u_\infty c$ increased rapidly in the inner region (Figure 20 a), and then gradually approached Γ_o as r became large. The slope of $\Gamma/u_\infty c$ for $r < r_c$ was smaller during pitch-up, and the hysteresis was observed to increase with κ. The self-similarity of the vortex was maintained throughout the cycle of oscillation (Figure 20 a), and $\Gamma/\Gamma_c(r/r_c)$ showed little variation from the static case with κ, despite the large differences in $\Gamma/u_\infty c$. The empirical constants fitting $\Gamma/\Gamma_c(r/r_c)$ to Equation 7 through an entire cycle of oscillation are listed in Table 4, with all autocorrelation coefficients greater than 99.8%.

Figure 21 shows the dynamic loops of the critical vortex quantities for the κ = 0.09 and 0.18 oscillation cases at the x/c = 1 measurement station. In all cases, α was compensated for the convection phase lag, as discussed above. The values of $\Gamma_o/u_\infty c$ were lower during the pitch-up phase of motion, and were generally lower for the oscillating cases than for the static case (Figure 21 a), which is consistent with the dynamic improvement of the boundary layer. For larger κ, the rate of change of vortex strength with α was greater both during pitch-up and pitch down, and the maximum vortex strength (occurring at $\alpha_{c,d} \approx 13.5°$) for the case of $\kappa = 0.18$ was 20% larger than the case of $\kappa = 0.09$. A significant hysteresis in the vortex strength which increased with κ was observed for both cases at lower incidences, though for $\alpha_c > 10°$ the hysteresis was small for the present attached-flow case. For wing oscillations within α_{ss}, the dynamic effects during pitch-up caused the boundary layer over the inboard region to remain laminar over the majority of the wing surface, rendering it more susceptible to the adverse pressure gradient and causing the flow to separate slightly earlier relative to the static case (Lee and Gerontakos, 2004), decreasing C_L and diffusing the tip vortex. During pitch down, the boundary layer tended to remain turbulent over the majority of the wing surface, enabling it to withstand the imposed pressure gradient and remain attached over a greater length of the chord, resulting in an increased C_L and a larger amount of streamwise vorticity and circulation in the tip vortex. The dynamic loops of $\Gamma_c/u_\infty c$ (Figure 21 b) exhibited much the same trends as $\Gamma_o/u_\infty c$, except that the rate of increase of the core circulation was not as significantly affected by κ. Throughout the cycle of motion, the ratio Γ_c/Γ_o remained between 60% (occurring at $\alpha_c = 2°$) and 85% (occurring at α_c = 14°), and varied little between pitch-up and pitch-down.

The peak tangential velocities were generally higher during a cycle of oscillation for $\kappa = 0.18$ case (Figure 21 e), and were also lower during pitch-down than during pitch-up. The degree of hysteresis in $v_{\theta max}/u_\infty$ was more significant than that observed in the $\Gamma_o/u_\infty c$ and $\Gamma_c/u_\infty c$ loops, and had an average value of ≈8% for $\kappa = 0.09$ and ≈20% for κ = 0.18. While the rates of increase of $v_{\theta max}/u_\infty$ with α_c were similar for the static case and the oscillation cases, the tangential velocities present in the static vortex were larger throughout the cycle. Figure 21 (f) shows the variation in $\zeta_c c/u_\infty$ through a cycle of oscillation for $\kappa = 0.09$ and 0.18. The trends were similar to those of $v_{\theta max}/u_\infty$, except that the degree of hysteresis increased more dramatically with κ. The value of $\zeta_c c/u_\infty$ for the oscillating cases was generally lower than the static case, with the exception of the portion of the downstroke when $12° > \alpha_{c,d} > 6°$ for $\kappa = 0.18$. The large increase in vorticity during pitch-down, together with the minimal hysteresis in $\Gamma_o/u_\infty c$, suggest that while the total strength of the vortex filaments produced at a given α_c was fairly insensitive to the sense of wing motion, the filaments were more concentrated around the vortex core during the pitch-down phase of motion.

The axial velocity at the unsteady vortex center is shown in Figure 21 (g). A considerable degree of hysteresis was observed, and increased with κ. The value of u_c/u_∞ tended to be much lower than the static value during pitch-up, while during pitch-down larger values of u_c/u_∞ were observed for the dynamic cases. For $\kappa = 0.09$, u_c/u_∞ was less than unity throughout the cycle, whereas for $\kappa = 0.18$, u_c exceeded the free-stream velocity for $13.5° > \alpha_{c,d} > 6°$. A dramatic increase in u_c/u_∞ was observed at the end up the upstroke and the beginning of the downstroke for $\kappa = 0.18$, from $u_c/u_\infty = 0.53$ at $\alpha_{c,u} = 12.1°$ to $u_c/u_\infty = 1.15$ at $\alpha_{c,d} = 12.4°$. Figures 21 (h) and (i) compare the dynamic loops of C_{Di} to the static values. The trends are similar to those of $\Gamma_o/u_\infty c$, and the magnitudes of C_{Di} are for the most part lower than the static values. It should be noted, however, that the discrepancy between the values of C_{Di} obtained using Equation 13 and Equation 17 increases with κ, as a result of the significant axial velocity gradients (Giles 1999). The dynamic vortex trajectories are plotted in Figures 21 (j) and (k). The oscillating vortex tended to follow the same trajectory as the static one, with only a slight difference between the pitch-up and pitch-down phases of motion. While the spanwise location of the vortex center varied negligibly with κ (Figure 21 j), larger excursions of the vortex center along the transverse axis were observed for larger values of κ. The degree of the excursions is more clearly presented in Figure 21 (l), in which the transverse location of the vortex center is plotted against its spanwise location.

The evolution of the dynamic loops of some selected critical vortex quantities with x/c is illustrated in Figure 22, for the case of $\kappa = 0.18$. In all cases, the hysteresis increased with increasing x/c. While $\Gamma_o/u_\infty c$, $\zeta c/u_\infty$ and v_θ/u_∞ exhibited significant increases in magnitude during pitch-down, the decrease in magnitude with x/c during pitch-up was small. Furthermore, since the variation of $\Gamma_c/u_\infty c$ with streamwise distance was small (Figure 22 b), these results indicate that a rapid development of the vortex in the near field was occurring during pitch-down as the additional shear layer vorticity was rolled up into the outer region of the vortex, and within the time- and length- scales considered, the effects of turbulent and viscous diffusion upon the development of the vortex were small relative to the unsteady effects.

The hysteresis in the u/u_∞ loops increased consistently with x/c (Figure 22 e) as the axial pressure gradient persisted throughout the range of measurement, though the rate of change decreased with increasing x/c. The induced drag yielded by Equation 17 was independent of x/c in the near field for $\alpha_{c,u} < 8°$ (Figure 22 f), while a gradual increase was observed with x/c during the downstroke. At $x/c = 0.5$, the vortex was yet insufficiently developed to accurately determine C_{Di} for larger incidences.

7.2.2 *Pitch oscillations beyond the static stall angle*

When the maximum wing incidence attained during a cycle of oscillation exceeded the static-stall angle (i.e. the deep-stall oscillation case), a significant change in the phase-locked, ensemble-averaged flow structures was observed as a result of the propagation of the region of flow reversal upstream from the trailing-edge and the formation growth and convection of a large LEV over the surface of the wing. Furthermore, the catastrophic spilling of the LEV from the trailing edge and subsequent massive flow separation was reflected in the near-field tip vortex characteristics, causing sharp gradients during stall and a large degree of hysteresis in the dynamic loops of most critical vortex quantities. Composite plots of contours of constant $\zeta c/u_\infty$, u/u_∞, and u'/u_∞ for the typical deep-stall case of $\alpha_o = 18°$ and $\Delta\alpha = 6°$, with $\kappa = 0.09$ are shown in Figure 23, at the $x/c = 1$ measurement station. The flow can clearly be divided into four parts: Between $\alpha_{c,u} \approx 12°$ and $\alpha_{c,u} \approx \alpha_{ss}$, the vortex was qualitatively similar to that formed in the low-amplitude oscillation case, as the flow remained for the most part attached to the wing, and the dynamic boundary layer improvement effects resulted in a slightly weaker vortex relative to the static case. From $\alpha_{c,u} \approx \alpha_{ss}$ to $\alpha_{c,u} \approx 22°$, the overall vortex strength increased while the vortex became less concentrated, as C_L continued to increase while the upstream propagation of the region of trailing-edge flow reversal caused an increase in the amount of disorganized, turbulent fluid entrained into the vortex. At $\alpha_u \approx 22°$, the onset of dynamic stall began as the LEV was shed and followed by massive flow separation, resulting in a more irregularly shaped vortex with a sharp decrease in vortex strength, and an increase in axial velocity and turbulence intensity. The dynamic stall process was essentially completed with the shedding of the LEV at $\alpha_{c,d} \approx 20°$, and the vortex strength remained fairly low, with a strong wake-like axial velocity profile and large axial RMS velocities (relative to the static case) throughout the remainder of the oscillation cycle, as the vortex entrained a large amount of turbulent, disorganized flow from the separated wake. An abrupt change in the vortex trajectory was also observed with the separation of the flow from the wing, causing a deflection of the vortex toward the suction side of the wing. In the latter part of the pitch-down phase of the motion, the vortex began to contract and become increasingly axisymmetric as a result of the re-attachment and re-establishment of the flow over the upper surface of the wing.

The details of the structures of the velocity, streamwise vorticity and turbulence fields are more clearly shown in Figure 24, which shows the velocity vectors and contour maps of $\zeta c/u_\infty$, u/u_∞, and u'/u_∞ at $\alpha_{c,u} = 13°$ (corresponding to the pre-stall, attached flow part of the oscillation cycle), $\alpha_{c,u} = 18°$ (slightly beyond α_{ss}, at a phase when the region of flow reversal begins to form and propagate upstream), and $\alpha_{c,u} = 22°$ (the onset of dynamic stall, at a phase when the LEV is increasing in strength over the wing and covering a significant area of the wing upper surface), at the $x/c = 1$ measurement station. For comparison, the flow structures at the same incidences during pitch-down are also shown, together with the static case results at both $\alpha_c = 13°$ and 18°.

At $\alpha_{c,u} = 13°$ (Figure 24 a), the vortex was highly symmetric and was characterized by circumferential flow around a concentrated vortex core (as with a typical turbulent line vortex), as the vorticity generated by the wing shear layer was continuously rolled into a tightening spiral. The velocity vectors described a nearly circular path around the vortex center on the outboard side of the vortex, however a significant radial component of velocity was observed to bring fluid outward from the vortex center on the inboard side of the vortex. The circumferential velocities were slightly lower at $\alpha_{c,u} = 13°$ relative to the static case at the same incidence (Figure 24 g), and the vortex was slightly weaker and less tightly wound. A considerable difference in the flow patterns was observed at $\alpha_{c,d} = 13°$ (Figure 24 f), as the flow was still undergoing the process of reattachment; the magnitudes of the cross-flow velocities decreased, and the vortex became weaker and more diffused. The inner region of the vortex increased disproportionately in size as well, with a value of r_c nearly 65% larger during the downstroke as a consequence of the entrainment of fluid originating from the large region of flow separation, which persisted as a result of the dynamic delay in boundary layer re-attachment.

A significant hysteresis between the pitch-up and pitch-down phases of motion at $\alpha_c = 13°$ was also apparent in the vorticity isocontours. During the pitch-up phase of the motion, the vortex was much more tightly wound, with nearly symmetric, evenly spaced contours of constant $\zeta c/u_\infty$, indicative of a fairly well-developed vortex. The outermost region of the vortex was still somewhat irregular in shape as the shear layer was continuously being rolled into the vortex from the inboard area of the wing. The vortex at $\alpha_{c,u} = 13°$ was of lesser strength (by approximately 35%) and had a lower concentration of vorticity in the inner region relative to the static case. At $\alpha_{c,d} = 13°$, the magnitude of $\zeta c/u_\infty$ decreased significantly relative to the pitch-up phase of motion, and the vortex was much more diffused with more irregularly shaped contours of constant $\zeta c/u_\infty$. The vortex was, however, beginning to become generally axisymmetric as the boundary layer was undergoing reattachment and the flow around the wing was being re-established. The u/u_∞ contours likewise were considerably different between the pitch-up and pitch-down phases of motion. While a fairly localized, irregularly shaped region of mildly wake-like axial velocity (with $u_{min}/u_\infty \approx 0.73$) was observed in the vicinity of the vortex core at $\alpha_{c,u} = 13°$, a large, generally symmetric region of significant velocity deficit (with $u_{min}/u_\infty \approx 0.61$) occurred at $\alpha_{c,d} = 13°$. The generally organized, consistently wake-like nature of the u/u_∞ distributions at $\alpha_{c,u} = 13°$ and $\alpha_{c,d} = 13°$ were in sharp contrast with those which were observed behind the static wing at the same incidence, in which the axial flow field was characterized by discrete islands of wake- and jet- like flow, with maximum velocity excesses and deficits not exceeding 20% of u_∞. The axial RMS velocity fields at $\alpha_{c,u}$ = 13° was dominated by the turbulence originating from the inboard wing shear layer as it was rolled into a spiral, forming the tip vortex. During pitch-up, the structure of the turbulence was similar both in form and in magnitude to the static case, though the peak turbulence was more localized for $\alpha_{c,u}$ = 13°, and coincided with the location of the vortex center. During pitch-down, the magnitude of u'/u_∞ was similar to the pitch-up case, though the area over which elevated turbulence levels were observed was larger, with a steeper gradient at the edge of the vortex, indicating that the bulk of the turbulence originated from the region of flow separation over the wing.

As α_c surpassed the static-stall angle, some distinct differences were observed in the flow. At $\alpha_{c,u}$ = 18° (Figure 24 b), the vortex had the same qualitative form as a turbulent line vortex and was fairly axisymmetric, though the magnitude of the cross-flow velocities were larger during the upstroke than the static case (Figure 24 h). While the outward radial flow persisted on the inboard side of the vortex, the magnitude of v_r was sufficiently large at $\alpha_{c,u}$ = 18° to distort the shape of the vortex. At the same wing incidence during pitch-down (Figure 24 e), the magnitudes of $(v^2 + w^2)^{1/2}$ were sufficiently small and the vorticity was sufficiently diffused to render the identification of a distinct vortex difficult. The distinct difference between $\alpha_{c,u}$ = 18° and $\alpha_{c,d}$ = 18° are further illustrated by the $\zeta c/u_\infty$ contours. During pitch-up, the vortex was of approximately the same shape as the static vortex, with a slightly lower peak vorticity. Also, the outer region of the vortex was more diffused as a result of the increasing size of the area of flow reversal over the wing and the entrainment of the enlarged wake. At $\alpha_{c,d}$ = 18°, the $\zeta c/u_\infty$ contours were highly disorganized, as the massive flow separation over the wing rendered the vortex indistinct. The flow separation also dominated the axial velocity distributions at $\alpha_{c,d}$ = 18°, resulting in a large area of significant velocity deficit (with $u_{min}/u_\infty \approx 0.51$), whereas during pitch-up, a number of small islands of wake-like flow developed within the vortex, of magnitudes slightly larger than the static case. In addition, a small island of slightly jet-like axial flow was observed at $\alpha_{c,u}$ = 18°, similar to those which occurred within the static vortex. As $\alpha_{c,u}$ increased beyond α_{ss} and the thin layer of flow reversal over the wing progressed forward from the trailing edge, the u'/u_∞ field became more distributed and less organized. The magnitudes of u'/u_∞ were smaller at $\alpha_{c,u} = 18°$ than the static case, as the flow was still largely attached to the wing as a result of the dynamic effects. During pitch-down, however, the peak magnitude of u'/u_∞ exceeded that of the static case, as did the size of the region of turbulent flow.

At the onset of dynamic stall ($\alpha_{c,u} = 22°$; Figure 24 c), as the LEV had begun to grow rapidly and convect over the surface of the wing, the shape of the tip vortex became increasingly distorted, though cross-flow velocities attained magnitudes as large as 75% of the free-stream value. The formation and growth of the LEV also resulted in a diffusion of the vortex, as the magnitude of the peak vorticity decreased relative to $\alpha_{c,u} = 18°$, and the $\zeta c/u_\infty$ contours became more sparsely spaced. Additionally, pockets of strong axial velocity excess and deficit were observed, with magnitudes ranging from 54% to 121% of u_∞. The magnitudes and distribution of turbulence did not change significantly from $\alpha_{c,u} = 18°$ to $\alpha_{c,u} = 22°$. Once dynamic stall had occurred and the LEV had convected beyond the trailing-edge of the wing ($\alpha_{c,d} = 22°$; Figure 24 d), the flow had become massively separated, causing the vortex to become highly diffused and indistinct. The peak cross-flow velocity and vorticity magnitudes decreased significantly from the pre-stall condition, and the axial velocity field became entirely wake-like with a minimum value of u/u_∞ of approximately 0.5. The turbulence also increased significantly both in peak magnitude and area with the highly disorganized flow from the separated wing wake at $\alpha_{c,d} = 22°$.

Figure 25 shows the evolution of v_θ/u_∞, $\zeta c/u_\infty$, u/u_∞, and u'/u_∞ with radial distance along a line passing transversely through the vortex center at the same selected angles of attack for the $\alpha_0 = 18°$, $\Delta\alpha = 6°$ deep-stall oscillation case. The tangential velocity distributions (Figure 25 a) were very symmetric and consistent with a generic turbulent line vortex for $\alpha_{c,u} = 13°$ and $18°$, with a linear core region surrounded by a region in which v_θ decayed with increasing radial distance. The velocity gradient within the inner region remained fairly constant with increasing incidence, while the peak magnitude of v_θ/u_∞ increased. At $\alpha_{c,u} = 22°$, the vortex began to lose its symmetry, as v_θ/u_∞ remained unchanged on the pressure side of the vortex, but the slope within the inner region decreased significantly on the suction side, as a consequence of the disturbance of the flow over the wing by the formation and growth of the LEV. Following the catastrophic flow separation, the vortex became highly asymmetric with a nonzero tangential velocity at the vortex center (defined as the location of maximum streamwise vorticity), and a greater peak value of v_θ/u_∞ on the suction side. As the wing incidence continued to decrease on the downstroke, the peak tangential velocity continued to occur on the suction side of the vortex, though the magnitude decreased with decreasing $\alpha_{c,d}$ and the vortex slowly began to regain its symmetry with the reattachment of the flow over the wing. At $\alpha_{c,d} = 13°$, the vortex was mostly symmetric, though the slope of the inner region and the peak magnitudes of v_θ/u_∞ were considerably diminished relative to the same incidence on the upstroke. The radial variation of $\zeta c/u_\infty$ (Figure 25) was symmetric at $\alpha_{c,u} = 13°$ with a nearly Gaussian shape, decaying to near zero magnitude by $r/c \approx 0.1$. At $\alpha_{c,u} = 18°$, though the peak vorticity increased only marginally and the distribution was still fairly symmetric, elevated levels of $\zeta c/u_\infty$ were observed away from the vortex center, with nearly 40% of the peak vorticity still present at $r/c = 0.1$. As $\alpha_{c,u}$ was increased to 22°, the peak vorticity decreased significantly and the distribution of $\zeta c/u_\infty$ was no longer symmetric, with only minimal decay of $\zeta c/u_\infty$ with radial distance toward the suction side. During the downstroke, $\zeta c/u_\infty$ remained small until the wing boundary layer began to reattach, and at $\alpha_{c,d} = 13°$, an increase in peak magnitude and the development of a symmetric distribution was again evident.

The axial velocity radial distributions (Figure 25 c) were dramatically different for $\alpha_{c,u} = 13°$ and 18° relative to the corresponding static cases. The axial velocity was highly asymmetric and entirely wake-like while the flow was attached to the wing and while the region of flow reversal was propagating upstream from the trailing edge. At $\alpha_{c,u} = 22°$, while the process of dynamic stall was underway, a large region of wake-like flow was observed at the vortex center, accompanied by a small region of jet-like flow on the suction side. After dynamic stall had occurred and the LEV was spilled, a large, nearly symmetric region of velocity deficit remained through the process of boundary layer re-attachment, with a fairly constant minimum magnitude of u/u_∞. Figure 25 (d) shows the radial distributions of u'/u_∞, and, as expected, the peak turbulence had decreased at $\alpha_{c,u} = 13°$ and 18° compared to the static cases, as a result of the dynamic boundary layer improvement. A very large difference at $\alpha_{c,u} = 18°$ was observed, as the static wing was mostly stalled, resulting in a large amount of wake turbulence. As $\alpha_{c,u}$ increased, u'/u_∞ increased in magnitude and became more broadly distributed. The turbulence distribution did not change significantly between the pre-and post-stall conditions ($\alpha_{c,u} = 22°$ to $\alpha_{c,d} = 22°$), and while the peak magnitudes decreased as the flow began to re-attach, the overall form of the distributions remained fairly constant.

Figure 26 (a) shows the radial distributions of vortex strength at $\alpha_{c,u} = \alpha_{c,d} = 13°$, 18° and 22° at $x/c = 1$, with $\kappa = 0.09$. During the upstroke, $d\Gamma/dr$ remains fairly constant within the inner region of the vortex, though the peak value of Γ increases with $\alpha_{c,u}$. At $\alpha_{c,d} = 22°$, a significant decrease in $d\Gamma/dr$ near the vortex center is observed, together with an increase in the radial length-scale caused by the diffusion of the vortex. The slope continues to decrease along with the peak value of Γ until $\alpha_{c,u}$, when the slope begins to increase while Γ_{max} further decreased. The self-symmetry of the vortex is maintained through most of the cycle, with the exception of the beginning of the downstroke (Figure 26 b), when the vortex was irregular and indistinct as a result of the catastrophic flow separation.

The variations of some of the phase-locked, ensemble-averaged vortex critical quantities with wing incidence over a cycle of deep-stall oscillation at the $x/c = 1$ measurement station are illustrated in Figure 27, for the case of $\kappa = 0.09$. It should be noted that because of the irregularity and asymmetry of the vortex while the flow over the wing was dominated by the LEV in the vicinity of α_{max}, the values of r_o, r_c, Γ_o and Γ_c at $\alpha \approx \alpha_{max}$ were calculated based on circumferential averages of the velocity and vorticity, and can only be considered as a qualitative reference. Figure 27 (a) shows the dynamic loops of $\Gamma_o/u_\infty c$ and $\Gamma_o/u_\infty c$, together with the static values. The value of $\Gamma_o/u_\infty c$ increased nearly linearly through $12° < \alpha_{c,u} < 21.5°$, with a slope slightly greater than the pre-stall static case, and a decrease in total vortex strength of approximately 30% relative to the static case for $\alpha_{c,u} < \alpha_{ss}$. For comparison, the slopes of selected critical quantities through the pre-stall upstroke are listed in Table 5. At $\alpha_{c,u} \approx 21.5°$, with the rapid growth of the

LEV, the vortex attained a maximum strength of $\Gamma_o/u_\infty c \approx 0.51$, and remained constant until the beginning of the pitch-down phase of motion. A rapid decrease in $\Gamma_o/u_\infty c$ was observed from $\alpha_{c,d} \approx 24°$ to $\alpha_{c,d} \approx 22°$, and once the LEV was released, $\Gamma_o/u_\infty c$ decreased more gradually with decreasing $\alpha_{c,d}$, with the progressive re-attachment of the flow to the wing surface. The vortex strength was consistently lower during the pitch-down phase of the motion (Figure 27 b), as a result of the massive flow separation following dynamic stall. The vortex core strength followed a similar trend, and through $12° < \alpha_{c,u} < 21.5°$, the ratio of Γ_c/Γ_o was consistently 81.5%, with a 4% variability. Both r_o/c and r_c/c were similar to the static values for $\alpha_{c,u} < \alpha_{ss}$ and exhibited nearly linear increases during the pre-stall upstroke, but both the vortex core and outer radii continued to increase, though at diminished rates, towards the onset of dynamic stall. On the downstroke, both r_o/c and r_c/c increased relative to the upstroke, though r_c/c remained fairly constant at 17% of the wing chord for $24° > \alpha_{c,d} > 18°$, while r_o/c continued to increase until the LEV was spilled at $\alpha_{c,d} \approx 22°$, attaining a maximum value of nearly 25% of the wing chord. A large hysteresis was observed in the dynamic loop of peak v_θ/u_∞ (Figure 27 c), increasing rapidly between $\alpha_{c,u} \approx 12°$ and $\alpha_{c,u} \approx 13°$, and then increasing linearly with $\alpha_{c,u}$ until the onset of dynamic stall, where it attained a maximum value of $v_\theta/u_\infty \approx 0.75$. After stall onset, the peak tangential velocity decreased rapidly, and continued decreasing throughout the remainder of the downstroke, reaching a minimum value of 25% of u_∞ at $\alpha_{c,d} \approx 13°$. for instantaneous wing incidences smaller than the static stall angle, the peak v_θ/u_∞ was lower than the corresponding static incidence.

Significant hysteresis was also observed in the dynamic loop of $\zeta c/u_\infty$ (Figure 27 d), with differences of as much as 60% between the pitch-up and pitch-down values at a given incidence. Furthermore, unlike the variation of most other critical vortex quantities, $\zeta c/u_\infty$ increased during the upstroke only until $\alpha_{c,u} \approx \alpha_{ss}$ (to a maximum of 21.5) and then decreased consistently until the shedding of the LEV. For $22° > \alpha_{c,d} > 15°$, a fairly constant, minimum value of $\zeta c/u_\infty \approx 5$ was maintained. The peak vorticity began to gradually recover for $\alpha_{c,d} < 15°$ while the flow over the wing was reattaching, until the rapid, dramatic increase which accompanied the full re-establishment of the flow around the wing. The axial velocities at the center of the vortex (Figure 27 e) tended to decrease very gradually with $\alpha_{c,u}$ during the upstroke, until $\alpha_{c,u} \approx \alpha_{ss}$. After the static-stall angle had been exceeded, u_c/u_∞ decreased at an accelerating rate until the onset of dynamic stall, at which point it began to increase rapidly until it recovered to its peak pre-stall value of $u_c/u_\infty \approx 0.8$ at $\alpha_{c,u} \approx \alpha_{max}$. As the downstroke began, the axial velocity decreased rapidly and attained a minimum value of approximately 50% of u_∞ before beginning a gradual increase for $22° > \alpha_{c,d} > 15°$, followed by a rapid increase with the beginning of the upstroke. The core axial velocity remained wake-like throughout the cycle of motion. The dynamic loop of core turbulence intensity is shown in Figure 27 (f), and has values very similar to the static wing during the upstroke, for $\alpha_{c,u} < \alpha_{ss}$. The turbulence levels at the vortex center rose sharply with the onset of dynamic stall, and decreased rapidly once the downstroke began.

The induced drag was calculated using Equation 17, and is shown in Figure 27 (g). The trend was fairly similar to those of Γ_c and Γ_o, with C_{Di} attaining a maximum value of approximately 0.013 just prior to dynamic stall and decreasing significantly thereafter to a reasonably constant post-stall value of 0.003. The rapid rise in C_D normally observed as a result of the formation and growth of the LEV (Figure 1a) was not reflected in C_{Di}, as the large disturbance caused by the LEV did not cause an increase in the mean kinetic energy associated with the tip vortex. Figure 27 (h) shows the trajectory of the vortex along the transverse and spanwise axes. The vortex trajectory was significantly different from the static case in the transverse direction, though it was similar to the static case during the beginning of the upstroke along the spanwise axis. During the upstroke, the vortex moved inboard and toward the pressure side of the wing, whereas during the downstroke, it progressed outboard and toward the suction side until $\alpha_{c,d} \approx 22°$, at which point it continued to move gradually outboard at approximately the same transverse location.

The spatial variation of selected characteristic vortex quantities in the region $0.5 \leq x/c \leq 1.5$ is shown in Figure 28, at $\kappa = 0.09$. While $\Gamma_o/u_\infty c$ and $\Gamma_c/u_\infty c$ (Figure 28 a-b) were fairly insensitive to streamwise location through most of the upstroke, both the total and core circulation increased with x/c during the downstroke, indicating that the more diffused, less tightly wound vortex produced after stall required a greater streamwise distance to develop. The vortex outer radius also remained fairly insensitive to x/c

through the upstroke (Figure 28 c), and varied inconsistently with $\alpha_{c,d}$ during the downstroke for x/c < 1, expecially at large wing incidences, suggesting that the vortex had yet to develop sufficiently well. For $x/c \geq 1$, r_o/c decreased with x/c for $\alpha_{c,d} > 18°$, and increased with x/c for $\alpha_{c,d} < 18°$, possibly due to some streamwise spatial smoothing of the flow structures resulting from the large wake-like axial velocities. A similar trend was observed for r_c/c (Figure 28 d), though at the $x/c = 0.5$ measurement station, the core radius was significantly smaller, especially at large incidences. The peak tangential velocities remained constant with increasing streamwise distance for $\alpha_{c,u} < \alpha_{ss}$ (Figure 28 e) but beyond the static-stall angle and throughout the downstroke, $v_{\theta,max}/u_\infty$ was substantially larger for x/c < 1. As x/c was increased to 1, $v_{\theta,max}/u_\infty$ became relatively insensitive to x/c throughout the cycle of oscillation. Figure 28 (f) shows that the peak value of $\zeta c/u_\infty$ was only affected by x/c through the upstroke for $\alpha_{c,u} > \alpha_{ss}$, decreasing in magnitude with increasing x/c as the vortex diffused with the continuous addition of the disorganized flow. A dramatic difference in the loops of the core axial velocity is observed (figure 28 g); as x/c was increased, the core value of u/u_∞ switched from being periodically jet-like to being entirely wake-like, with the peak value decreasing from approximately 107% u_∞ (at $\alpha_{c,u} \approx 22°$) to 80% u_∞ (at $\alpha_{c,u} \approx 13°$) between $x/c = 0.5$ and 1. The hysteresis also decreased significantly with increasing x/c, as the axial velocity fields responded to the severe streamwise pressure gradient. Figure 28 (h) shows the evolution of the C_{Di} loops with streamwise distance, and indicates that the vortex development was yet insufficiently complete to yield an accurate estimate of C_{Di} at x/c = 0.5. As expected, however, the induced drag was insensitive to increasing streamwise distance for larger x/c.

7.2.3 *Variation of vortex properties with mean incidence*

In order to quantify the effects of the wing mean incidence upon the unsteady tip vortex, the tip vortex flow structure and critical vortex quantities were compared at α_o = 8°, 14° and 18°, corresponding to the attached-flow, light-stall and deep-stall cases, while x/c, κ and $\Delta\alpha$ were kept constant at 1, 0.09 and 6°, respectively. Decreasing α_o from 18°

to 14° reduced the maximum incidence from 24° to 20°, causing the growth of the LEV to be interrupted. As the wing began to pitch downward, the recirculating, vortical fluid in the leading-edge region which would otherwise have grown into the LEV was forced to detach prematurely. Interestingly, for the light stall oscillation case, at $\kappa = 0.18$, the boundary-layer reattachment was sufficiently promoted by the oscillation that the flow over the wing was mostly re-established by the early part of the downstroke, causing the tip vortex to resemble that of the attached-flow case. On the other hand, at $\kappa = 0.09$, the boundary layer was insufficiently energized by the surface motion to re-attach as early, causing some flow quantities to behave as in the deep-stall case.

For the light-stall oscillation case with $\kappa = 0.18$, the catastrophic separation associated with deep stall was absent, and the associated diffusion of the tip vortex during pitch-down was likewise not observed. While the turbulent breakdown of the wing boundary layer occurred during pitch-up similarly to the deep-stall oscillation case, since the LEV formation was aborted, the stalling mechanism was primarily the forward motion of the trailing-edge separation point (Lee and Gerontakos, 2004). To illustrate the effects of this phenomenon on the tip vortex, Figure 29 shows a composite plot of $\zeta c/u_\infty$, u/u_∞ and u'/u_∞ isocontours as they evolve through a cycle of oscillation for $\alpha_o = 14°$, $\Delta\alpha = 6°$ and $\kappa = 0.18$, at the $x/c = 1$ measurement station. The normalized vorticity contours (Figure 29 a) were similar to the deep-stall case during pitch-up, and though the vortex became somewhat more diffused at the beginning of the downstroke as the turbulent, vortical fluid from the undeveloped LEV was drawn into the tip vortex, as the wing pitched beyond $\alpha_d \approx 18°$ during the downstroke, the tip vortex was well-organized, and more concentrated than during the upstroke. The distributions of u/u_∞ (Figure 29 b) and u'/u_∞ (Figure 29 c) more closely resembled the attached-flow case than the deep-stall case, indicating that the flow had re-attached early in the downstroke ($\alpha_d \approx 18°$), and that no massive flow separation had occurred.

Details of the vortex flow structure at selected incidences, including the cross-flow velocity vectors and normalized vorticity, and axial mean and RMS velocity isocontours, are shown in Figure 30 for the same light-stall case at $\kappa = 0.18$, and $x/c = 1$. At $\alpha_{c,u} = 13°$ (Figure 30 a), the vortex was similar to the attached-flow case at the same incidence. The cross-flow velocity vectors described a circumferential path about the vortex center, with a radial distribution of magnitude qualitatively similar to a generic turbulent line vortex. However, some radial flow outward from the vortex on the inboard side was observed. The vorticity contours were highly symmetric with evenly spaced increments within the inner region, while the outer region was dominated by the remnants of the shear layer vorticity still being wound into the vortex. The axial velocity was symmetric about the vortex center and was wake-like, with the same core value (u_c/u_∞ = 54%) as the attached-flow case. The turbulence structure was dominated by the rolling-up of the wing shear layer into the vortex, and also had a core magnitude similar to the attached-flow case, with $u'_c/u_\infty \approx 6\%$. At $\alpha_{c,u} = 18°$ (Figure 30 b), the vortex was qualitatively similar to the deep-stall case at the same incidence, as the upstream influence of the previously shed deep-stall LEV was small. The vortex had increased in size, and the cross-flow velocities had become significantly larger, though the inboard radial outflow persisted.

The contours of $\zeta c/u_\infty$ were still fairly symmetric and increased in magnitude from $\alpha_{c,u} = 13°$, though the vortex had begun to become somewhat more irregular as a result of the thickening wing wake. The u/u_∞ contours had also become less symmetric, while the core axial velocity deficit increased to 50%. The magnitude and size of the u'/u_∞ contours had likewise increased, and the individual turns of the shear layer had become less distinct with the entrainment of the additional turbulence. At the maximum incidence ($\alpha_c = 20°$; Figure 30 c), the vortex had become irregular and highly diffused as a result of the entrainment of the highly disorganized, turbulent recirculating flow from the undeveloped LEV. The axial velocity profile was wake-like, though the peak deficit decreased relative to $\alpha_{c,u} = 18°$. The axial turbulence was highly concentrated in the vicinity of the vortex center, with a peak value of u'/u_∞ of over 22%. By $\alpha_{c,u} = 18°$ (Figure 30 d) the flow had begun to reattach to the wing surface, and similar to the attached-flow case, the vortex was stronger and more concentrated during the downstroke as a result of the dynamic improvement of the boundary layer (Figure 30 d-e). At $\alpha_{c,u}$ = 18°, u/u_∞ was wake-like at the vortex center, but the vortex inner region was surrounded by pockets of velocity excess, and by $\alpha_{c,u} = 13°$, the axial velocity was entirely jet-like.

The behaviour of the tip vortex through the light-stall oscillations with $\kappa = 0.18$ is summarized in Figure 31, which shows the dynamic loops of selected vortex quantities thorough a cycle of oscillation. The total and core vortex strengths (Figure 31 a) increase nearly linearly throughout the upstroke, at greater rates than the static cases. While a small hysteresis was present in the total vortex strength (with greater magnitudes during the downstroke), the core strength was nearly unchanged between the pitch-up and pitch-down phases of motion, with the exception of a small increase with the entrainment of the aborted LEV. The vortex outer and core radii were for the most part smaller during the downstroke than the upstroke (Figure 31 b), indicative of a more concentrated vortex during pitch-down. Again, a brief enlargement of the vortex was observed at the beginning of the downstroke. The peak tangential velocity increased linearly during the upstroke as well (Figure 31 c), and continued to increase until $\alpha_{c,d} \approx 18°$, and then decreased rapidly and nonlinearly until the end of the cycle.

Figure 31 (d) shows the peak vorticity through a cycle of oscillation. Significant hysteresis ($\approx 50\%$) was observed between the upstroke and downstroke for $\alpha_c > 10°$. The vorticity increased from the beginning of the upstroke to $\alpha_{c,u} \approx 10°$, remained relatively insensitive to wing incidence for $10° < \alpha_{c,u} < 18°$, and then decreased gradually until the beginning of the downstroke. A sharp increase occurred from $\alpha_c \approx 20°$ to $\alpha_{c,d} \approx 18°$, followed by a gradual (though accelerating) decrease through to the end of the downstroke. A similarly dramatic difference between the upstroke and downstroke was observed in u/u_∞, ranging from a minimum of $u/u_\infty \approx 50\%$ during the upstroke to a maximum of $u/u_\infty \approx 1.3\%$ during the downstroke. The core axial RMS velocity was greater during the pitch-down phase of motion than during pitch-up (Figure 31f), and was only a weak function of α for $\alpha_c < 18°$. A sharp spike was observed at $20° > \alpha_{c,d} > 18°$, as the highly turbulent fluid from the leading-edge region was entrained into the tip vortex. The induced drag (calculated using Equation 17) was similar in magnitude to the attached case for $\alpha_{c,u} < 18°$, and followed a trend similar to the tangential velocity. Figure 31 (h) depicts the vortex trajectory as a function of α_c, and shows that the transverse location of the vortex center varied only marginally from the static case, though some significant excursions in the spanwise direction were observed, with the vortex passing outboard of the wing tip for $\alpha_c < 10°$.

As with the attached-flow case, the self-symmetry of the vortices was maintained throughout the oscillation cycle. The empirical constants which relate the present results to Equation 7 are presented in Table 6. Additionally, the radial distributions of circulation were fitted to the polynomial relationship of Equation 6 with the coefficients $A_1 = 1.7303$, $A_2 = -0.9799$, and $A_3 = 0.2428$. In all cases, the autocorrelation coefficients were greater than 99.7%.

Figure 32 shows a comparison of some of the critical vortex quantities through a cycle of each of the attached-flow, light-stall and deep-stall oscillations at $\kappa = 0.09$. The loops of $\Gamma_o/u_\infty c$ and $\Gamma_c/u_\infty c$ show that the hysteresis between the pitch-up and pitch-down phases of motion increased with α_o, as the severity of the dynamic stall and the strength of the LEV increased (Figure 32 a-b). Similarly, r_o/c and r_c/c increased progressively with α_o for a given instantaneous wing incidence, and the vortices were larger during pitch-down only for the deep-stall oscillation case Figure 32 (c-d). The loops of $v_{\theta\,max}/u_\infty$, shown in Figure 32 (c), demonstrate as well the increasing hysteresis with α_o, as the peak tangential velocities decreased with increasing mean incidence, while the pitch-up values remained fairly insensitive to α_o. The incomplete development of the LEV in the light-stall case resulted in increases in peak vorticity and core axial velocity during the start of the downstroke for $\kappa = 0.09$ (Figure 32 f-g) otherwise not observed, while the variation of $\zeta_{max}c/u_\infty$ with α_c during the upstroke was qualitatively similar between the light-stall and deep-stall cases. The induced drag (Figure 32 h) varied with α_o in a similar manner as the vortex tangential velocity, with the degree of hysteresis increasing significantly with α_o.

7.3 *Control of the unsteady tip vortex*

In order to quantify the relative advantage of an active blade tip-vortex control system, the effects of a number of common passive flow control techniques upon the development of the tip vortex were evaluated. In all cases, the wing model used was the same rectangular, square-tipped NACA 0015 with no twist, oscillating in the light-stall regime with $\alpha_o = 14°$, $\Delta\alpha = 8°$ and $\kappa = 0.09$, while measurements were made at the x/c = 2 streamwise location. Note that the amplitude of oscillation was increased in order to increase the phase resolution of the active control system, while deep-stall oscillations have been avoided as any means of tip vortex control through geometrical modifications of the trailing-edge were expected to have little effect on the massively separated flow resulting from the growth and shedding of the LEV.

7.3.1 Passive control of the unsteady tip vortex

First, short-span trailing-edge spoilers were attached to the tip of the wing in various configurations (Figure 33) to either increase or decrease the effective camber of the local airfoil section in the vicinity of the wing tip, altering the spanwise distribution of lift near the tip and thereby controlling vortex roll-up process (Russell *et. al.*, 1997; Liu *et. al.*, 2001).

The cross-flow velocity vectors, together with contours of constant $\zeta c/u_\infty$, u/u_∞ and u'/u_∞, for the case of the inverted spoiler with h = 0.023c (where h is the height of the spoiler) are compared to the clean wing in Figures 34 and 35 at selected instantaneous incidences. The height of the spoiler was selected to correspond to a TE flap deflection of approximately 5°, which will provide some control over the vortex strength while resulting in a small drag penalty (Russell *et. al.*, 1997). At $\alpha_{c,u} = 8°$ (Figure 35 a), the cross-flow velocities were fairly symmetric and described a circumferential path around the vortex center for the case of the inverted spoiler, resulting in flow fields which were qualitatively similar to the clean wing case. The effective increase in local camber (and, as a consequence, wing loading) had the effect of increasing the magnitude and concentration of the vorticity associated with the tip vortex relative to the clean wing case, while the vortex remained well-defined and nearly axisymmetric, with regularly spaced contours of constant $\zeta c/u_\infty$. The axial velocity fields between the case of the clean wing and the case of the inverted TE spoiler were similar as well, primarily wake-like in the region of the vortex and with similar magnitudes. The turbulence structures in the vicinity of the tip vortex, however, were very different. While the turbulence was concentrated in the tip vortex and wing wake for the case of the clean wing, the inverted TE spoiler generated higher levels of turbulence throughout the measurement plane, as a result of the increased size of the wing wake region and the displacement of the boundary layer separation points resulting from the increase in effective camber.

As $\alpha_{c,u}$ was increased to 18° (Figure 35 b), the region of flow reversal over the wing had begun to affect the development of the tip vortex, distorting and diffusing it. For the case of the inverted TE spoiler, while the vortex was still well-defined, the distortions were more pronounced. A significant radial outflow from the vortex center was visible on the inboard side, and the circumferential variation of tangential velocity magnitude showed a higher degree of variability relative to the case of the clean wing. The contours of normalized vorticity also show that the vortex was less concentrated and more irregularly shaped, indicating that the trailing-edge to leading-edge progression of the flow separation point was occurring earlier in the tip region as a result of the increased local camber, causing a larger amount of turbulent, disorganized fluid to be entrained into the tip vortex. The axial velocity field continued to be wake-like, and was not significantly different from the clean wing, though the magnitude of the axial velocity deficit was slightly greater for the case of the inverted spoiler as a result of the entrainment of the additional low-momentum fluid. In addition, the contours of constant u'/u_∞ revealed a highly concentrated region of turbulence at the location of the vortex core for the case of the inverted spoiler.

At $\alpha_{c,u} = 21°$ (Figure 35c), as the process of dynamic stall was underway, the tip vortex had become highly distorted for both the case of the inverted TE spoiler and the clean wing, with the cross-flow velocity vectors for both cases showing an enlarged core region and a larger radial component relative to the pre-stalled condition. The $\zeta c/u_\infty$ isocontours were neither symmetric nor regularly spaced, though the distortions were greater for the case of the inverted TE spoiler. The vortex was also more diffused and had a lower peak magnitude, as the effect of the inverted spoiler on the pressure gradients resulted in the earlier separation of the flow in the tip region. The axial velocities were again of similar magnitude and distribution as the case of the clean wing, though the turbulence was still concentrated in a small region around the location of the vortex core.

During the downstroke, some significant differences between the tip vortex produced by the wing with the inverted TE spoiler and the baseline case were observed. At $\alpha_{c,d} = 18°$ (Figure 35 d), the clean wing tip vortex had become mostly symmetric, with a small, concentrated core, similar to a generic turbulent line vortex. The wing with the inverted TE spoiler, however, had an enlarged core region with a significant radial velocity component, resulting in a somewhat elongated, elliptic vortex. This difference is further illustrated by the isovorticity contours, which show that the vortex was more distorted and diffused, and had a significantly lower peak vorticity than the baseline case. The effect of the promoted boundary layer separation in the tip region was also reflected in the axial velocity fields, where the axial velocities were very weakly jet-like in the vicinity of the vortex core (with an 1.4% velocity excess at the vortex center), compared to the stronger jet-like axial velocities (with a 20% velocity excess at the vortex center) observed for the case of the clean wing. The axial RMS velocity field showed that the turbulence was more highly concentrated in the vicinity of the vortex center relative to the baseline case, and that the magnitudes were somewhat larger. At $\alpha_{c,d} = 8°$ (Figure 34 e), the flow had begun the reattachment process for both the cases of the inverted TE spoiler and the clean wing, and the tip vortices had once again become fairly well-defined though with diminished cross-flow velocity magnitudes relative to the corresponding incidence angle during the upstroke. The vorticity distributions were symmetric, and the contour lines were evenly distributed within the vortex inner region, with similar magnitudes as the baseline case. The axial velocity fields were somewhat different from the baseline case, with a velocity deficit at the vortex center and clearly discernable wing wake, where the clean wing axial velocity field was characterized by pockets of jet-like flow away from the vortex center, with local minimum values of u/u_∞ of nearly unity at the vortex center. The turbulence distributions were similar in form to the case of the clean wing, though elevated magnitudes of u'/u_∞ were observed as a result of the presence of the spoiler and the resulting increase in wake size and turbulence.

Figure 36 shows similarly the cross-flow velocity vectors and contours of constant $\zeta c/u_\infty$, u/u_∞ and u'/u_∞ for the case of a plain trailing-edge spoiler with $h = 0.023$. At $\alpha_{c,u} = 8°$ (Figure 36 a) the velocity vectors show that though some circulating sructures existed within the flow fields, a distinct, discrete vortex was not observed. The vorticity isocontours show that the distortion of the tip vortex was due to a secondary vortical structure which originated at the inboard wing-spoiler junction and was entrained into the tip vortex. While the $\zeta c/u_\infty$ contours in the inner region of the tip vortex were generally symmetric and fairly concentrated, the magnitudes were significantly lower than the baseline case. The u/u_∞ contours were similar to the baseline case, with islands of velocity excess observed in the region surrounding the tip vortex, and a core axial velocity which was very weakly wake-like. The u'/u_∞ contours showed elevated turbulence levels in the region around both the tip and spoiler vortices, though the peak values were observed between the two vortical structures. As $\alpha_{c,u}$ increased to 18° (Figure 36 b), the vortex had begun to more closely resemble a generic turbulent line vortex, with a generally symmetric distribution of tangential velocities. Some radial outflow was observed, however, on the outboard side of the vortex. The contours of constant normalized vorticity were mostly symmetric and evenly spaced as well, and were of similar size and shape relative to the baseline case, though of lesser magnitude as a result of the decrease in effective local camber. The suppression of the spoiler vortex at larger incidences could be attributed to the increased rate of tip vortex roll-up accelerating the entrainment of the spoiler vortex, but the lack of a corresponding increase in vorticity suggested instead that the suppression was due to the increase in the boundary layer thickness. The axial velocities were wake-like and were more regular and symmetric, with a greater peak velocity deficit compared to the baseline case, as a result of the increase in the amount of low-momentum wake fluid being entrained. Also, the u'/u_∞ contours show an increased area of elevated levels of turbulence in the vicinity of the vortex relative to the baseline case, consistent with an increase in wake turbulence.

At $\alpha_{c,u} = 21°$ (Figure 36 c), the tip vortex was qualitatively similar to the baseline case, though the magnitudes of the tangential velocities were somewhat diminished. The cross-flow velocity vectors show that the vortex was becoming distorted and that the core region had increased in size. The vorticity isocontours were irregular in shape and distribution , though they were generally similar to the baseline case but with slightly decreased magnitudes in the core region. The axial velocity contours were also qualitatively similar to the baseline case in the core region, with a single local minimum of 54% u_∞ at the location of the vortex center. Outside of the core region, on the other hand, islands of both velocity excess and deficit were observed for the baseline case, with a minimum value of 64% u_∞ at the vortex center and a maximum excess of 125% u_∞ inboard of the vortex center. The axial RMS velocity fields were also basically unchanged from the baseline case.

As the downstroke began and the flow was massively separated, the trailing-edge spoiler had little effect on the flow field relative to the baseline case (Figure 36 d-e), aside from a small decrease in vortex strength which became insignificant at smaller incidences. The spoiler vortex was not observed until the beginning of the upstroke, indicating that throughout the downstroke and while the re-attachment process was underway, the flow was generally separated in the vicinity of the trailing edge.

The effects of a trailing-edge strip (extending symmetrically 0.023 wing chords above and below the trailing edge as illustrated in Figure 33), similar to the strip tested by Liu *et. al.* (2001) was also investigated, and the velocity vectors and contours of constant $\zeta c/u_\infty$, u/u_∞ and u'/u_∞ are shown in Figure 36 at the same selected wing incidences. At $\alpha_{c,u}$ = 8° (Figure 37 a), it can be seen from the cross-flow velocity vectors that the vortex is larger and more diffused than the baseline case, and that no secondary vortex structure was produced by the inboard junction between the strip and the trailing edge. The contours of constant normalized vorticity were axisymmetric and regularly spaced, indicative of a well-developed vortex, though the vortex was highly diffused relative to the other cases tested. The contours of u/u_∞ were largely wake-like in the vicinity of the vortex but with regions of velocity excess on the pressure side, similar to the case of the spoiler, though a greater velocity deficit at the vortex center was observed. The u'/u_∞ contours were similar in form to the baseline case, but with shallower radial gradients. The magnitude of the turbulence was larger than the case of the spoiler, as the additional width of the strip further increased the size of the wake. At $\alpha_{c,u}$ = 18° (Figure 37 b), the vortex was of similar size, but less concentrated than the baseline case. The inner region of the vortex exhibited a fair degree of axisymmetry, and the vorticity contours were evenly distributed, while the concentration and magnitude of the vorticity within the vortex was significantly lower than the baseline case. As expected, the increased size of the wake resulted in an axial velocity in the vortex region which was fairly symmetric and strongly wake-like in nature, with a core value of $u/u_\infty \approx 54\%$. The axial RMS velocities were also fairly symmetric about the vortex center, and were qualitatively similar to the baseline case.

At $\alpha_{c,u} = 21°$ (Figure 37 c), the vortex had become more irregular, and the contours of $\zeta c/u_\infty$ were similar in shape and magnitude to the case of the inverted TE spoiler, suggesting that the presence of the strip on the pressure surface at $\alpha_{c,u} = 21°$ had a more significant effect on the diffusion of the vortex than the strip on the suction surface, since the boundary layer had begun to separate as the dynamic stalling process was underway, and the strip on the suction surface was in a region of mostly separated, recirculating flow. The axial velocity was mostly wake-like, with a core value of 48% of u_∞, while the axial RMS velocities were considerably larger than the other cases, with the peak value occurring near r_c on the inboard side of the vortex.

During the pitch-down phase of wing motion, at $\alpha_{c,d} = 18°$ and 8° (Figure 37 d-e), the vortex had become once again fairly symmetric, though with some distortion still evident at larger incidences. The isovorticity contours exhibited a high degree of axisymmetry, but the vortex was more diffused than the baseline case. The axial mean velocity was wake-like throughout the downstroke, and was qualitatively similar to the case of the inverted spoiler for smaller incidences. The u'/u_∞ contours were likewise similar to the case of the inverted spoiler.

The evolution of the v_θ/u_∞, $\zeta c/u_\infty$, u/u_∞ and u'/u_∞ distributions with phase are more easily compared between the cases of the baseline wing, the TE spoiler, the inverted TE spoiler and the symmetric TE strip in Figure 37, where the variation of these quantities along a line passing transversely through the vortex center at selected wing incidences is shown. The tangential velocities are shown in Figure 38 (a), and with the exception of the case of the spoiler at $\alpha_{c,u} = 8°$ (when the secondary vortex structure was distorting the tip vortex), the tangential velocities increased fairly linearly within the inner region and decayed outside of r_c, similar to the generic turbulent line vortex. More variation between the cases was observed during the upstroke relative to the downstroke, as the effectiveness of the trailing-edge devices decreased when the flow was mostly separated. The highest peak tangential velocities were consistently generated by the inverted spoiler, while the slope of the inner region was approximately the same as the baseline case throughout the cycle. For the case of the spoiler and the symmetric strip, the peak tangential velocities were generally lower than the baseline case, with the spoiler generating larger peak values of v_θ/u_∞ with steeper slopes in the linear region than the symmetric strip though most of the cycle. While the flow is re-attaching, though, the spoiler had produced lower tangential velocities than the strip.

The radial variation of $\zeta c/u_\infty$ likewise showed little difference between the cases while the flow was detached (Figure 38 b). At $\alpha_{c,u} = 8°$, the baseline case and the inverted spoiler produced nearly identical, highly concentrated vorticity distributions (with a core magnitude of $\zeta c/u_\infty \approx 15$). The vorticity distributions for the case of the spoiler and symmetric strip were also fairly similar to each other, with a peak value of $\zeta c/u_\infty \approx 7$, though the vorticity gradient was somewhat more steep near the vortex center for the case of the spoiler. A secondary peak was observed for the case of the spoiler, corresponding to the location of the spoiler vortex. At $\alpha_{c,u} = 18°$, the vorticity distributions for the case of the baseline wing, the case of the spoiler and the case of the inverted spoiler were nearly identical for $y/c > 0.1$ and $y/c < -0.1$, while the symmetric strip produced a much more diffused vorticity distribution. Within the range $-0.1 < y/c < 0.1$, the inverted spoiler resulted in a decreased peak value of vorticity and diminished gradient relative to the baseline case, and closely approached the distribution observed for the case of the symmetric strip. The spoiler resulted in a slightly higher concentration of vorticity near the vortex center than the inverted spoiler. By $\alpha_{c,u} = 21°$, the difference in the vorticity distributions between the cases was fairly small.

The axial velocity across the vortex center, on the other hand, showed more variability during the downstroke, when both wake-like and jet-like axial velocity distributions were observed, than during the upstroke, when the distributions were generally wake-like (Figure 38 c). For all cases, the axial velocity distributions were mostly symmetric about the vortex center. During pitch-up, the baseline case exhibited the lowest amount of velocity deficit, as it was generating the narrowest wake in the tip region. An interesting result is observed at $\alpha_{c,d} = 18°$, where the symmetric strip generated a wake-like distribution of u/u_∞, the inverted spoiler yielded a nearly constant axial velocity with a magnitude close to u_∞, and both the baseline case and the case of the spoiler had jet-like axial velocity distributions in the vortex region. The jet-like velocities subsided by $\alpha_{c,d} = 8°$.

The most significant difference between the cases was observed in the radial distributions of axial RMS velocity (Figure 38 d). At $\alpha_{c,u} = 8°$, the spoiler and symmetric strip produced similar levels of turbulence compared to the baseline case, but over a larger region of the vortex. The inverted spoiler generated a nearly constant distribution of u'/u_∞ within the region of nonzero vorticity. At $\alpha_{c,u} = 18°$, the distribution of axial RMS velocity was similar for the cases of the baseline wing, the spoiler and the symmetric strip, while a sharp increase in the turbulence intensity was observed in the range $-0.1 < y/c < 0.1$ for the case of the inverted spoiler, with a peak magnitude over 100% larger than the other cases. At $\alpha_{c,u} = 21°$, the sharp increase in the range $-0.1 < y/c < 0.1$ was observed for the baseline and spoiler cases as well, though will lower magnitudes than the case of the inverted spoiler. A slight local minima at the location of the vortex center was also observed for the case of the baseline wing, the spoiler and the symmetric strip. During the downstroke, a broad area of elevated turbulence levels was observed for all cases.

The effects of the various passive trailing-edge spoiler and strip configurations are summarized in Figure 39, which shows the variation of several critical vortex quantities with phase. The loops of $\Gamma_o/u_\infty c$ (Figure 39 a) show that for all of the cases tested, the tip vortex circulation was greater during the upstroke relative to the downstroke, indicating that the trailing-edge modifications did not prevent the massive separation in the tip region at the end of the upstroke associated with the dynamic stall phenomenon. The inverted spoiler caused the vortex strength to increase throughout the cycle relative to the baseline case by a nearly constant amount of $\Gamma_o/u_\infty c \approx 0.08$, resulting in an increase in the maximum vortex strength (occurring in all cases at $\alpha_{c,d} \approx 21°$) by 11%. The plain spoiler caused the vortex strength to decrease significantly relative to the baseline case for $6° < \alpha_{c,u} < 11°$, though the difference decreased with increasing $\alpha_{c,u}$, as a result of the partitioning of the total circulation into two discrete vortices (only the tip vortex was considered when determining the value of $\Gamma_o/u_\infty c$). From $\alpha_{c,u}$ 11° through to the end of the upstroke, a nearly constant decrease of $\Gamma_o/u_\infty c \approx 0.04$ relative to the baseline case was observed, and through the downstroke the difference decreased to $\Gamma_o/u_\infty c \approx 0.02$. Surprisingly, the symmetric strip had little effect on the strength of the tip vortex. During the upstroke, the difference between the strength of the tip vortex produced by the wing fitted with a symmetric strip and the baseline wing was within the experimental error, while during the downstroke, the symmetric strip resulted in a slight increase in the vortex strength. While the symmetric strip decreased the peak vorticity significantly, the vortex radius increased proportionally to yield only a small net difference in total strength.

The circulation around the vortex core followed similar trends (Figure 39 b), though with some important differences. While the variations in $\Gamma_c/u_\infty c$ between the different configurations tested were basically due to a small and constant linear shift throughout the cycle of oscillation similar to $\Gamma_o/u_\infty c$, the division of the total circulation between the tip vortex and the secondary vortex for the case of the plain spoiler resulted in a significantly reduced tip vortex core strength during pitch-up relative to the other cases, reducing the hysteresis.

The variation of the vortex outer radius through a cycle of oscillation is illustrated in Figure 39 (c), which shows that all configurations resulted in an increase in vortex size. The inverted spoiler and the symmetric strip yielded vortices of similar radii throughout the cycle, suggesting that when flow separation was promoted by the pressure gradients generated by the presence of the inverted spoiler, the addition of the plain spoiler (into the region of primarily separated flow) had little effect. The high-frequency fluctuations in r_o/c observed for the case of the symmetric strip at larger values of $\alpha_{c,u}$ was indicative of a larger degree of random variation in vortex size from cycle to cycle. For both the cases of the inverted spoiler and the symmetric strip, a decrease in the hysteresis was observed relative to the baseline case. At smaller incidences, the hysteresis nearly vanished, suggesting that the presence of the spoiler on the pressure surface promoted flow re-attachment, narrowing the wake and reducing the vortex size. For the case of the plain spoiler, during the beginning of the upstroke, r_o/c increased rapidly as the spoiler vortex was further entrained into the tip vortex, enhancing the diffusion of the vortex. For larger $\alpha_{c,u}$, the spoiler resulted in a vortex which was larger than the baseline case, by a nearly constant amount. During the beginning of the downstroke ($22° > \alpha_{c,d} >$

13°), a region of massive flow separation was present over the trailing-edge of the wing where the spoiler was situated, and the difference in r_o/c relative to the baseline case was marginal. For $\alpha_{c,d} < 13°$, the pressure gradients resulting from the presence of the spoiler inhibited flow re-attachment, causing the completion of the leading-edge to trailing-edge re-attachment process to occur more abruptly at the end of the downstroke, when the direction of $d\alpha/dt$ reversed.

The variation in r_c/c between the different configurations, as well as the individual case hysteresis, was small relative to those observed for r_o/c (Figure 39 d). The baseline case and the case of the spoiler had vortices with nearly identical core radii, though only after the spoiler vortex had been fully merged into the tip vortex. The addition of the symmetric strip caused almost no variation or hysteresis for $\alpha < 18°$, and yielded values nearly identical to the case of the inverted spoiler in the range $21° > \alpha_{c,d} > 9°$. The vortex generated with the inverted spoiler exhibited values of r_c/c which varied considerably through the cycle relative to the other cases, though the hysteresis was of similar magnitude. In all cases, a rapid rise in r_c/c was observed prior to the onset of the downstroke. The amount of the increase was significantly less for the cases of the spoiler and the symmetric strip.

The loops of peak tangential velocity are shown in Figure 39 (e). The peak tangential velocities were similar between the case of the inverted spoiler and the baseline case, and exhibited a similar degree of hysteresis. The peak values of v_θ/u_∞ were greater for the case of the inverted spoiler for $\alpha_c < 11°$, likely as a result of the promotion of boundary layer re-attachment in the tip region. The cases of the plain spoiler and the symmetric strip were also similar to each other throughout most of the cycle of oscillation, and are characterized by lower peak tangential velocities and less hysteresis than the baseline case, though the division of the circulation into a tip vortex and a spoiler vortex had little effect on the peak magnitudes of v_θ/u_∞.

The variation of peak vorticity thorough a cycle of oscillation showed some interesting differences between the various configurations tested (Figure 39 f). The maximum vorticity was attained by the baseline wing during pitch-up, where the value remained constant at $\zeta c/u_\infty \approx 18$ within the range $9° < \alpha_{c,u} < 18°$; in contrast, within the same range, the peak vorticity increased for the case of the spoiler and symmetric strip, and decreased for the case of the inverted spoiler. During the beginning of the pitch-down phase of motion, a brief recovery of the peak vorticity levels was observed for both the baseline case and the case of the spoiler, though for the range $18° > \alpha_{c,d} > 8°$ there was little variation with the configuration. At the end of the downstroke, the vorticity levels increased more rapidly for the case of the inverted spoiler and baseline wing, while an increase in peak vorticity did not occur until the beginning of the upstroke for the cases of the spoiler and symmetric strip. The lowest levels of vorticity were observed for the case of the symmetric strip, which also exhibited the lowest degree of hysteresis in the $\zeta c/u_\infty$ loop.

Figure 39 (g) shows the loops of axial mean velocity measured at the vortex center. During the upstroke, the core axial velocity was consistently wake-like and had lower values of u_c/u_∞ than the baseline case, which is consistent with the increase in the axial momentum deficit caused by the presence of the spoilers. For the case of the inverted spoiler, a rapid increase of u/u_∞ was observed for $\alpha_{c,u} > 18°$, followed by an abrupt decrease at the beginning of the downstroke. The axial velocity was consistently larger during the downstroke at the $x/c = 2$ measurement plane, with a local maximum occurring at $\alpha_{c,d} \approx 19°$, which was consistent with the results from the deep stall case discussed in section 7.2.2. The baseline wing and the case of the plain spoiler attained core axial velocities well in excess of the free-stream at certain times during the cycle, but remained fairly constant at $u_c/u_\infty \approx 1$ from $\alpha_{c,d} \approx 16°$ to the beginning of the upstroke. For the cases of the inverted spoiler and the symmetric strip, the core axial velocity loops were similar in general form, but remained wake-like throughout the cycle.

The axial RMS velocity loops showed little variation between the different configurations (Figure 39 h). A local maximum was observed at the beginning of the downstroke, with a slightly greater magnitude for the cases of the baseline wing and the plain spoiler, and at a slightly earlier phase.

The loops of induced drag are shown in Figure 39 (i), which exhibited trends reflective of the vortex strength. C_{Di} was consistently larger during the upstroke, and varied nearly linearly with $\alpha_{c,u}$. The induced drag increased with increasing effective camber, and was insensitive to the axial momentum deficit, as expected. It should be noted that the spoilers would cause a pressure drag penalty to be incurred as well, and that the variation in induced drag was not necessarily reflective of the variation in total drag.

The vortex trajectory in the spanwise direction showed some variability with the spoiler configuration during the pitch-up phase of motion, but was less sensitive to the presence of trailing-edge modifications through the downstroke (Figure 39 j). The transverse trajectory of the vortex, however, showed smaller variability between the configurations at larger incidences during both the upstroke and the downstroke. The spoiler had almost no influence on the transverse trajectory during the downstroke, but caused a significant shift toward the suction side during the early part of the pitch-up phase of motion. During the downstroke, the transverse trajectory was also nearly identical between the cases of the inverted spoiler and the symmetric strip, shifting in both cases toward the pressure side. On the other hand, during pitch-up, the symmetric strip had almost no effect on the transverse trajectory, while the inverted spoiler displaced the vortex toward the pressure side.

The self-similarity of vortices produced by the modified wing was also investigated, and in most cases, the vortex was found to fit well to the model of Equation 7. The empirical constants, together with the autocorrelation coefficients, are shown in Table 7 for some selected wing incidences.

The effects of a constant tab deflection $\delta = 5.3°$ and $-5.3°$ (where $\delta > 0$ when the tab deflection increased the camber of the local airfoil section, and $\delta < 0$ when the tab deflection decreased the camber of the local airfoil section, as illustrated in Figure 33) were also investigated. The tab deflection angle was selected such that the displacement of the trailing edge would be equal to the height of the spoilers tested earlier.

Figures 40 and 41 show the cross-flow velocity vectors, together with contours of constant $\zeta c/u_\infty$, u/u_∞ and u'/u_∞, at selected instantaneous wing incidences for the cases of $\delta = 5.3°$ and $\delta = -5.3°$, respectively. The near-field flow structures produced in the tip vortex region by the wing with $\delta = 5.3°$ and $\delta = -5.3°$ were similar to those produced by the wing fitted with the inverted spoiler and the spoiler, respectively, though with some distinct differences. First, while a secondary tab vortex was observed for the case of $\delta = -5.3°$, it was of greater strength than the spoiler vortex and persisted throughout the upstroke. The trajectory of the tab vortex was similar to the trajectory of the spoiler vortex. The tip vortex was also of greater strength through the entire cycle. The vortex produced with $\delta = 5.3°$ was of somewhat greater strength and concentration for large α_c during the upstroke relative to the case of the inverted spoiler, but the vortex strengths were fairly similar during the rest of the cycle. Similar trends were observed in the normalized axial velocity fields. During pitch-up, the RMS velocity fields produced by the case of $\delta = -5.3°$ were similar in form to those of the case of the spoiler, though the magnitudes were larger and the turbulence was concentrated within the primary and secondary vortices. A significant difference between the case of $\delta = 5.3°$ and the case of the inverted spoiler was observed during pitch-up, with the deflected tab resulting in a more well-defined concentration of turbulence within the vortex and the wing wake.

The effects of the tab deflection on the vortex critical quantities through a cycle of oscillation are illustrated in Figure 42. The vortex strength remained unchanged through most of the cycle for the case of $\delta = 5.3°$ (Figure 42 a), except during the beginning of the downstroke ($\alpha_{c,d} > 20°$) where the deflected tab decreased the vortex strength significantly. Since trailing-edge modifications were expected to have little effect once the flow had become massively separated from the wing, these results suggest that the positive tab deflection caused an earlier separation in the tip region relative to the baseline case. For the case of $\delta = -5.3°$, the total circulation was lower than the baseline case through most of the upstroke as a result of the decrease in the section camber in the tip region and the partitioning of the total circulation between the tip vortex and the tab vortex. The tip vortex strength increased at approximately the same rate as the baseline case, but for $\alpha_{c,u} > 20°$, the circulation increased rapidly and attained a maximum of $\Gamma_o/u_\infty c \approx 0.71$ at $\alpha_{c,d} \approx 21°$. Through the downstroke, the variation of $\Gamma_o/u_\infty c$ was similar to the baseline case, resulting in a significant reduction in the hysteresis for $\alpha_c < 20°$.

The evolution of the vortex core strength with phase is shown in Figure 42 (b). For the case of $\delta = 5.3°$, the core circulation was similar to the baseline case for $\alpha_c < 12°$, and within the range $12° < \alpha_c < 20°$, the value of $\Gamma_c/u_\infty c$ was lower than the baseline case through both the upstroke and the downstroke. For $\alpha_c > 20°$, the core circulation for the case of $\delta = 5.3°$ was again similar to the baseline case, indicating that the increased effective camber resulted in a delay in the growth of the vortex core. For the case of $\delta =$

$-5.3°$, $\Gamma_c/u_\infty c$ was lower than the baseline case throughout the cycle, and less hysteresis was observed. While significant reductions in core strength were achieved with both $\delta = 5.3°$ and $\delta = -5.3°$ during pitch-up, the massive flow separation occurring during pitch-down limited the effectiveness of the trailing-edge modifications, and resulted only in small differences between the cases.

Considerable variation in the evolution of the vortex radius through a cycle of oscillation was observed for the different tab deflections tested (Figure 42 c). For the case of $\delta = 5.3°$, the vortex was larger relative to the baseline case through the entire upstroke, and grew rapidly for $\alpha_{c,u} < 18°$. The vortex radius remained fairly constant until the beginning of the downstroke, decreased rapidly (attaining a minimum of $r_o/c \approx 0.2$ at $\alpha_{c,d} \approx 21°$) and then increased again for $21° > \alpha_{c,d} > 18°$, to values slightly larger than those observed during the upstroke. For $\alpha_{c,d} < 18°$, the magnitudes of r_o/c was basically unchanged from the baseline case. On the other hand, when $\delta = -5.3°$, during the upstroke, the vortex was of similar size and grew at a similar rate compared to the baseline case. During the downstroke, however, for $20° > \alpha_{c,d} > 10°$, the vortex was smaller relative to the baseline case. The vortex core radius showed less variability between the configurations tested (Figure 42 d). For $\delta = 5.3°$, the core radius was slightly greater than the baseline case through most of the upstroke. A rapid increase was observed for $\alpha_{c,u} > 20°$ to a maximum of $r_c/c \approx 0.25$ at $\alpha_c = 22°$ (compared to a maximum of $r_c/c \approx 0.19$ for the baseline case), but during the downstroke, for $\alpha_{c,d} < 20°$, the core radius was basically the same as the baseline case. For the case of $\delta = -5.3°$, the core radius was smaller throughout the cycle, and the hysteresis was negligible through most of the cycle.

The loops of peak tangential velocity were fairly similar between the case of $\delta = 5.3°$ and the baseline case (Figure 42 e), though the positive tab deflection resulted in a slight decrease in tangential velocity during the upstroke. For $\delta = -5.3°$, a significant decrease in peak tangential velocity was observed during the upstroke, together with a similar decrease in the hysteresis between the upstroke and the downstroke, similar to the case of the trailing-edge spoiler. The difference between the different cases, however, was small for $\alpha_c > 21°$. A similar comparison could be made in the loops of peak vorticity (Figure 42 f). The positive tab deflection resulted in a trend similar to the baseline case but with lower magnitudes, with a nearly constant value of $\zeta c/u_\infty \approx 14$ in the range $7° < \alpha_{c,u} < \alpha_{ss}$, followed by a gradual decrease through the remainder of the upstroke. For $\delta = -5.3°$, on the other hand, the peak vorticity increased rapidly from $\zeta c/u_\infty \approx 4$ at the beginning of the upstroke to $\zeta c/u_\infty \approx 15$ at $\alpha_{c,u} \approx \alpha_{ss}$, and then remained basically constant until $\alpha_{c,u} \approx 20°$. At the beginning of the upstroke the peak vorticity increased rapidly, achieving a maximum of $\zeta c/u_\infty \approx 17$, and then decreased through the remainder of the downstroke, resulting in a small degree of hysteresis relative to the other cases. The trend observed for $\delta = -5.3°$ was again similar to the case of the trailing-edge spoiler, but with somewhat larger magnitudes.

The core axial velocity (Figure 42 g) was basically the same during the upstroke for the case of $\delta = 5.3°$ as the baseline case, while the magnitudes of u_c/u_∞ were reduced during the downstroke, possibly due to the increase in the wake width. With $\delta = 5.3°$, a larger axial velocity deficit at the vortex center was observed during the upstroke, and during the downstroke, jet-like velocities of similar magnitude as the baseline case were observed, resulting in an overall increase in hysteresis. The axial RMS velocity (Figure 42 h) was consistently larger (smaller) through a cycle of oscillation for the case of positive (negative) tab deflection.

The loops of C_{Di} are shown in Figure 42 (i). Both positive and negative tab deflection resulted in a decrease in induced drag relative to the baseline case. During the upstroke, for $\alpha_{c,u} < 19°$, a greater reduction in induced drag was achieved with $\delta = -5.3°$, while for $\alpha_{c,u} > 19°$ and through the downstroke with $\alpha_{c,d} > 14°$, a slightly greater decrease in induced drag is yielded by the $\delta = 5.3°$ case.

The deflection of the trailing-edge tabs also caused a change in the vortex trajectories, as is illustrated in Figures 42 (j) and (k). Positive tab deflection caused little change in the spanwise location of the vortex center at the $x/c = 2$ measurement station, while a negative deflection shifted the vortex further outboard through most of the cycle, possibly as a result of the influence of the secondary vortex. In contrast, along the transverse axis, positive tab deflection had almost no effect on the location of the vortex center, where negative tab deflection resulted in a significant displacement towards the pressure side of the wing.

While the deflection of the trailing-edge tab resulted in some significant differences in the tip vortices, the vortices remained fairly self-similar; the empirical constants fitting the circulation distributions to the model presented in Equation 7 are included in Table 7, together with the corresponding autocorrelation coefficients.

7.3.2 *Active control of the unsteady tip vortex*

After having evaluated the effectiveness of various passive trailing-edge devices at controlling the tip vortex produced by an oscillating wing, the trailing-edge tab was used to actively control the tip vortex by actuating in response to the phase angle. The use of actively actuated tabs has already been shown to be effective in controlling the flow around a full-scale rotor blade tip (Enenkl *et. al.*, 2002), though the effect of the active tabs upon the flow fields were not reported. In the present study, a number of different tab deflection time-histories were tested, and are illustrated in Figure 43. The time required to deflect the tab was approximately 8% λ (where λ is the time required for the wing to undergo one full cycle of oscillation), and varied between cycles by less than 1% λ. In all cases, the wing was oscillated with $\alpha_o = 14°$, $\Delta\alpha = 8°$ and $\kappa = 0.09$, and measurements were taken at the $x/c = 2$ downstream station.

First, the tab deflection was initiated at $\alpha_u \approx \alpha_{ss}$ and the return stroke was terminated at $\alpha_d \approx \alpha_{ss}$ (corresponding to a total deflection time equal to approximately 36% λ. Both positive and negative tab deflections were tested (cases A and B, respectively), while the magnitude of the deflection $|\delta|$ was maintained constant at 5.3°. The effects of the tab actuation upon the flow structures are summarized in Figure 44, which shows the loops of critical vortex quantities for both cases. The detailed flow structures are documented in Appendix 3.

The vortex strength (Figure 44 a) exhibited no abrupt, dramatic changes in magnitude or slope as a result of the transient tab displacement, though the tab actuation did result in a change in the $\Gamma_o/u_\infty c$ loops relative to the baseline case which was observed throughout the cycle. The values of $\Gamma_o/u_\infty c$ observed for case A were nearly identical to those observed for the case of constant $\delta = 5.3°$, indicating that the increased camber had little influence on the tip vortex during the end of the downstroke through to the formation of the region of flow reversal near the trailing-edge during the following upstroke. For case B, during the beginning of the upstroke, the $\Gamma_o/u_\infty c$ loop showed significantly more hysteresis than the case of $\delta = 5.3°$, increasing at approximately the same rate as the baseline case but with a magnitude somewhat lower. As the wing incidence increased beyond the static stall angle, the slope of $\Gamma_o/u_\infty c$ decreased gradually and the curve began to approach the values observed for the case of $\delta = -5.3°$. A local maximum of was recorded for case B at $\alpha_{c,d} \approx 21°$, similar to both the baseline case and the case of $\delta = -5.3°$, with a somewhat smaller peak value of $\Gamma_o/u_\infty c \approx 0.6$. For $18° > \alpha_{c,d} > 6°$, the vortex strength was nearly identical to the case of $\delta = -5.3°$, indicating that once the flow had separated, the position or motion of the tab did not have a significant effect on the vortex.

The vortex core strength (Figure 44 b) was again nearly unchanged from the case of $\delta = 5.3°$ for case A, though a decrease in the slope of $\Gamma_c/u_\infty c$ was observed during the upstroke once the tab had been actuated. For $\alpha_{ss} < \alpha_{c,u} < 22°$, the core strength continued to increase at approximately the same rate as the case of $\delta = 5.3°$, but with a phase lag of approximately 2°. The phase lag decreased rapidly towards the end of the upstroke, and once the flow had completely separated from the wing, the phase lag vanished. During the downstroke, the values of $\Gamma_c/u_\infty c$ for case A were identical to the case of $\delta = 5.3°$. For case B, a less significant reduction in the magnitude of $\Gamma_c/u_\infty c$ was observed through the upstroke relative to the case of $\delta = -5.3°$, but after the deflection of the tab, a decrease in the rate of increase of the core strength was observed, attaining a peak value lower than either the baseline case or the case of $\delta = -5.3°$, with $\Gamma_c/u_\infty c \approx 0.33$.

Some interesting differences were observed in the loops of r_o/c (Figure 44 c). For case A, strong local maxima were observed at $\alpha_{c,u} \approx 9°$ and $\alpha_{c,u} \approx \alpha_{ss}$. Also, a significant decrease in the vortex size relative to the case of $\delta = 5.3°$ was observed for $\alpha_{c,u} \approx \alpha_{ss}$. These transient increases may be attributed to the unsteady effects of the rapid deflection of the tab. During the downstroke, the vortex radius for case A was nearly identical to the case of $\delta = 5.3°$. A local maximum was also observed at $\alpha_{c,u} \approx 9°$ for case B, but in the range $10° < \alpha_{c,u} < 18°$, the vortex radius increased steadily and exhibited no transient behaviour. From $\alpha_{c,u} \approx 18°$ to $\alpha_{c,u} \approx 20°$, the vortex radius remained fairly constant (with $r_o/c \approx 0.22$), and then increased sharply with the onset of dynamic stall and the beginning of the downstroke. During the downstroke, the vortex radius for case B was fairly similar to the baseline case. The evolution of the vortex core radius (Figure 44 d) showed less variation between the cases. The values of r_c/c for case A were nearly identical to the case of $\delta = 5.3°$, though with somewhat larger values for $\alpha_{ss} < \alpha_{c,u} < 21°$. For case B, the core radius was larger than for the case of $\delta = -5.3°$, except for $\alpha_c > 21°$.

The variations in the loops of peak tangential velocity are shown in Figure 44 (e). For case A, there was little difference compared to the case of static positive tab deflection. For case B, v_θ/u_∞ was larger than the case of $\delta = -5.3°$ by a nearly constant amount during the upstroke for $\alpha_{c,u} < 18°$, but through the rest of the cycle, the values were similar to the case of $\delta = -5.3°$.

Figure 44 (f) shows the loops of peak vorticity, and some interesting differences are observed. First, both cases A and B had lower values of peak vorticity than the baseline case through the upstroke, indicating that the actuation of the tab at the end of the upstroke and beginning of the downstroke affected the vortex concentration throughout the cycle of oscillation. For case A, a small but nearly constant decrease in peak vorticity was observed through the upstroke relative to the case of $\delta = 5.3°$, and the difference vanished at the beginning of the downstroke. For case B, on the other hand, the peak vorticity remained nearly constant throughout the entire upstroke (with $\zeta c/u_\infty \approx 13$), following more closely the trend of the baseline case rather than the case of $\delta = -5.3°$. During the downstroke, a slight local maximum was observed at $\alpha_{c,u} \approx 21°$, followed by a gradual decrease, with magnitudes similar to the baseline case.

The loops of core axial velocity are shown in Figure 44 (g). Case A followed fairly closely the trend of the baseline case, characterized by wake-like flow during the upstroke with a magnitude of u_c/u_∞ which decreased linearly until the beginning of the upstroke, and a rapid increase to jet-like flow and a local maximum at $\alpha_{c,d} \approx 19°$. The axial velocity was more wake-like throughout the upstroke for case A than for the case of $\delta = 5.3°$, but the difference between the cases became small during the downstroke. For case B, the core axial velocity remained fairly constant (with $u_c/u_\infty \approx 0.72$) from the actuation of the tab until $\alpha_{c,u} \approx 20°$, and then increased to reach an earlier local maximum at $\alpha_{c,d} \approx 20°$. For $\alpha_{c,d} < 20°$, the core axial velocity for case B followed a trend similar to the baseline case, with magnitudes significantly lower than the case of $\delta = -5.3°$. No significant differences in the core axial RMS velocity were observed (Figure 44 h), except for a decrease in the peak turbulence intensity during the beginning of the downstroke for case B.

Figure 44 (i) shows the loops of induced drag, and very little difference was observed between case A and the case of $\delta = -5.3°$. For case B, however, a reduction in the induced drag relative to the case of static tab deflection was observed for the duration of tab actuation, resulting in a diminished maximum C_{Di}.

The vortex trajectories along the spanwise and vertical axes through a cycle of oscillation are shown in Figures 44 (j) and (k), respectively. Positive tab actuation tended to shift the vortex outboard and toward the pressure side, whereas negative tab actuation tended to shift the vortex inboard and toward the suction side. Along the spanwise axis, little variation was observed between the active control cases and the baseline case while the instantaneous tab deflection angle was 0°. Along the trasnverse axis, both cases A and B resulted in a deflection of the vortex toward the pressure side, though the trajectory of the vortex was nearly identical for cases A and B prior to and after tab actuation. During actuation, the vortex approached the trajectories observed for the corresponding cases of static tab deflection.

For the next tab actuation cases tested, the tab deflection was initiated at the beginning of the upstroke and was terminated at the end of the upstroke (corresponding to a total deflection time equal to approximately 50% λ). Again, both positive and negative tab deflections with a constant magnitude $|\delta| = 5.3°$ were tested (cases C and D, respectively). The results are summarized by the loops of critical vortex quantities, shown for both cases C and D in Figure 45.

The variation of vortex strength through a cycle of oscillation for cases C and D are compared to the corresponding cases of static tab deflection in Figure 45 (a). For case C, the transient tab deflection at the beginning of the upstroke had little effect on the magnitude of the vortex strength relative to the case of $\delta = 5.3°$. At the beginning of the downstroke, the local minimum in vortex strength was absent, and through the remainder of the downstroke, the vortex strength was slightly decreased relative to the case of δ = 5.3°. For case D, the vortex strength was larger relative to the case of $\delta = -5.3°$ for $\alpha_{c,u} < 16°$, but corresponded fairly well to the case of static tab deflection for $16° < \alpha_{c,u} < 21°$. During the downstroke, the large peak at $\alpha_{c,d} \approx 21°$ was again absent, but for $\alpha_{c,d} < 20°$, the vortex strength remained unchanged from the case of $\delta = -5.3°$. These results show that a transient, negative tab motion at the beginning of the upstroke had a significant effect on the vortex, while a positive tab motion at the beginning of the upstroke had almost no effect.

Somewhat different trends were observed in the loops of vortex core strength, which are shown in Figure 45 (b). For case C, an increase in both the slope and magnitudes of $\Gamma_c/u_\infty c$ during pitch-up relative to the case of $\delta = 5.3°$, together with a fairly constant decrease in core strength during the pitch-down phase of motion, resulted in a significant increase in the degree of hysteresis. It is interesting to note that the values of $\Gamma_c/u_\infty c$ during pitch-up for case C were nearly unchanged from the baseline case. For case D, a small increase (decrease) in $\Gamma_c/u_\infty c$ during the pitch-up (pitch-down) phase of motion relative to the case of $\delta = -5.3°$ resulted in a nearly negligible degree of hysteresis, while the peak magnitude increased by approximately 13%.

The loops of r_o/c are shown in Figure 45 (c). For case C, the vortex radius followed the case of $\delta = 5.3°$ fairly closely, but without the local minimum at the beginning of the downstroke, and with slightly diminished magnitudes through the remainder of the pitch-down phase. For case D, during the upstroke, the vortex radius can only be considered as a reference, as the values were affected by the presence of a system of multiple secondary vortices, rendering the determination of the vortex radii (based on Equation 10) inaccurate. These secondary vortices contained more of the total circulation compared to the case of static tab deflection, which resulted in a dramatic increase in the effective size of the vortex and diffusion of the vorticity.

The determination of the core radius was not affected by the presence of multiple vortex structures, and as such may be compared directly (Figure 45 d). For case C, a much larger vortex core was observed during the upstroke relative to the case of $\delta = 5.3°$, which, together with a somewhat smaller value of r_c/c through the downstroke, resulted in a significant degree of hysteresis. This trend is similar to $\Gamma_c/u_\infty c$, indicating that the increase in core strength during the pitch-up phase of motion was a result of an increase in the core size rather than an increase in the magnitude of the vorticity. For case D, r_c/c was approximately the same through the upstroke as the case of $\delta = -5.3°$, but at the end of the upstroke and the beginning of the downstroke, a large increase in core size was observed. Through the downstroke, the magnitude of r_c/c for case D remained consistently larger than the case of $\delta = -5.3°$.

The deflection of the tab through the pitch-up phase of motion had almost no effect on the peak tangential velocities observed (Figure 45 e), however the loops of peak vorticity (Figure 45 f), exhibited some interesting differences between the cases. For case C, a decrease in the magnitude of peak vorticity through the upstroke relative to the case of $\delta = 5.3°$ was observed, together with a slight increase in the magnitude of the local maximum occurring at the beginning of the downstroke. For case D, the magnitude of $\zeta c/u_\infty$ remained nearly constant through the upstroke, compared to the rapid increase observed for the case of $\delta = -5.3°$. Through the downstroke, the variation in peak vorticity was similar to the baseline case, but with reduced magnitudes.

Figure 45 (g) shows the loops of core axial velocity. For case C, the tab deflection resulted in a large increase in the velocity deficit during the upstroke (to 49% u_∞), together with an increase in the peak velocity excess observed during the downstroke (to 130% u_∞). For $16° > \alpha_{c,d} > 8°$, the core axial velocity remained fairly constant at the free-stream value, which is a slight increase relative to the case of $\delta = 5.3°$. For case D, only minor deviations in the u_c/u_∞ loop were observed compared to the baseline case. The axial RMS velocity (Figure 45 h) had decreased throughout the cycle for case C (relative to the static tab deflection), whereas a larger increase in the turbulence intensity was observed for case D, as compared to the case of $\delta = -5.3°$. No significant increase in the peak turbulence intensity was observed at the $x/c = 2$ measurement station as a consequence of the tab actuation.

The induced drag loop was unaffected by the positive tab actuation of case C (figure 45 i), aside from a very slight decrease during the pitch-down phase of the motion. For case D, a significant decrease was observed throughout the cycle relative to the case of $\delta = -5.3°$.

The vortex trajectories are shown in Figures 45 (j) and (k), and indicate that for case C, the vortex experienced greater excursions along the transverse axis, but smaller excursions along the spanwise axis, relative to the case of $\delta = -5.3°$. For case D, the vortex was shifted outboard during the downstroke, but was displaced toward the pressure side throughout the cycle.

8 Conclusions

The tip vortex produced by an oscillating NACA 0015 wing has been studied, and the effectiveness of a number of passive and active means of vortex control using trailing-edge spoilers, strips and tabs in the tip region were evaluated. The following brief conclusions may be drawn:

i For the static wing, the tip vortex continued to gain strength and develop in the near field. Downstream of the $x/c = 0.5$ measurement station, the vortex had become nearly fully developed and axisymmetric, and only a small variation in circulation, radius, tangential velocity, and peak vorticity was observed with increasing downstream distance. As the wing incidence increased, the nearly linear increase in lift for $\alpha < \alpha_{ss}$ was reflected by a similarly linear increase in vortex strength. The inner region of the axisymmetric tip vortex was self symmetric, and the radial distribution of circulation agreed remarkably well with previous studies.

ii For a wing oscillated through the attached-flow regime, the vortex was qualitatively similar to the static case, remaining fairly concentrated and axisymmetric throughout the cycle of oscillation. The vortex strength was slightly greater during the pitch-down phase of motion than during pitch-up, and the hysteresis increased with the oscillation frequency. The vortex was of similar radius as the static case, but with lower peak tangential velocity and vorticity. The axial velocity at the vortex center varied dramatically over a cycle of oscillation, from being wake-like during the upstroke to jet-like during the downstroke. The inner region of the vortex remained strongly self-similar, with a nearly constant ratio of Γ_c / Γ_o, independent of the phase.

iii As the wing was subjected to deep-stall oscillations, significant hysteresis between the upstroke and the downstroke was observed in most of the critical vortex quantities. During most of the pitch-up phase of motion, the boundary layer remained attached over the inboard region of the wing, producing a well-organized and less turbulent wake structure which rolled up into a concentrated tip vortex. Once the LEV was spilled from the trailing-edge, the flow became massively separated, resulting in a highly disorganized, turbulent wake and a more irregular and diffused vortex. No transient increase in vortex strength was observed during the process of dynamic stall, suggesting that the spanwise vorticity contained within the LEV did not contribute to the strength of the tip vortex for $x/c < 1.5$. Some variation in the vortex critical properties with downstream distance was observed during the pitch-up phase of motion, while during pitch-down, the vortex properties remained fairly insensitive to x/c.

iv For light-stall oscillations, the structure of the tip vortex was dependant upon the oscillation frequency. For lower frequencies, the vortex was more irregular and more diffused during the pitch-down phase of motion, possibly as a result of the entrainment of the highly agitated, vortical fluid convected downstream from the leading-edge area as the formation of the LEV was interrupted. The axial velocity at the vortex center was wake-like throughout the cycle with the exception of the beginning of the downstroke, when a small jet-like region was observed. For higher frequencies, the vortex remained fairly symmetric and self-similar throughout the cycle and increased in strength during the downstroke, similar to the attached-flow case. The vortex size and trajectory were basically unchanged from the static case, while the axial velocity at the vortex center was strongly wake-like during the upstroke and jet-like during the downstroke.

v The inverted spoiler had the effect of increasing the strength and size of the tip vortex at the $x/c = 2$ measurement station, together with the induced drag, throughout the cycle of oscillation. A mostly wake-like axial velocity and a large increase in maximum axial RMS velocity was also observed. For the case of the plain spoiler, a smaller vortex strength and larger size was observed relative to the baseline case, together with lower values of peak vorticity and tangential velocity, indicating that the vortex was more diffused. The symmetric trailing-edge strip resulted in little change in vortex strength relative to the baseline case, but the vortex was larger with a larger core. Also, the peak tangential velocity, vorticity and core RMS velocity were substantially decreased. The trailing-edge modifications generally had less effect on the critical vortex properties during the downstroke than during the upstroke, as the flow was mostly separated over the wing.

vi A positive, constant 5.3° tab deflection had little effect on the strength or size of the tip vortex, and resulted in only small decreases in the peak tangential and core axial velocities, but did have a significant effect on the vortex trajectory. A constant tab deflection of −5.3° also resulted in a decrease in the vortex size, as well as a dramatic decrease in the vortex strength. Furthermore, the hysteresis in the circulation was nearly eliminated. The tangential velocity, vorticity and induced drag were also significantly reduced, though the axial velocity at the vortex center and the vortex trajectory remained similar to the baseline case.

vii A number of time-dependent tab deflections were tested with deflection durations of up to half of the oscillation period. A short-duration, positive deflection while the wing incidence was larger than the static-stall angle (case A) produced little change in the critical vortex properties compared to a static positive tab deflection of the same amplitude. A similar tab deflection time-history but with negative amplitudes (case B) reduced the vortex strength, peak tangential velocity and vorticity relative to the baseline case throughout the cycle, though not as effectively as the static deflection for smaller incidences. At larger incidences, once the tab was deflected, the critical vortex quantities began to approach those observed for the case of the constant tab deflection. Positive tab deflection during the upstroke (case C) produced a vortex of similar strength as the baseline case, but with lower peak vorticity and a larger radius, while the negative tab deflection during the upstroke (case D) resulted only in a significant increase in vortex radius together with a smaller increase in vortex strength during the upstroke relative to the static tab deflection.

9 References

AGARD report R-781 (1990) "Aerodynamics of Rotorcraft" (VKI Special Course)

Anderson, E. and Lawton, T. (2003) "Correlation between vortex strength and axial velocity in a trailing vortex." Journal of Aircraft 40(4):699-704.

Anderson, J., Streitlein, K., Barrett, D and Triantafyllou, M. (1998) "Oscillating foils of high propulsive efficiency." Journal of Fluid Mechanics, 360:41-72.

Batchelor, G. (1964) "Axial flow in trailing line vortices." Journal of Fluid Mechanics, 20(4):645-658.

Betz, A. (1932) "Verhalten von wirbelsystemen." *Zeitschrift fuer Angewandte Mathematik und Mechanik*, 12(3):164-174. (Translation included in NACA Technical Memorandum TM-71, 1932).

Birch, D. and Lee, T. (2000) "Non-intrusive measurement of the boundary layer developed on an oscillating airfoil." Proceedings of the 6th International Symposium of Fluid Control, Measurement and Visualization, Sherbrooke, Quebec.

Birch, D. and Lee, T. (2003) "The structure and induced drag of a tip vortex." Proceedings of the 10th Aerodynamics Symposium of the Canadian Aeronautics and Space Institute, Montreal, Quebec.

Birch, D., Lee, T., Mokhtarian, F. and Kafyeke, F. (2003) "Rollup and near-field behavior of a tip vortex." Journal of Aircraft, 40(3):603-607.

Birch, D., Lee, T., Mokhtarian, F. and Kafyeke, F. (2004) "Structure and induced drag of a tip vortex." Journal of Aircraft, 41(5):1138-1145.

Bousman, W. (2000) "Evaluation of airfoil dynamic stall characteristics for maneuverability". Proceedings of the 26th European Rotorcraft Forum, Netherlands: 1-21.

Brentner, K and Farassat, F. (1994) "Helicopter noise prediction: the current status and future direction." Journal of Sound and Vibration, 170(1): 79-96.

Carr, L. (1987) "Progress in analysis of dynamic stall." Journal of Aircraft, 25(1):6-17.

Chandrasekhara, M., Wilder, M. and Carr, L. (1998) "Unsteady stall control using dynamically deforming airfoils." AIAA Journal, 36(10):1792-1800.

Chang, J. and Park, S. (2000) "Measurements in the tip vortex roll-up region of an oscillating wing." AIAA Journal, 38(6):1092-1095.

Chopra, I. and McCloud, J. (1983) "A numerical simulation study of open-loop and adaptive multicyclic control systems". Journal of the American Helicopter Society, 28(1):63-77.

Choudhuri, P., Knight, D. and Visbal, M. (1994) "Two-dimensional unsteady leading-edge separation on a pitching airfoil." AIAA Journal, 32(4):673-681.

Chow, J., Zilliac, G., and Bradshaw, P. (1997) "Mean and turbulence measurements in the near field of a wingtip vortex." AIAA Journal, 35(10):1561-1567.

Cimbala, J. M. and Park, W. J. (1990) "A direct hot-wire calibration technique to account for ambient temperature drift in incompressible flow". Experiments in Fluids, 8(5):299-300.

Conlisk, A. (1997) "Modern Helicopter Aerodynamics". Annual Review of Fluid Mechanics, 29:515-567.

Dacles-Mariani, J., Zilliac, G., Chow, S. and Bradshaw, P. (1995) "Numerical/experimental study of a wingtip vortex in the near field." AIAA Journal, 33(9):1561-1568.

Devenport, W., Rife, M., Liapis, S. and Follin, G. (1996) "The structure and development of a wing-tip vortex." Journal of Fluid Mechanics, 312:67-106.

Dumitrescu, H. and Cardos, V. (1999) "Moving wall effect on unsteady boundary layers." Journal of Aircraft, 37(2):341-345.

Ekaterinaris, J. (2002) "Numerical investigations of dynamic stall active control for incompressible and compressible flows." Journal of Aircraft, 39(1):71-78.

Enenkl, B., Klöppel, V. and Preissler, D. (2002) "Full scale rotor with piezoelectric actuated blade flaps". Proceedings of the 28th European Rotorcraft Forum, Bristol, U.K.

Ericsson, L. "Revisiting unresolved dynamic stall phenomena". Journal of Aircraft; 37:6, 1117-1122.

Ericsson, L. and Beyers, M. "Universality of the moving-wall effect". Journal of Aircraft, 2000; 37:3, 508-513.

Ericsson, L. and Reding, J. (1988) "Fluid mechanics of dynamic stall, Part I: Unsteady flow concepts." Journal of Fluids and Structures, 2:1-33.

Ericsson, L. and Reding, J. (1988 b) "Fluid mechanics of dynamic stall, Part II: Prediction of full scale characteristics." Journal of Fluids and Structures, 2:113-143.

Francis, M. and Keesee, J. (1985) "Airfoil dynamic stall performance with large-amplitude motions." AIAA Journal, 23(11):1653-1659.

Francis, T. and Katz, J. (1988) "Observations on the development of a tip vortex on a rectangular hydrofoil." Journal of Fluids Engineering, 110:208-215.

Freymuth, P., Finaish, F. and Bank, W. (1986) "Visualization of wing tip vortices in accelerating and steady flow." Journal of Aircraft, 23(9):730-733.

Giles, M and Cummings, R. (1999) "Wake Integration for Three-Dimensional Flowfield Computations: Theoretical Development". Journal of Aircraft, 36(2):357-365.

Govindaraju, S. and Saffman, P. (1971) "Flow in a turbulent trailing vortex." Physics of Fluids, 14(10):2074-2080.

Green, S. and Acosta, A. (1991) "Unsteady flow in trailing vortices." Journal of Fluid Mechanics, 227:107-134.

Greentblatt, D., Neuburger, D., and Wygnanski, I. (2001) "Dynamic stall control by intermittent periodic excitation." Journal of aircraft, 38(1):188-190.

Hammond, C. (1983) "Wind tunnel results showing rotor vibratory loads reduction using higher harmonic blade pitch". Journal of the American Helicopter Society, 28(1):10-15.

Han, Y. and Leishman, J. (2004) "Investigation of helicopter rotor-blade-tip-vortex alleviation using a slotted tip." AIAA Journal, 42(3):524-535.

Haverkamp, S., Neuwerth, G. and Jacob, D. (2003) "Studies on the influence of outboard flaps on the vortex wake of a rectangular wing." Aerospace Science and Technology 7:331-339.

Haverkamp, S., Neuwerth, G. and Jacob, D. (2004) "Active and passive vortex wake mitigation using control surfaces." Aerospace Science and Technology, 9:5-18.

Hoffmann, E. and Joubert, P. (1963) "Turbulent line vortices." Journal of Fluid Mechanics, 16:365-411.

Huffman, G. D., Rabe, D. C. and Poti, N. D. (1980) "Flow Direction Probes from a Theoretical and Experimental Point of View". Journal of Physics Engineering Scientific Instruments, 13(7):751-760

Johnson, W. and Ham, N. (1972) "On the mechanism of dynamic stall." AHS Journal, 17(4):36-45.

Katz, J. and Walters, R. (1995) "Effects of large blockage in wind-tunnel testing." Journal of Aircraft, 32(5):1149-1152.

Kuzunose, K. (1997) “Development of a Universal Wake Survey Data Analysis Code”. AIAA paper A97-31757.

Kuzunose, K. (1998) “Drag Prediction Based on a Wake Integral Method”. AIAA paper A98-32446.

Lee, T. and Basu, S. (1998) “Measurement of unsteady boundary layers developed on an oscillating airfoil using multiple hot-film sensors.” Experiments in Fluids, 25:108-117.

Lee, T. and Gerontakos, P. (2004) “Investigation of flow over an oscillating airfoil.” Journal of Fluid Mechanics 512:313-341.

Lee, T. and Petrakis, G. “Boundary-layer transition, separation and re-attachment on an unsteady airfoil.” Journal of Aircraft, 1999; 37:2, 360-365.

Leishman, G. and Bagai, A. “Challenges in understanding the vortex dynamics of helicopter rotor wakes.” AIAA Journal, 1998; 36:7, 1130-1140.

Lekakis, I. C., Adrian, R. J. and Jones, B. G. (1989) “Measurement of velocity vectors with orthogonal and non-orthogonal triple-sensor probes”. Experiments in fluids, 7:228-240.

Leung, R. and So, R. “Noise generation of blade-vortex resonance.” Journal of Sound and Vibration, 2001; 245:2, 217-237.

Liu, Z., Russell, J., Sankar, L. and Hassan, A. (2001) “A study of rotor tip vortex alteration techniques.” Journal of Aircraft, 38(3):473-477.

Lorber, P., McCormick, D., Anderson, T., Wake, B., MacMartin, D., Pollack, M., Corke, T and Breuer, K. (2000) “Rotorcraft retreating blade stall control.” AIAA paper 2000-2475, presented at the FLUIDS 2000 conference and exhibit, June 19-22, Denver, CO.

Magill, J., Bachmann, M., Rixon, G. and McManus, K. (2003) “Dynamic stall control using a model-based observer.” Journal of Aircraft, 40(2):355-360.

Mahalingham, R., Wong, O. and Komerath, N. “Experiments on the Origin of Tip-Vortices”. AIAA paper 2000-0278.

Martin, J., Empey, R., McCroskey, W. and Caradonna, F. (1974) “An experimental analysis of dynamic stall on an oscillating airfoil.” AHS Journal, 19(1):26-32.

Maskell, E. (1973) “Progress Towards a Method for the Measurement of the Components of the Drag of a Wing of Finite Span”. Royal Aircraft Establishment Technical Report 72232.

Mathioudakis, K. and Breugelmans, F. (1985) "Use of triple hot wires to measure unsteady flows with large direction changes". Journal of Pphysics Engineering and Scientific Measurement, 18(5):414-419.

McAlister, K. and Takahashi, R. (1991) "NACA 0015 wing pressure and trailing vortex measurements." NASA Technical Paper 3151:1-144.

McCormick, B., Tangler, J. and Sherrieb, H. "Structure of Trailing Vortices." Journal of Aircraft, 1968; 5:3, 260-267.0

McCroskey, W. (1973) "Inviscid flowfield of an unsteady airfoil." AIAA Journal, 11(8):1130-1137.

McCroskey, W. (1982) "Unsteady airfoils." Annual Review of Fluid Mechanics, 14:285-311.

McCroskey, W. and Philippe, J. (1975) "Unsteady viscous flow on oscillating airfoils." AIAA Journal, 13(1):71-79.

McCroskey, W., Carr, L. and McAlister, K. (1976) "Dynamic stall experiments on oscillating airfoils." AIAA Journal, 14(1):57-63.

McCroskey, W., McAlister, K., Carr, L., Pucci, S., Lambert, O. and Indergrand, R. (1981) "Dynamic stall on advanced airfoil sections." AHS Journal, 26(3):40-50.

Moore, D. and Saffman, P. (1973) "Axial Flow in Laminar Trailing Vortices." Proceedings of the Royal Society of London. 333:491-508.

Muller, U. (1992) "Comparison of turbulence measurements with single, X and triple hot-wire probes". Experiments in Fluids, 13:208-216.

Naik, D. and Ostowari, C. (1990) "Effects of nonplanar wing forms on a wing." Journal of Aircraft, 27(2):117-122.

Nguyen, K. (1998) "Active control of helicopter blade stall." Journal of Aircraft, 325(1):91-98.

Oshima, H. and Ramaprian, B. (1997) "Velocity measurements over a pitching airfoil." AIAA Journal, 35(1):119-126.

Panda, J. and Zaman, Q. (1994) "Experimental investigation of the flow field of an oscillating airfoil and estimation of lift from wake surveys." Journal of Fluid Mechanics, 265:65-95.

Payne, F. M., Ng, T. T. and Nelson, R. C. (1989) "Seven Hole Probe Measurement of Leading Edge Vortex Flows". Experiments in Fluids, 7(1):1-8

Phillips, W. (1981) "The turbulent trailing vortex during roll-up." Journal of Fluid Mechanics, 105:451-467.

Phillips, W. and Graham, J. (1984) "Reynolds stress measurements in a turbulent trailing vortex." Journal of Fluid Mechanics, 174:353-371.

Ramaprian, B. and Zheng, Y. (1997) "Measurements in the roll-up region of the tip vortex from a rectangular wing." AIAA Journal, 35(12):1837-1843

Ramaprian, B. and Zheng, Y. (1998) "Near field of the tip vortex behind an oscillating rectangular wing." AIAA Journal, 36(7):1263-1269.

Rediniotis, O. K. and Vijayagopal, R. (1999) "Miniature Multihole Pressure Probes and their Neural-Network-Based Calibration." AIAA Journal, 37(6):666-674

Rokhsaz, K., Foster, s. and Miller, S. (2000) "Exploratory study of aircraft wake vortex filaments in a water tunnel." Journal of Aircraft, 37(6):1022-1027

Russell, J., Sankar, L., Tung, C., and Patterson, M. (1997) "Alterations of the tip vortex structure from a hovering rotor using passive tip devices." Proceedings of the 53rd Annual Forum of the American Helicopter Society, Virginia Beach, Virginia, April 29 - May 1.

Schell, I., Ozger, E. and Jacob, D. (2000) "Influence of different flap settings on the wake-vortex structure of a rectangular wing with flaps and means of alleviation with wing fins." Aerospace Science and Technology 4:79-90.

Shaw, J., Albion, N., Hanker, E., and Teal, R. (1989) "Higher harmonic control: wind tunnel demonstration of fully effective vibratory hub forces suppression". Journal of the American Helicopter Society, 34(1):14-25.

Shekarriz, A., Fu, t., Katz, J. and Huang, T. (1993) "Near-field behavior of a tip vortex." AIAA Journal, 31(1):112-118.

Spalart, P.(1998) "Airplane trailing vortices." Annual Review of Fluid Mechanics, 30: 107-138.

Spencer, M., Sanner, R., and Chopra, I. (2002) "Closed-loop neurocontroller tests on piezoactuated smart rotor blades in hover". AIAA Journal, 40(8):1596-1602.

Spreiter, J. and Sacks, A. (1951) "The Rolling Up of the Trailing Vortex and its Effect on the Downwash Behind Wings." Journal of Aeronautical Sciences, 18(1):21-32

Stepniewski, W. and Keys, C. "Rotary-Wing Aerodynamics". Dover Press, 1984.

Treaster, A.L. and Yocum, A. M. (1979) "The Calibration and Application of Five-Hole Probes". ISA Transactions, 18(3):23-24

Viswamurthy, S. and Ganguli, R. (2004) "An optimization approach to vibration reduction in helicopter rotors with multiple active trailing edge flaps." Aerospace Science and Technology, 8:185-194.

Vukoslavcevic, P., Balint, J. and Wallace, J. (1989) "A multi-sensor hot-wire probe to measure vorticity and velocity in turbulent flows." Journal of Fluids Engineering, 111:220-224.

Wenger, C. W. and Devenport, W. J. (1999) "Seven-Hole Pressure Probe Calibration Method Utilizing Look-Up Error Tables." AIAA Journal, 37(6):675-679

Westphal, R., and Mehta, R. (1989) "Interaction of an oscillating vortex with a turbulent boundary layer." Experiments in Fluids, 1989:405-411.

Widnall, S. (1975) "The structure and dynamics of vortex filaments." Annual Review of Fluid Mechanics, 7:141-165.

x/c	A_i	A_o	B_o
0.3	1.393	2.215	0.946
0.5	1.566	2.230	0.994
0.75	1.667	2.110	0.974
1	1.786	1.942	0.962
1.25	1.611	2.208	0.997
1.5	1.805	1.927	0.965
1.75	1.707	2.042	0.969
2	2.029	1.893	0.994

Table 1 Vortex self-symmetry curve-fit constants for static tip vortex, $\alpha = 10°$.

α	A_i	A_o	B_o
4°	1.727	1.969	0.994
6°	1.574	1.985	0.955
8°	1.666	2.010	0.972
10°	1.566	2.230	0.994
12°	1.619	1.197	0.978
14°	1.811	2.154	0.986
16°	1.586	2.178	0.994
18°	1.609	2.070	0.970

Table 2 Vortex self-symmetry curve-fit constants for static tip vortex, $x/c = 1$.

$u_{conv} = u_\infty$

α_u	$\kappa = 0.09$	$\kappa = 0.12$	$\kappa = 0.18$
2°	2.0000°	2.0000°	2.0000°
4°	3.4839°	3.3238°	3.0090°
6°	5.0954°	4.8150°	4.2632°
8°	6.9307°	6.5992°	5.9470°
10°	9.0306°	8.7301°	8.1387°
12°	11.3703°	11.1750°	10.7909°

α_d	$\kappa = 0.09$	$\kappa = 0.12$	$\kappa = 0.18$
14°	14.1343°	14.1759°	14.2578°
12°	12.6297°	12.8250°	13.2091°
10°	10.9694°	11.2699°	11.8613°
8°	9.0693°	9.4008°	10.0530°
6°	6.9046°	7.1850°	7.7368°
4°	4.5161°	4.6762°	4.9910°
2°	2.0000°	2.0000°	2.0000°

	$u_{conv} =$				
α_u	local u_∞	u_{avg}	u_{min}	u_{max}	u_∞
2°	2.0000°	2.0000°	2.0000°	2.0000°	2.0000°
4°	3.4476°	3.4593°	3.3628°	3.5080°	3.4839°
6°	5.0218°	5.0425°	4.8715°	5.1288°	5.0954°
8°	6.8201°	6.8451°	6.6388°	6.9491°	6.9307°
10°	8.8886°	8.9122°	8.7179°	9.0102°	9.0306°
12°	11.2118°	11.2285°	11.0907°	11.2980°	11.3703°

α_d	local u_∞	u_{avg}	u_{min}	u_{max}	u_∞
14°	14.2845°	14.2784°	14.3282°	14.2533°	14.1343°
12°	12.7882°	12.7715°	12.9093°	12.7020°	12.6297°
10°	11.1114°	11.0878°	11.2821°	10.9898°	10.9694°
8°	9.1799°	9.1549°	9.3612°	9.0509°	9.0693°
6°	6.9782°	6.9575°	7.1285°	6.8712°	6.9046°
4°	4.5524°	4.5407°	4.6372°	4.4920°	4.5161°
2°	2.0000°	2.0000°	2.0000°	2.0000°	2.0000°

Data for case $\alpha = 8° + 6°\sin(\omega t)$, $\kappa = 0.09$, $x/c = 1$

Table 3 Angles of attack compensated for convection time lag at $x/c = 1$, with comparison of various possible convection velocities.

$\kappa = 0.09$							
α_u	A_i	A_o	B_o	α_d	A_i	A_o	B_o
2°	1.4349	2.3646	0.9940	14°	1.6814	2.1982	0.9884
4°	1.4288	2.2972	0.9878	12°	1.4748	2.3599	0.9969
6°	1.4279	2.3376	0.9910	10°	1.4806	2.2820	0.9906
8°	1.4600	2.2847	0.9911	8°	1.4473	2.2914	0.9924
10°	1.6691	2.0937	0.9880	6°	1.5275	2.1750	0.9870
12°	1.7251	2.0751	0.9796	4°	1.4060	2.3258	0.9872

$\kappa = 0.12$							
α_u	A_i	A_o	B_o	α_d	A_i	A_o	B_o
2°	1.3606	2.4152	0.9905	14°	1.7530	2.2496	0.9974
4°	1.4310	2.3147	0.9905	12°	1.6922	2.2214	1.0053
6°	1.5246	2.1331	0.9827	10°	1.4842	2.3530	0.9972
8°	1.5771	2.1589	0.9854	8°	1.5464	2.1987	0.9898
10°	1.6073	2.2021	0.9957	6°	1.4549	2.2569	0.9889
12°	1.6937	2.1525	0.9852	4°	1.4785	2.1946	0.9880

$\kappa = 0.18$							
α_u	A_i	A_o	B_o	α_d	A_i	A_o	B_o
2°	3.2467	1.6895	1.0692	14°	1.7859	2.0783	0.9855
4°	1.6842	1.7548	0.9648	12°	1.6667	2.2570	1.0075
6°	1.4258	2.2435	0.9820	10°	1.5147	2.2946	0.9936
8°	1.4790	2.1067	0.9774	8°	1.4166	2.3100	0.9910
10°	1.4823	2.2105	0.9858	6°	1.4666	2.2309	0.9862
12°	1.5521	2.2815	0.9848	4°	1.3807	2.4348	0.9950

Table 4 Vortex self-symmetry curve-fit constants for the case $\alpha_o = 8°$ and $\Delta\alpha = 6°$, at $x/c = 1$.

Quantity	a	b
r_o/c	0.0106	-0.0321
r_c/c	0.0118	-0.0848
$\Gamma_o/u_\infty c$	0.0387	-0.2728
$\Gamma_c/u_\infty c$	0.0375	-0.3150
v_θ/u_∞	0.0324	0.0921
C_{Di} (Eq. 17)	0.0012	-0.0102

Table 5 Empirical coefficients fitting selected vortex properties to the line $a\times\alpha_{c,u} + b$, in the range $13° < \alpha_{c,u} < 21°$, for the case of $\alpha_o = 18°$, $\Delta\alpha = 6°$ and $\kappa = 0.09$, at the $x/c = 1$ measurement station.

$\kappa = 0.09$

α_u	Ai	A_o	B_o	α_d	A_i	A_o	B_o
8	1.4169	2.3199	0.9887	20	-	-	-
10	1.7163	2.1614	0.9860	18	1.7111	2.2546	1.0001
12	1.7834	2.1761	1.0024	16	1.6265	2.2810	1.0104
14	1.9166	2.0713	0.9931	14	1.6648	2.1744	0.9889
16	1.9965	2.0384	0.9966	12	1.5670	2.1794	0.9815
18	1.8726	2.2093	1.0106	10	1.3957	2.3880	0.9927

$\kappa = 0.18$

α_u	A_i	A_o	B_o	α_d	A_i	A_o	B_o
8°	1.5047	2.3255	0.9951	20°	-	-	-
10°	1.4510	2.2713	0.9891	18°	1.8380	2.0901	0.9952
12°	1.5923	2.2067	0.9928	16°	1.8007	2.2151	1.0122
14°	1.5301	2.1957	0.9816	14°	1.7546	2.2161	0.9981
16°	1.6262	2.1432	0.9786	12°	1.7035	2.2187	1.0074
18°	1.7882	2.1811	0.9913	10°	1.5409	2.1750	0.9866

Table 6 Vortex self-symmetry curve-fit constants for the case $\alpha_o = 14°$ and $\Delta\alpha = 6°$, at $x/c = 1$.

Baseline case

α	A_i	A_o	B_o	R^2
$\alpha_u = 8°$	1.4328	2.2888	0.9863	0.9991
$\alpha_u = 18°$	1.6919	2.2056	0.9952	0.9993
$\alpha_u = 21°$	1.5435	2.1695	0.9887	0.9991
$\alpha_d = 18°$	1.6384	2.2155	0.9971	0.9987
$\alpha_d = 8°$	1.4714	2.2129	0.9854	0.9995

Inverted spoiler, $h = 2.3\%$

α	A_i	A_o	B_o	R^2
$\alpha_u = 8°$	1.6476	2.1296	0.9973	0.9991
$\alpha_u = 18°$	1.5936	2.2244	1.0010	0.9993
$\alpha_u = 21°$	1.6952	2.2046	1.0131	0.9996
$\alpha_d = 18°$	1.7939	2.1578	0.9973	0.9995
$\alpha_d = 8°$	1.6798	2.1775	1.0023	0.9996

Plain spoiler, $h = 2.3\%$

α	A_i	A_o	B_o	R^2
$\alpha_u = 8°$	1.6909	2.0757	0.9973	0.9994
$\alpha_u = 18°$	1.6474	2.2292	0.9988	0.9995
$\alpha_u = 21°$	1.6519	2.1619	0.9983	0.9995
$\alpha_d = 18°$	1.7067	2.1237	0.9951	0.9997
$\alpha_d = 8°$	1.6450	2.2257	1.0027	0.9996

Symmetric strip, $2h = 2.3\%$

α	A_i	A_o	B_o	R^2
$\alpha_u = 8°$	1.6415	2.0998	0.9833	0.9994
$\alpha_u = 18°$	1.7572	2.1284	0.9934	0.9994
$\alpha_u = 21°$	1.6320	2.2304	0.9940	0.9994
$\alpha_d = 18°$	1.6435	2.2262	0.9967	0.9996
$\alpha_d = 8°$	1.5497	2.1343	0.9817	0.9992

25% trailing-edge tab, $\delta = 5.3°$

α	A_i	A_o	B_o	R^2
$\alpha_u = 8°$	1.4397	2.1362	0.9847	0.9988
$\alpha_u = 18°$	2.0124	2.2001	1.0291	0.9983
$\alpha_u = 21°$	1.7704	2.2746	1.0337	0.9978
$\alpha_d = 18°$	1.6691	2.1801	0.9978	0.9990
$\alpha_d = 8°$	1.4436	2.2919	0.9892	0.9994

25% trailing-edge tab, $\delta = -5.3°$

α	A_i	A_o	B_o	R^2
$\alpha_u = 8°$	1.4242	2.3117	0.9906	0.9990
$\alpha_u = 18°$	1.5809	2.2610	0.9983	0.9994
$\alpha_u = 21°$	1.5965	2.1222	0.9800	0.9992
$\alpha_d = 18°$	1.5030	2.2169	0.9970	0.9988
$\alpha_d = 8°$	1.4797	2.2808	0.9965	0.9994

Table 7 Vortex self-symmetry curve-fit constants for the case $\alpha_o = 14°$ and $\Delta\alpha = 8°$ with $\kappa = 0.09$, at $x/c = 2$, for the different trailing-edge configurations.

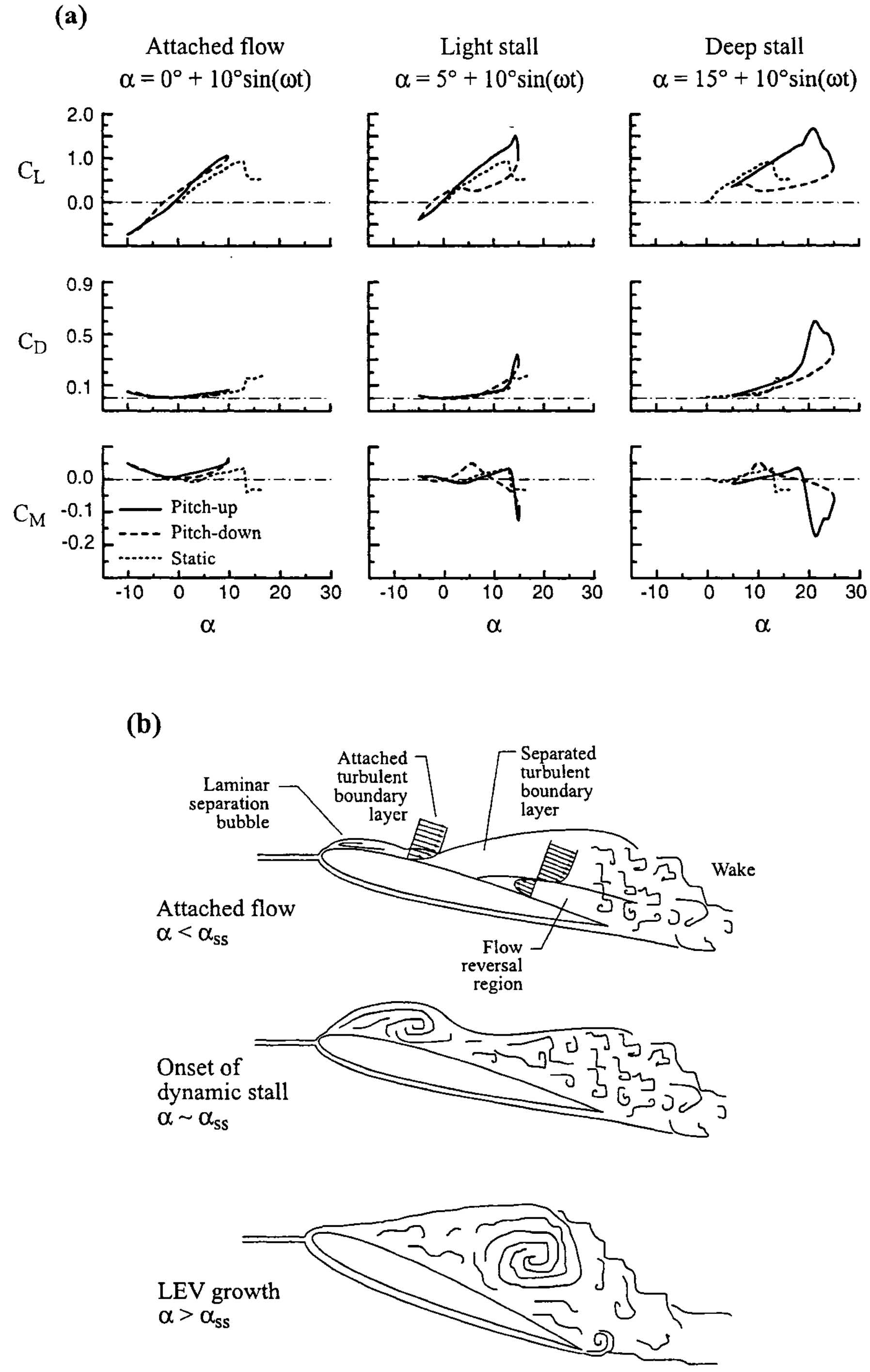

Figure 1 Typical loads and flow patterns for an oscillating, two-dimensional airfoil. (a) Comparison of loads between attached flow, light stall and deep stall cases (reproduced from Lee and Gerontakos, 2004); (b) conceptual sketch of flow patterns; (c) illustration of the progression of major boundary layer and flow events through a cycle of oscillation (reproduced from Carr, 1987).

(c)

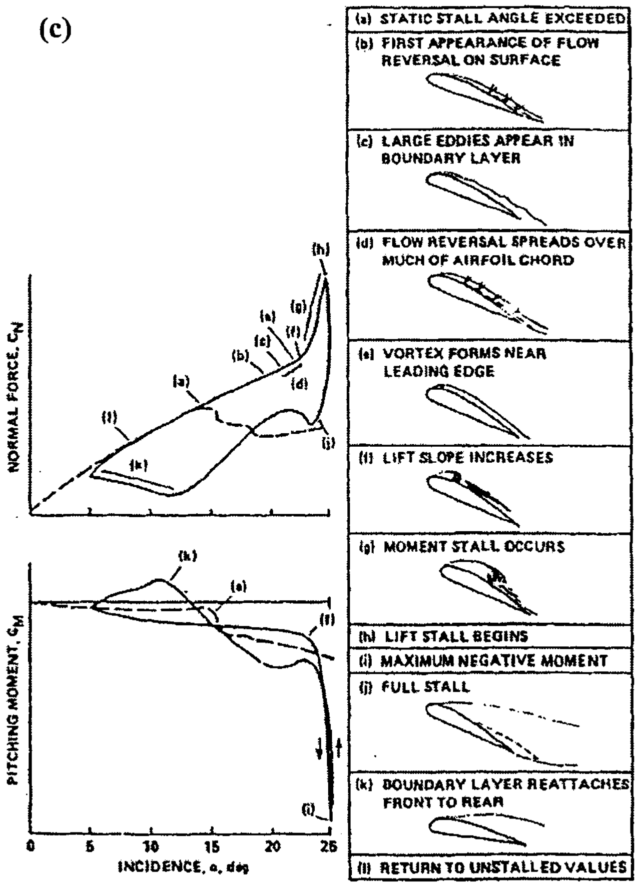

Figure 1 Typical loads and flow patterns for an oscillating, two-dimensional airfoil. (a) Comparison of loads between attached flow, light stall and deep stall cases (reproduced from Lee and Gerontakos, 2004); (b) conceptual sketch of flow patterns; (c) illustration of the progression of major boundary layer and flow events through a cycle of oscillation (reproduced from Carr, 1987).

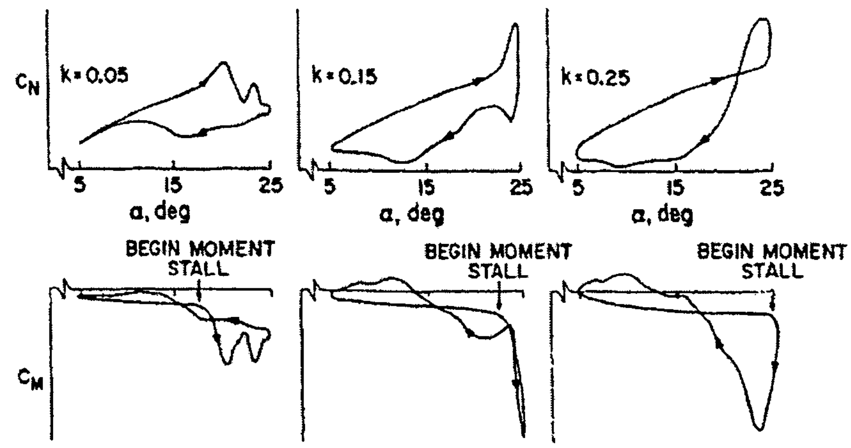

Figure 2 Variation of airfoil loads with frequency for an oscillating, two-dimensional airfoil (reproduced from McCroskey et. al., 1976)

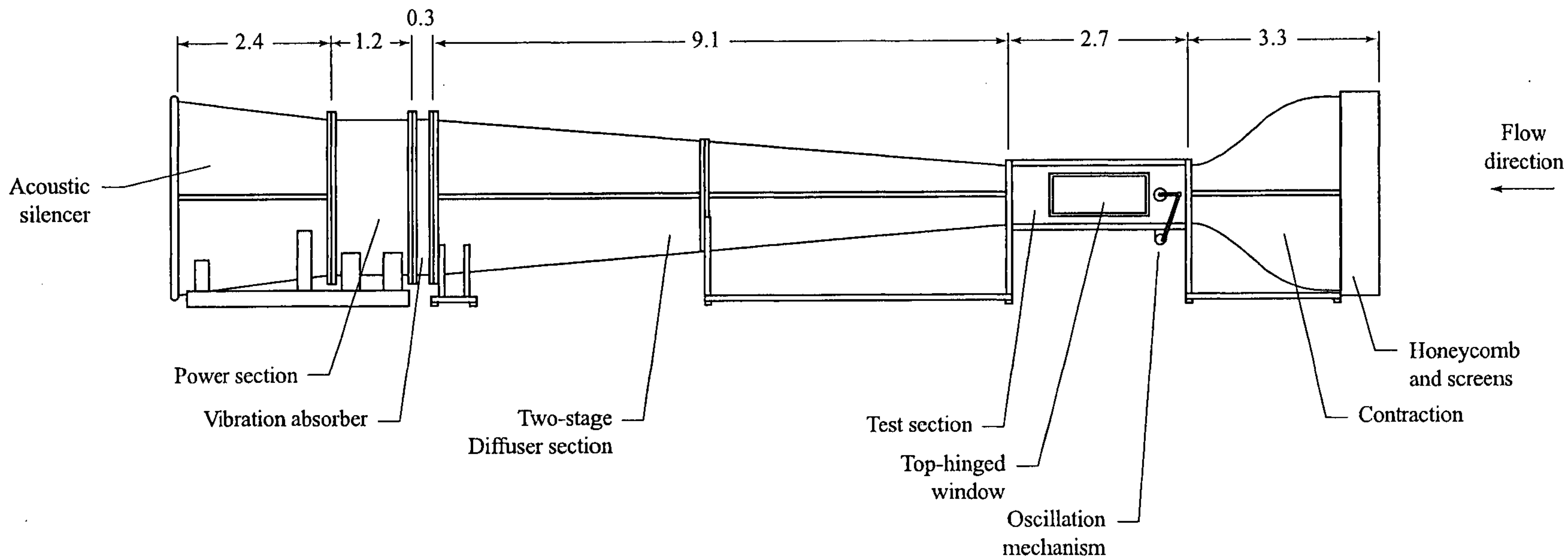

Figure 3 Schematic of the J.A. Bombardier low-turbulence wind-tunnel. All dimensions indicated are in meters.

a)

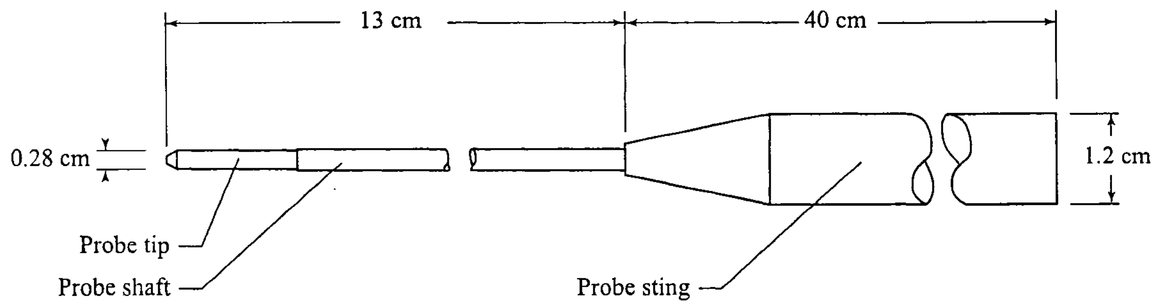

b)

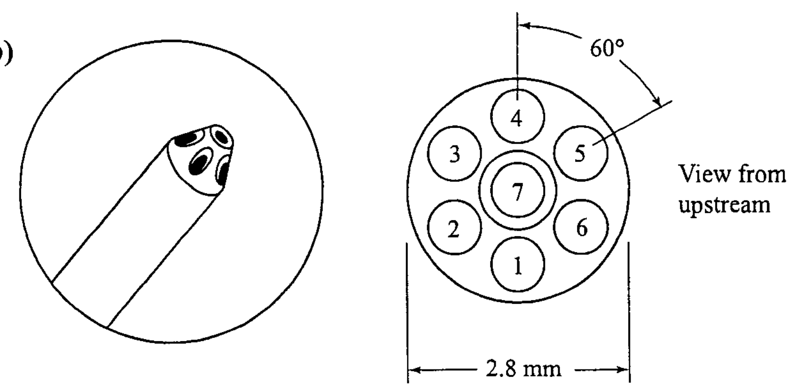

Figure 4 Seven-hole probe geometry. (a) Probe shaft and sting assembly; (b) probe tip geometry. Numbers indicate hole index.

a)

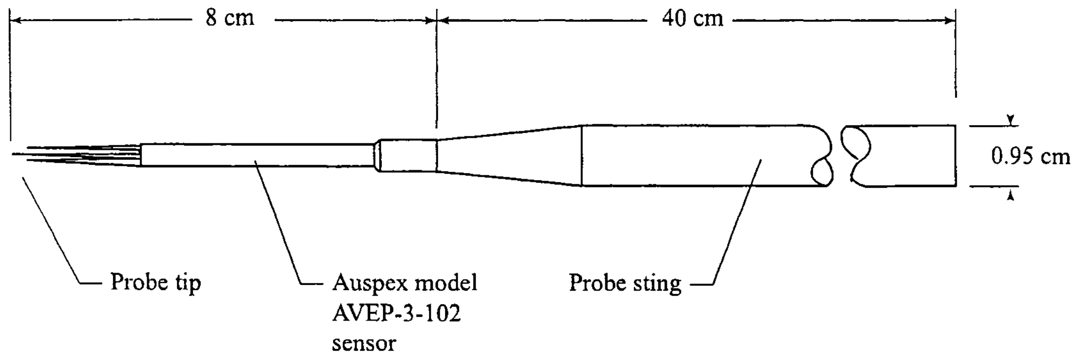

b)

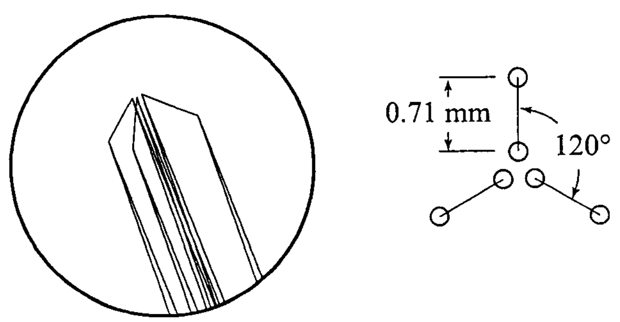

Figure 5 Triple-sensor hot-wire probe geometry. (a) Sensor and sting assembly; (b) sensor tip geometry.

a)

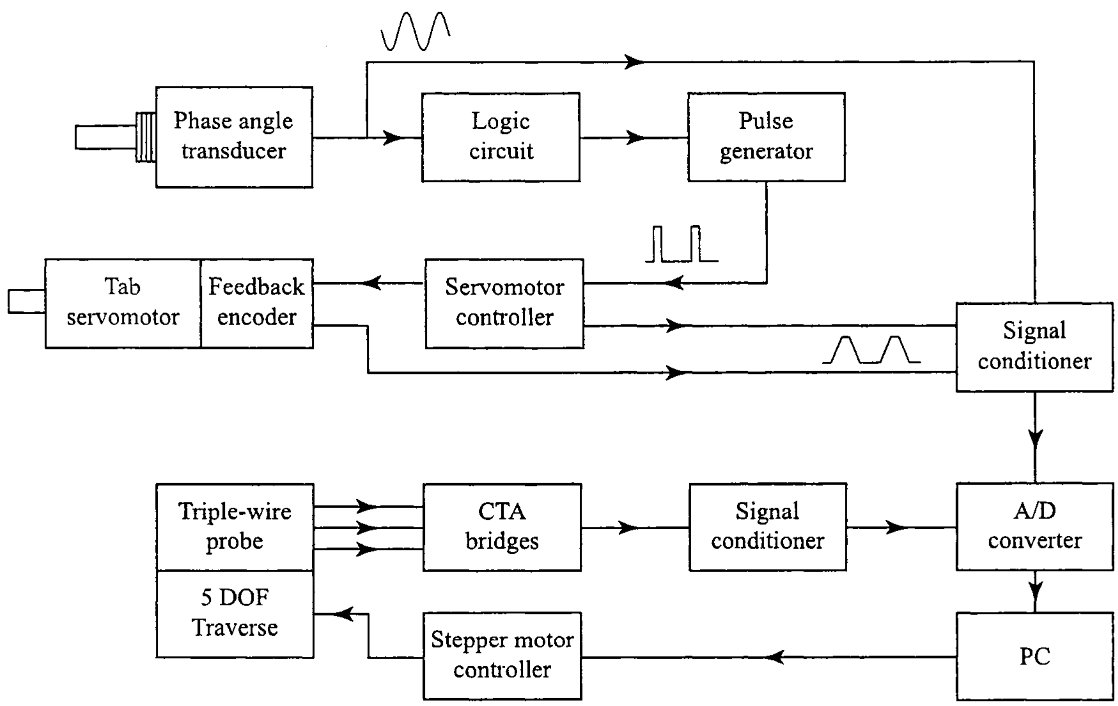

Figure 6 (a) Instrumentation setup for triple-sensor hot-wire measurement; (b) wing model with actuated tab, and (c) oscillation mechanism output.

b)

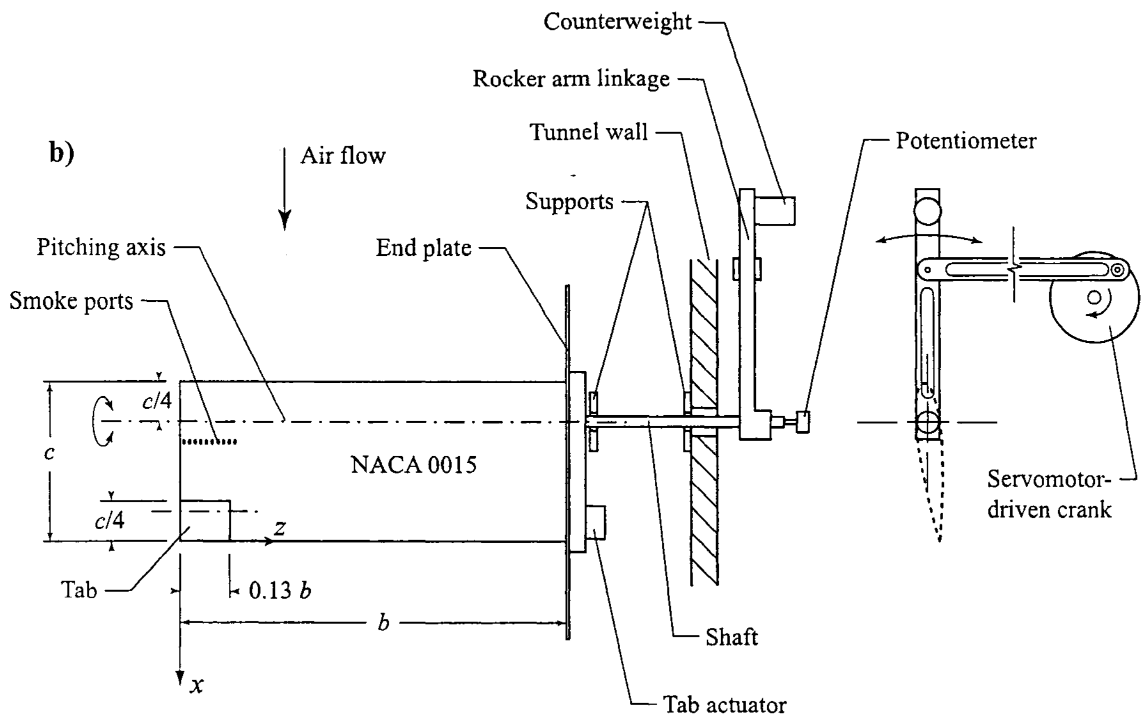

c)

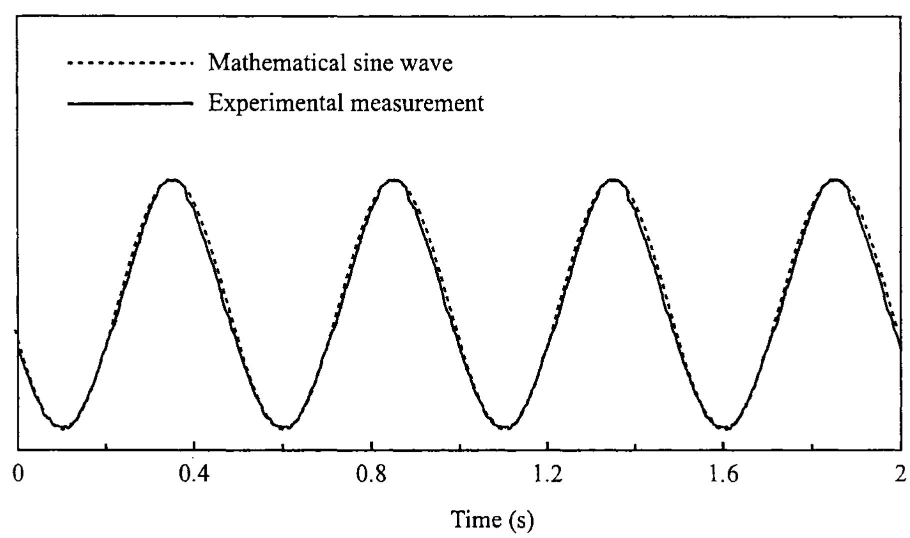

Figure 6 (a) Instrumentation setup for triple-sensor hot-wire measurement; (b) wing model with actuated tab, and (c) oscillation mechanism output.

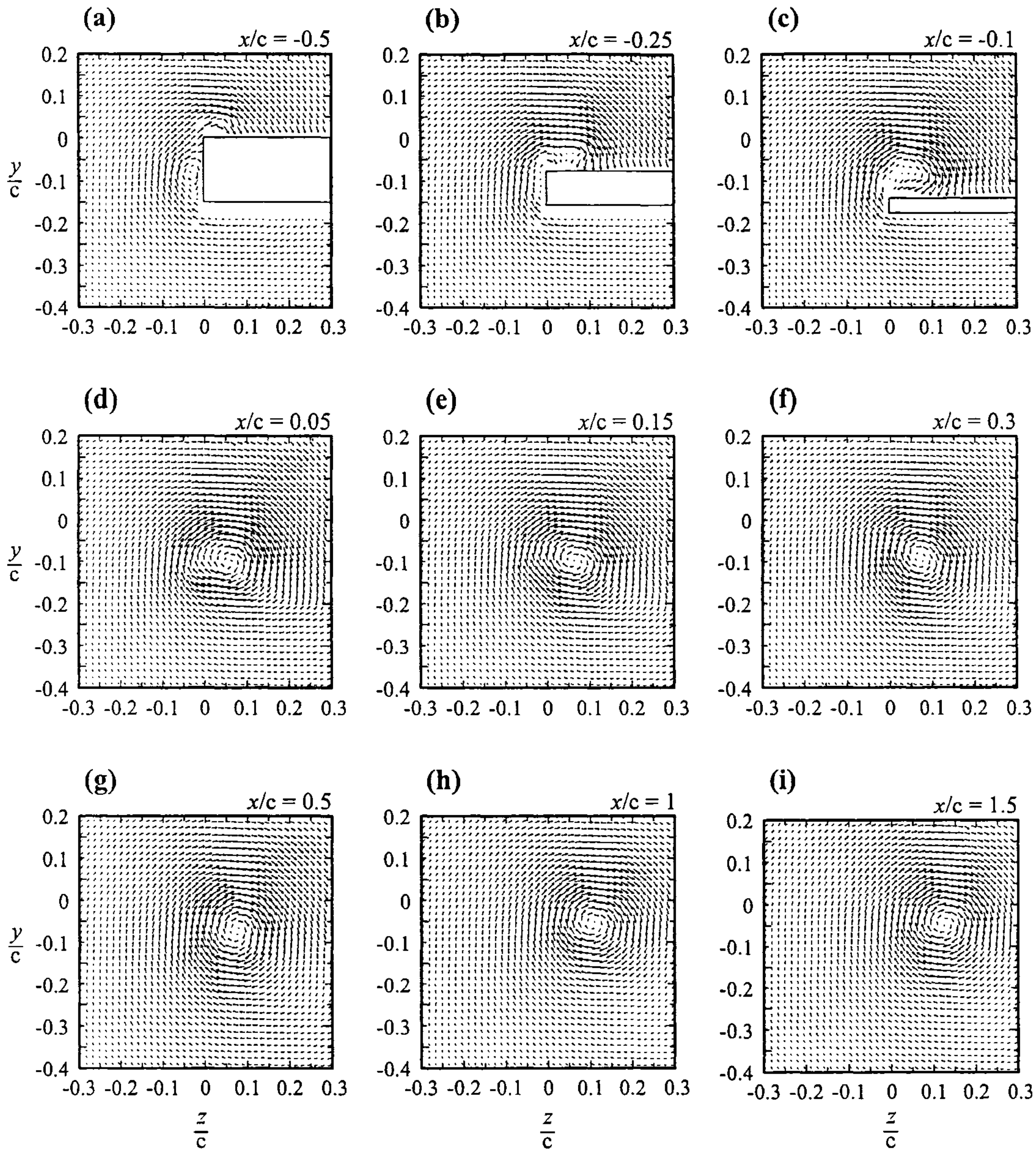

Figure 7 Cross-flow velocity fields behind a static wing at $\alpha = 10°$. Rectangles inset in (a), (b) and (c) represent local wing cross-section.

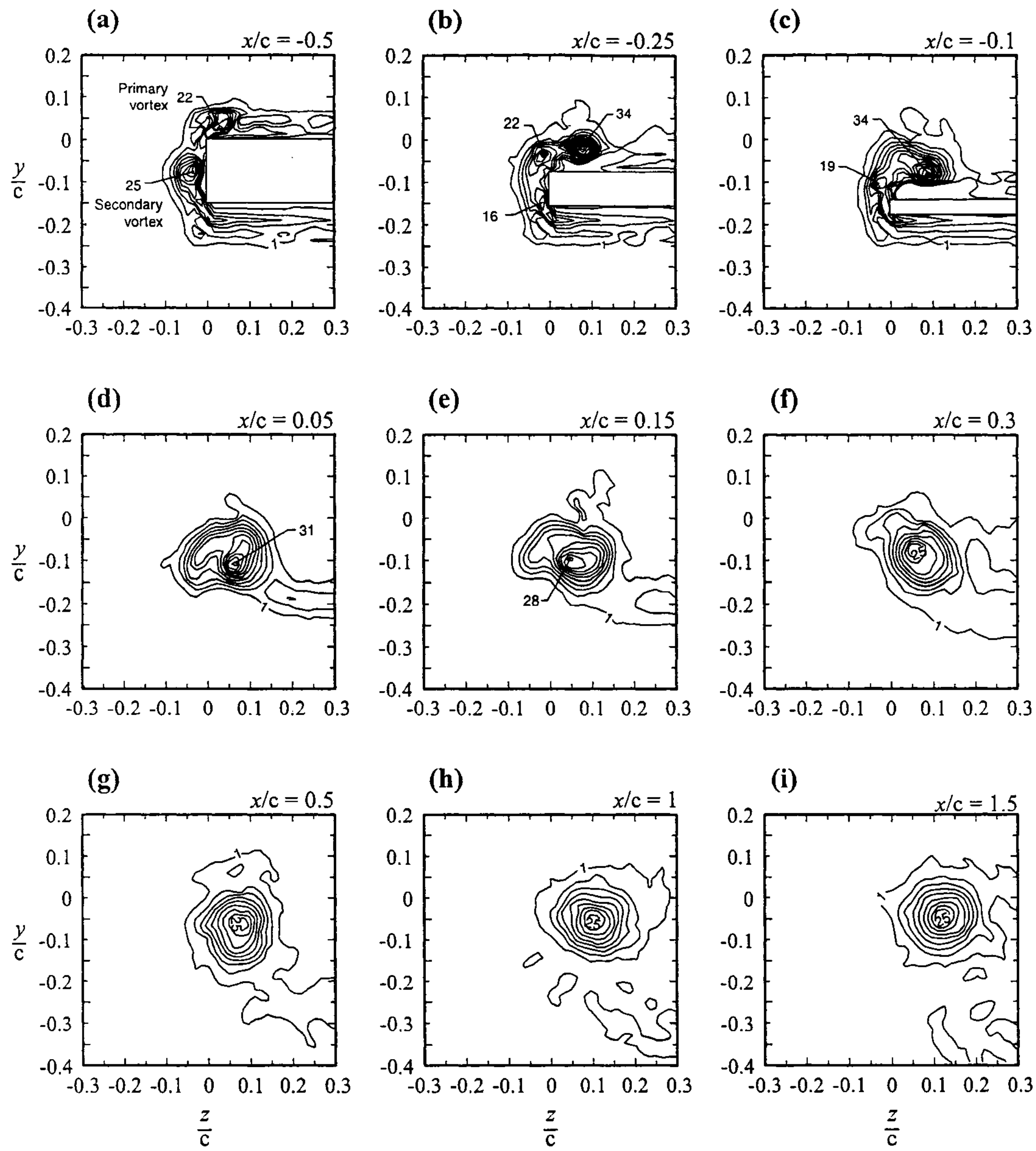

Figure 8 Contours of constant $\zeta c/u_\infty$ behind a static wing at α = 10°, with constant contour level increments of $\zeta c/u_\infty$ = 3. Rectangles inset in (a), (b) and (c) represent local wing cross-section.

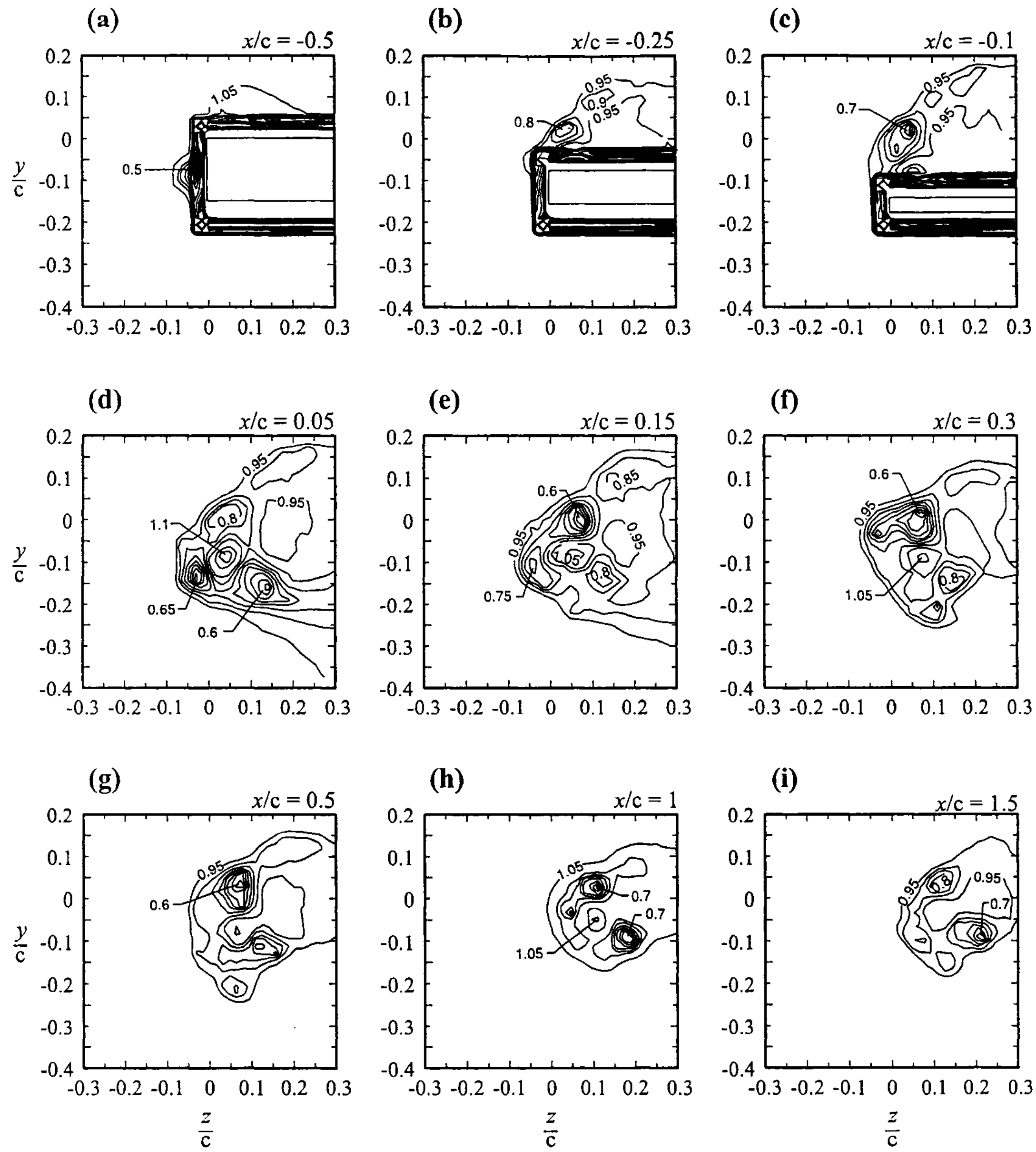

Figure 9 Contours of constant u/u_∞ behind a static wing at $\alpha = 10°$, with constant contour level increments of $u/u_\infty = 0.05$. Rectangles inset in (a), (b) and (c) represent local wing cross-section.

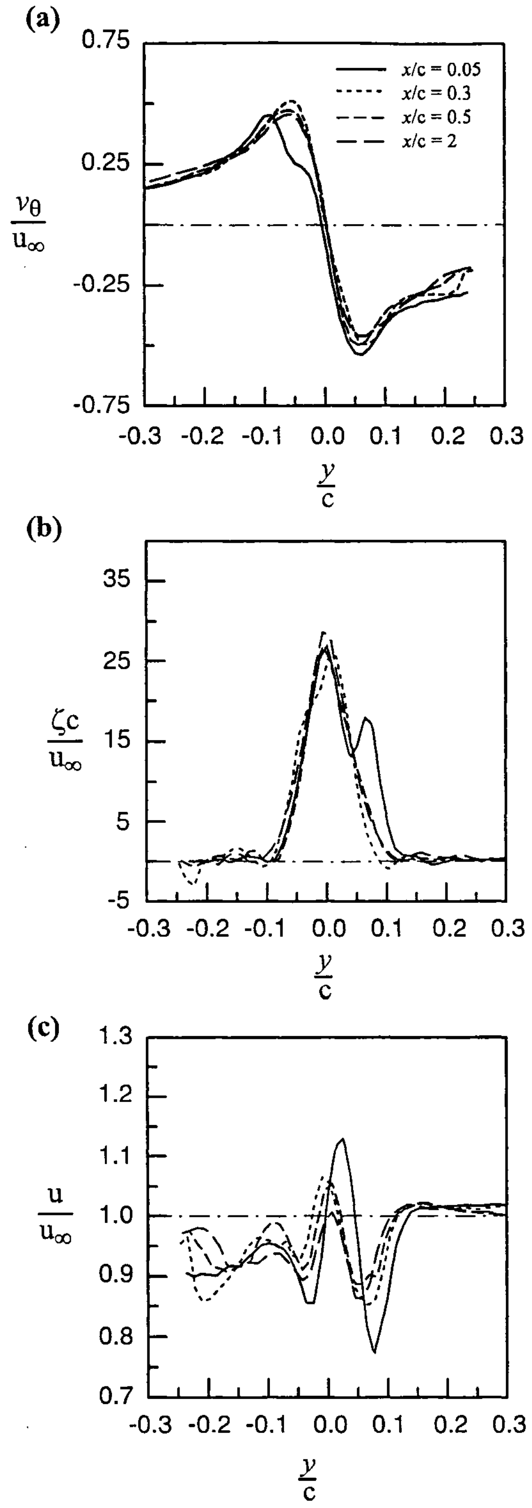

Figure 10 Vortex flow quantities measured across the static vortex center, with $\alpha = 10°$. (a) Tangential velocity; (b) vorticity and (c) axial velocity.

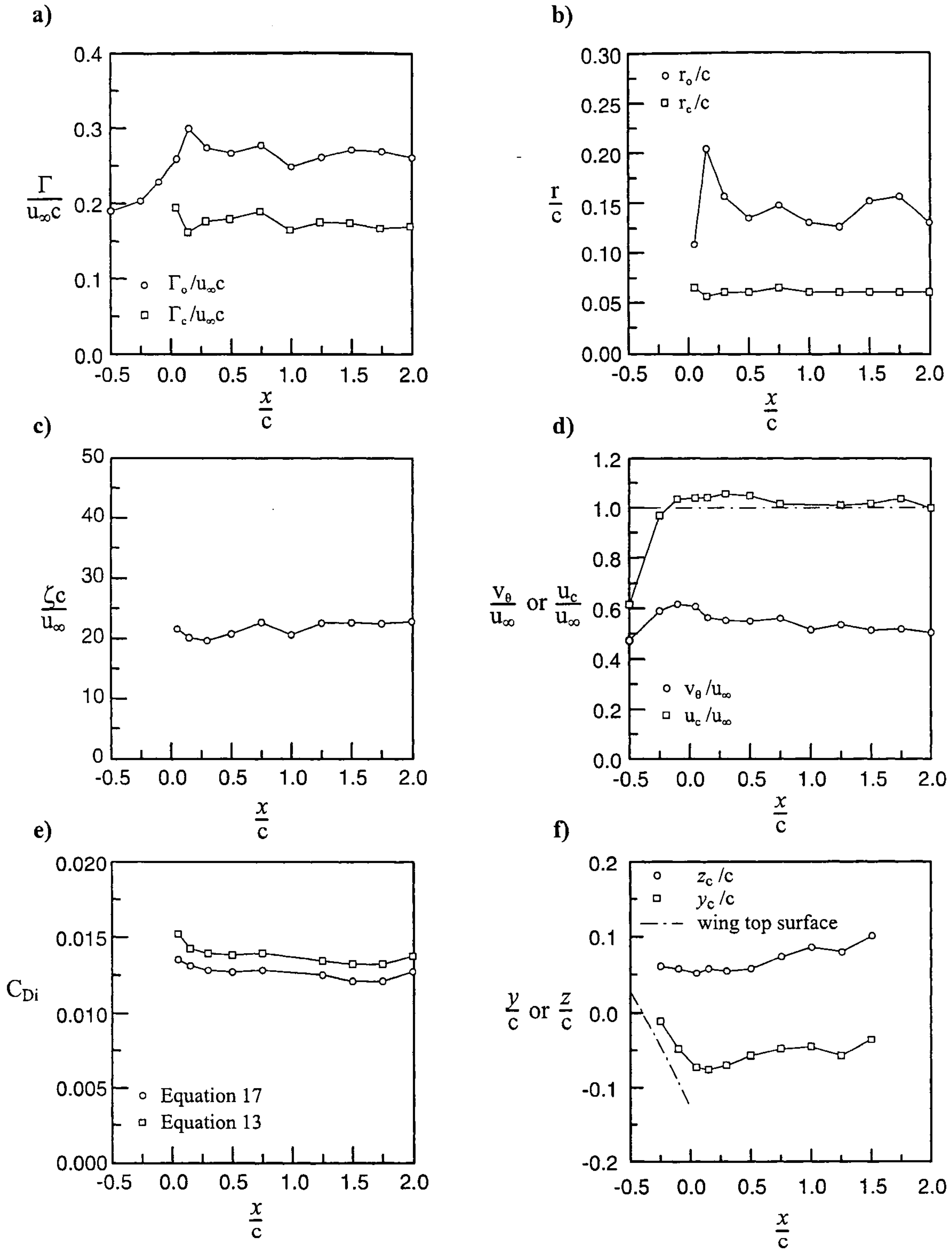

Figure 11 Variation of critical vortex quantities with x/c, for α = 10°. (a) Core and outer circulation; (b) core and outer radius; (c) peak vorticity; (d) peak tangential and core axial velocity; (e) induced drag, and (f) vortex trajectory.

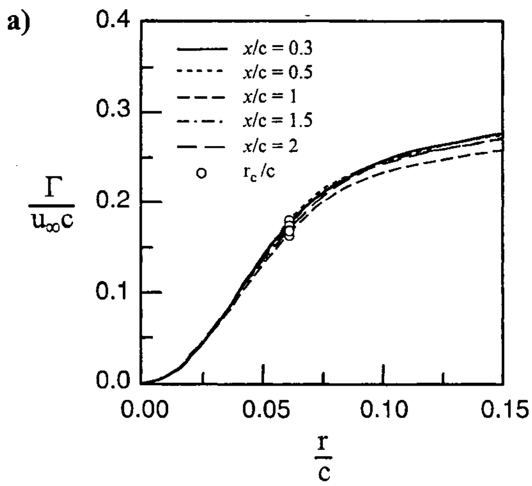

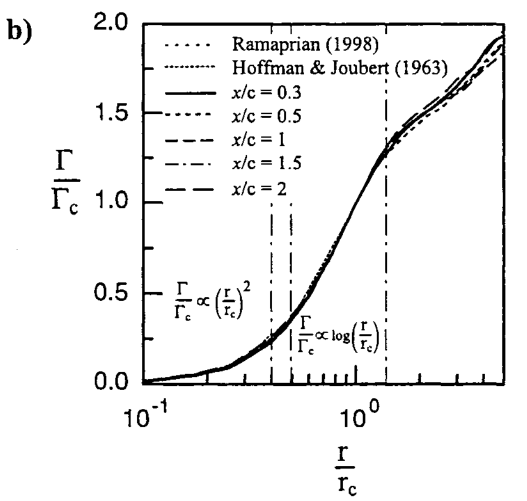

Figure 12 Radial circulation distribution for the static vortex at α = 10°. (a) normalized against $u_{\infty}c$; (b) self-scaled.

(a)

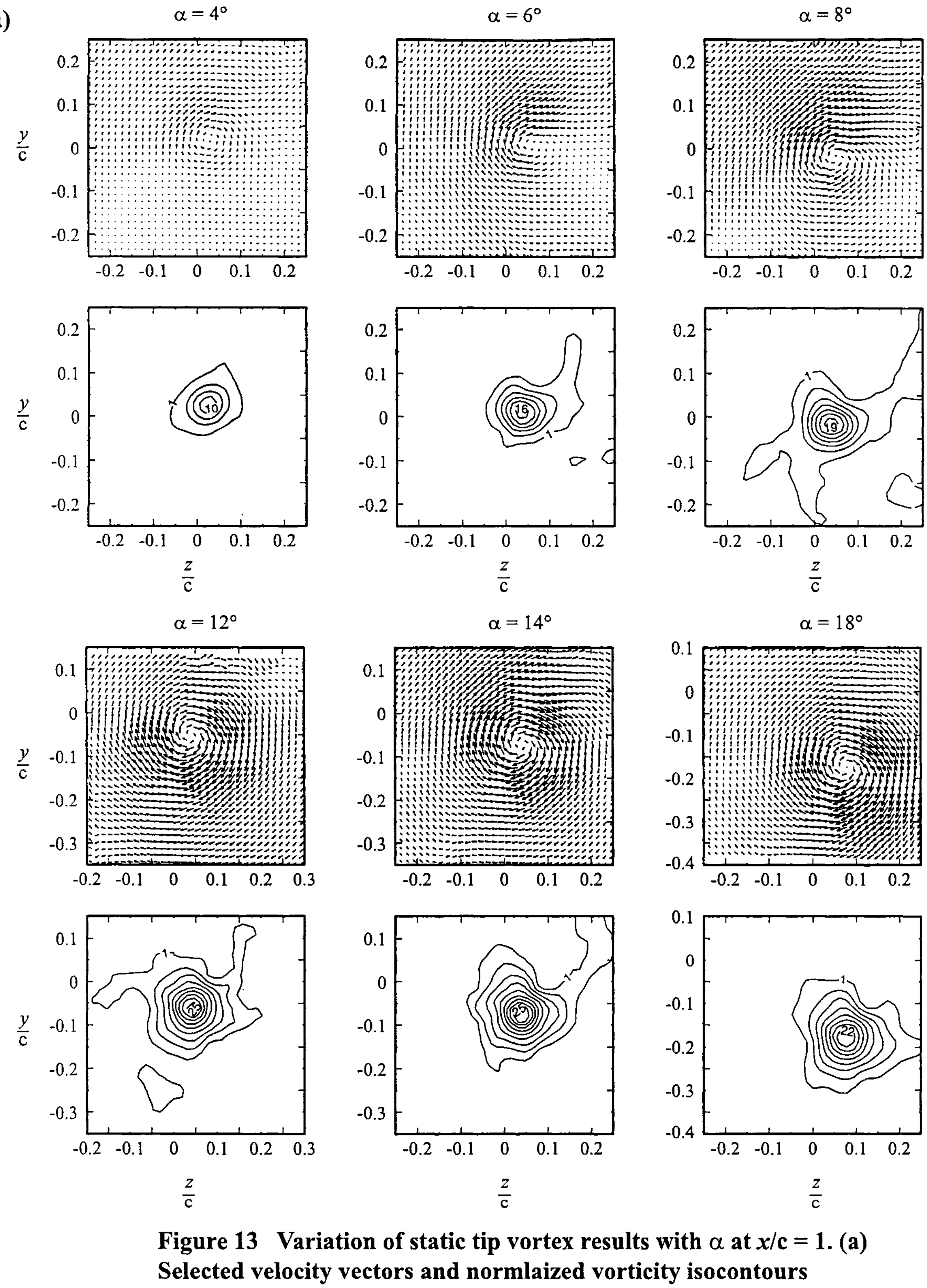

Figure 13 Variation of static tip vortex results with α at $x/c = 1$. (a) Selected velocity vectors and normlaized vorticity isocontours (with a constant increment $\zeta c/u_\infty = 3$), and composite plots of the (b) normalized vorticity, (c) normalized axial mean velocity, and (c) axial RMS velocity. Numerical values in (b) - (d) denote $\zeta c/u_\infty$, u/u_∞ and u'/u_∞ (%) levels with constant increments of 3, 0.05 and 2, respectively.

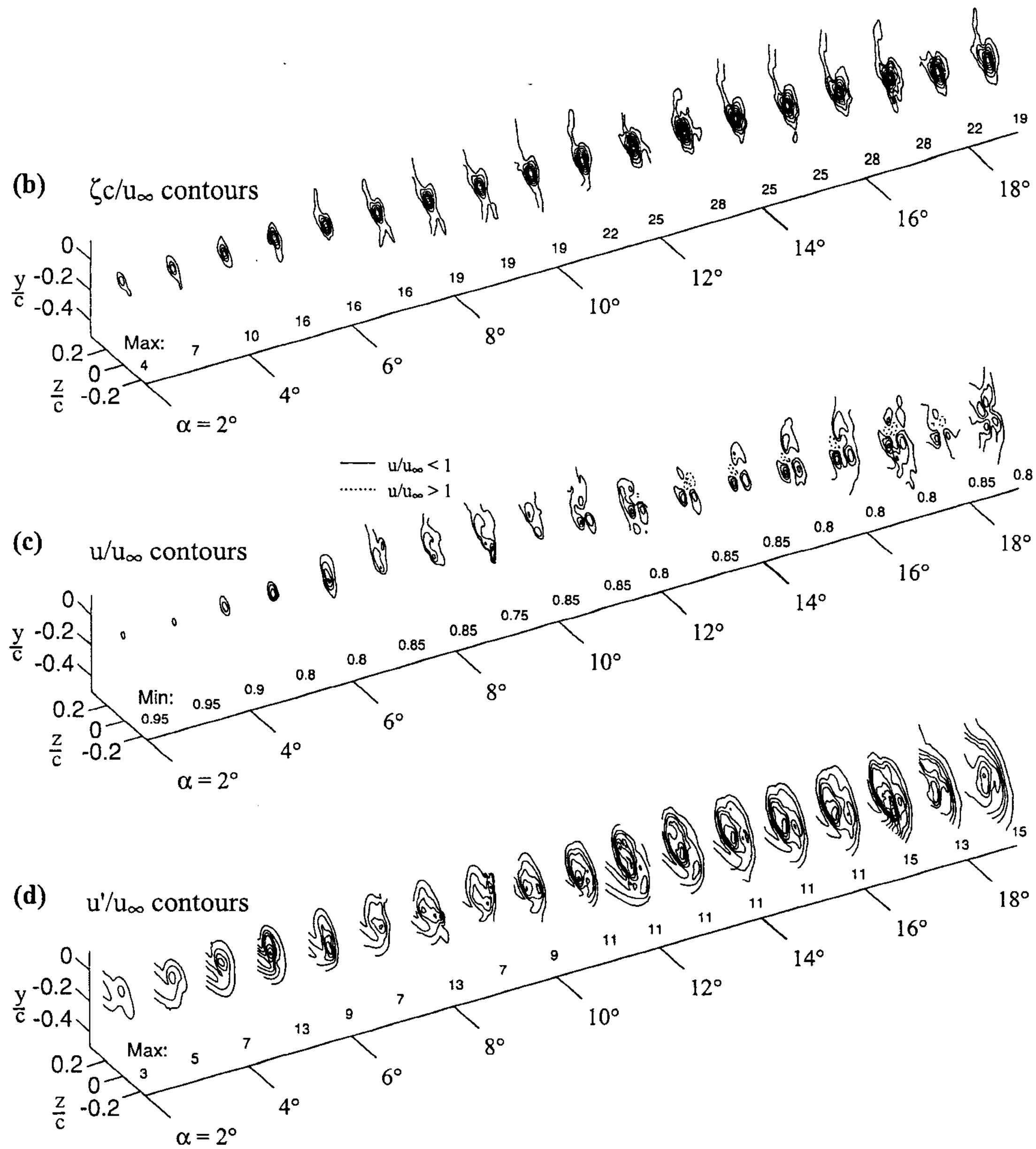

Figure 13 Variation of static tip vortex results with α at $x/c = 1$. (a) Selected velocity vectors and normlaized vorticity isocontours (with a constant increment $\zeta c/u_\infty = 3$), and composite plots of the (b) normalized vorticity, (c) normalized axial mean velocity, and (c) axial RMS velocity. Numerical values in (b) - (d) denote $\zeta c/u_\infty$, u/u_∞ and u'/u_∞ (%) levels with constant increments of 3, 0.05 and 2, respectively.

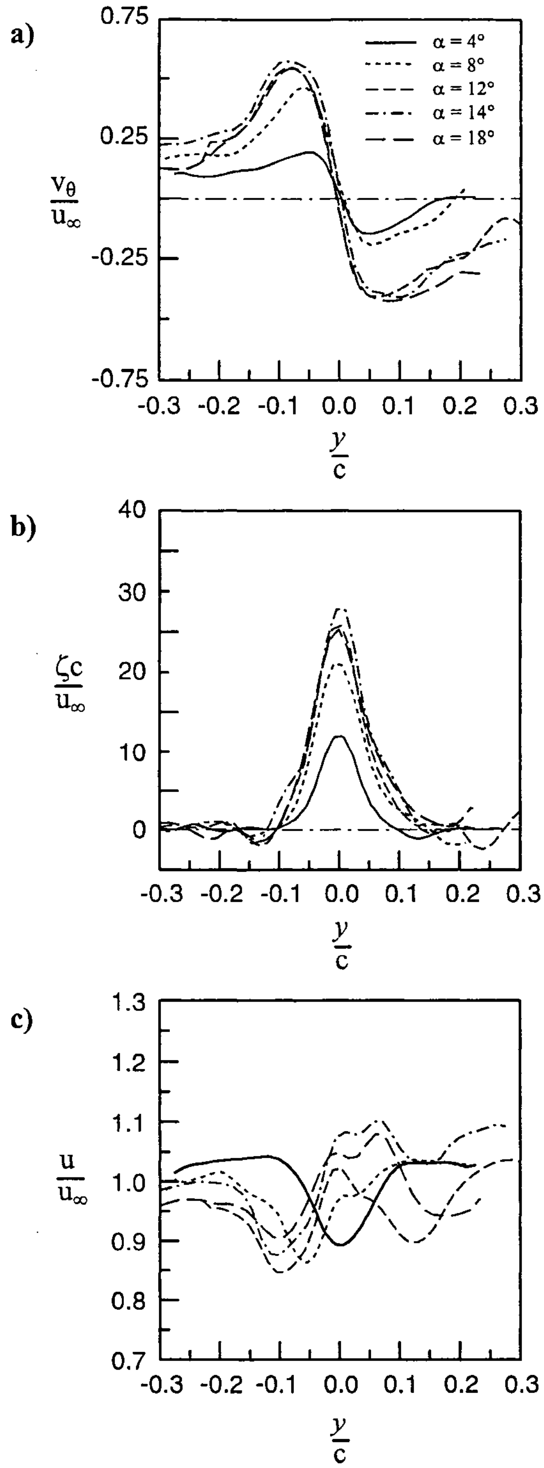

Figure 14 Vortex flow quantities measured across the static vortex center, with $x/c = 1$. (a) Tangential velocity; (b) vorticity, and (c) axial velocity.

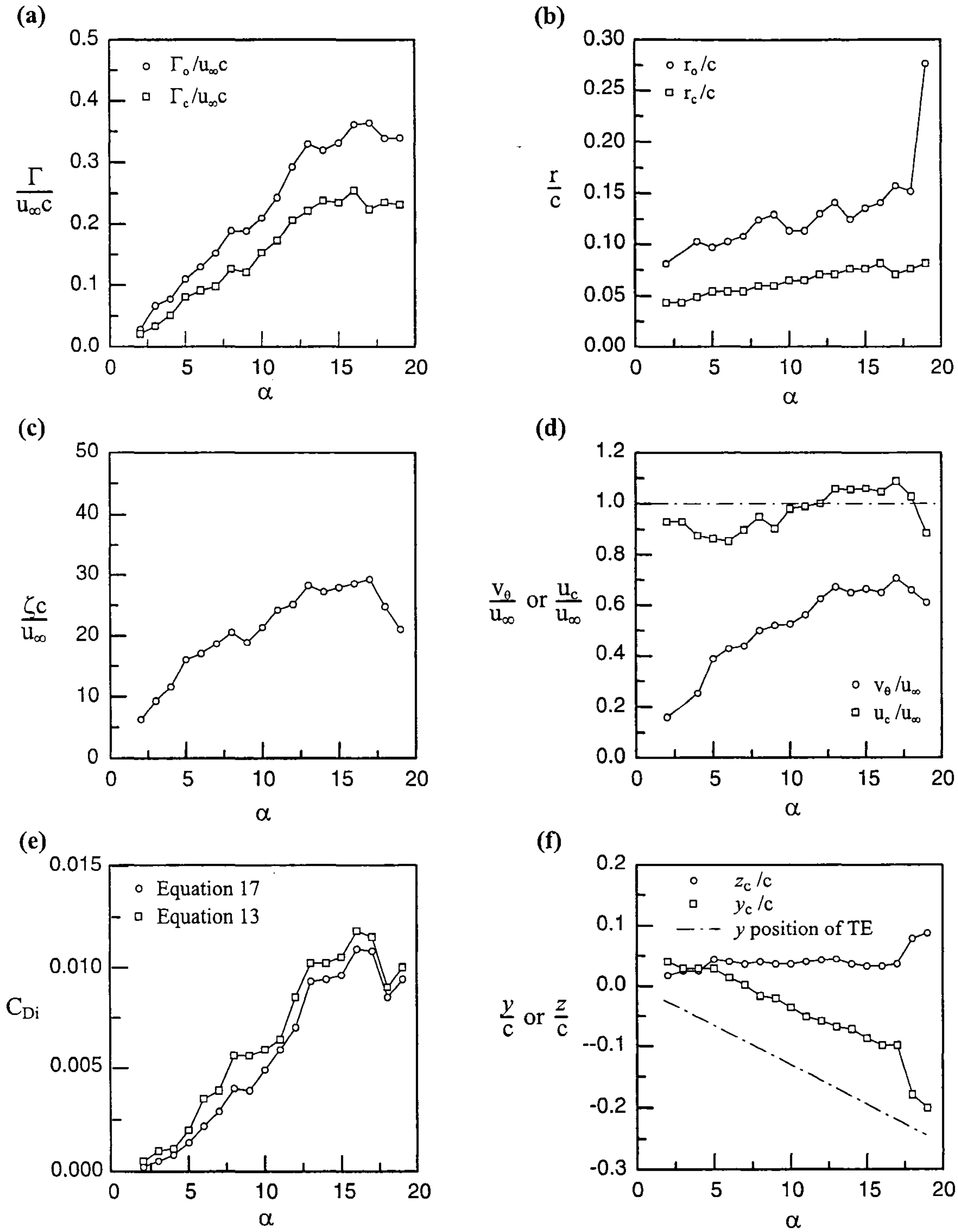

Figure 15 Variation of critical vortex quantities with α for x/c,= 1. (a) Core and outer circulation; (b) core and outer radius; (c) peak vorticity; (d) peak tangential and core axial velocity; (e) induced drag, and (f) vortex trajectory.

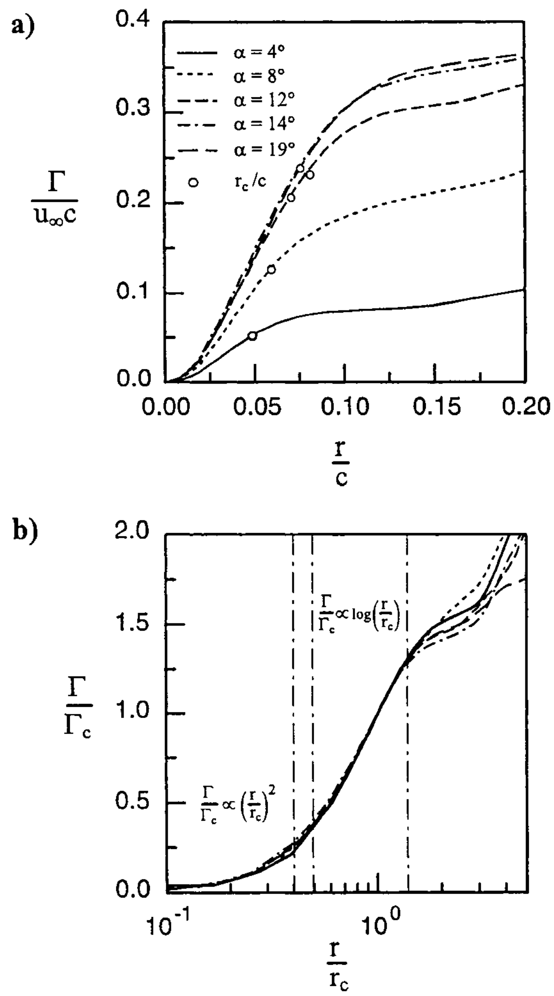

Figure 16 Radial circulation distribution for the static vortex at ***x*/c = 1. (a) normalized against $u_\infty c$; (b) self-scaled.**

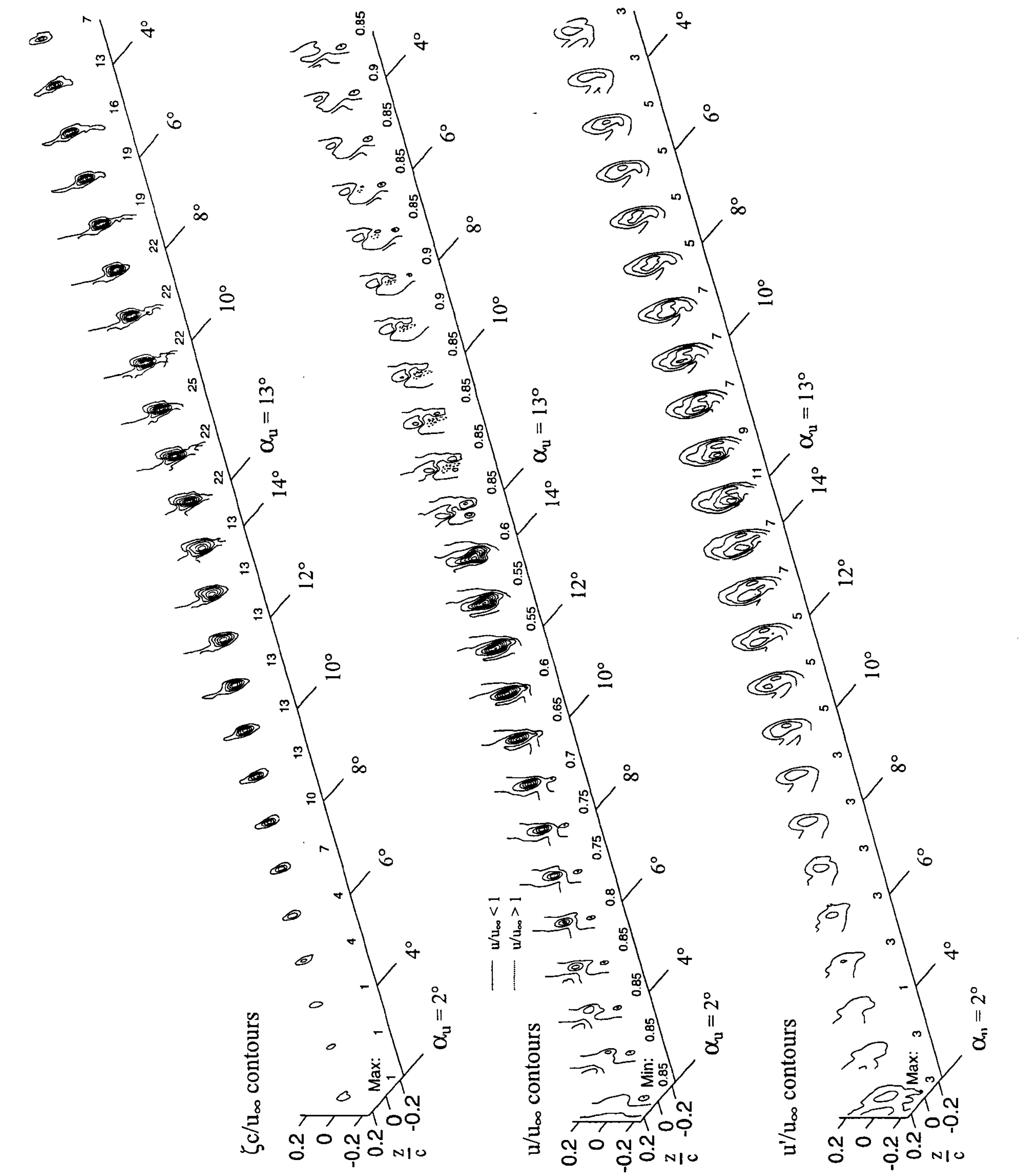

Figure 17 Variation of vortex results for the attached flow case of $\alpha = 8° + 6°\sin(\omega t)$ and $\kappa = 0.18$ at $x/c = 1$. (a) Vorticity; (b) axial mean velocity, and (c) axial RMS velocity. Numerical values denote $\zeta c/u_\infty$, u/u_∞ and u'/u_∞ (%) levels with constant increments of 3, 0.05 and 2, respectively.

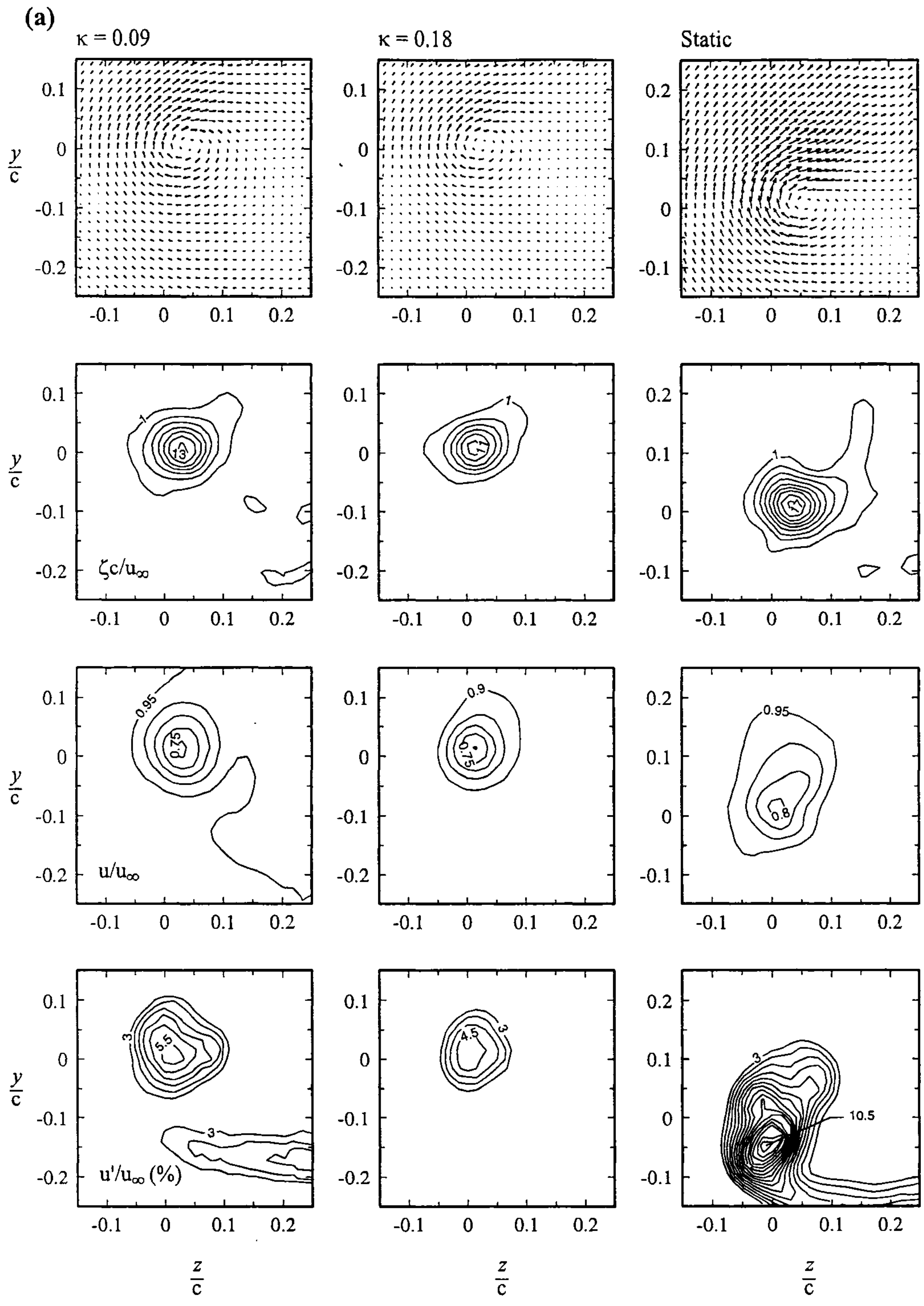

Figure 18 Velocity vectors and contours of constant vorticity, axial mean and RMS velocities at $x/c = 1$. (a) $\alpha_{c,u} = 6°$; (b) $\alpha_{c,u} = 12°$; (c) $\alpha_{c,d} = 12°$; (d) $\alpha_{c,d} = 6°$.

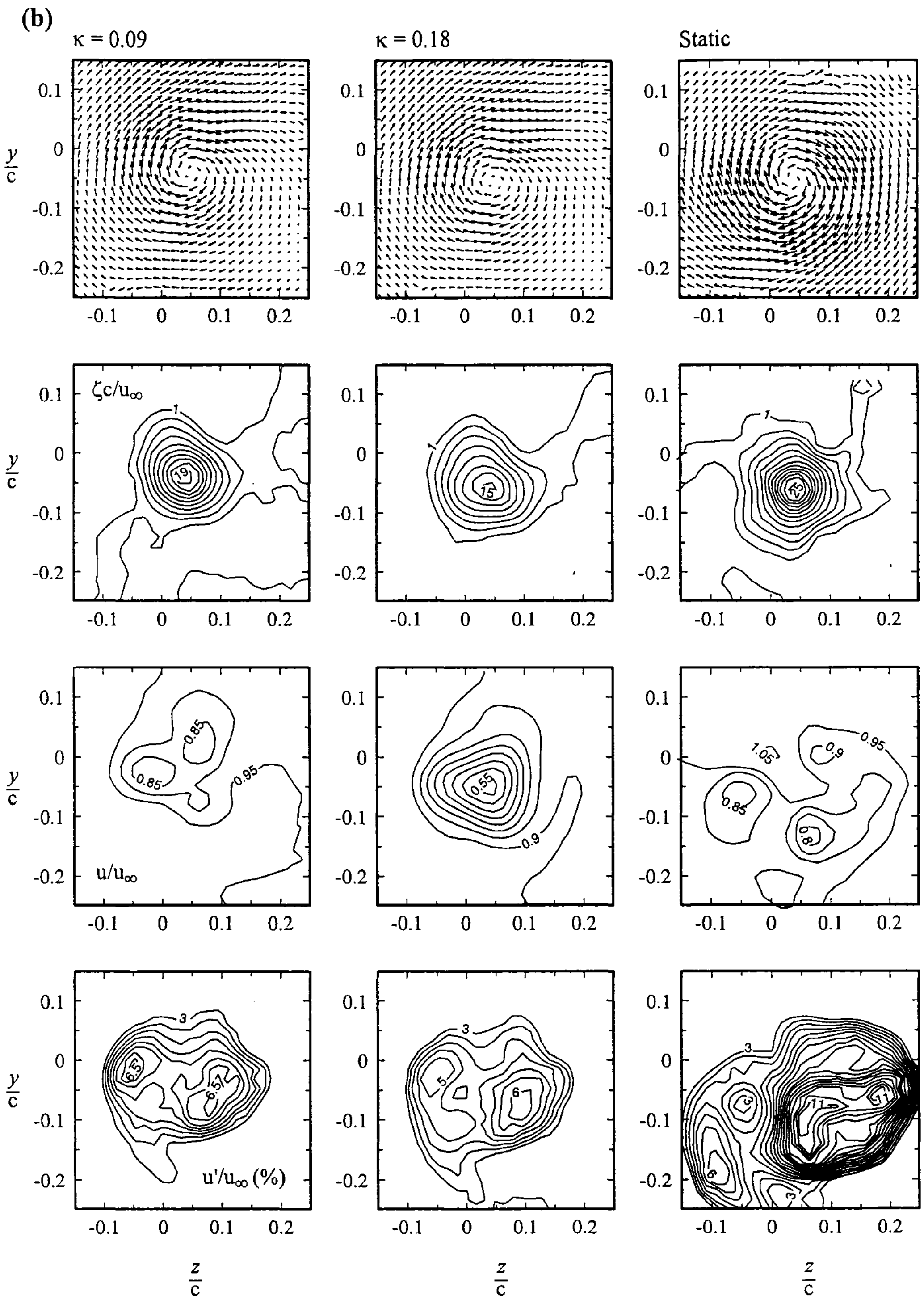

Figure 18 Velocity vectors and contours of constant vorticity, axial mean and RMS velocities at $x/c = 1$. (a) $\alpha_{c,u} = 6°$; (b) $\alpha_{c,u} = 12°$; (c) $\alpha_{c,d} = 12°$; (d) $\alpha_{c,d} = 6°$.

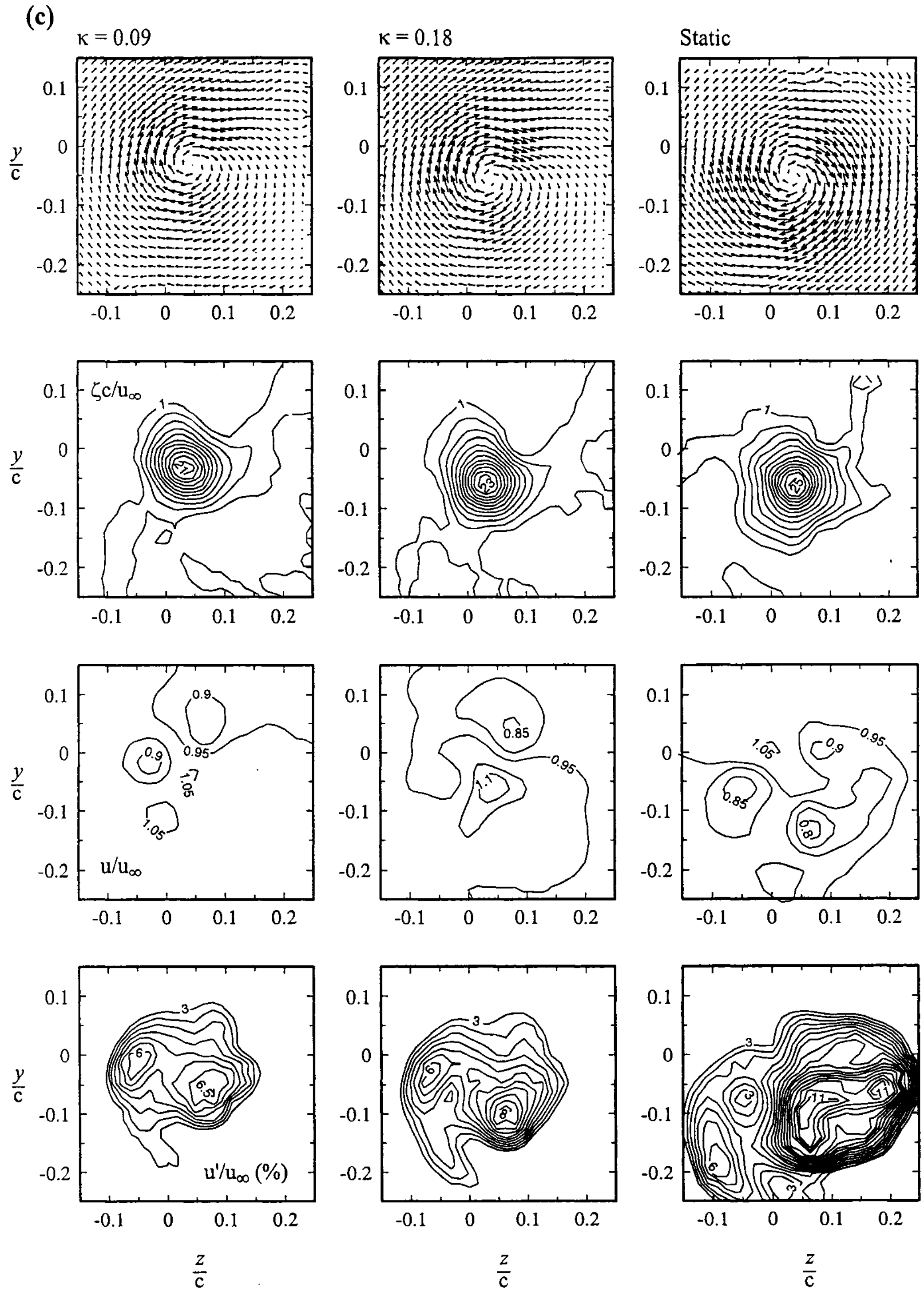

Figure 18 Velocity vectors and contours of constant vorticity, axial mean and RMS velocities at $x/c = 1$. (a) $\alpha_{c,u} = 6°$; (b) $\alpha_{c,u} = 12°$; (c) $\alpha_{c,d} = 12°$; (d) $\alpha_{c,d} = 6°$.

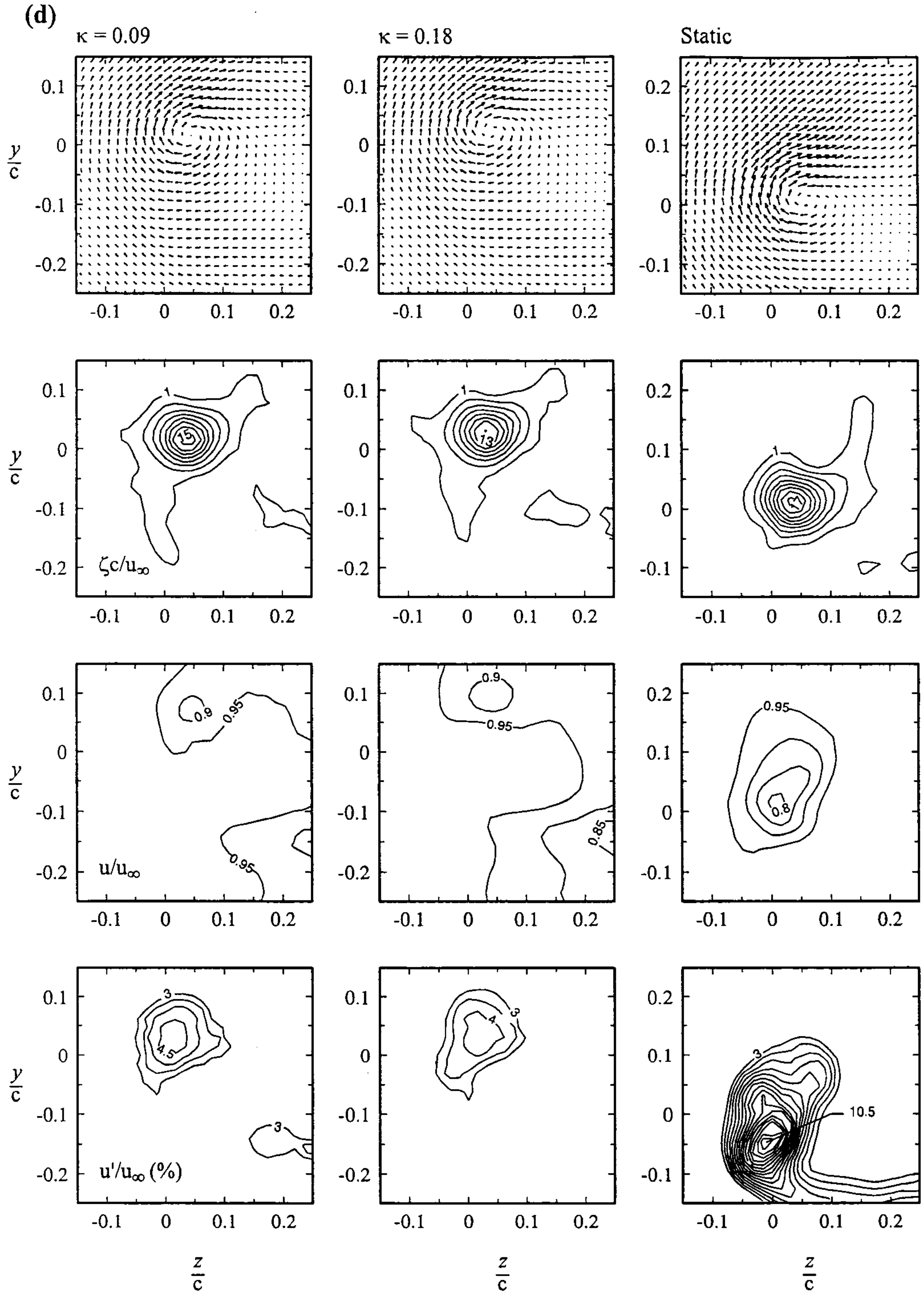

Figure 18 Velocity vectors and contours of constant vorticity, axial mean and RMS velocities at $x/c = 1$. (a) $\alpha_{c,u} = 6°$; (b) $\alpha_{c,u} = 12°$; (c) $\alpha_{c,d} = 12°$; (d) $\alpha_{c,d} = 6°$.

a)

b)

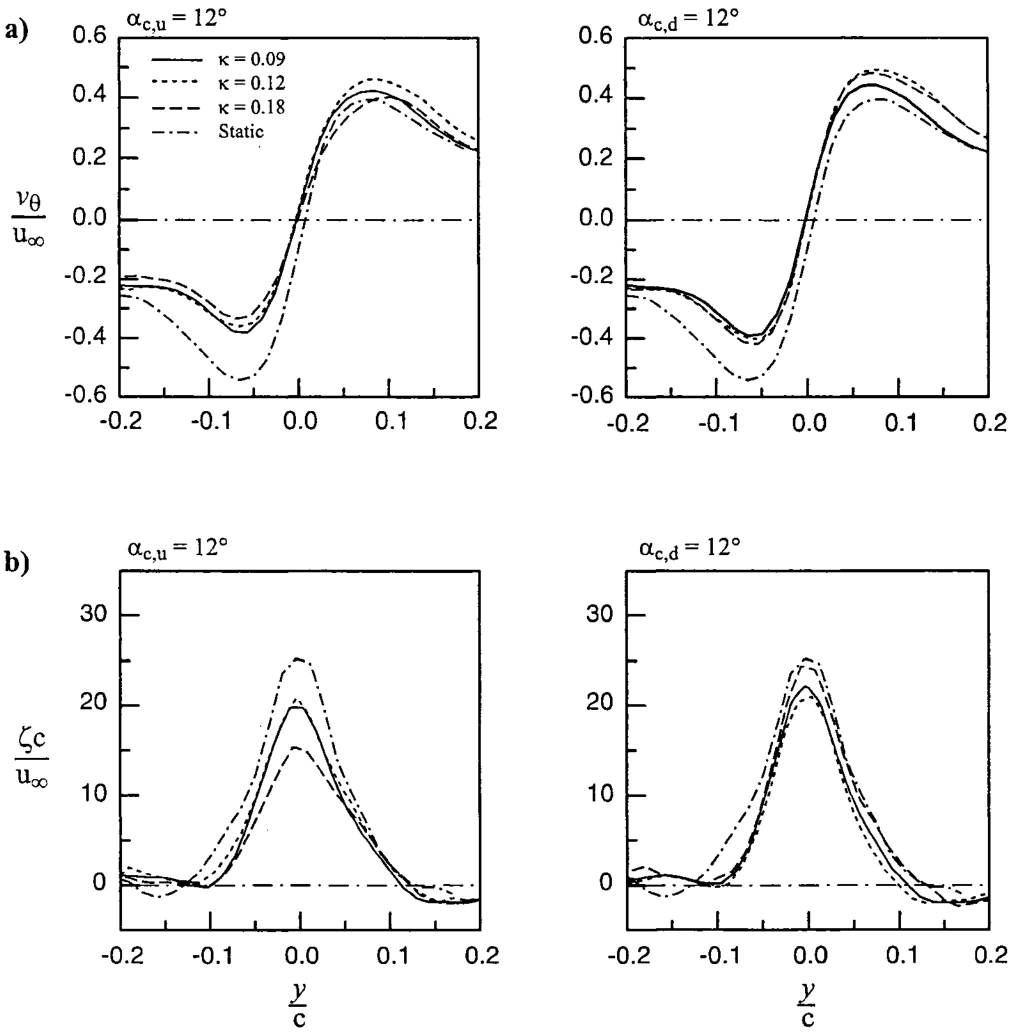

Figure 19 Vortex flow quantities measured across the vortex center at $x/c = 1$, with $\alpha = 8° + 6°\sin(\omega t)$. (a) Tangential velocity; (b) vorticity; (c) axial velocity; (d) axial RMS velocity, and (e) scaled axial RMS velocity.

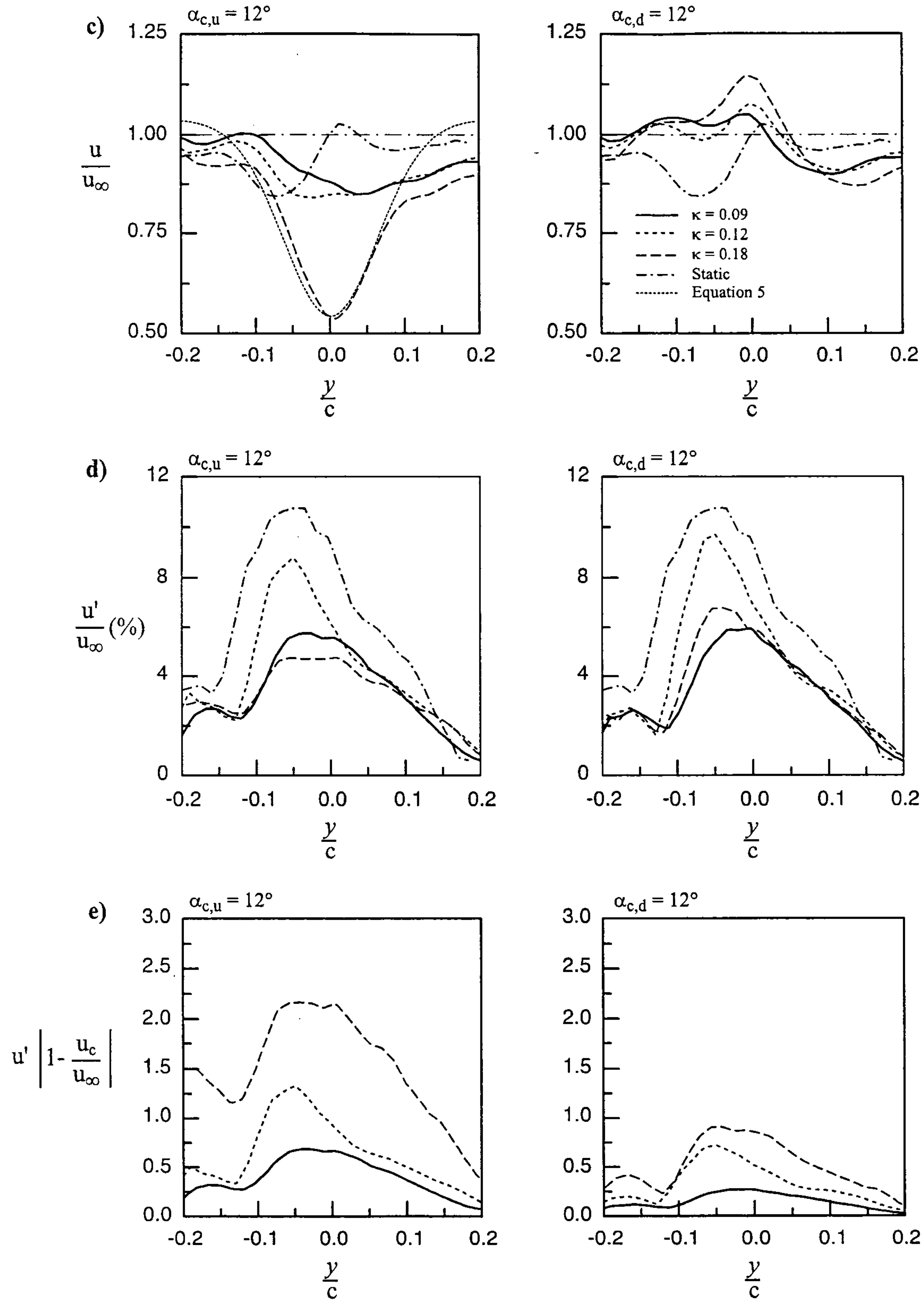

Figure 19 Vortex flow quantities measured across the vortex center at $x/c = 1$, with $\alpha = 8° + 6°\sin(\omega t)$. (a) Tangential velocity; (b) vorticity; (c) axial velocity; (d) axial RMS velocity, and (e) scaled axial RMS velocity.

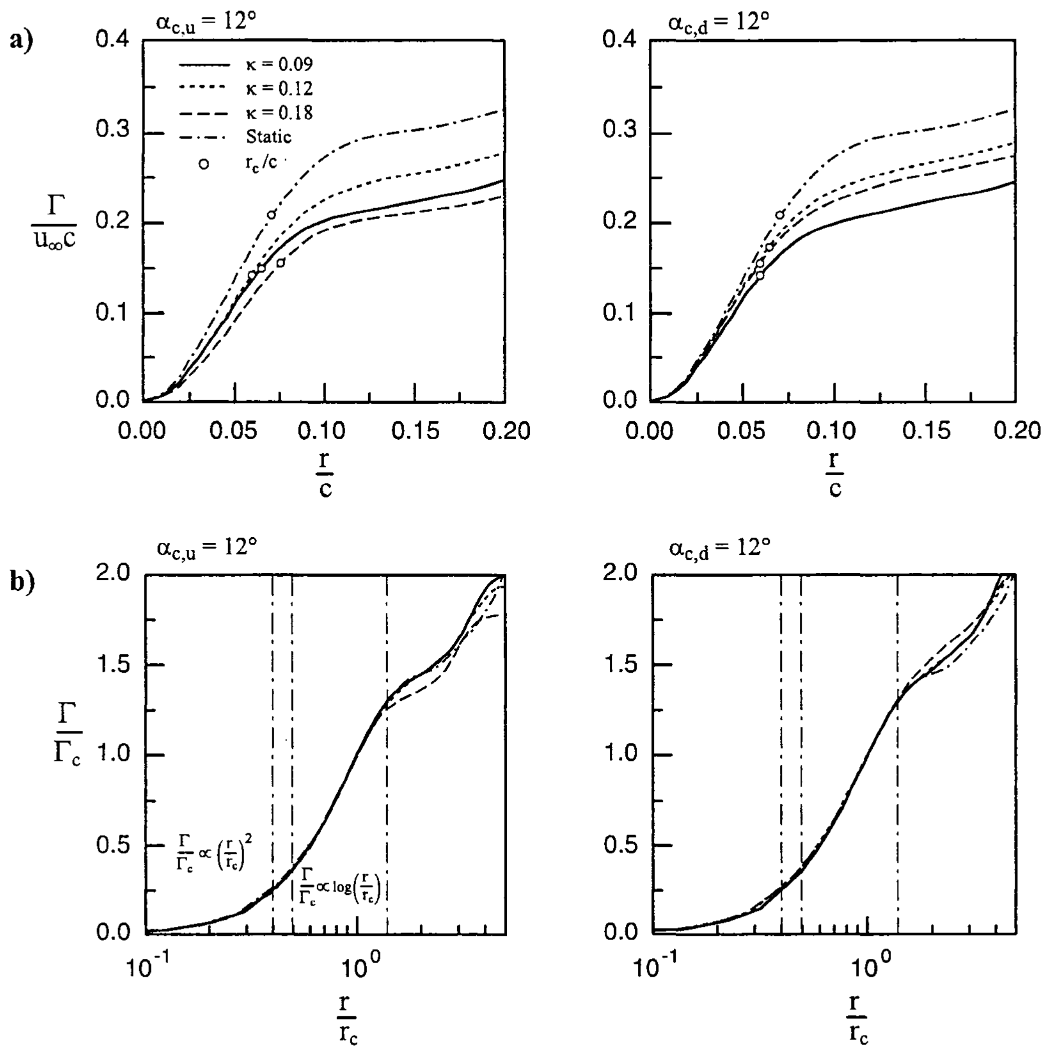

Figure 20 Radial circulation distribution for the vortex at x/c = 1 with $\alpha = 8° + 6°\sin(\omega t)$. (a) normalized against $u_\infty c$; (b) self-scaled.

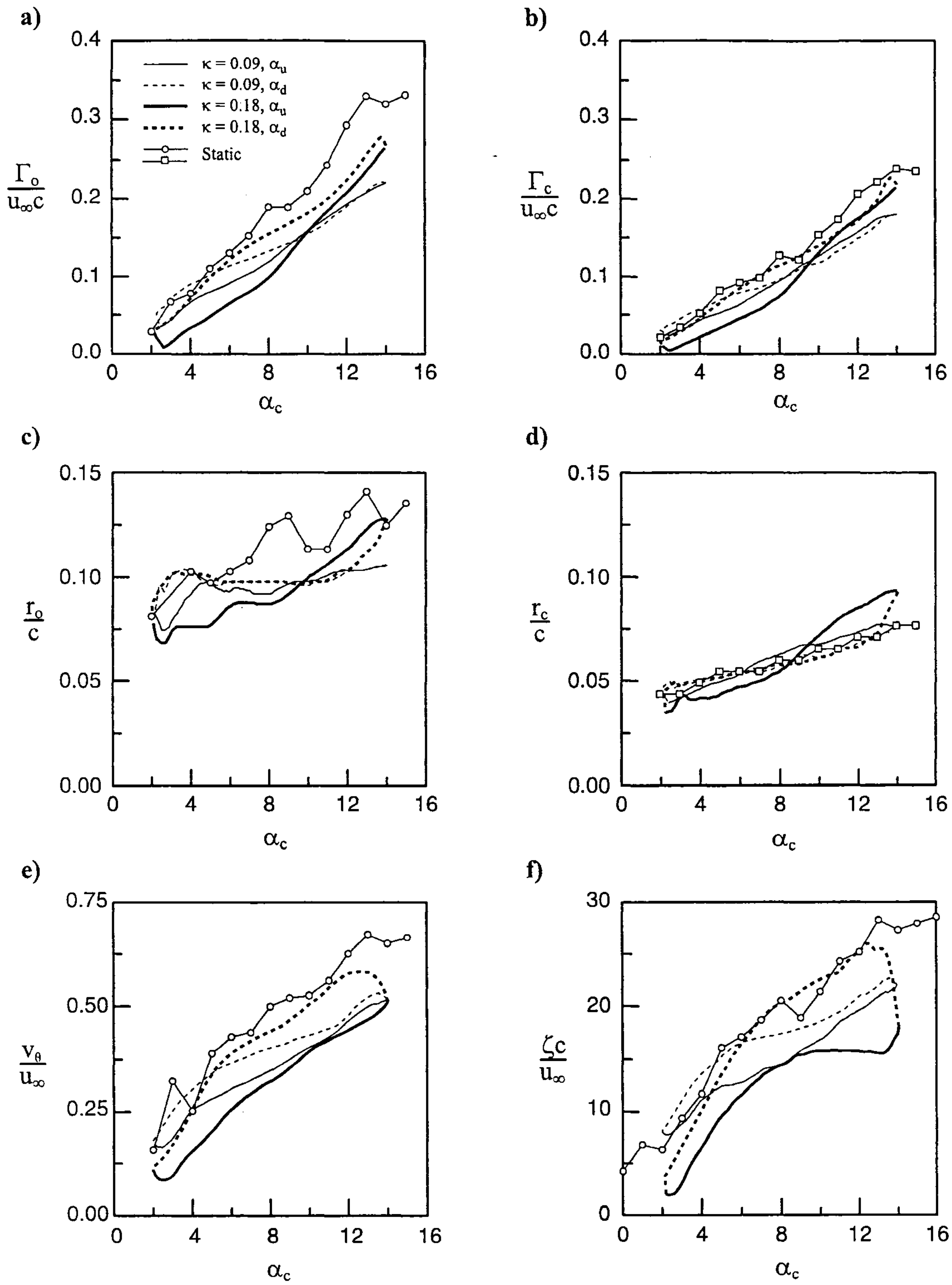

Figure 21 Variation of critical vortex quantities with κ at $x/c = 1$, for $\alpha = 8° + 6°\sin(\omega t)$. (a) Total circulation; (b) core circulation; (c) outer radius; (d) core radius; (e) tangential velocity; (f) peak vorticity; (g) axial velocity; (h) C_{Di} (Equation 13); (i) C_{Di} (Equation 17); (j-l) vortex trajectory.

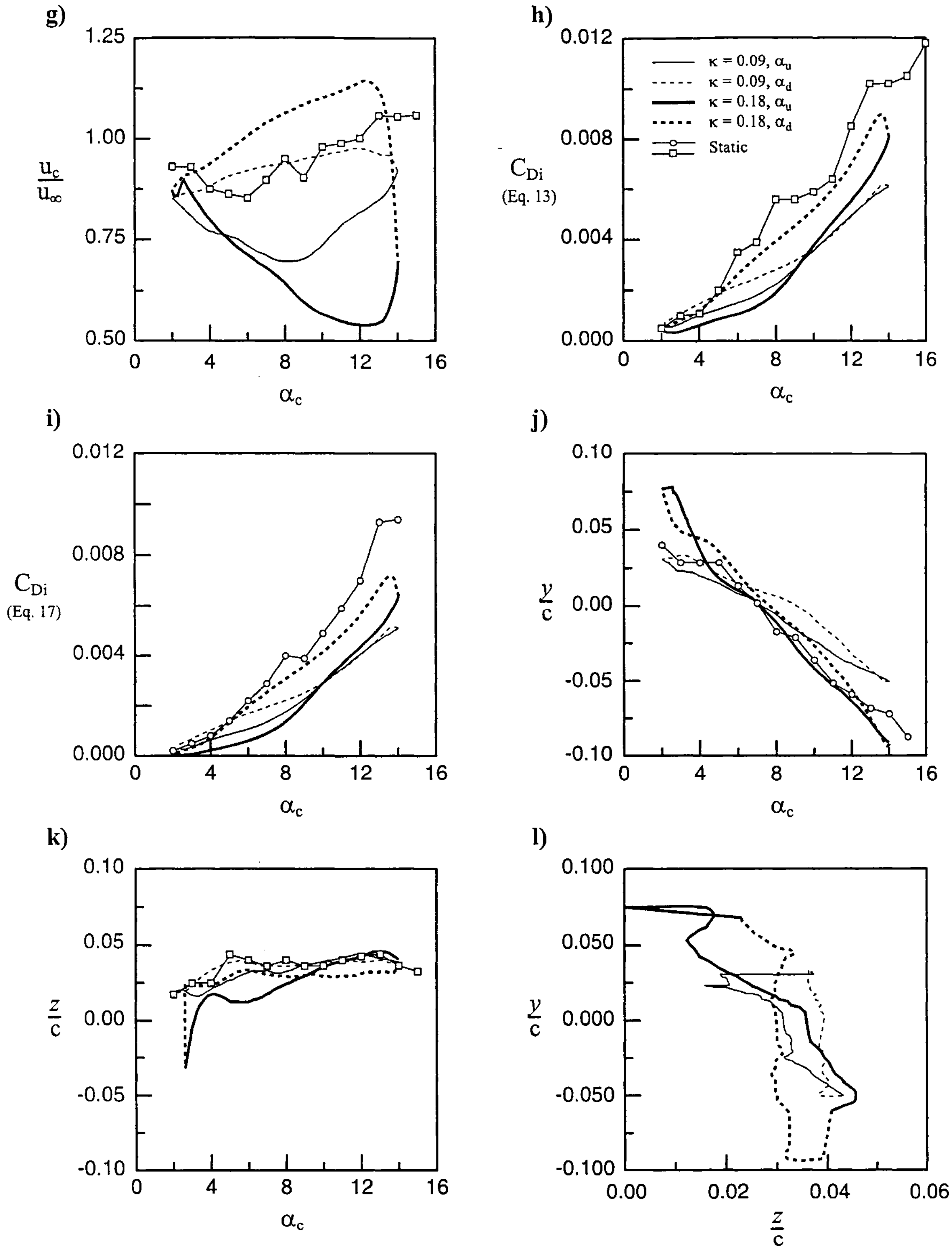

Figure 21 Variation of critical vortex quantities with κ at $x/c = 1$, for $\alpha = 8° + 6°\sin(\omega t)$. (a) Total circulation; (b) core circulation; (c) outer radius; (d) core radius; (e) tangential velocity; (f) peak vorticity; (g) axial velocity; (h) C_{Di} (Equation 13); (i) C_{Di} (Equation 17); (j-l) vortex trajectory.

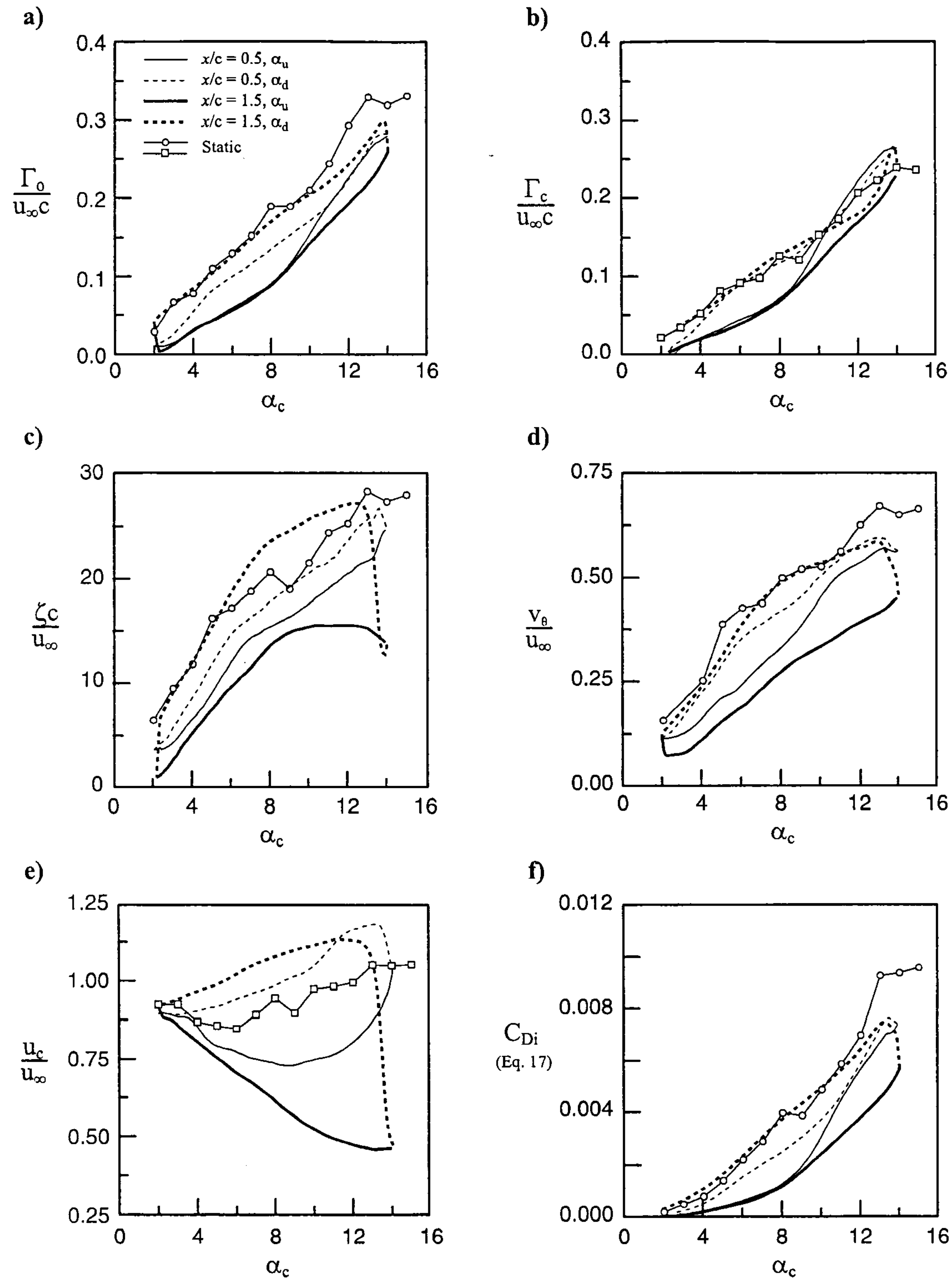

Figure 22 Variation of critical vortex quantities with x/c, for $\alpha = 8° + 6°\sin(\omega t)$. (a) Total circulation; (b) core circulation; (c) peak vorticity; (d) tangential velocity; (e) axial velocity, and (f) C_{Di} (Equation 17).

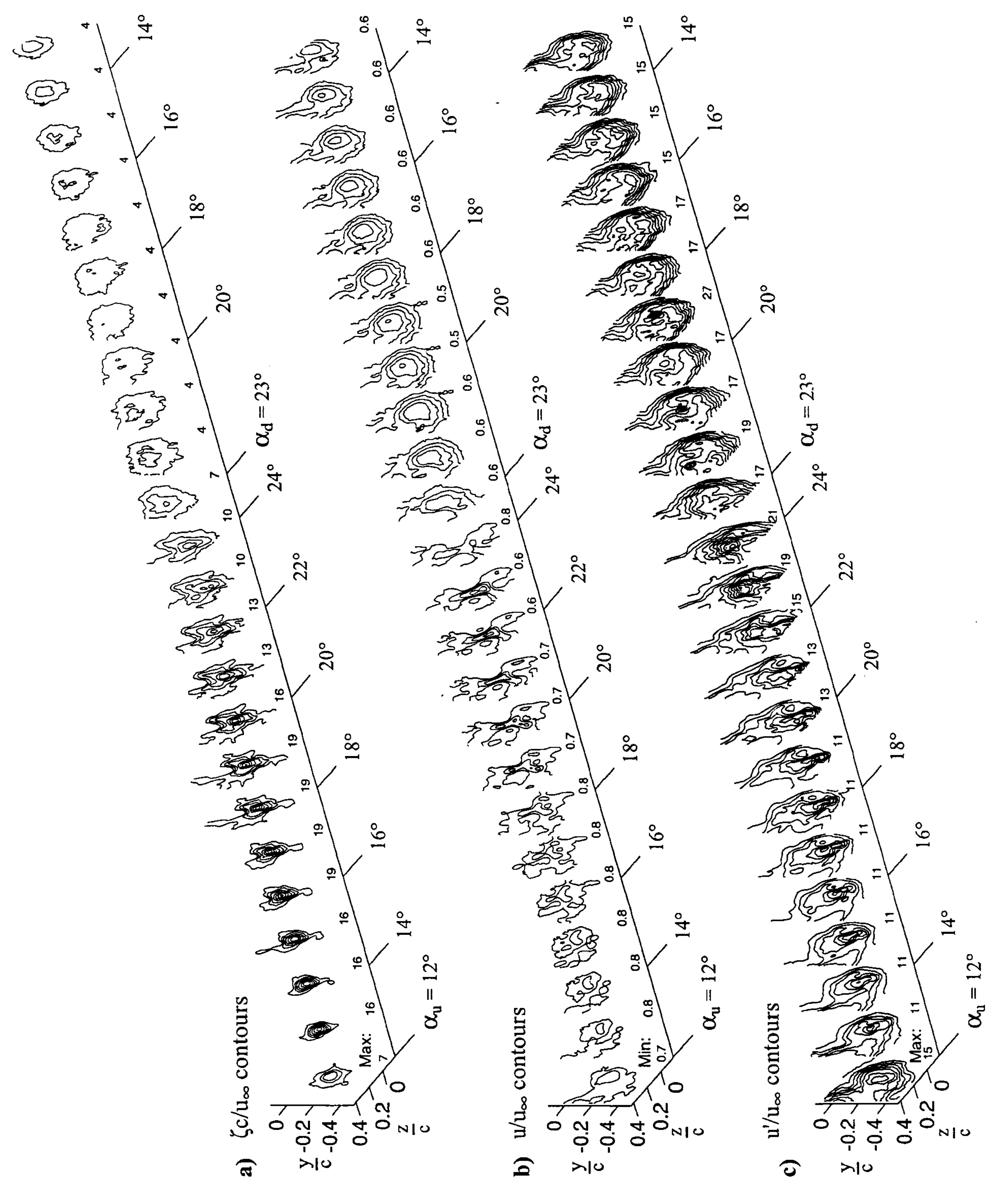

Figure 23 Variation of vortex results for the deep-stall case of $\alpha = 18° + 6°\sin(\omega t)$ and $\kappa = 0.09$ at $x/c = 1$. (a) Vorticity; (b) axial mean velocity, and (c) axial RMS velocity. Numerical values denote $\zeta c/u_\infty$, u/u_∞ and u'/u_∞ (%) levels with constant increments of 3, 0.1 and 2, respectively.

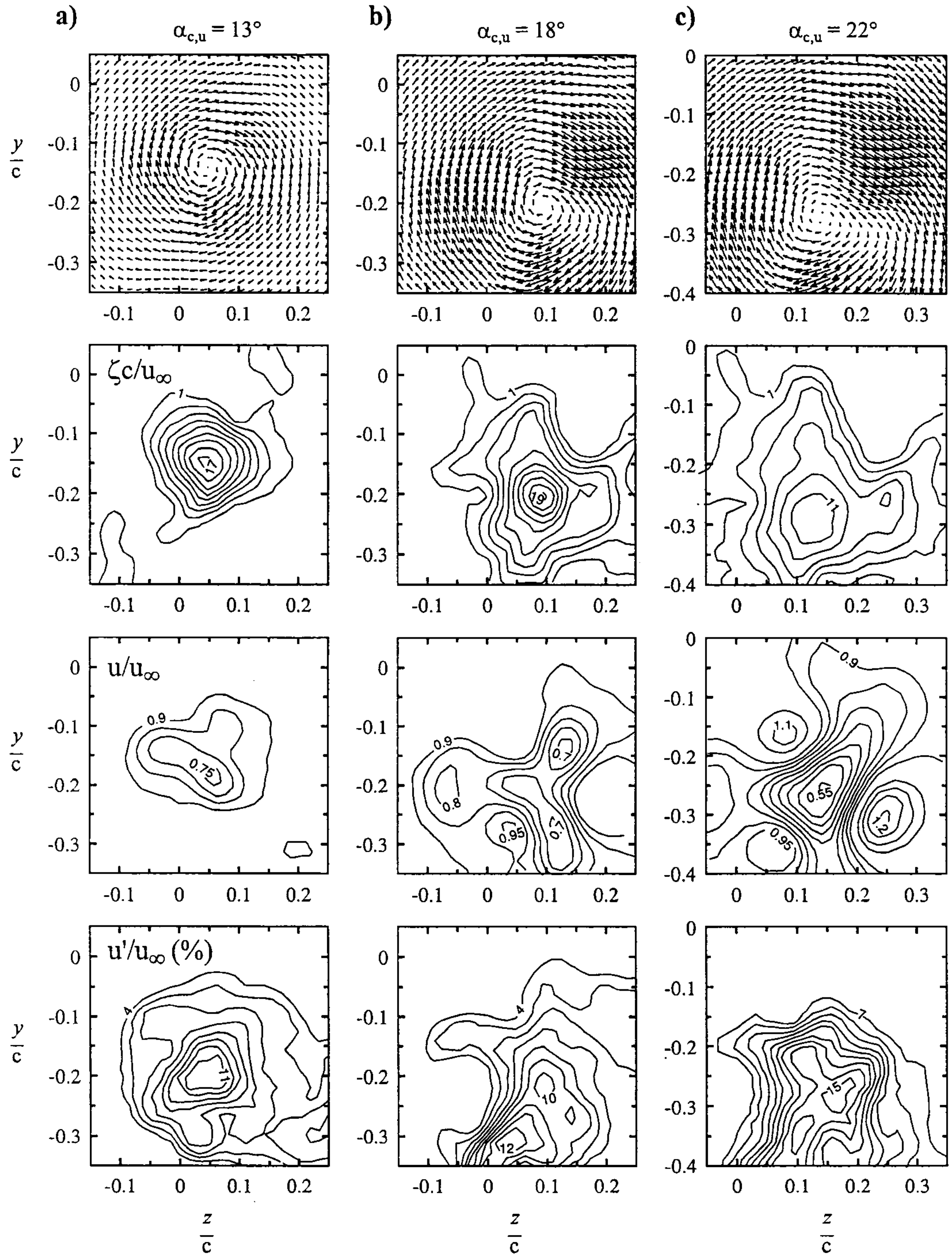

Figure 24 Velocity vectors and contours of constant vorticity, axial mean and RMS velocities at $x/c = 1$, for $\alpha = 18° + 6°\sin(\omega t)$. (a) $\alpha_{c,u} = 13°$; (b) $\alpha_{c,u} = 18°$; (c) $\alpha_{c,u} = 22°$; (d) $\alpha_{c,d} = 22°$; (e) $\alpha_{c,d} = 18°$; (f) $\alpha_{c,d} = 13°$; (g) $\alpha_{static} = 13°$; (h) $\alpha_{static} = 18°$.

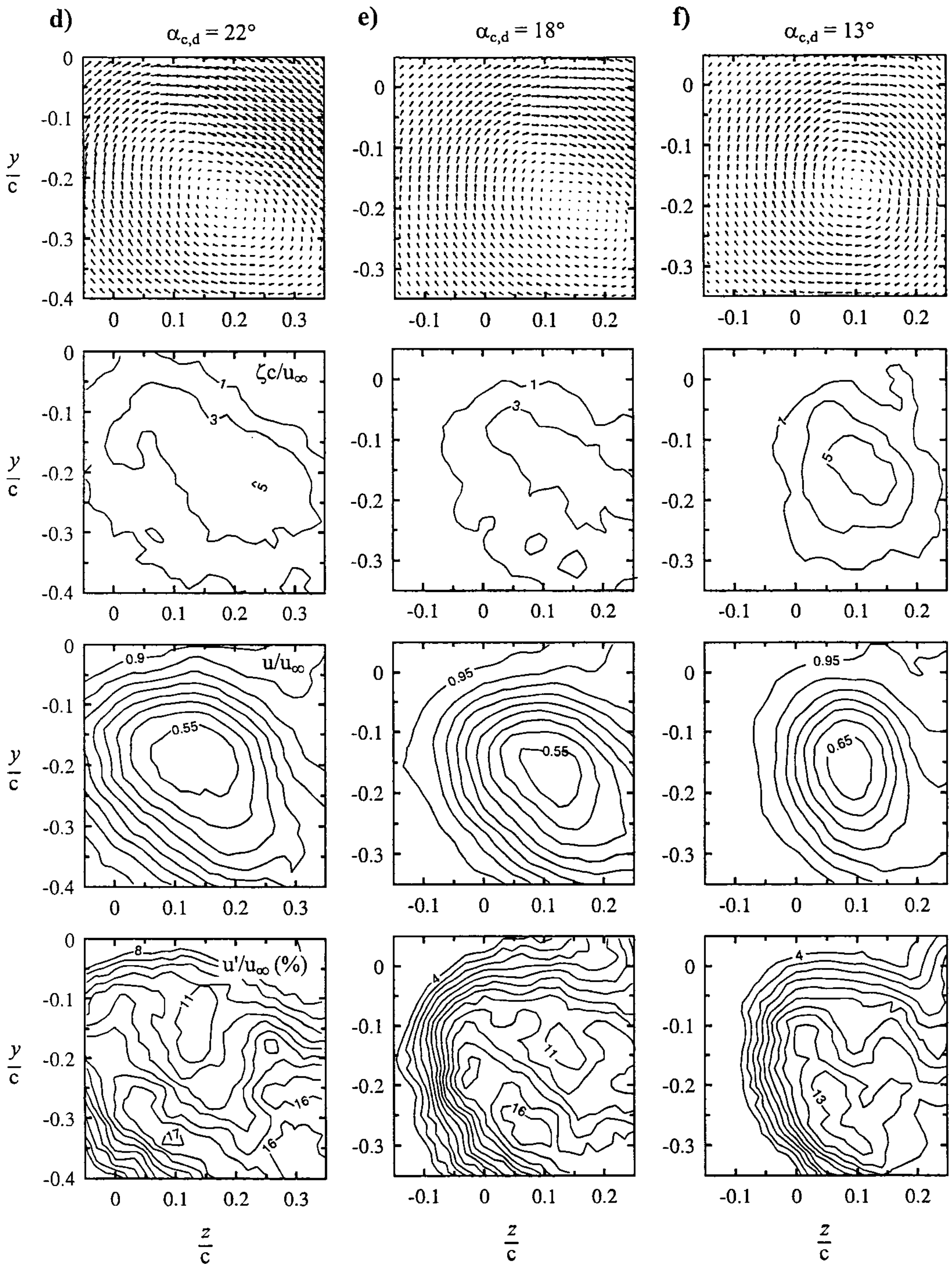

Figure 24 Velocity vectors and contours of constant vorticity, axial mean and RMS velocities at $x/c = 1$, for $\alpha = 18° + 6°\sin(\omega t)$. (a) $\alpha_{c,u} = 13°$; (b) $\alpha_{c,u} = 18°$; (c) $\alpha_{c,u} = 22°$; (d) $\alpha_{c,d} = 22°$; (e) $\alpha_{c,d} = 18°$; (f) $\alpha_{c,d} = 13°$; (g) $\alpha_{static} = 13°$; (h) $\alpha_{static} = 18°$.

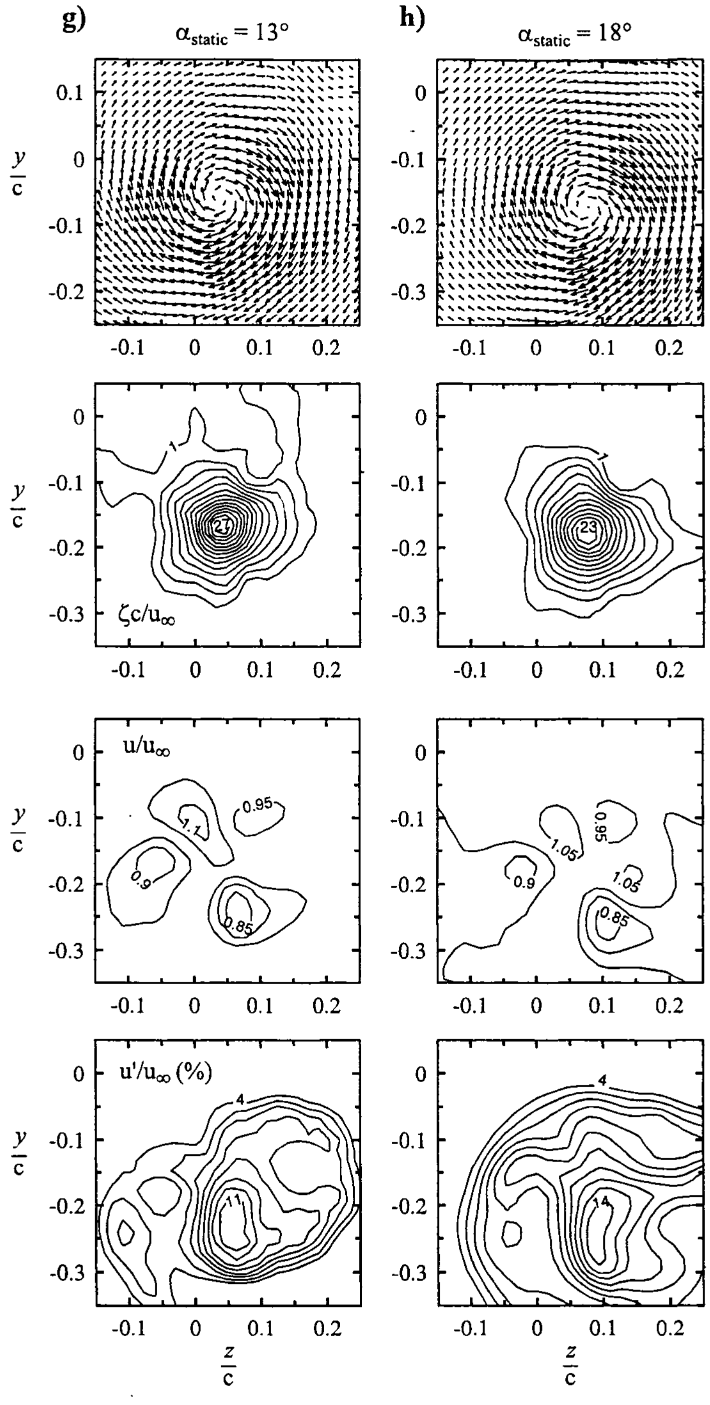

Figure 24 Velocity vectors and contours of constant vorticity, axial mean and RMS velocities at $x/c = 1$, for $\alpha = 18° + 6°\sin(\omega t)$. (a) $\alpha_{c,u} = 13°$; (b) $\alpha_{c,u} = 18°$; (c) $\alpha_{c,u} = 22°$; (d) $\alpha_{c,d} = 22°$; (e) $\alpha_{c,d} = 18°$; (f) $\alpha_{c,d} = 13°$; (g) $\alpha_{static} = 13°$; (h) $\alpha_{static} = 18°$.

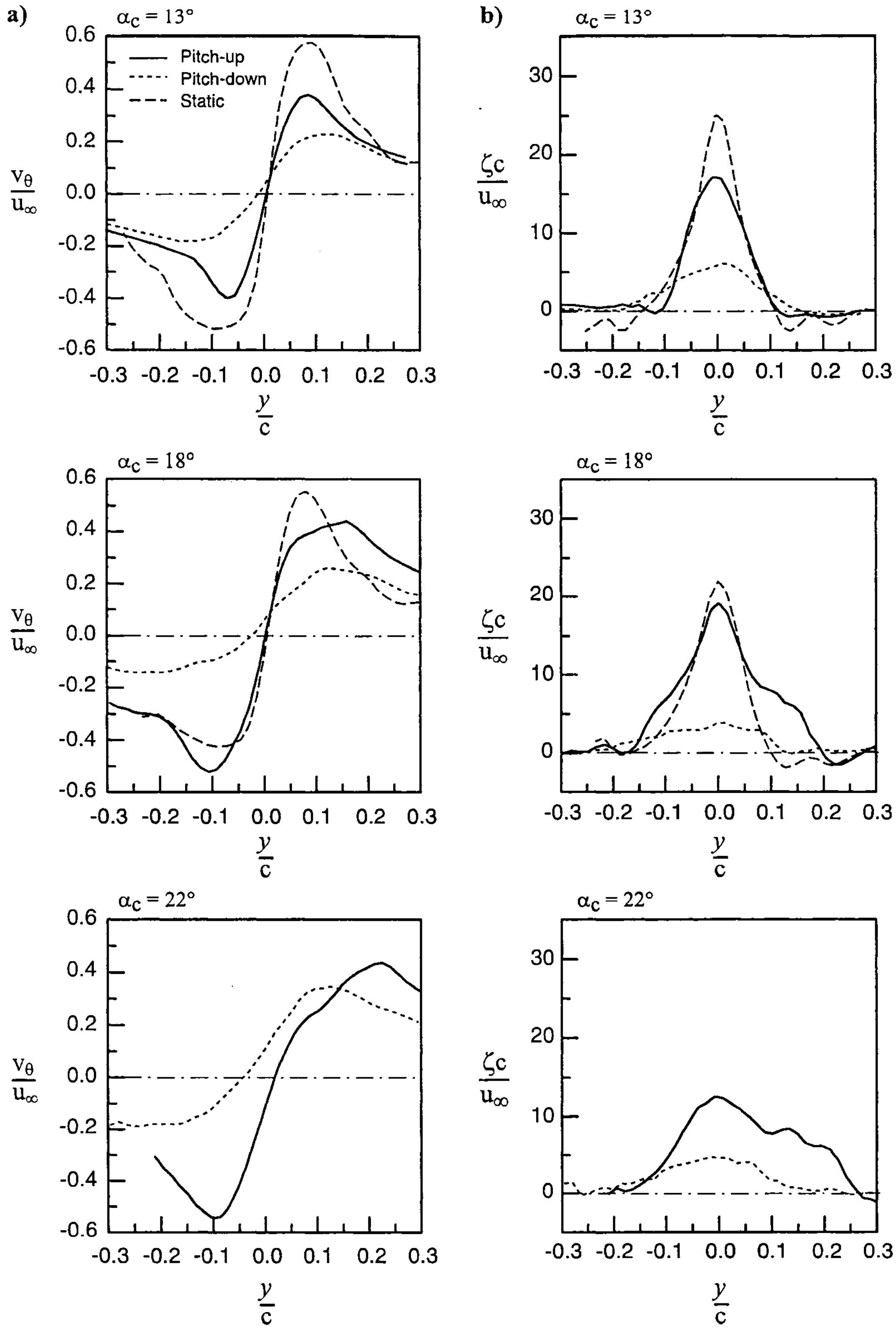

Figure 25 Vortex flow quantities measured across the vortex center at $x/c = 1$, with $\alpha = 18° + 6°\sin(\omega t)$. (a) Tangential velocity; (b) vorticity; (c) axial velocity, and (d) axial RMS velocity.

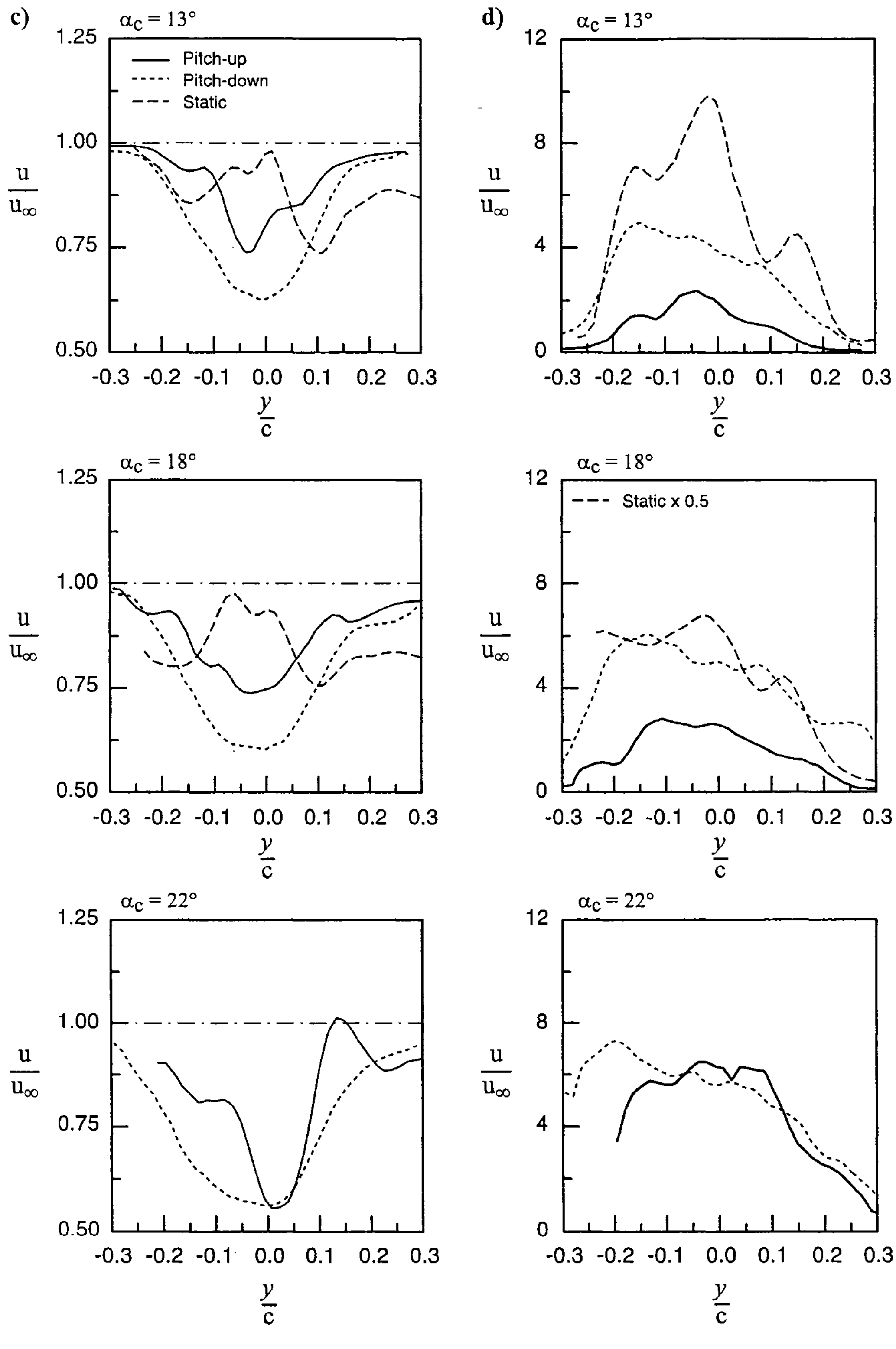

Figure 25 Vortex flow quantities measured across the vortex center at $x/c = 1$, with $\alpha = 18° + 6°\sin(\omega t)$. (a) Tangential velocity; (b) vorticity; (c) axial velocity, and (d) axial RMS velocity.

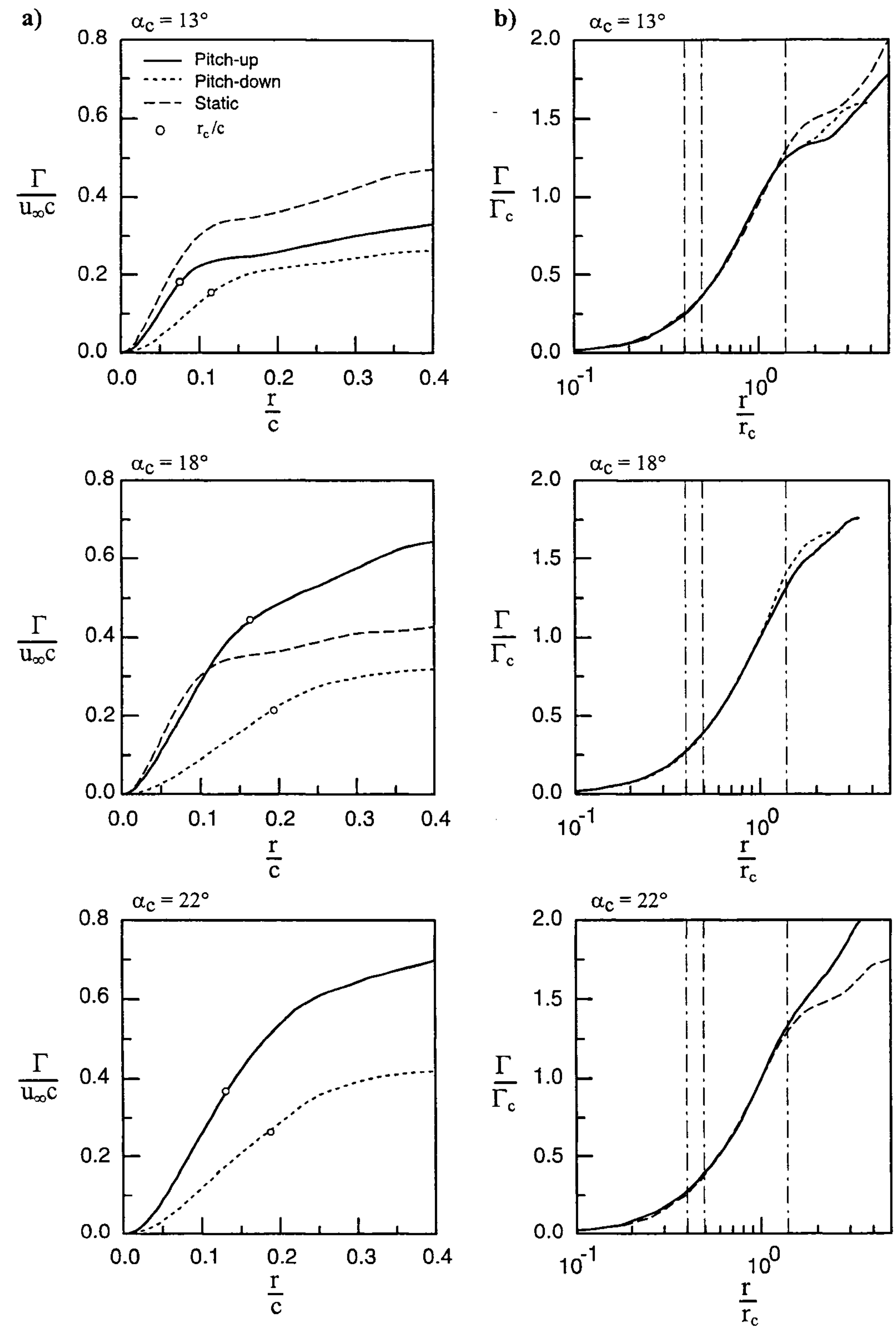

Figure 26 Radial circulation distribution for the vortex at x/c = 1 with $\alpha = 18° + 6°\sin(\omega t)$. (a) normalized against $u_\infty c$; (b) self-scaled.

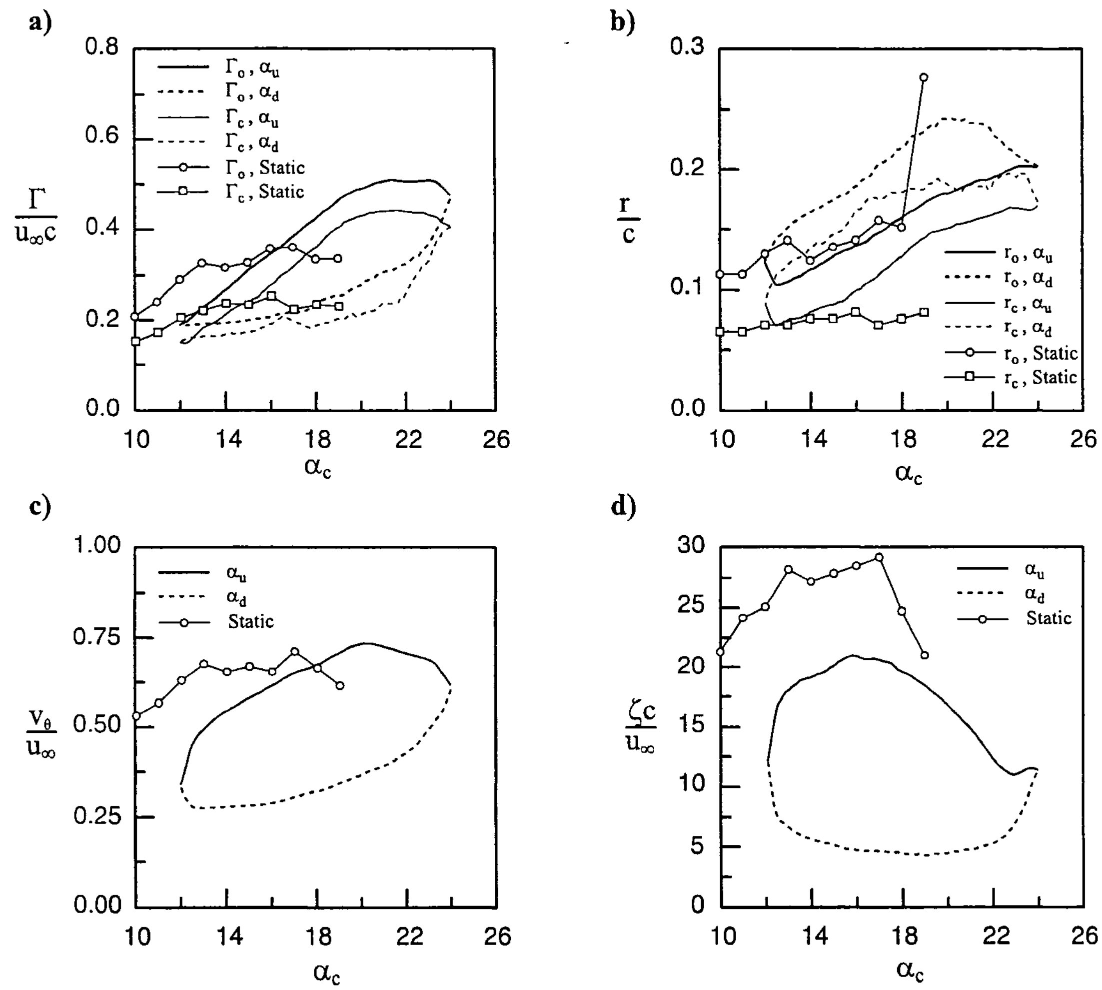

Figure 27 Variation of critical vortex quantities at $x/c = 1$, for $\alpha = 18° + 6°\sin(\omega t)$ and $\kappa = 0.09$. (a) Total and core circulation; (b) outer and core radii; (c) tangential velocity; (d) peak vorticity; (e) axial velocity; (f) core RMS velocity; (g) C_{Di} (Equation 17); (h) vortex trajectory.

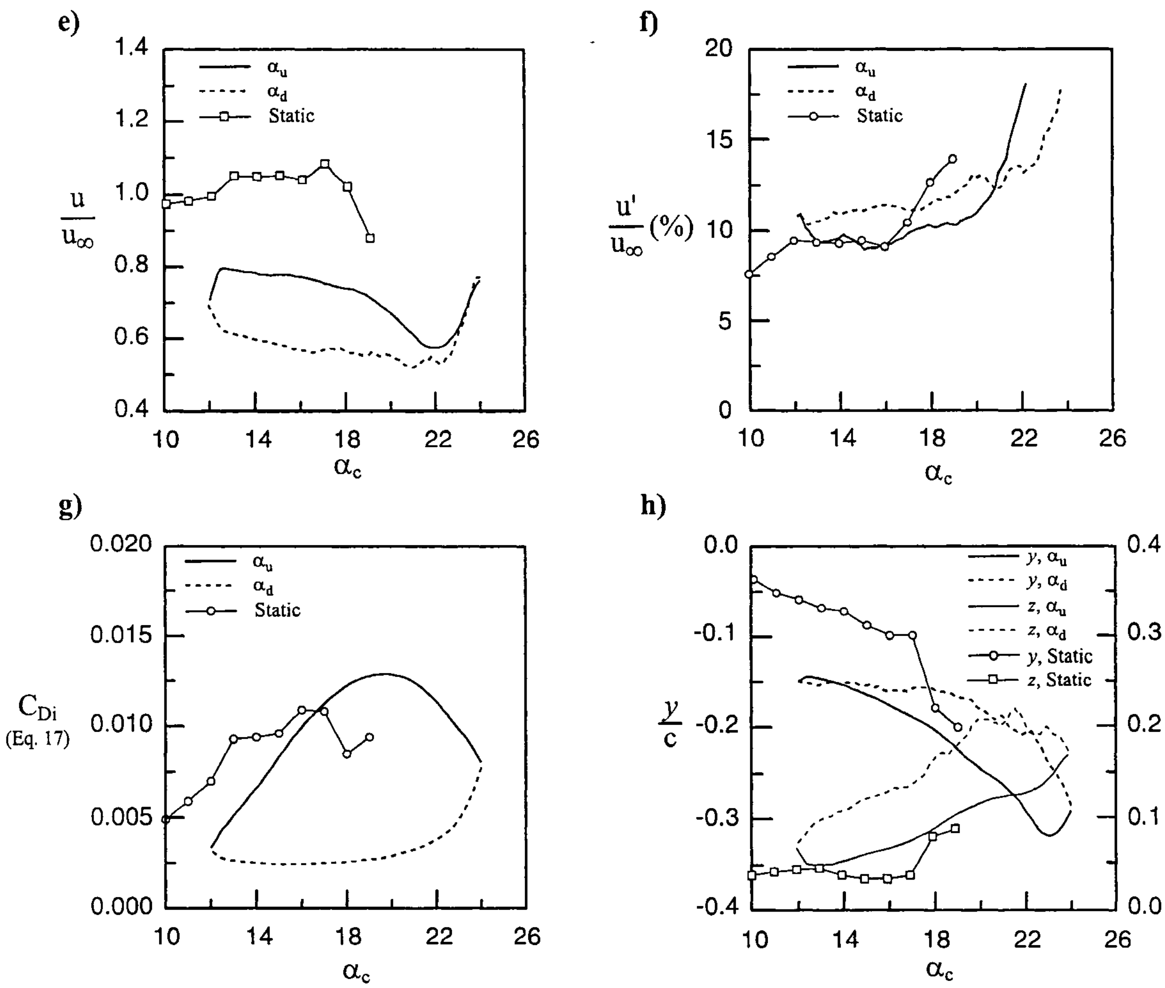

Figure 27 Variation of critical vortex quantities at $x/c = 1$, for $\alpha = 18° + 6°\sin(\omega t)$ and $\kappa = 0.09$. (a) Total and core circulation; (b) outer and core radii; (c) tangential velocity; (d) peak vorticity; (e) axial velocity; (f) core RMS velocity; (g) C_{Di} (Equation 17); (h) vortex trajectory.

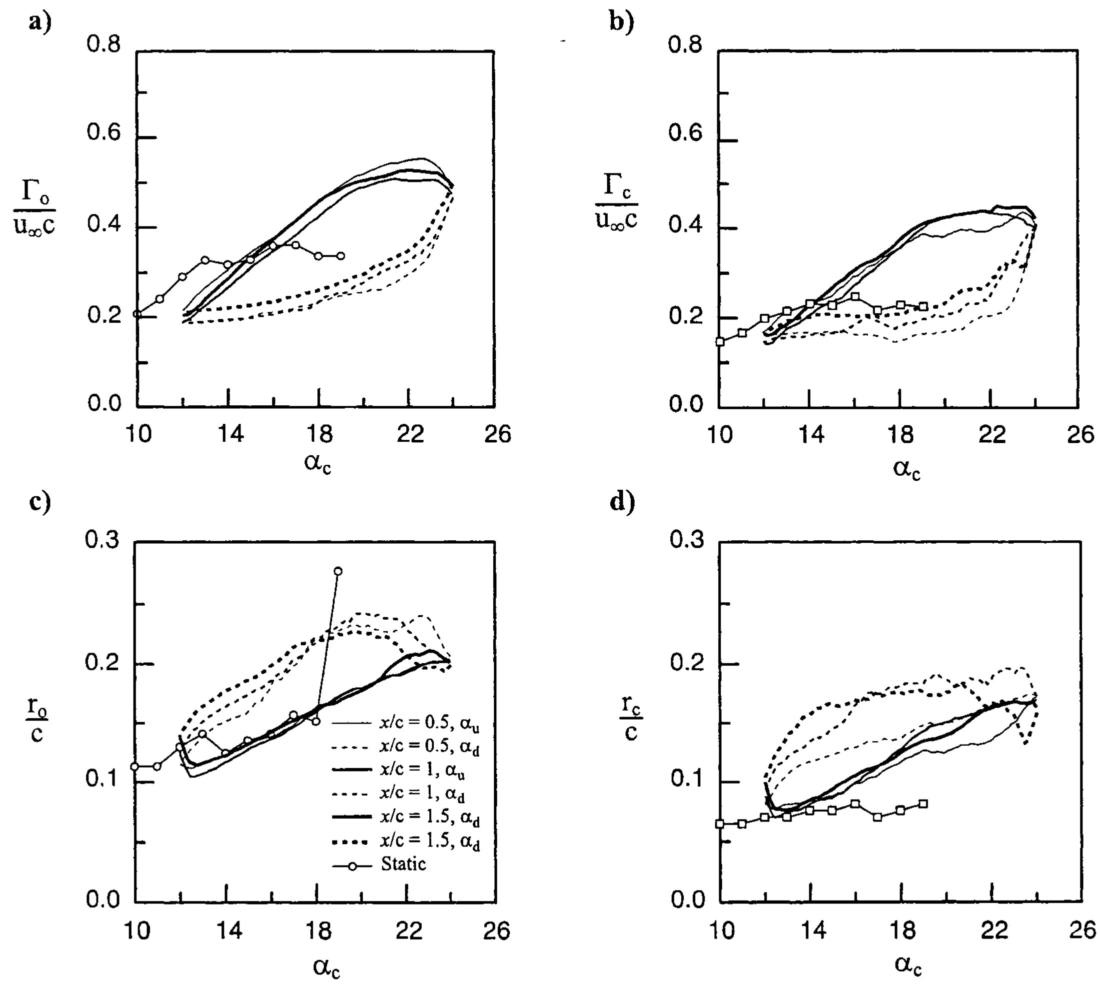

Figure 28 Variation of critical vortex quantities with x/c for $\kappa = 0.09$ and $\alpha = 18° + 6°\sin(\omega t)$. (a) Total circulation; (b) core circulation; (c) outer radius; (d) core radius; (e) tangential velocity; (f) peak vorticity; (g) core axial velocity and (h) induced drag

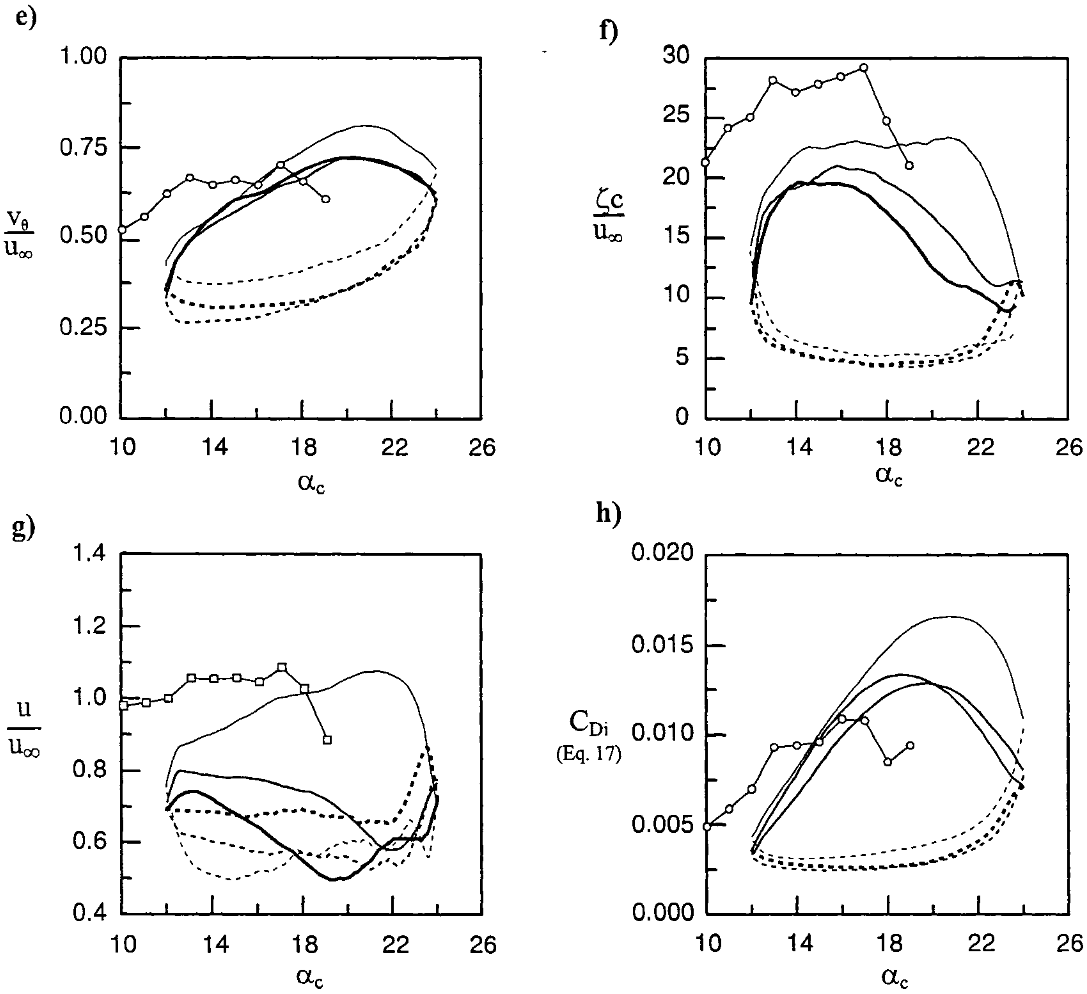

Figure 28 Variation of critical vortex quantities with x/c for κ = 0.09 and $\alpha = 18° + 6°\sin(\omega t)$. (a) Total circulation; (b) core circulation; (c) outer radius; (d) core radius; (e) tangential velocity; (f) peak vorticity; (g) core axial velocity and (h) induced drag.

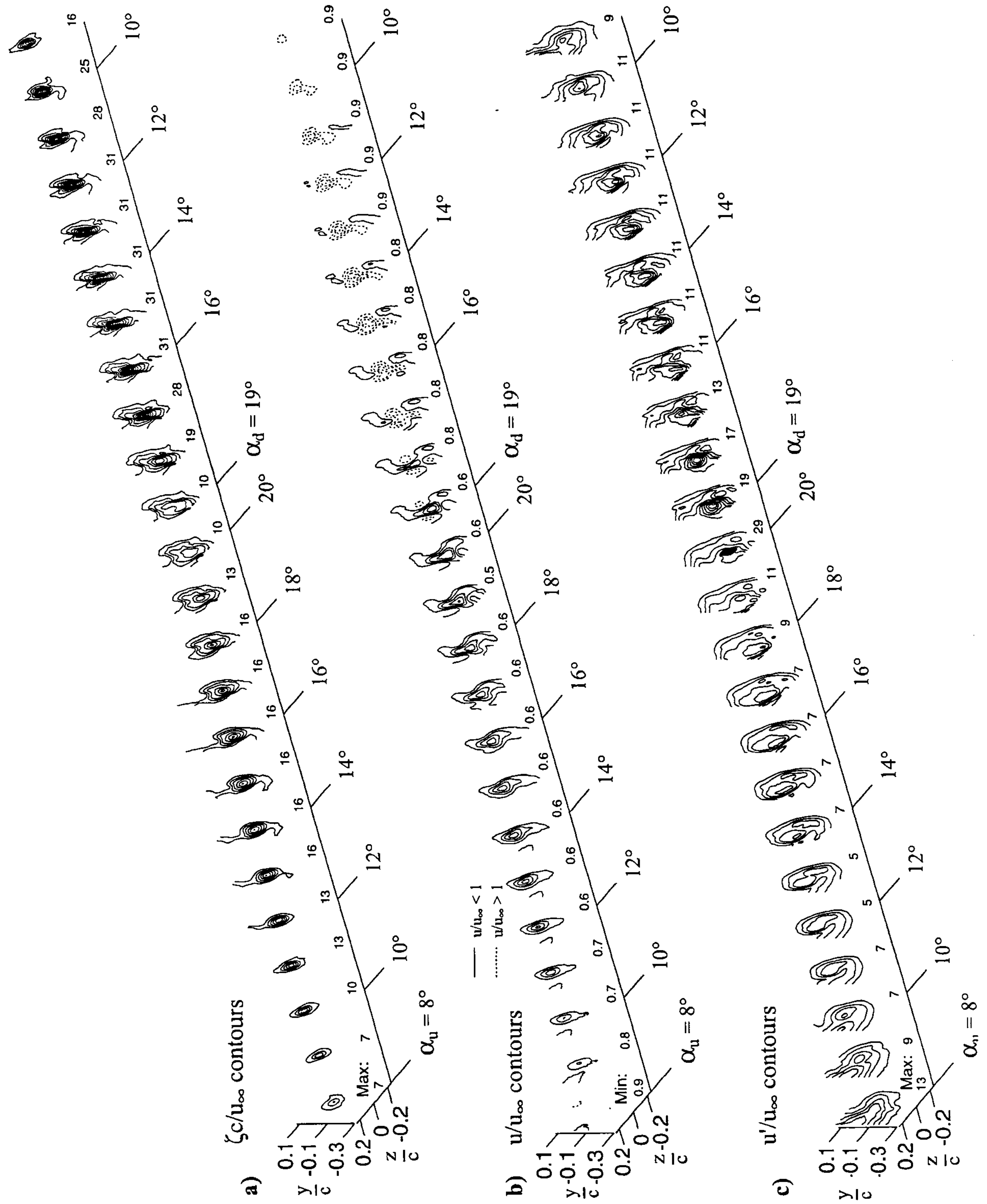

Figure 29 Variation of vortex results for the light-stall flow case of $\alpha = 14° + 6°\sin(\omega t)$ and $\kappa = 0.18$ at $x/c = 1$. (a) Vorticity; (b) axial mean velocity, and (c) axial RMS velocity. Numerical values denote $\zeta c/u_\infty$, u/u_∞ and u'/u_∞ (%) levels with constant increments of 3, 0.05 and 2, respectively.

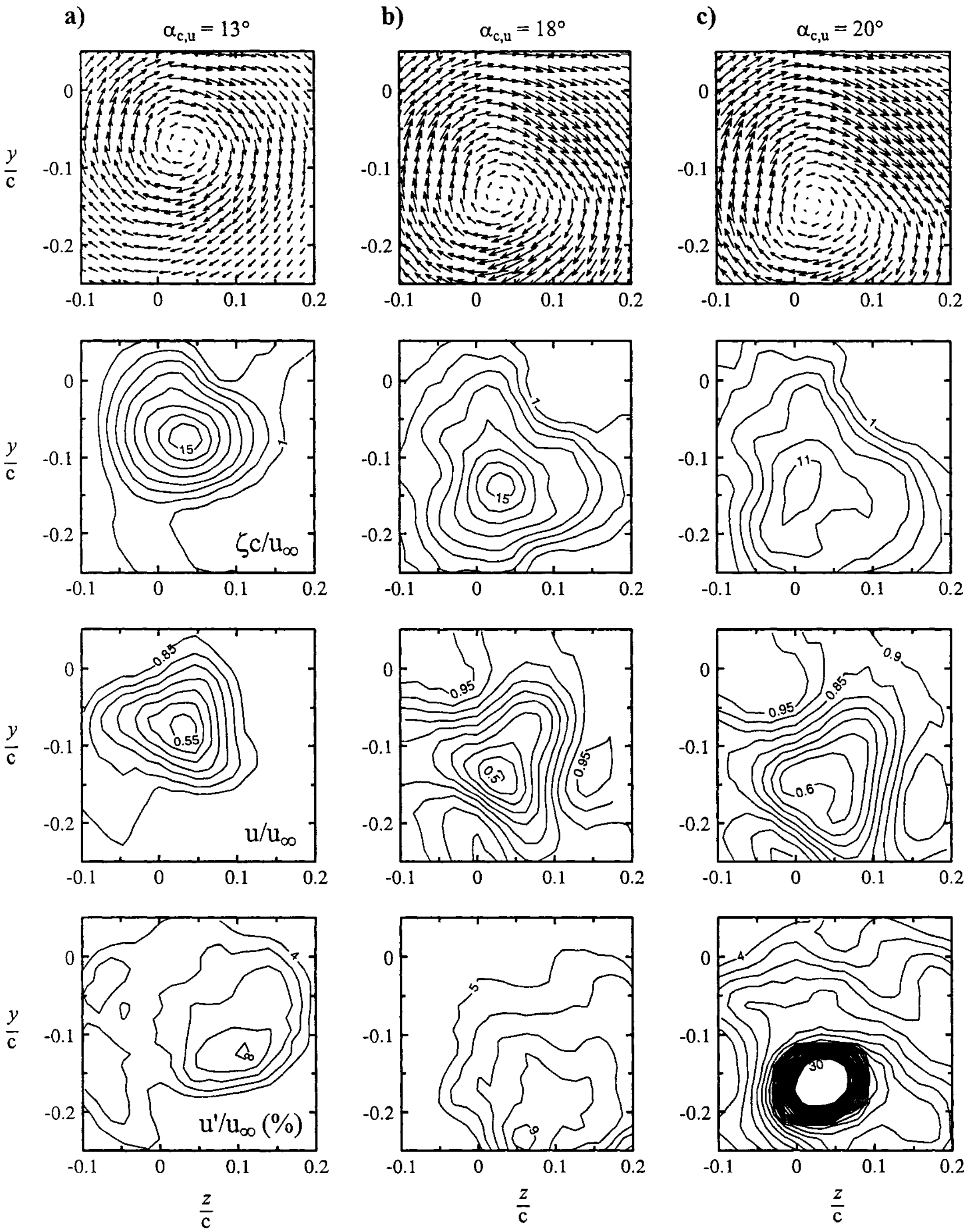

Figure 30 Velocity vectors and contours of constant vorticity, axial mean and RMS velocities for $\alpha = 14° + 6°\sin(\omega t)$ and $\kappa = 0.18$, at $x/c = 1$. (a) $\alpha_{c,u} = 13°$; (b) $\alpha_{c,u} = 18°$; (c) $\alpha_{c,u} = 20°$; (d) $\alpha_{c,d} = 18°$; (e) $\alpha_{c,d} = 13°$.

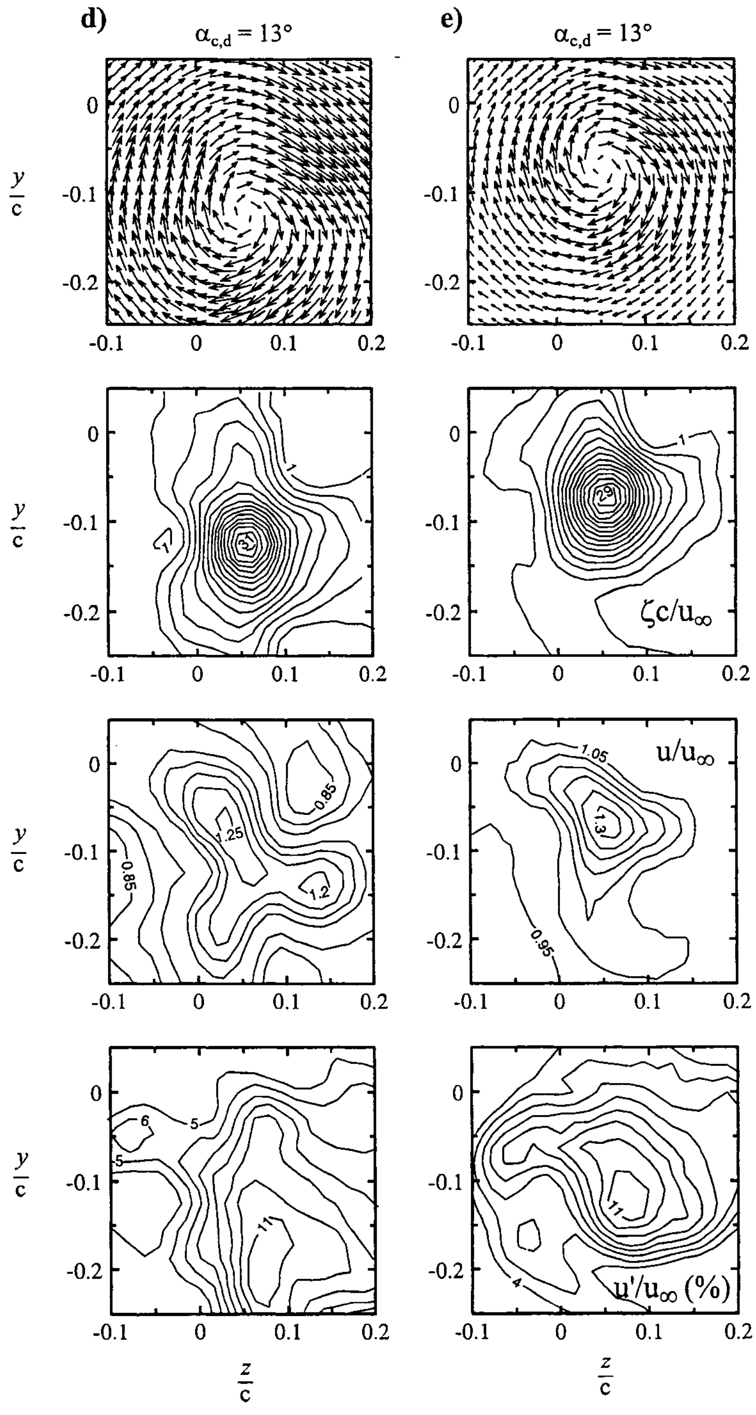

Figure 30 Velocity vectors and contours of constant vorticity, axial mean and RMS velocities for $\alpha = 14° + 6°\sin(\omega t)$ and $\kappa = 0.18$, at $x/c = 1$. (a) $\alpha_{c,u} = 13°$; (b) $\alpha_{c,u} = 18°$; (c) $\alpha_{c,u} = 20°$; (d) $\alpha_{c,d} = 18°$; (e) $\alpha_{c,d} = 13°$.

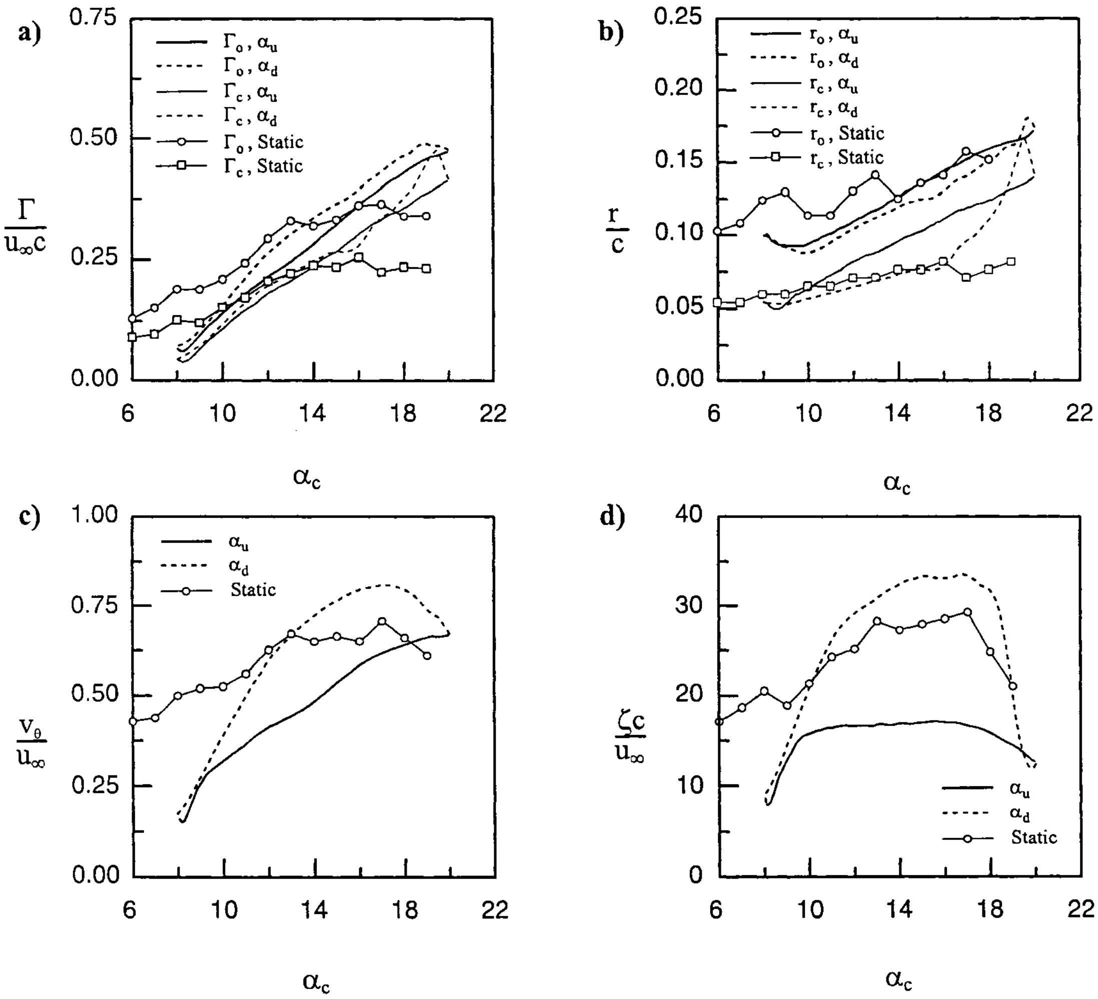

Figure 31 Variation of critical vortex quantities at $x/c = 1$, for $\alpha = 14° + 6°\sin(\omega t)$ and $\kappa = 0.18$. (a) Total and core circulation; (b) outer and core radii; (c) tangential velocity; (d) peak vorticity; (e) axial velocity; (f) core RMS velocity; (g) C_{Di} (Equation 17); (h) vortex trajectory.

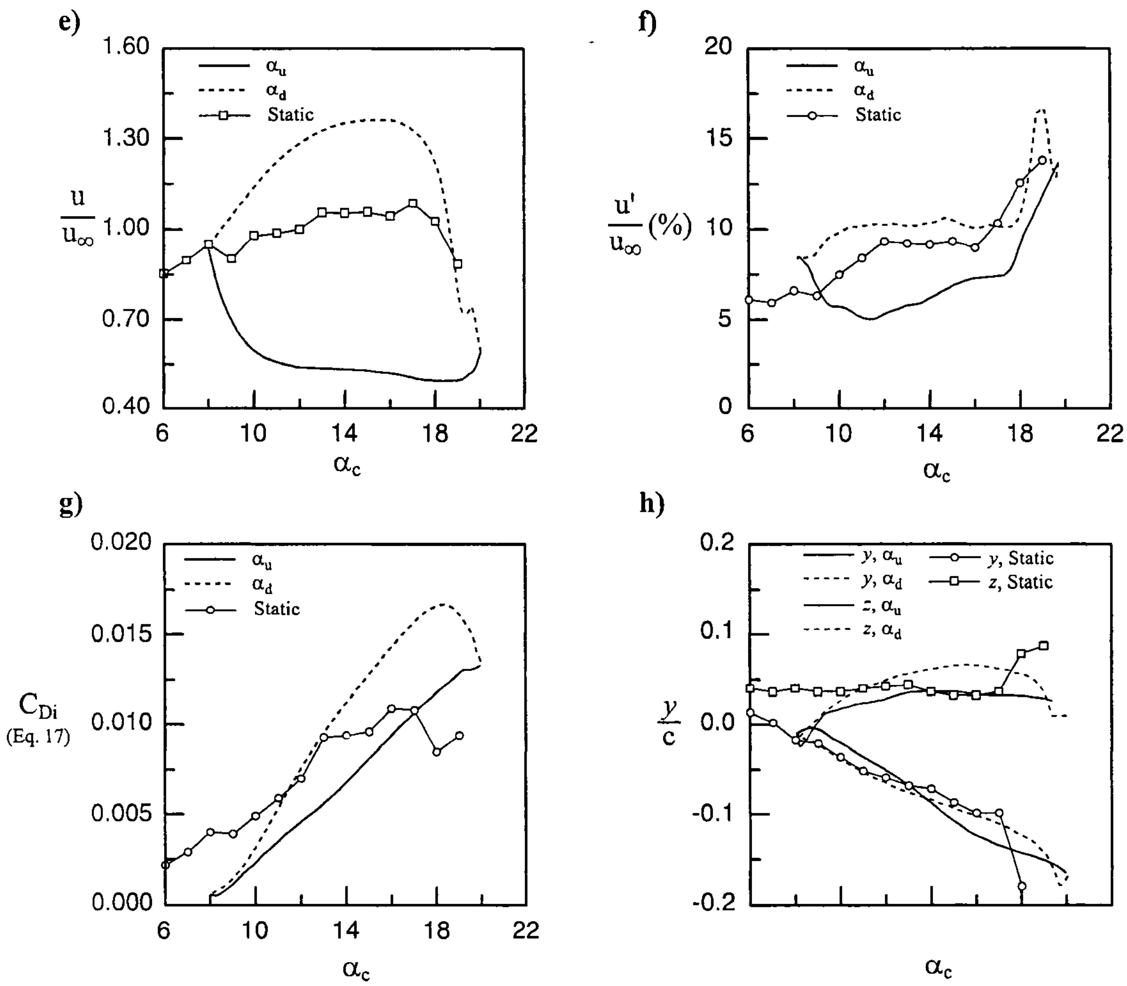

Figure 31 Variation of critical vortex quantities at $x/c = 1$, for $\alpha = 14° + 6°\sin(\omega t)$ and $\kappa = 0.18$. (a) Total and core circulation; (b) outer and core radii; (c) tangential velocity; (d) peak vorticity; (e) axial velocity; (f) core RMS velocity; (g) C_{Di} (Equation 17); (h) vortex trajectory.

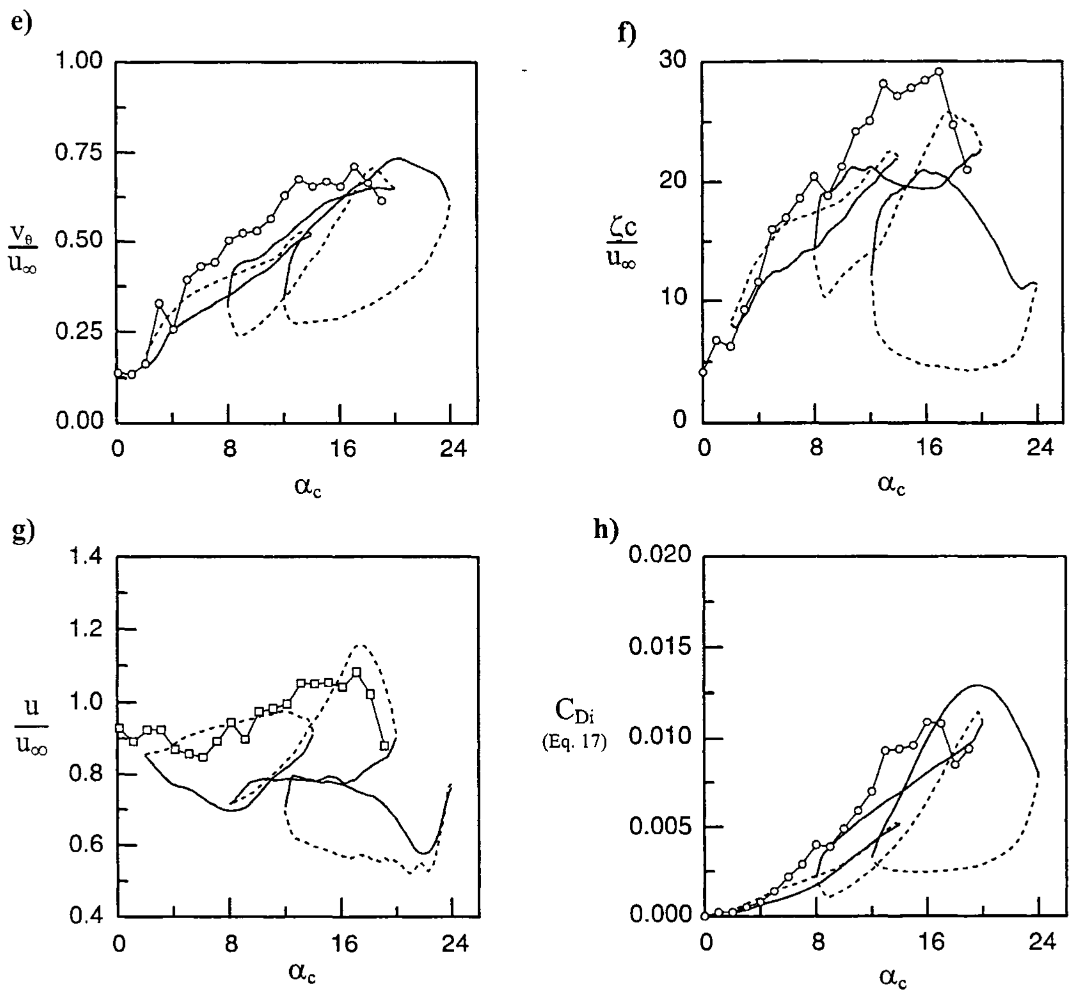

Figure 32 Variation of critical vortex quantities with α_o at $x/c = 1$, for $\Delta\alpha = 6°$ and $\kappa = 0.09$. (a) Total circulation; (b) core circulation; (c) outer radius; (d) core radius; (e) peak tangential velocity; (f) peak vorticity; (g) core axial velocity; (h) C_{Di} (Equation 17).

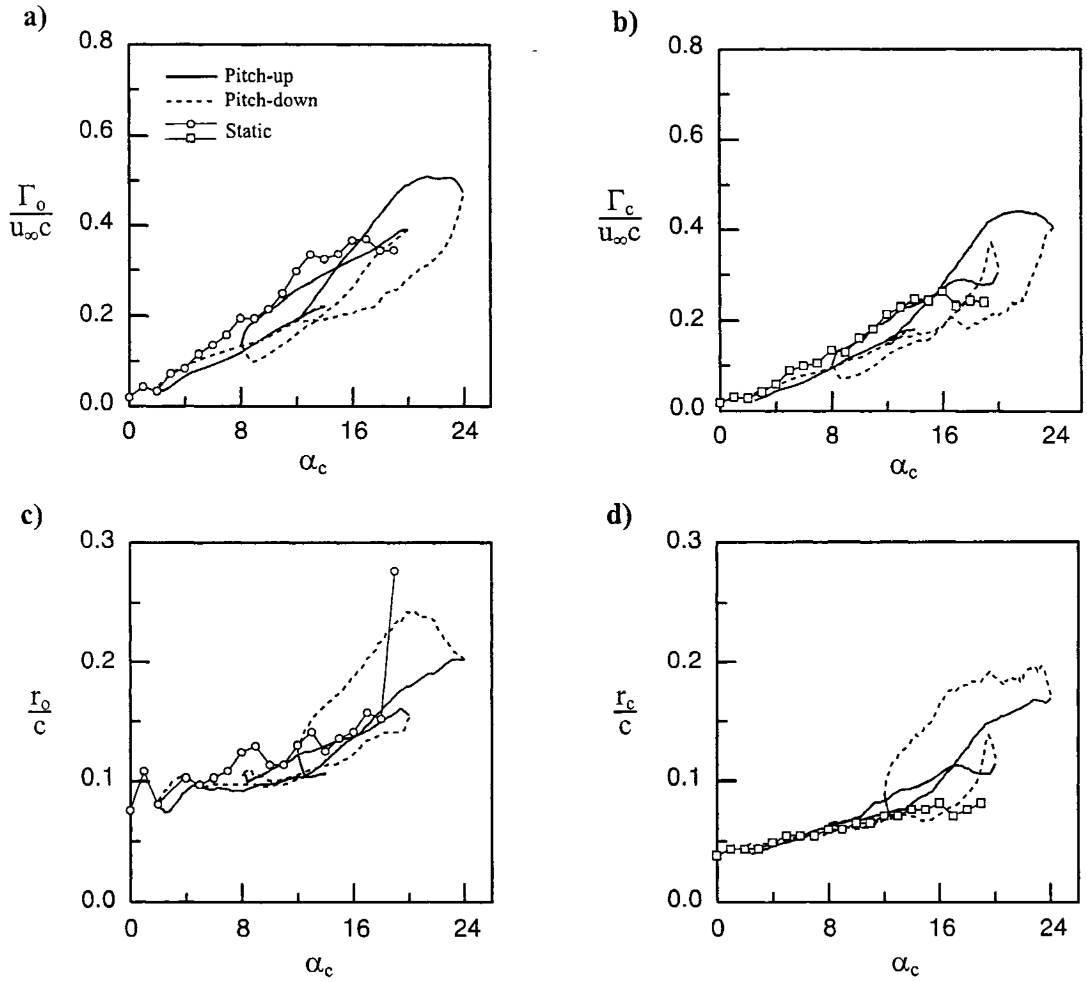

Figure 32 Variation of critical vortex quantities with α_0 at $x/c = 1$, for $\Delta\alpha = 6°$ and $\kappa = 0.09$. (a) Total circulation; (b) core circulation; (c) outer radius; (d) core radius; (e) peak tangential velocity; (f) peak vorticity; (g) core axial velocity; (h) C_{Di} (Equation 17).

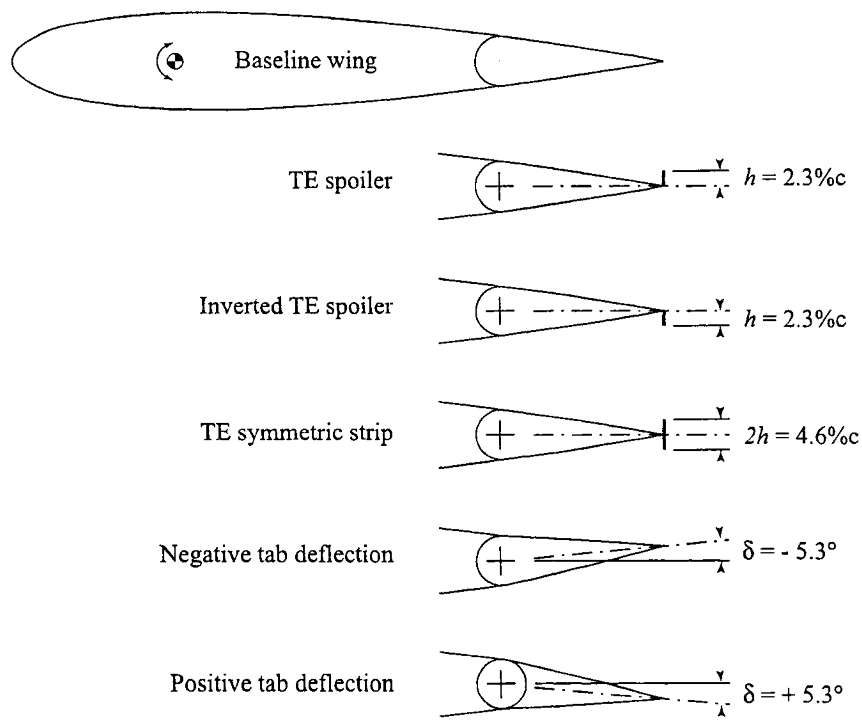

Figure 33 Trailing-edge geometrical configurations tested for passive vortex control.

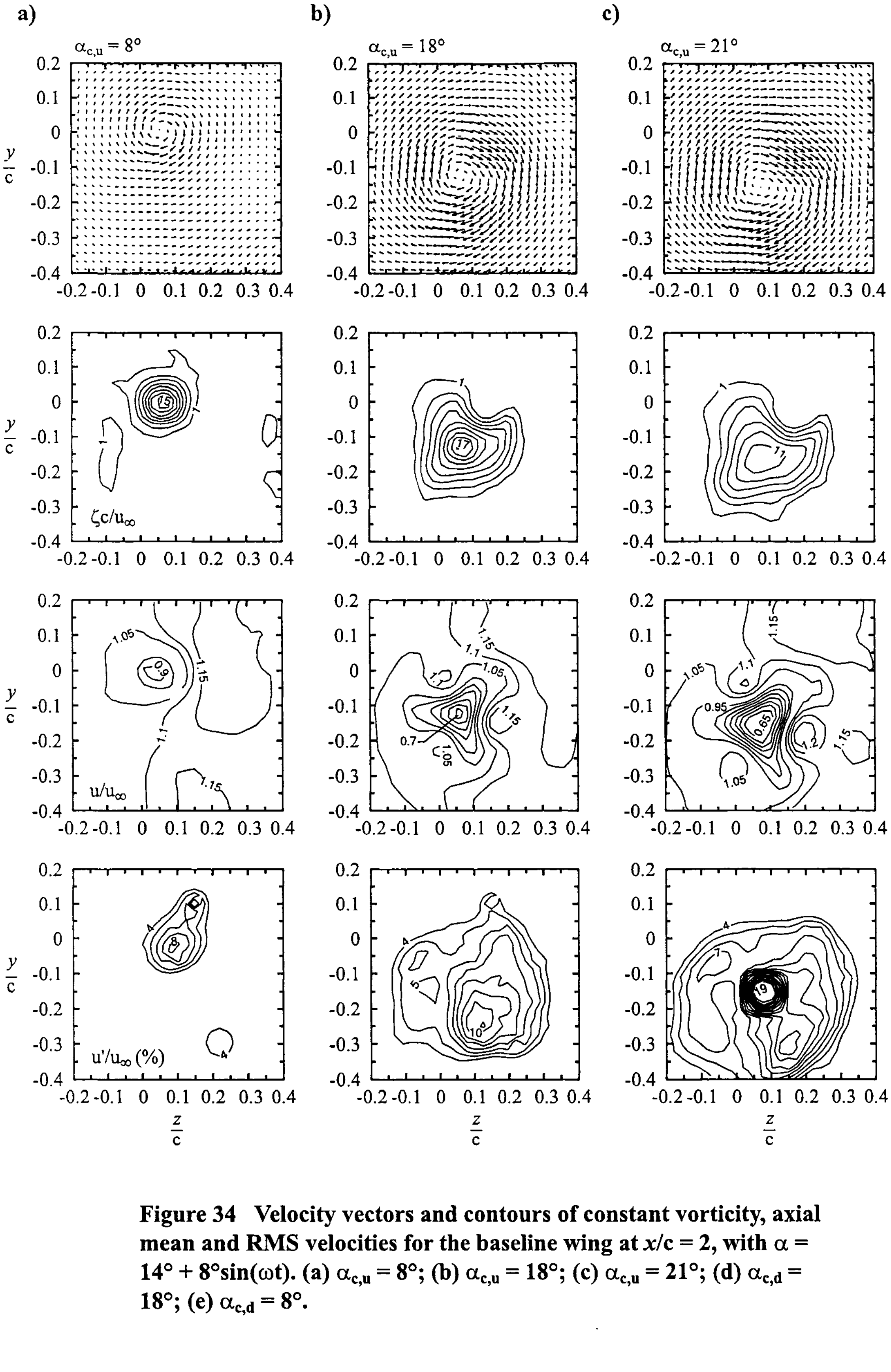

Figure 34 Velocity vectors and contours of constant vorticity, axial mean and RMS velocities for the baseline wing at $x/c = 2$, with $\alpha = 14° + 8°\sin(\omega t)$. (a) $\alpha_{c,u} = 8°$; (b) $\alpha_{c,u} = 18°$; (c) $\alpha_{c,u} = 21°$; (d) $\alpha_{c,d} = 18°$; (e) $\alpha_{c,d} = 8°$.

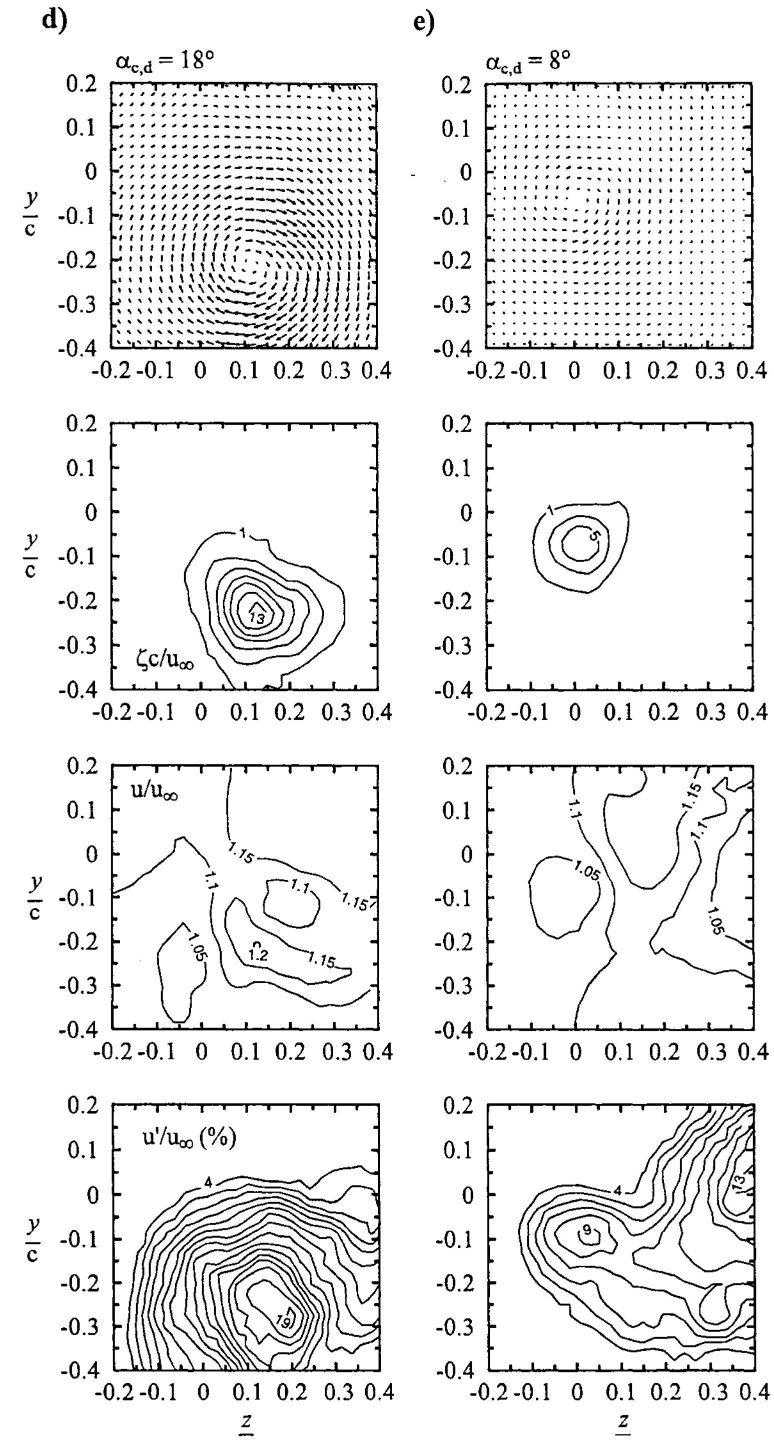

Figure 34 Velocity vectors and contours of constant vorticity, axial mean and RMS velocities for the baseline wing at $x/c = 2$, with $\alpha = 14° + 8°\sin(\omega t)$. (a) $\alpha_{c,u} = 8°$; (b) $\alpha_{c,u} = 18°$; (c) $\alpha_{c,u} = 21°$; (d) $\alpha_{c,d} = 18°$; (e) $\alpha_{c,d} = 8°$.

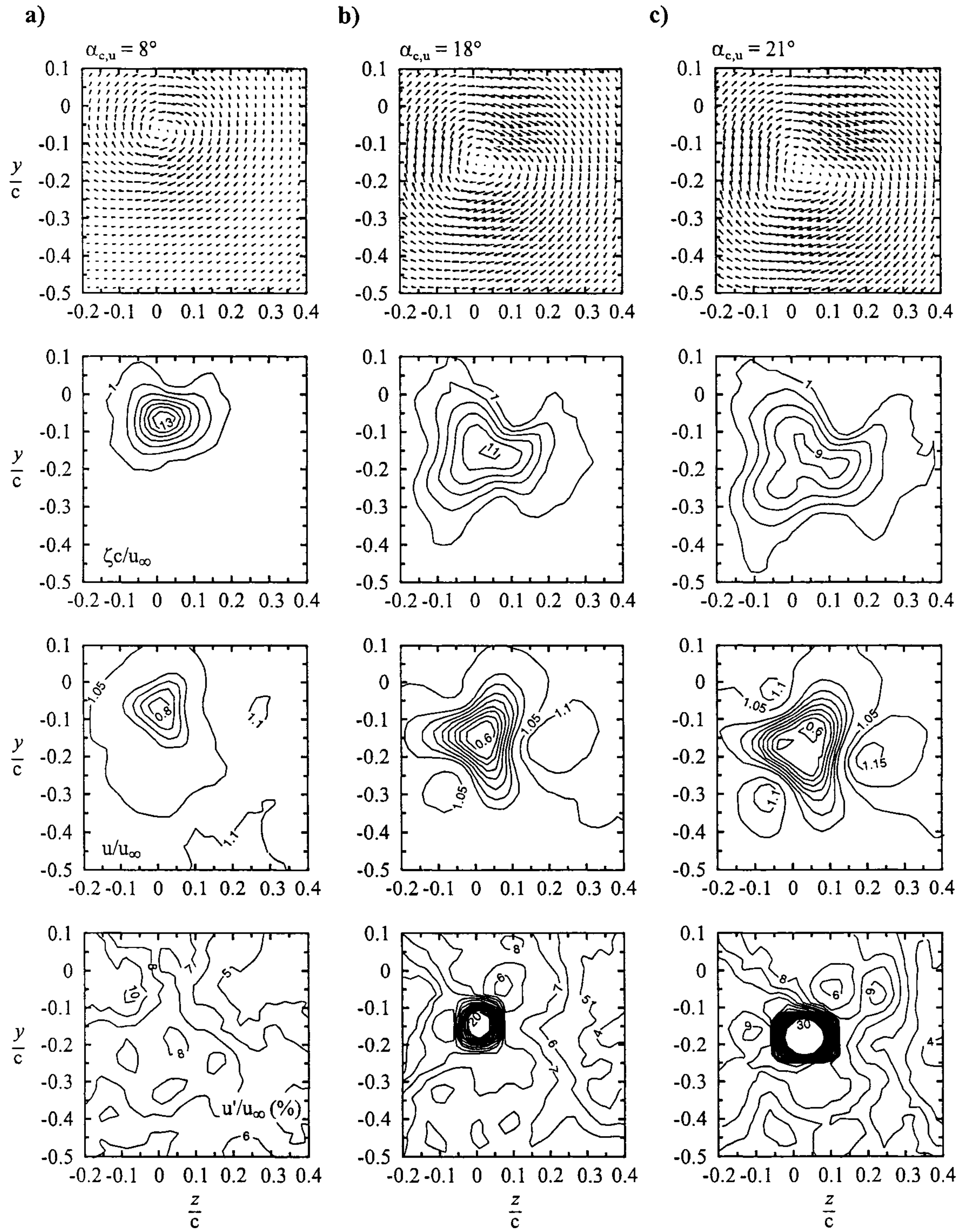

Figure 35 Velocity vectors and contours of constant vorticity, axial mean and RMS velocities for the case of the inverted spoiler at $x/c = 2$, with $\alpha = 14° + 8°\sin(\omega t)$. (a) $\alpha_{c,u} = 8°$; (b) $\alpha_{c,u} = 18°$; (c) $\alpha_{c,u} = 21°$; (d) $\alpha_{c,d} = 18°$; (e) $\alpha_{c,d} = 8°$.

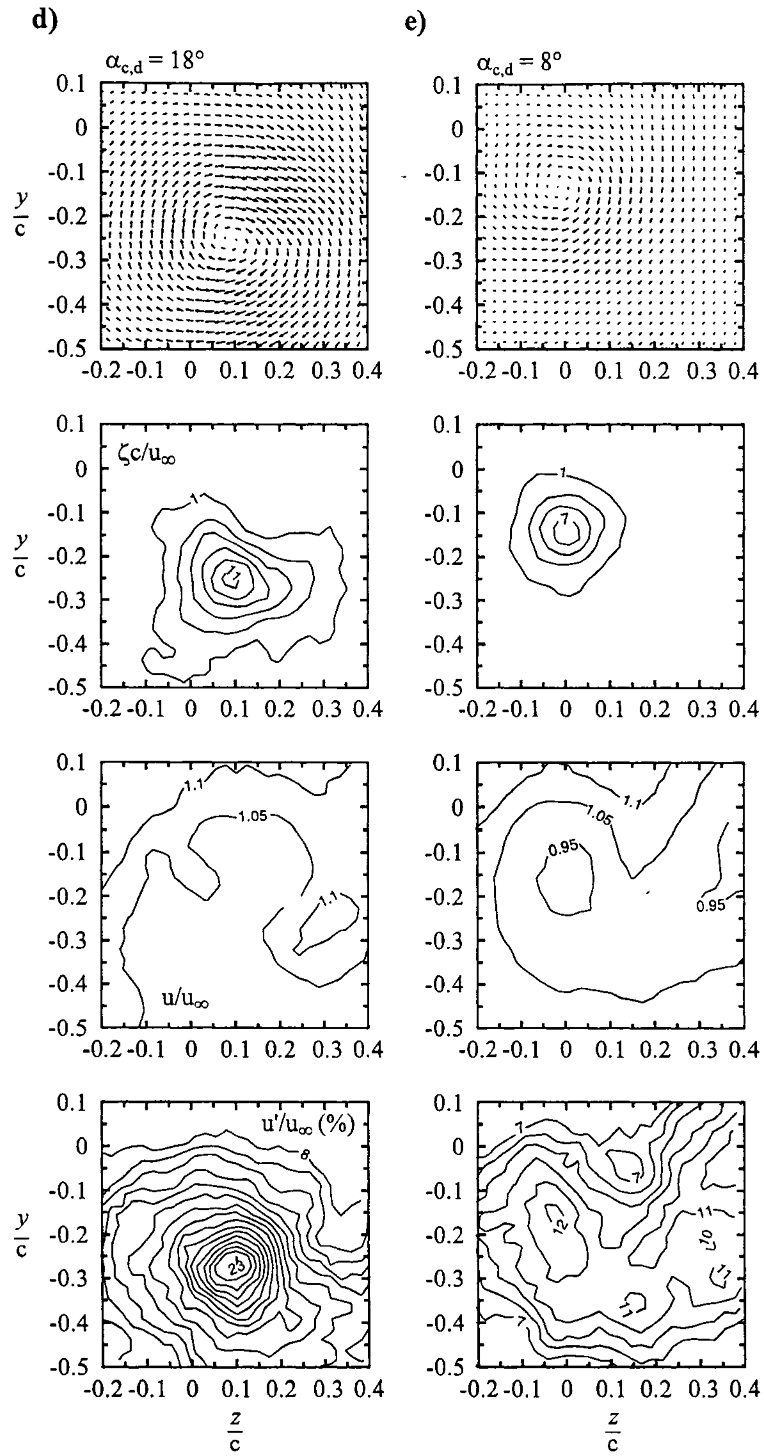

Figure 35 Velocity vectors and contours of constant vorticity, axial mean and RMS velocities for the case of the inverted spoiler at x/c = 2, with $\alpha = 14° + 8°\sin(\omega t)$. (a) $\alpha_{c,u} = 8°$; (b) $\alpha_{c,u} = 18°$; (c) $\alpha_{c,u} = 21°$; (d) $\alpha_{c,d} = 18°$; (e) $\alpha_{c,d} = 8°$.

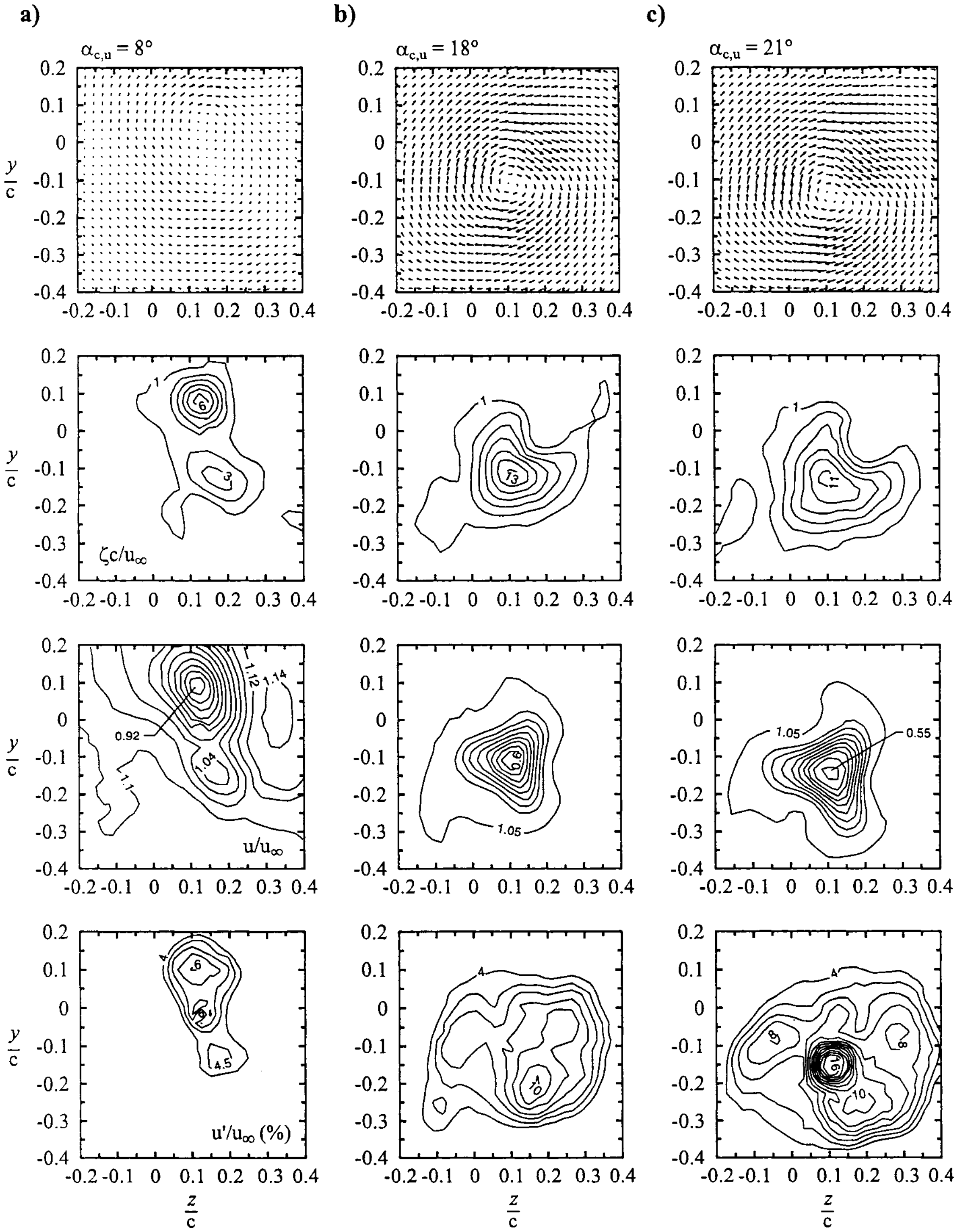

Figure 36 Velocity vectors and contours of constant vorticity, axial mean and RMS velocities for the case of the non-inverted spoiler at $x/c = 2$, with $\alpha = 14° + 8°\sin(\omega t)$. (a) $\alpha_{c,u} = 8°$; (b) $\alpha_{c,u} = 18°$; (c) $\alpha_{c,u} = 21°$; (d) $\alpha_{c,d} = 18°$; (e) $\alpha_{c,d} = 8°$.

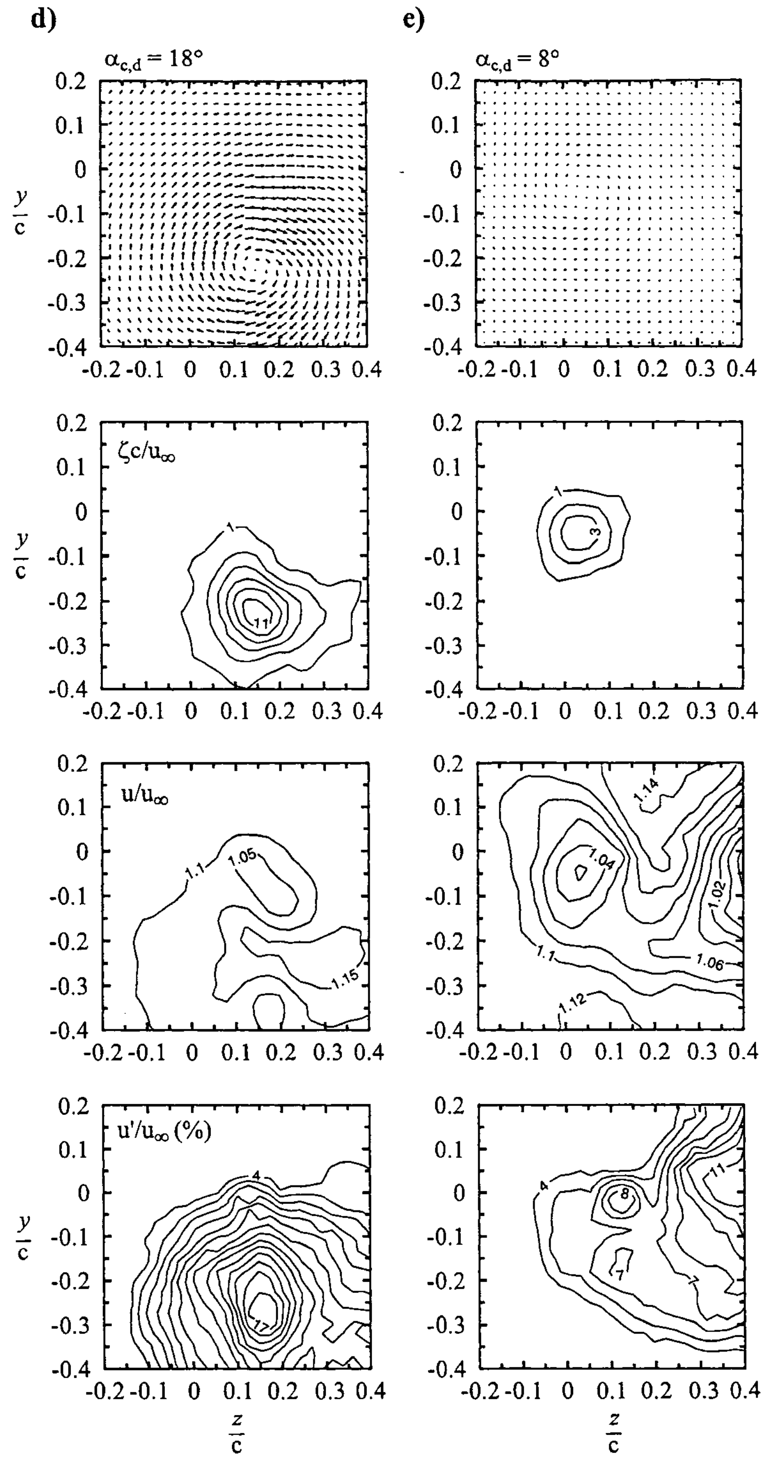

Figure 36 Velocity vectors and contours of constant vorticity, axial mean and RMS velocities for the case of the non-inverted spoiler at $x/c = 2$, with $\alpha = 14° + 8°\sin(\omega t)$. (a) $\alpha_{c,u} = 8°$; (b) $\alpha_{c,u} = 18°$; (c) $\alpha_{c,u} = 21°$; (d) $\alpha_{c,d} = 18°$; (e) $\alpha_{c,d} = 8°$.

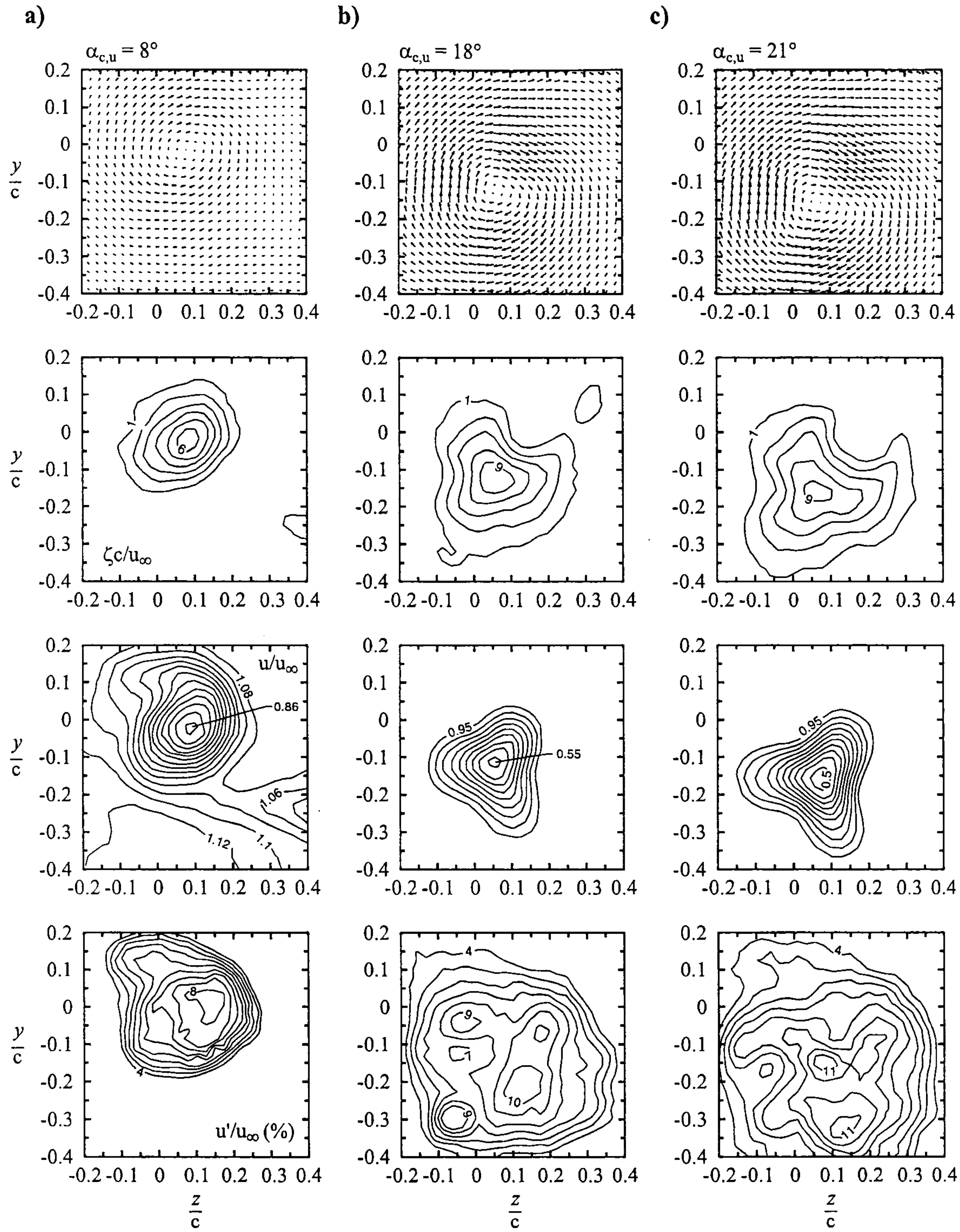

Figure 37 Velocity vectors and contours of constant vorticity, axial mean and RMS velocities for the case of the symmetric strip at x/c = 2, with $\alpha = 14° + 8°\sin(\omega t)$. (a) $\alpha_{c,u} = 8°$; (b) $\alpha_{c,u} = 18°$; (c) $\alpha_{c,u} = 21°$; (d) $\alpha_{c,d} = 18°$; (e) $\alpha_{c,d} = 8°$.

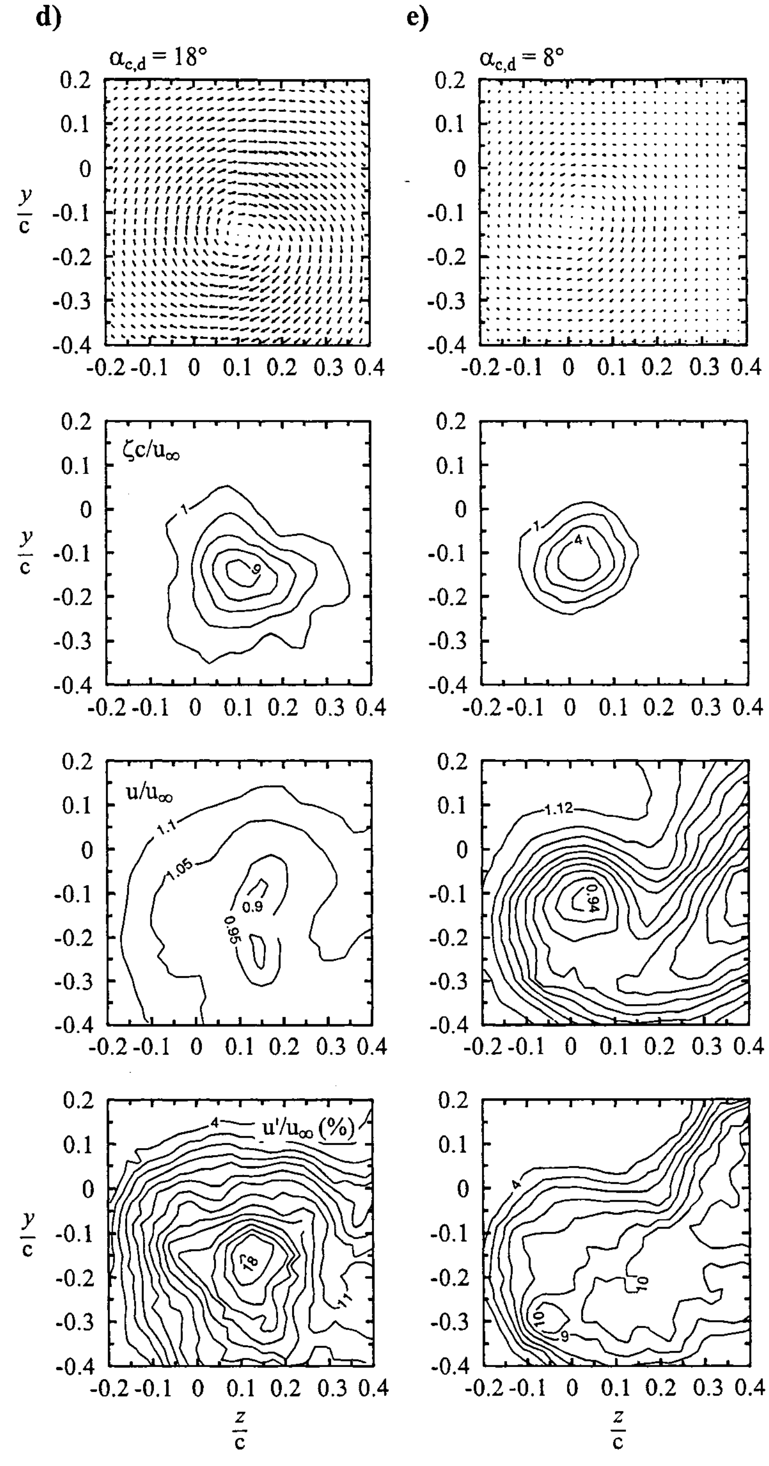

Figure 37 Velocity vectors and contours of constant vorticity, axial mean and RMS velocities for the case of the symmetric strip at x/c = 2, with $\alpha = 14° + 8°\sin(\omega t)$. (a) $\alpha_{c,u} = 8°$; (b) $\alpha_{c,u} = 18°$; (c) $\alpha_{c,u} = 21°$; (d) $\alpha_{c,d} = 18°$; (e) $\alpha_{c,d} = 8°$.

a)

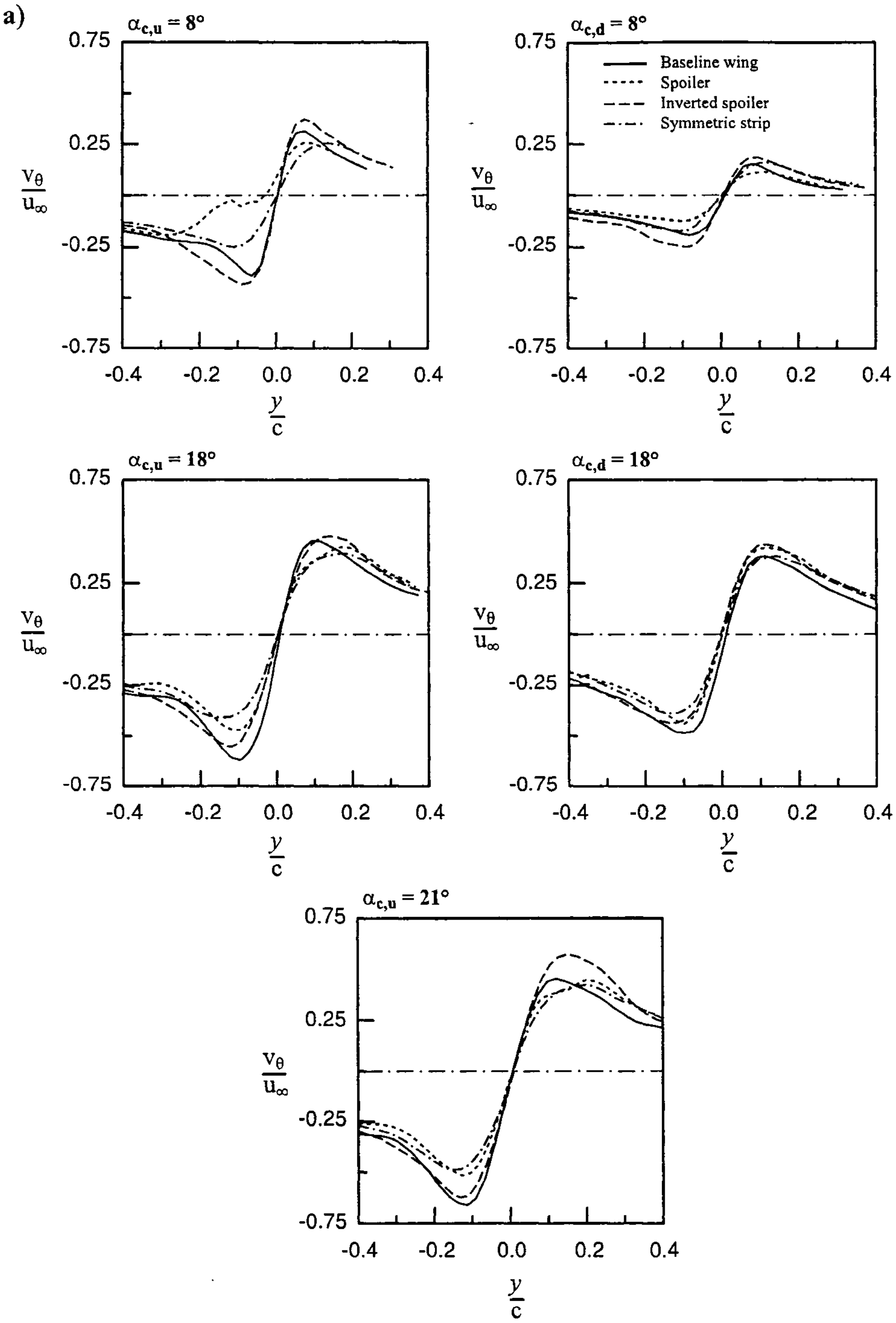

Figure 38 Vortex flow quantities measured across the vortex center at selected incidences with different trailing-edge spoiler configurations, for $x/c = 2$ and $\alpha = 14° + 8°\sin(\omega t)$. (a) Tangential velocity; (b) vorticity; (c) axial mean velocity; (d) axial RMS velocity.

b)

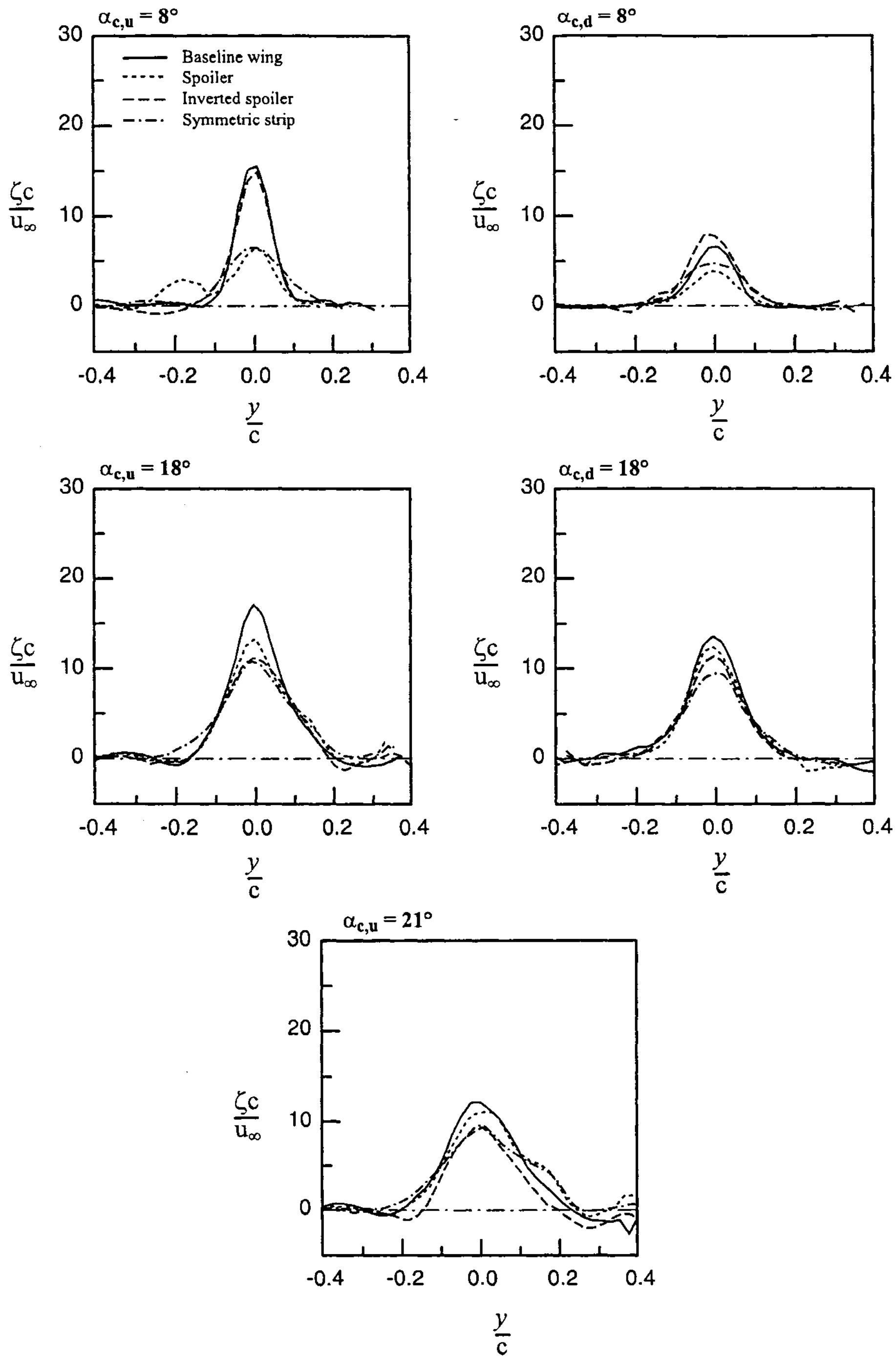

Figure 38 Vortex flow quantities measured across the vortex center at selected incidences with different trailing-edge spoiler configurations, for $x/c = 2$ and $\alpha = 14° + 8°\sin(\omega t)$. (a) Tangential velocity; (b) vorticity; (c) axial mean velocity; (d) axial RMS velocity.

c)

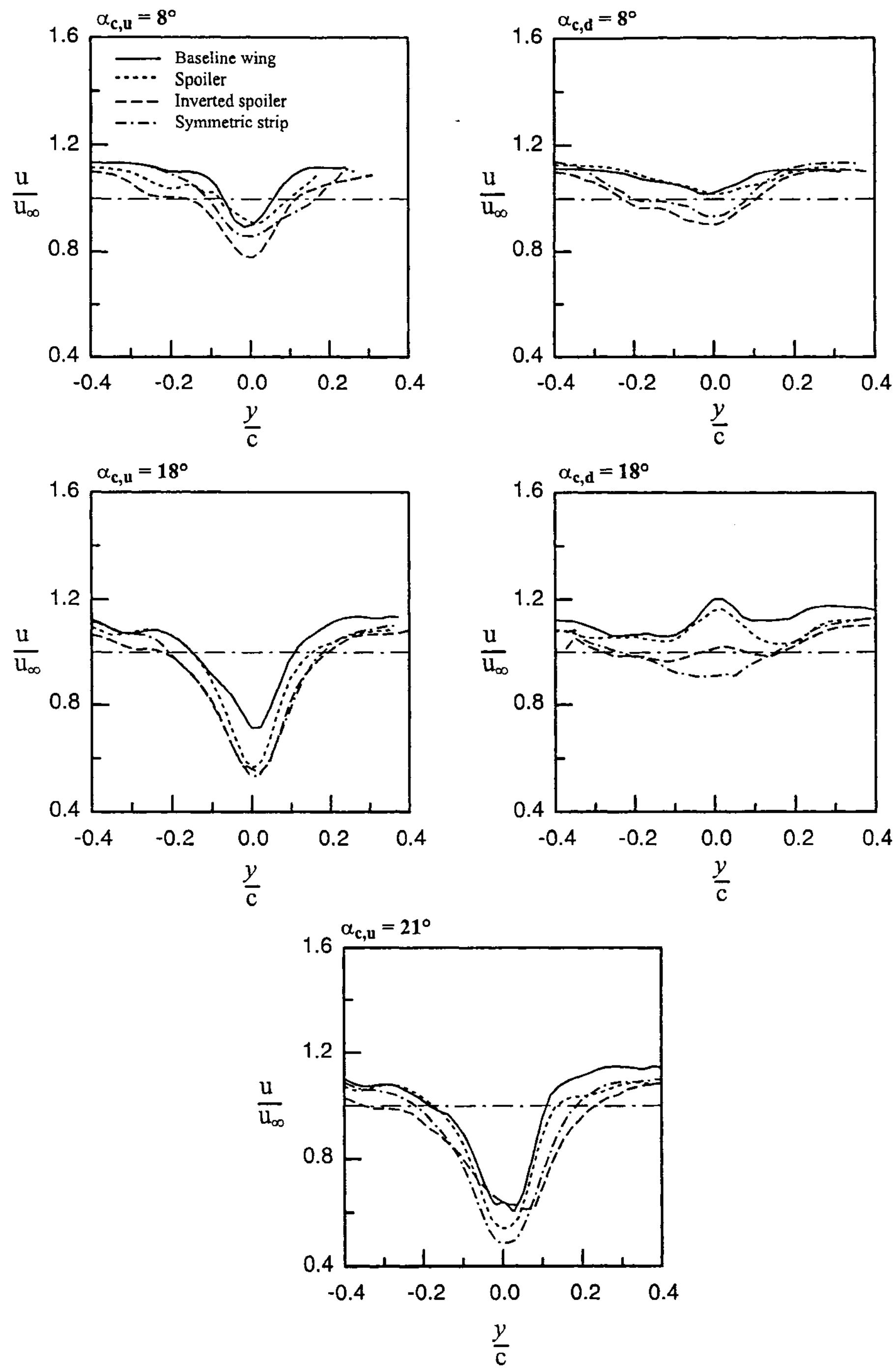

Figure 38 Vortex flow quantities measured across the vortex center at selected incidences with different trailing-edge spoiler configurations, for $x/c = 2$ and $\alpha = 14° + 8°\sin(\omega t)$. (a) Tangential velocity; (b) vorticity; (c) axial mean velocity; (d) axial RMS velocity.

d)

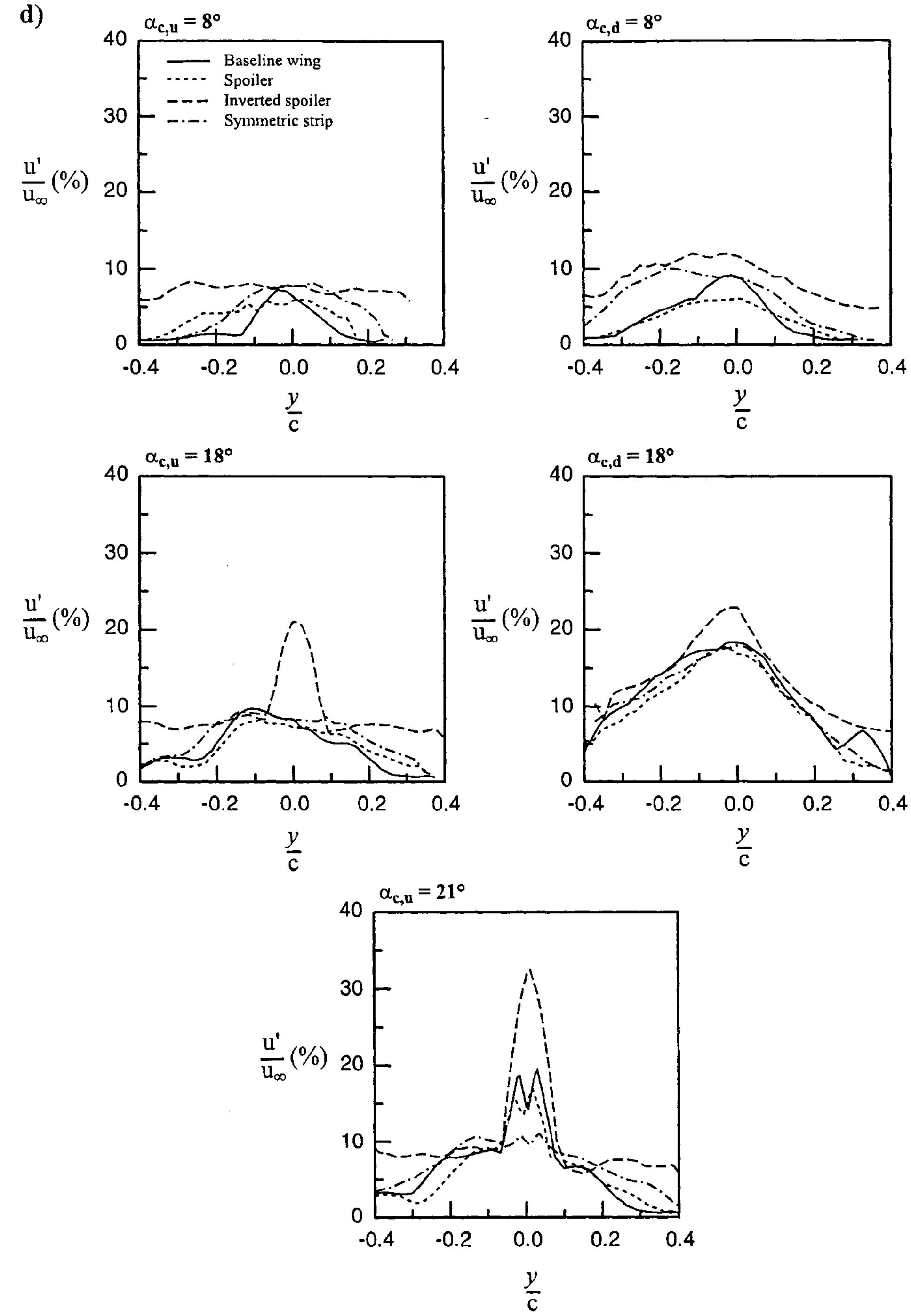

Figure 38 Vortex flow quantities measured across the vortex center at selected incidences with different trailing-edge spoiler configurations, for $x/c = 2$ and $\alpha = 14° + 8°\sin(\omega t)$. (a) Tangential velocity; (b) vorticity; (c) axial mean velocity; (d) axial RMS velocity.

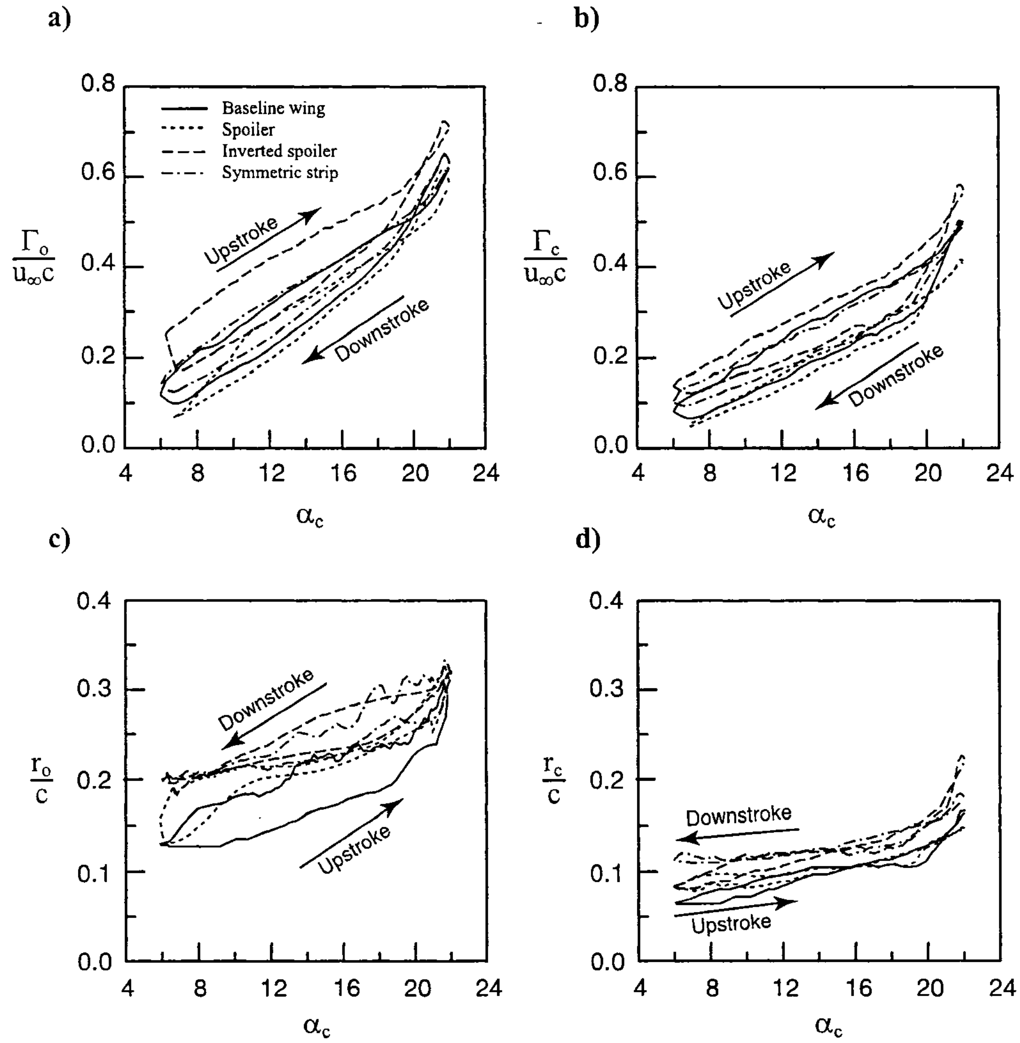

Figure 39 Variation of critical vortex quantities at $x/c = 2$, for $\alpha = 14° + 8°\sin(\omega t)$ and $\kappa = 0.09$. (a) Total circulation; (b) core circulation; (c) outer radius; (d) core radius; (e) peak tangential velocity; (f) peak vorticity; (g) core axial velocity; (h) core RMS velocity; (i) induced drag, and (j-k) fortex trajectory.

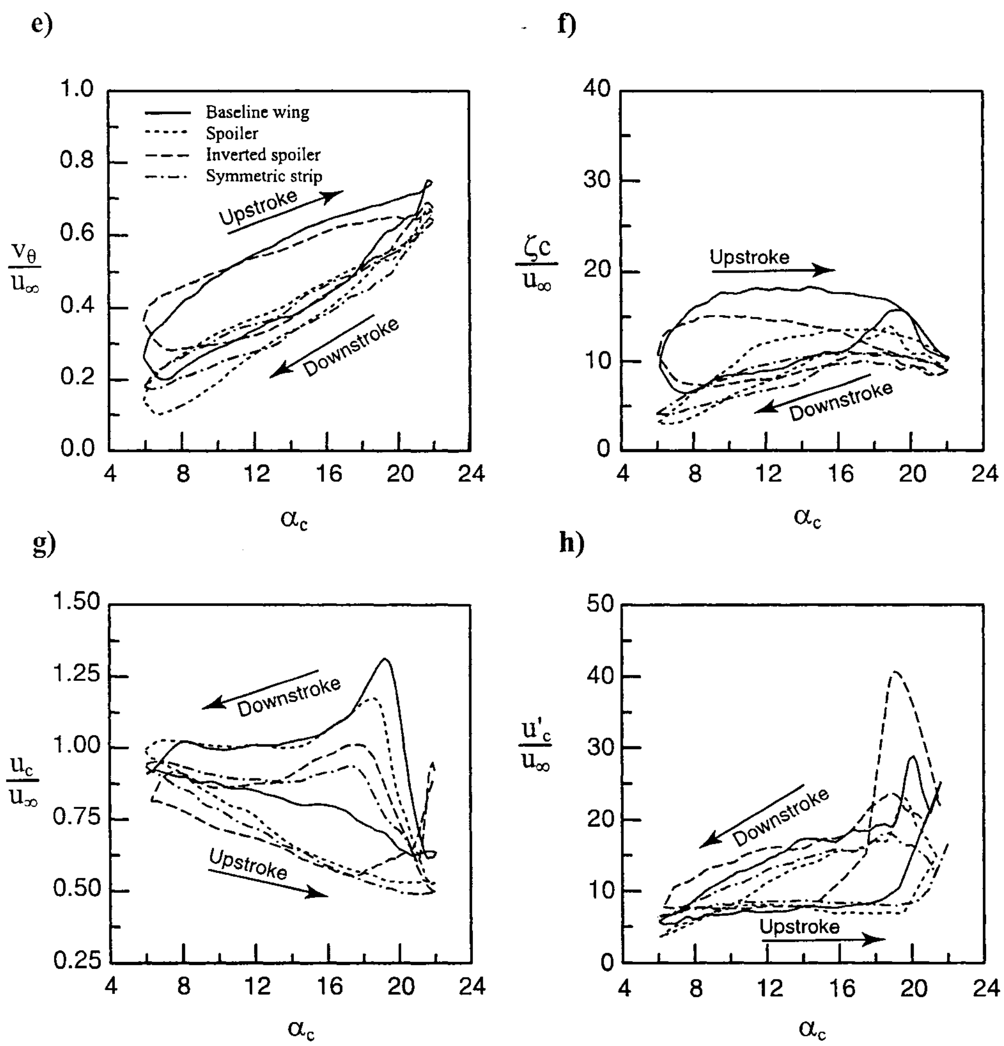

Figure 39 Variation of critical vortex quantities at $x/c = 2$, for $\alpha = 14° + 8°\sin(\omega t)$ and $\kappa = 0.09$. (a) Total circulation; (b) core circulation; (c) outer radius; (d) core radius; (e) peak tangential velocity; (f) peak vorticity; (g) core axial velocity; (h) core RMS velocity; (i) induced drag, and (j-k) fortex trajectory.

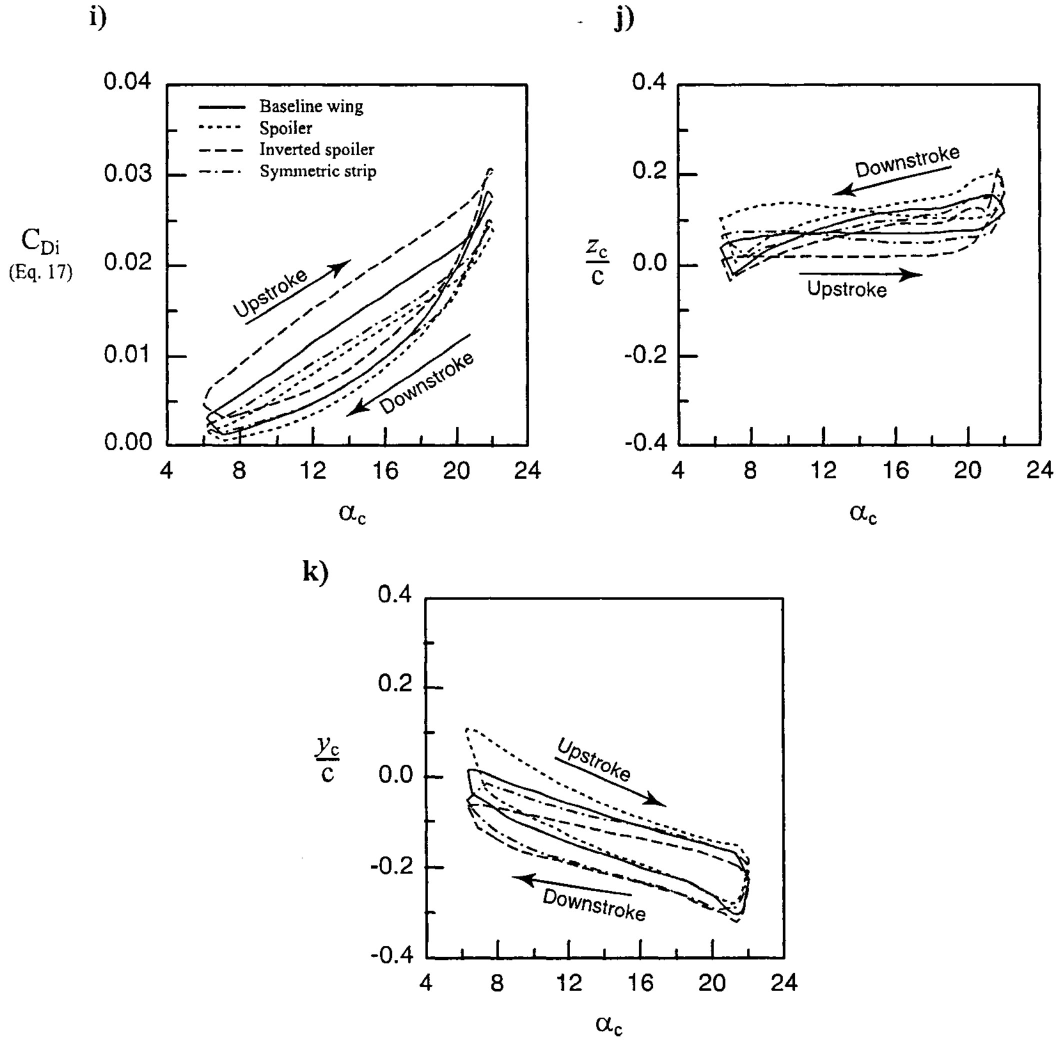

Figure 39 Variation of critical vortex quantities at $x/c = 2$, for $\alpha = 14° + 8°\sin(\omega t)$ and $\kappa = 0.09$. (a) Total circulation; (b) core circulation; (c) outer radius; (d) core radius; (e) peak tangential velocity; (f) peak vorticity; (g) core axial velocity; (h) core RMS velocity; (i) induced drag, and (j-k) vortex trajectory.

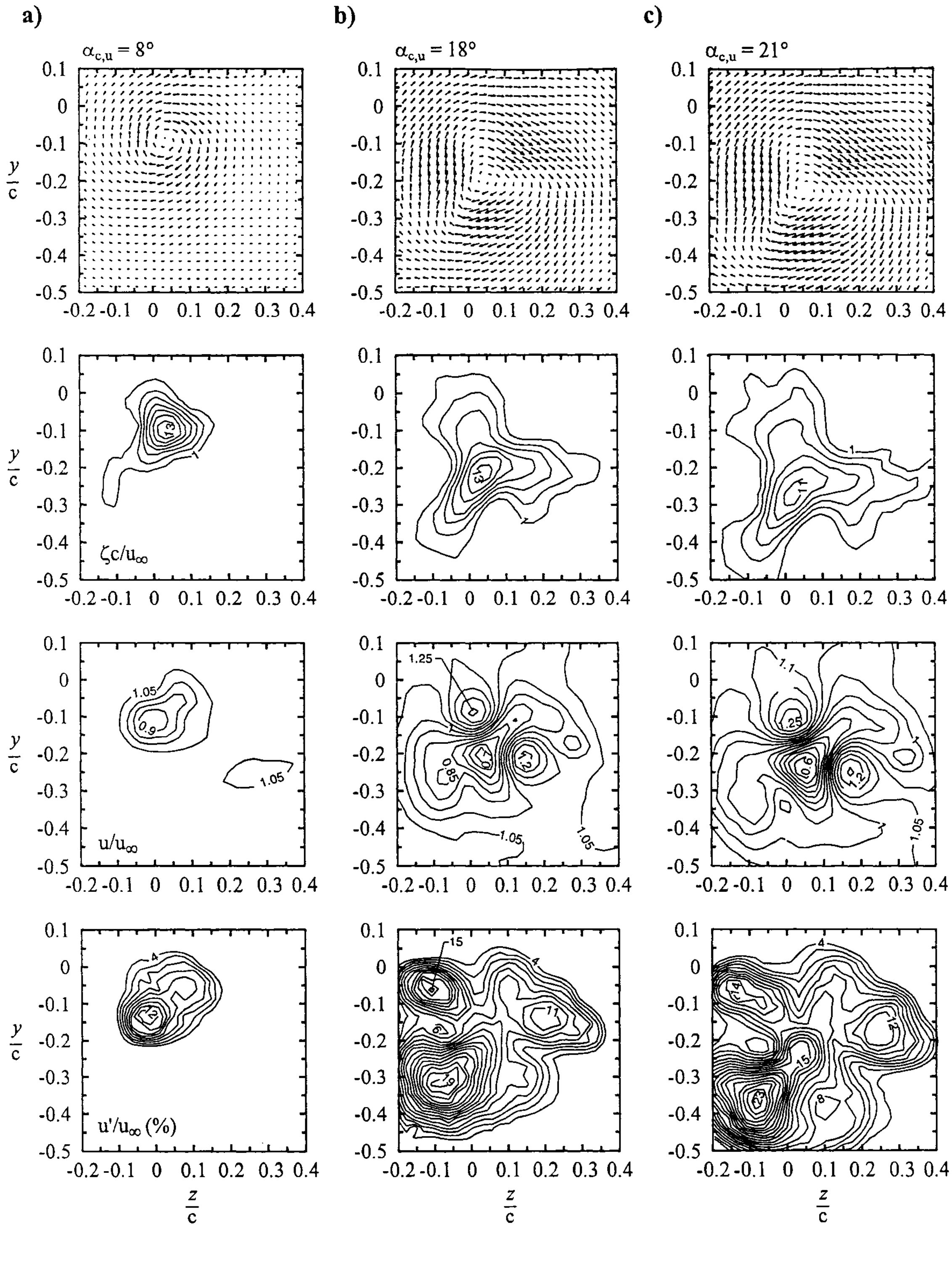

Figure 40 Velocity vectors and contours of constant vorticity, axial mean and RMS velocities for the case of the 25% TE tab deflected with $\delta = 5.3°$ at $x/c = 2$, with $\alpha = 14° + 8°\sin(\omega t)$. (a) $\alpha_{c,u} = 8°$; (b) $\alpha_{c,u} = 18°$; (c) $\alpha_{c,u} = 21°$; (d) $\alpha_{c,d} = 18°$; (e) $\alpha_{c,d} = 8°$.

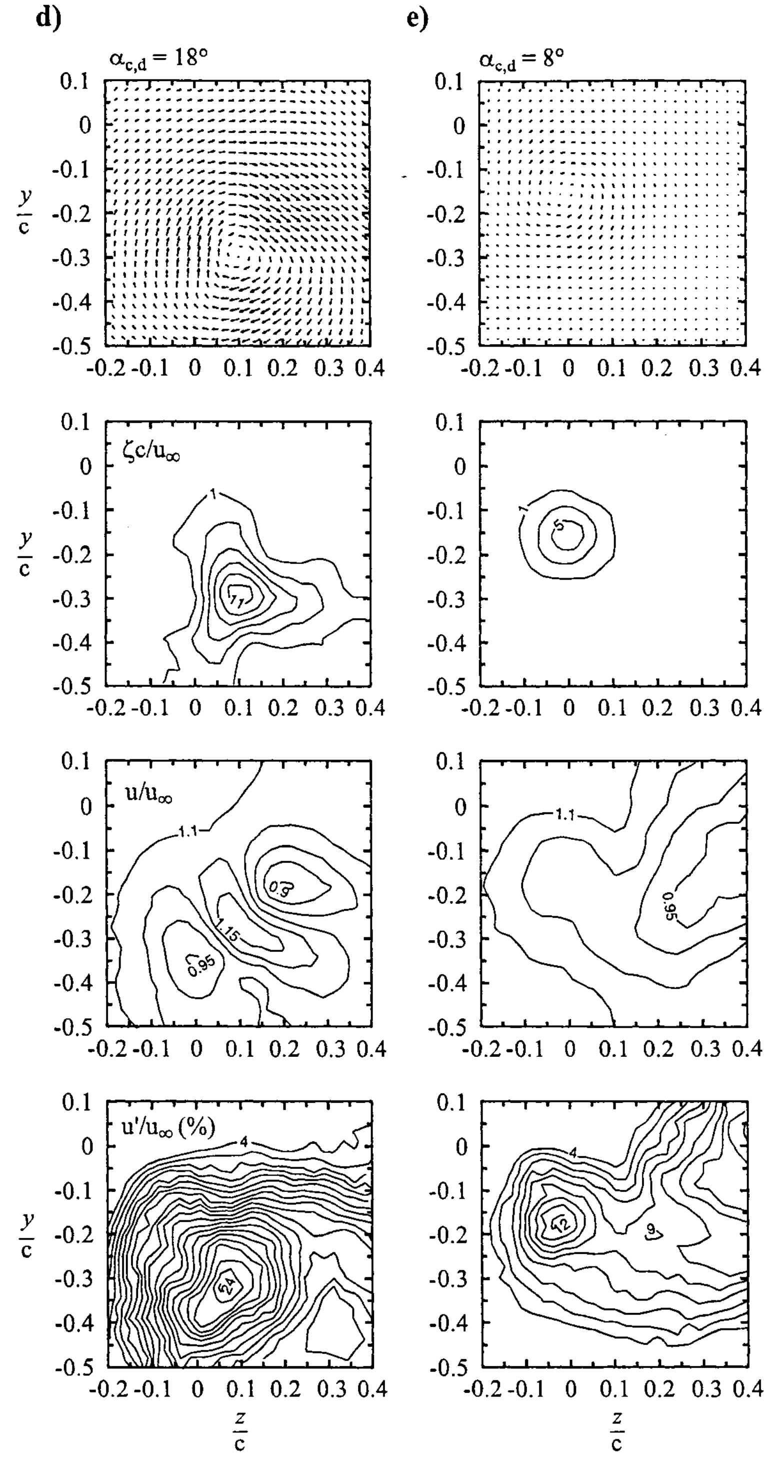

Figure 40 Velocity vectors and contours of constant vorticity, axial mean and RMS velocities for the case of the 25% TE tab deflected with $\delta = 5.3°$ at $x/c = 2$, with $\alpha = 14° + 8°\sin(\omega t)$. (a) $\alpha_{c,u} = 8°$; (b) $\alpha_{c,u} = 18°$; (c) $\alpha_{c,u} = 21°$; (d) $\alpha_{c,d} = 18°$; (e) $\alpha_{c,d} = 8°$.

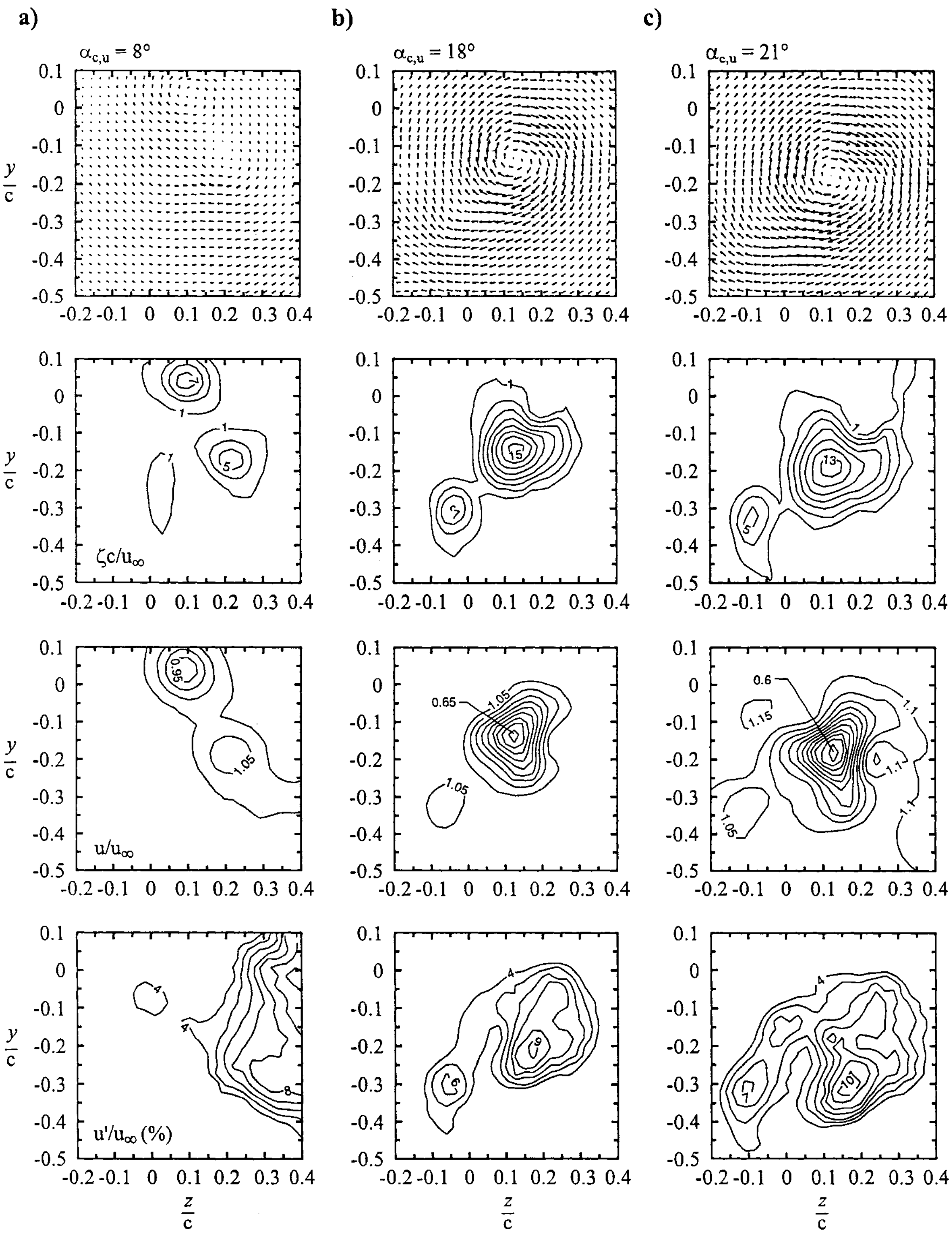

Figure 41 Velocity vectors and contours of constant vorticity, axial mean and RMS velocities for the case of the 25% TE tab deflected with δ = -5.3° at x/c = 2, with α = 14° + 8°sin(ωt). (a) $\alpha_{c,u}$ = 8°; (b) $\alpha_{c,u}$ = 18°; (c) $\alpha_{c,u}$ = 21°; (d) $\alpha_{c,d}$ = 18°; (e) $\alpha_{c,d}$ = 8°.

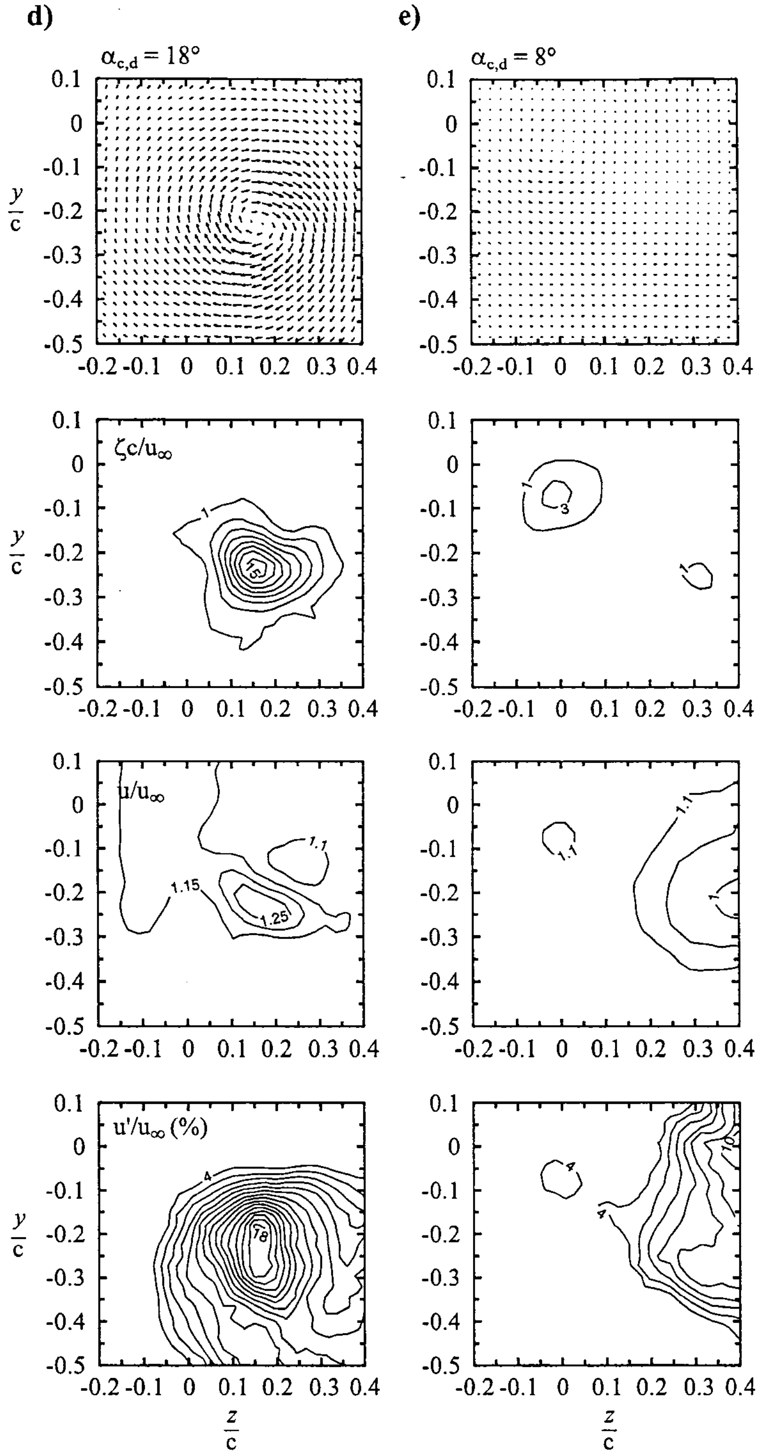

Figure 41 Velocity vectors and contours of constant vorticity, axial mean and RMS velocities for the case of the 25% TE tab deflected with δ = -5.3° at x/c = 2, with α = 14° + 8°sin(ωt). (a) $\alpha_{c,u}$ = 8°; (b) $\alpha_{c,u}$ = 18°; (c) $\alpha_{c,u}$ = 21°; (d) $\alpha_{c,d}$ = 18°; (e) $\alpha_{c,d}$ = 8°.

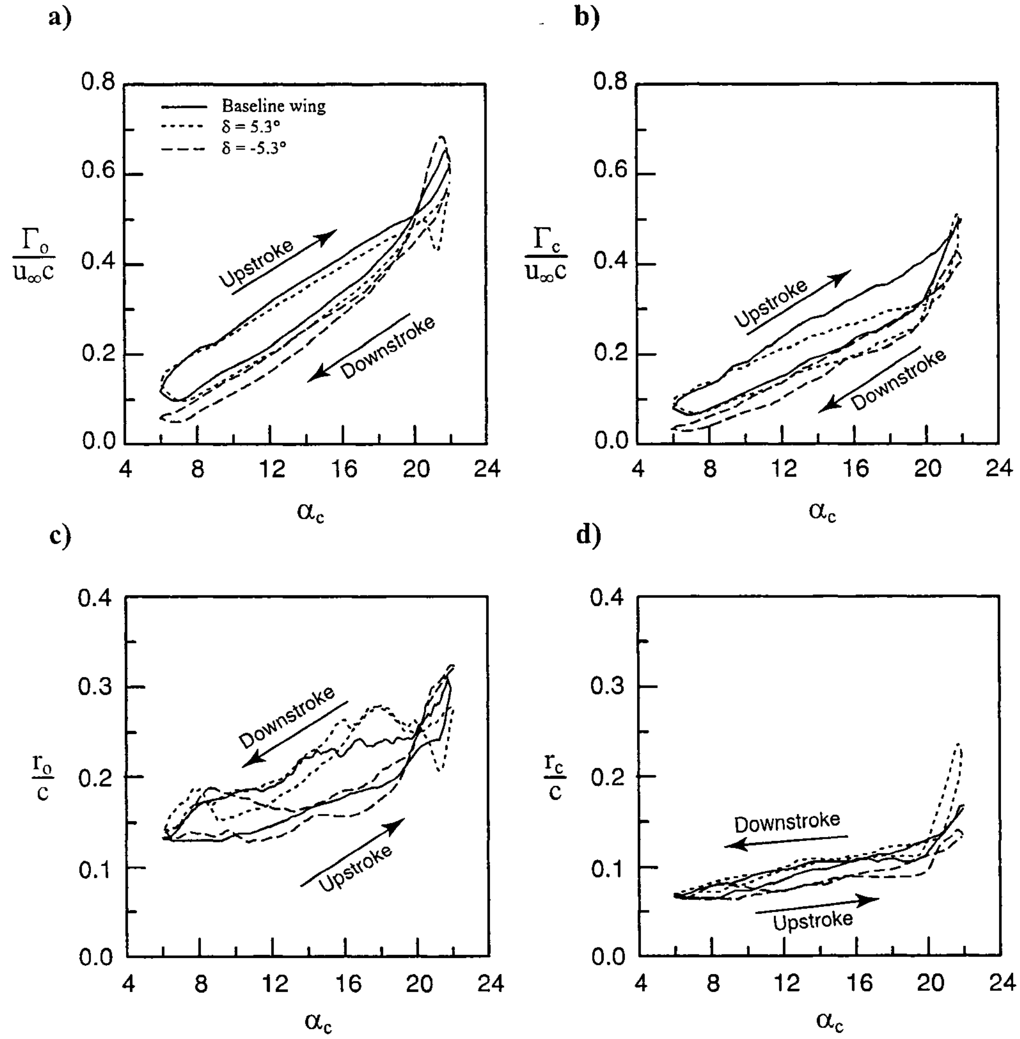

Figure 42 Variation of critical vortex quantities at $x/c = 2$, for $\alpha = 14° + 8°\sin(\omega t)$ and $\kappa = 0.09$. (a) Total circulation; (b) core circulation; (c) outer radius; (d) core radius; (e) peak tangential velocity; (f) peak vorticity; (g) core axial velocity; (h) core RMS velocity; (i) induced drag, and (j-k) fortex trajectory.

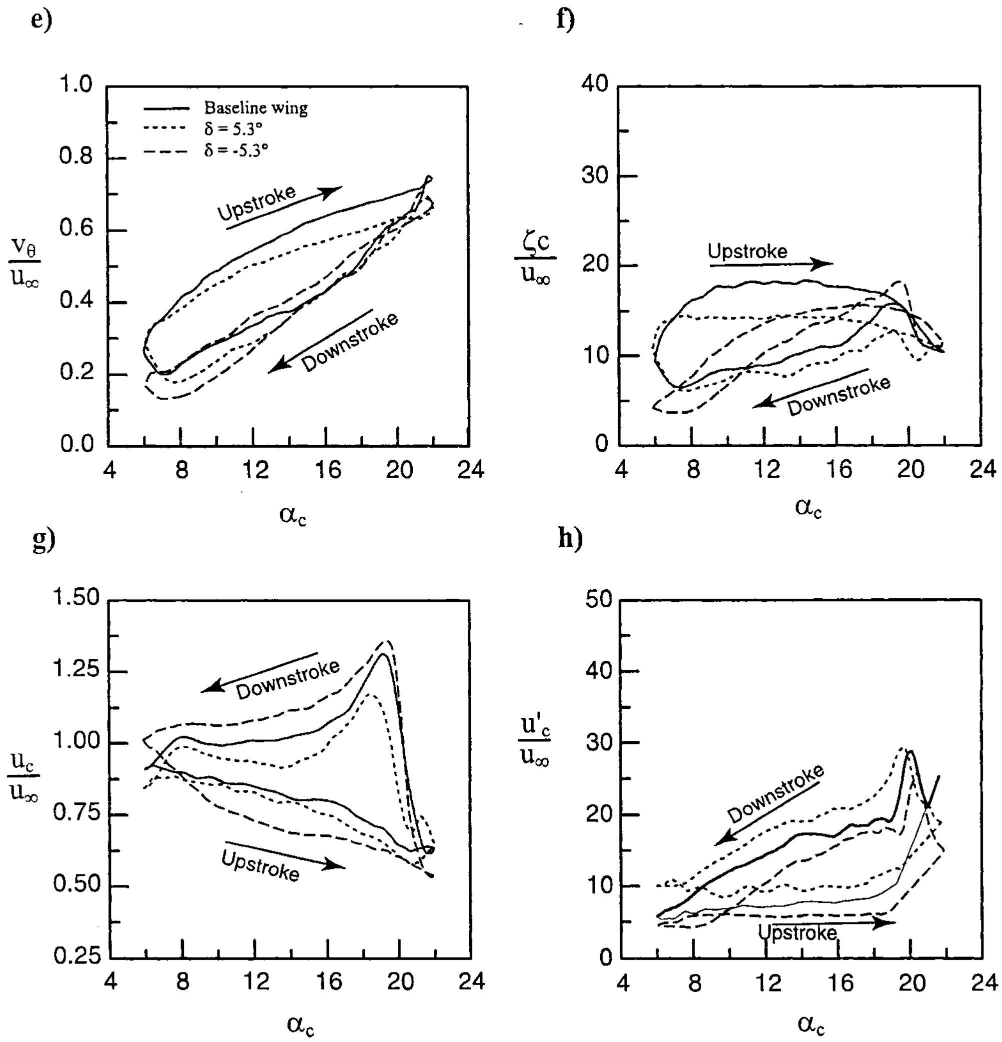

Figure 42 Variation of critical vortex quantities at $x/c = 2$, for $\alpha = 14° + 8°\sin(\omega t)$ and $\kappa = 0.09$. (a) Total circulation; (b) core circulation; (c) outer radius; (d) core radius; (e) peak tangential velocity; (f) peak vorticity; (g) core axial velocity; (h) core RMS velocity; (i) induced drag, and (j-k) fortex trajectory.

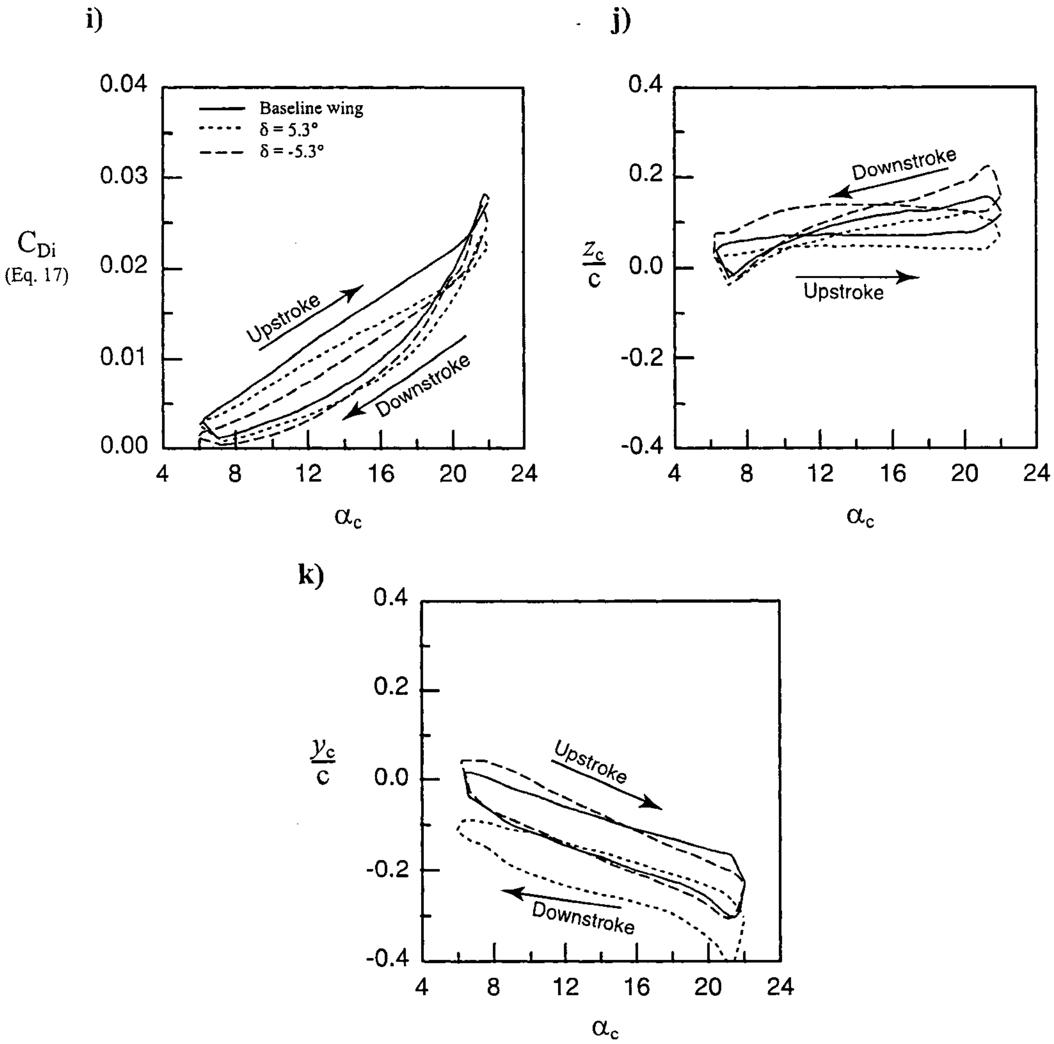

Figure 42 Variation of critical vortex quantities at $x/c = 2$, for $\alpha = 14° + 8°\sin(\omega t)$ and $\kappa = 0.09$. (a) Total circulation; (b) core circulation; (c) outer radius; (d) core radius; (e) peak tangential velocity; (f) peak vorticity; (g) core axial velocity; (h) core RMS velocity; (i) induced drag, and (j-k) vortex trajectory.

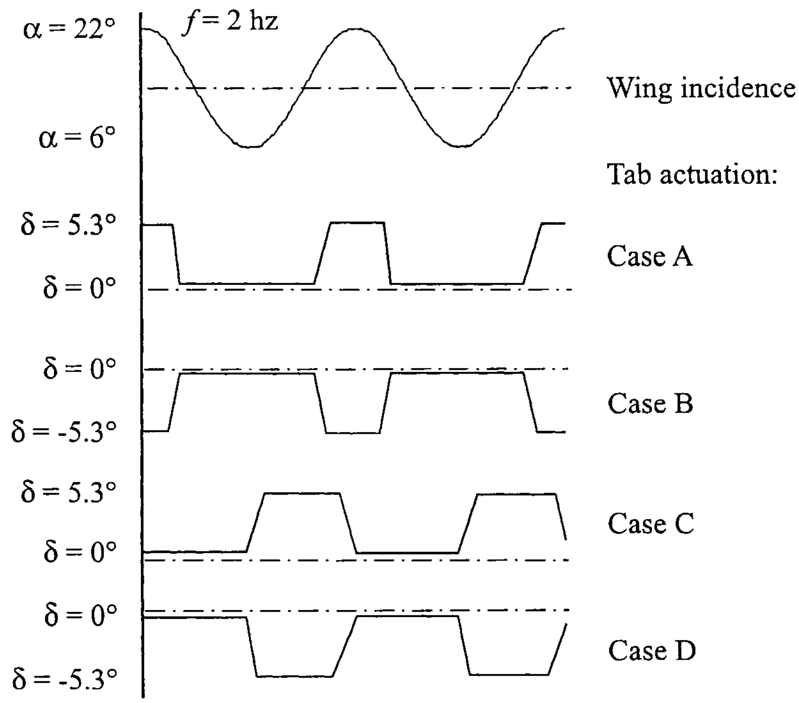

Figure 43 Tab deflection time-histories tested for active tip vortex control.

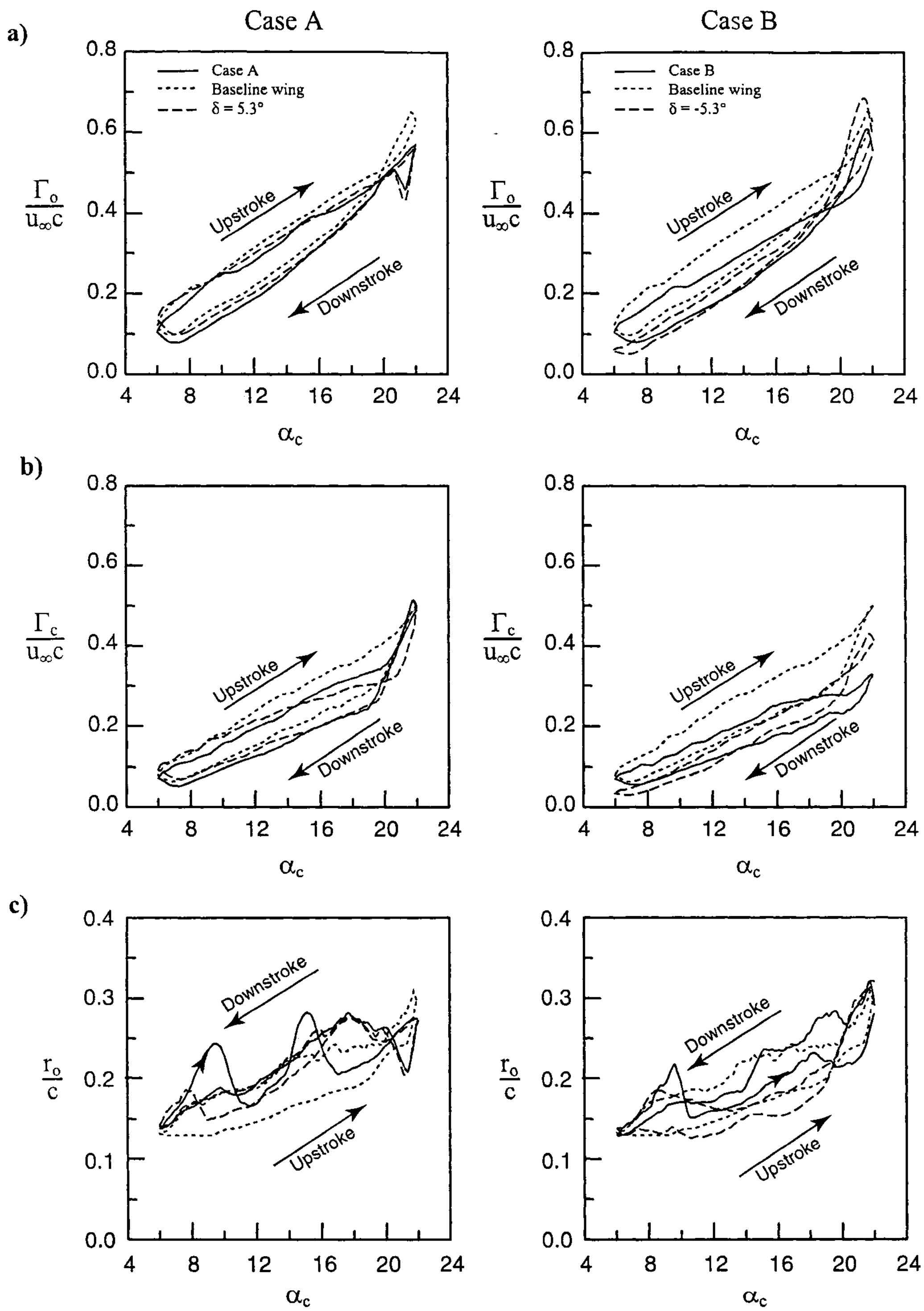

Figure 44 Variation of critical vortex quantities at $x/c = 2$, for $\alpha = 14° + 8°\sin(\omega t)$ and $\kappa = 0.09$. (a) Total circulation; (b) core circulation; (c) outer radius; (d) core radius; (e) peak tangential velocity; (f) peak vorticity; (g) core axial velocity; (h) core RMS velocity; (i) induced drag, and (j-k) vortex trajectory.

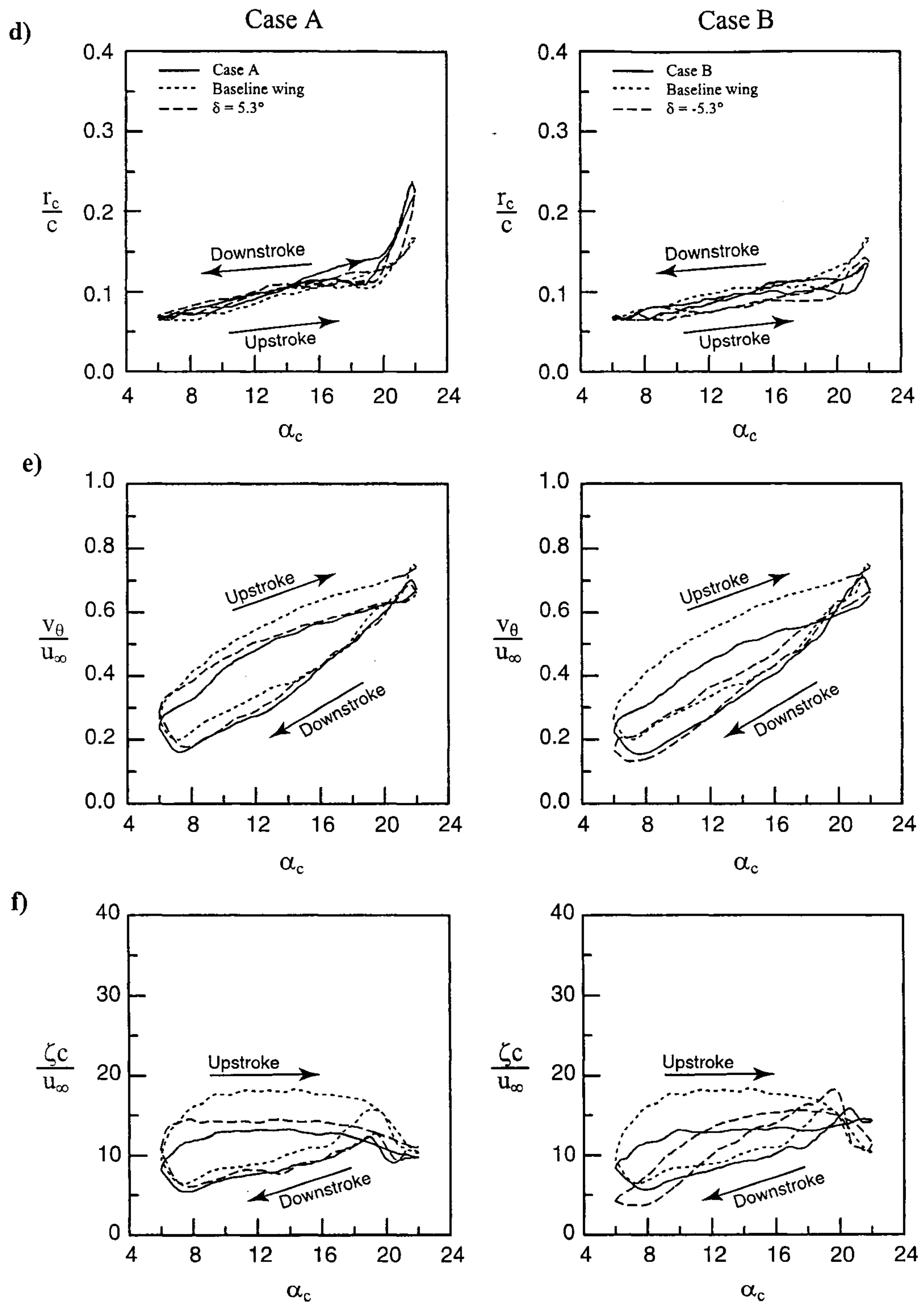

Figure 44 Variation of critical vortex quantities at $x/c = 2$, for $\alpha = 14° + 8°\sin(\omega t)$ and $\kappa = 0.09$. (a) Total circulation; (b) core circulation; (c) outer radius; (d) core radius; (e) peak tangential velocity; (f) peak vorticity; (g) core axial velocity; (h) core RMS velocity; (i) induced drag, and (j-k) vortex trajectory.

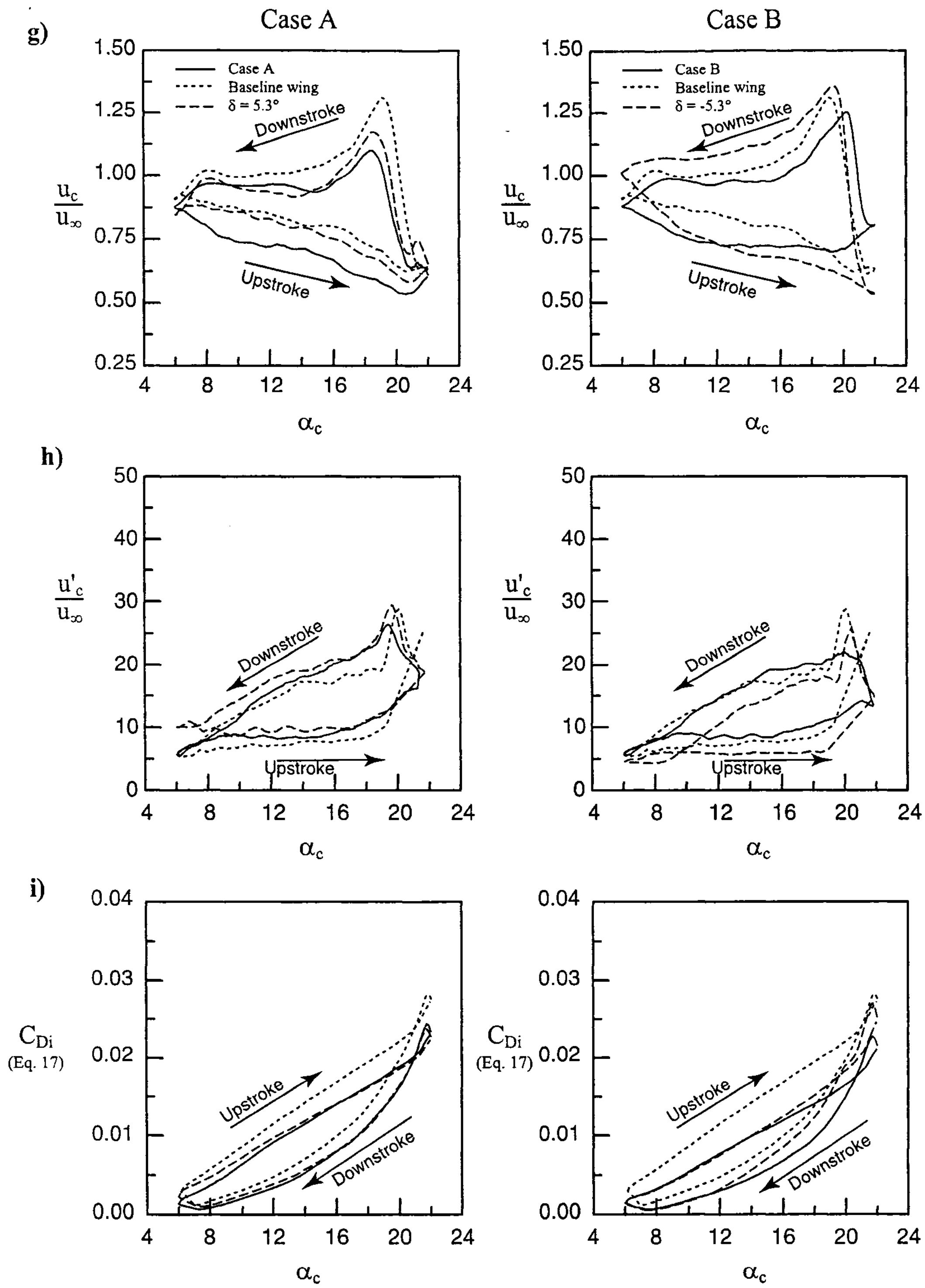

Figure 44 Variation of critical vortex quantities at $x/c = 2$, for $\alpha = 14° + 8°\sin(\omega t)$ and $\kappa = 0.09$. (a) Total circulation; (b) core circulation; (c) outer radius; (d) core radius; (e) peak tangential velocity; (f) peak vorticity; (g) core axial velocity; (h) core RMS velocity; (i) induced drag, and (j-k) vortex trajectory.

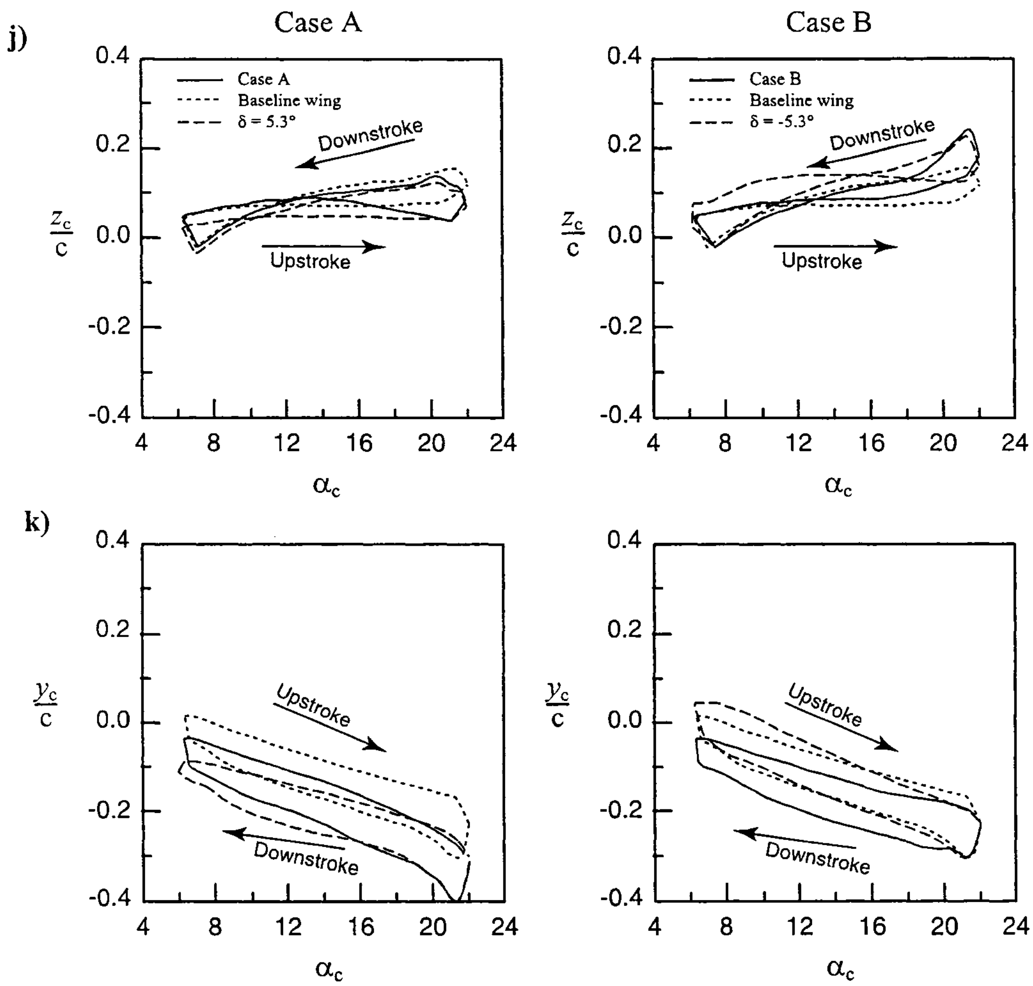

Figure 44 Variation of critical vortex quantities at $x/c = 2$, for $\alpha = 14° + 8°\sin(\omega t)$ and $\kappa = 0.09$. (a) Total circulation; (b) core circulation; (c) outer radius; (d) core radius; (e) peak tangential velocity; (f) peak vorticity; (g) core axial velocity; (h) core RMS velocity; (i) induced drag, and (j-k) vortex trajectory.

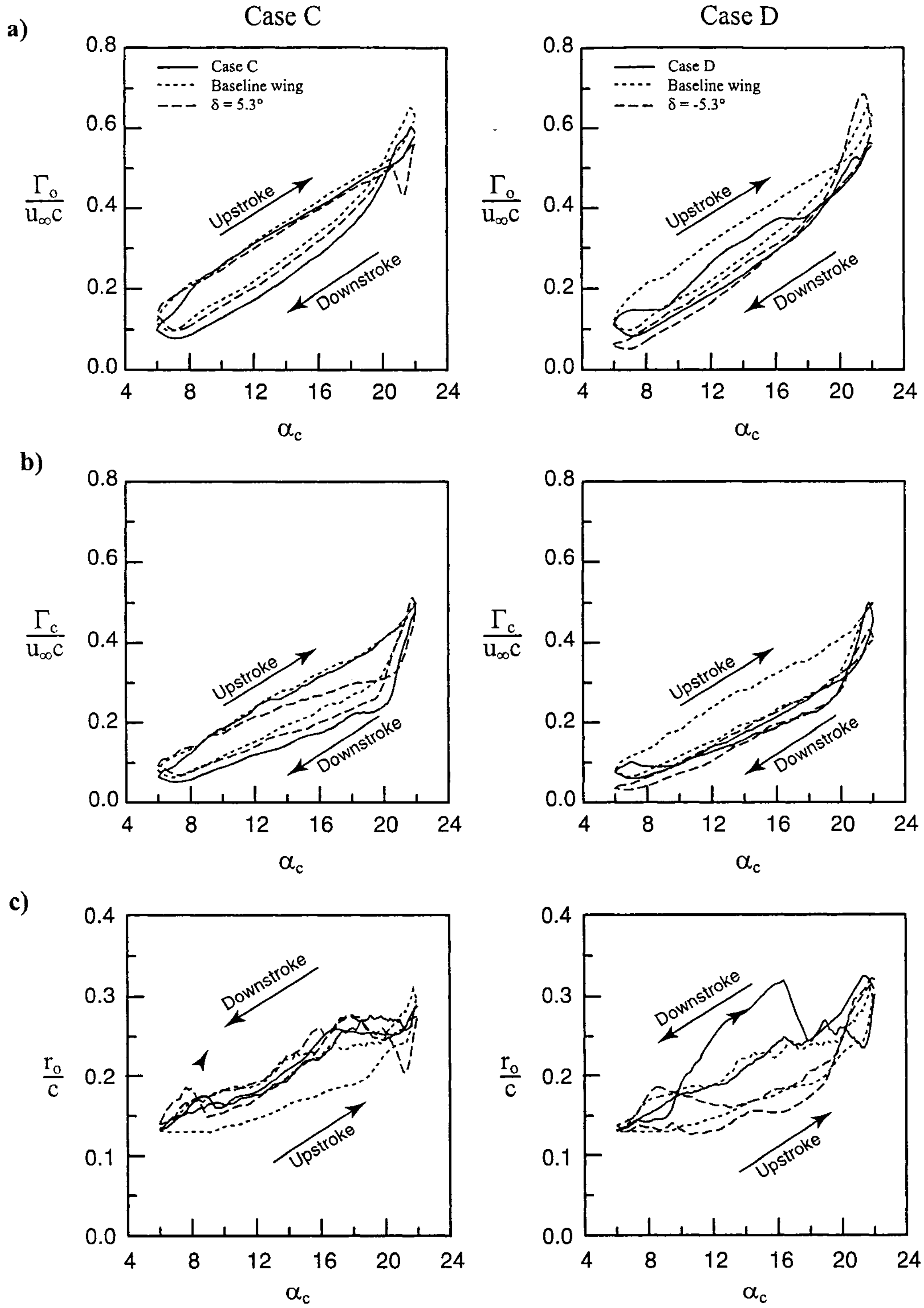

Figure 45 Variation of critical vortex quantities at x/c = 2, for $\alpha = 14° + 8°\sin(\omega t)$ and $\kappa = 0.09$. (a) Total circulation; (b) core circulation; (c) outer radius; (d) core radius; (e) peak tangential velocity; (f) peak vorticity; (g) core axial velocity; (h) core RMS velocity; (i) induced drag, and (j-k) vortex trajectory.

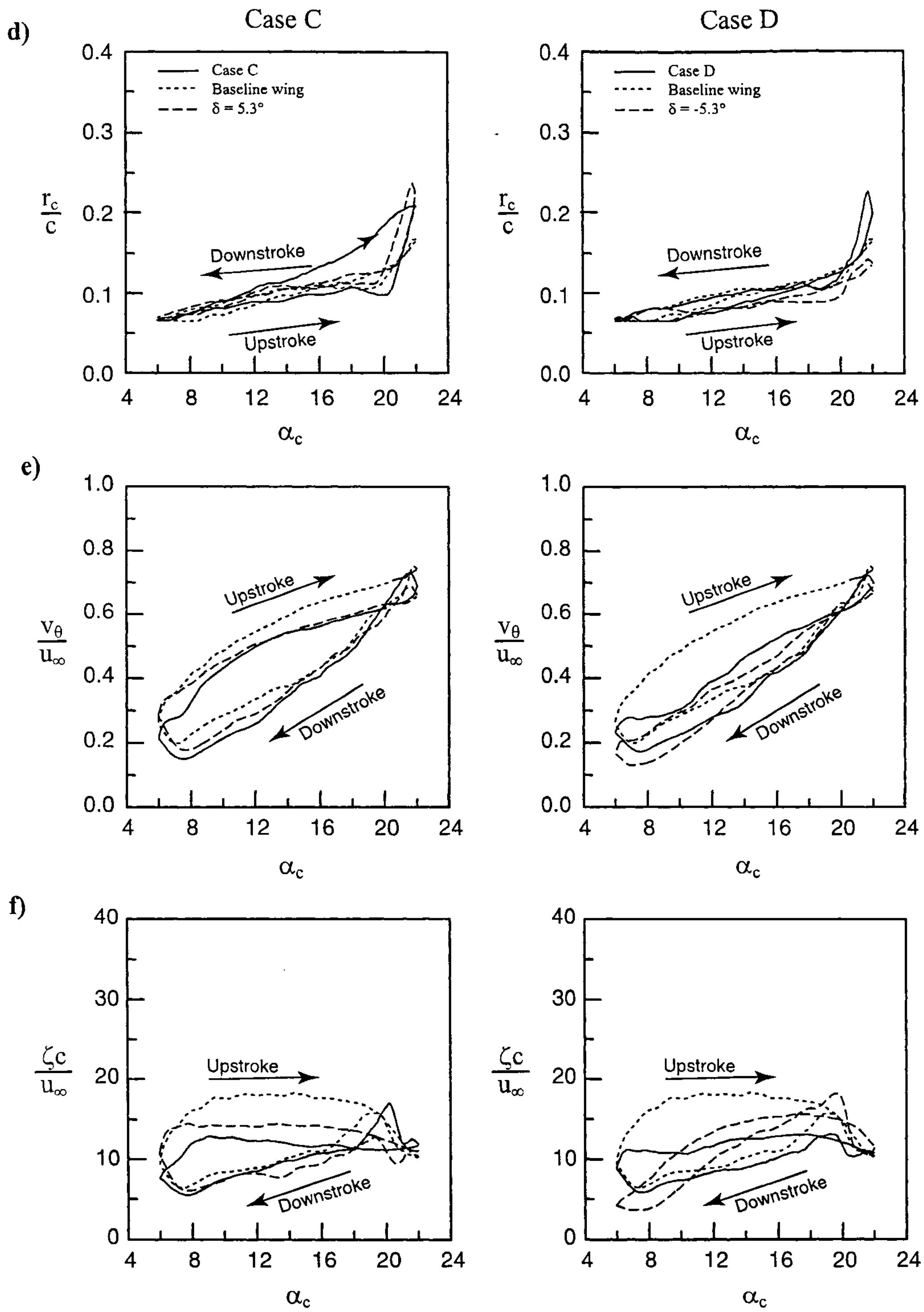

Figure 45 Variation of critical vortex quantities at $x/c = 2$, for $\alpha = 14° + 8°\sin(\omega t)$ and $\kappa = 0.09$. (a) Total circulation; (b) core circulation; (c) outer radius; (d) core radius; (e) peak tangential velocity; (f) peak vorticity; (g) core axial velocity; (h) core RMS velocity; (i) induced drag, and (j-k) vortex trajectory.

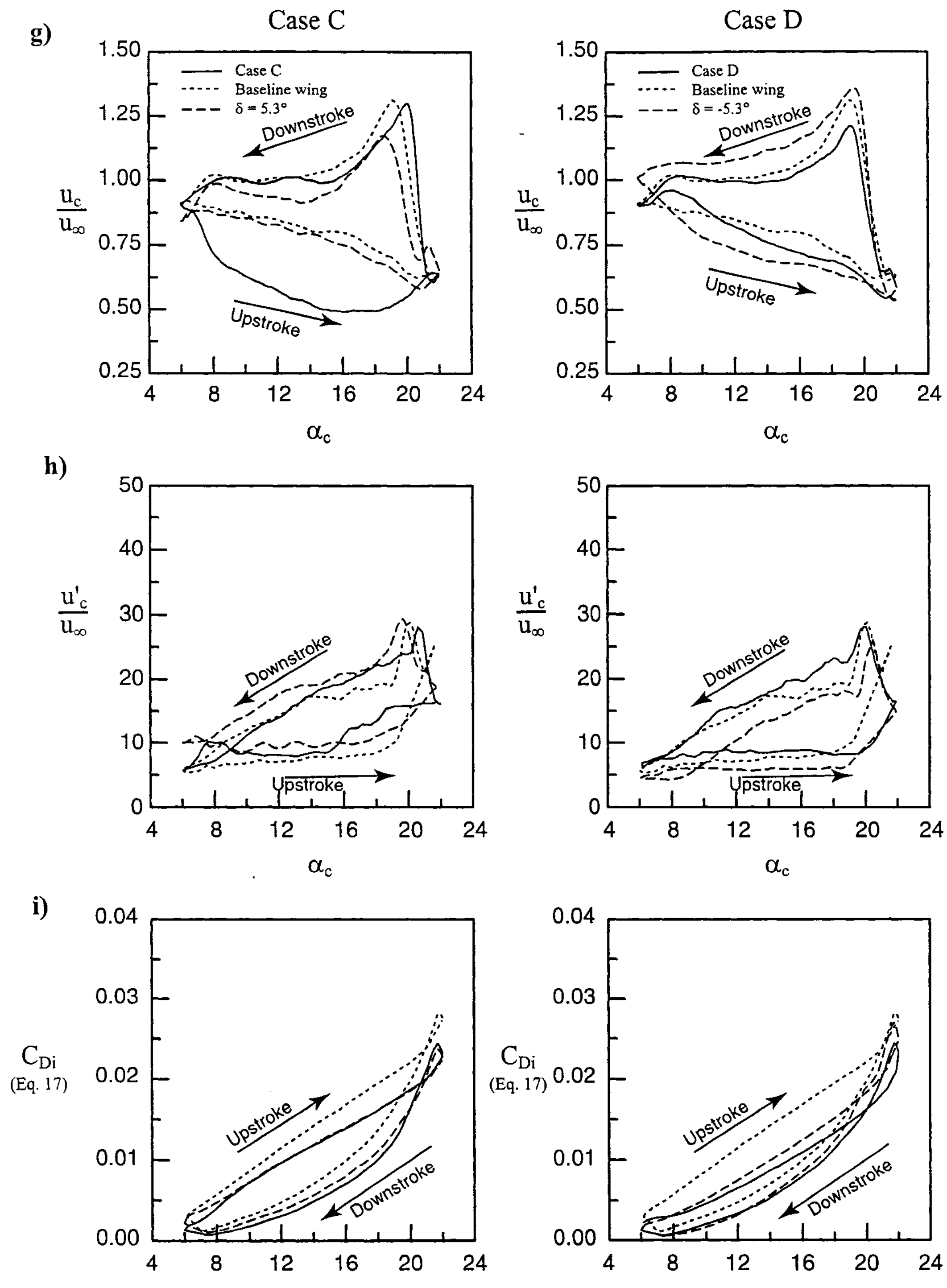

Figure 45 Variation of critical vortex quantities at $x/c = 2$, for $\alpha = 14° + 8°\sin(\omega t)$ and $\kappa = 0.09$. (a) Total circulation; (b) core circulation; (c) outer radius; (d) core radius; (e) peak tangential velocity; (f) peak vorticity; (g) core axial velocity; (h) core RMS velocity; (i) induced drag, and (j-k) vortex trajectory.

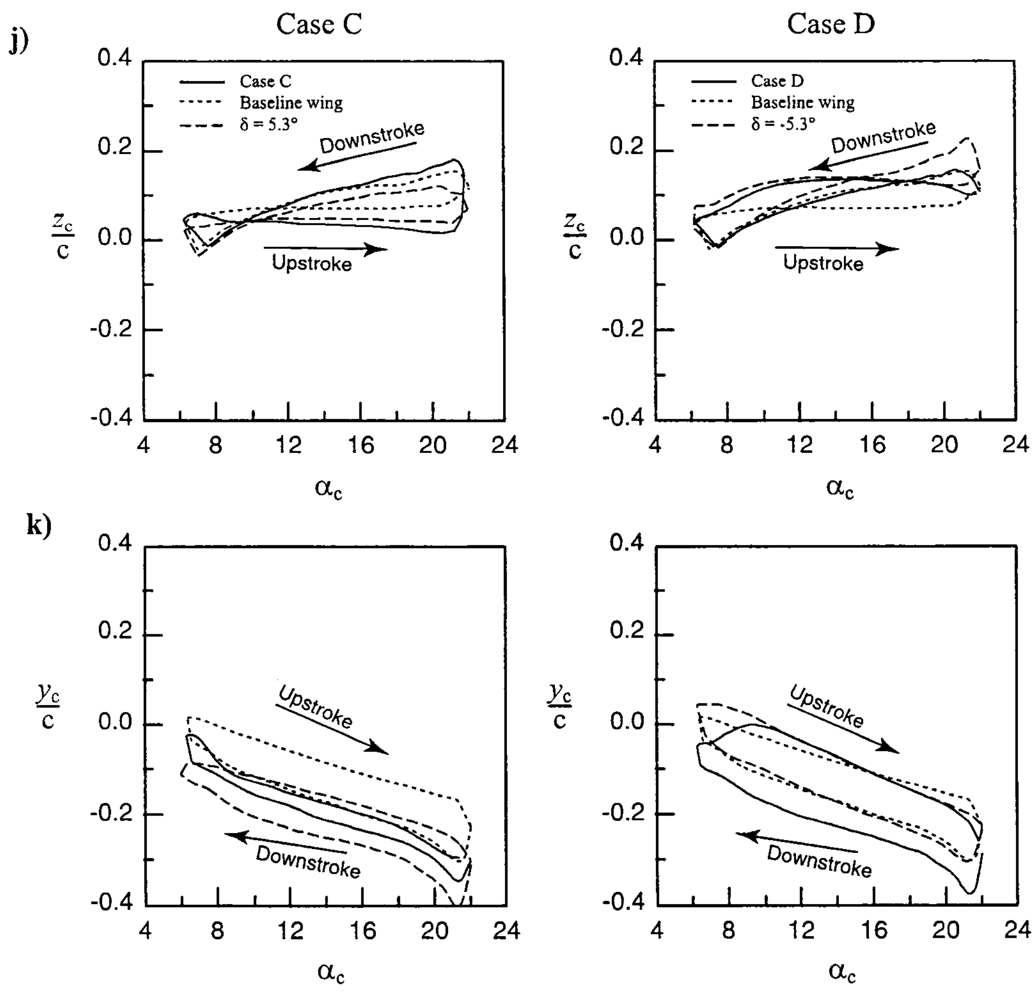

Figure 45 Variation of critical vortex quantities at $x/c = 2$, for $\alpha = 14° + 8°\sin(\omega t)$ and $\kappa = 0.09$. (a) Total circulation; (b) core circulation; (c) outer radius; (d) core radius; (e) peak tangential velocity; (f) peak vorticity; (g) core axial velocity; (h) core RMS velocity; (i) induced drag, and (j-k) vortex trajectory.

Appendix A: Seven hole pressure probe calibration technique

The seven-hole pressure probe (7HP) measures the time-averaged magnitude and direction of the flow in the vicinity of the probe tip. The probe tip is a series of seven pressure taps arranged in close-packed configuration in a truncated 30° cone. By convention, the holes are numbered 1 through 7, with hole 7 located at the center and holes 1 through 6 numbered clockwise from the bottom, as seen from upstream. By comparing the relative magnitudes of the pressures recorded at the different tap locations, the local flow velocity vector can be obtained. Due to the time-lag and damping effect of the length of tubing connecting the probe tip to the pressure transducer array, the 7HP is limited to measurement of time-mean values. Also, the probe is only sensitive to flow cone angles less than ≈70° from the axis of the probe.

In order to calibrate the 7HP, an empirical function must be found which is homeomorphic within the range of measurement and can relate the pressure at the seven holes $\mathbf{P} = (P_1, P_2, \ldots, P_7)$ to the local velocity $\mathbf{v} = (u, v, w)$. In order to determine the values of this empirical function, the physics governing the sensor must be considered. First, since the magnitude of the velocity can be calculated from the difference between the static and stagnation pressures using Bernoulli's principle, and the 7HP provides local pressure measurements, the velocity magnitude can be computed directly rather than inferred from the calibration, reducing the order of the problem.

Since the magnitude of the velocity vector can be eliminated from the calibration parameter space, it becomes convenient to express the velocity in terms of magnitude and direction such that $\mathbf{v} = \{|\mathbf{v}|, \theta, \phi\}$ or $\mathbf{v} = \{|\mathbf{v}|, \alpha, \beta\}$, where θ is the cone angle, ϕ is the roll angle, α is the pitch angle and β is the yaw angle. The cone, roll, pitch and yaw angles are related to the orthogonal components of velocity as

$$u = |\mathbf{v}| \cos(\beta) \cos(\alpha) = |\mathbf{v}| \cos(\theta) \tag{A1}$$

$$v = |\mathbf{v}| \cos(\beta) \sin(\alpha) = |\mathbf{v}| \sin(\theta) \sin(\phi) \tag{A2}$$

$$w = |\mathbf{v}| \sin(\beta) = |\mathbf{v}| \sin(\theta) \cos(\phi) \tag{A3}$$

These relationships are illustrated graphically in Figure A1.

Furthermore, at larger flow angles, the flow will separate from the tip of the 7HP and at least one of the pressure taps will be located in a wake region. Since surface pressures in wake regions are relatively insensitive to changes in flow magnitude or direction, the function relating **P** and **v** must be defined piecewise, depending on (a) whether or not there is flow separation over the probe tip, and if there is separation, (b) which taps are in the separated region. Since the probe tip is a 30° cone and the flow is known to remain attached everywhere on the probe tip when the probe is oriented parallel to the flow, and since the pressure in regions of separated flow is known to be higher than in regions of attached flow, the flow is assumed to be attached everywhere on the probe tip if the maximum pressure is recorded at the center tap.

In the case where the maximum pressure is recorded at the center tap and the flow is attached everywhere on the probe tip, the difference in the pressures between the top hole and the bottom hole will be a homeomorphic function of α (defined as C_α), and the difference in the pressure between the holes on the left and right sides will be a homeomorphic function of β (defined as C_β). Since the magnitude of the pressures will be a function of |**v**| and |**v**| has been eliminated from the parameter set, the pressures can be normalized against the local dynamic pressure P_{TOT} - P_{STAT}. The total pressure is taken as the pressure at the center tap, and the static pressure is approximated as the average of the pressure at all of the peripheral taps. Also, since there are six peripheral taps, there are two taps on each of the left and right sides and the average of the two side pressures are used. Thus,

$$C_\alpha = \frac{P_4 - P_1}{P_7 - P_{AV}} \tag{A4}$$

$$C_\beta = \frac{\frac{1}{2}(P_5 + P_6) - \frac{1}{2}(P_3 + P_2)}{P_7 - P_{AV}} \tag{A5}$$

$$P_{AV} = \sum_{k=1}^{6} \frac{P_k}{6} \tag{A6}$$

where k indicates the hole index number.

In the event that the maximum pressure is recorded at some hole i where $i \neq 7$, then the flow can only be assumed to be attached in the immediate vicinity of the stagnation point, where the hole i is located. As a result, only the hole i and the three holes adjacent to it are used to determine the values of the functions. The pressure difference between hole 7 and hole i will be a homeomorphic function of the cone angle θ (defined as C_θ), and the pressure difference between the holes located peripherally adjacent to the ith hole will be a homeomorphic function of the roll angle φ (defined as C_ϕ). The total pressure is taken as the maximum recorded pressure P_i, and the static pressure is approximated as the average of the pressures at the two peripherally adjacent holes P_{CW} and P_{CCW} (where the subscripts CW and CCW indicate the adjacent hole going around the probe tip clockwise and counterclockwise as seen from upstream, respectively).

$$C_{\theta i} = \frac{P_i - P_7}{P_i - P_{AV}} \qquad i = 1, 2, ..., 6 \qquad \text{(A7)}$$

$$C_{\phi i} = \frac{P_{CW} - P_{CCW}}{P_i - P_{AV}} \qquad \text{(A8)}$$

$$P_{AV} = \frac{P_{CW} + P_{CCW}}{2} \qquad \text{(A9)}$$

The spherical co-ordinates are used in the case of $i \neq 7$ because the centers of the four holes used describe a 120° segment of a cone, and it is more convenient to describe this geometry in terms of cone and roll angles. The functions C_θ and C_ϕ are defined independently for each hole $i = 1, 2, ..., 6$.

Finally, since the magnitude of the velocity is computed based on approximate values of the static and total pressures, the measurement accuracy can be significantly improved by further defining functions $C_{STAT\,i}$ and $C_{TOT\,i}$, where $i = 1, 2, ..., 7$, which are homeomorphic functions relating the approximate and actual values of the static and total pressures, respectively.

$$C_{STATi} = \frac{P_i - P_{STAT}}{P_i - P_{AV}} \qquad i = 1, 2, \ldots, 6 \tag{A10}$$

$$C_{TOTi} = \frac{P_i - P_{TOT}}{P_i - P_{AV}} \tag{A11}$$

where P_{AV} is the approximated value of the static pressure, the definition of which depends on i and is given by equations A6 and A9.

To calibrate the probe, data is collected at a single free-stream velocity close to the expected velocities in the measurement region, and at many angles in pitch and yaw. The 7HP's measurement space is limited to the region $-70° \leq \alpha \leq 70°$, $-70° \leq \beta \leq 70°$. Above or below 70° in pitch or yaw, the functions described above are no longer sufficiently sensitive to the angles to be considered homeomorphic. The data is then used to construct seven calibration grids (Figure A2), with one grid associated with each of the seven holes. The calibration grids consist of a number of points in (C_α, C_β) or (C_θ, C_ϕ) space of known flow angle, C_{STAT}, and C_{TOT}. Then, given any experimental pressure measurements, the hole registering the maximum pressure is determined and the corresponding calibration grid is used to interpolate the values of α and β (or θ and ϕ), together with C_{STAT}, and C_{TOT}. Then, substituting equations A10 and A11 into the Bernoulli equation yields the magnitude of the velocity,

$$|\mathbf{v}| = \sqrt{\frac{2}{\rho}(P_i - P_{AV})(C_{STAT} - C_{TOT})} \tag{A12}$$

The orthogonal components of the velocity vector can then be calculated from equations A1, A2 and A3.

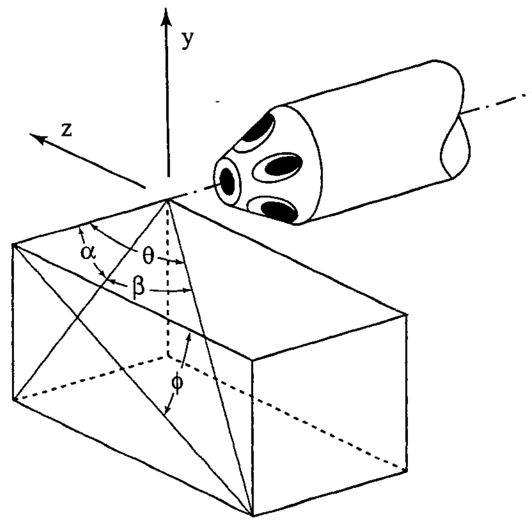

Figure A1 Representation of angular co-ordinate systems. α = pitch angle; β = yaw angle; θ = cone angle; φ = roll angle.

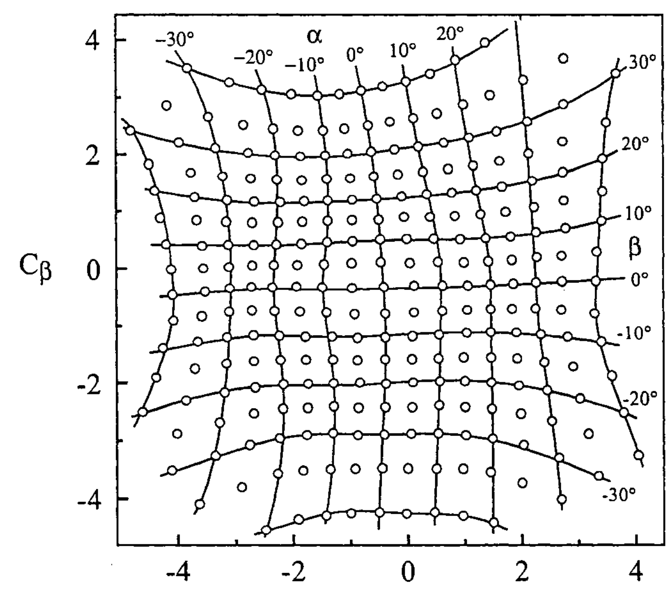

Figure A2 Typical low-angle calibration data for seven-hole probe. α = pitch angle; β = yaw angle.

Appendix B: Triple-sensor hot-wire probe calibration technique

The triple-wire probe outputs a set of three voltage signals $\mathbf{E} = (E_1, E_2, E_3)$. Since the probe has three degrees of freedom each capable of responding independently to the flow direction and magnitude, and since the velocity vector $\mathbf{v}$ also has three degrees of freedom such that $\mathbf{v}$ = (u, v, w), then some empirical function $f(\mathbf{v})$ must be found such that $f(\mathbf{v}) = \mathbf{E}$. Being able to invert the function f such that $f^{-1}(\mathbf{E}) = \mathbf{v}$ necessarily requires that the function f be homeomorphic within the domain of $\mathbf{E}$. For the triple-wire probe, the voltage output $\mathbf{E}$ is only homeomorphic in $\mathbf{v}$ when the cone angle of the flow is less than the cone angle of the wires, so the inequality $-45° < \theta < 45°$ (where θ is the cone angle of the flow relative to the sting) must be satisfied in order for $f^{1}(\mathbf{E})$ to be homeomorphic. However, if $f^{1}(\mathbf{E})$ is not homeomorphic but only has one degree of ambiguity, then $f(\mathbf{v})$ will have only two solutions within the domain of $\mathbf{E}$- one solution corresponding to the case when the inequality is satisfied, and one corresponding to the case when it is not. It may be possible, then, to invert the function $f(\mathbf{v})$ for cases where the cone angle of the flow exceeds that of the wires, but only if the condition of the inequality is known.

Without simplification, it would be possible to determine the function f^{1} directly by calibration. An exhaustive look-up table could be constructed by measuring $\mathbf{E}$ at many angles in pitch, at many angles in yaw and at many speeds, but since the triple-wire must be frequently recalibrated, the amount of time required to collect the necessary look-up table reference data would be prohibitive. Some analytical methods exist to determine f^{1} geometrically from a very limited set of calibration data, but these methods require knowledge of the precise orientation of the sensor wires relative to the sting axis.

Instead, some simplifying approximations are made in order to determine f^{1}. First, consider the probe being subjected to flow with an angle (α, β) with respect to the axis of the sting, where α and β are the pitch and yaw angles of the flow relative to the axis of the sting, respectively. Then, for the kth wire, King's law can be expressed as

$$Q_k^2 = a_k^2 v_{||k}^2 + b_k^2 v_{\perp k}^2 \qquad k = 1, 2, 3 \qquad \text{(B1)}$$

where Q_k is the effective cooling velocity experienced by the kth wire of the array, $v_{||k}$ is the component of velocity parallel to the kth wire, $v_{\perp k}$ is the component of velocity perpendicular to the kth wire, and a_k and b_k are constants that depend on the properties of the wire. Since $v_{||k}$ and $v_{\perp k}$ are themselves functions of α, β, and the cone and roll angles θ_k and ϕ_k of the kth wire relative to the sting, and are proportional to $|\mathbf{v}|$, Q_k can be re-expressed as

$$Q_k = |\mathbf{v}|\, p(\alpha, \beta, \theta_k, \phi_k) \qquad k = 1, 2, 3 \qquad \text{(B2)}$$

where p is some vector function dependant upon geometry only. This expression can be normalized against the effective cooling velocity Q_0 for the case when the flow is parallel to the sting

$$Q_{0\,k} = |\mathbf{v}|\, p(0, 0, \theta_k, \phi_k) \qquad k = 1, 2, 3 \qquad \text{(B3)}$$

Then, equations B2 and B3 can be combined as

$$Q_k \,/\, Q_{0\,k} = p^*(\alpha, \beta, \theta_k, \phi_k) \qquad k = 1, 2, 3 \qquad \text{(B4)}$$

where p^* is the vector function $p(\alpha, \beta, \theta_k, \phi_k)$ adjusted such that it absorbs the function $p(0, 0, \theta_k, \phi_k)$, which will be constant for each wire since θ_k, and ϕ_k will not change during the process of measurement. In general, for inclined hot-wires the relationship between Q and E can be expressed as a second-order polynomial for velocities reasonably larger than 0. Therefore, if the quotient $Q_k / Q_{0\,k}$ is independent of $|\mathbf{v}|$, then the quotient $E_k / E_{0\,k}$ (where $E_{o\,k}$ is the voltage response of the kth wire when $\alpha = 0$ and $\beta = 0$) is expected to be independent of $|\mathbf{v}|$, and the homeomorphic functions g_k and h_k can be defined such that

$$g_k(Q_k \,/\, Q_{0\,k}) = h_k(E_k \,/\, E_{0\,k}) \qquad k = 1, 2, 3 \qquad \text{(B5)}$$

The independence of $E_k / E_{o\,k}$ from $|\mathbf{v}|$ was validated experimentally. Combining Equations B4 and B5 yields

$$g_k(Q_k / Q_{o\,k}) = h_k(E_k / E_{o\,k}) = g_k(\,p^*(\alpha, \beta, \theta_k, \phi_k)\,) \qquad k = 1, 2, 3 \qquad \text{(B6)}$$

Since h_k is homeomorphic, it can be inverted to yield another homeomorphic function h_k^{-1}, and the quotient $E_k / E_{o\,k}$ can be isolated from equation B6 as

$$E_k / E_{o\,k} = h_k^{-1}(g_k(\,p^*(\alpha, \beta, \theta_k, \phi_k)\,)\,) \qquad \text{(B7)}$$

The right-hand side of equation B7 represents a function that will vary only with the angle of the flow, and the denominator of the left-hand side will vary only with the magnitude of the velocity and the wire geometry. For simplicity, combine the right-hand side functions as

$$E_k/E_{o\,k} = q_k(\alpha, \beta) \qquad k = 1, 2, 3 \qquad \text{(B8)}$$

The angles (θ_k, ϕ_k) have been dropped, since they will remain constant throughout the calibration procedure and experimental measurement. Since the values E_k are measured voltages, it is possible for $E_{o\,k}$ to approach zero, resulting in a singular point in the function q. Consequently, it is convenient to add a constant, such as

$$\frac{E_k + \Delta E}{E_{o\,k} + \Delta E} = q_k(\alpha, \beta) \equiv E_k^* \qquad k = 1, 2, 3 \qquad \text{(B9)}$$

where ΔE should be at least equal to the minimum signal voltage level.

Let the three-dimensional parameter space $\mathbf{S}$ be defined, such that $\mathbf{S} = \{E_1^*, E_2^*, E_3^*\}$. Then, if n values of $\mathbf{E}^* = (E_1^*, E_2^*, E_3^*)$ are collected at a single, known flow speed but at many angles α and β, each $\mathbf{E}^*$ vector will represent a single point in $\mathbf{S}$, and all of the n $\mathbf{E}^*$ vectors together will define a continuous surface A in $\mathbf{S}$ which represents the function q_k, and is independent of the magnitude of the velocity. This surface A is the locus of all possible combinations of E_1^*, E_2^* and E_3^* which could result from flow over the sensor array, and each point on the surface A corresponds to a unique flow direction (α, β).

In order to solve for $\mathbf{E}^*$ given an experimental data point $\mathbf{E}$ with unknown α, β and $|\mathbf{v}|$, it is necessary to know the values of $E_{o\,k}$, which requires that the magnitude of the velocity vector be known. However, if $\mathbf{E}^*$ is plotted in $\mathbf{S}$ as a function of $E_{o\,k}$, the result will be a curve which can intersect A at only one point. By measuring $E_{o\,k}$ at many velocities but with $\alpha = 0$ and $\beta = 0$, and applying the method of least-squares, the curve describing the locus of possible values $\mathbf{E}^*$ in $\mathbf{S}$ can be expressed parametrically, as

$$\mathbf{E}^* = \{\mathbf{a}\} + \{\mathbf{b}\}t + \{\mathbf{c}\}t^2 \qquad \text{(B10)}$$

where $\{\mathbf{a}\}$, $\{\mathbf{b}\}$ and $\{\mathbf{c}\}$ are arrays of known constants, and for flows with reasonably small cone angles, the constants $\{\mathbf{c}\}$ will vanish. The parameter t is a function of $|\mathbf{v}|$, and $t(\,|\mathbf{v}|\,)$ can be reasonably approximated as a second-order polynomial. Least-squares analysis can once again be used to determine the coefficients of this polynomial relationship.

The problem of converting some experimental values $\mathbf{E}$ into velocities $\mathbf{v}$ has thus been reduced to finding the point of intersection of the line described by equation B10 and the surface A, and is illustrated graphically in Figure B1. Since α and β are known at every calibration point on A, the point of intersection can be interpolated to yield the pitch and yaw angles of the flow. Also, the parameter t of the line of $\mathbf{E}$ at the point of intersection can be used to calculate $|\mathbf{v}|$. Then, u, v, and w can be obtained from the geometry as

$$u = |\mathbf{v}| \cos(\beta) \cos(\alpha) \qquad \text{(B11)}$$

$$v = |\mathbf{v}| \cos(\beta) \sin(\alpha) \qquad \text{(B12)}$$

$$w = |\mathbf{v}| \sin(\beta) \qquad \text{(B13)}$$

It is significant to note that the triple-wire probe calibration scheme outlined above places no requirement on the actual cone and roll angles of the probe sensor wires, other than to set a limit on the domain in which the functions q_k* are homeomorphic, so the actual roll angle of the probe in the sting assembly is irrelevant.

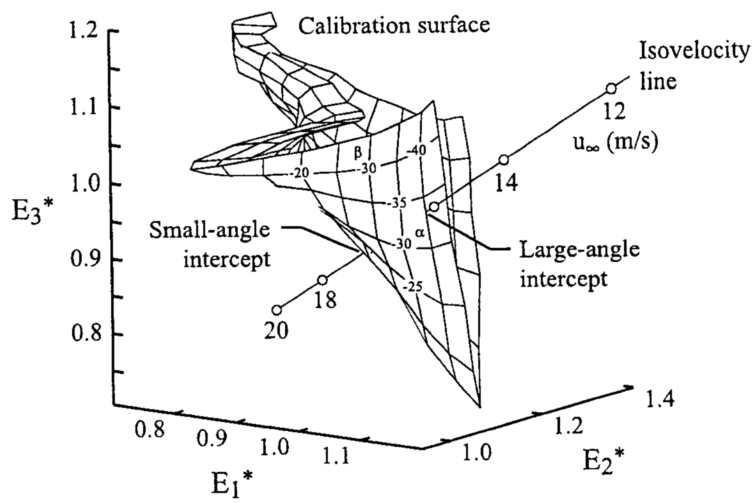

Figure B1 Typical triple-sensor hot-wire data conversion from normalized voltages to velocity components.

Appendix C: Discussion of vortex meandering

Because the tip vortex velocity fields were obtained by means of discrete, pointwise measurements, the random, low-frequency meandering of the vortex would cause the long time-average vorticity to appear more diffused and decrease the measured peak tangential velocity. Furthermore, the low-frequency, broadband velocity fluctuations resulting from the random vortex motion would be erroneously interpreted as large-scale turbulence and would cause an overestimation of the root-mean-square velocity fluctuations and turbulent stresses. While it is assumed that the very small level of free-stream turbulence in the present study will result in meandering amplitudes sufficiently small relative to the vortex size to be neglected, a quantification of the error expected as a result of the random, bulk motion of the vortex structure would nonetheless be valuable.

Devenport *et. al.* (1996) present a general solution for the error resulting from vortex meandering by modeling the vortex by expressing the vorticity in the form of a series of the form

$$\bar{\zeta}(y,z) = \sum_{i=1}^{n} A_i \exp\left(-\frac{y^2+z^2}{a_i^2}\right) \tag{C1}$$

where A_i and a_i are arrays of constants which must be determined, and where y and z are taken relative to the instantaneous location of the vortex center. The tangential velocity, then, can be expressed as

$$\bar{v}_\theta = \sum_{i=1}^{n} \frac{B_i}{r}\left(1-\exp\left(-\frac{y^2+z^2}{a_i^2}\right)\right) \tag{C2}$$

where B_i is a constant. The individual terms in the series can be recognized as being of the form of the Batchelor (1964) vortex described in Equations (4) and (5), and as such the model is expected to apply well to a measured trailing vortex. If the vortex position is expected to vary randomly in time as a result of the meandering, the instantaneous location of the vortex center may be assumed to correspond to a non-isotropic Gaussian probability density function of the form

$$p(y_c,z_c)=\frac{1}{2\pi\sigma_y\sigma_z\left(1-e^2\right)^{1/2}}\exp\left(-\frac{1}{2\left(1-e^2\right)}\left(\frac{z_c^2}{\sigma_z^2}+\frac{y_c^2}{\sigma_y^2}-\frac{2y_cz_c}{\sigma_y\sigma_z}\right)\right) \tag{C3}$$

where σ_y and σ_z are the root-mean-square amplitudes of vortex meandering in the transverse and spanwise directions, respectively, and e is the correlation coefficient. Once the relative positions y and z in equation (C1) have been adjusted by Equation (C3), the measured time-mean vorticity can be re-expressed as

$$\bar{\zeta}(y,z)=\sum_{i=1}^{n}C_i\exp\left(-E_i\left(y^2\left(2\sigma_z^2+a_i^2\right)+z^2\left(2\sigma_y^2+a_i^2\right)-4yze\sigma_y\sigma_z\right)\right) \tag{C4}$$

where C_i and E_i are functions of σ_y and σ_z. Some manipulation of the equations may then extract the time-mean vorticity independent of the meandering.

For the present case, the vortex meandering will be assumed isotropic, such that $\sigma_y = \sigma_z = \sigma$. Also, because the mean vortex profiles corresponded fairly well to the Batchelor laminar solution for r/c < 0.15, the tangential velocity distribution will be fitted to Equation (4), with $K = A_o$ taken as an empirical constant, which is essentially a first-order approximation of the general model presented above. With these simplifications, Equations (C2) and (C3) reduce to (Devenport 1996)

$$\bar{v}_\theta = v_{\theta\max}\left(1+\frac{0.5}{A_o}\right)\frac{r_c}{r}\left(1-\exp\left(-A_o\frac{r^2}{r_c^2}\right)\right) \tag{C5}$$

$$p(y_c,z_c)=\frac{1}{2\pi\sigma^2}\exp\left(-\frac{y_c^2+z_c^2}{2\sigma^2}\right) \tag{C6}$$

and when Equation (C5) is corrected to include the effects of meandering, the time-mean tangential velocity is expressed as

$$\bar{v}_\theta = v_{\theta\max}\left(1+\frac{0.5}{A_o}\right)\frac{r_c}{r}\left(1-\exp\left(-A_o\frac{r^2}{r_c^2+2A_o\sigma^2}\right)\right) \tag{C7}$$

and the corrected v_θ approaches the uncorrected v_θ as σ becomes small. The error incurred in long time-measurements as a result of vortex meandering is then expressed as

$$\Delta v_\theta = \left(1-2A_o\frac{\sigma^2}{r_c^2}\right)^{1/2} \tag{C8}$$

The evaluation of the meandering error in the time-mean velocity fields then requires the determination of the empirical constant A_0 and the RMS amplitude of the meandering of the location of the vortex center σ.

To isolate the effects of meandering from the effects of small-scale turbulence, the time-domain cross-flow velocity data was low-pass filtered at 20 Hz to eliminate the fluctuations due to small-scale turbulence. If the large-scale turbulence is assumed small relative to the effects of meandering, then what remains is a measure of the effect of the motion of the vortex center upon the local velocity. By subtracting the low-pass filtered component from the time-domain data and recomputing the RMS velocity fluctuations, the difference between the measured RMS fields and the RMS field corrected for vortex meandering can be quantified. Figures C1a and C1b show the uncorrected and corrected values of u'/u_∞ for the typical case of $\alpha = 6°$ and $x/c = 1$, and the difference is seen to be negligible.

To determine a first-order approximation of the magnitude of σ, the random motion of the vortex center was assumed to have only a negligible effect on the velocity gradient dv_θ/dr. Then, the time-dependent distance between the measurement location and the location of the vortex center could be directly calculated from time-domain cross-flow velocity data at a scan grid location very close to the vortex center. The value of the empitical constant $A_0 \approx 1.32$ was calculated by least-squares (compared to the theoretical value of 1.26 for a laminar vortex), and the comparison between the tangential velocity determined using Equation (C5) and experimental data for the same typical case of $\alpha = 6°$ and $x/c = 1$ is shown in Figure C1c. The meandering error on the mean cross-flow velocity field was then computed using Equation C8, and was found to be 0.74%, which is well below the measurement uncertainty. For reference purposes, typical axial velocity time traces across the vortex are included in Figure C2.

Because of the very small effect of the vortex meandering upon the present measurements, no corrections for vortex meandering were applied.

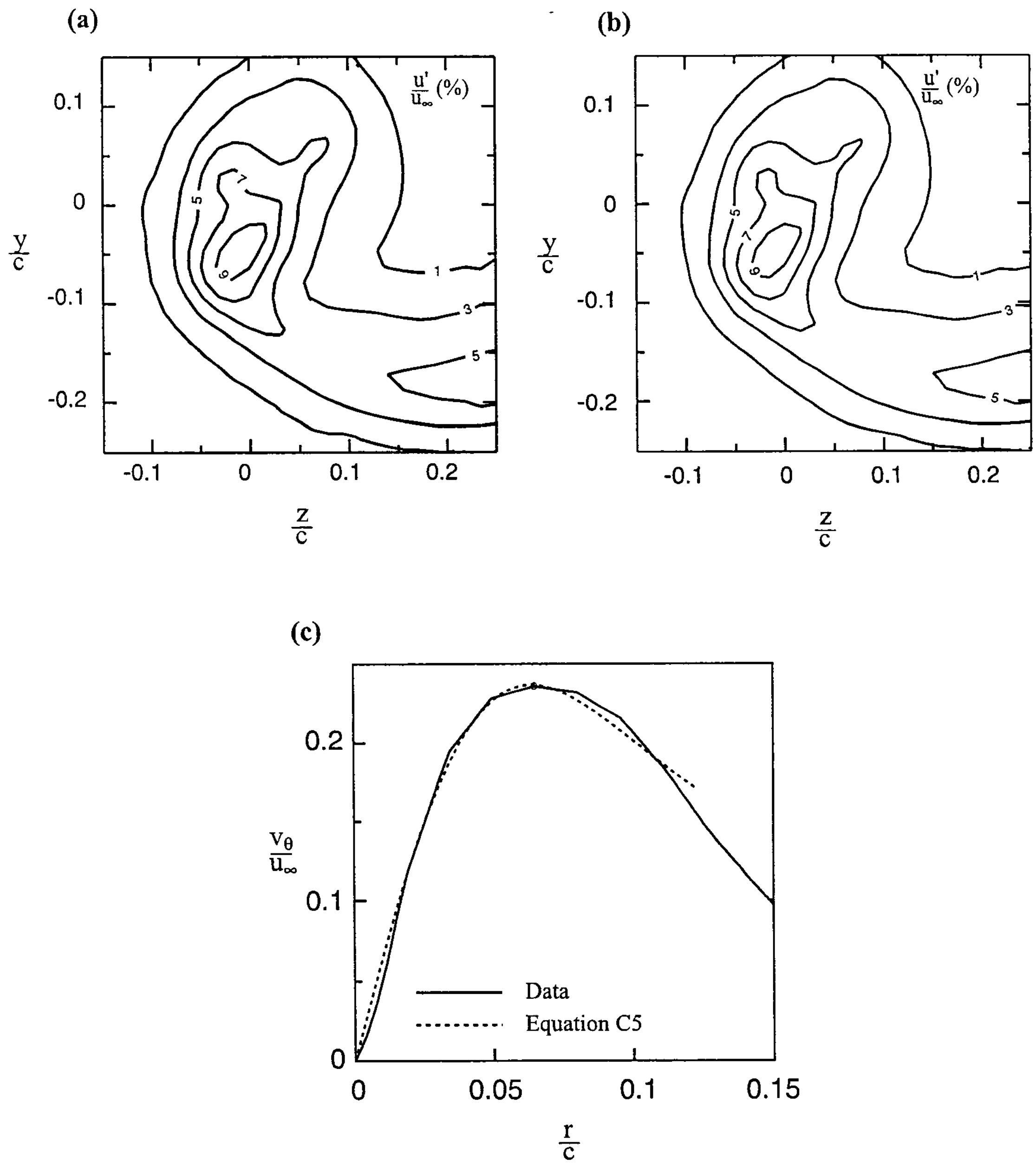

Figure C1 Measured root-mean-square velocity contours (a) and those corrected for vortex meandering (b), for the static vortex with $\alpha = 6°$ and $x/c = 1$; (c) comparison between measured tangential velocity and Equation C5.

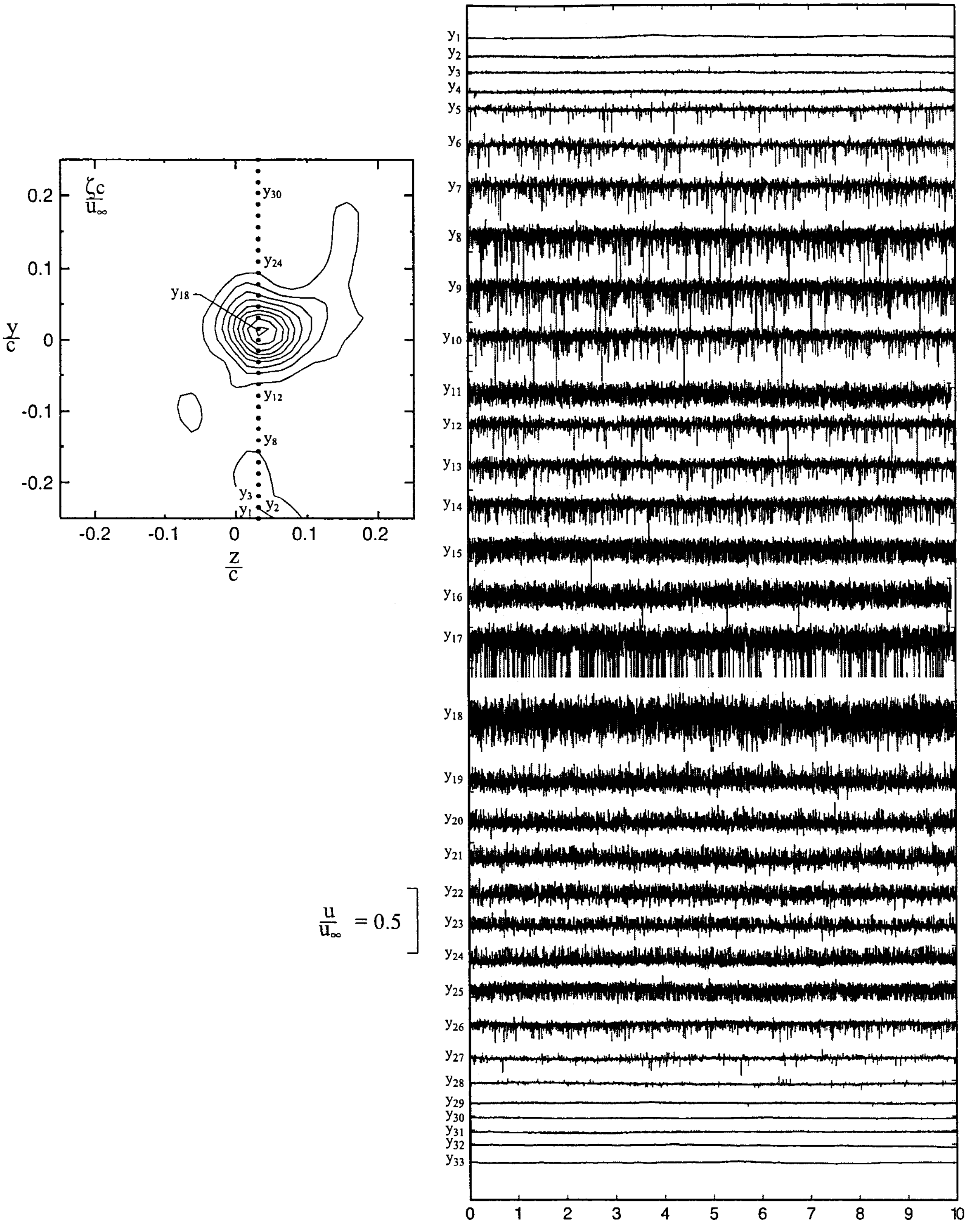

Figure C2 Normalized axial velocity time-traces at selected stations across the static vortex, $\alpha = 6°$, $x/c = 1$.

Appendix D: Experimental uncertainty

Part I: Uncertainty due to data acquisition

The following table lists the experimental uncertainty resulting from the triple-wire sensor system, the wind tunnel and traverse mechanism, and the data conditioning and acquisition. These values were all either measured directly or supplied by the equipment manufacturer.

Quantity	Uncertainty (% full-scale)
Experimental parameters (constant)	
Free-stream velocity	0.8%
Model profile	0.5%
Maximum normalization error:	**1.3%**
Measurement	
Angular position	0.2%
Traverse position	0.4%
CTA calibration error	0.48%
Analogue signal processing	
Amplifier reference voltage	0.06%
Amplifier drift (approx)	0.2%
Analogue-to-digital conversion	
10 V FS, 16 bit A/D conversion of 3V signal	0.01%
Sampling discretization & SNR mean error	0.05%
Maximum error due to data acquisition:	**1.4%**

Note that the sampling discretization and signal-to-noise ratio error was calculated based on a synthesized signal with known mean value, combined with an artificially imposed 60 Hz signal noise. The errors were combined additively as a worst-case approximation.

Part II: Uncertainty due to data reduction

Because of the complex algorithm used to convert the triple-wire measured voltages into velocities, the error incurred is a strong function of the direction of the flow. The uncertainties cited below are averaged over a typical measurement field. Also, the number of cycles collected for the oscillating cases was limited, as larger samples would have rendered the sampling times prohibitively long.

Quantity	Uncertainty (% full-scale)
Data reduction	
Data conversion	3%
Data field conditioning	0.5%
Total error in velocity fields:	**3.5%**
Calculation error	
Maximum error in vorticity finite-difference calculation	2.1%
Maximum vorticity error, including velocity error	7.5%

The error in the vorticity finite-difference calculation was estimated based on a typical time-mean data set for the case of a centered finite-difference calculation of vorticity. The calculation error was approximated as the mean of the small-amplitude discontinuities in a typical velocity field, additively combined with the traverse position error. The total uncertainty in the vorticity fields includes a weighted sum of the velocity uncertainty over the $2\Delta y\Delta z$ range of the finite-difference gradient.

An error in the determination of the vortex core and outer radii of 4% was estimated, as a result of the measurement grid resolution, as well as a 1.7% error in the determination of the location of the vortex center.

For oscillating cases, phase-locked ensemble-averages were computed by interpolating the time-domain measurements at a specific instant in oscillation phase, based on the reference signal from the potentiometer mounted on the wing shaft. Mean and RMS velocities were then computed based on the interpolated time-domain measurements, with an effective sample size of one per phase. Similarly to the time-mean measurements, the phase-locked ensemble-averages were checked for convergence against a larger sample and values were found to converge to within 4%.

Appendix E: Additional data

a)

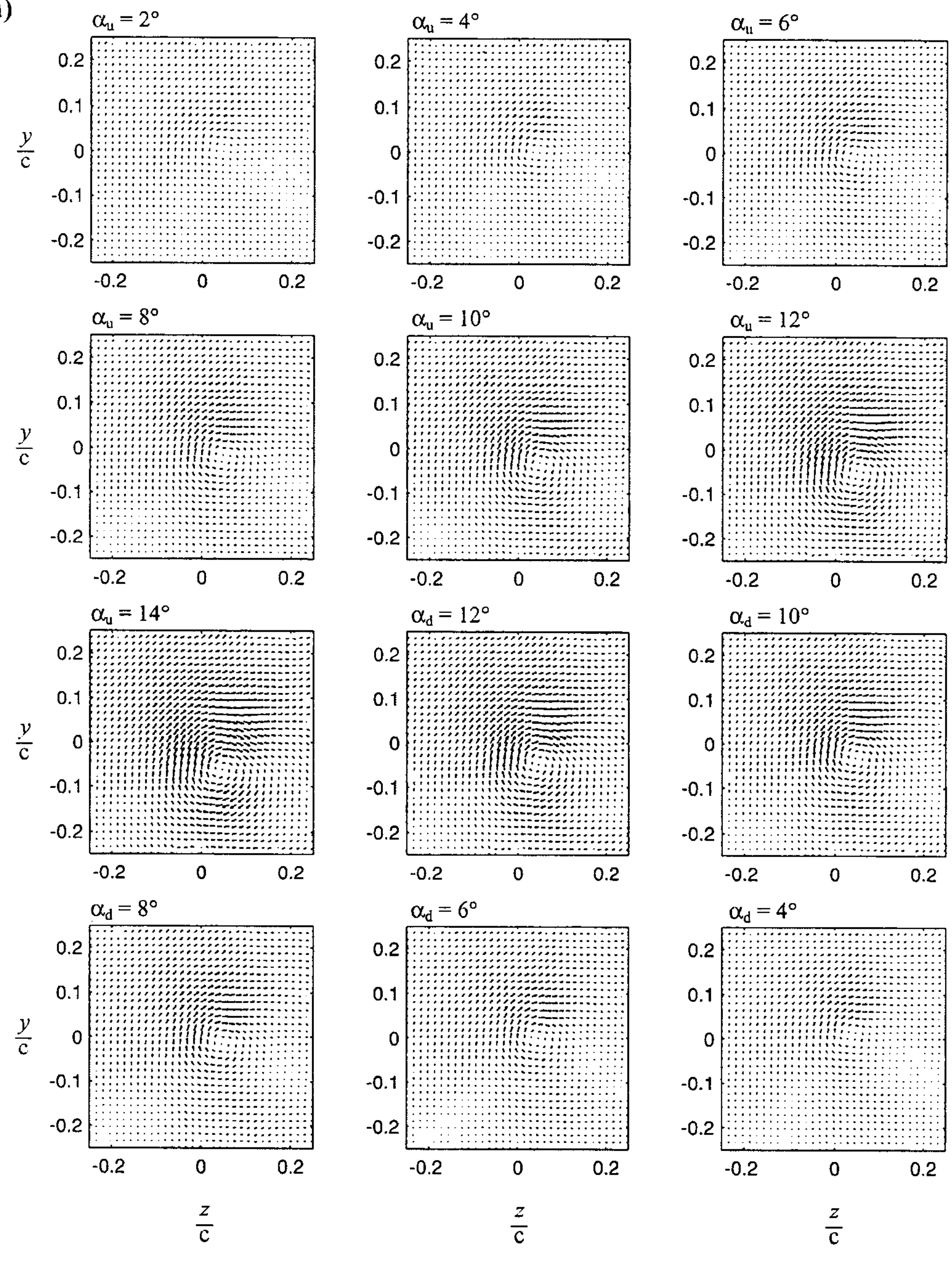

Figure E1 (a) Cross-flow velocity vectors, and contours of constant (b) $\zeta c/u_\infty$, (c) u/u_∞, and (d) u'/u_∞ (%) for the case of α_o = 8°, $\Delta\alpha$ = 6° and κ = 0.09 at the x/c = 0.5 measurement station.

b)

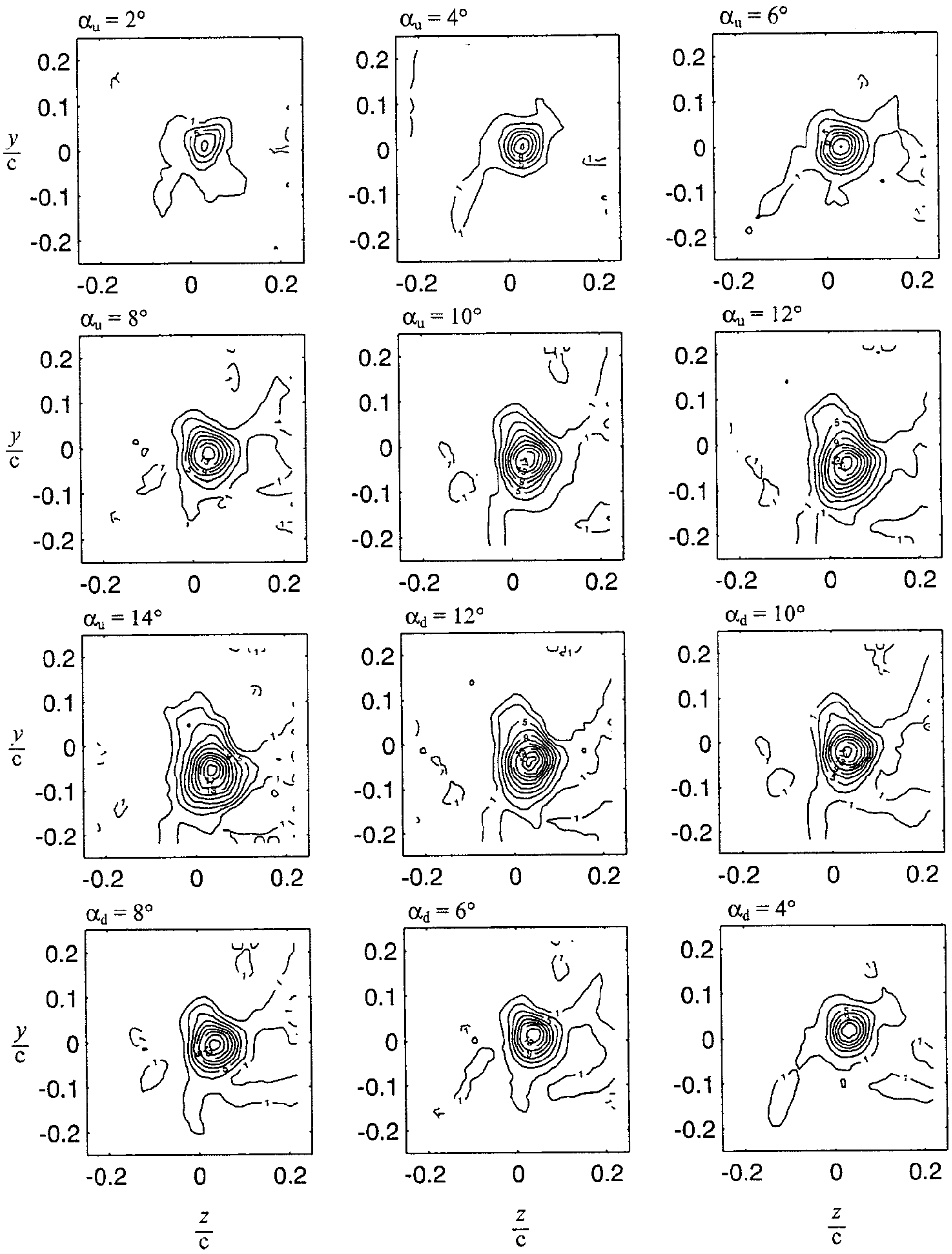

Figure E1 (a) Cross-flow velocity vectors, and contours of constant (b) $\zeta c/u_\infty$, (c) u/u_∞, and (d) u'/u_∞ (%) for the case of α_0 = 8°, $\Delta\alpha$ = 6° and κ = 0.09 at the x/c = 0.5 measurement station.

c)

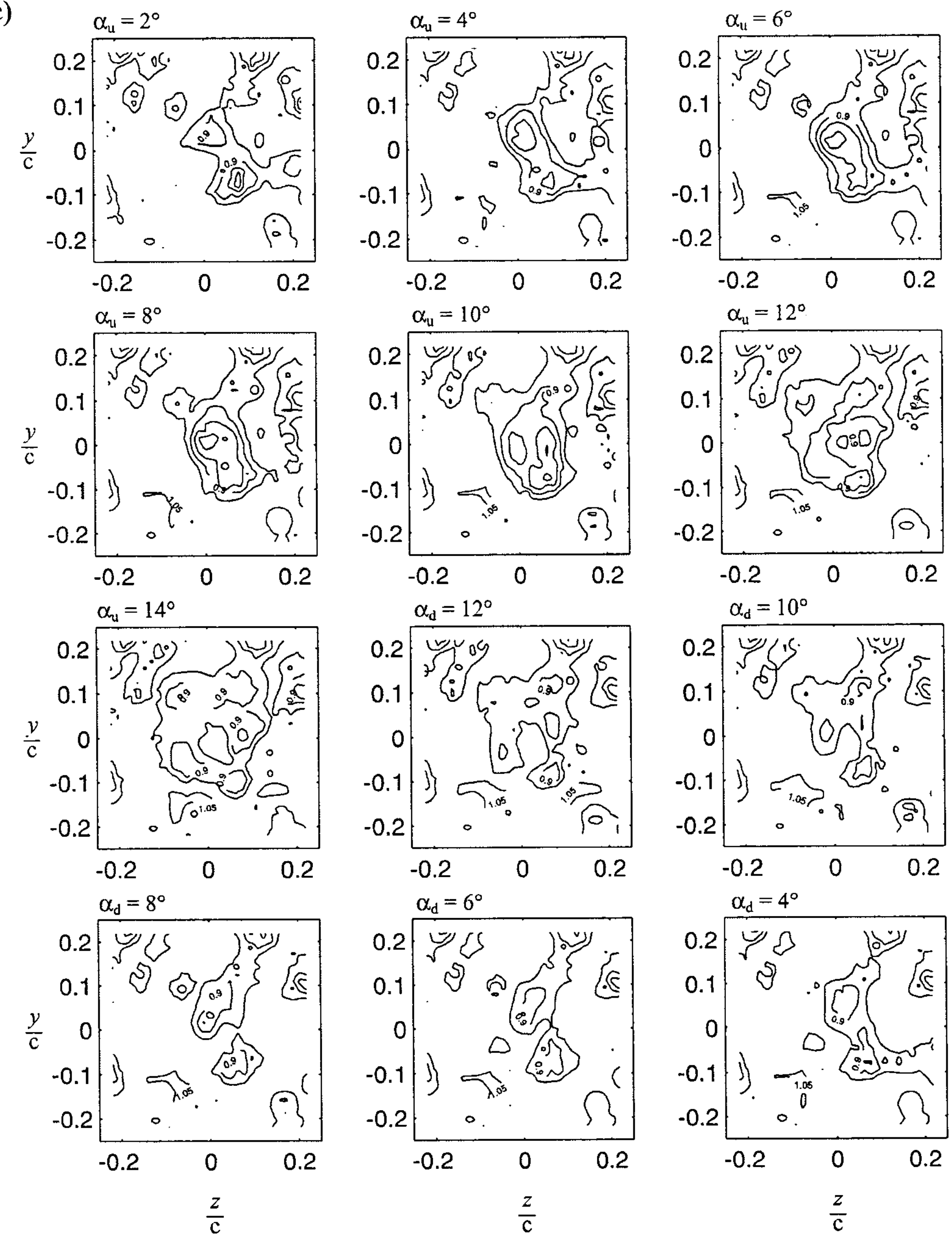

Figure E1 (a) Cross-flow velocity vectors, and contours of constant (b) $\zeta c/u_\infty$, (c) u/u_∞, and (d) u'/u_∞ (%) for the case of α_o = 8°, $\Delta\alpha$ = 6° and κ = 0.09 at the x/c = 0.5 measurement station.

d)

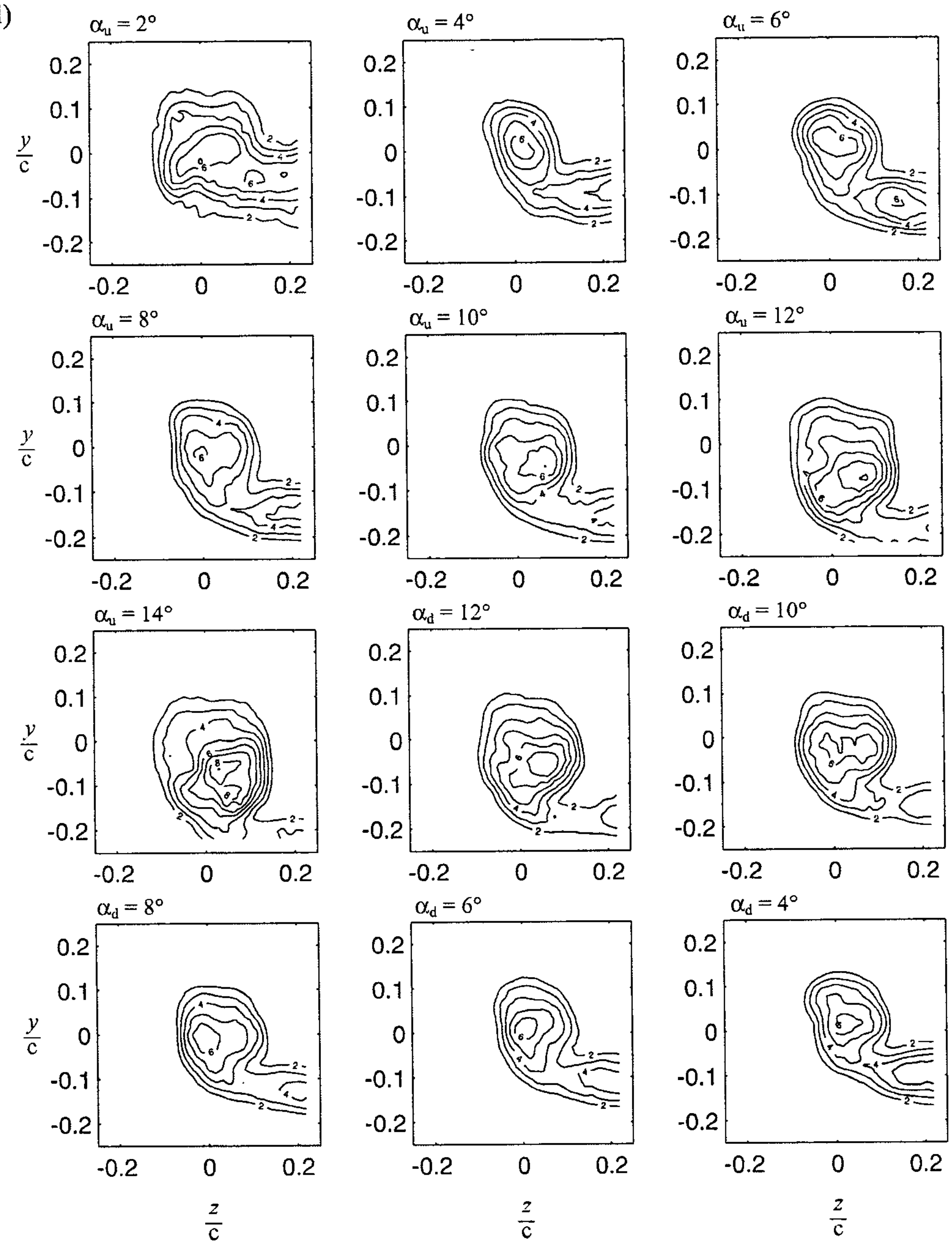

Figure E1 (a) Cross-flow velocity vectors, and contours of constant (b) $\zeta c/u_\infty$, (c) u/u_∞, and (d) u'/u_∞ (%) for the case of α_0 = 8°, $\Delta\alpha$ = 6° and κ = 0.09 at the x/c = 0.5 measurement station.

a)

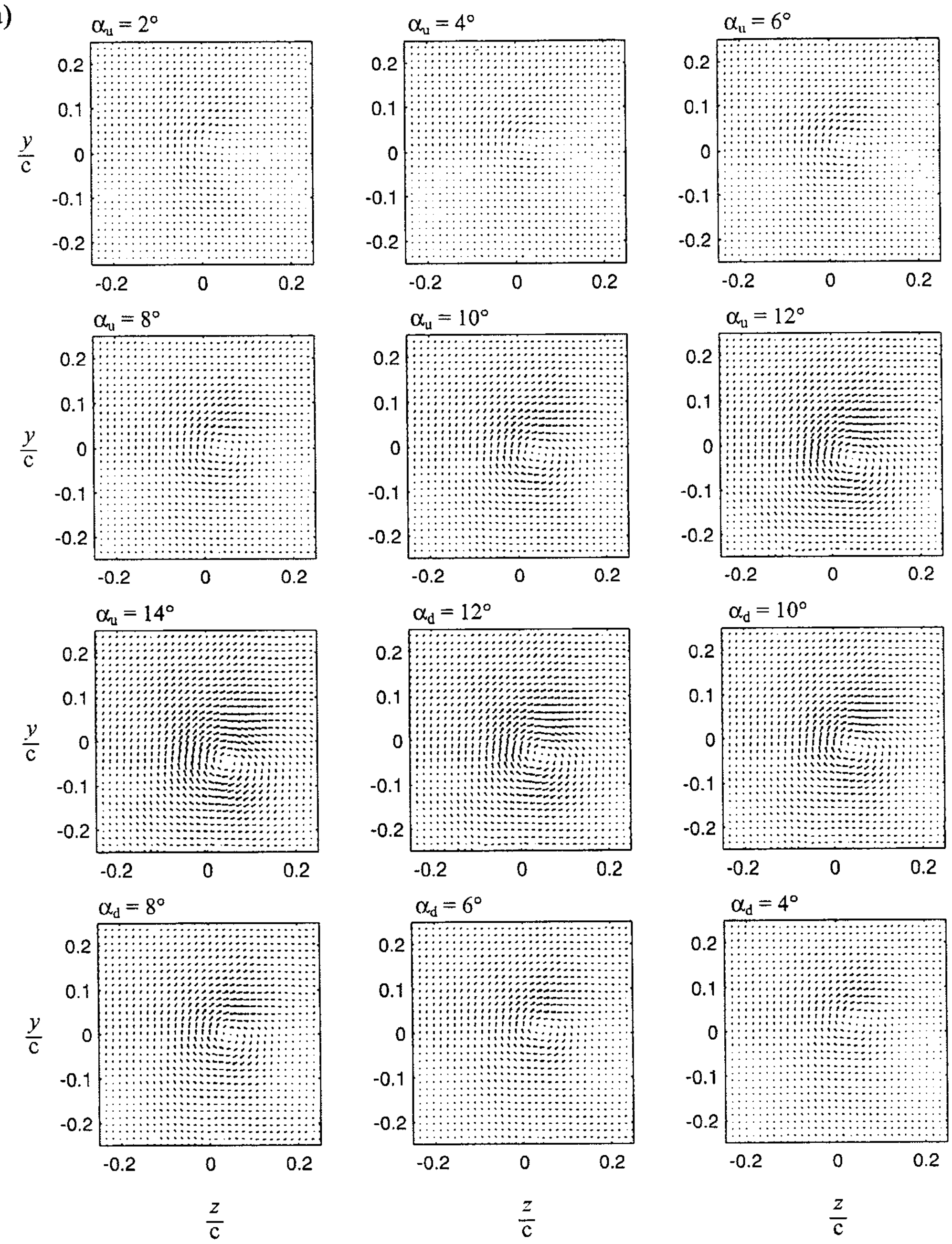

Figure E2 (a) Cross-flow velocity vectors, and contours of constant (b) $\zeta c/u_\infty$, (c) u/u_∞, and (d) u'/u_∞ (%) for the case of α_0 = 8°, $\Delta\alpha$ = 6° and κ = 0.09 at the x/c = 1 measurement station.

b)

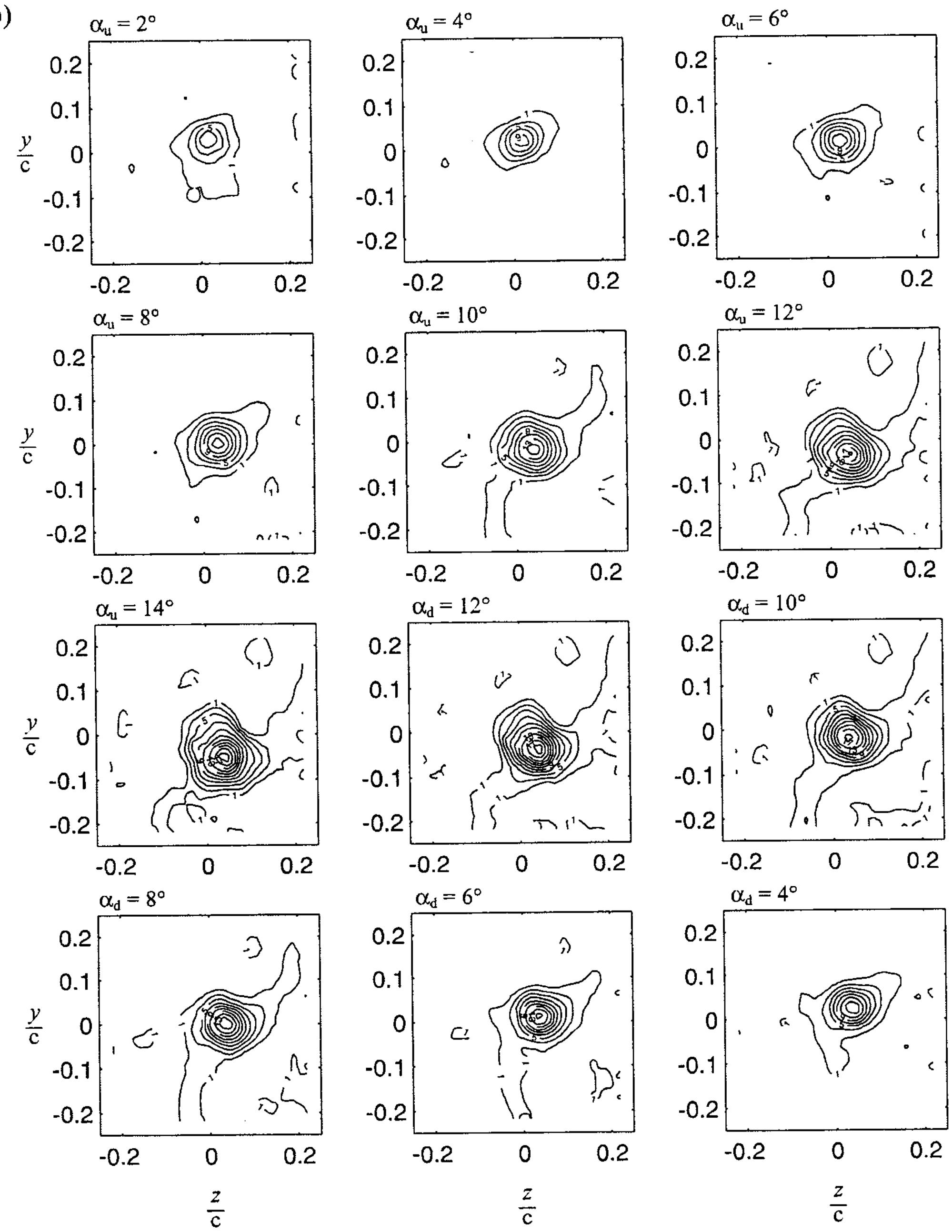

Figure E2 (a) Cross-flow velocity vectors, and contours of constant (b) $\zeta c/u_\infty$, (c) u/u_∞, and (d) u'/u_∞ (%) for the case of $\alpha_0 = 8°$, $\Delta\alpha = 6°$ and $\kappa = 0.09$ at the $x/c = 1$ measurement station.

c)

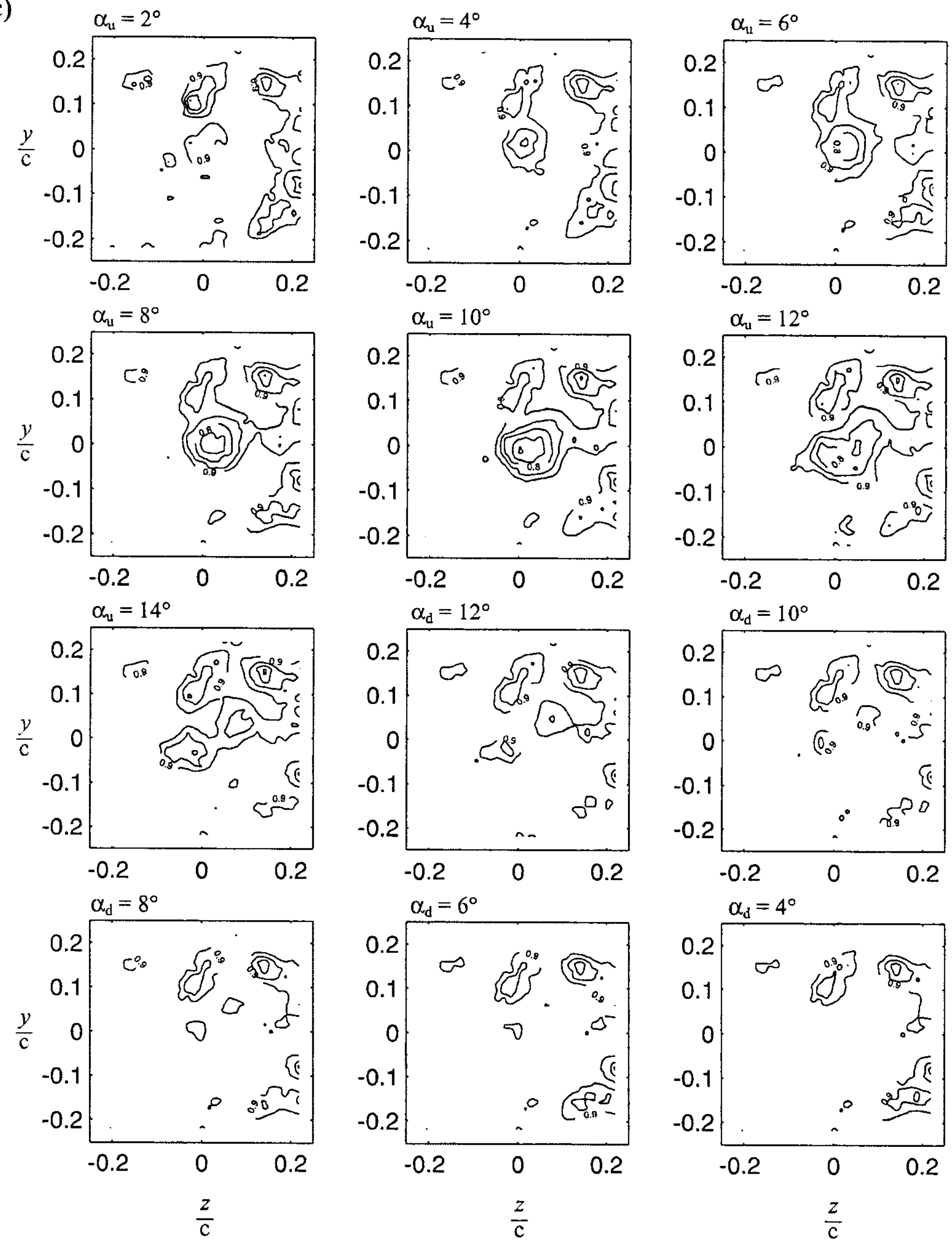

Figure E2 (a) Cross-flow velocity vectors, and contours of constant (b) $\zeta c/u_\infty$, (c) u/u_∞, and (d) u'/u_∞ (%) for the case of α_o = 8°, $\Delta\alpha$ = 6° and κ = 0.09 at the x/c = 1 measurement station.

d)

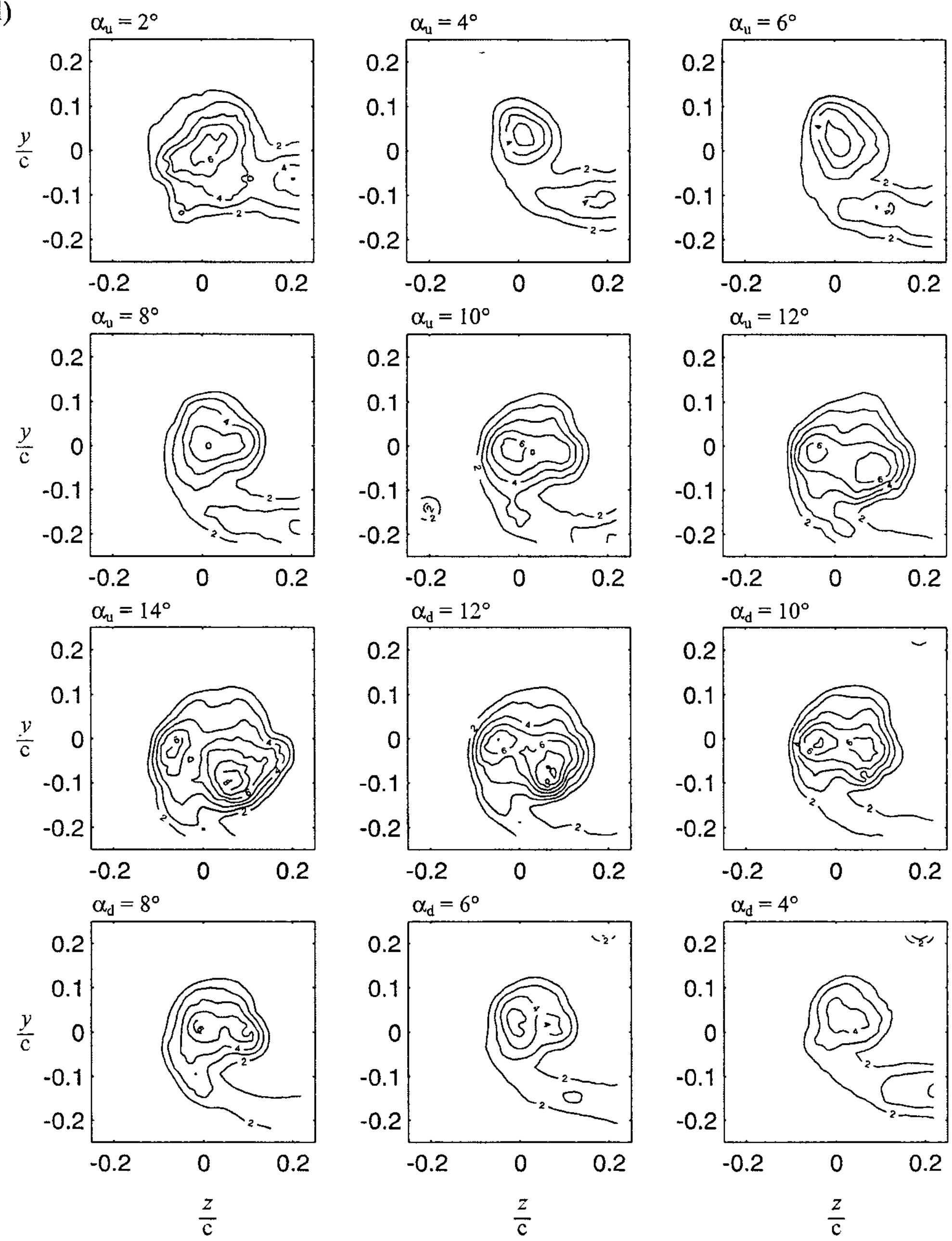

Figure E2 (a) Cross-flow velocity vectors, and contours of constant (b) $\zeta c/u_\infty$, (c) u/u_∞, and (d) u'/u_∞ (%) for the case of α_o = 8°, $\Delta\alpha$ = 6° and κ = 0.09 at the x/c = 1 measurement station.

a)

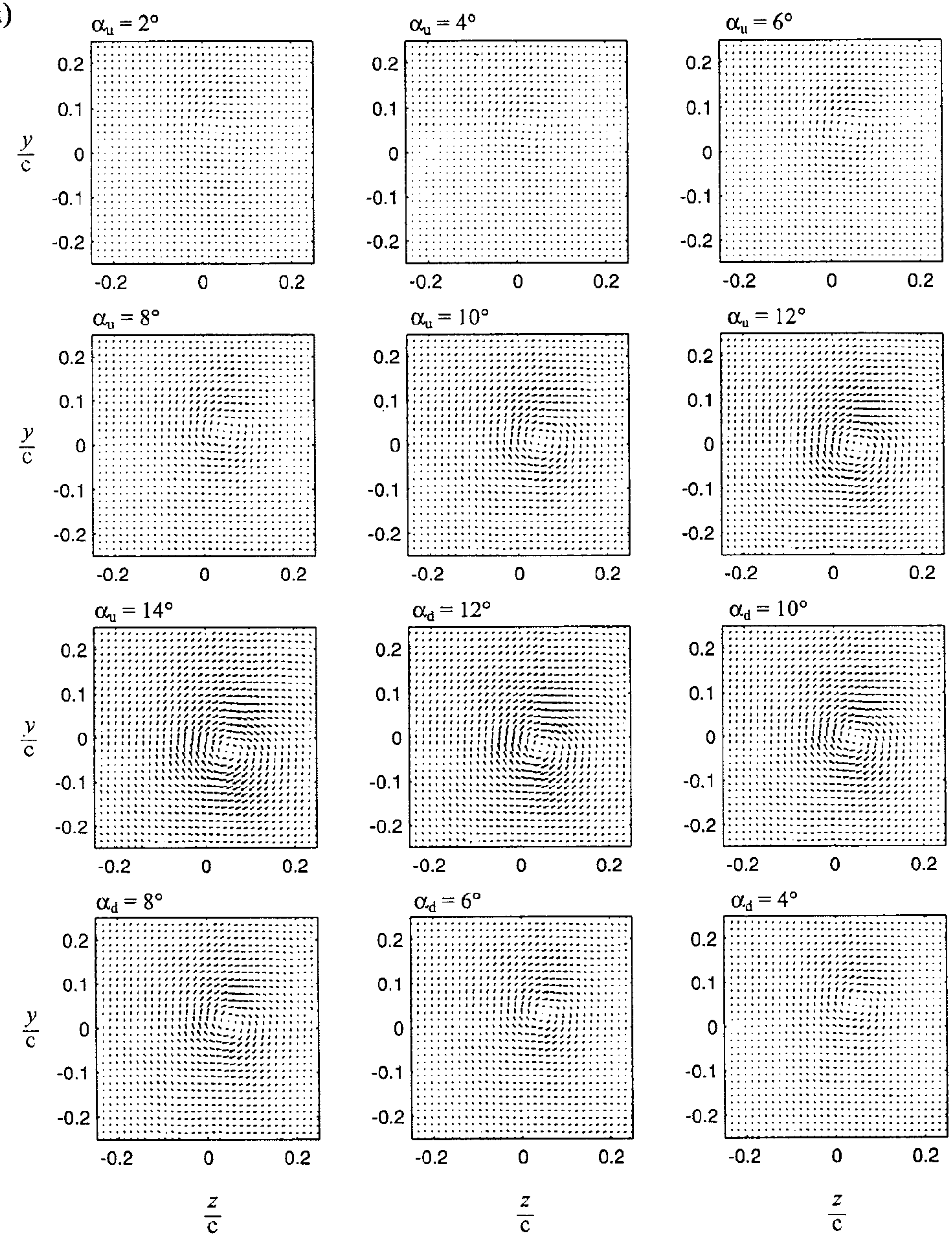

Figure E3 (a) Cross-flow velocity vectors, and contours of constant (b) $\zeta c/u_\infty$, (c) u/u_∞, and (d) u'/u_∞ (%) for the case of α_o = 8°, $\Delta\alpha$ = 6° and κ = 0.09 at the x/c = 1.5 measurement station.

b)

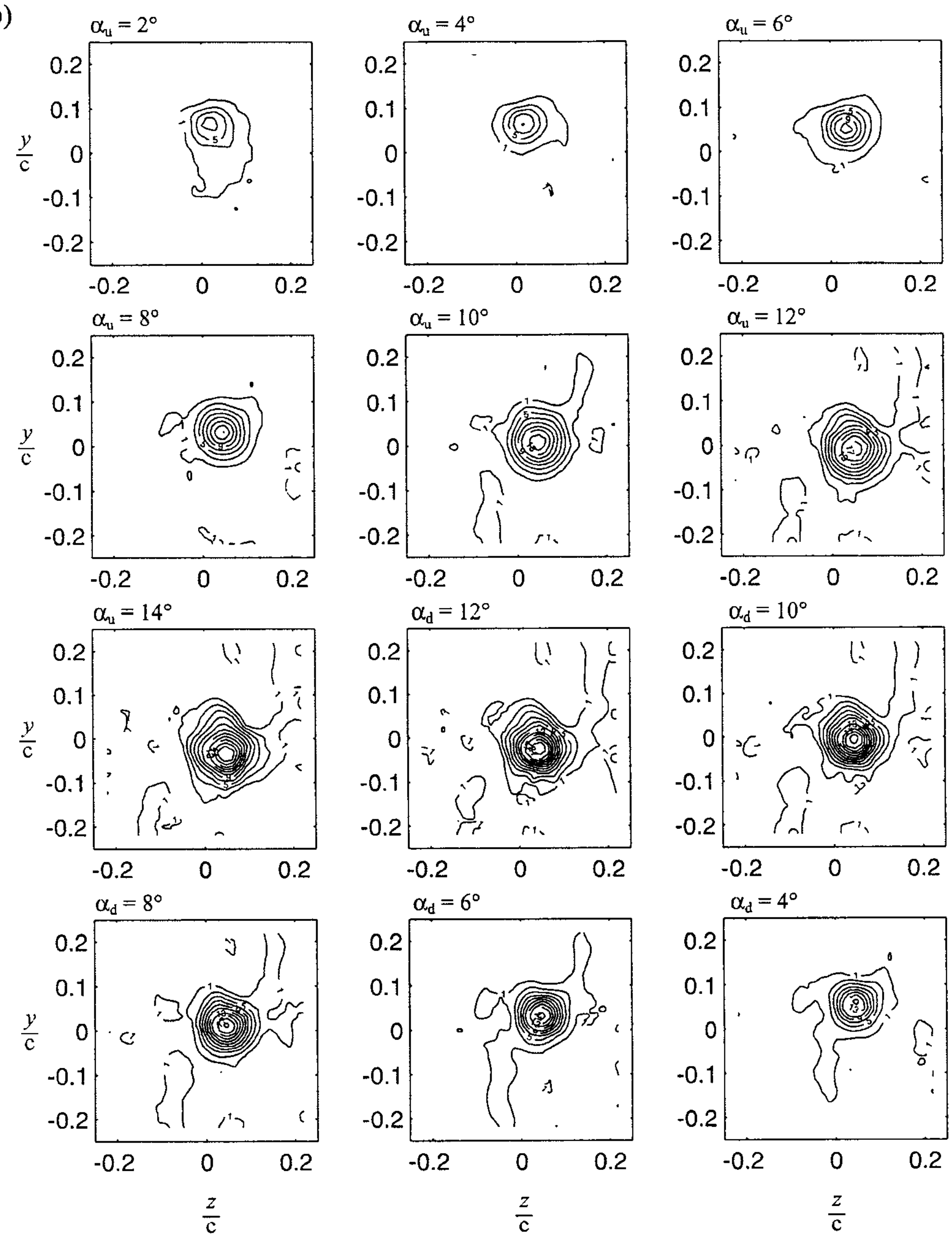

Figure E3 (a) Cross-flow velocity vectors, and contours of constant (b) $\zeta c/u_\infty$, (c) u/u_∞, and (d) u'/u_∞ (%) for the case of $\alpha_0 = 8°$, $\Delta\alpha = 6°$ and $\kappa = 0.09$ at the $x/c = 1.5$ measurement station.

c)

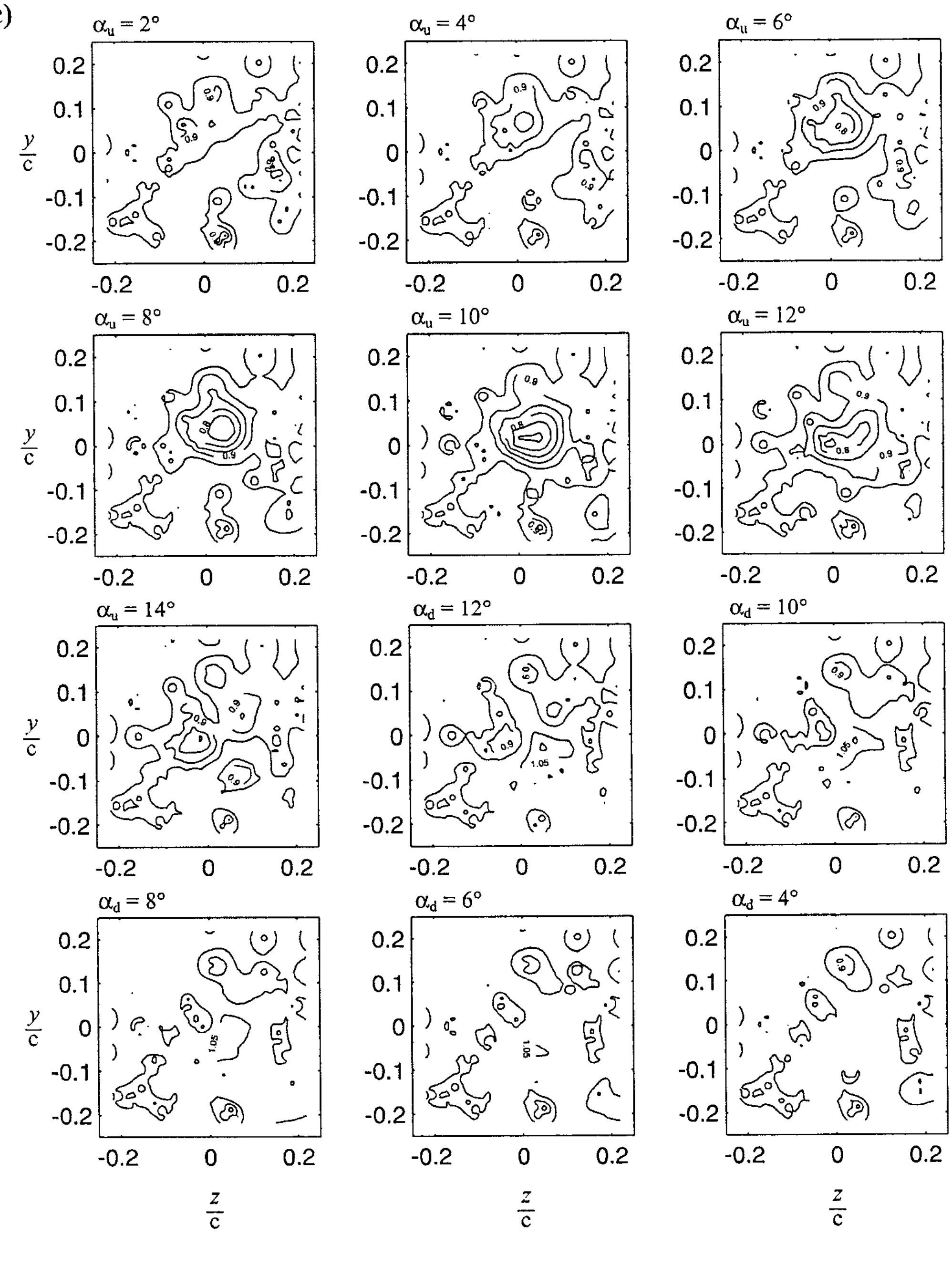

Figure E3 (a) Cross-flow velocity vectors, and contours of constant (b) $\zeta c/u_\infty$, (c) u/u_∞, and (d) u'/u_∞ (%) for the case of α_0 = 8°, $\Delta\alpha$ = 6° and κ = 0.09 at the x/c = 1.5 measurement station.

d)

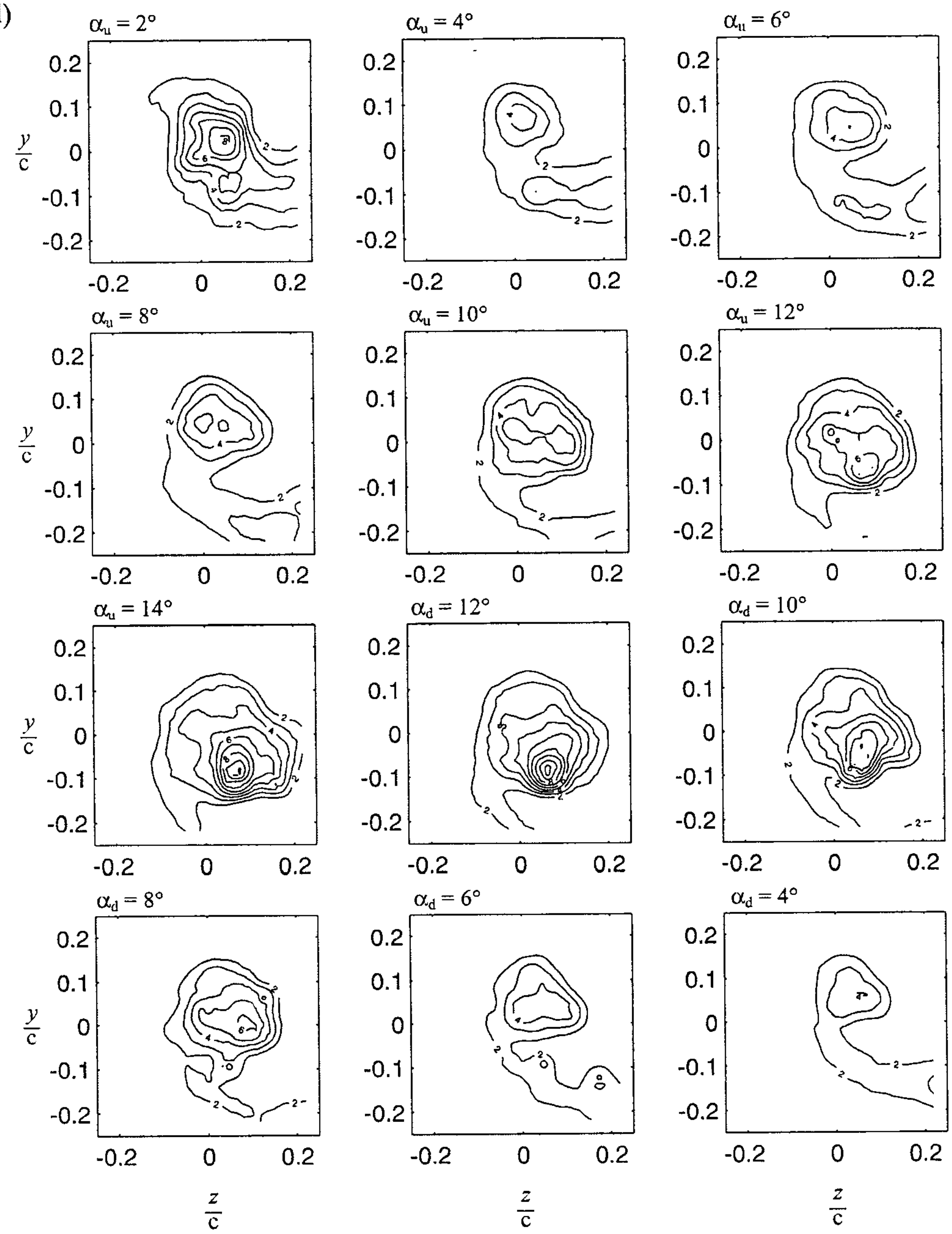

Figure E3 (a) Cross-flow velocity vectors, and contours of constant (b) $\zeta c/u_\infty$, (c) u/u_∞, and (d) u'/u_∞ (%) for the case of α_o = 8°, $\Delta\alpha$ = 6° and κ = 0.09 at the x/c = 1.5 measurement station.

a)

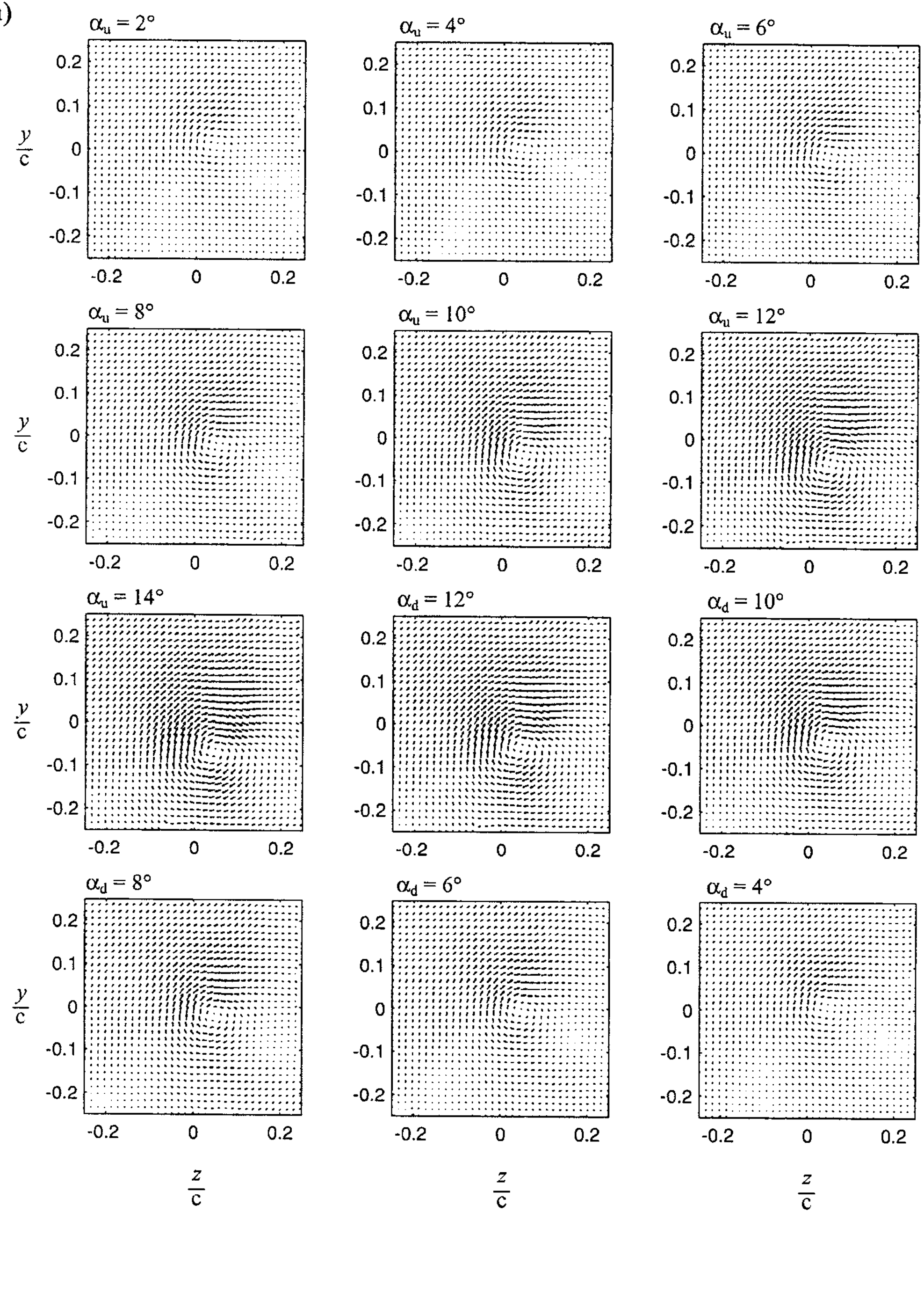

Figure E4 (a) Cross-flow velocity vectors, and contours of constant (b) $\zeta c/u_\infty$, (c) u/u_∞, and (d) u'/u_∞ (%) for the case of $\alpha_0 = 8°$, $\Delta\alpha = 6°$ and $\kappa = 0.12$ at the $x/c = 0.5$ measurement station.

b)

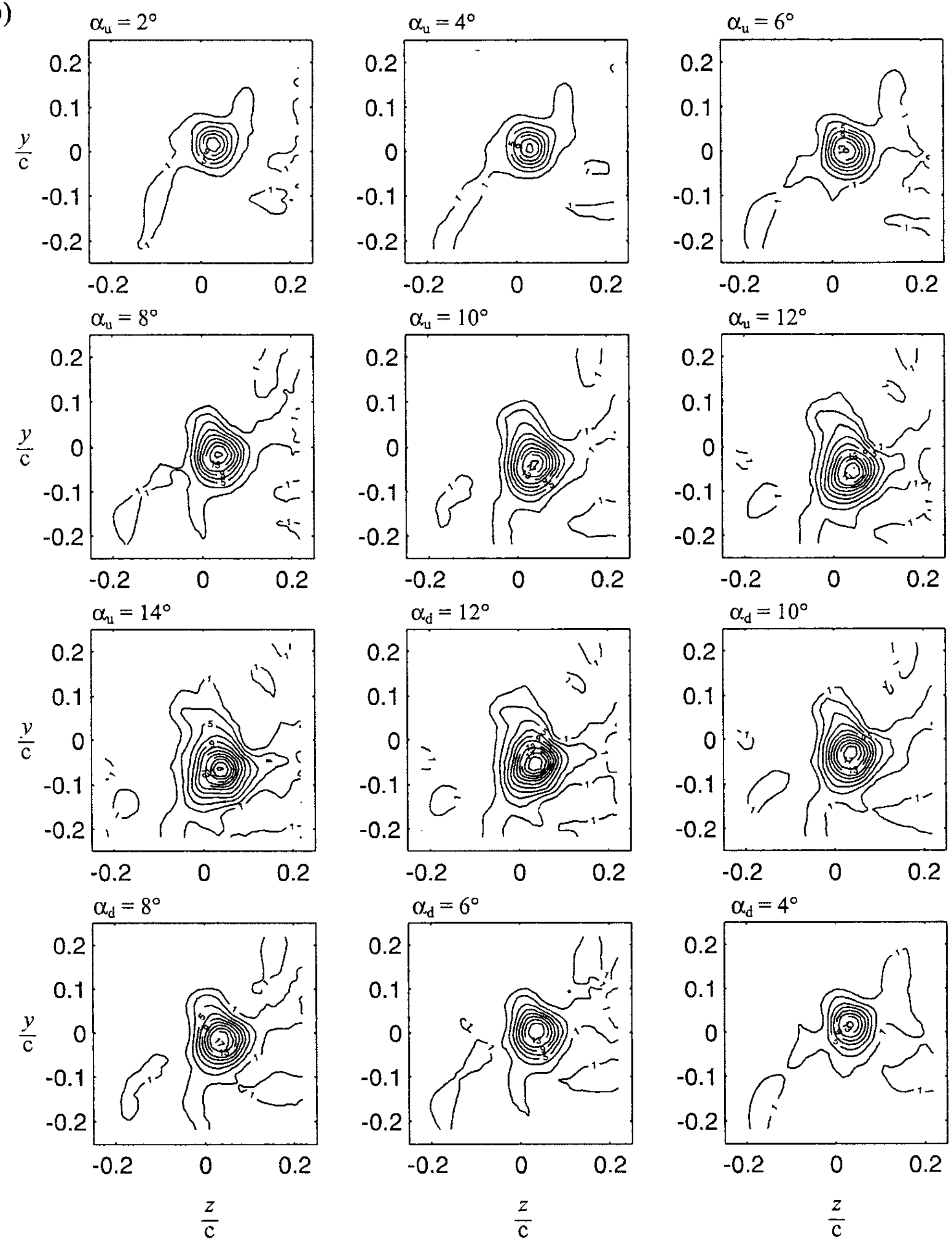

Figure E4 (a) Cross-flow velocity vectors, and contours of constant (b) $\zeta c/u_\infty$, (c) u/u_∞, and (d) u'/u_∞ (%) for the case of α_0 = 8°, $\Delta\alpha$ = 6° and κ = 0.12 at the x/c = 0.5 measurement station.

c)

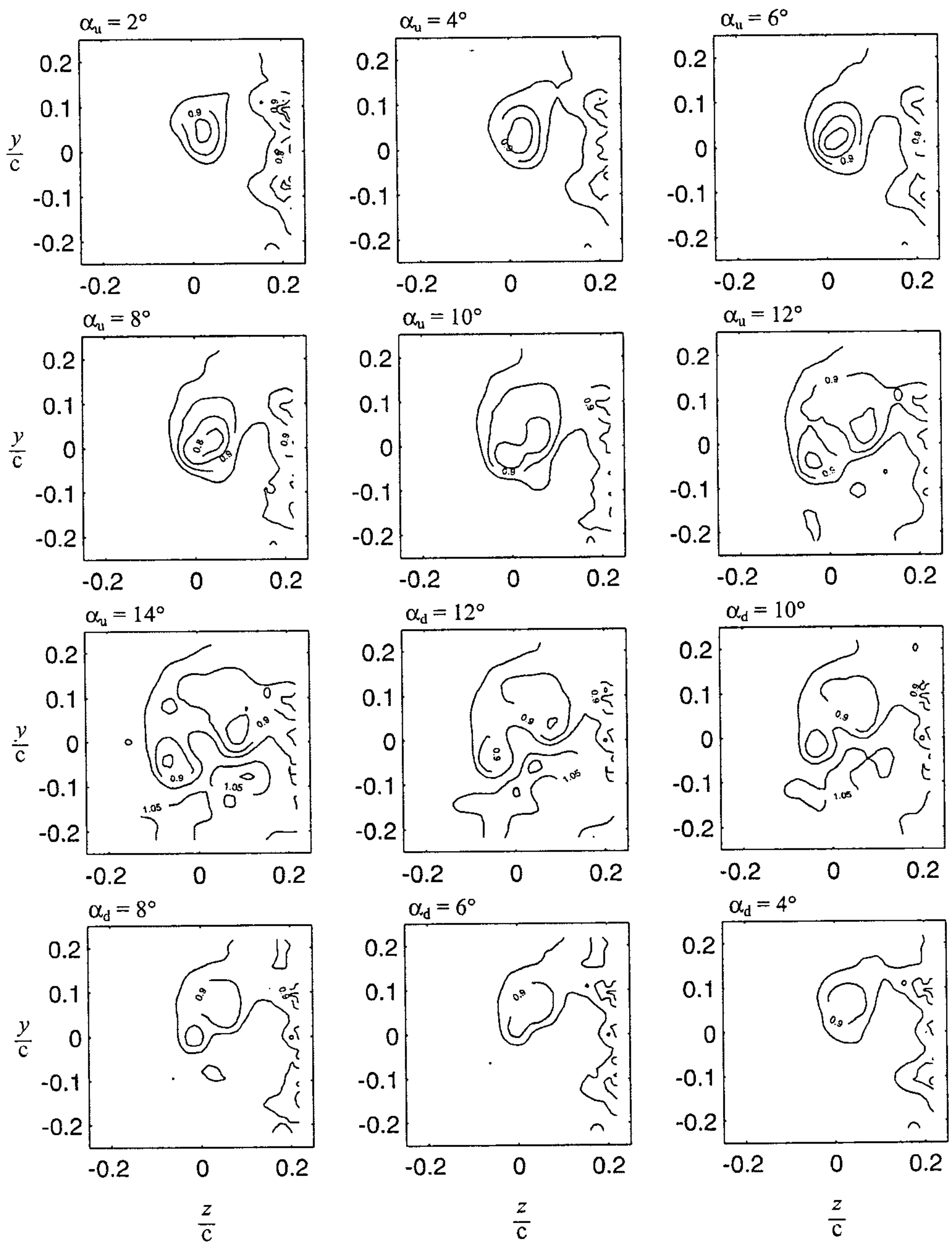

Figure E4 (a) Cross-flow velocity vectors, and contours of constant (b) $\zeta c/u_\infty$, (c) u/u_∞, and (d) u'/u_∞ (%) for the case of α_o = 8°, $\Delta\alpha$ = 6° and κ = 0.12 at the x/c = 0.5 measurement station.

d)

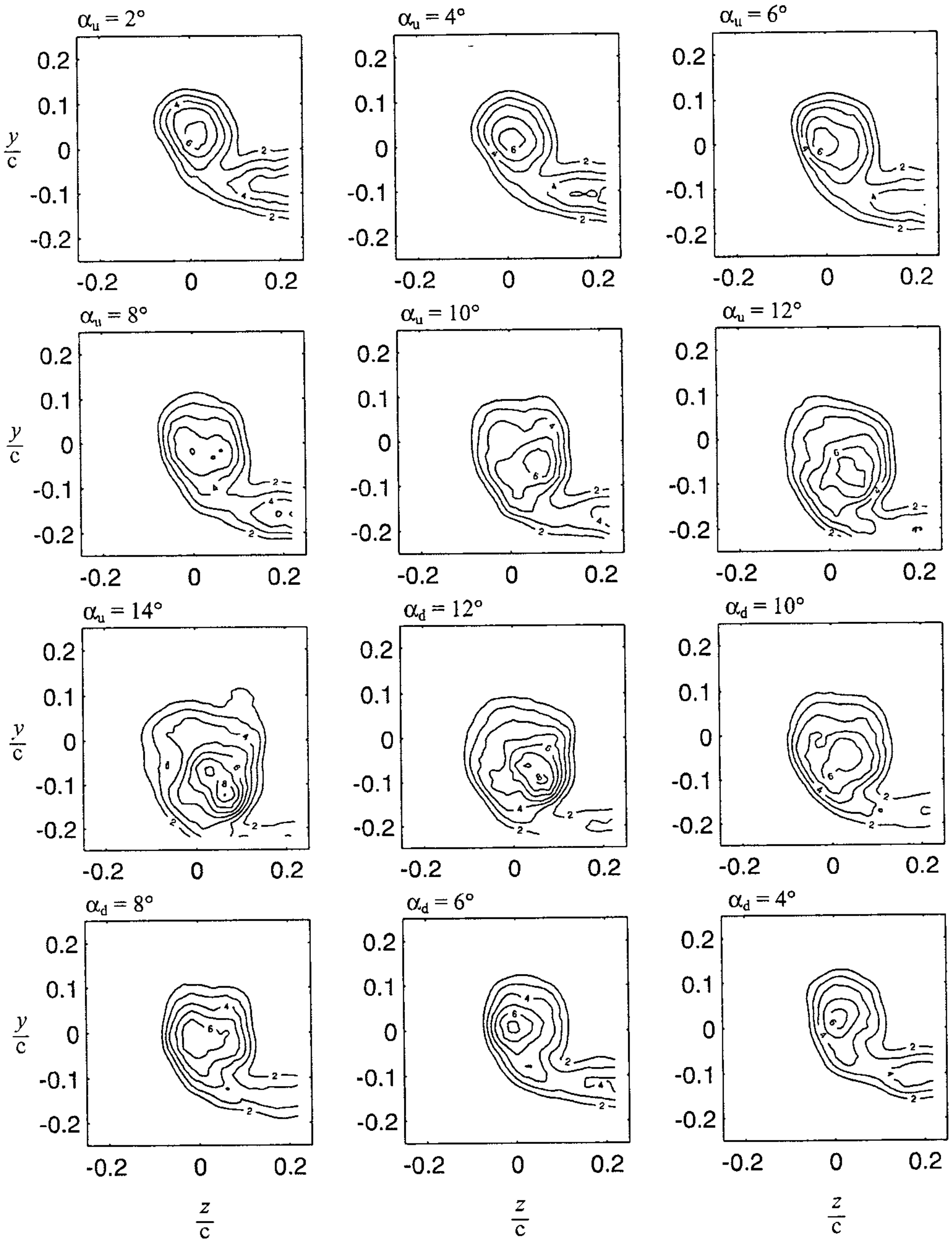

Figure E4 (a) Cross-flow velocity vectors, and contours of constant (b) $\zeta c/u_\infty$, (c) u/u_∞, and (d) u'/u_∞ (%) for the case of α_o = 8°, $\Delta\alpha$ = 6° and κ = 0.12 at the x/c = 0.5 measurement station.

a)

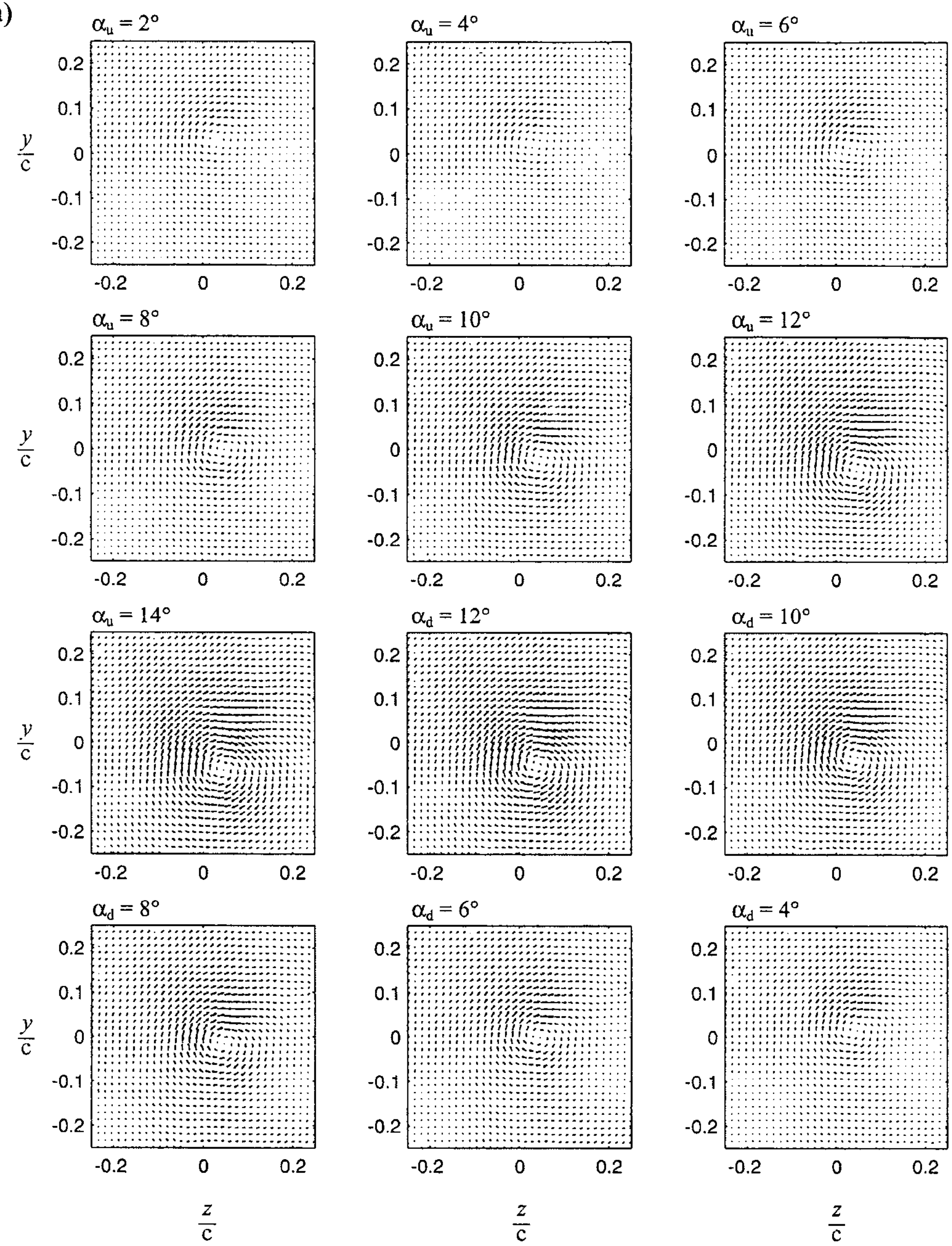

Figure E5 (a) Cross-flow velocity vectors, and contours of constant (b) $\zeta c/u_\infty$, (c) u/u_∞, and (d) u'/u_∞ (%) for the case of α_0 = 8°, $\Delta\alpha$ = 6° and κ = 0.12 at the x/c = 1 measurement station.

b)

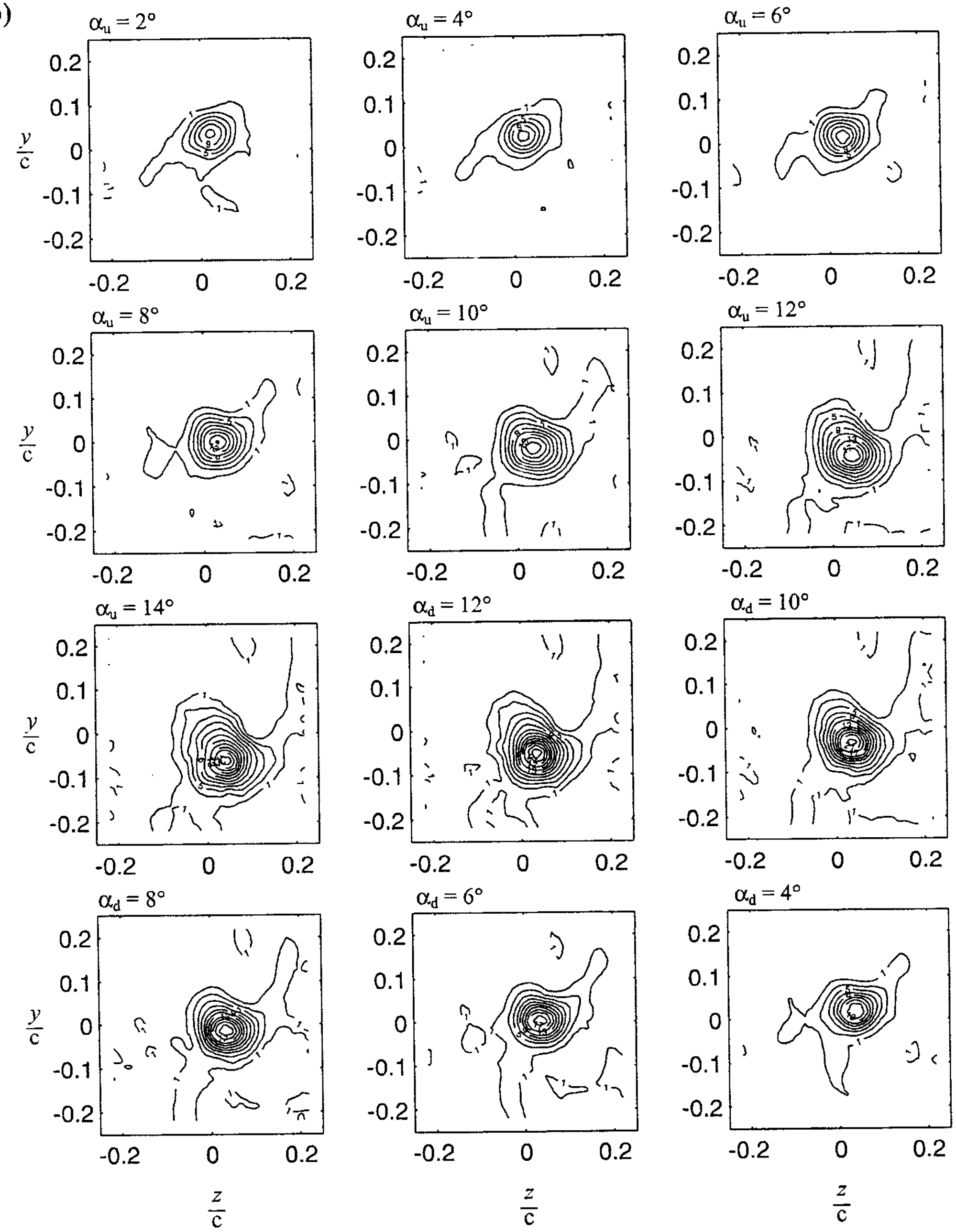

Figure E5 (a) Cross-flow velocity vectors, and contours of constant (b) $\zeta c/u_\infty$, (c) u/u_∞, and (d) u'/u_∞ (%) for the case of α_o = 8°, $\Delta\alpha$ = 6° and κ = 0.12 at the x/c = 1 measurement station.

c)

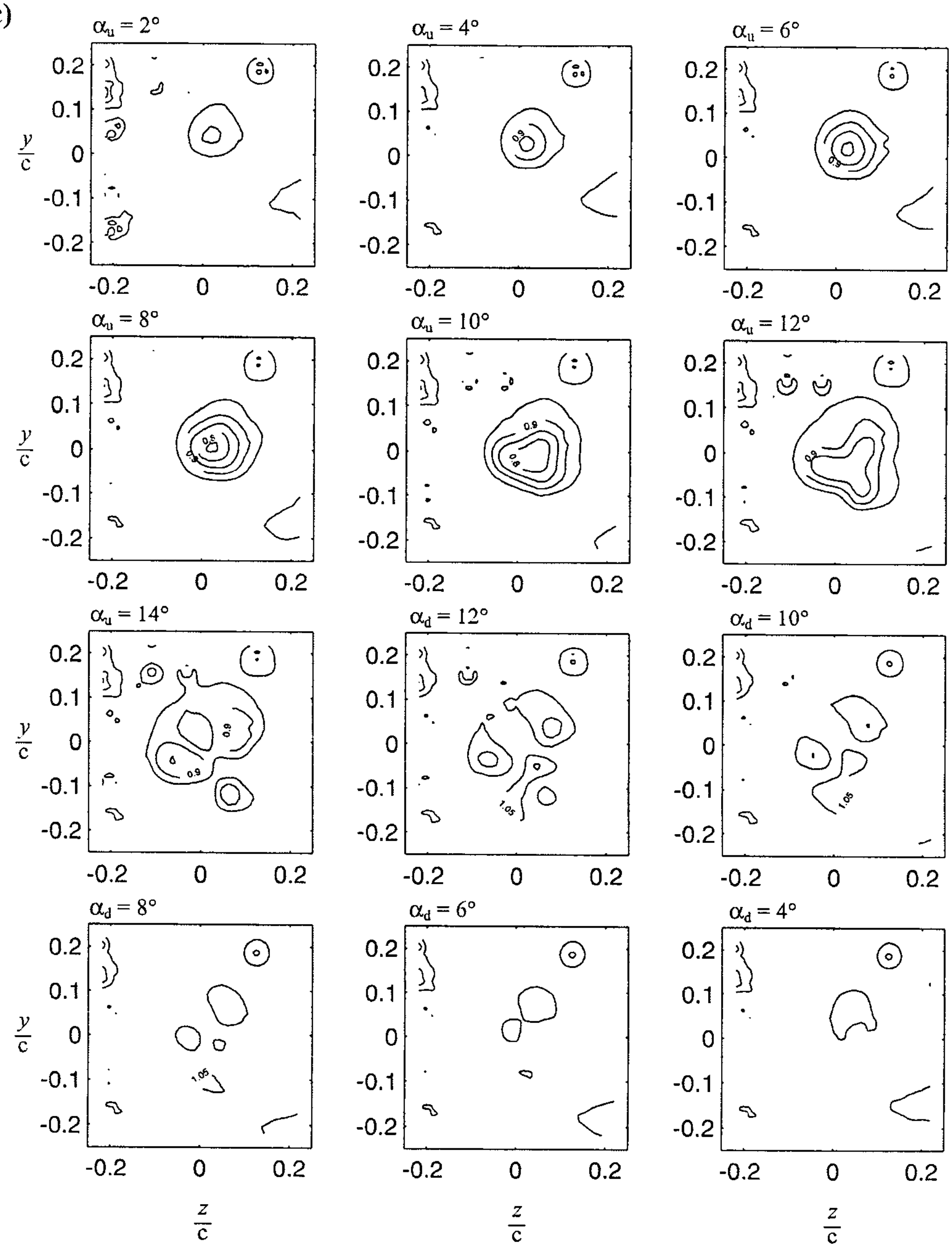

Figure E5 (a) Cross-flow velocity vectors, and contours of constant (b) $\zeta c/u_\infty$, (c) u/u_∞, and (d) u'/u_∞ (%) for the case of α_0 = 8°, $\Delta\alpha$ = 6° and κ = 0.12 at the x/c = 1 measurement station.

d)

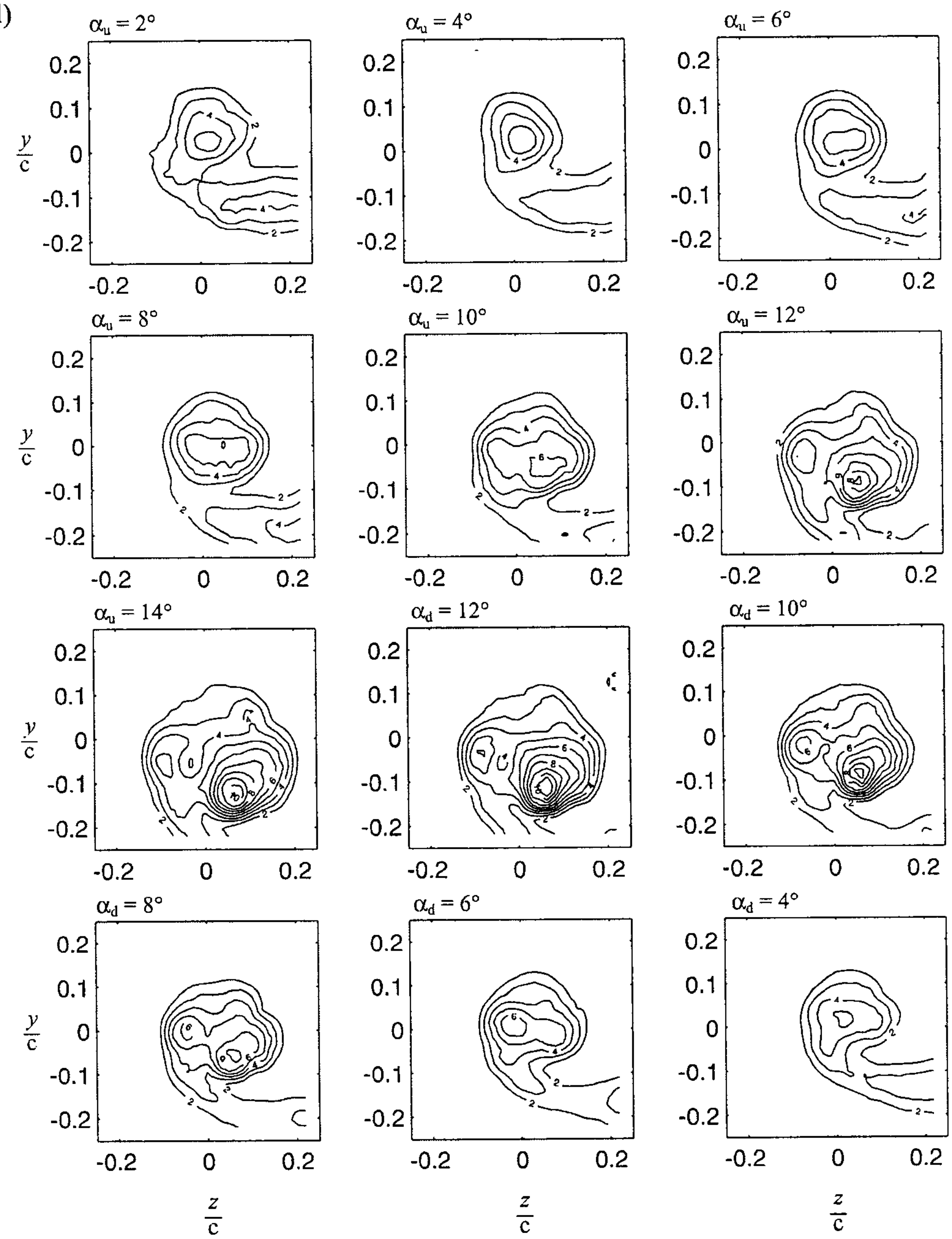

Figure E5 (a) Cross-flow velocity vectors, and contours of constant (b) $\zeta c/u_\infty$, (c) u/u_∞, and (d) u'/u_∞ (%) for the case of α_o = 8°, $\Delta\alpha$ = 6° and κ = 0.12 at the x/c = 1 measurement station.

a)

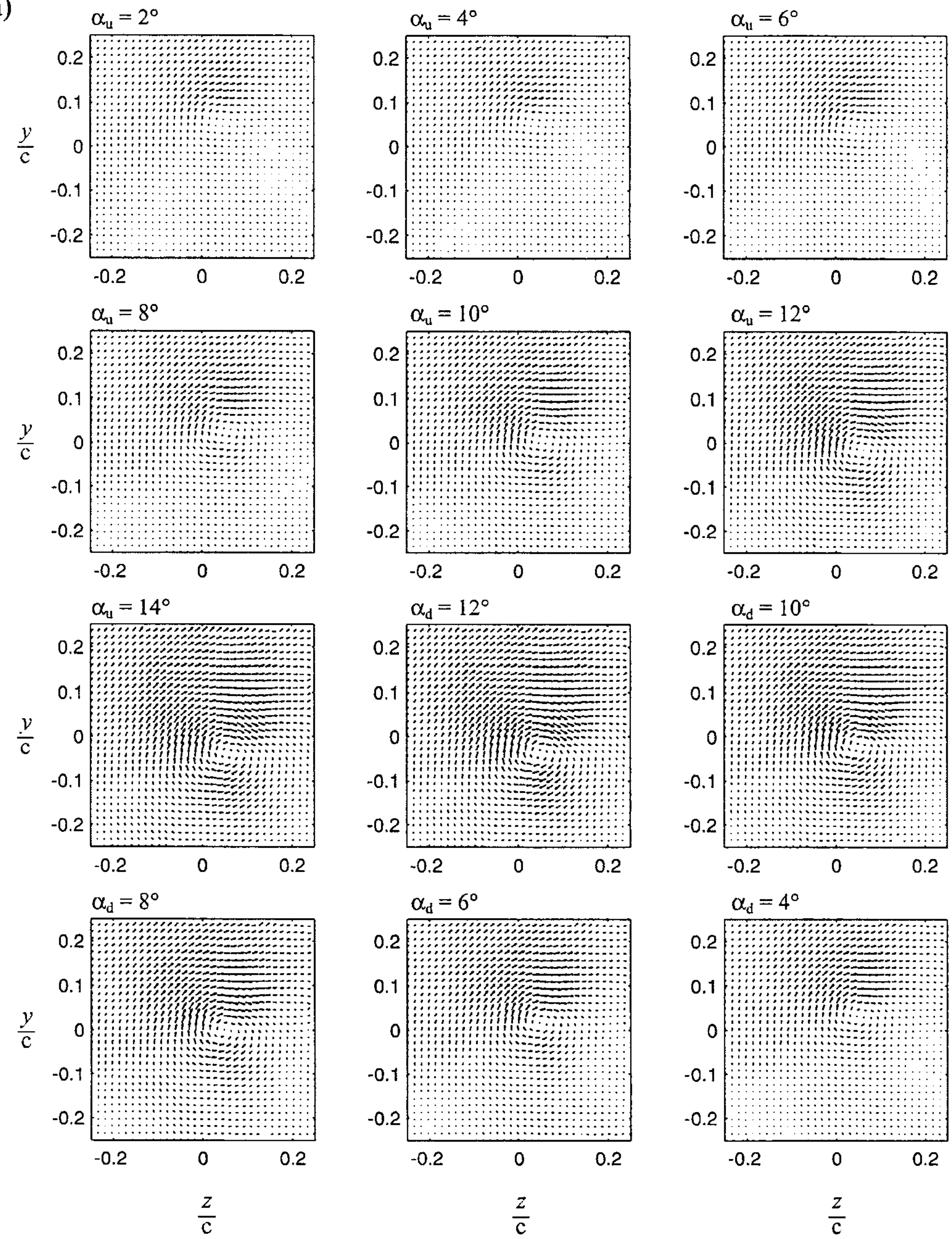

Figure E6 (a) Cross-flow velocity vectors, and contours of constant (b) $\zeta c/u_\infty$, (c) u/u_∞, and (d) u'/u_∞ (%) for the case of α_0 = 8°, $\Delta\alpha$ = 6° and κ = 0.12 at the x/c = 1.5 measurement station.

b)

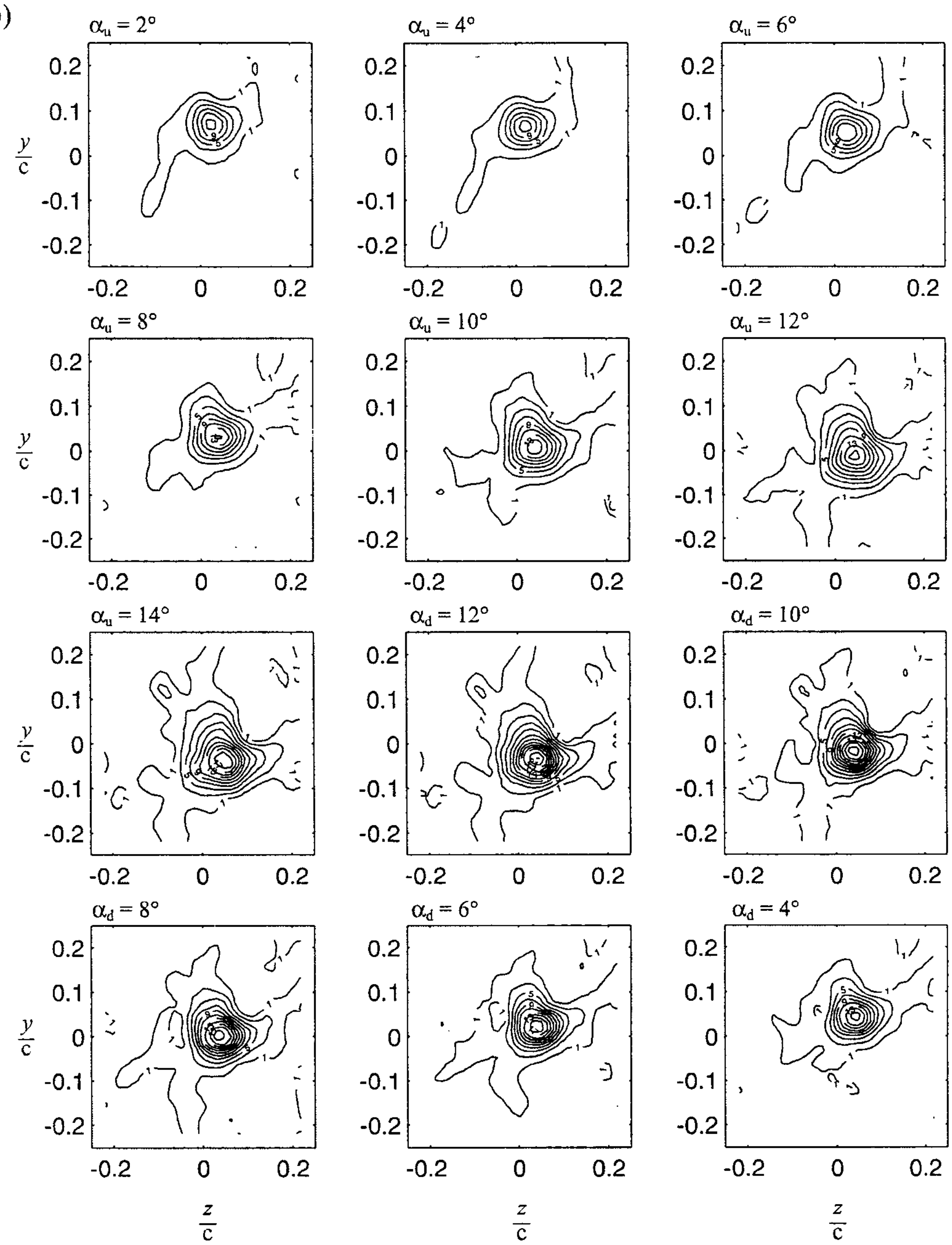

Figure E6 (a) Cross-flow velocity vectors, and contours of constant (b) $\zeta c/u_\infty$, (c) u/u_∞, and (d) u'/u_∞ (%) for the case of α_0 = 8°, $\Delta\alpha$ = 6° and κ = 0.12 at the *x*/c = 1.5 measurement station.

c)

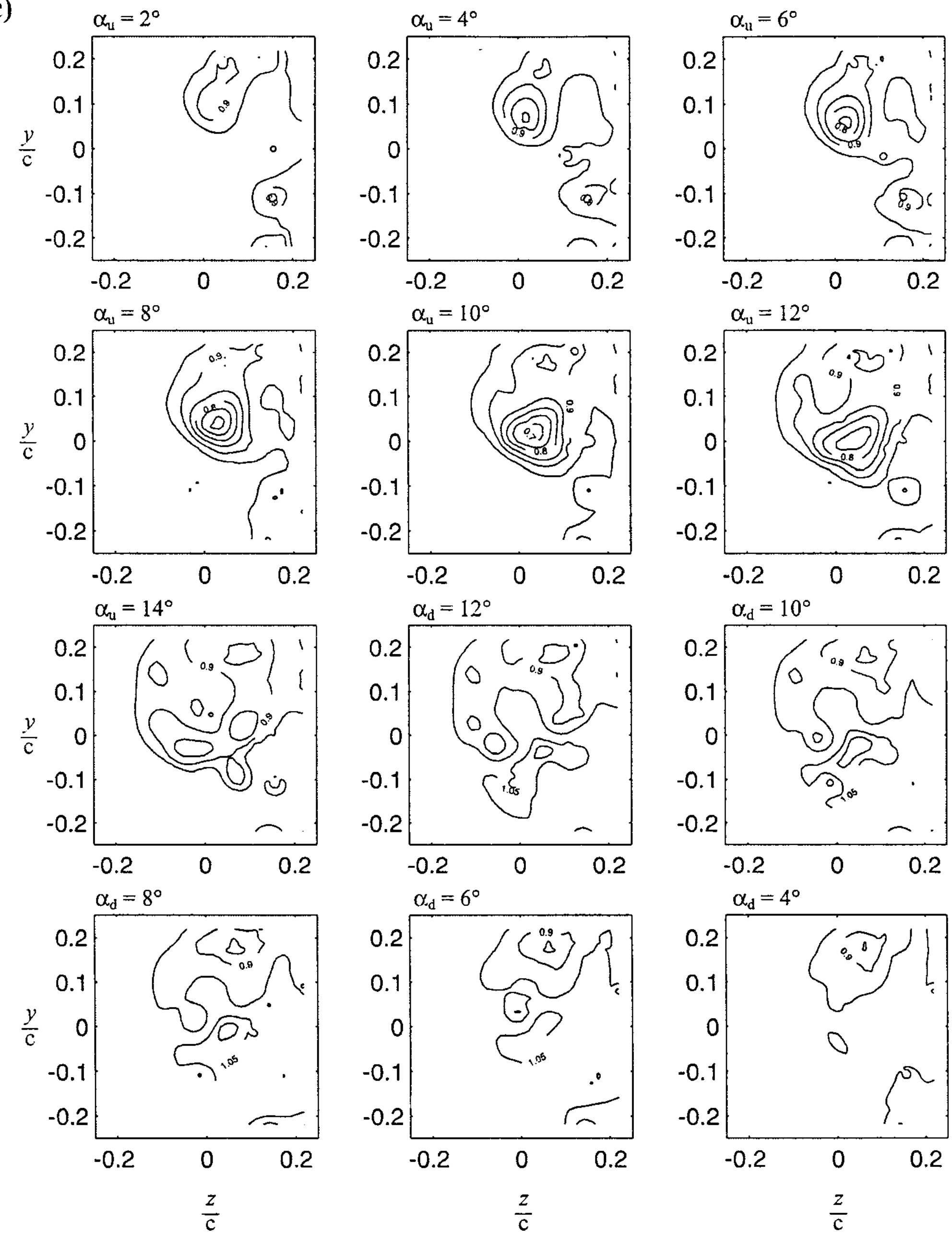

Figure E6 (a) Cross-flow velocity vectors, and contours of constant (b) $\zeta c/u_\infty$, (c) u/u_∞, and (d) u'/u_∞ (%) for the case of α_0 = 8°, $\Delta\alpha$ = 6° and κ = 0.12 at the x/c = 1.5 measurement station.

d)

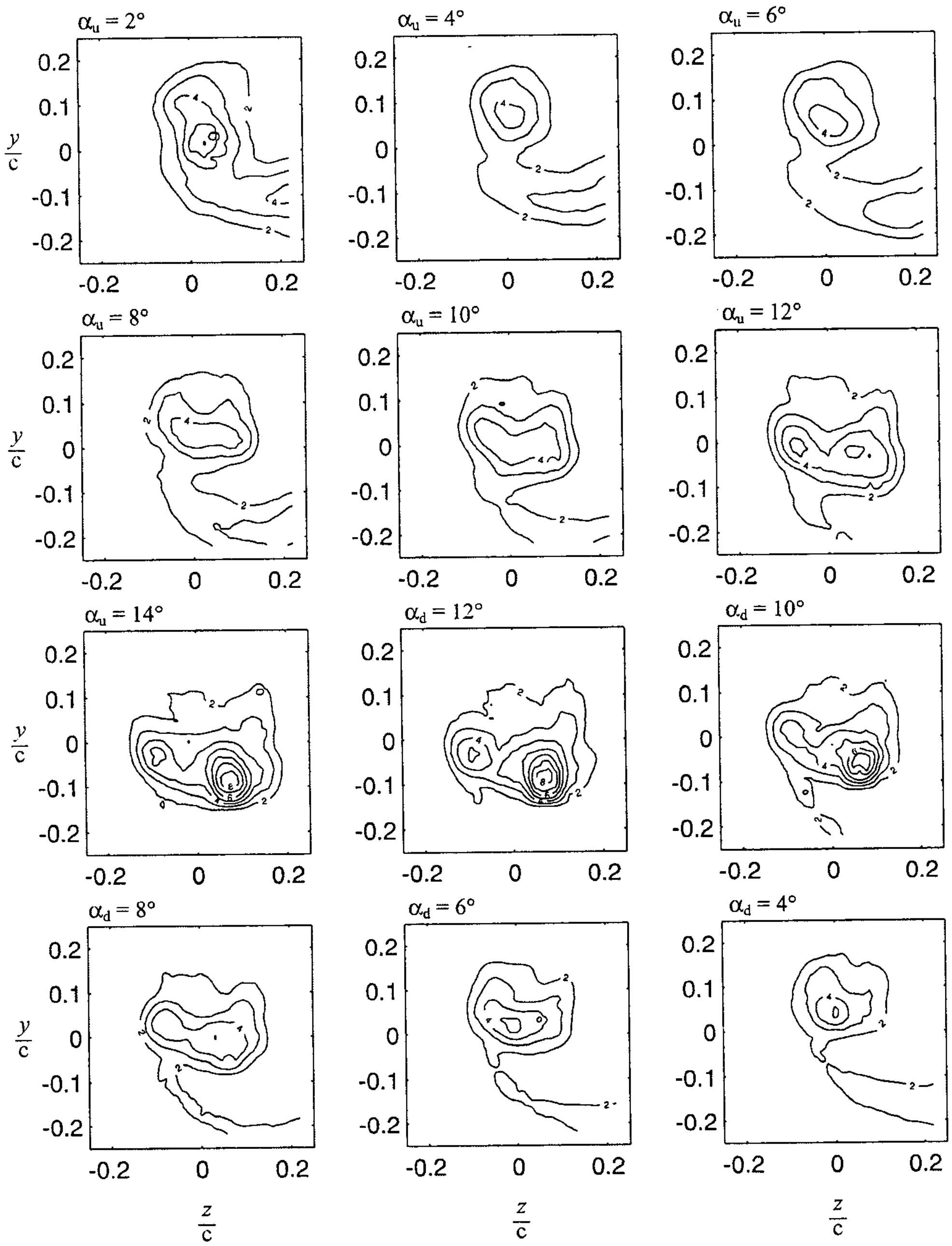

Figure E6 (a) Cross-flow velocity vectors, and contours of constant (b) $\zeta c/u_\infty$, (c) u/u_∞, and (d) u'/u_∞ (%) for the case of α_0 = 8°, $\Delta\alpha$ = 6° and κ = 0.12 at the x/c = 1.5 measurement station.

a)

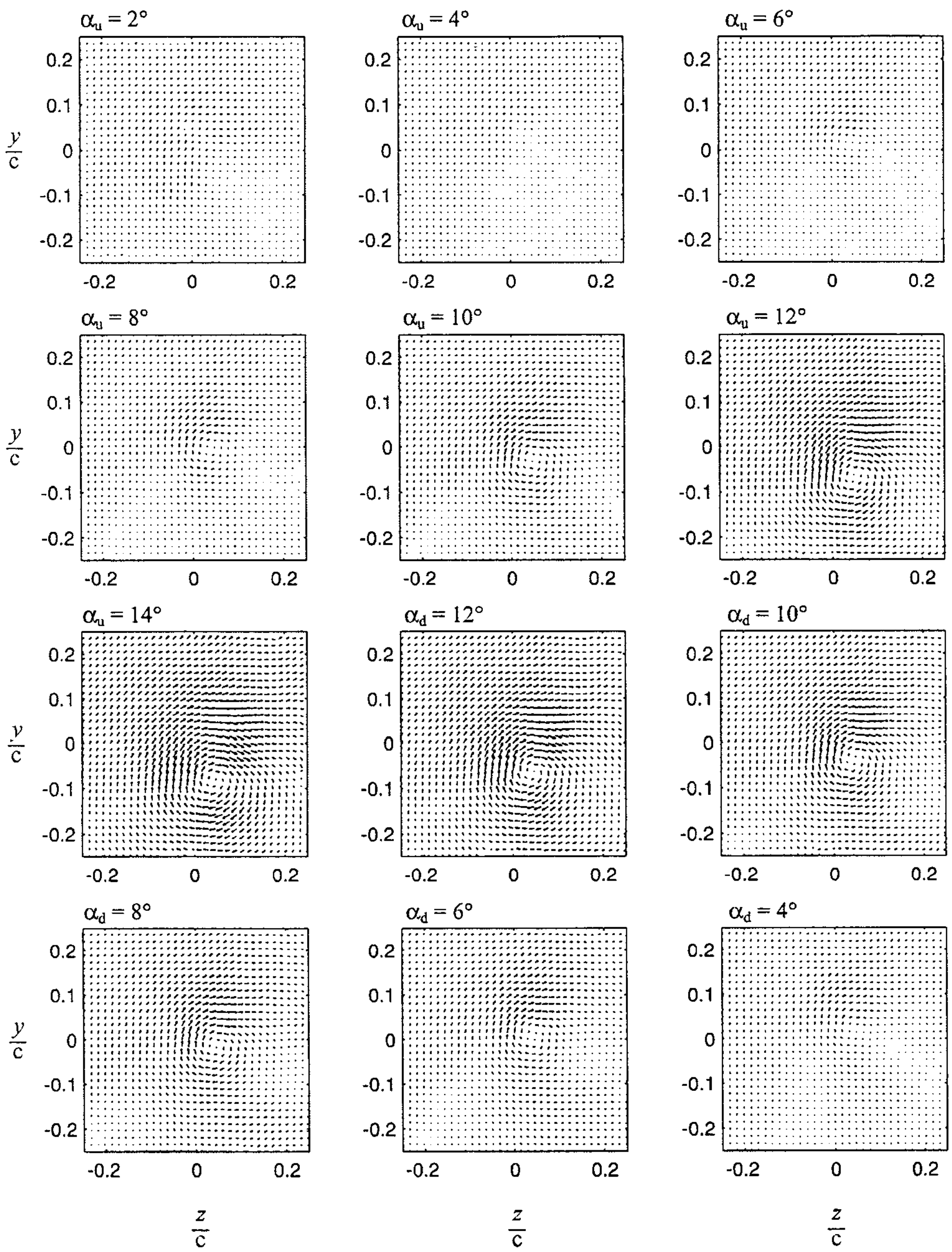

Figure E7 (a) Cross-flow velocity vectors, and contours of constant (b) $\zeta c/u_\infty$, (c) u/u_∞, and (d) u'/u_∞ (%) for the case of α_o = 8°, $\Delta\alpha$ = 6° and κ = 0.18 at the x/c = 0.5 measurement station.

b)

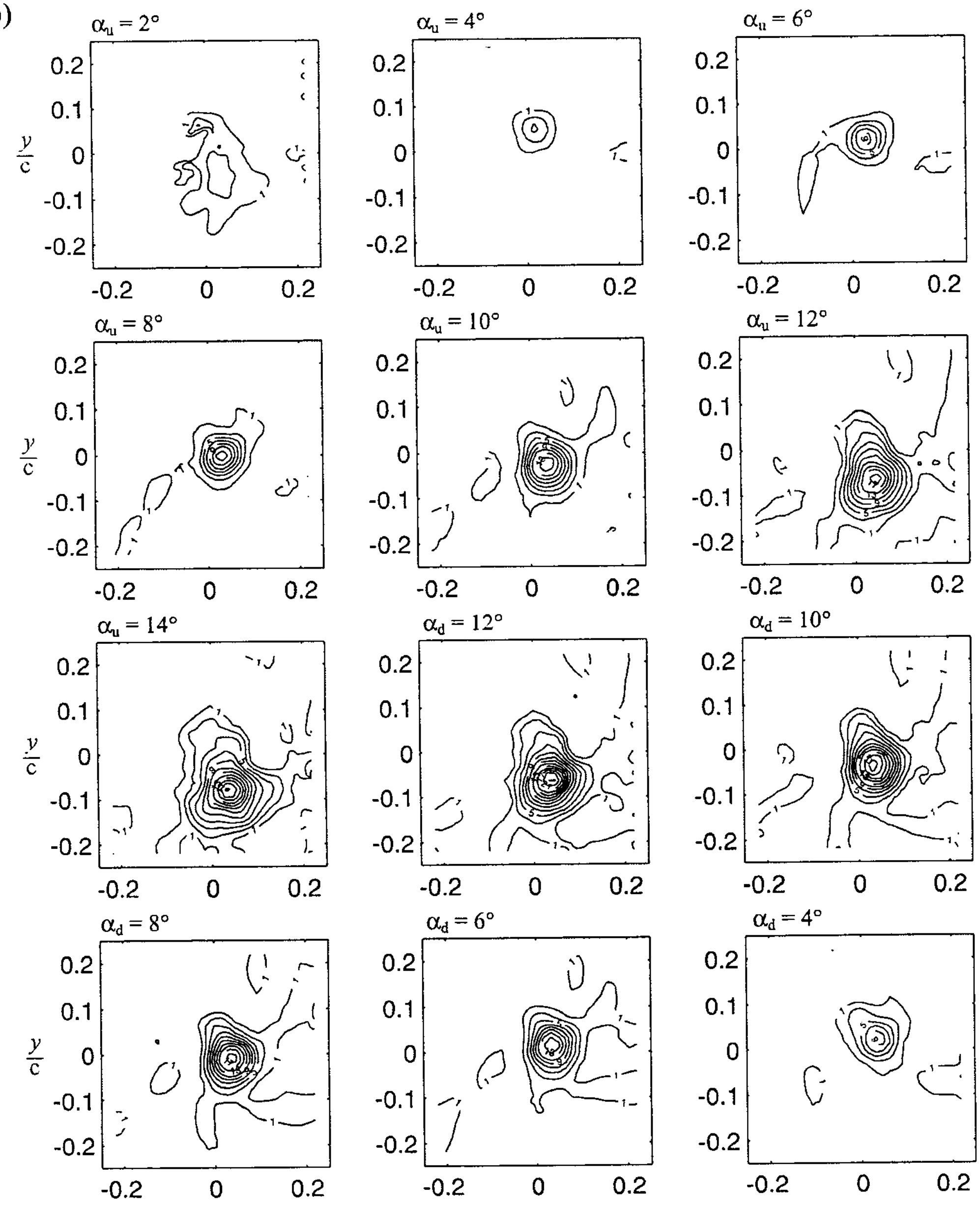

Figure E7 (a) Cross-flow velocity vectors, and contours of constant (b) $\zeta c/u_\infty$, (c) u/u_∞, and (d) u'/u_∞ (%) for the case of α_o = 8°, $\Delta\alpha$ = 6° and κ = 0.18 at the x/c = 0.5 measurement station.

c)

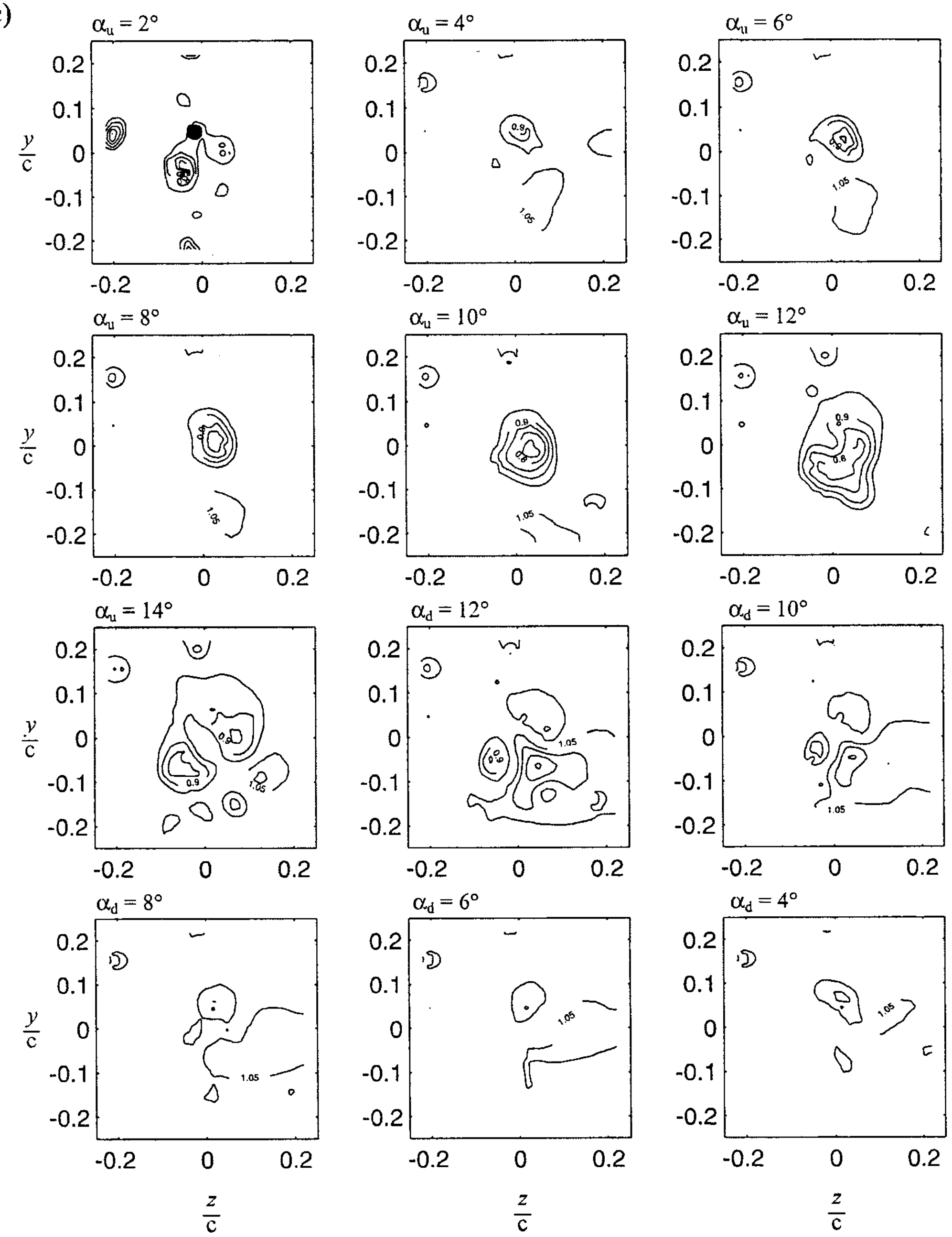

Figure E7 (a) Cross-flow velocity vectors, and contours of constant (b) $\zeta c/u_\infty$, (c) u/u_∞, and (d) u'/u_∞ (%) for the case of α_o = 8°, $\Delta\alpha$ = 6° and κ = 0.18 at the x/c = 0.5 measurement station.

d)

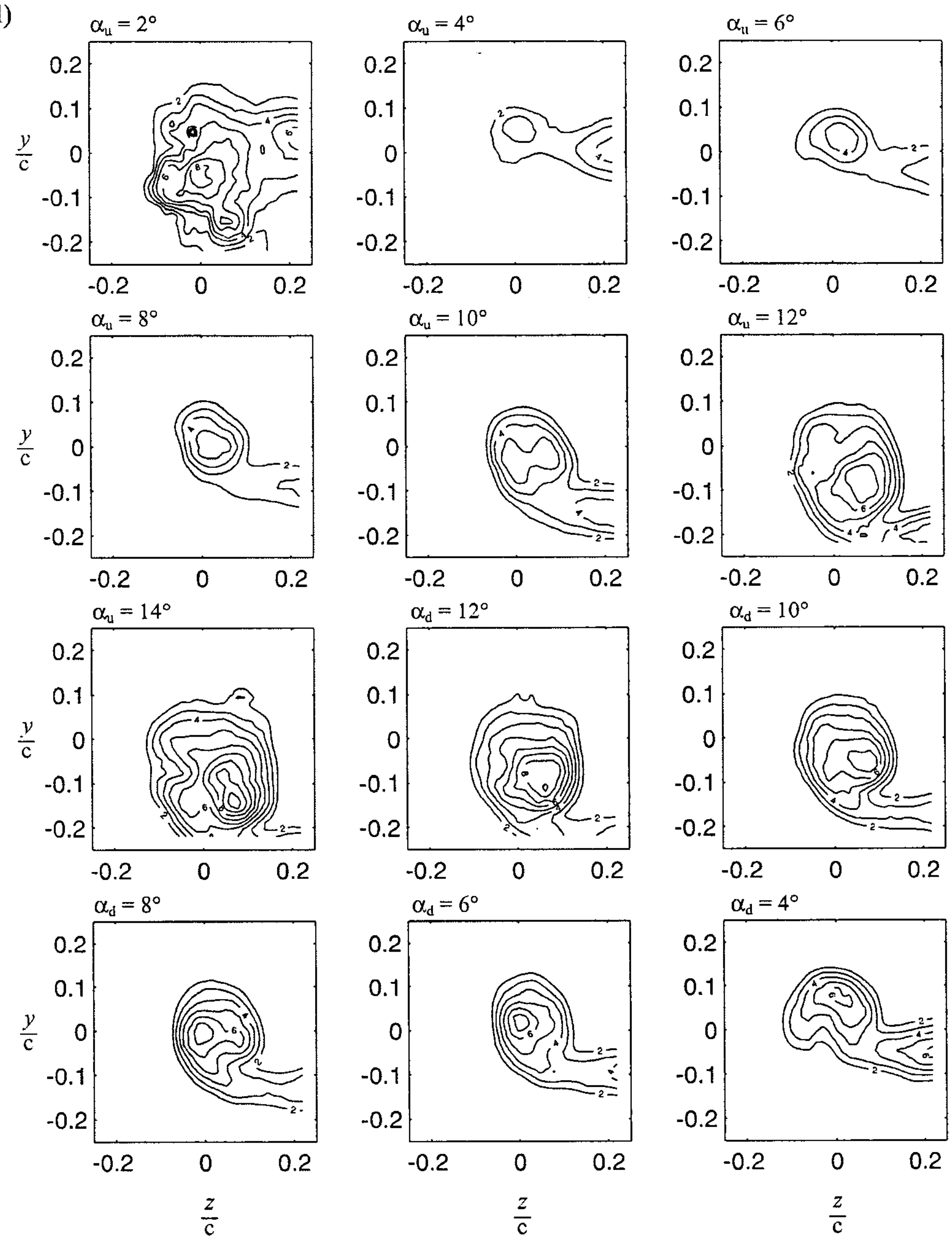

Figure E7 (a) Cross-flow velocity vectors, and contours of constant (b) $\zeta c/u_\infty$, (c) u/u_∞, and (d) u'/u_∞ (%) for the case of α_o = 8°, $\Delta\alpha$ = 6° and κ = 0.18 at the x/c = 0.5 measurement station.

a)

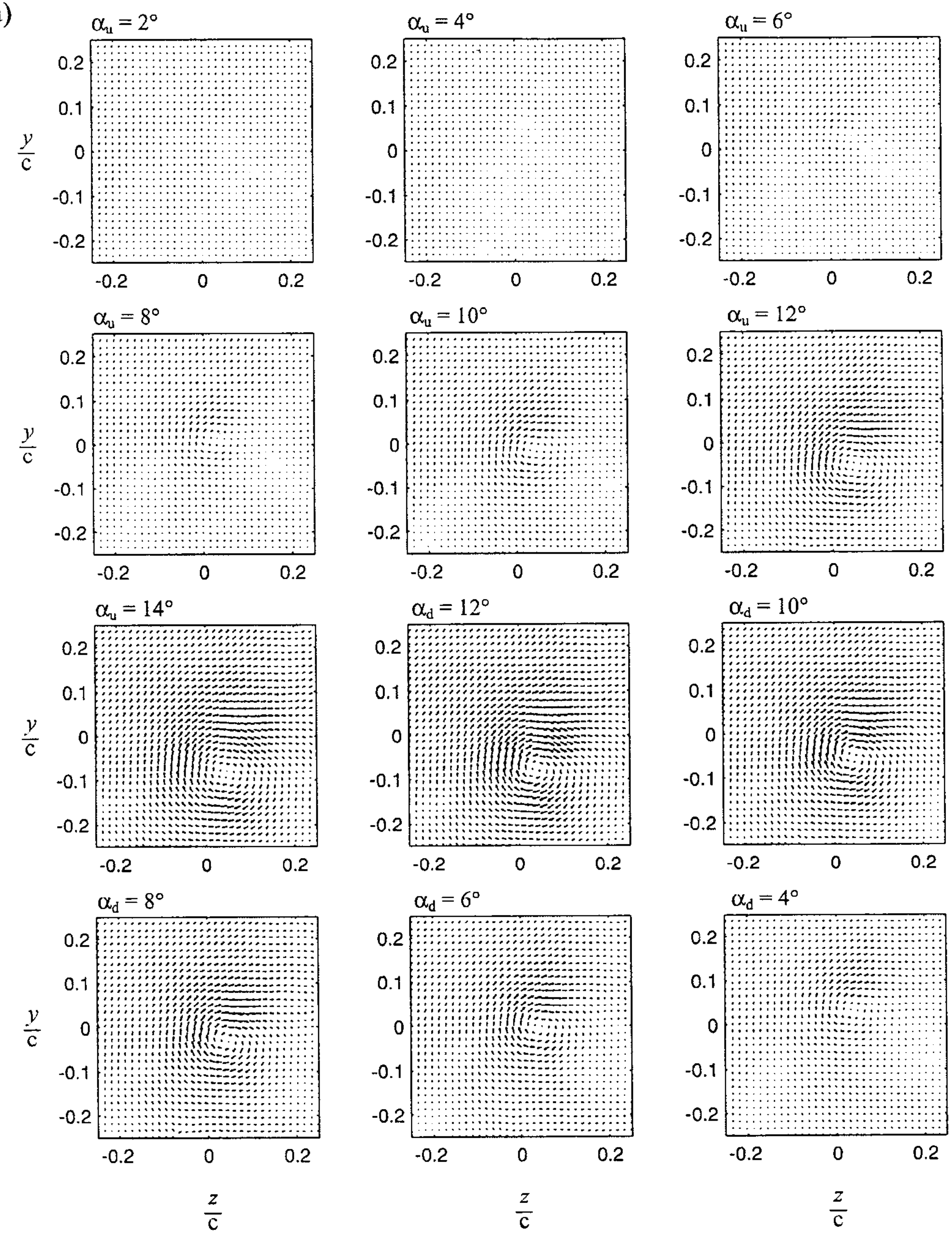

Figure E8 (a) Cross-flow velocity vectors, and contours of constant (b) $\zeta c/u_\infty$, (c) u/u_∞, and (d) u'/u_∞ (%) for the case of α_o = 8°, $\Delta\alpha$ = 6° and κ = 0.18 at the x/c = 1 measurement station.

b)

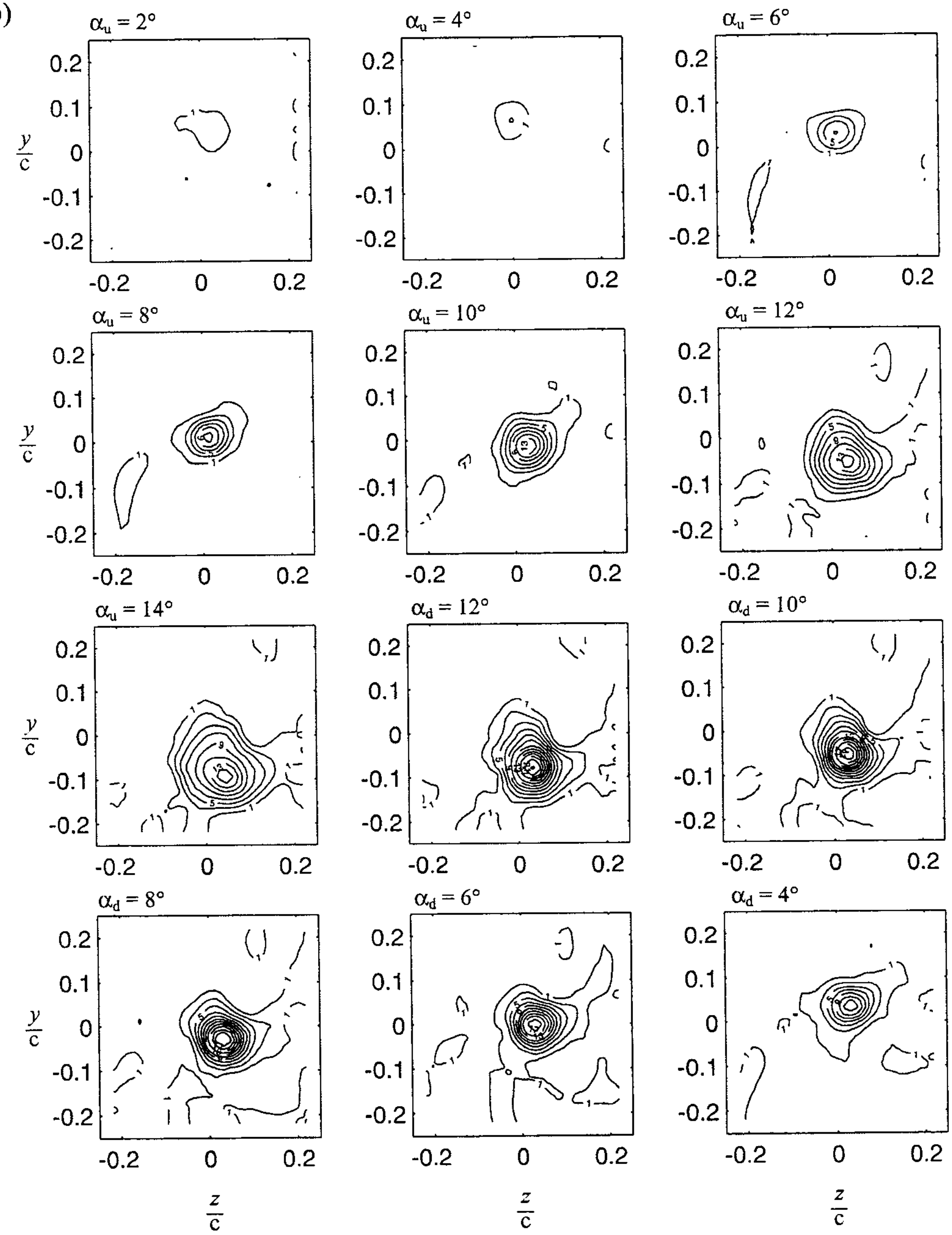

Figure E8 (a) Cross-flow velocity vectors, and contours of constant (b) $\zeta c/u_\infty$, (c) u/u_∞, and (d) u'/u_∞ (%) for the case of α_o = 8°, $\Delta\alpha$ = 6° and κ = 0.18 at the x/c = 1 measurement station.

c)

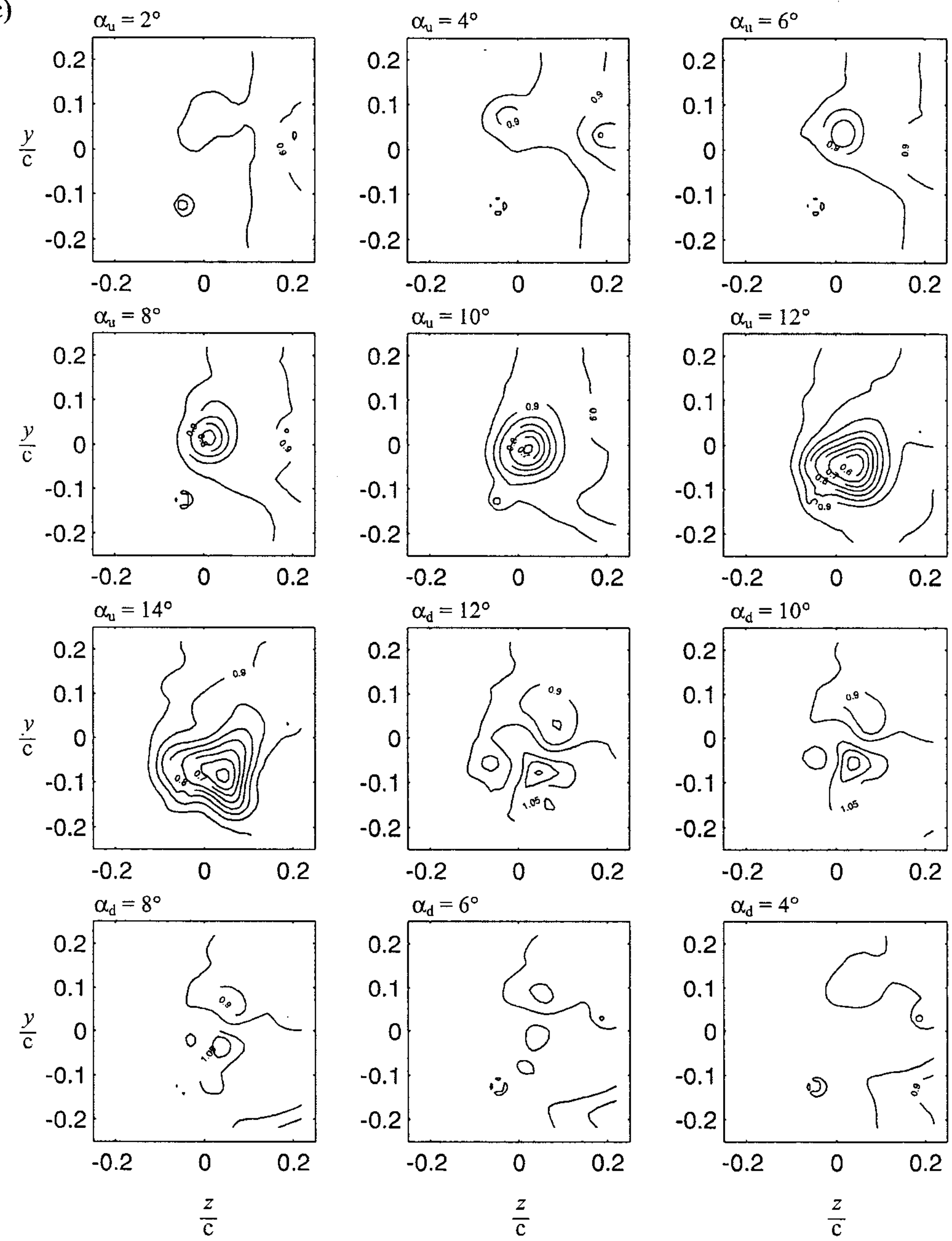

Figure E8 (a) Cross-flow velocity vectors, and contours of constant (b) $\zeta c/u_\infty$, (c) u/u_∞, and (d) u'/u_∞ (%) for the case of α_o = 8°, $\Delta\alpha$ = 6° and κ = 0.18 at the x/c = 1 measurement station.

d)

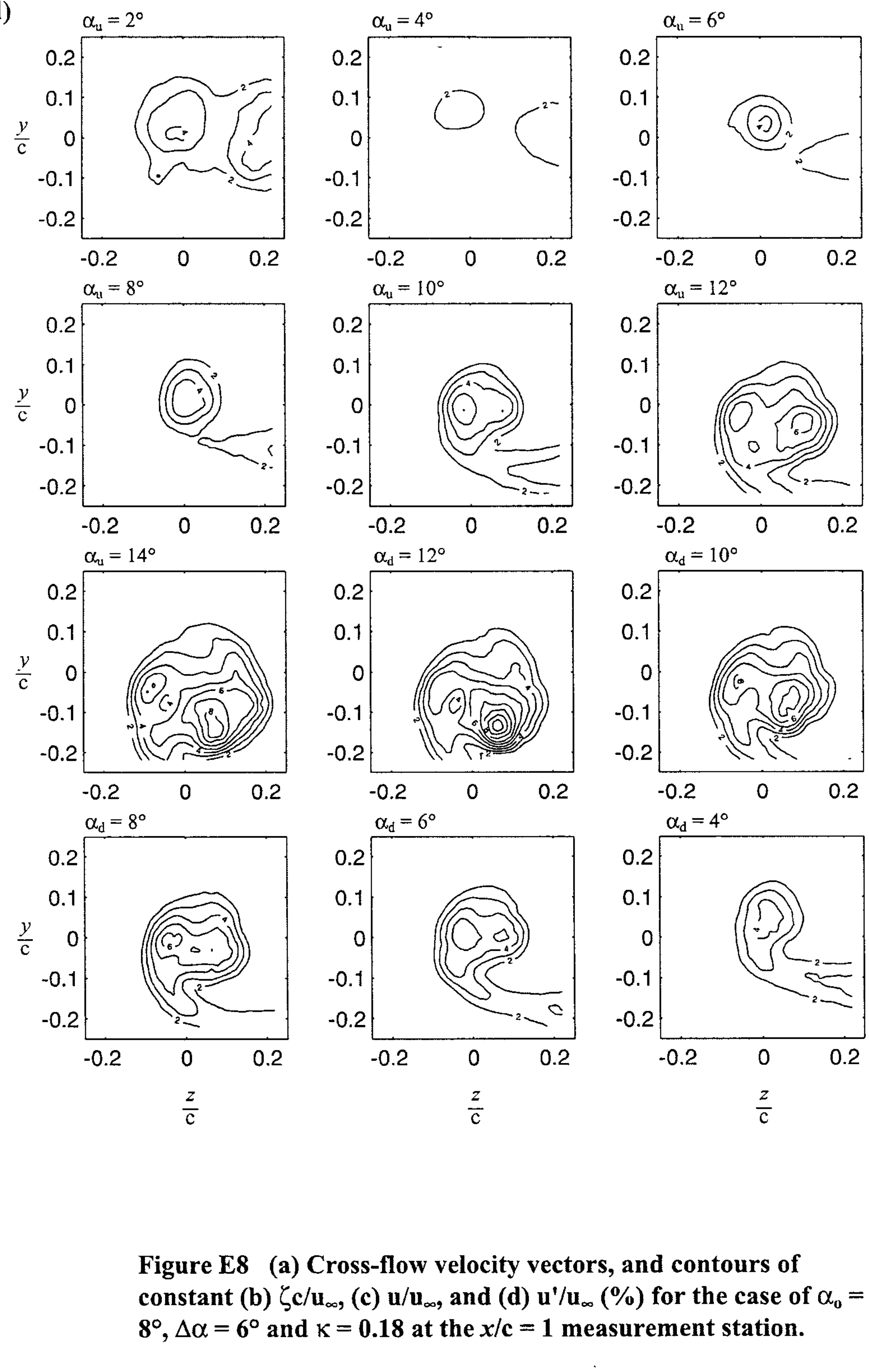

Figure E8 (a) Cross-flow velocity vectors, and contours of constant (b) $\zeta c/u_\infty$, (c) u/u_∞, and (d) u'/u_∞ (%) for the case of α_o = 8°, $\Delta\alpha$ = 6° and κ = 0.18 at the x/c = 1 measurement station.

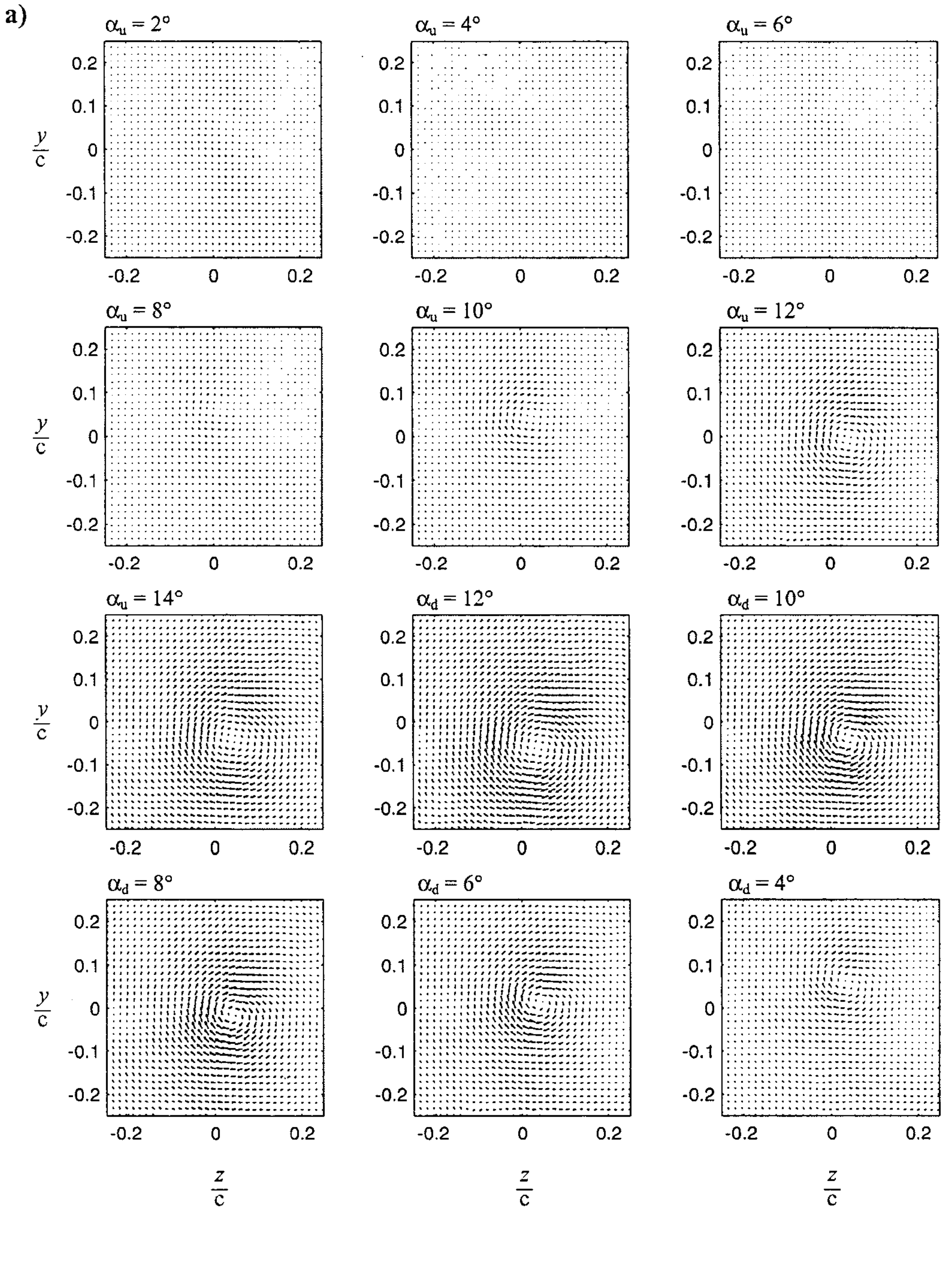

Figure E9 (a) Cross-flow velocity vectors, and contours of constant (b) $\zeta c/u_\infty$, (c) u/u_∞, and (d) u'/u_∞ (%) for the case of α_o = 8°, $\Delta\alpha$ = 6° and κ = 0.18 at the x/c = 1.5 measurement station.

b)

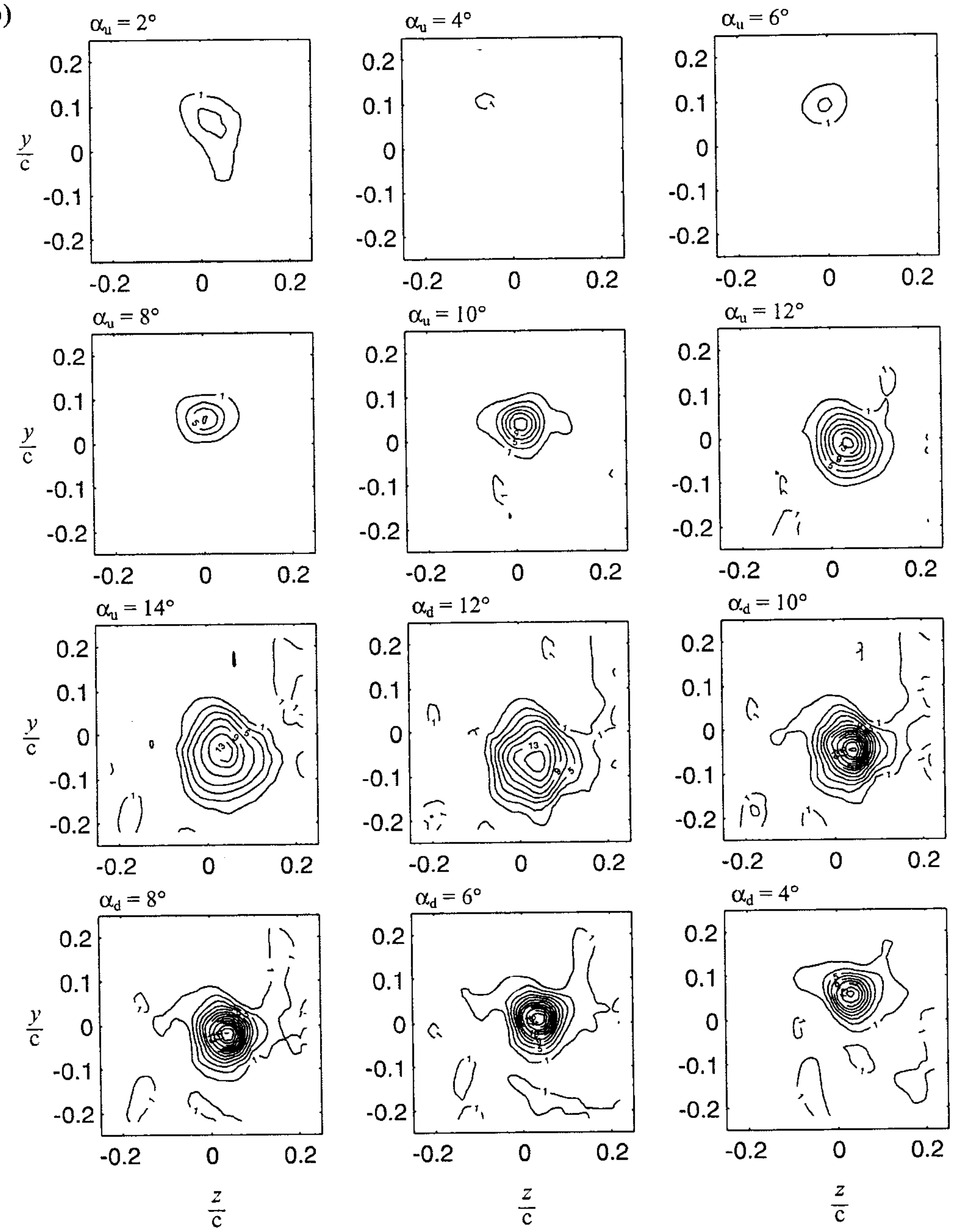

Figure E9 (a) Cross-flow velocity vectors, and contours of constant (b) $\zeta c/u_\infty$, (c) u/u_∞, and (d) u'/u_∞ (%) for the case of α_o = 8°, $\Delta\alpha$ = 6° and κ = 0.18 at the x/c = 1 measurement station.

c)

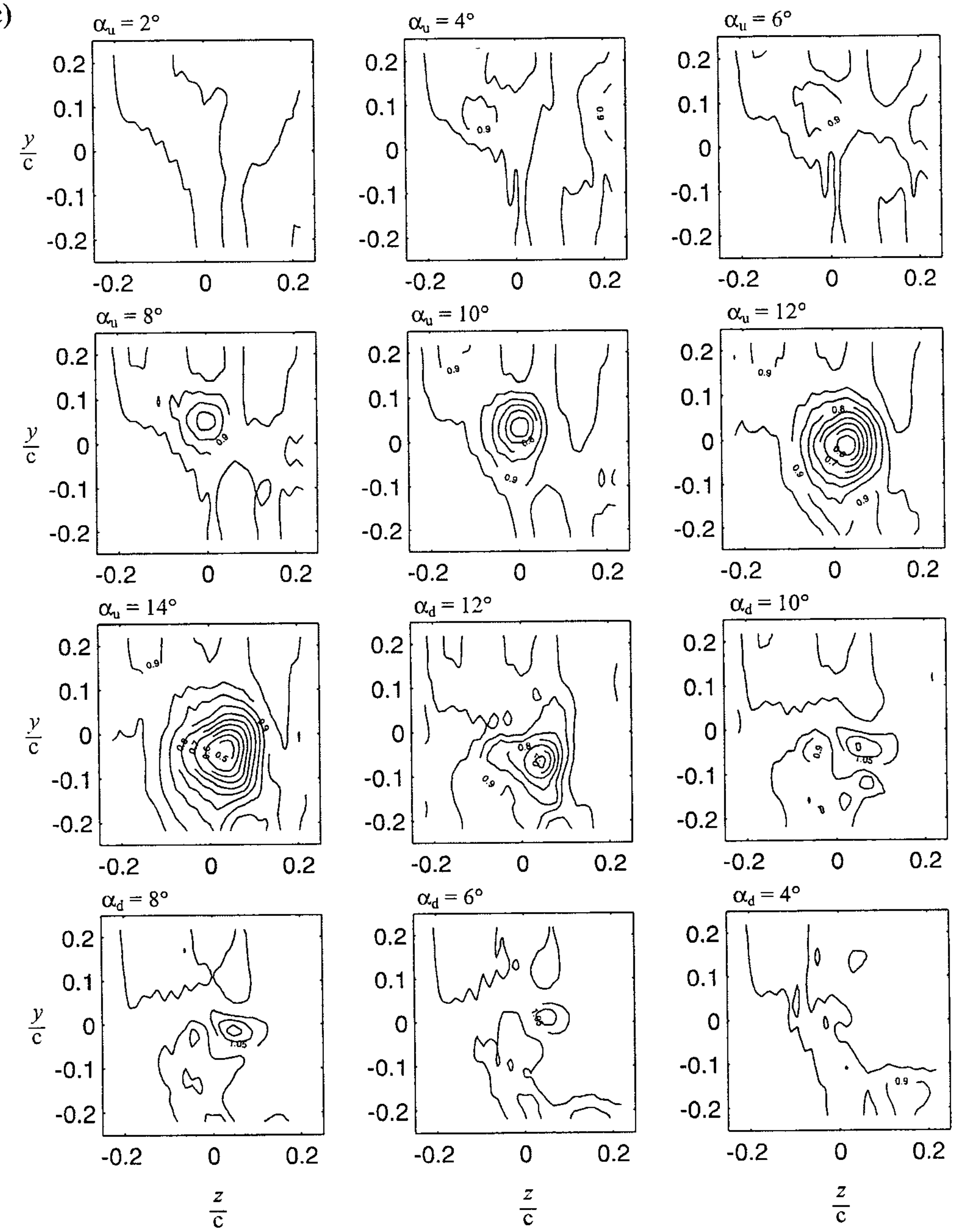

Figure E9 (a) Cross-flow velocity vectors, and contours of constant (b) $\zeta c/u_\infty$, (c) u/u_∞, and (d) u'/u_∞ (%) for the case of $\alpha_0 = 8°$, $\Delta\alpha = 6°$ and $\kappa = 0.18$ at the $x/c = 1$ measurement station.

d)

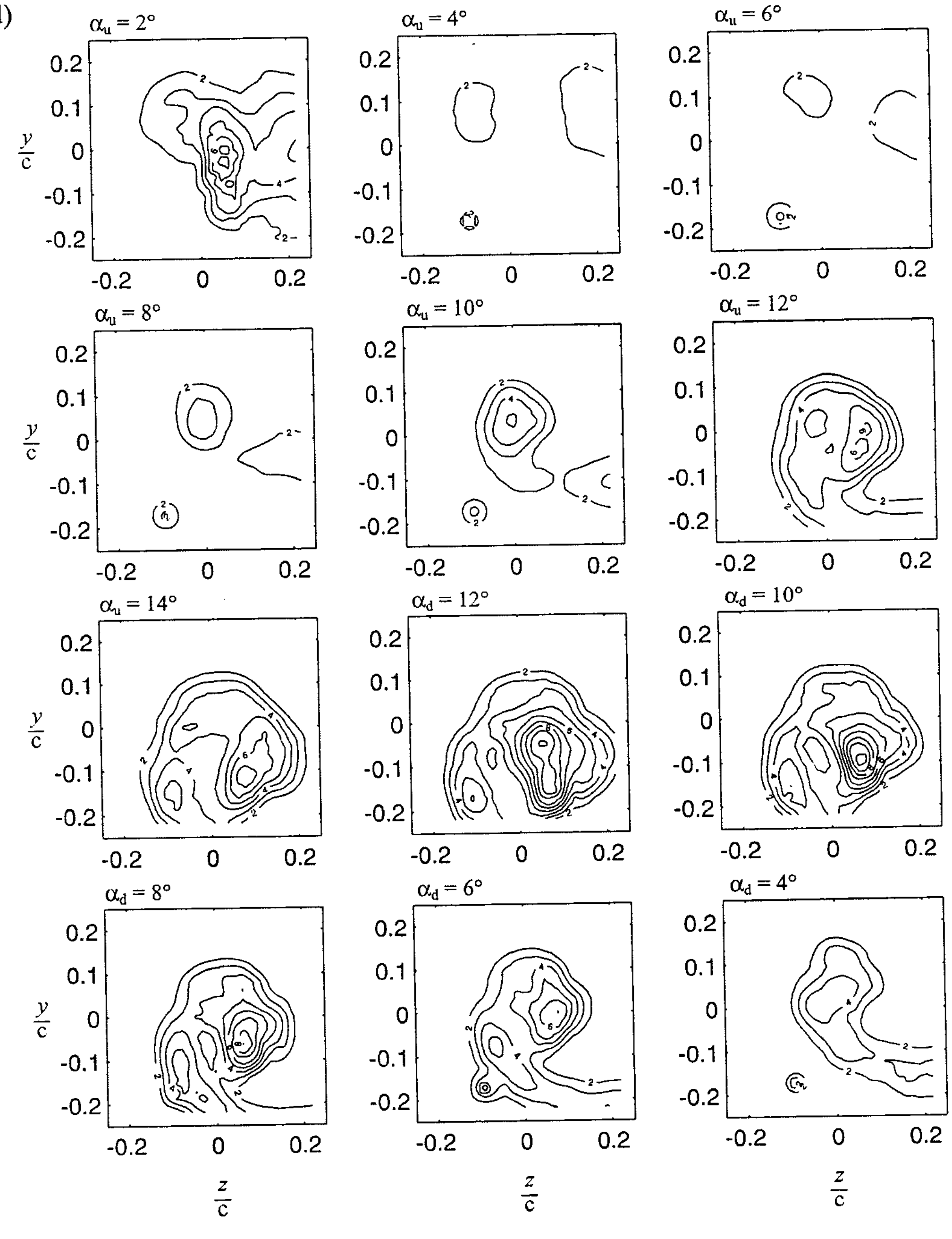

Figure E8 (a) Cross-flow velocity vectors, and contours of constant (b) $\zeta c/u_\infty$, (c) u/u_∞, and (d) u'/u_∞ (%) for the case of $\alpha_0 = 8°$, $\Delta\alpha = 6°$ and $\kappa = 0.18$ at the $x/c = 1$ measurement station.

a)

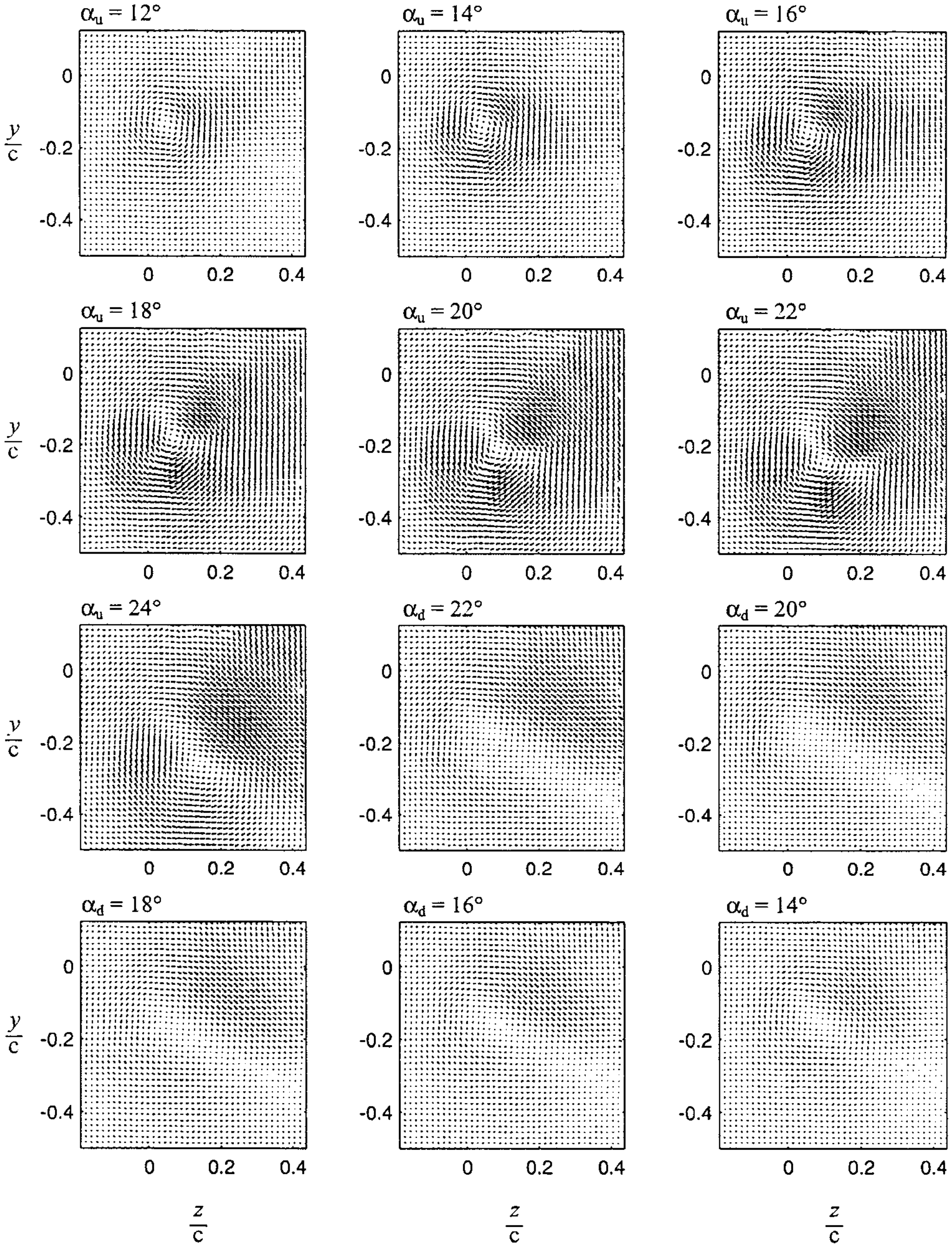

Figure E10 (a) Cross-flow velocity vectors, and contours of constant (b) $\zeta c/u_\infty$, (c) u/u_∞, and (d) u'/u_∞ (%) for the case of α_0 = 18°, $\Delta\alpha$ = 6° and κ = 0.09 at the x/c = 0.5 measurement station.

b)

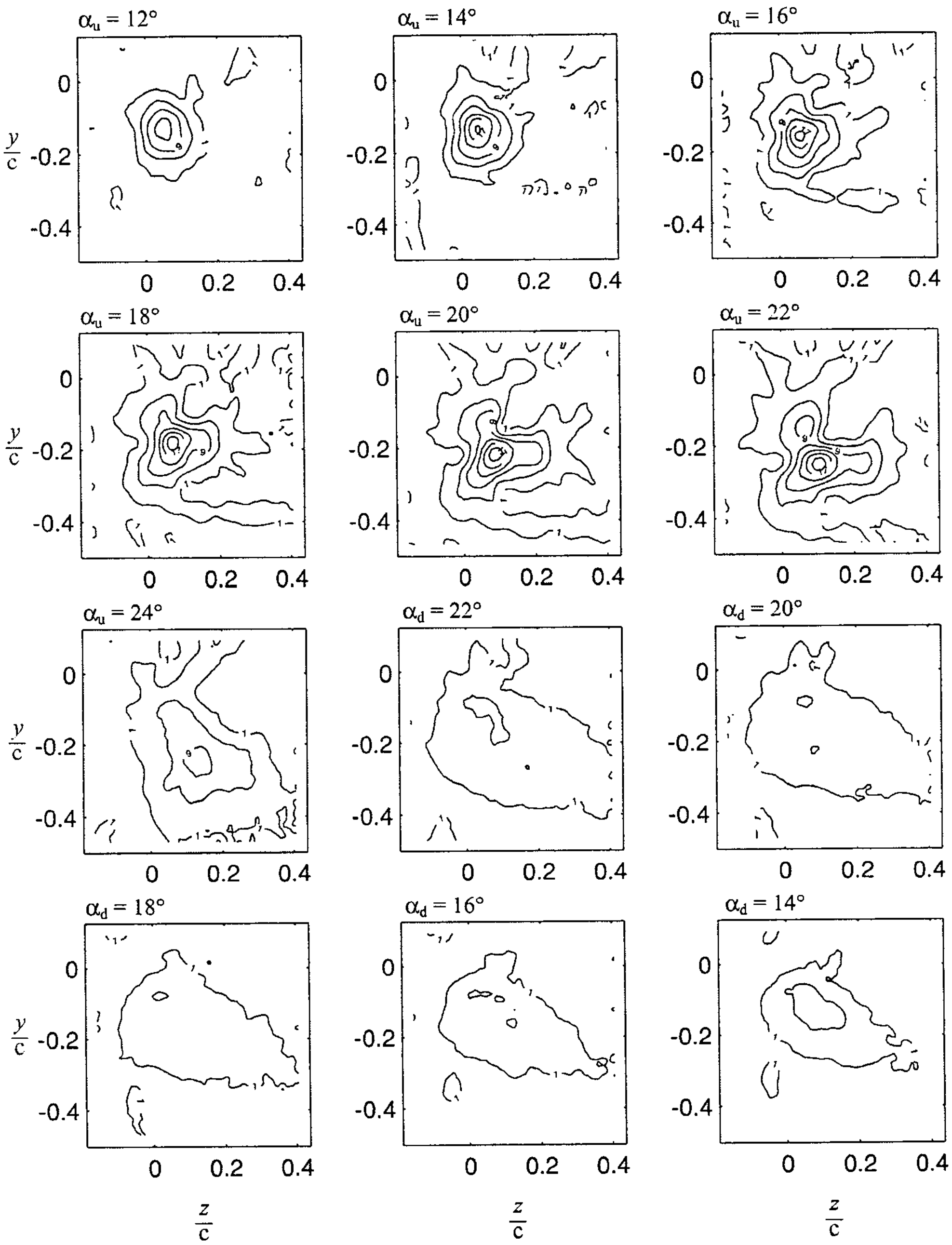

Figure E10 (a) Cross-flow velocity vectors, and contours of constant (b) $\zeta c/u_\infty$, (c) u/u_∞, and (d) u'/u_∞ (%) for the case of α_0 = 18°, $\Delta\alpha$ = 6° and κ = 0.09 at the x/c = 0.5 measurement station.

c)

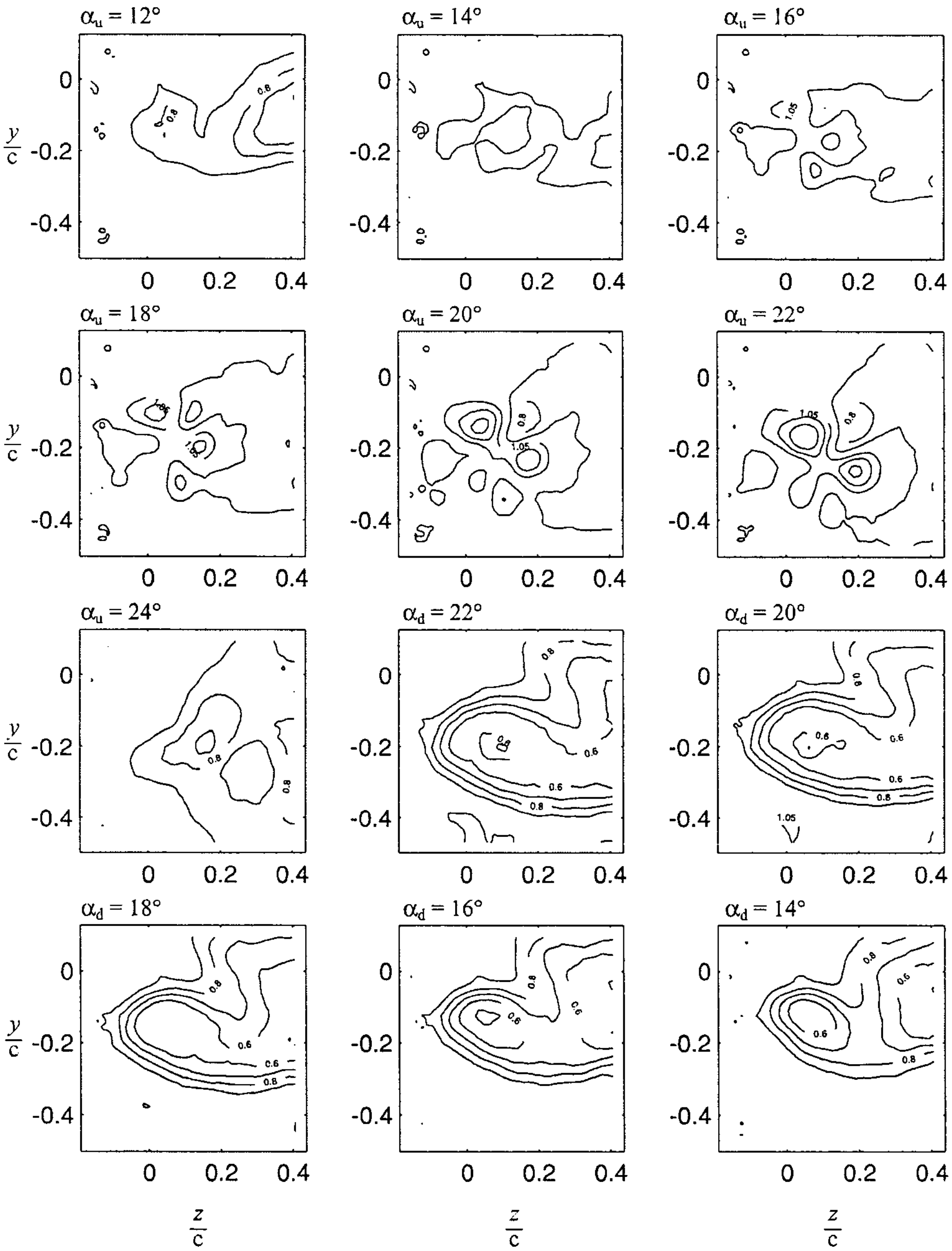

Figure E10 (a) Cross-flow velocity vectors, and contours of constant (b) $\zeta c/u_\infty$, (c) u/u_∞, and (d) u'/u_∞ (%) for the case of $\alpha_0 = 18°$, $\Delta\alpha = 6°$ and $\kappa = 0.09$ at the $x/c = 0.5$ measurement station.

d)

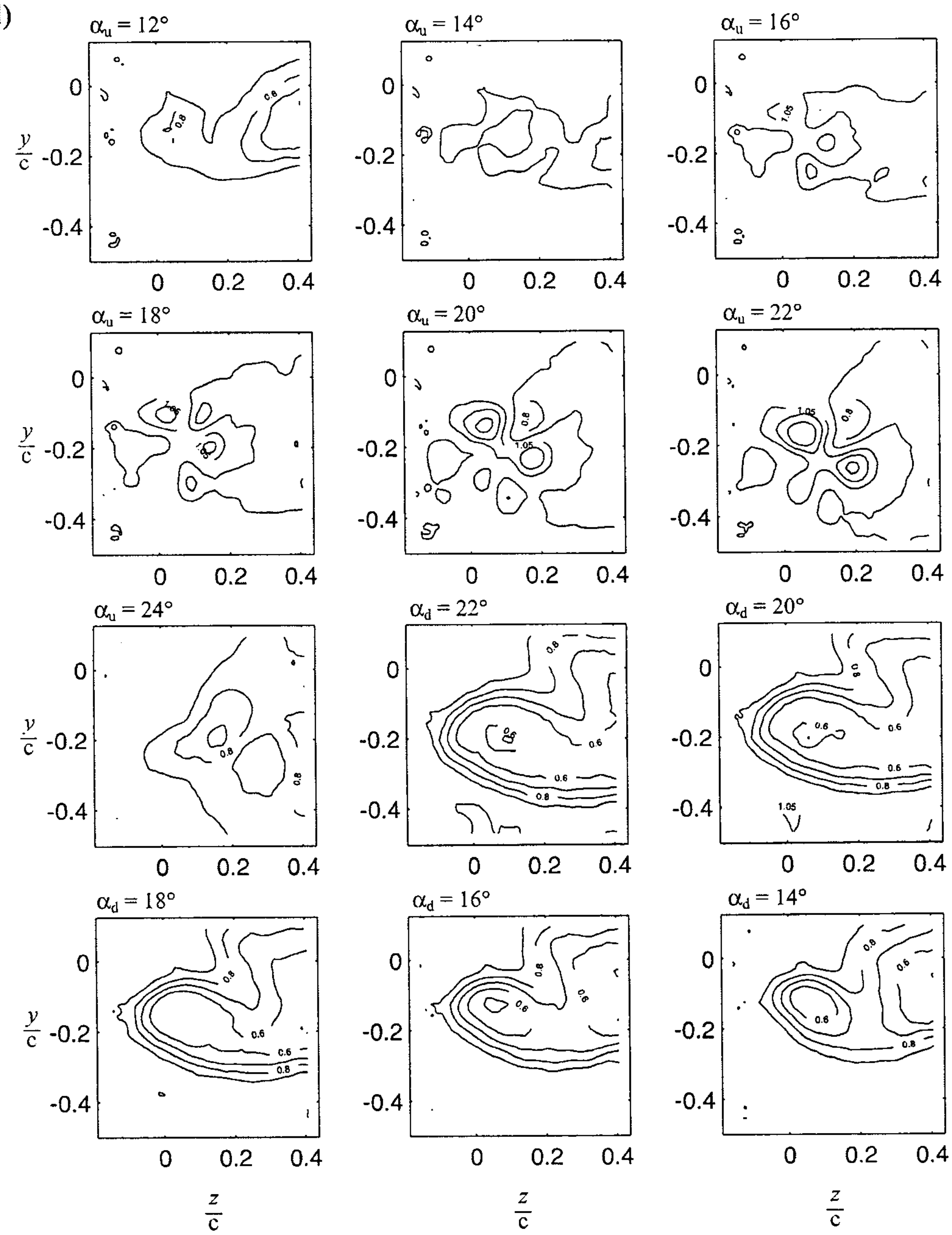

Figure E10 (a) Cross-flow velocity vectors, and contours of constant (b) $\zeta c/u_\infty$, (c) u/u_∞, and (d) u'/u_∞ (%) for the case of α_0 = 18°, $\Delta\alpha$ = 6° and κ = 0.09 at the x/c = 0.5 measurement station.

a)

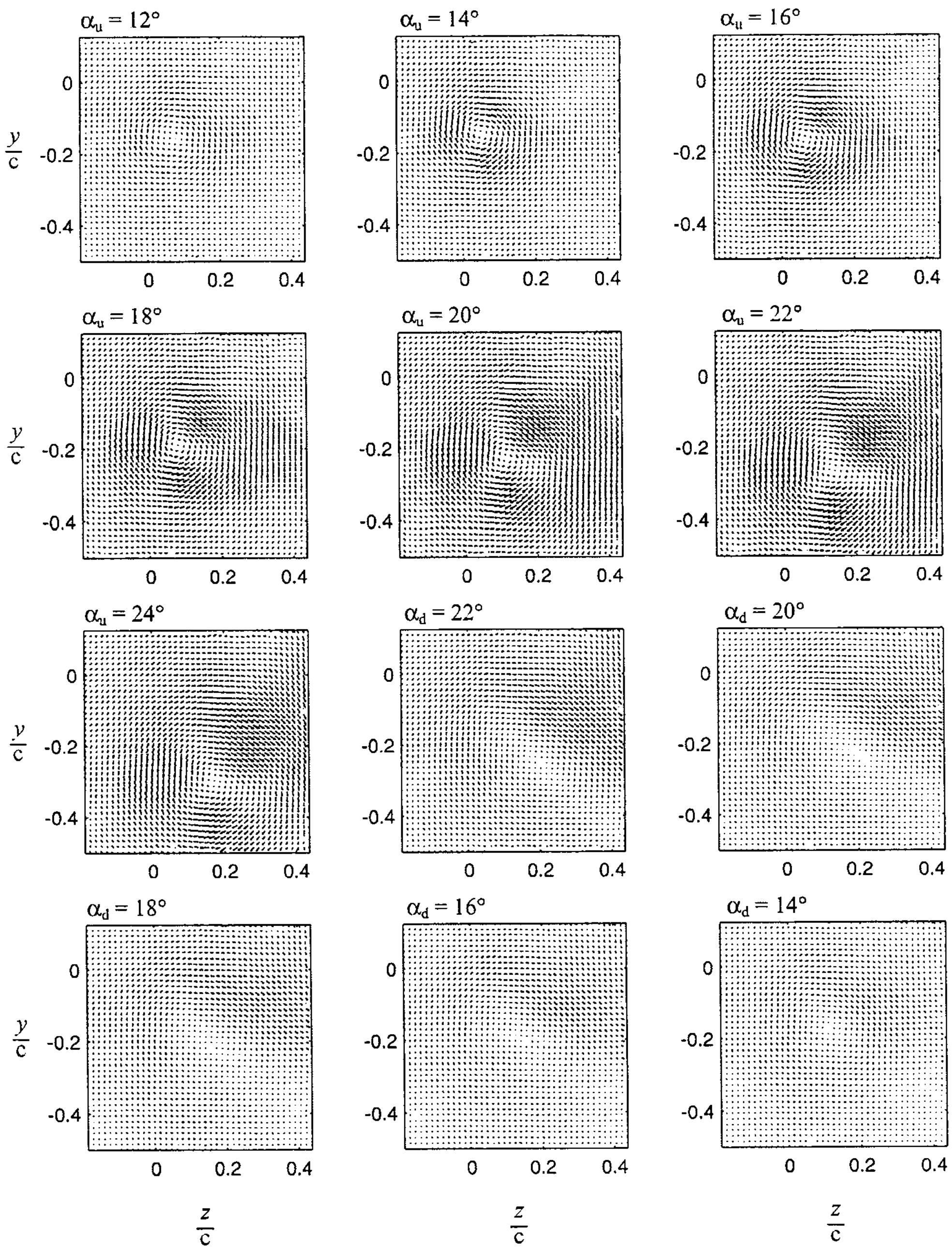

Figure E11 (a) Cross-flow velocity vectors, and contours of constant (b) $\zeta c/u_\infty$, (c) u/u_∞, and (d) u'/u_∞ (%) for the case of α_o = 18°, $\Delta\alpha$ = 6° and κ = 0.09 at the x/c = 1 measurement station.

b)

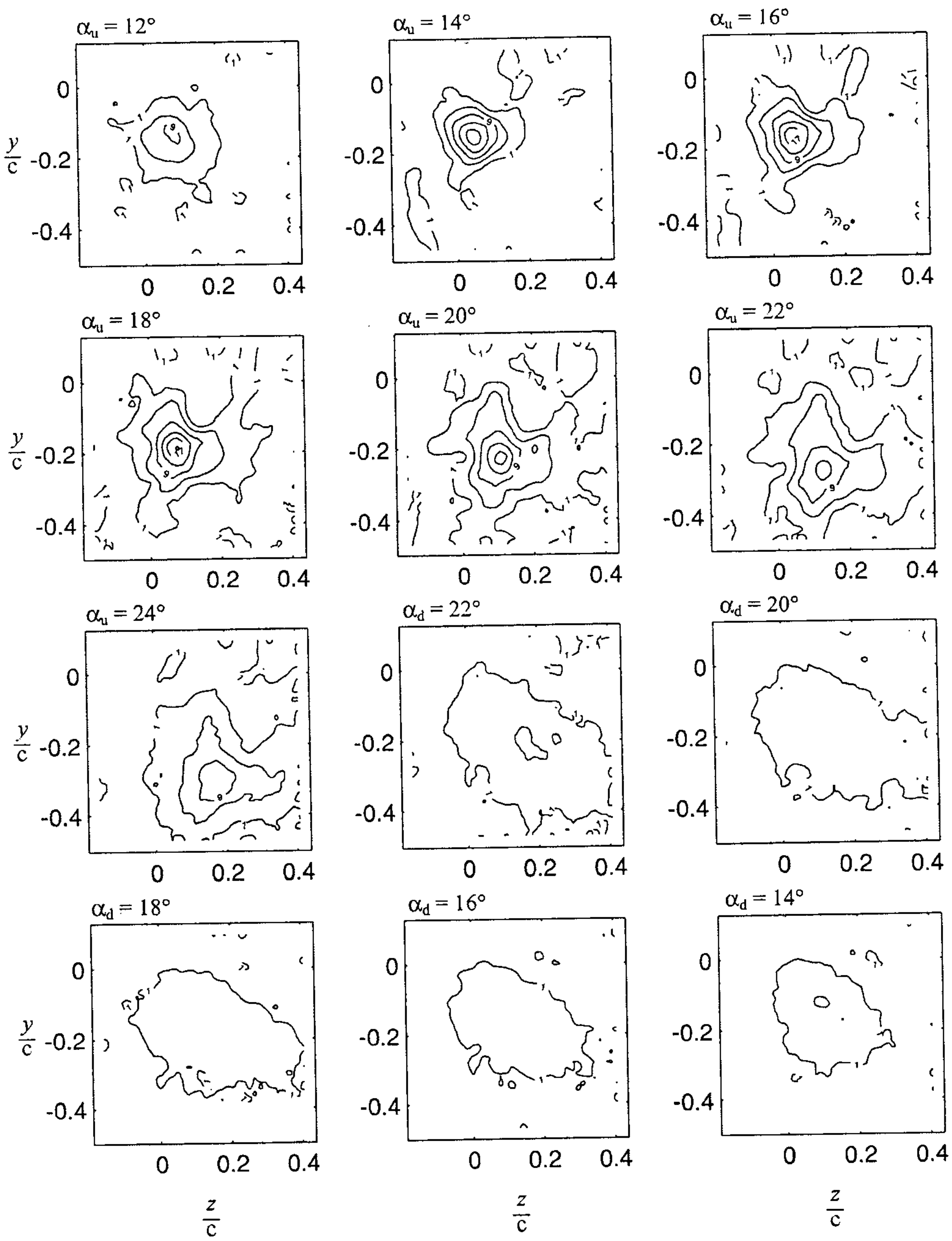

Figure E11 (a) Cross-flow velocity vectors, and contours of constant (b) $\zeta c/u_\infty$, (c) u/u_∞, and (d) u'/u_∞ (%) for the case of α_o = 18°, $\Delta\alpha$ = 6° and κ = 0.09 at the x/c = 1 measurement station.

c)

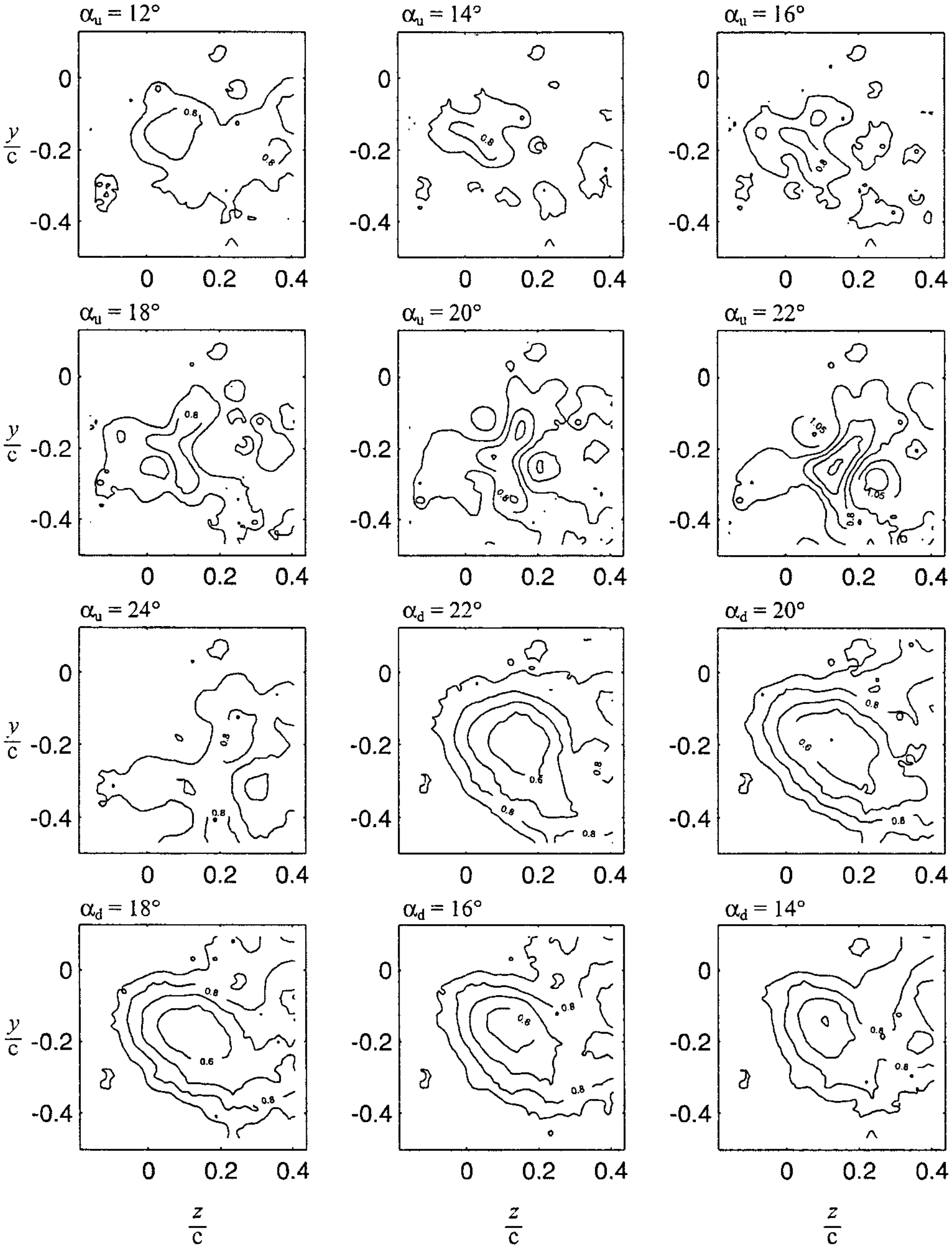

Figure E11 (a) Cross-flow velocity vectors, and contours of constant (b) $\zeta c/u_\infty$, (c) u/u_∞, and (d) u'/u_∞ (%) for the case of α_o = 18°, $\Delta\alpha$ = 6° and κ = 0.09 at the x/c = 1 measurement station.

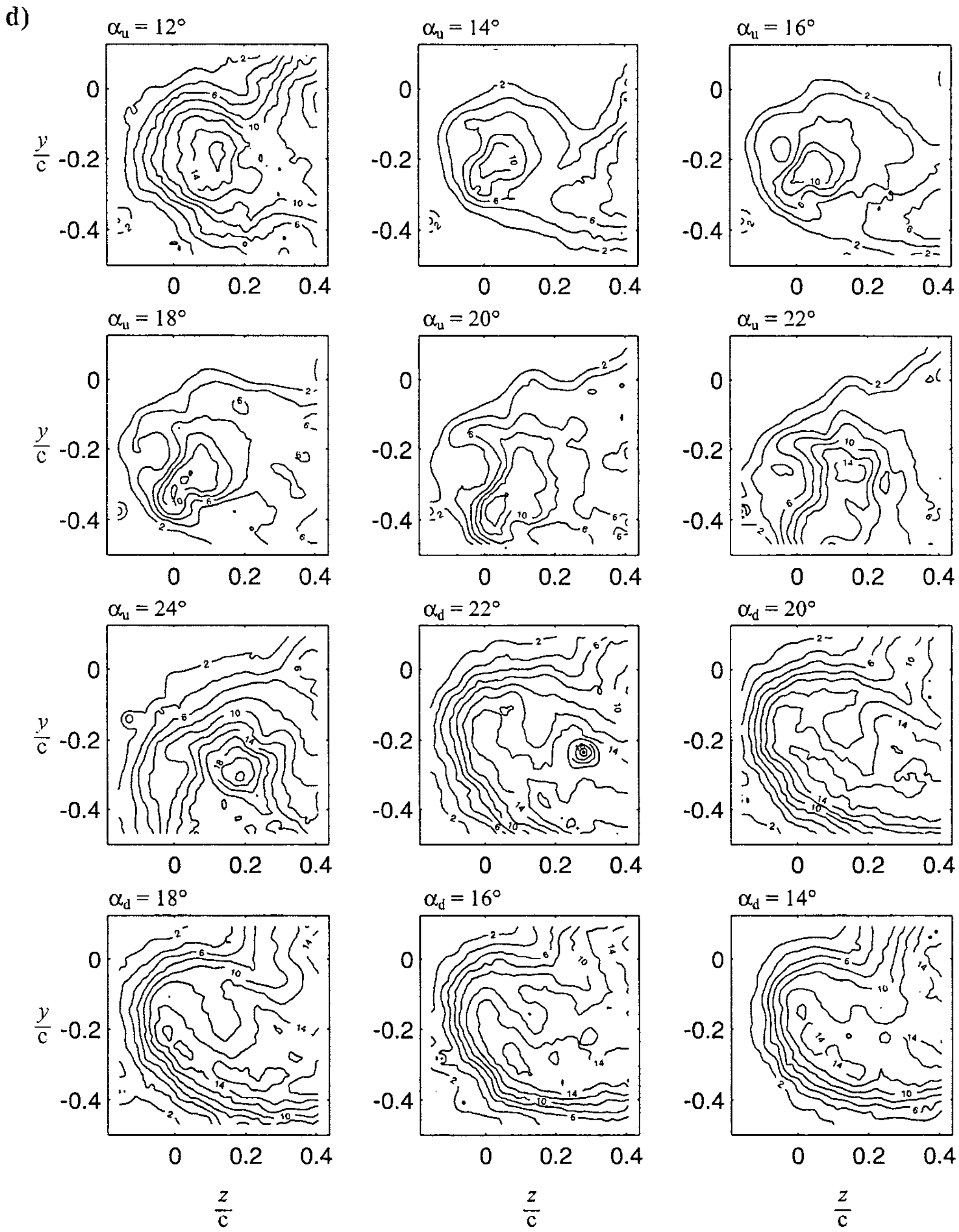

Figure E11 (a) Cross-flow velocity vectors, and contours of constant (b) $\zeta c/u_\infty$, (c) u/u_∞, and (d) u'/u_∞ (%) for the case of $\alpha_0 = 18°$, $\Delta\alpha = 6°$ and $\kappa = 0.09$ at the $x/c = 1$ measurement station.

a)

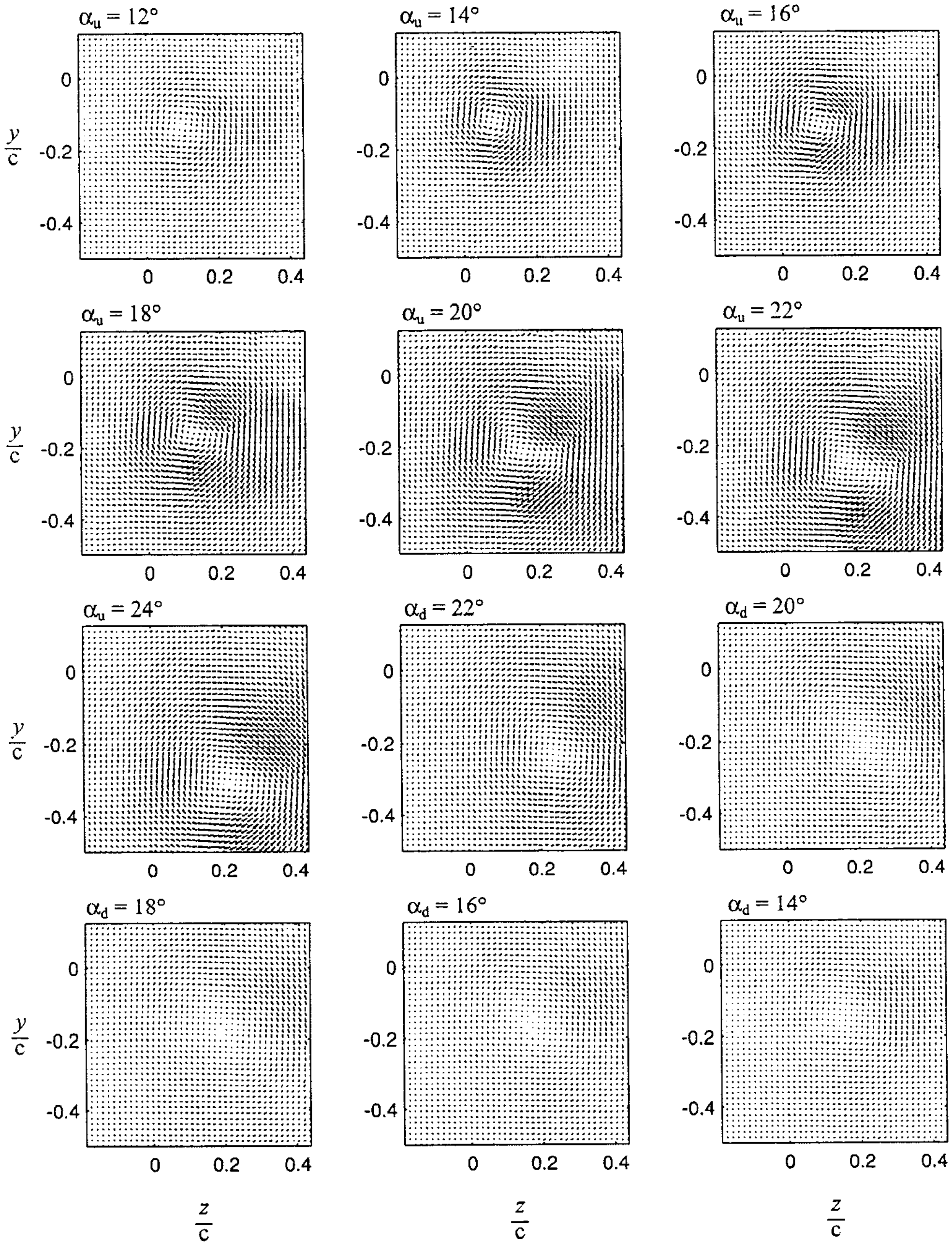

Figure E12 (a) Cross-flow velocity vectors, and contours of constant (b) $\zeta c/u_\infty$, (c) u/u_∞, and (d) u'/u_∞ (%) for the case of α_o = 18°, $\Delta\alpha$ = 6° and κ = 0.09 at the x/c = 1.5 measurement station.

b)

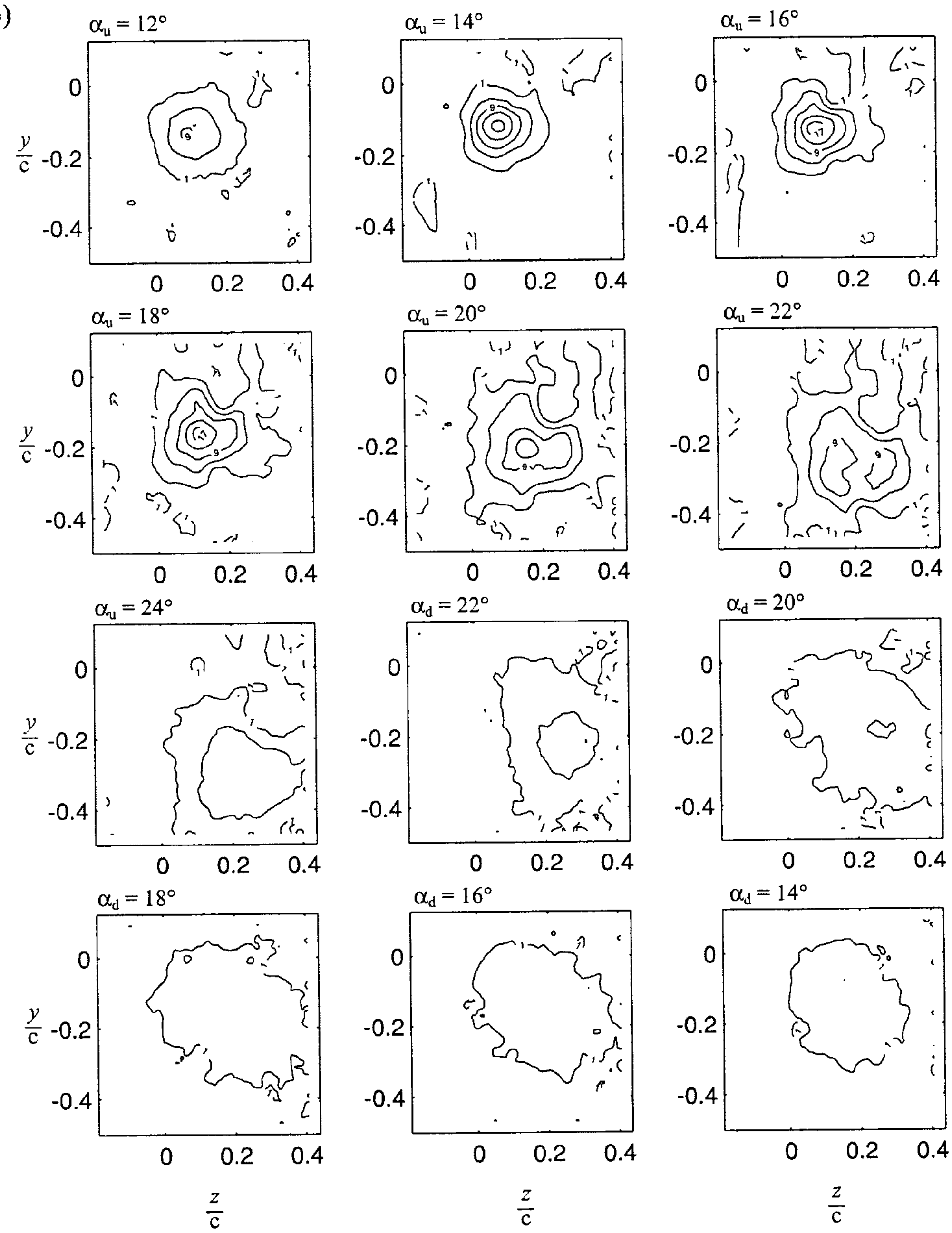

Figure E12 (a) Cross-flow velocity vectors, and contours of constant (b) $\zeta c/u_\infty$, (c) u/u_∞, and (d) u'/u_∞ (%) for the case of $\alpha_0 = 18°$, $\Delta\alpha = 6°$ and $\kappa = 0.09$ at the $x/c = 1.5$ measurement station.

c)

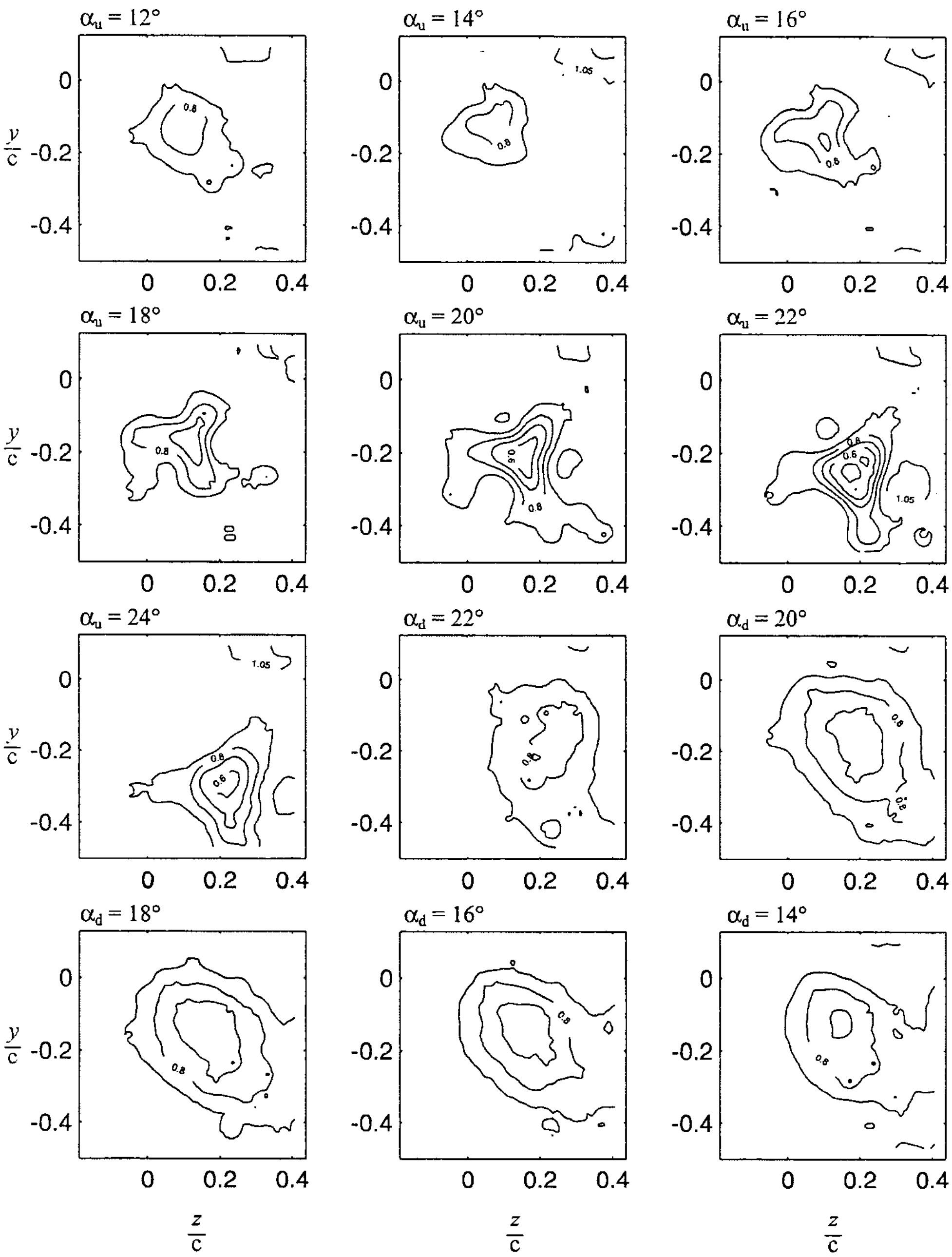

Figure E12 (a) Cross-flow velocity vectors, and contours of constant (b) $\zeta c/u_\infty$, (c) u/u_∞, and (d) u'/u_∞ (%) for the case of α_o = 18°, $\Delta\alpha$ = 6° and κ = 0.09 at the x/c = 1.5 measurement station.

d)

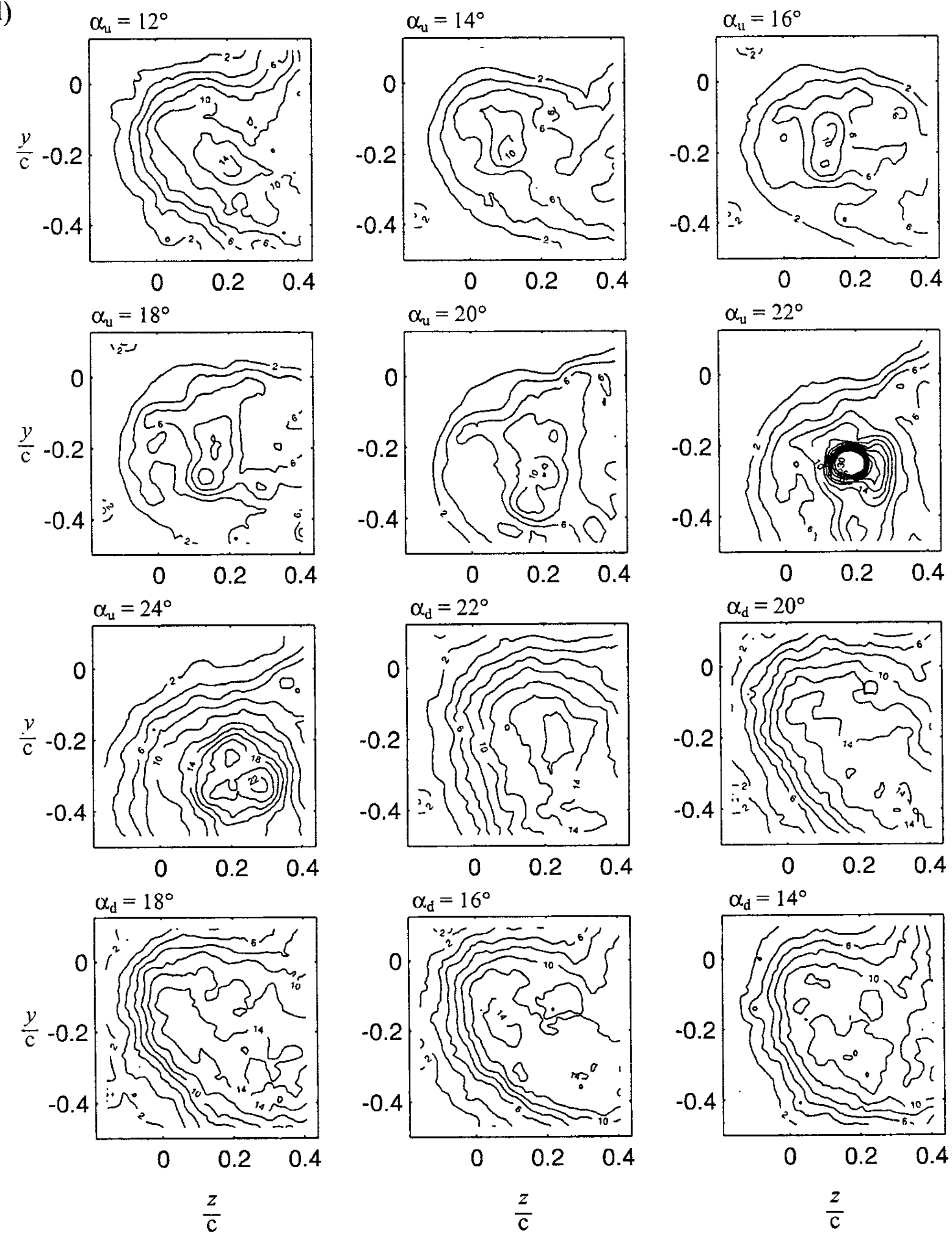

Figure E12 (a) Cross-flow velocity vectors, and contours of constant (b) $\zeta c/u_\infty$, (c) u/u_∞, and (d) u'/u_∞ (%) for the case of $\alpha_o = 18°$, $\Delta\alpha = 6°$ and $\kappa = 0.09$ at the $x/c = 1.5$ measurement station.

a)

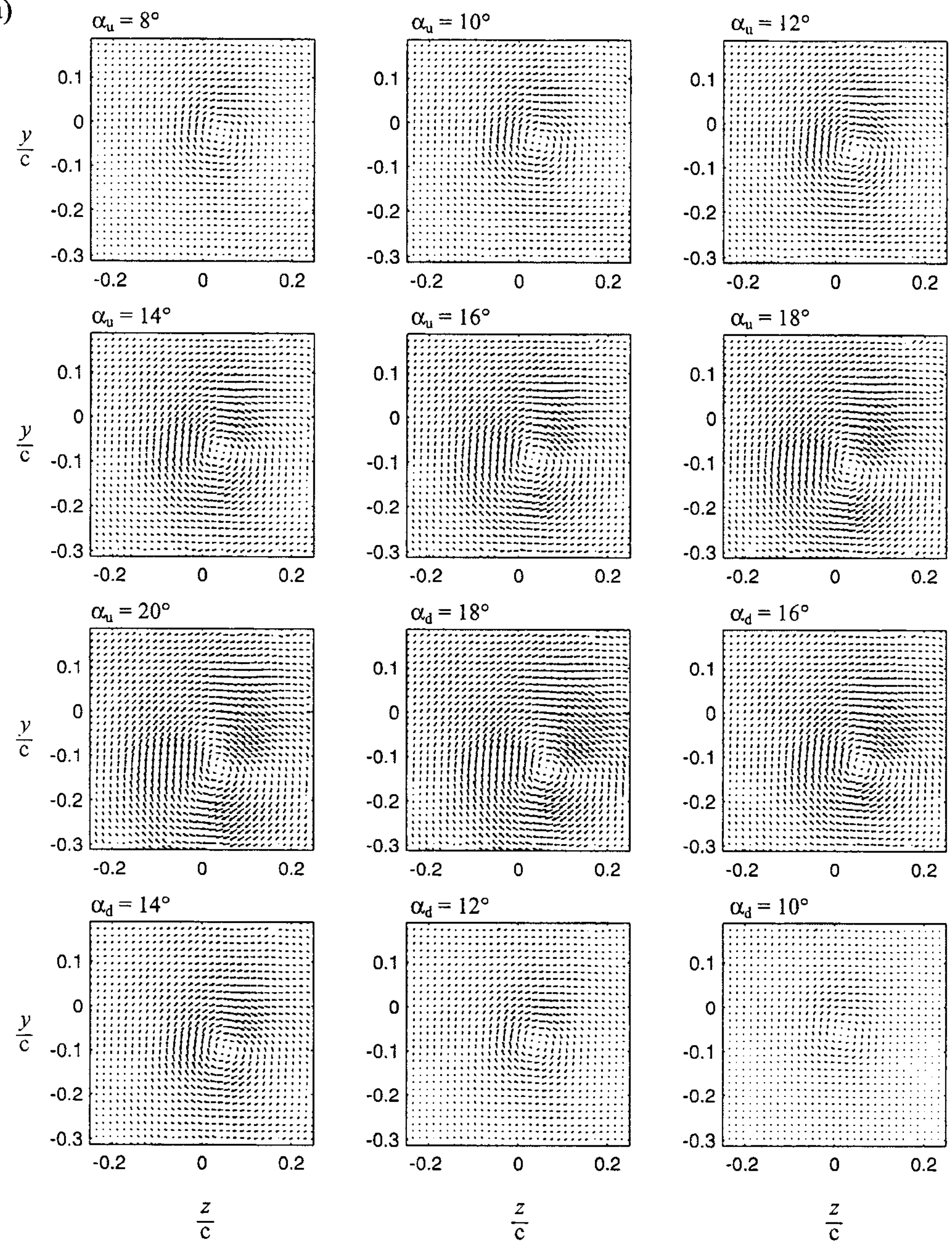

Figure E13 (a) Cross-flow velocity vectors, and contours of constant (b) $\zeta c/u_\infty$, (c) u/u_∞, and (d) u'/u_∞ (%) for the case of α_o = 14°, $\Delta\alpha$ = 6° and κ = 0.09 at the x/c = 0.5 measurement station.

b)

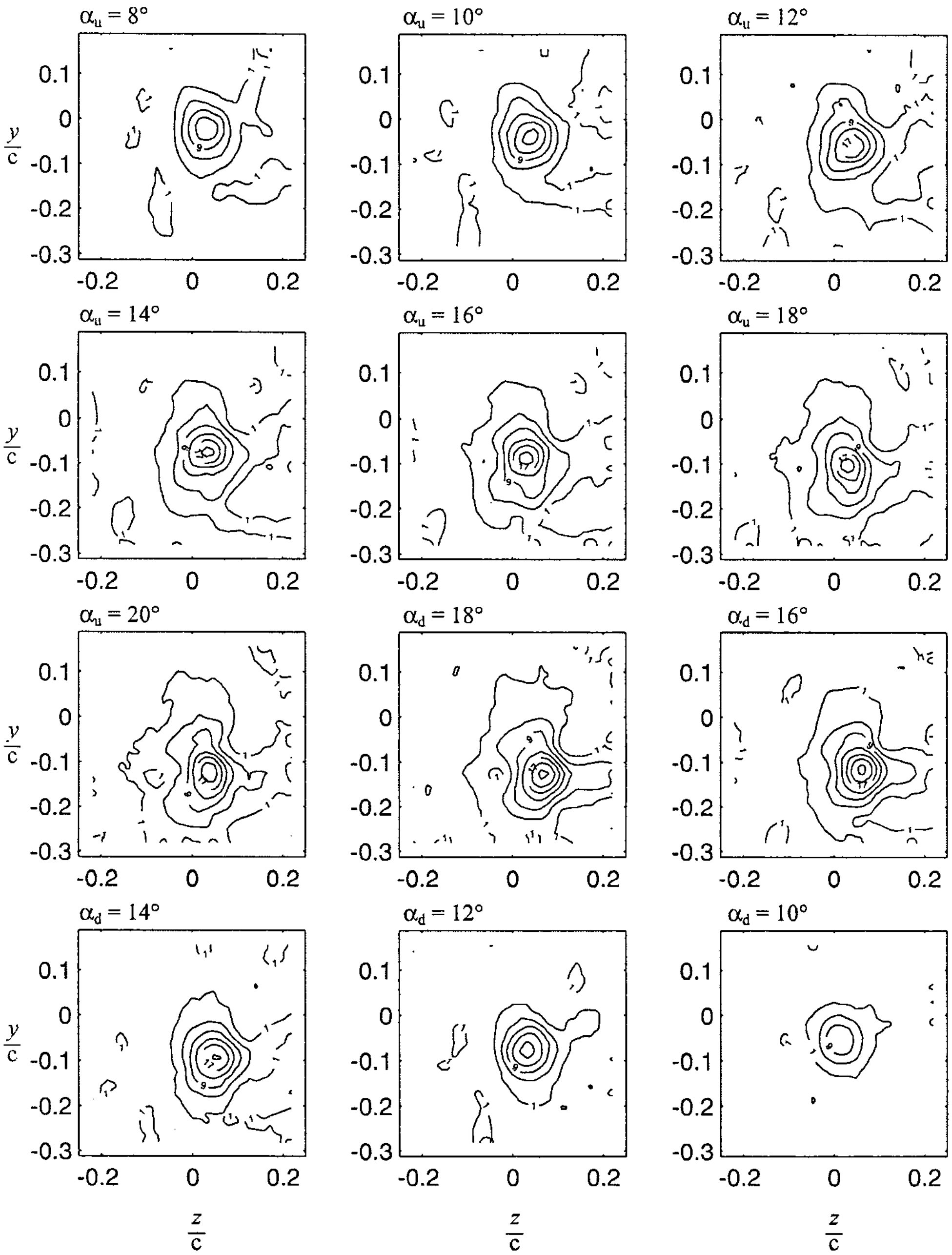

Figure E13 (a) Cross-flow velocity vectors, and contours of constant (b) $\zeta c/u_\infty$, (c) u/u_∞, and (d) u'/u_∞ (%) for the case of α_o = 14°, $\Delta\alpha$ = 6° and κ = 0.09 at the x/c = 0.5 measurement station.

c)

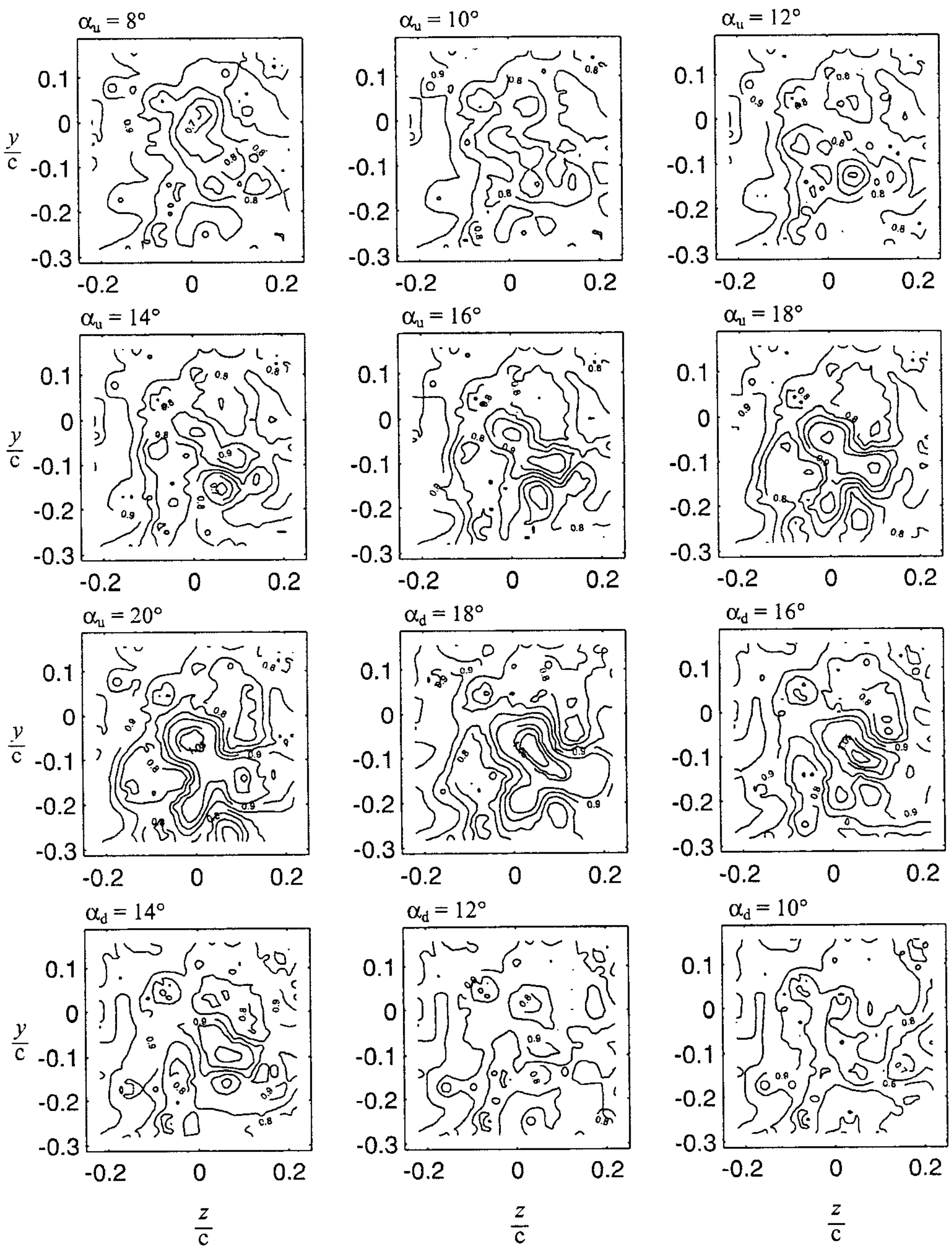

Figure E13 (a) Cross-flow velocity vectors, and contours of constant (b) $\zeta c/u_\infty$, (c) u/u_∞, and (d) u'/u_∞ (%) for the case of α_0 = 14°, $\Delta\alpha$ = 6° and κ = 0.09 at the x/c = 0.5 measurement station.

d)

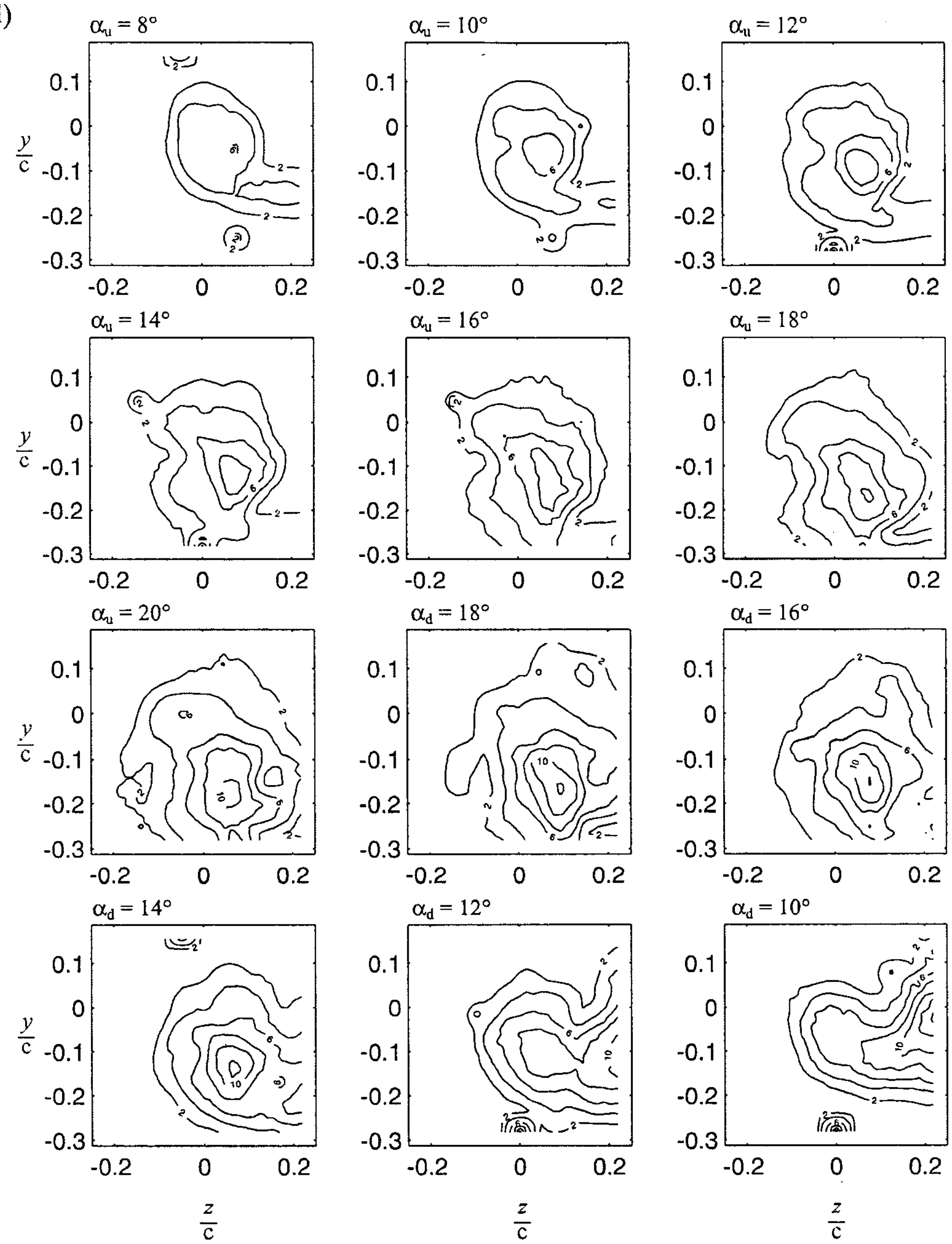

Figure E13 (a) Cross-flow velocity vectors, and contours of constant (b) $\zeta c/u_\infty$, (c) u/u_∞, and (d) u'/u_∞ (%) for the case of $\alpha_0 = 14°$, $\Delta\alpha = 6°$ and $\kappa = 0.09$ at the $x/c = 0.5$ measurement station.

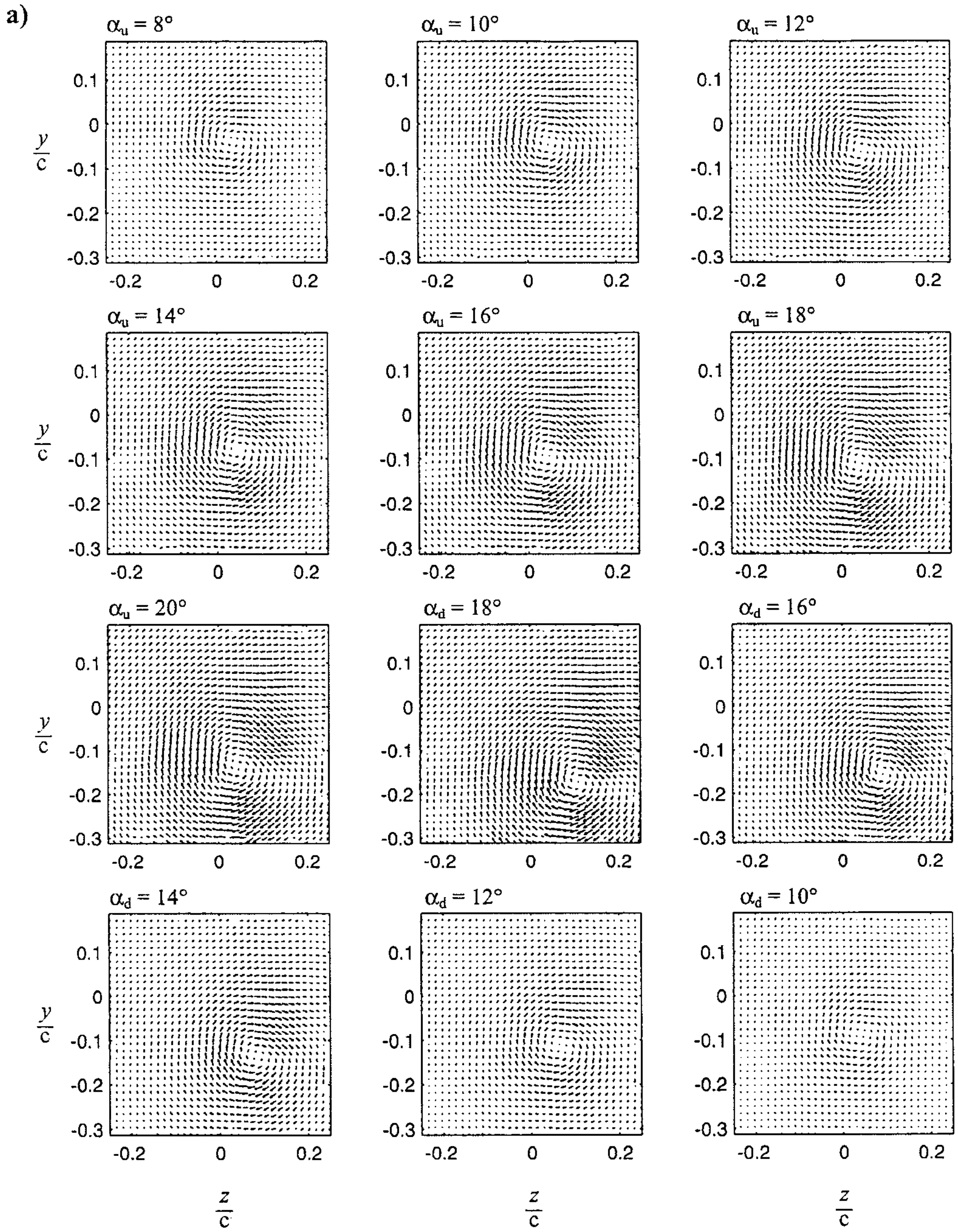

Figure E14 (a) Cross-flow velocity vectors, and contours of constant (b) $\zeta c/u_\infty$, (c) u/u_∞, and (d) u'/u_∞ (%) for the case of α_0 = 14°, $\Delta\alpha$ = 6° and κ = 0.09 at the x/c = 1 measurement station.

b)

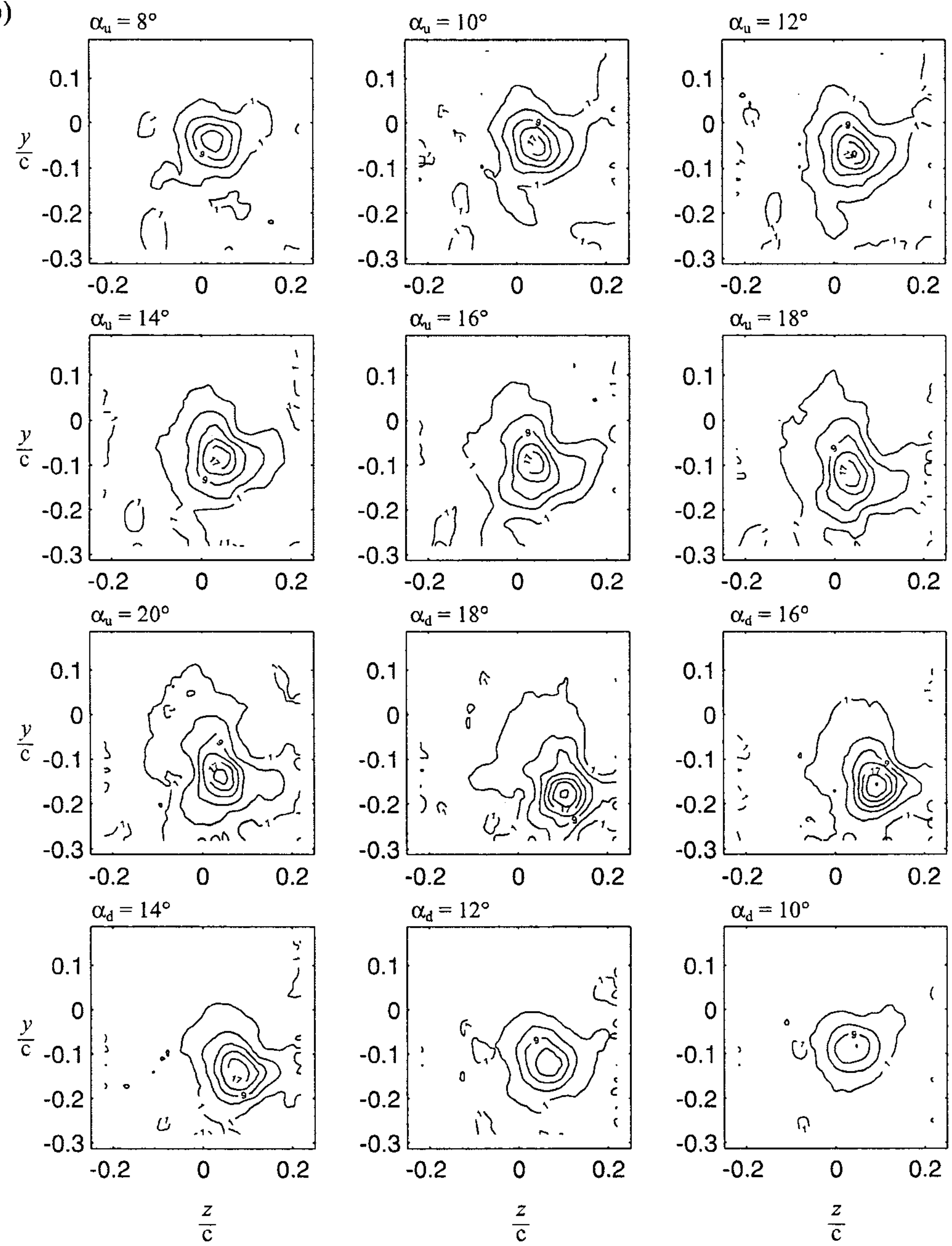

Figure E14 (a) Cross-flow velocity vectors, and contours of constant (b) $\zeta c/u_\infty$, (c) u/u_∞, and (d) u'/u_∞ (%) for the case of $\alpha_0 = 14°$, $\Delta\alpha = 6°$ and $\kappa = 0.09$ at the $x/c = 1$ measurement station.

c)

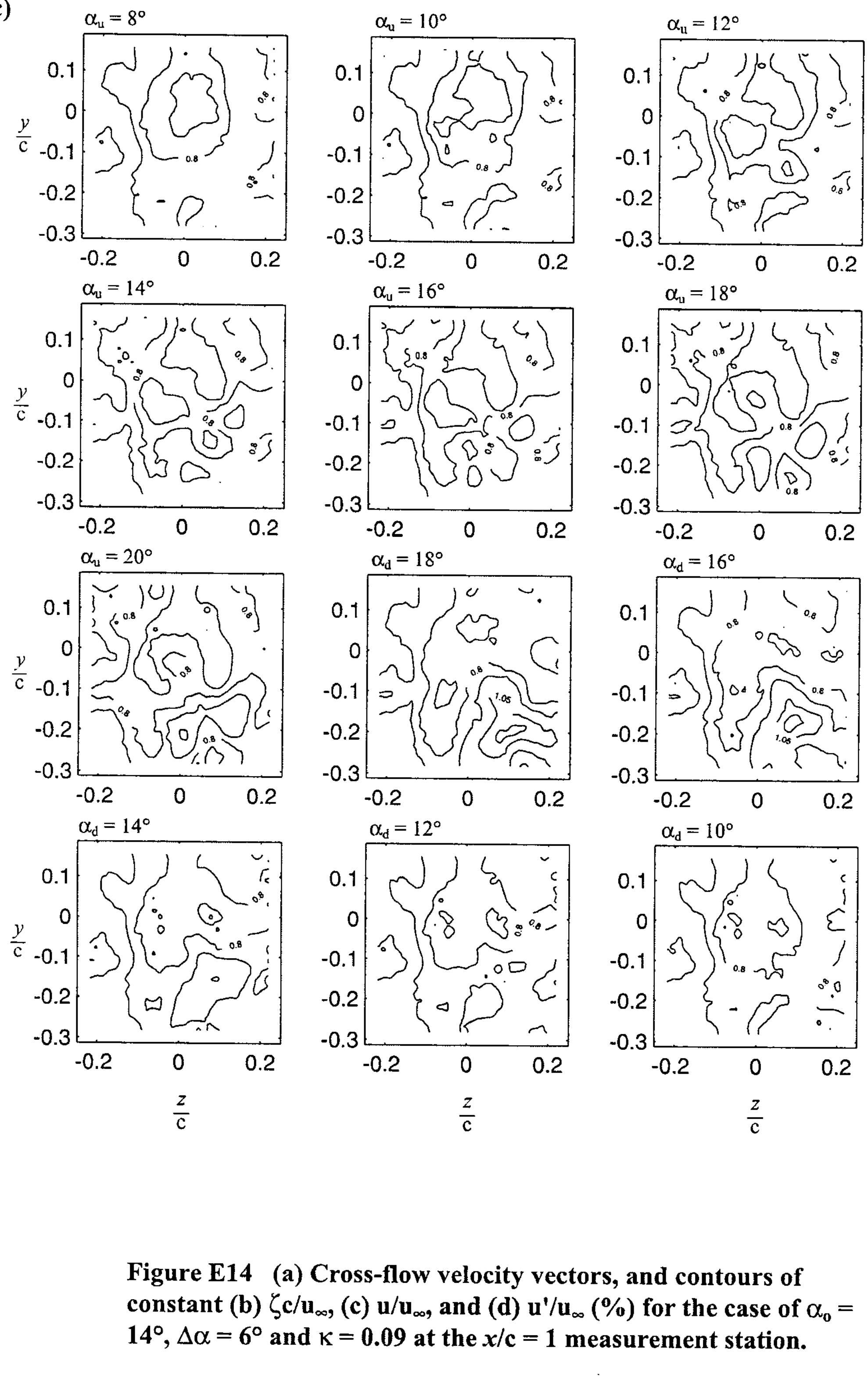

Figure E14 (a) Cross-flow velocity vectors, and contours of constant (b) $\zeta c/u_\infty$, (c) u/u_∞, and (d) u'/u_∞ (%) for the case of α_0 = 14°, $\Delta\alpha$ = 6° and κ = 0.09 at the x/c = 1 measurement station.

d)

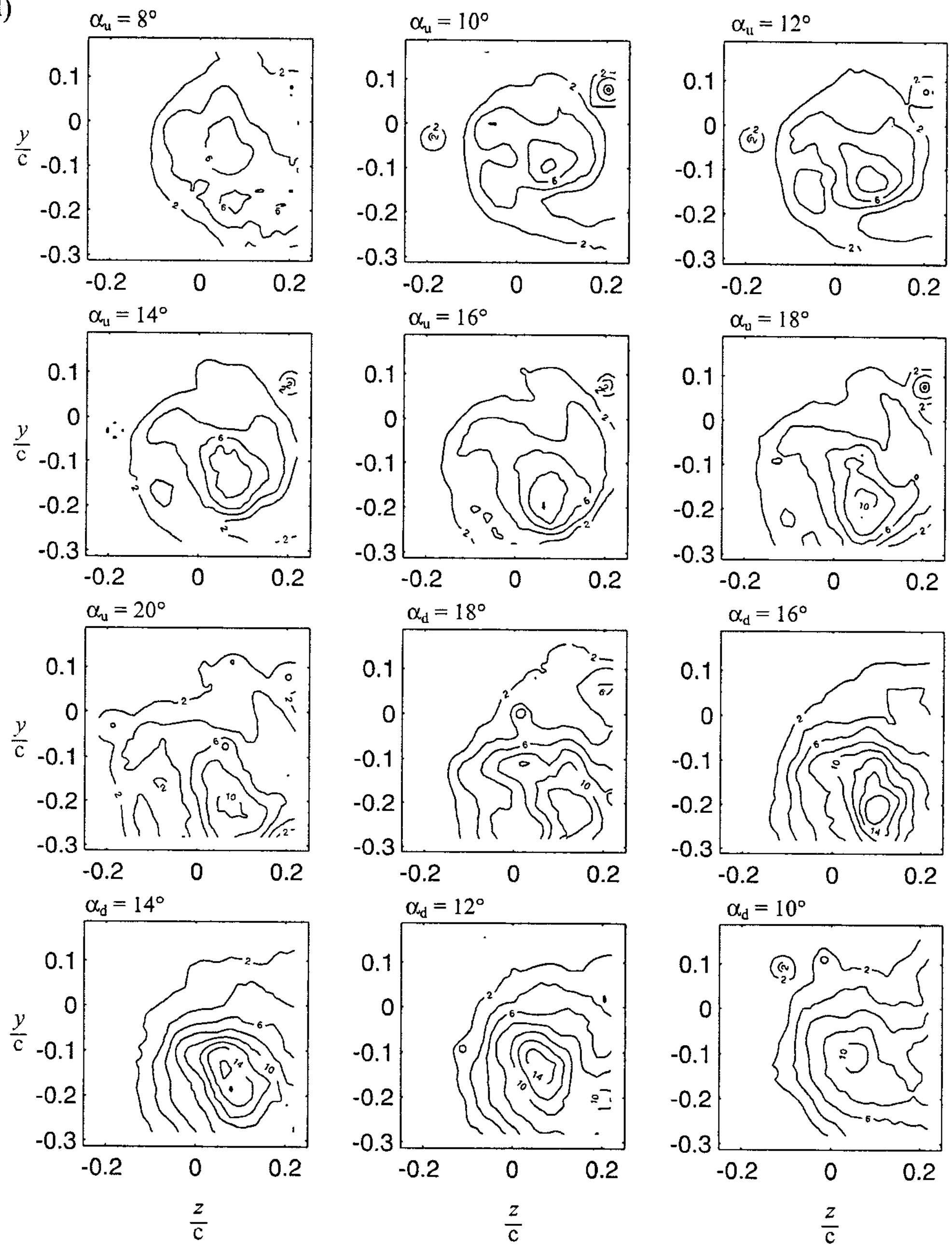

Figure E14 (a) Cross-flow velocity vectors, and contours of constant (b) $\zeta c/u_\infty$, (c) u/u_∞, and (d) u'/u_∞ (%) for the case of α_0 = 14°, $\Delta\alpha$ = 6° and κ = 0.09 at the x/c = 1 measurement station.

a)

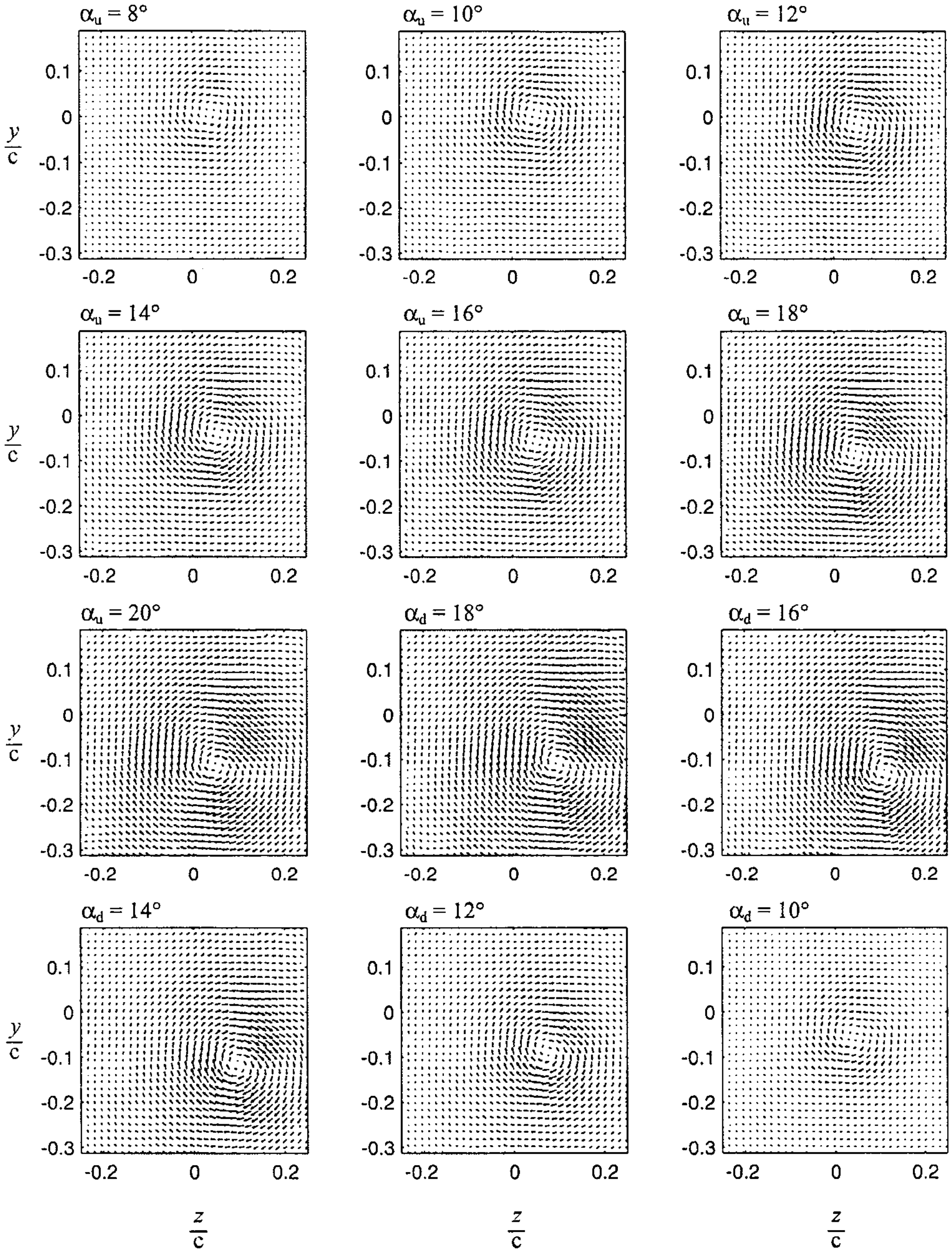

Figure E15 (a) Cross-flow velocity vectors, and contours of constant (b) $\zeta c/u_\infty$, (c) u/u_∞, and (d) u'/u_∞ (%) for the case of α_o = 14°, $\Delta\alpha$ = 6° and κ = 0.09 at the x/c = 1.5 measurement station.

b)

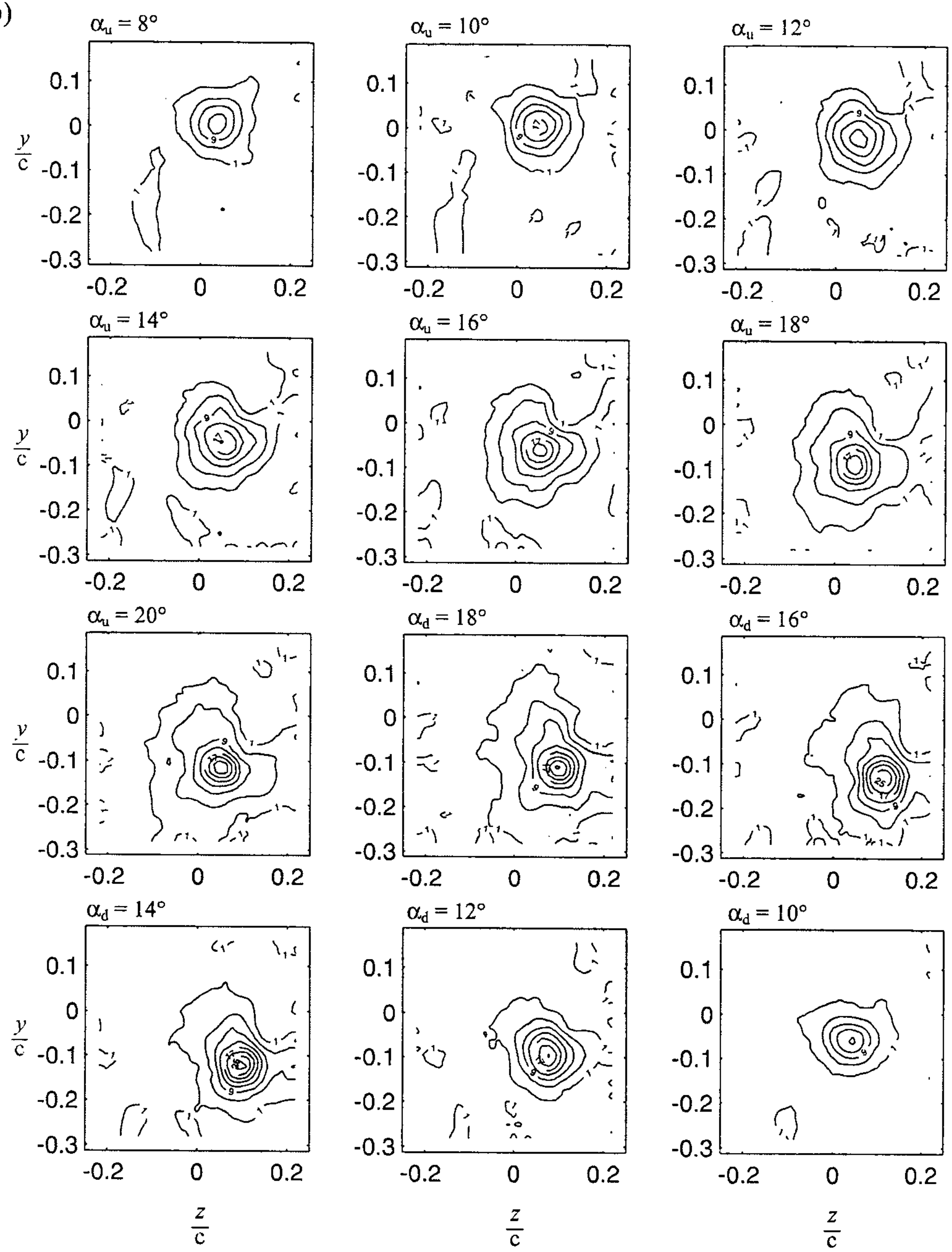

Figure E15 (a) Cross-flow velocity vectors, and contours of constant (b) $\zeta c/u_\infty$, (c) u/u_∞, and (d) u'/u_∞ (%) for the case of α_o = 14°, $\Delta\alpha$ = 6° and κ = 0.09 at the x/c = 1.5 measurement station.

c)

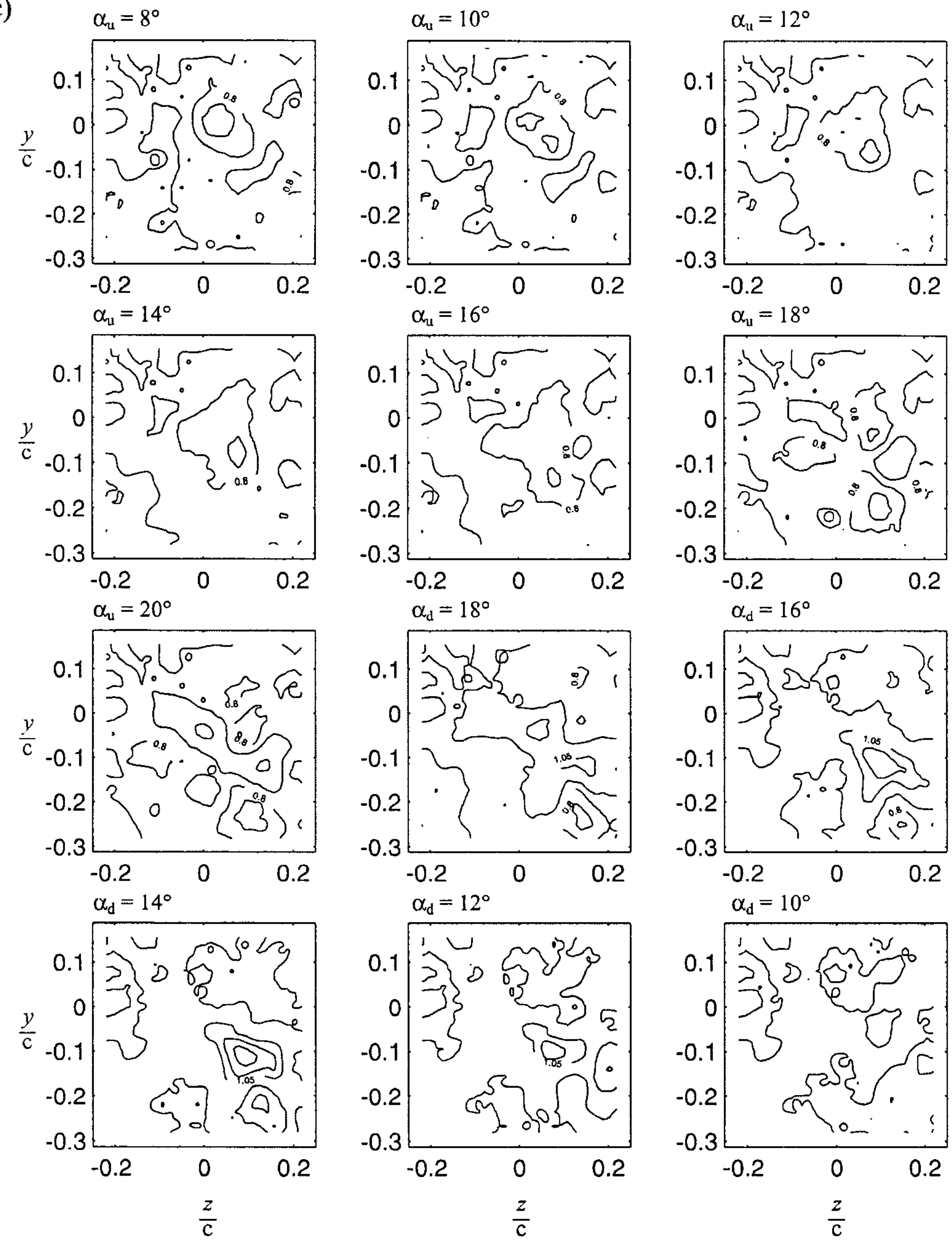

Figure E15 (a) Cross-flow velocity vectors, and contours of constant (b) $\zeta c/u_\infty$, (c) u/u_∞, and (d) u'/u_∞ (%) for the case of $\alpha_0 = 14°$, $\Delta\alpha = 6°$ and $\kappa = 0.09$ at the $x/c = 1.5$ measurement station.

d)

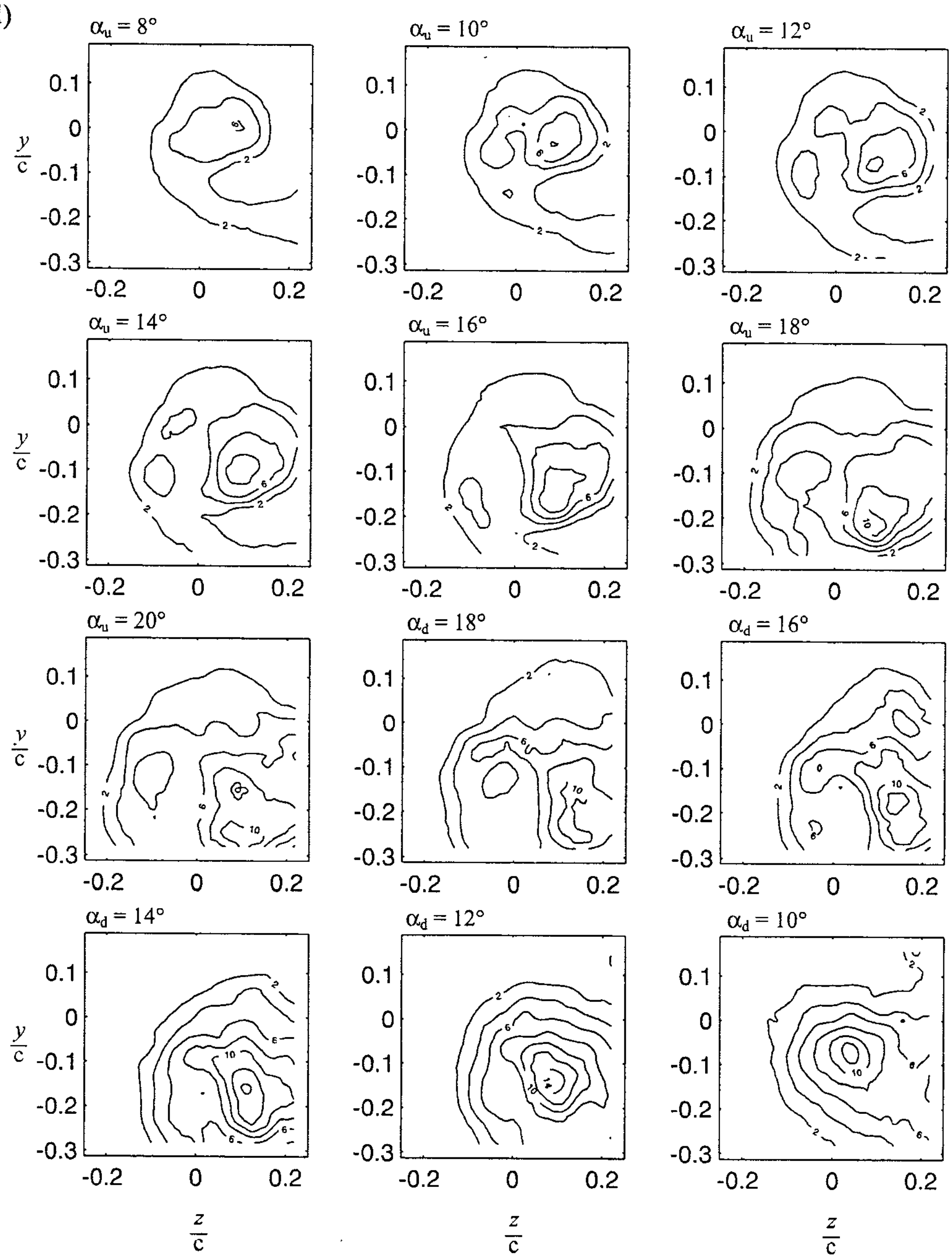

Figure E15 (a) Cross-flow velocity vectors, and contours of constant (b) $\zeta c/u_\infty$, (c) u/u_∞, and (d) u'/u_∞ (%) for the case of α_0 = 14°, $\Delta\alpha$ = 6° and κ = 0.09 at the x/c = 1.5 measurement station.

a)

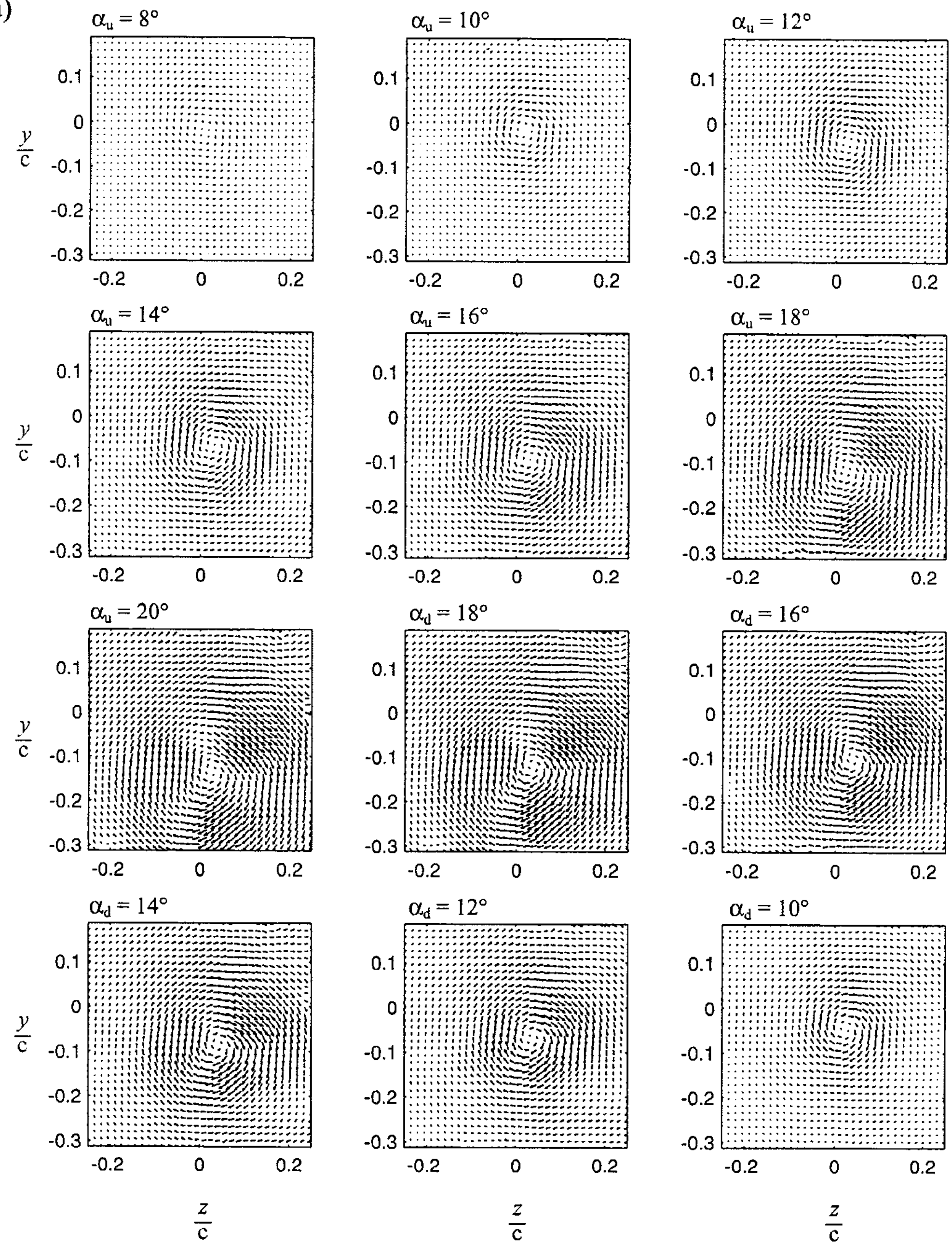

Figure E16 (a) Cross-flow velocity vectors, and contours of constant (b) $\zeta c/u_\infty$, (c) u/u_∞, and (d) u'/u_∞ (%) for the case of α_0 = 14°, $\Delta\alpha$ = 6° and κ = 0.18 at the x/c = 0.5 measurement station.

b)

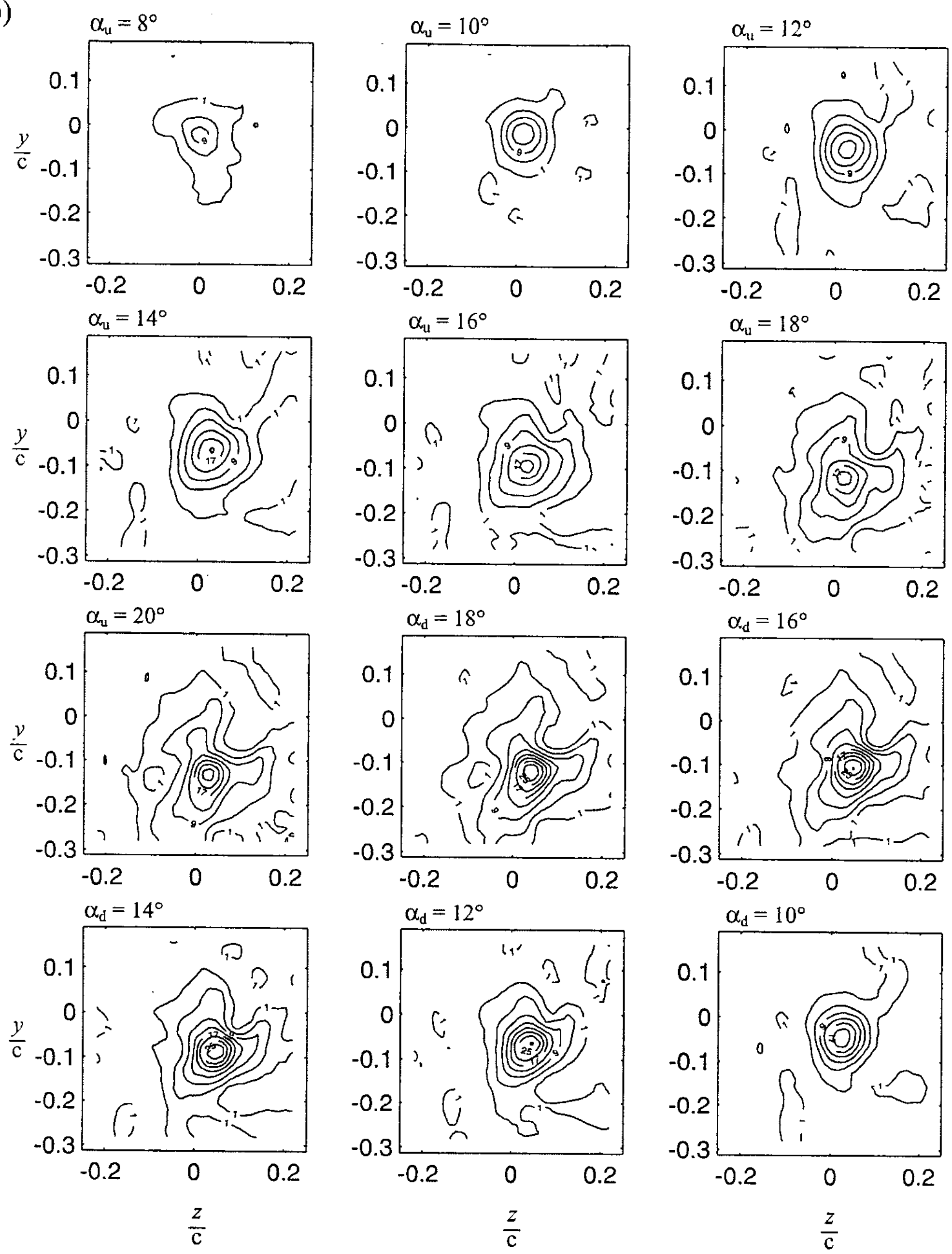

Figure E16 (a) Cross-flow velocity vectors, and contours of constant (b) $\zeta c/u_\infty$, (c) u/u_∞, and (d) u'/u_∞ (%) for the case of α_0 = 14°, $\Delta\alpha$ = 6° and κ = 0.18 at the x/c = 0.5 measurement station.

c)

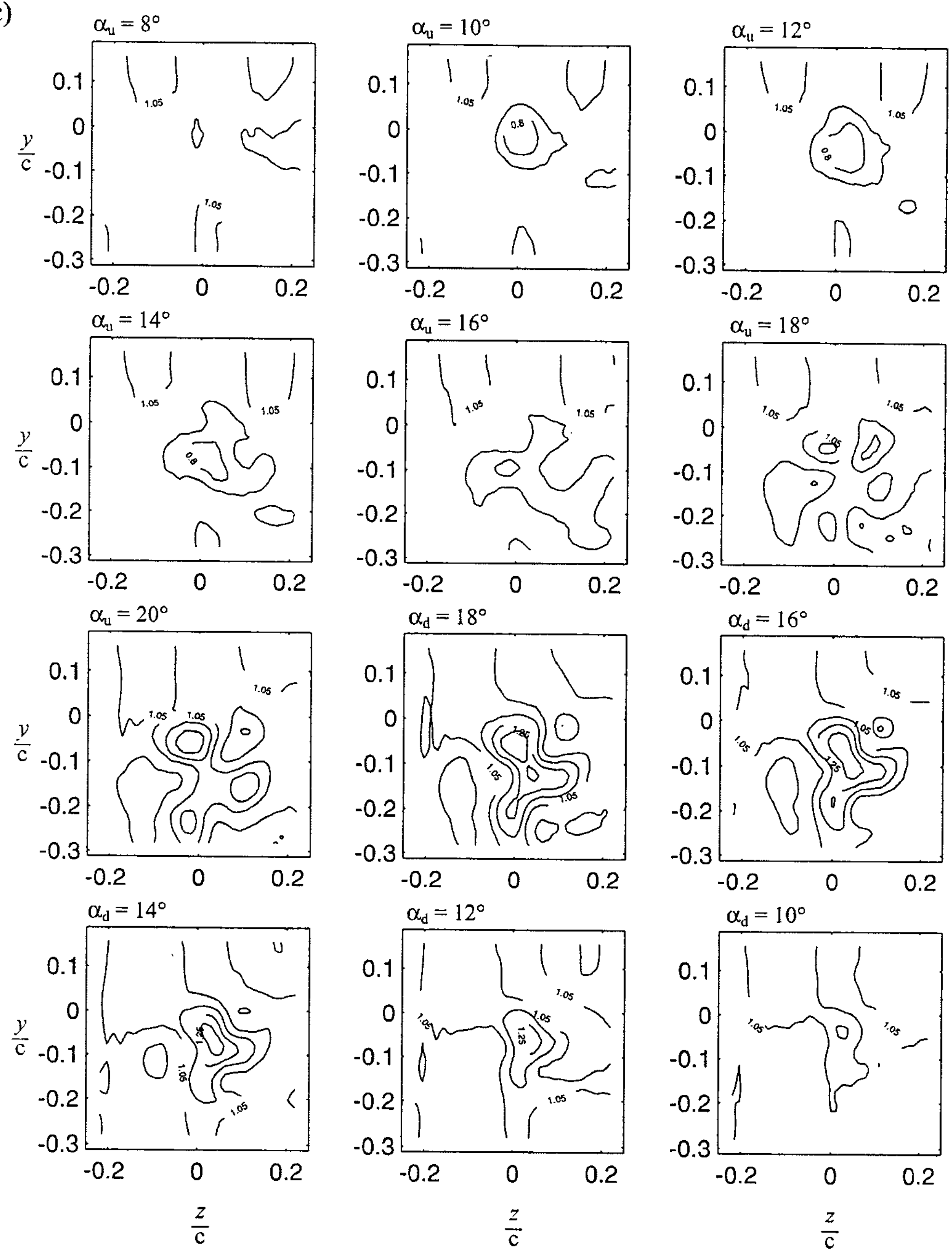

Figure E16 (a) Cross-flow velocity vectors, and contours of constant (b) $\zeta c/u_\infty$, (c) u/u_∞, and (d) u'/u_∞ (%) for the case of α_0 = 14°, $\Delta\alpha$ = 6° and κ = 0.18 at the *x*/c = 0.5 measurement station.

d)

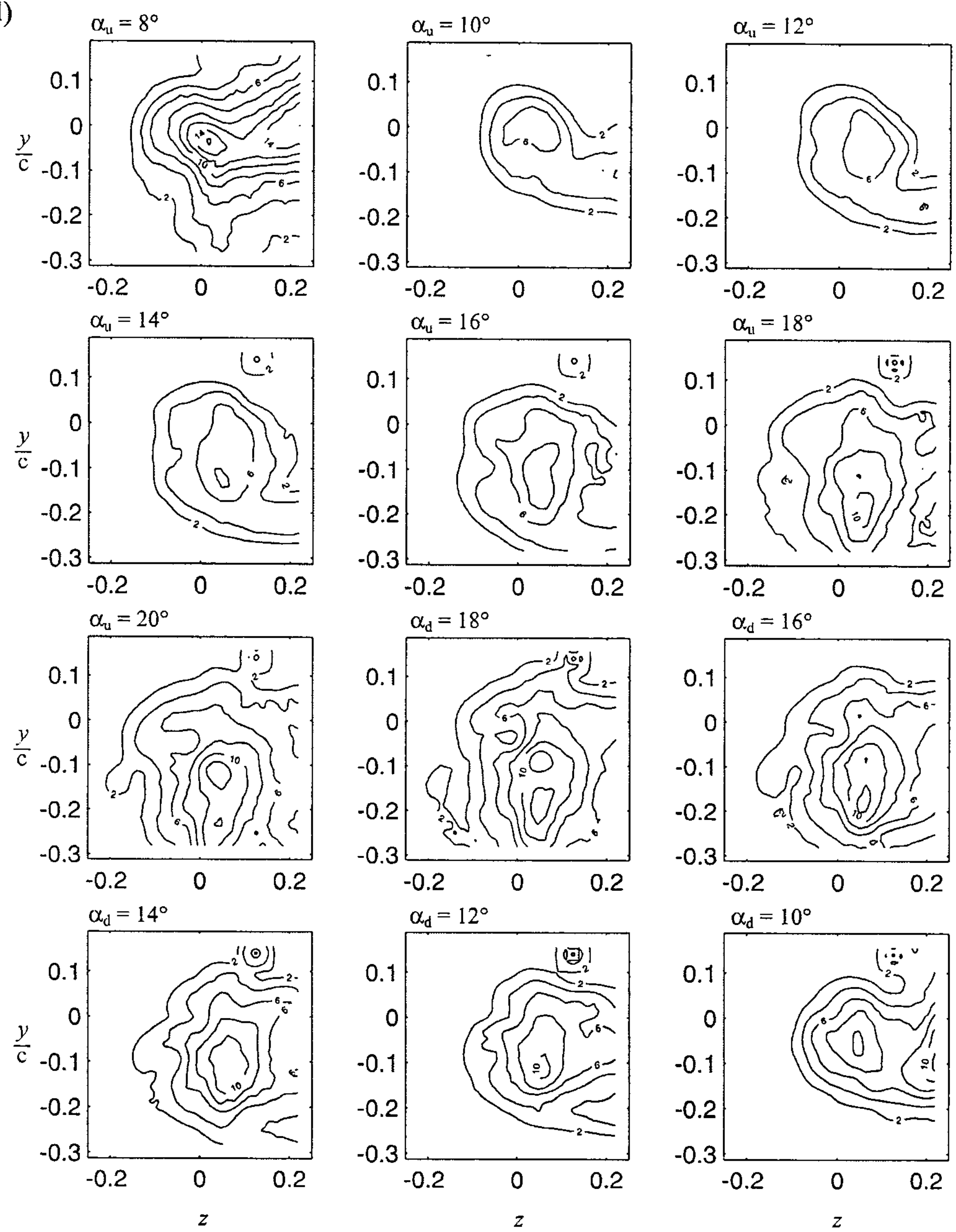

Figure E16 (a) Cross-flow velocity vectors, and contours of constant (b) $\zeta c/u_\infty$, (c) u/u_∞, and (d) u'/u_∞ (%) for the case of α_0 = 14°, $\Delta\alpha$ = 6° and κ = 0.18 at the x/c = 0.5 measurement station.

a)

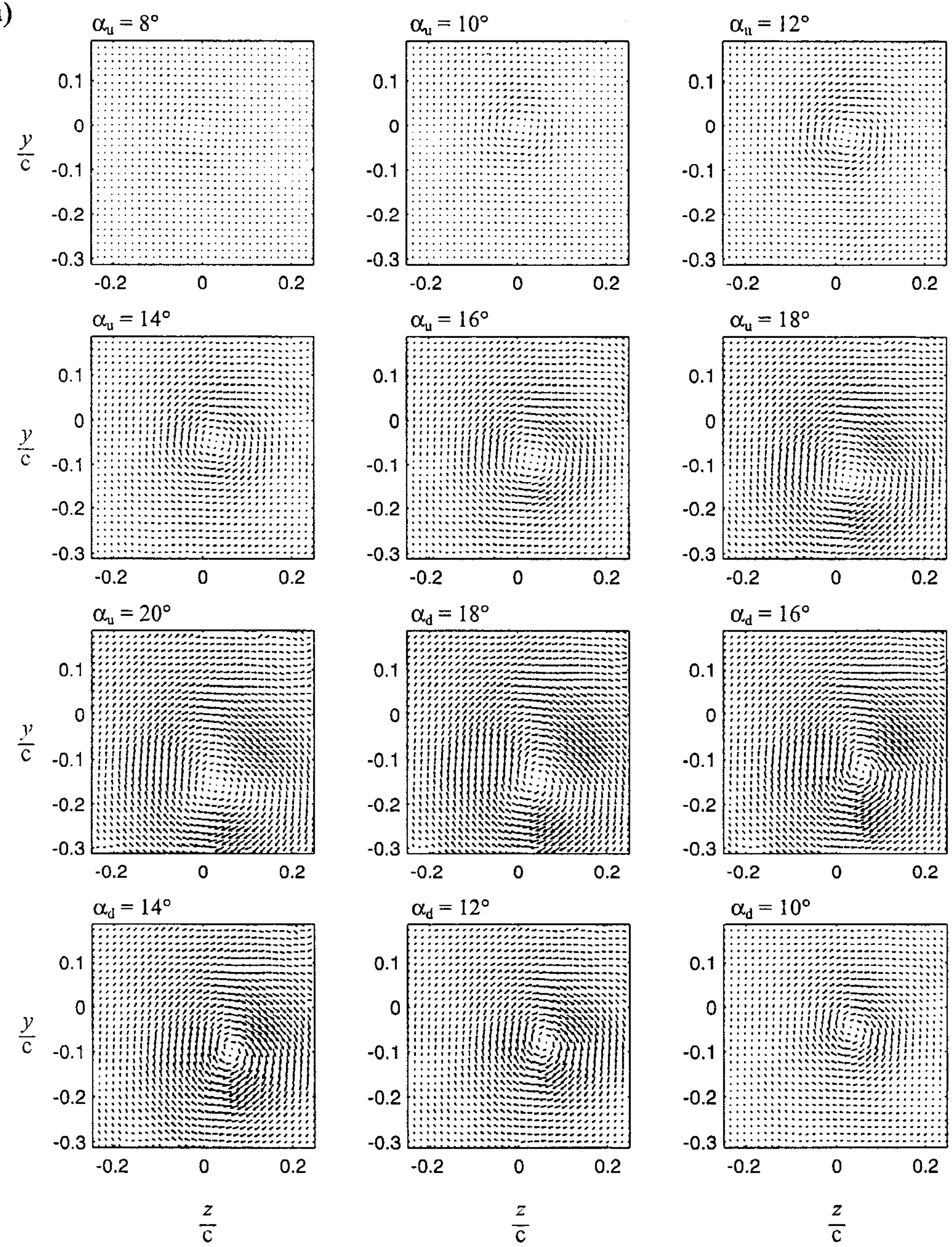

Figure E17 (a) Cross-flow velocity vectors, and contours of constant (b) $\zeta c/u_\infty$, (c) u/u_∞, and (d) u'/u_∞ (%) for the case of α_o = 14°, $\Delta\alpha$ = 6° and κ = 0.18 at the x/c = 1 measurement station.

b)

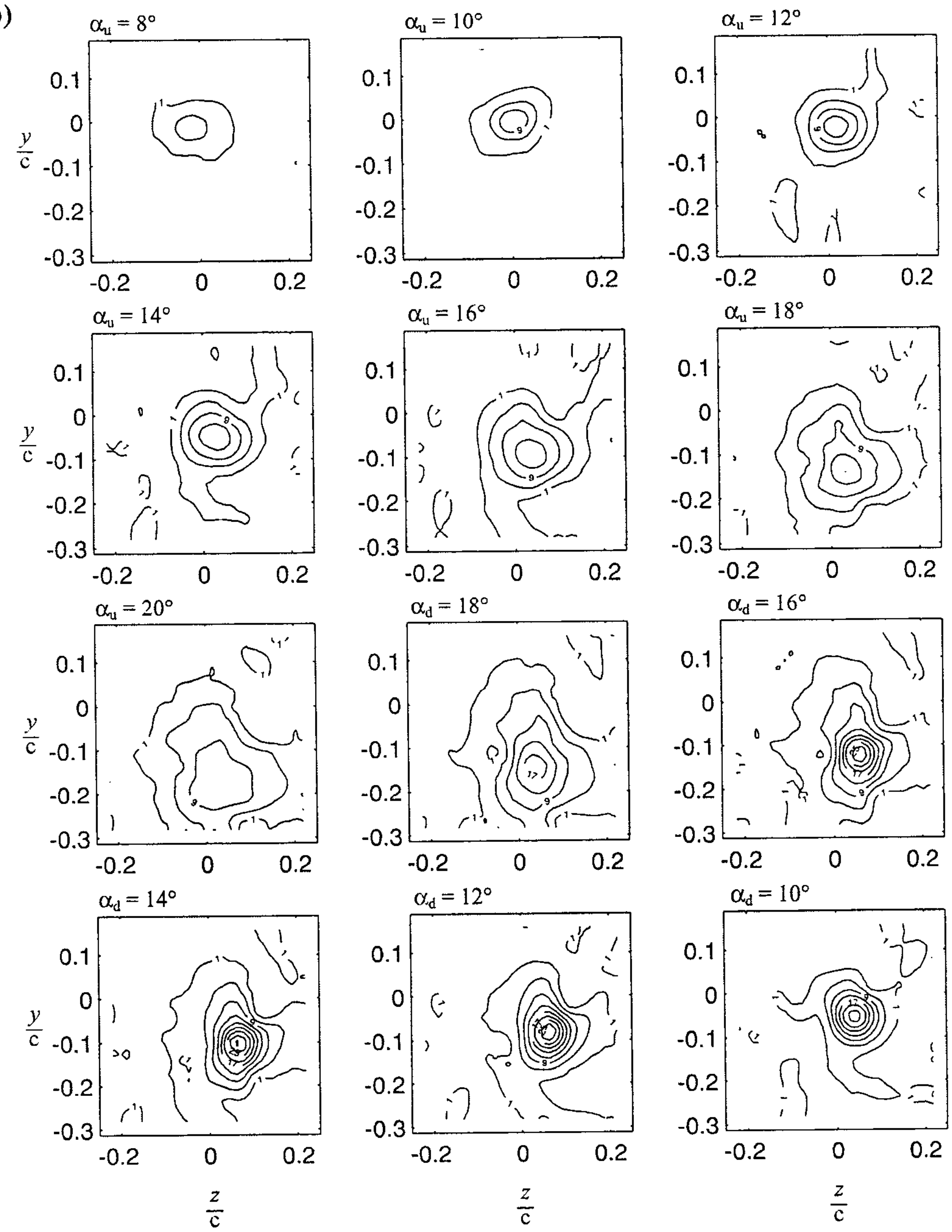

Figure E17 (a) Cross-flow velocity vectors, and contours of constant (b) $\zeta c/u_\infty$, (c) u/u_∞, and (d) u'/u_∞ (%) for the case of $\alpha_0 = 14°$, $\Delta\alpha = 6°$ and $\kappa = 0.18$ at the $x/c = 1$ measurement station.

c)

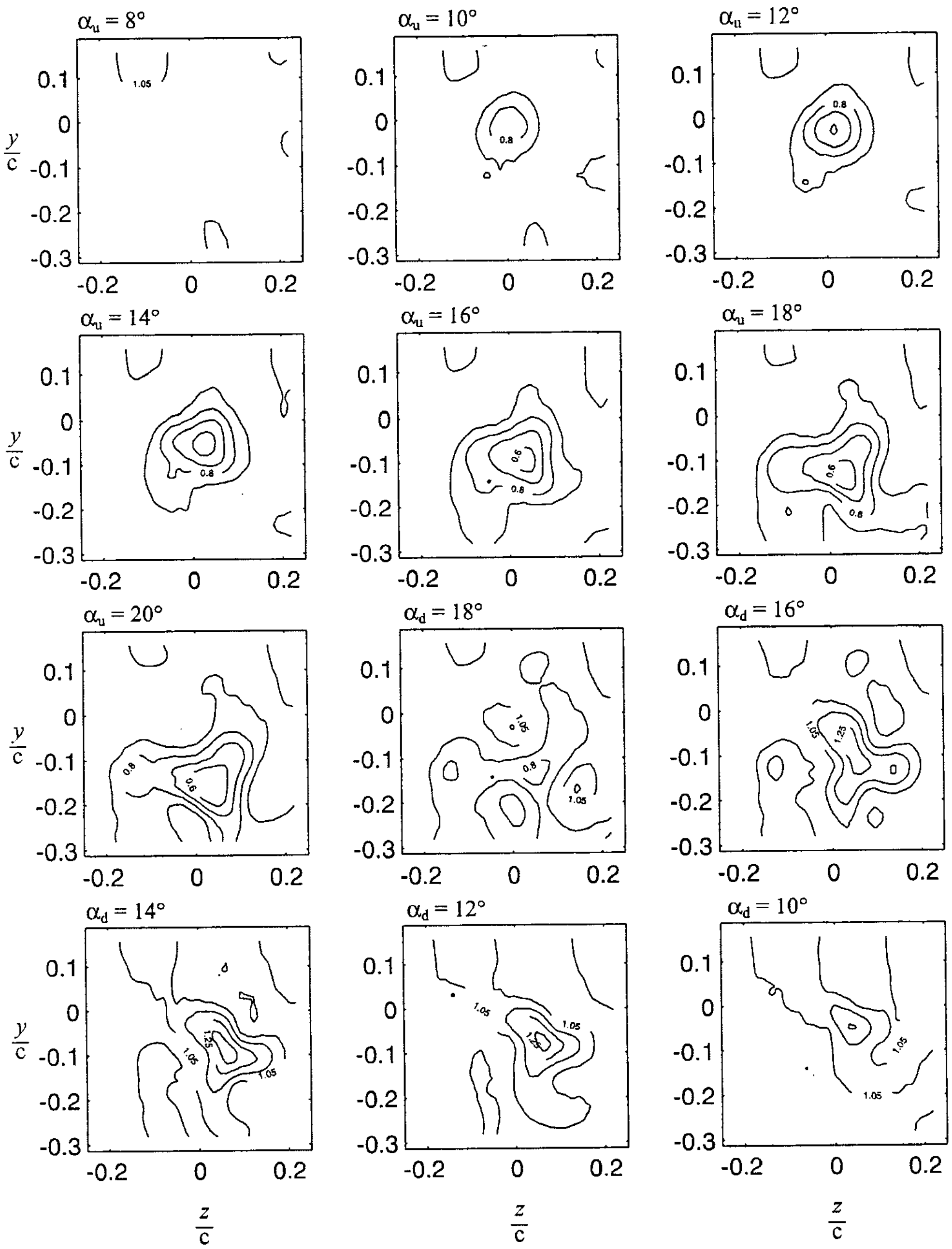

Figure E17 (a) Cross-flow velocity vectors, and contours of constant (b) $\zeta c/u_\infty$, (c) u/u_∞, and (d) u'/u_∞ (%) for the case of α_0 = 14°, $\Delta\alpha$ = 6° and κ = 0.18 at the x/c = 1 measurement station.

d)

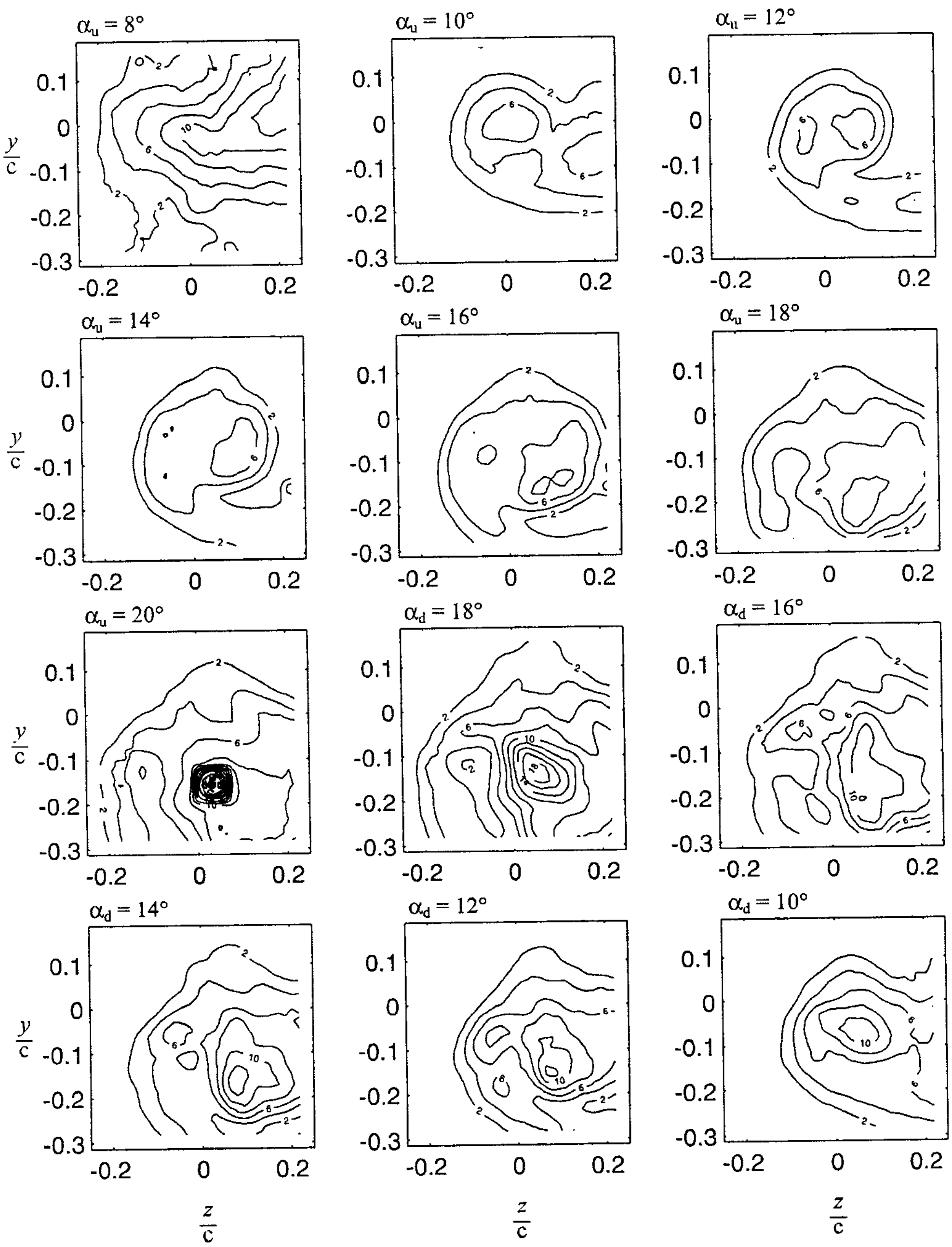

Figure E17 (a) Cross-flow velocity vectors, and contours of constant (b) $\zeta c/u_\infty$, (c) u/u_∞, and (d) u'/u_∞ (%) for the case of α_o = 14°, $\Delta\alpha$ = 6° and κ = 0.18 at the x/c = 1 measurement station.

a)

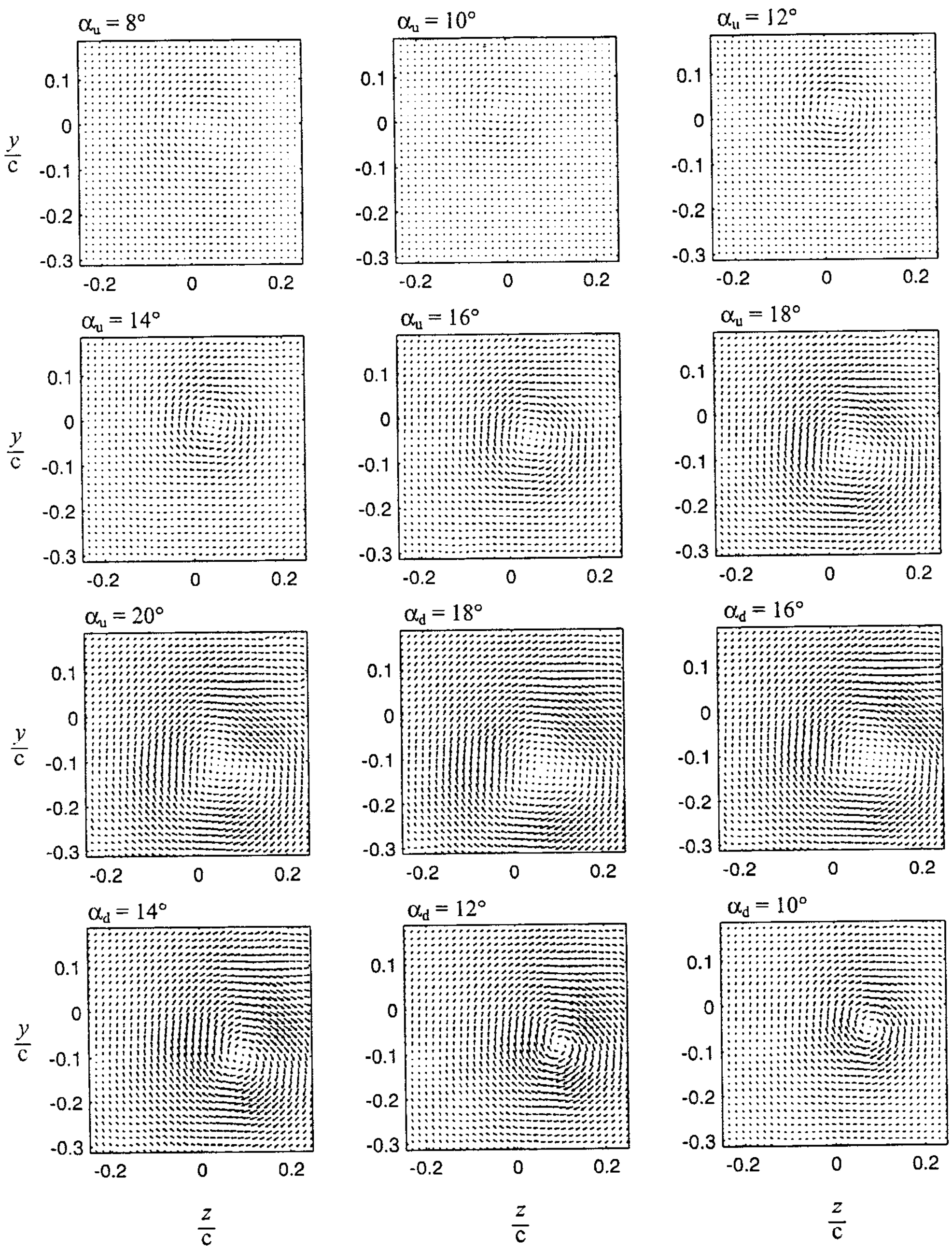

Figure E18 (a) Cross-flow velocity vectors, and contours of constant (b) $\zeta c/u_\infty$, (c) u/u_∞, and (d) u'/u_∞ (%) for the case of α_o = 14°, $\Delta\alpha$ = 6° and κ = 0.18 at the x/c = 1.5 measurement station.

b)

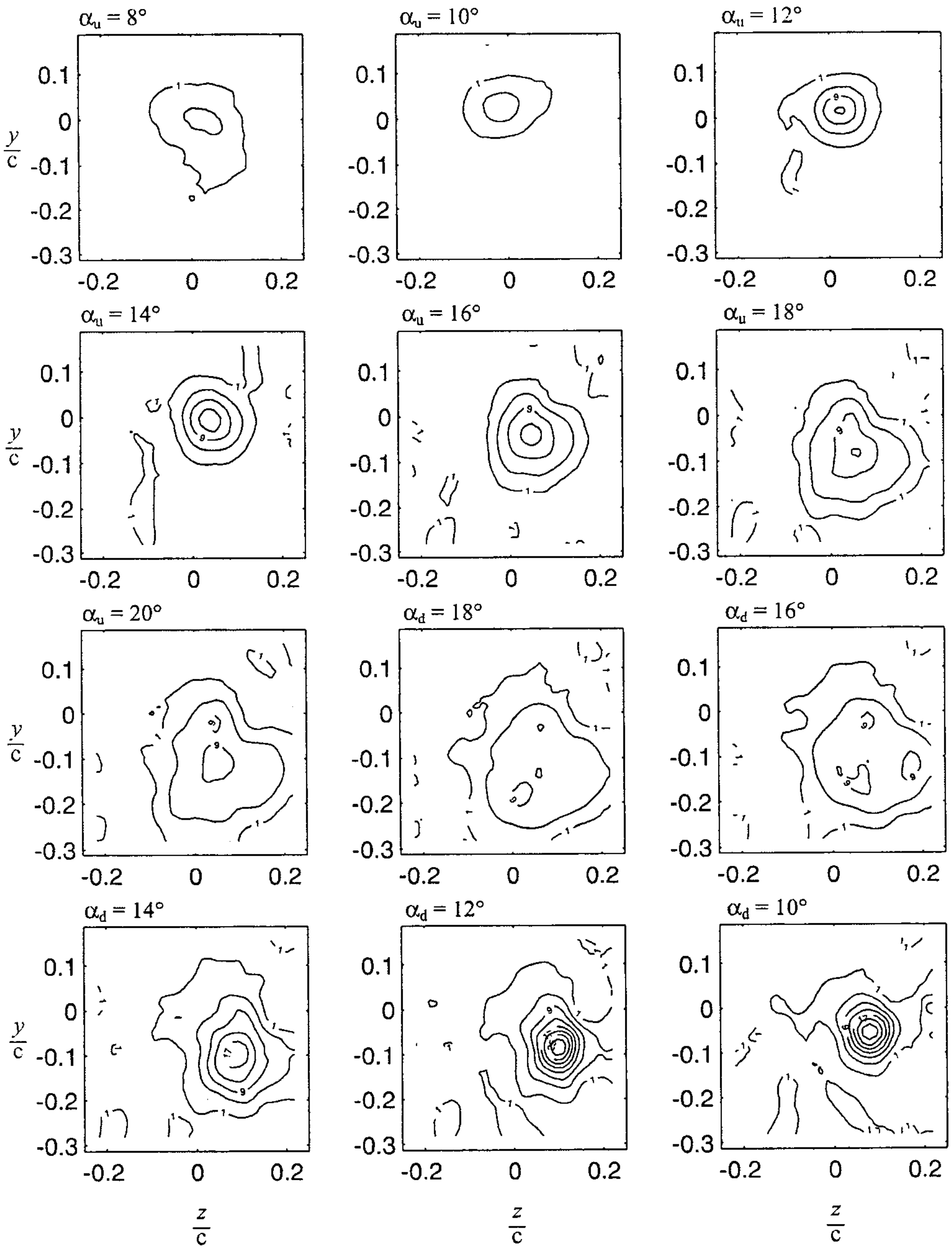

Figure E18 (a) Cross-flow velocity vectors, and contours of constant (b) $\zeta c/u_\infty$, (c) u/u_∞, and (d) u'/u_∞ (%) for the case of α_o = 14°, $\Delta\alpha$ = 6° and κ = 0.18 at the x/c = 1.5 measurement station.

c)

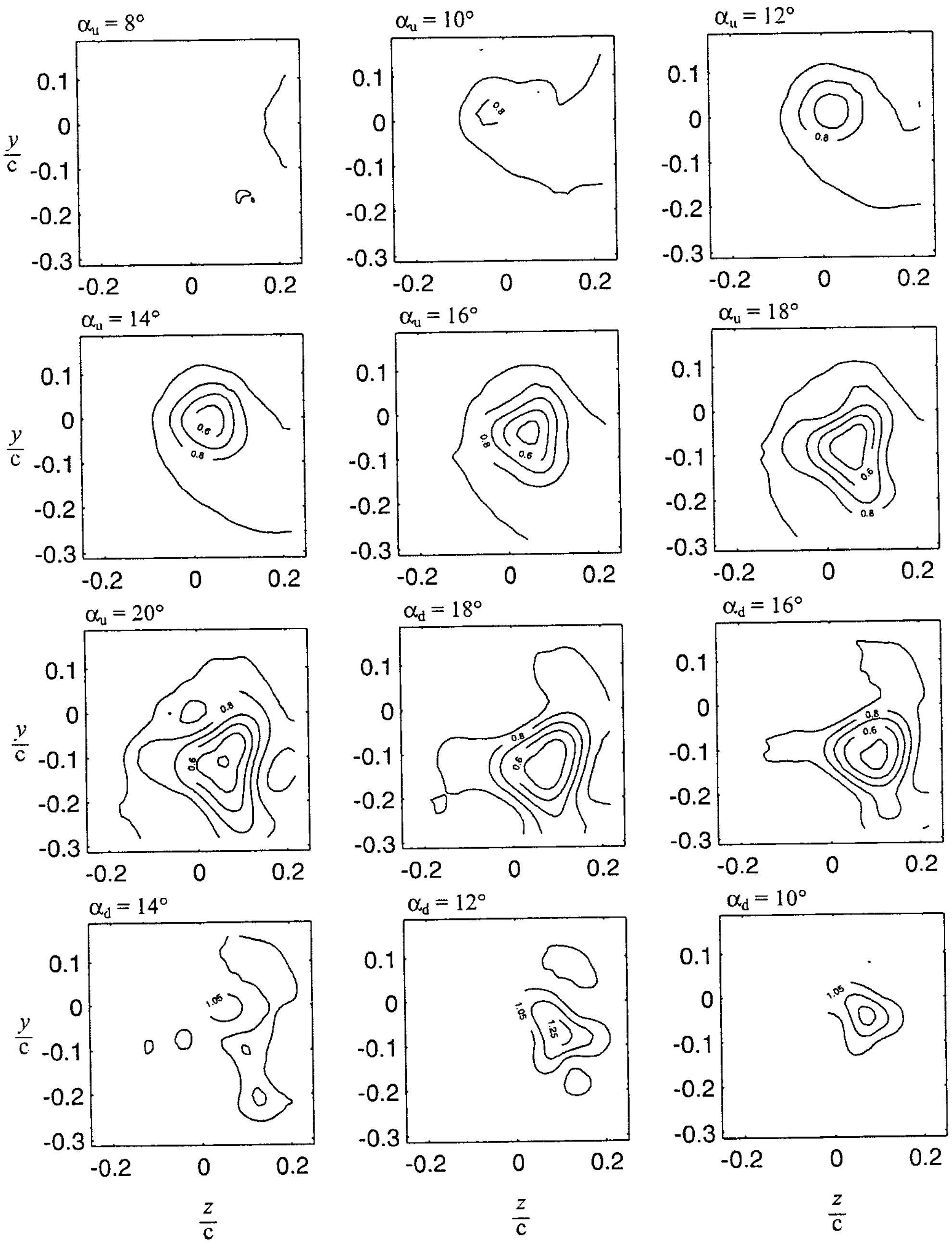

Figure E18 (a) Cross-flow velocity vectors, and contours of constant (b) $\zeta c/u_\infty$, (c) u/u_∞, and (d) u'/u_∞ (%) for the case of α_o = 14°, $\Delta\alpha$ = 6° and κ = 0.18 at the x/c = 1.5 measurement station.

d)

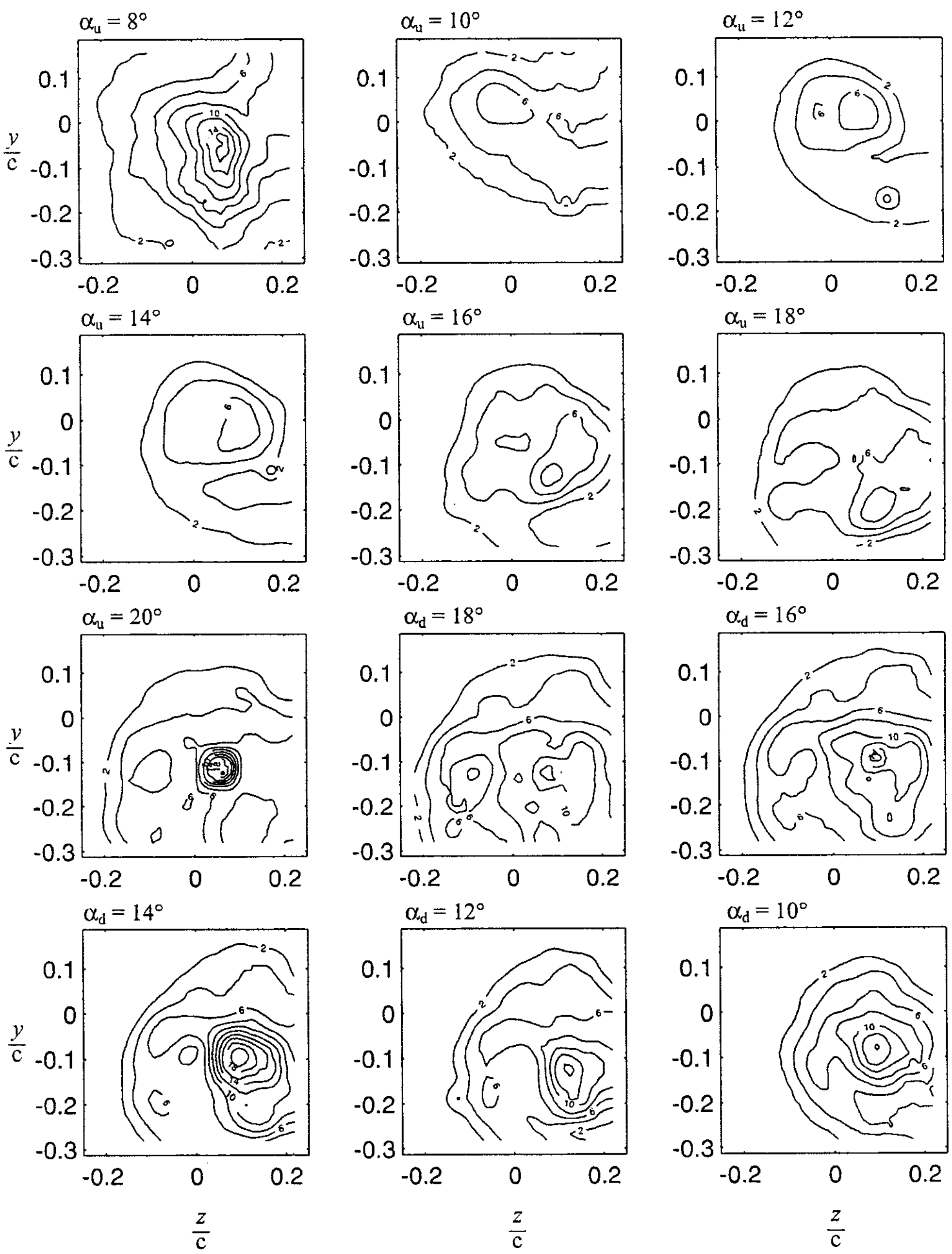

Figure E18 (a) Cross-flow velocity vectors, and contours of constant (b) $\zeta c/u_\infty$, (c) u/u_∞, and (d) u'/u_∞ (%) for the case of α_o = 14°, $\Delta\alpha$ = 6° and κ = 0.18 at the x/c = 1.5 measurement station.

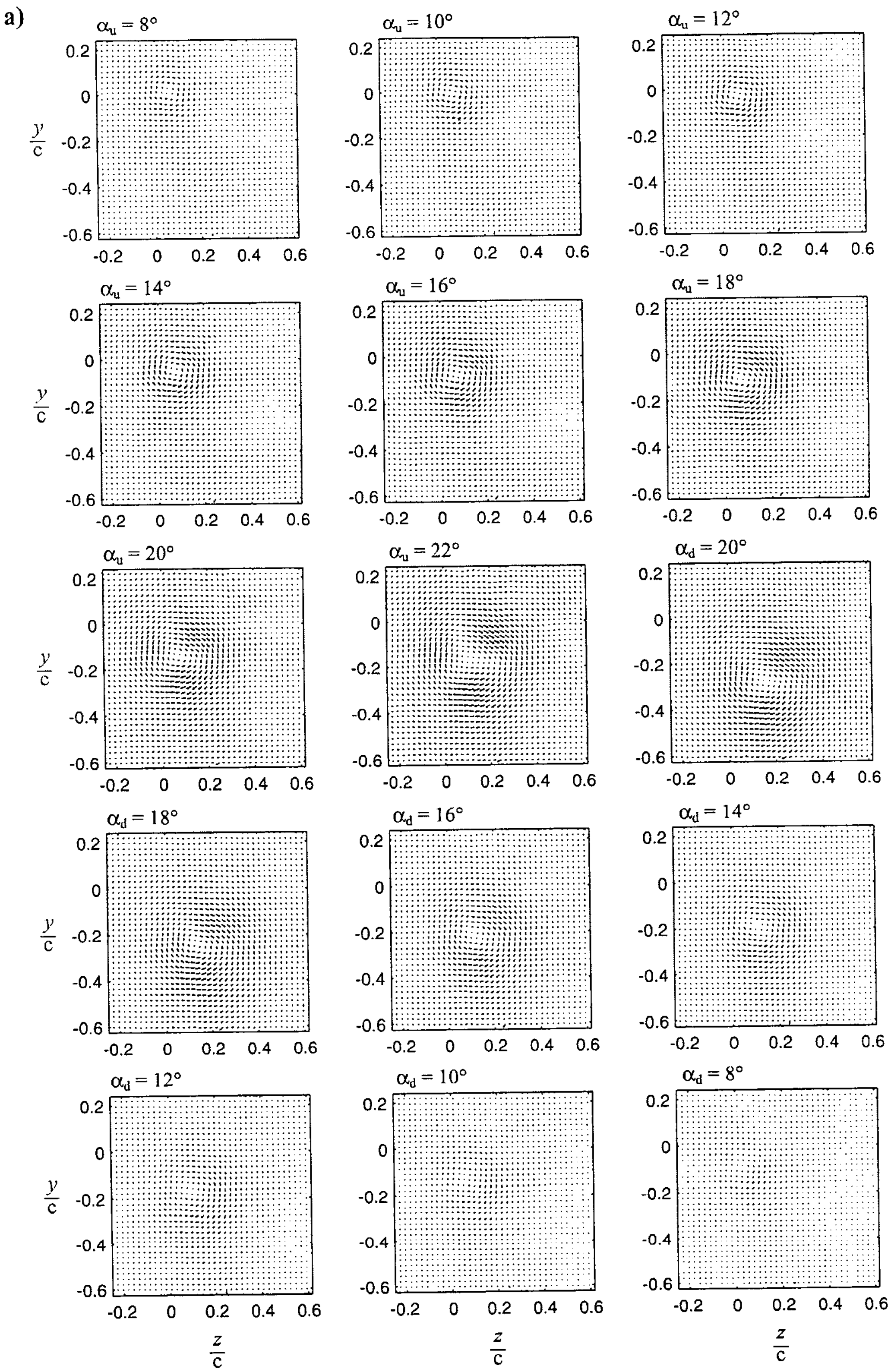

Figure E19 (a) Cross-flow velocity vectors, and contours of constant (b) $\zeta c/u_\infty$, (c) u/u_∞, and (d) u'/u_∞ (%) for the case of α_o = 14°, $\Delta\alpha$ = 8° and κ = 0.09 at the x/c = 2 measurement station.

b)

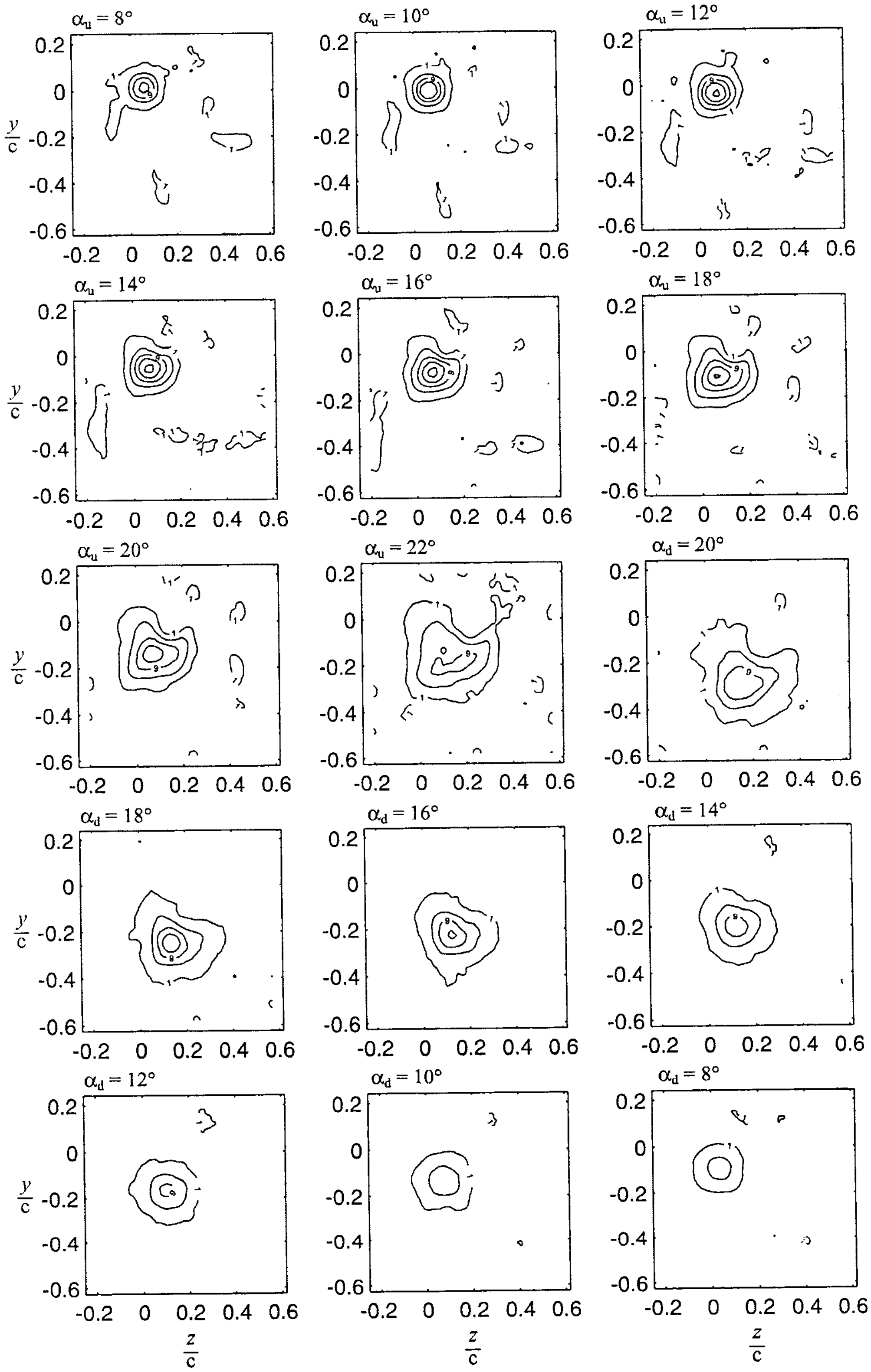

Figure E19 (a) Cross-flow velocity vectors, and contours of constant (b) $\zeta c/u_\infty$, (c) u/u_∞, and (d) u'/u_∞ (%) for the case of α_0 = 14°, $\Delta\alpha$ = 8° and κ = 0.09 at the x/c = 2 measurement station.

c)

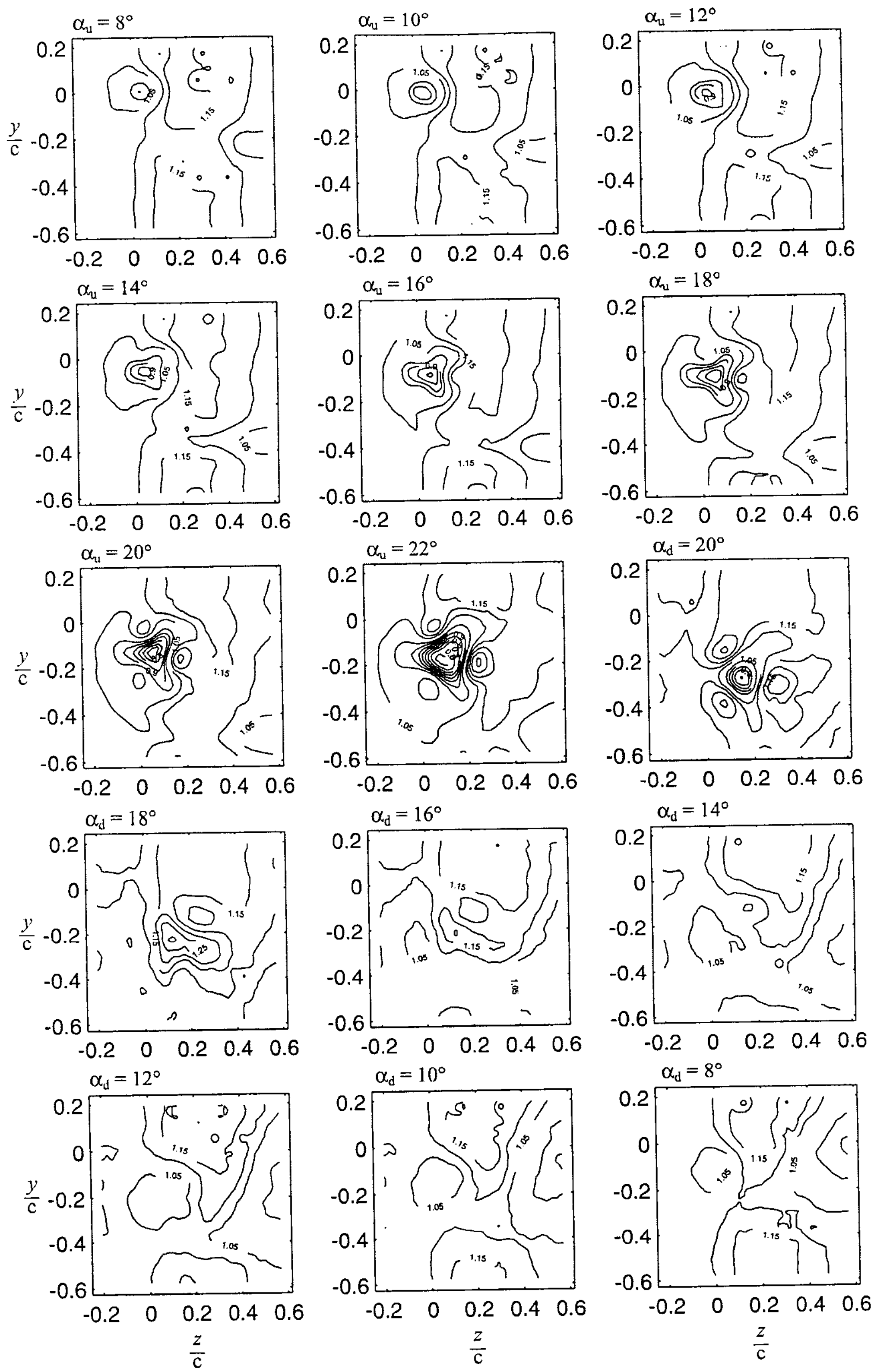

Figure E19 (a) Cross-flow velocity vectors, and contours of constant (b) $\zeta c/u_\infty$, (c) u/u_∞, and (d) u'/u_∞ (%) for the case of α_o = 14°, $\Delta\alpha$ = 8° and κ = 0.09 at the x/c = 2 measurement station.

d)

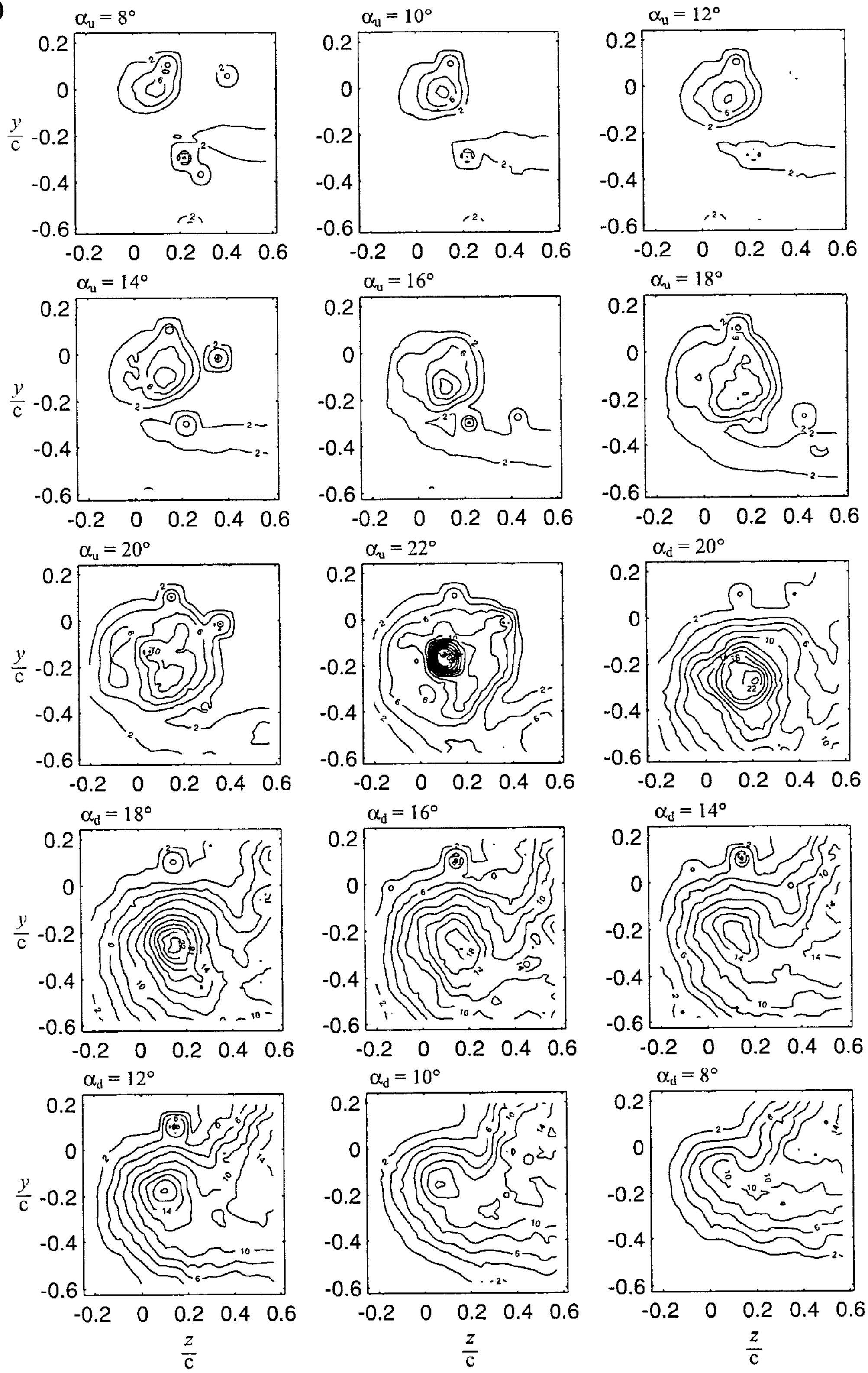

Figure E19 (a) Cross-flow velocity vectors, and contours of constant (b) $\zeta c/u_\infty$, (c) u/u_∞, and (d) u'/u_∞ (%) for the case of α_o = 14°, $\Delta\alpha$ = 8° and κ = 0.09 at the x/c = 2 measurement station.

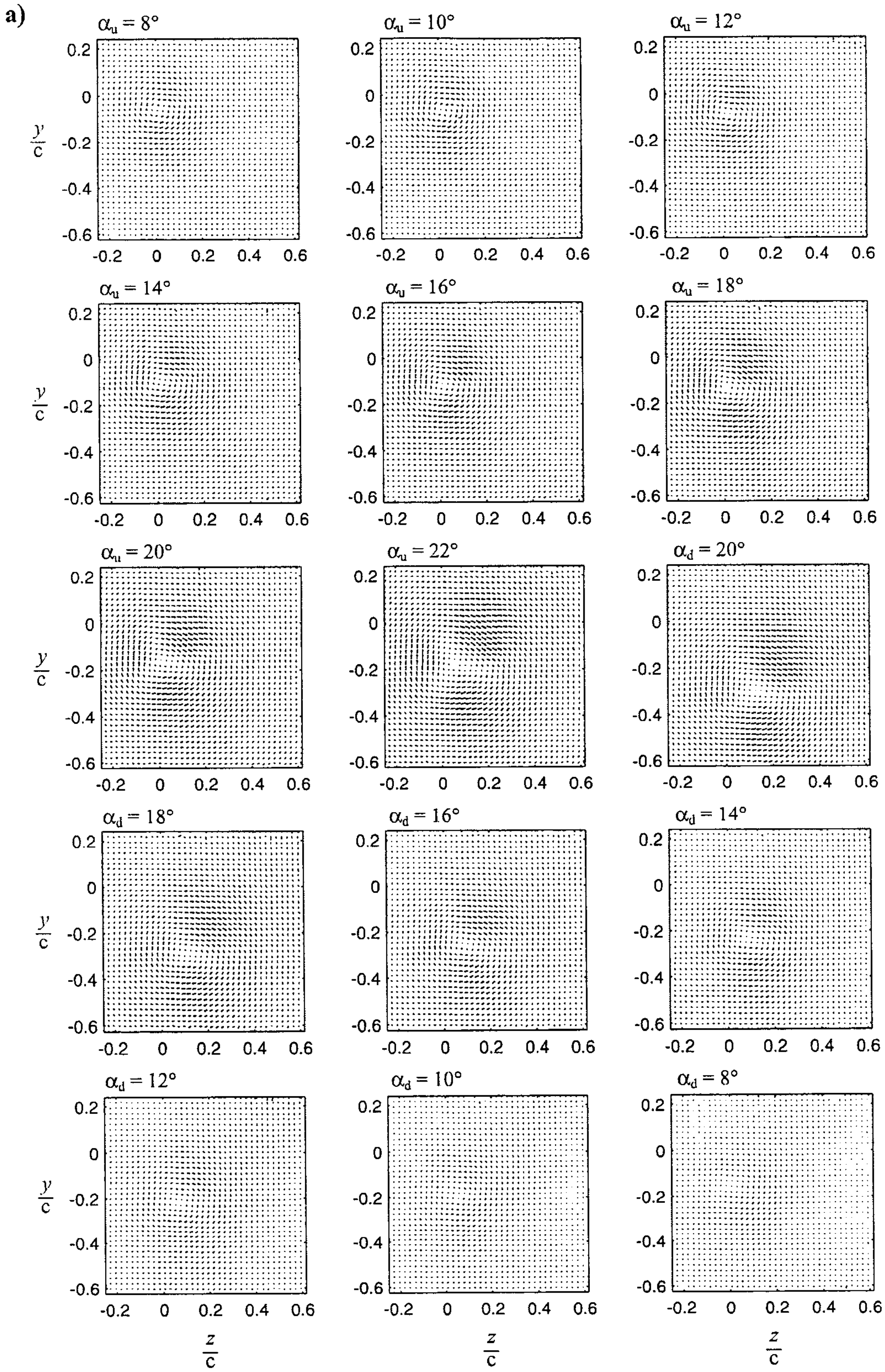

Figure E20 (a) Cross-flow velocity vectors, and contours of constant (b) $\zeta c/u_\infty$, (c) u/u_∞, and (d) u'/u_∞ (%) for the case of the inverted trailing-edge spoiler

b)

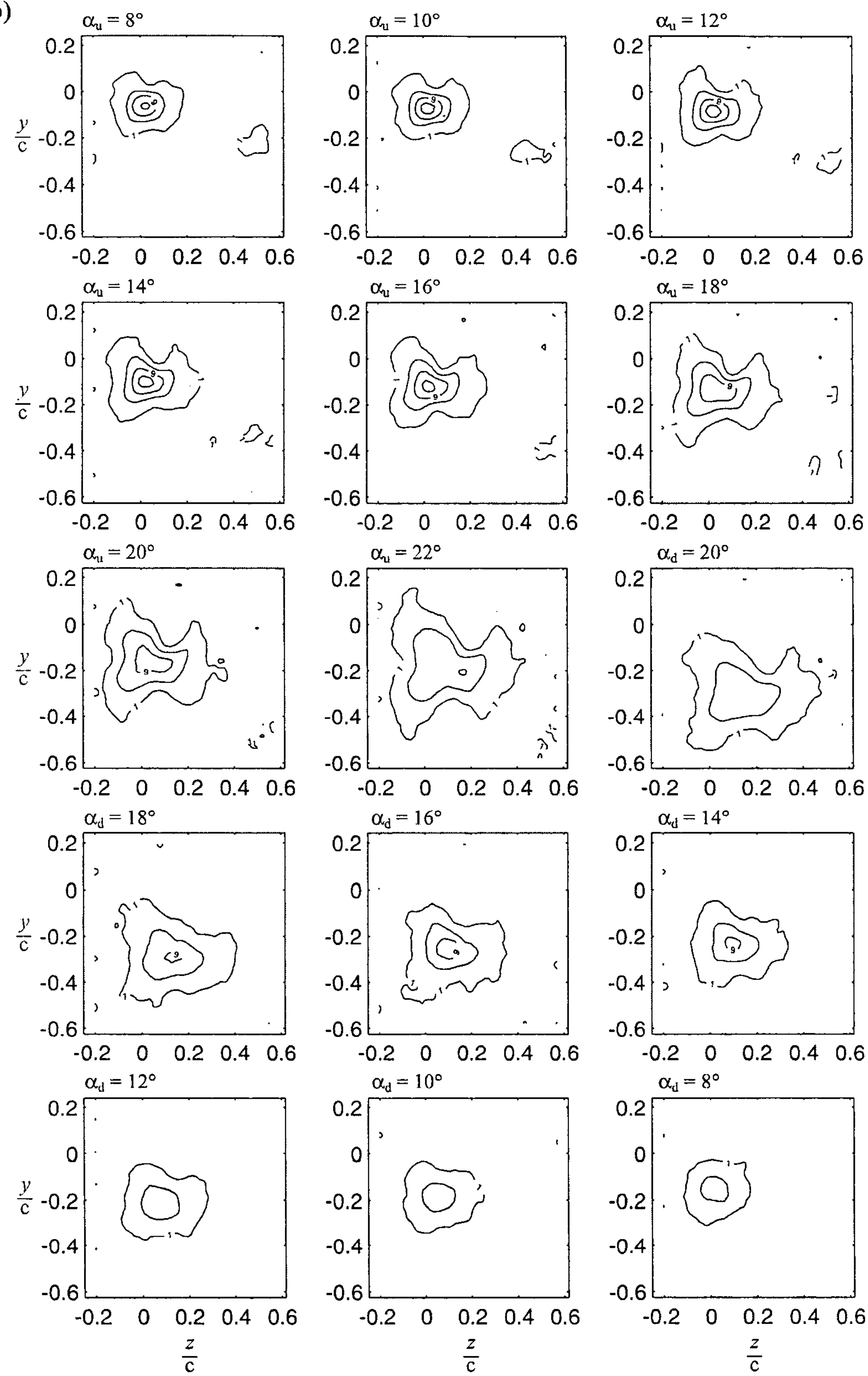

Figure E20 (a) Cross-flow velocity vectors, and contours of constant (b) $\zeta c/u_\infty$, (c) u/u_∞, and (d) u'/u_∞ (%) for the case of the inverted trailing-edge spoiler

c)

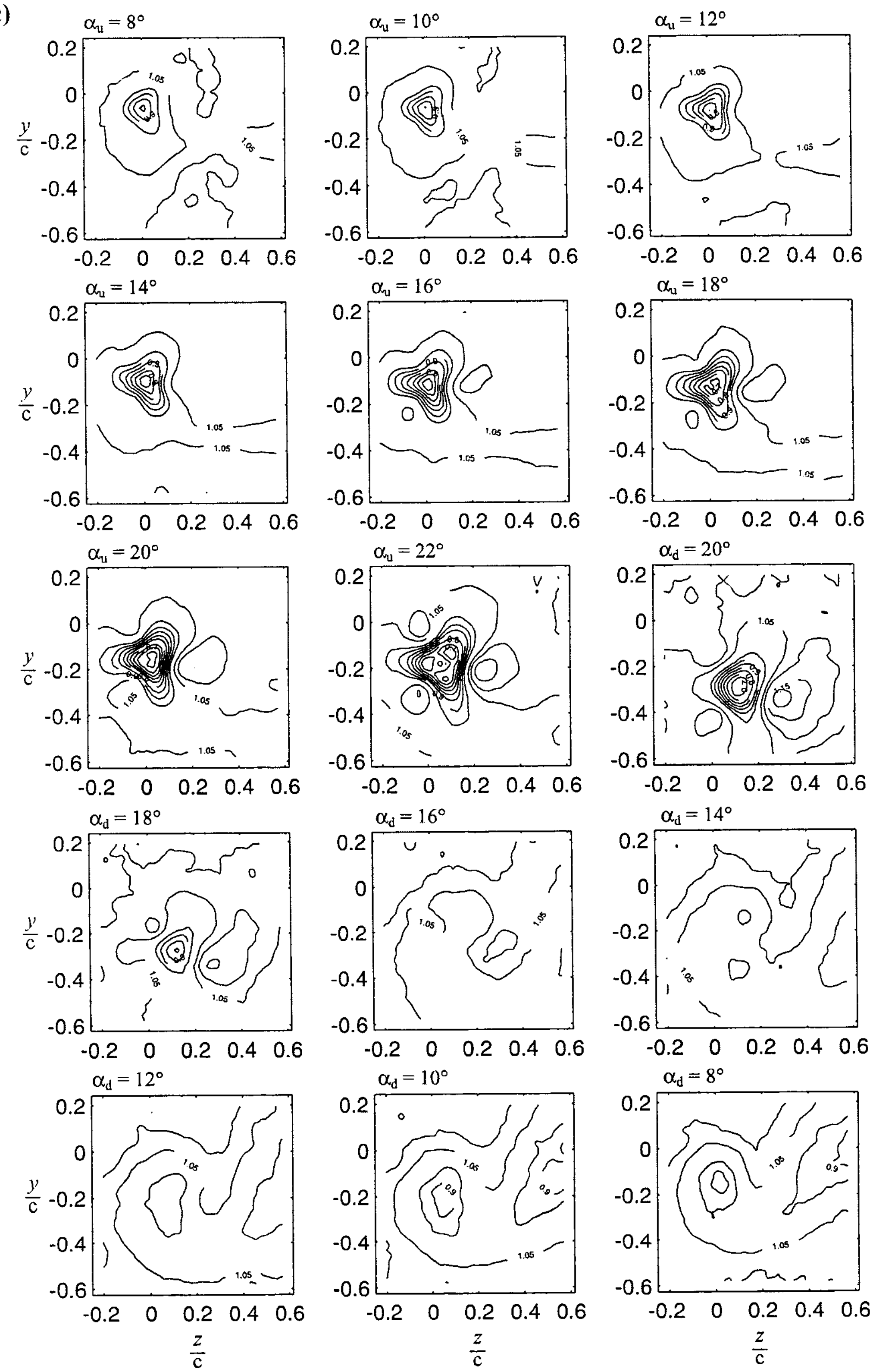

Figure E20 (a) Cross-flow velocity vectors, and contours of constant (b) $\zeta c/u_\infty$, (c) u/u_∞, and (d) u'/u_∞ (%) for the case of the inverted trailing-edge spoiler

d)

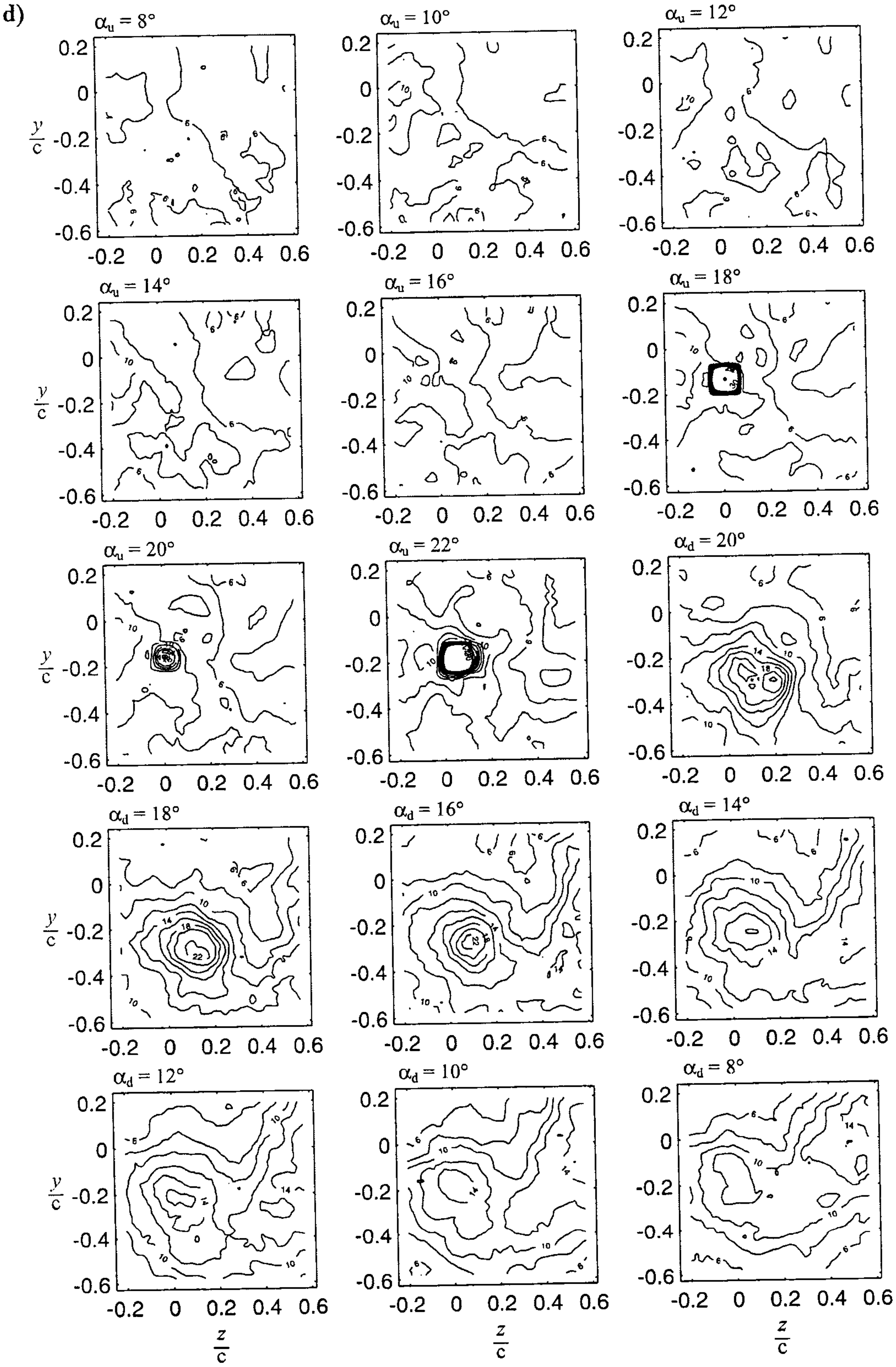

Figure E20 (a) Cross-flow velocity vectors, and contours of constant (b) $\zeta c/u_\infty$, (c) u/u_∞, and (d) u'/u_∞ (%) for the case of the inverted trailing-edge spoiler

a)

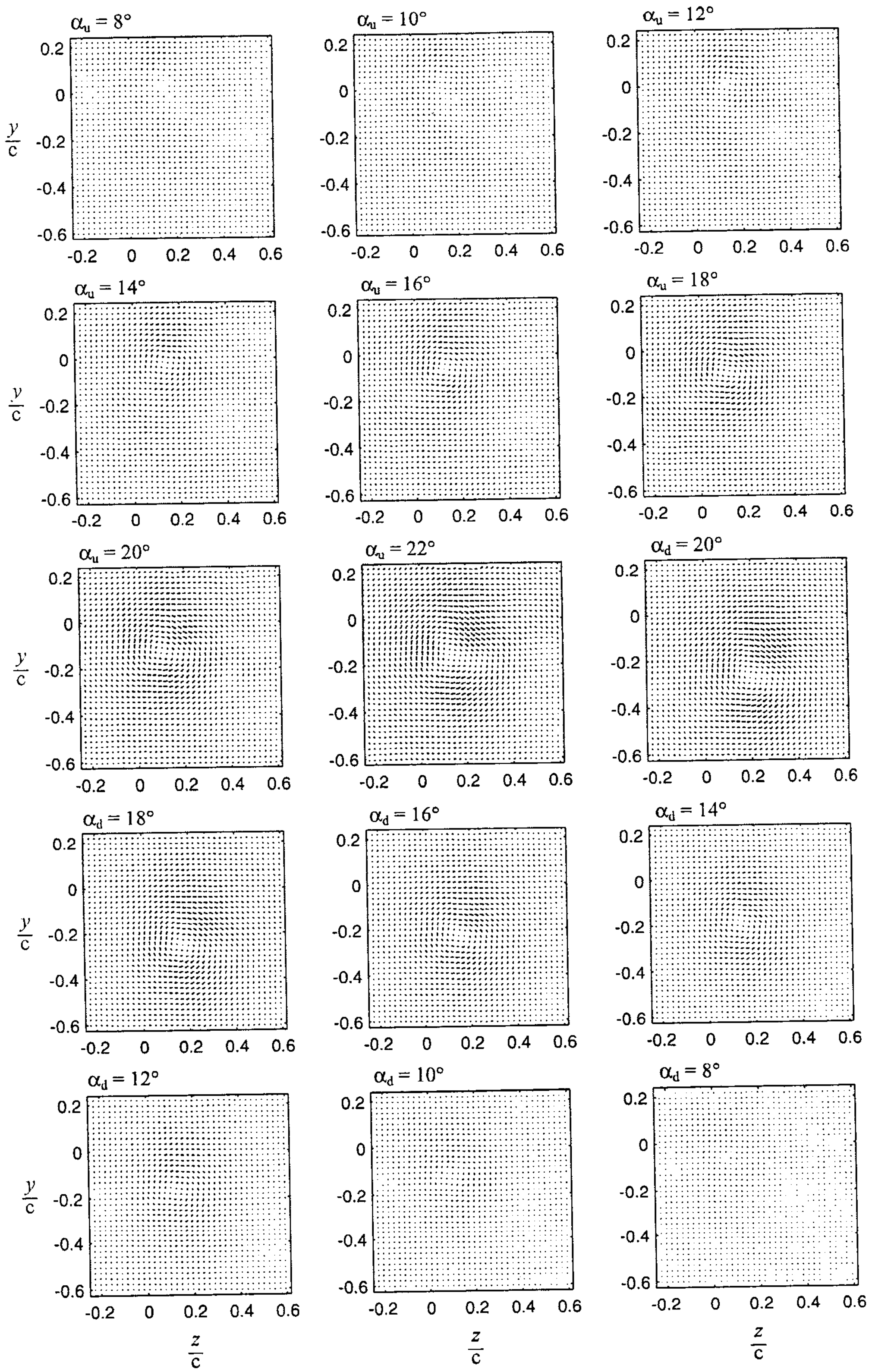

Figure E21 (a) Cross-flow velocity vectors, and contours of constant (b) $\zeta c/u_\infty$, (c) u/u_∞, and (d) u'/u_∞ (%) for the case of the trailing-edge spoiler

b)

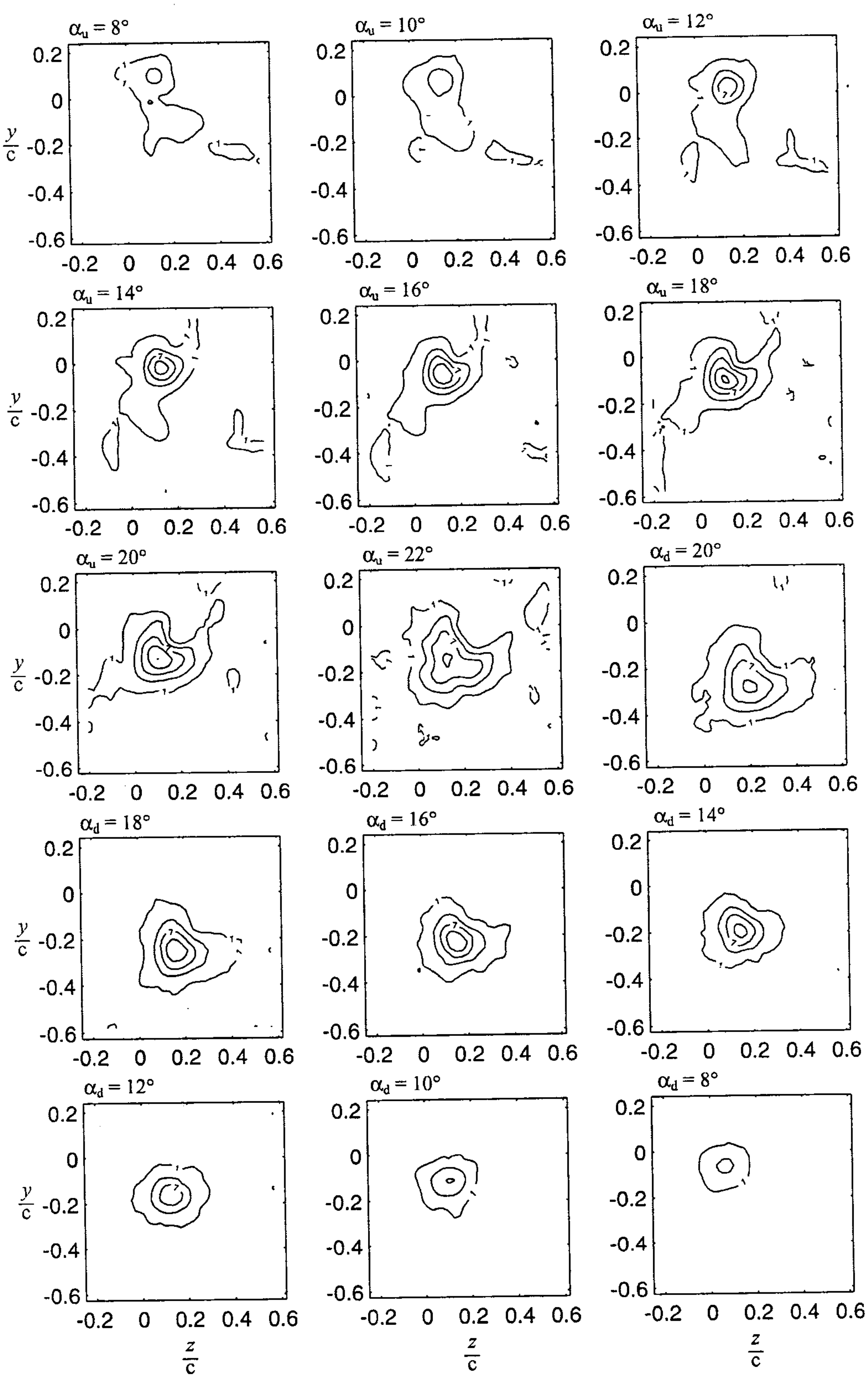

Figure E21 (a) Cross-flow velocity vectors, and contours of constant (b) $\zeta c/u_\infty$, (c) u/u_∞, and (d) u'/u_∞ (%) for the case of the trailing-edge spoiler

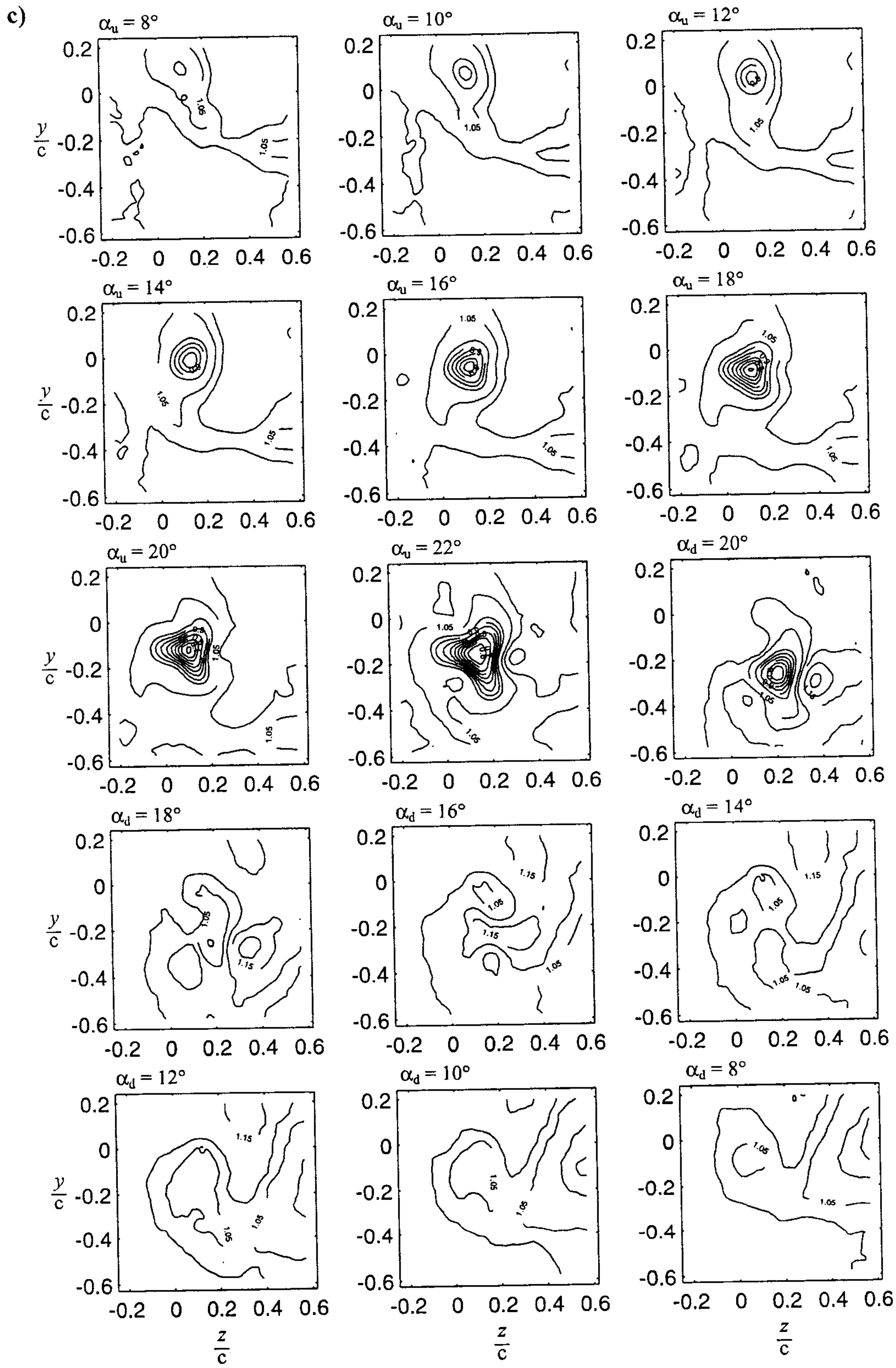

Figure E21 (a) Cross-flow velocity vectors, and contours of constant (b) $\zeta c/u_\infty$, (c) u/u_∞, and (d) u'/u_∞ (%) for the case of the trailing-edge spoiler

d)

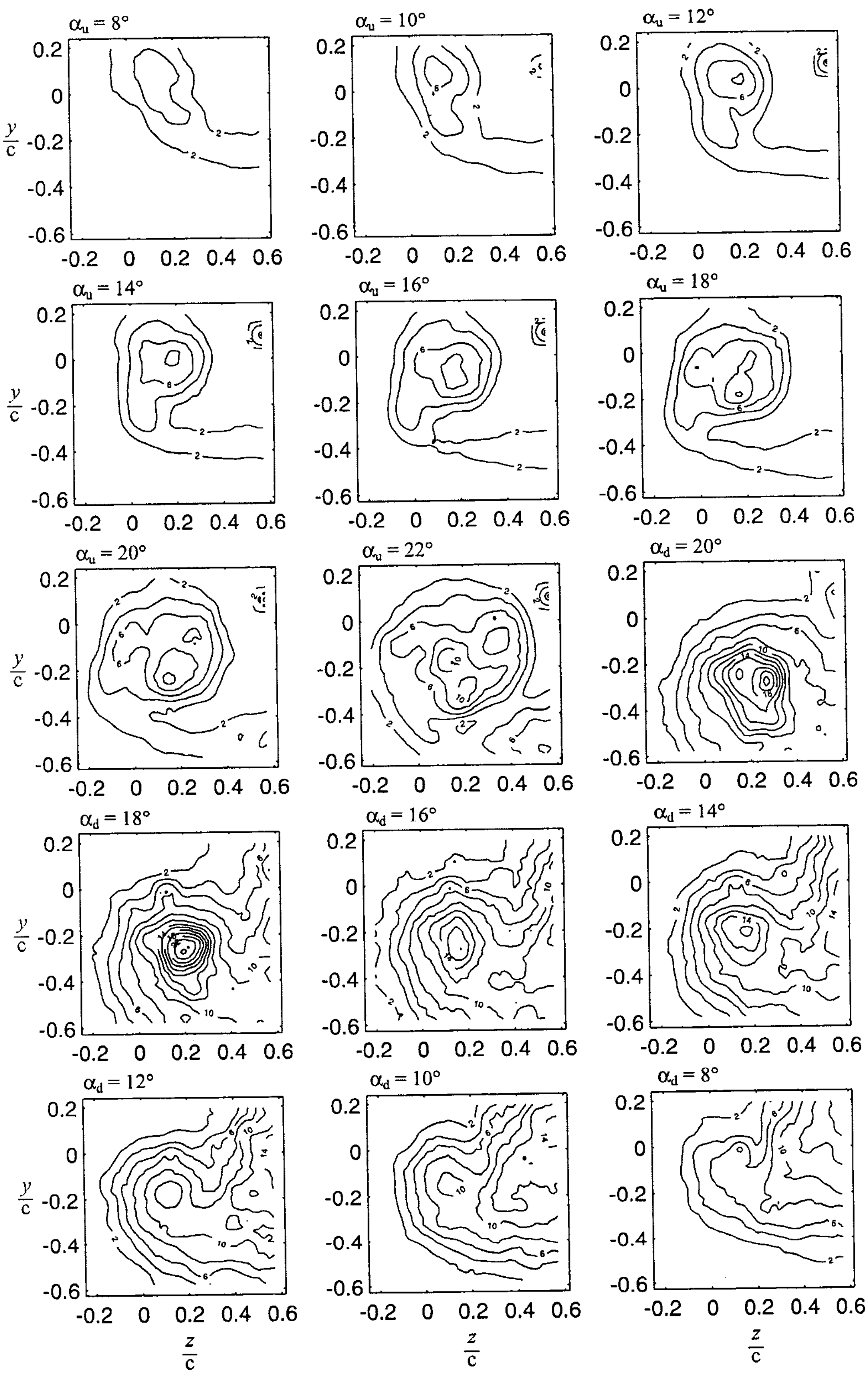

Figure E21 (a) Cross-flow velocity vectors, and contours of constant (b) $\zeta c/u_\infty$, (c) u/u_∞, and (d) u'/u_∞ (%) for the case of the trailing-edge spoiler

a)

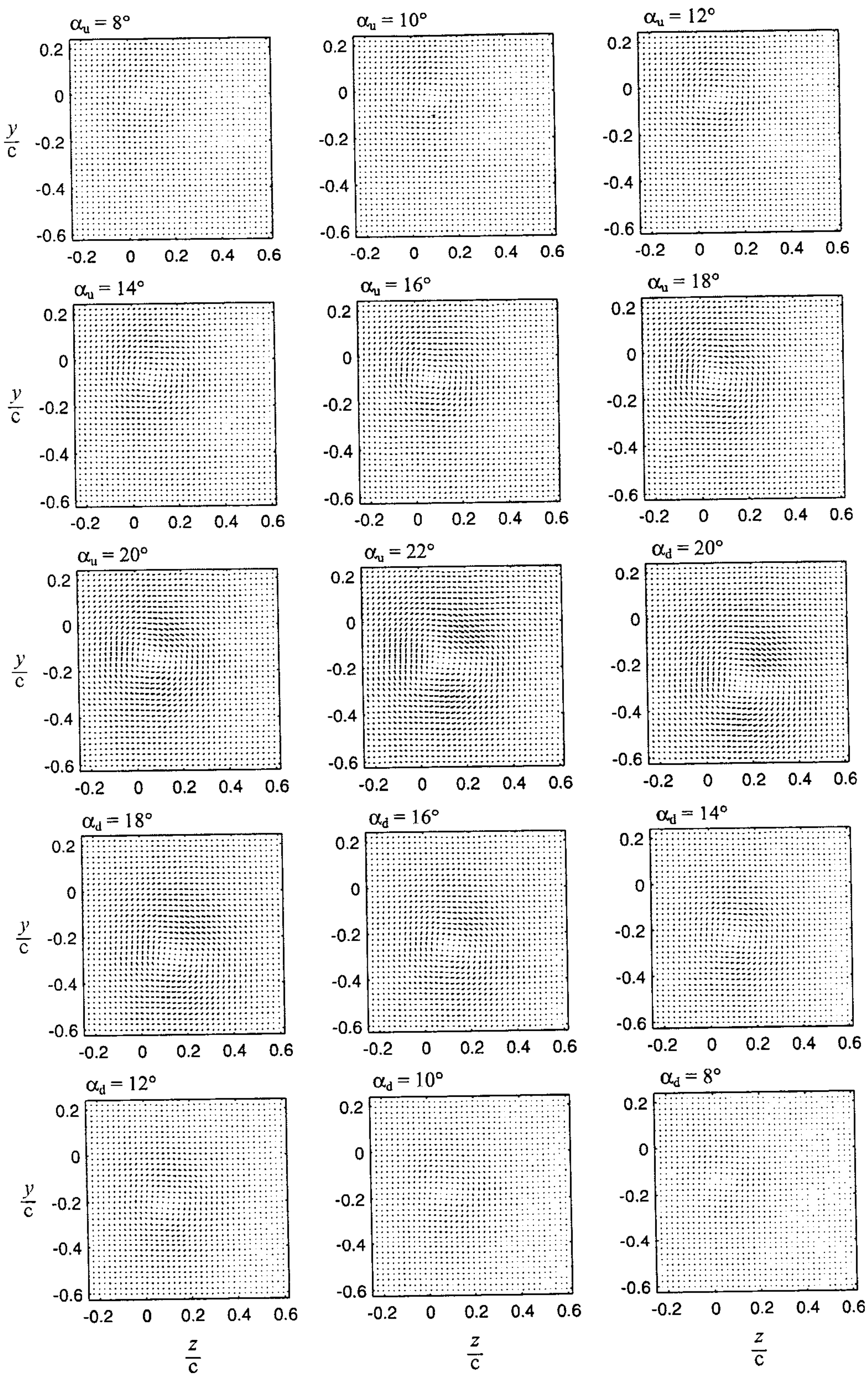

Figure E22 (a) Cross-flow velocity vectors, and contours of constant (b) $\zeta c/u_\infty$, (c) u/u_∞, and (d) u'/u_∞ (%) for the case of the symmetric trailing-edge strip

b)

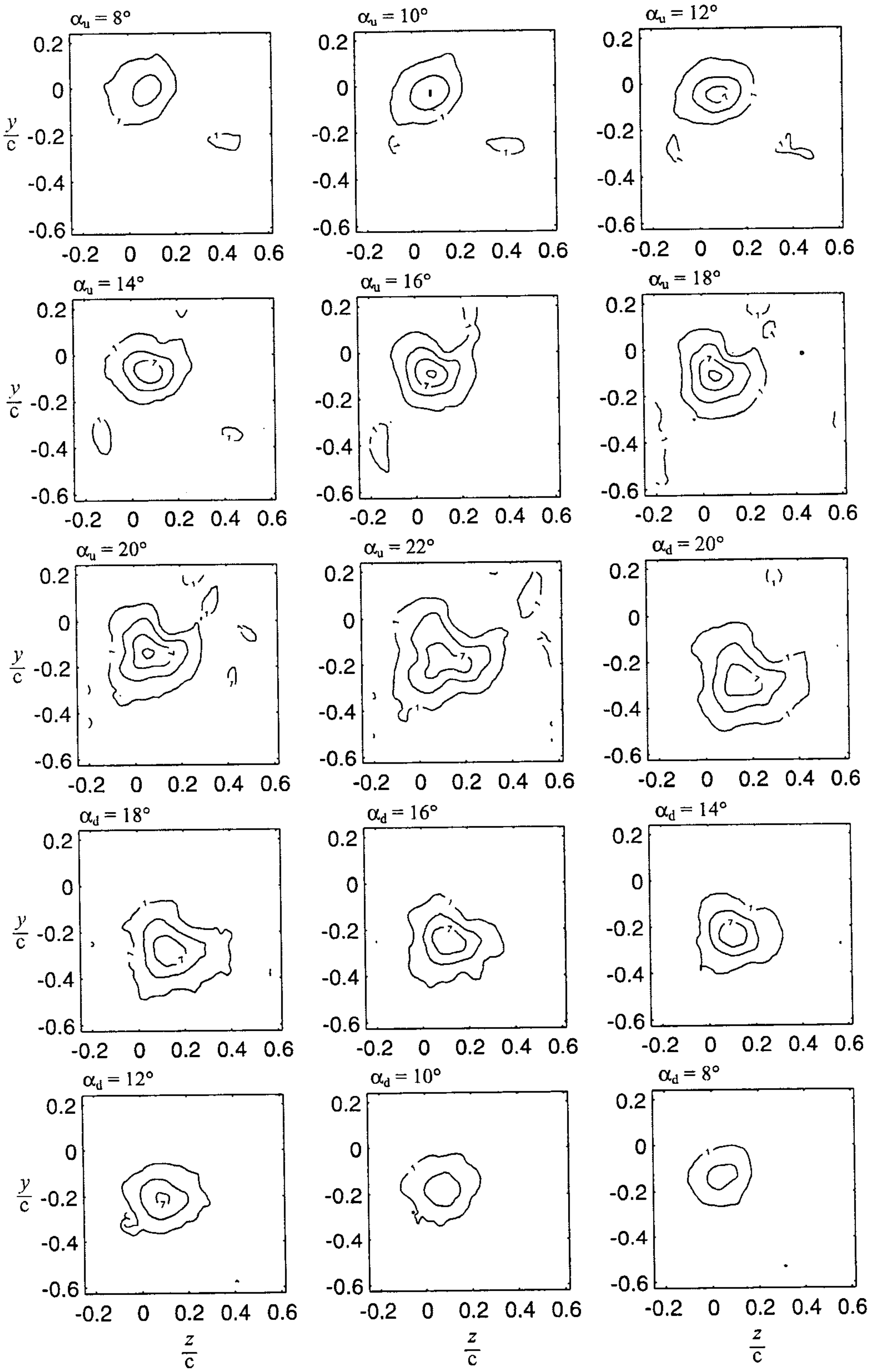

Figure E22 (a) Cross-flow velocity vectors, and contours of constant (b) $\zeta c/u_\infty$, (c) u/u_∞, and (d) u'/u_∞ (%) for the case of the symmetric trailing-edge strip

c)

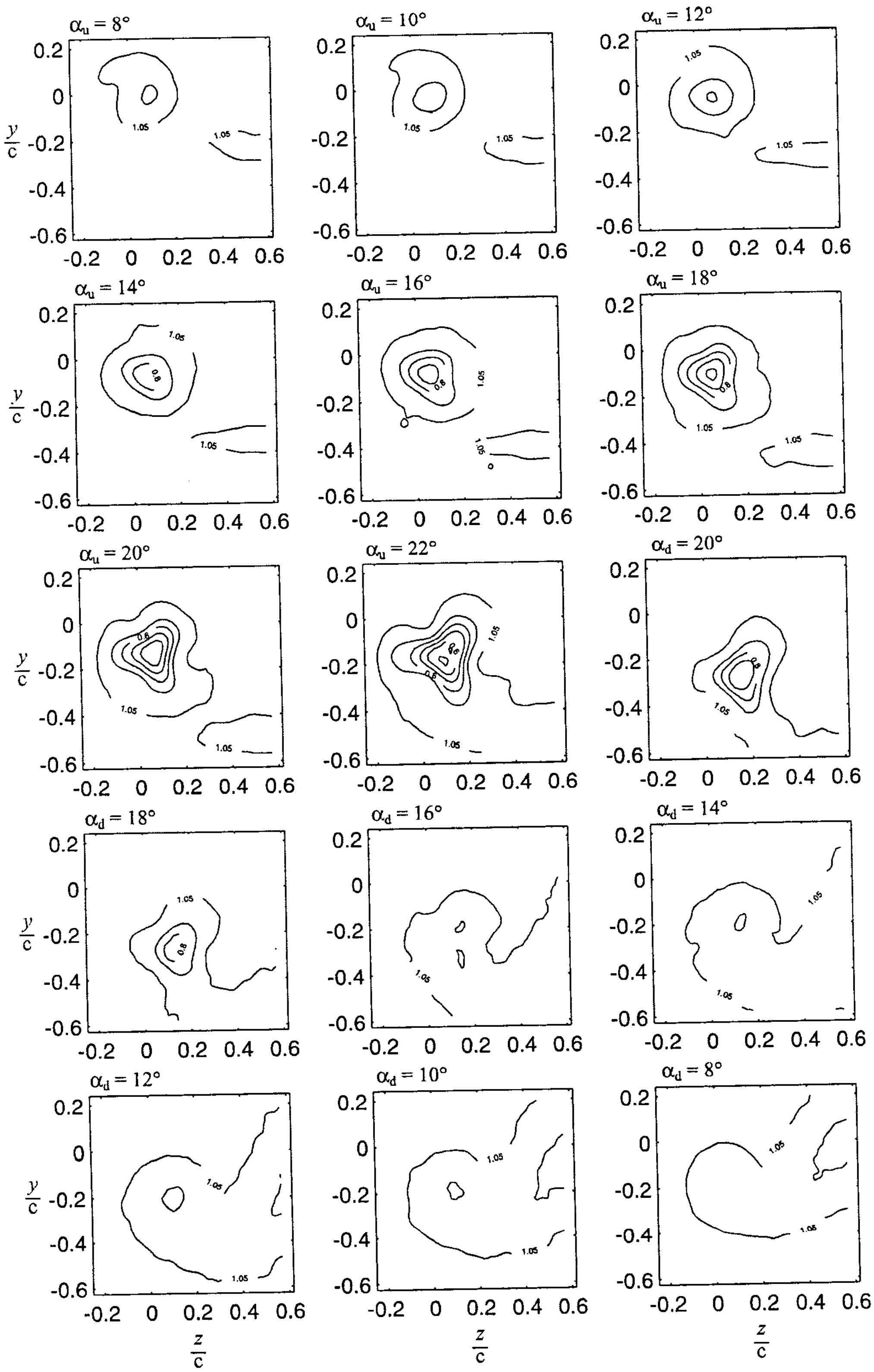

Figure E22 (a) Cross-flow velocity vectors, and contours of constant (b) $\zeta c/u_\infty$, (c) u/u_∞, and (d) u'/u_∞ (%) for the case of the symmetric trailing-edge strip

d)

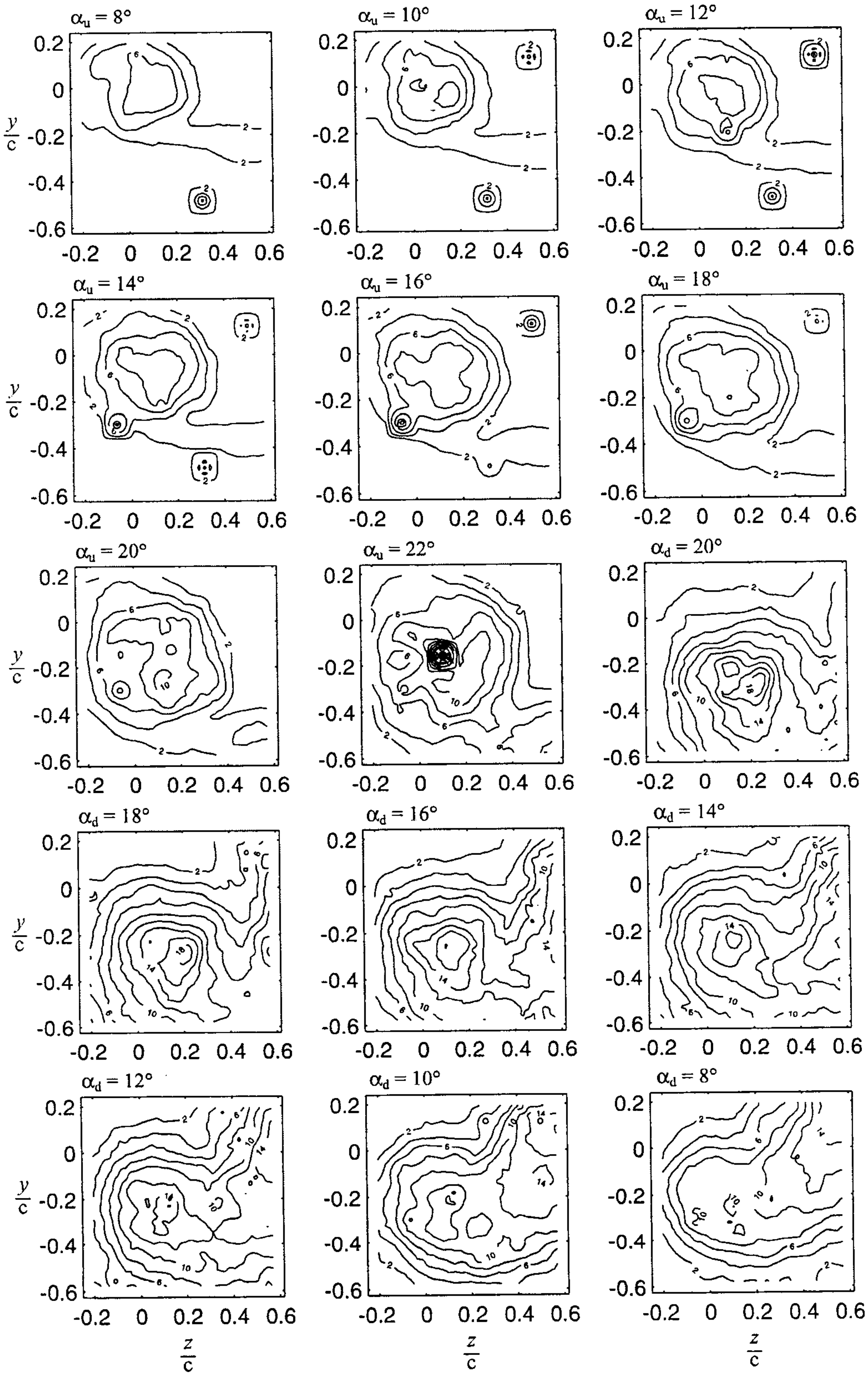

Figure E22 (a) Cross-flow velocity vectors, and contours of constant (b) $\zeta c/u_\infty$, (c) u/u_∞, and (d) u'/u_∞ (%) for the case of the symmetric trailing-edge strip

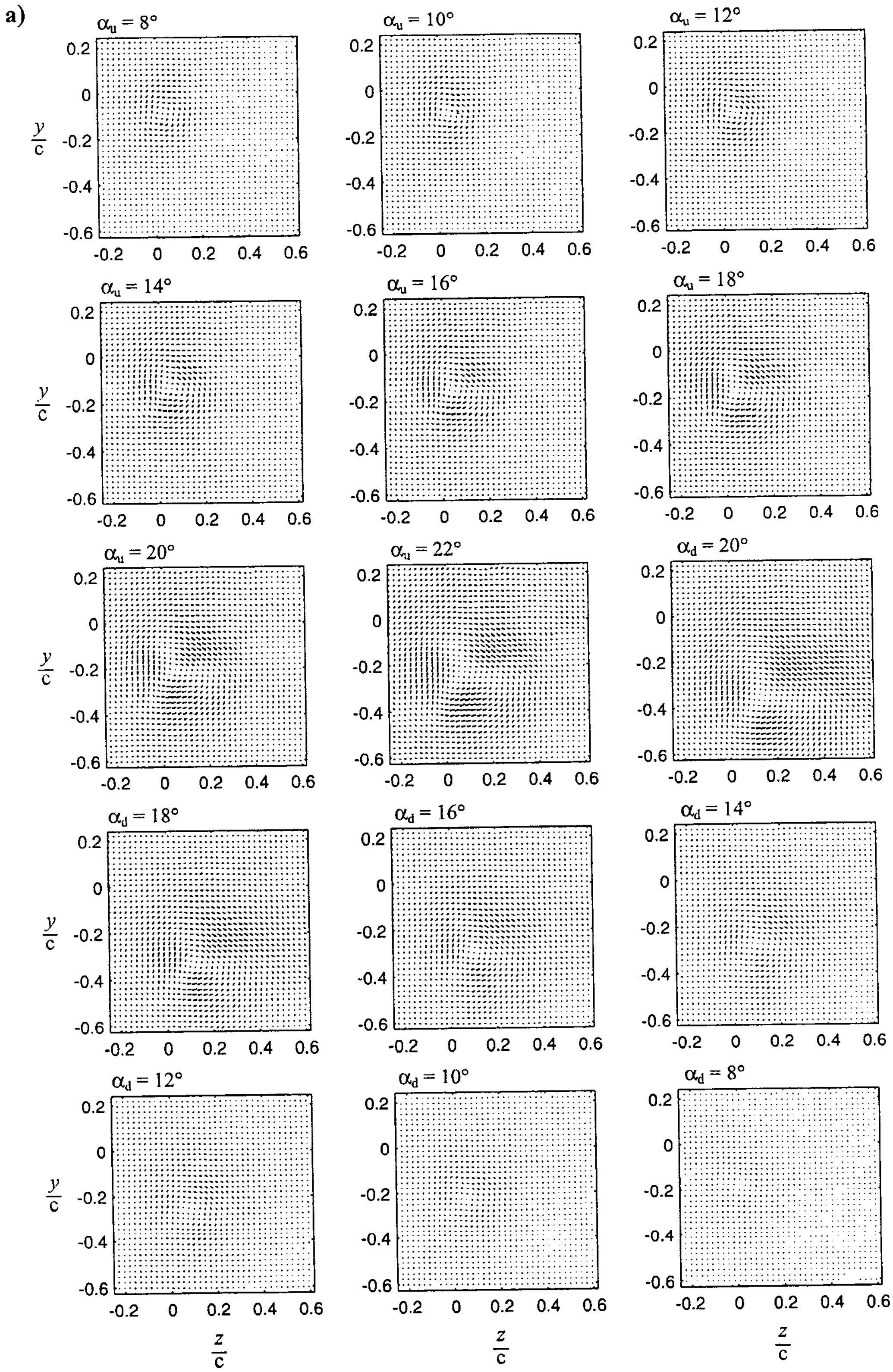

Figure E23 (a) Cross-flow velocity vectors, and contours of constant (b) $\zeta c/u_\infty$, (c) u/u_∞, and (d) u'/u_∞ (%) for the case of δ = 5.3°.

b)

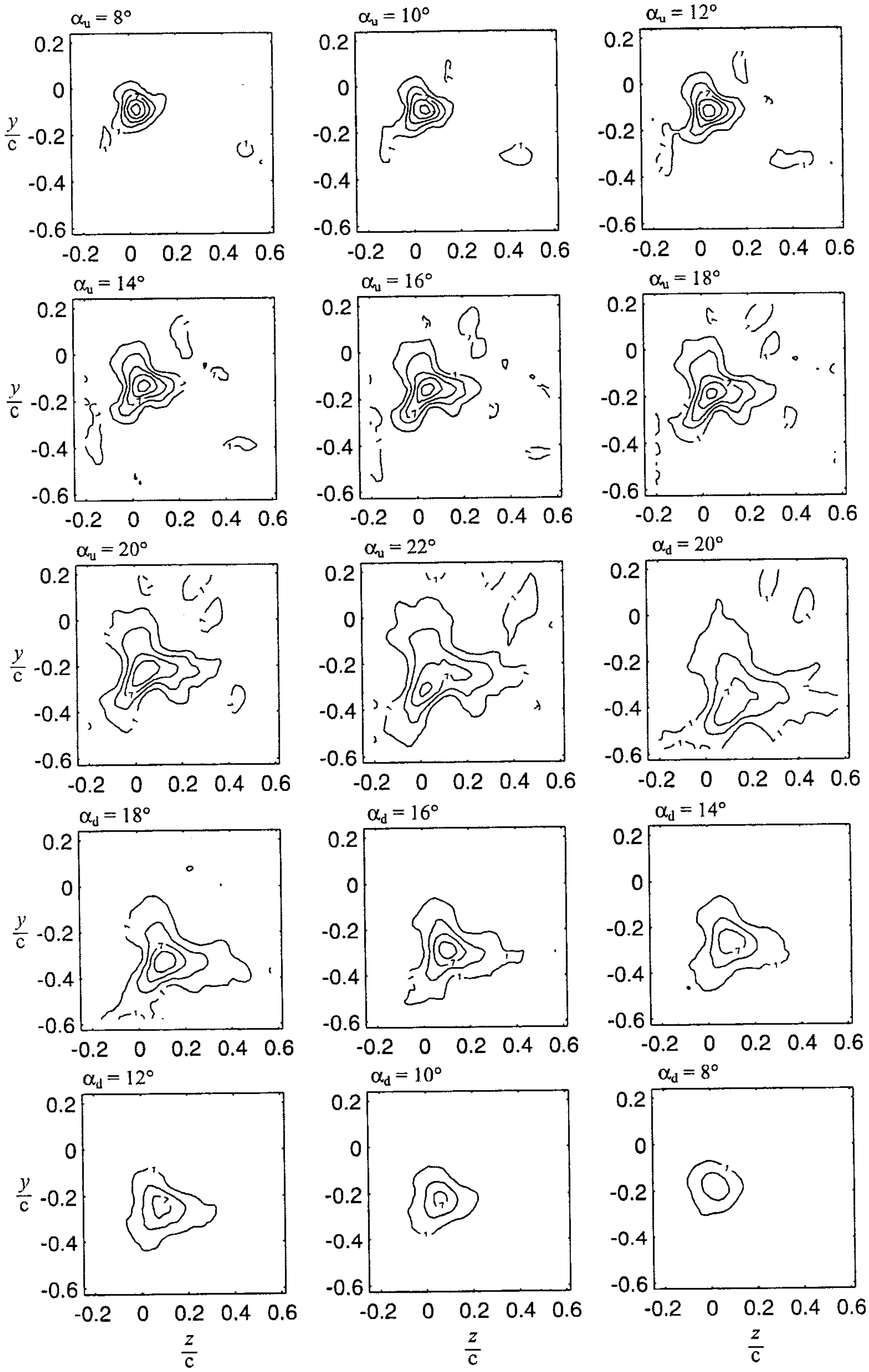

Figure E23 (a) Cross-flow velocity vectors, and contours of constant (b) $\zeta c/u_\infty$, (c) u/u_∞, and (d) u'/u_∞ (%) for the case of $\delta =$ 5.3°.

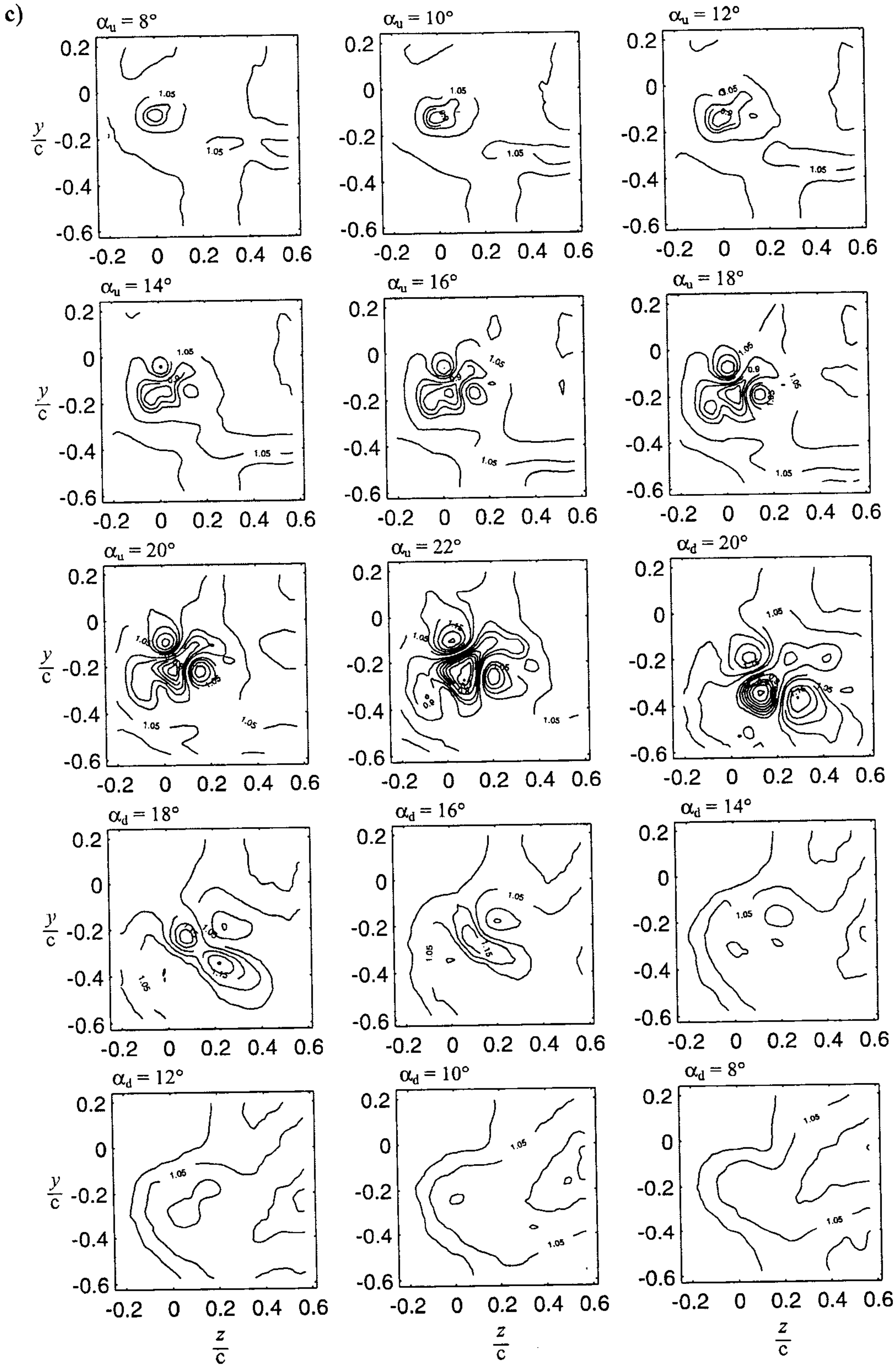

Figure E23 (a) Cross-flow velocity vectors, and contours of constant (b) $\zeta c/u_\infty$, (c) u/u_∞, and (d) u'/u_∞ (%) for the case of δ = 5.3°.

d)

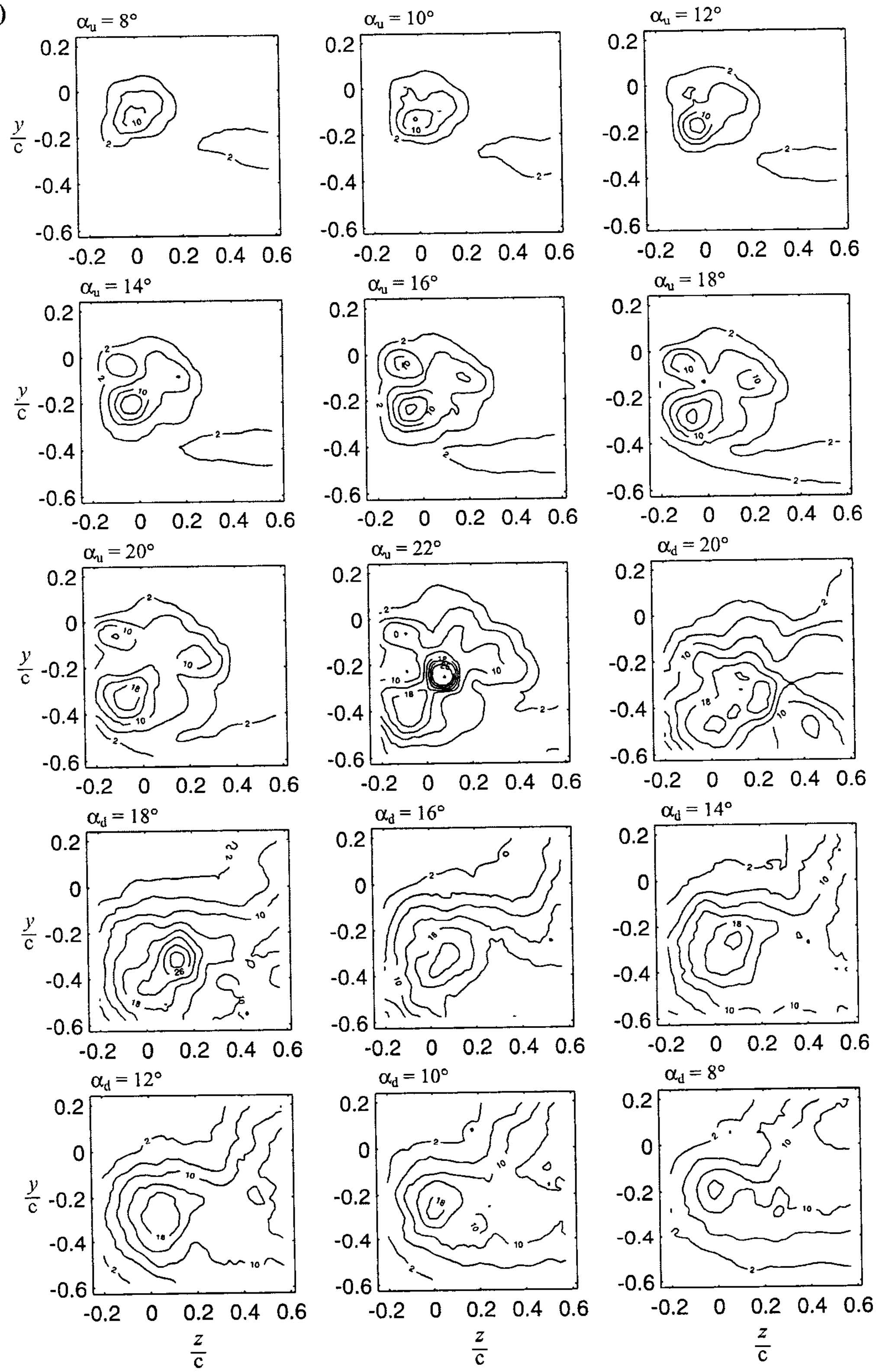

Figure E23 (a) Cross-flow velocity vectors, and contours of constant (b) $\zeta c/u_\infty$, (c) u/u_∞, and (d) u'/u_∞ (%) for the case of $\delta = 5.3°$.

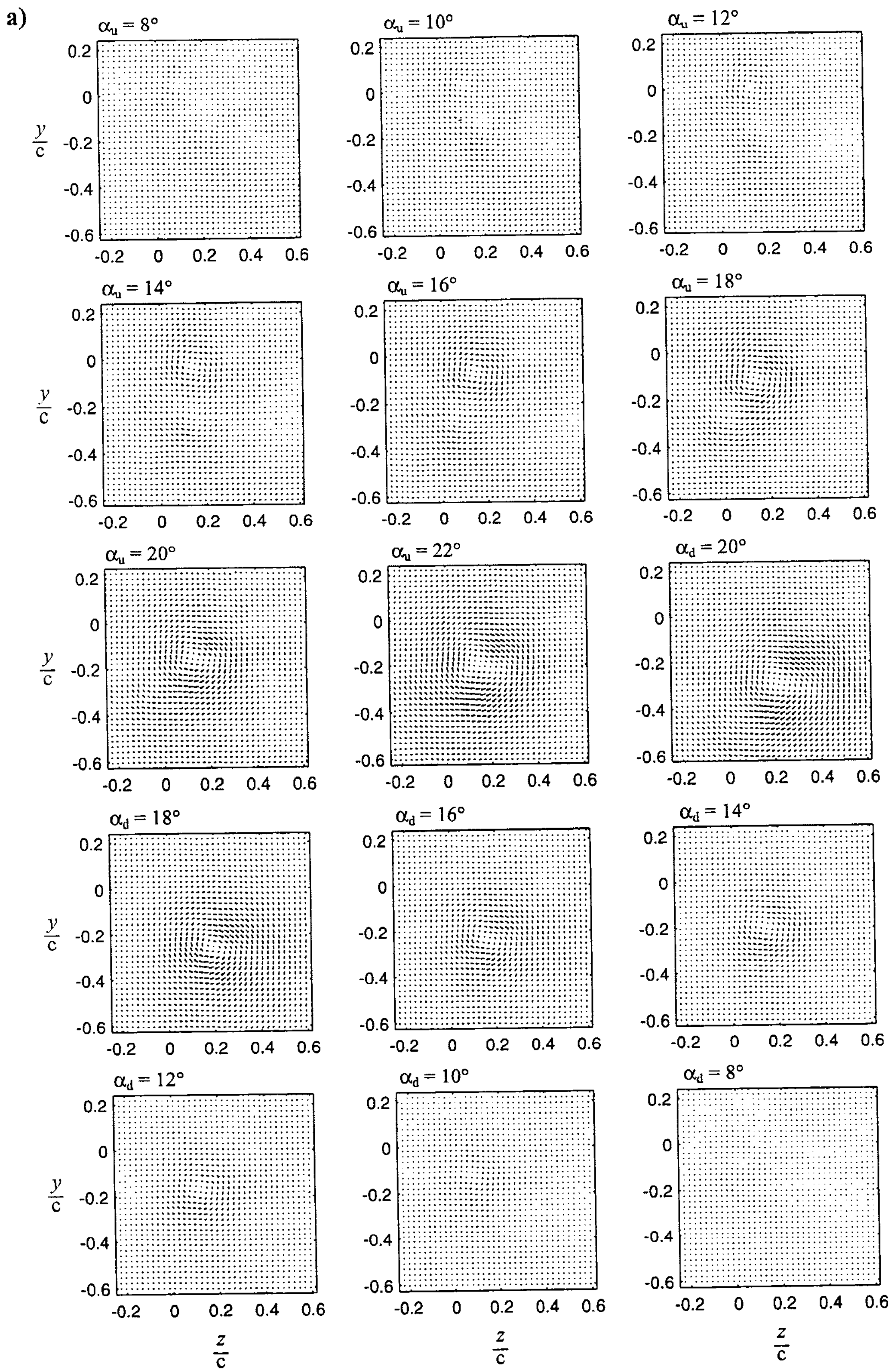

Figure E24 (a) Cross-flow velocity vectors, and contours of constant (b) $\zeta c/u_\infty$, (c) u/u_∞, and (d) u'/u_∞ (%) for the case of δ = -5.3°.

b)

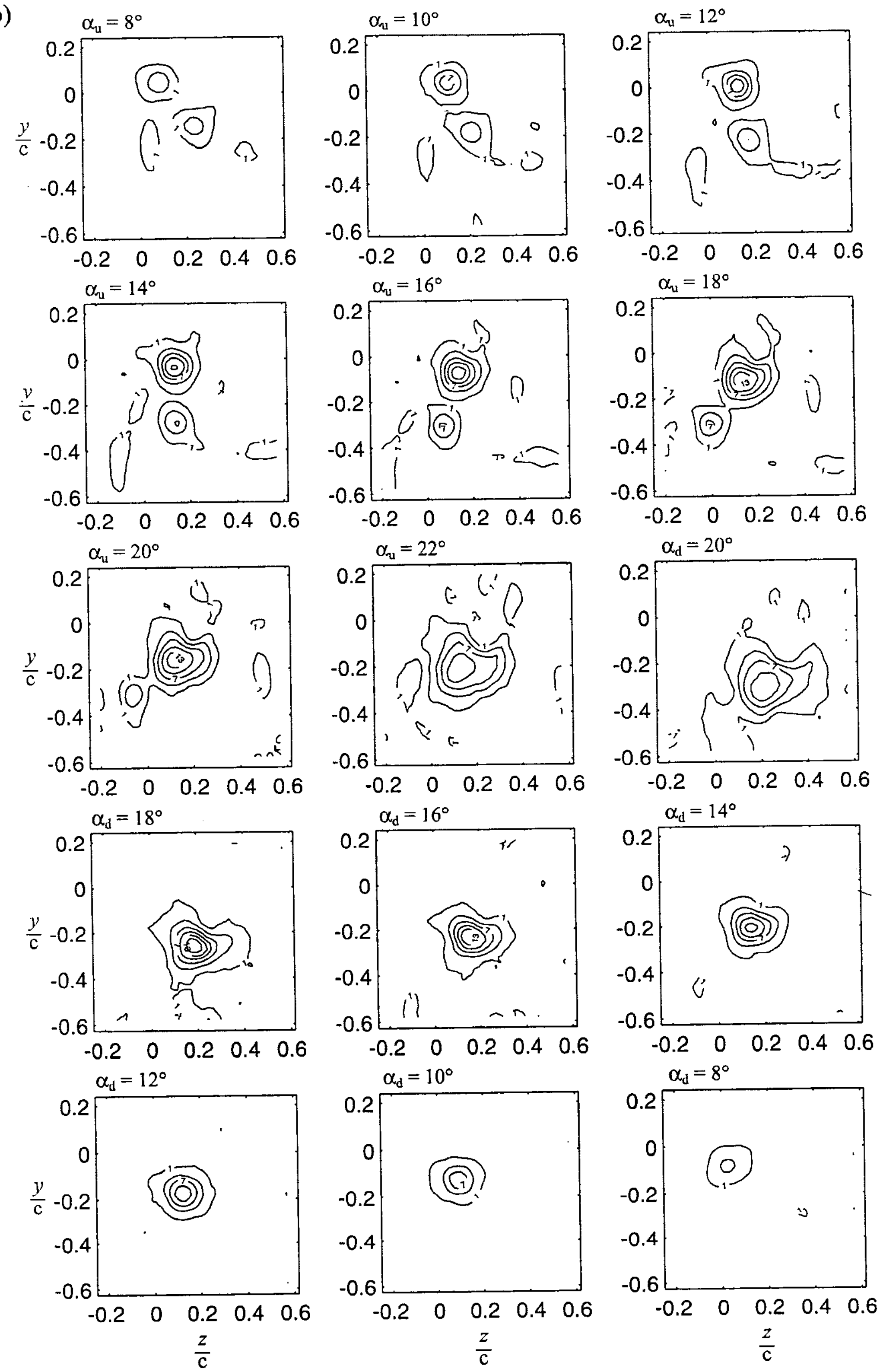

Figure E24 (a) Cross-flow velocity vectors, and contours of constant (b) $\zeta c/u_\infty$, (c) u/u_∞, and (d) u'/u_∞ (%) for the case of δ = -5.3°.

c)

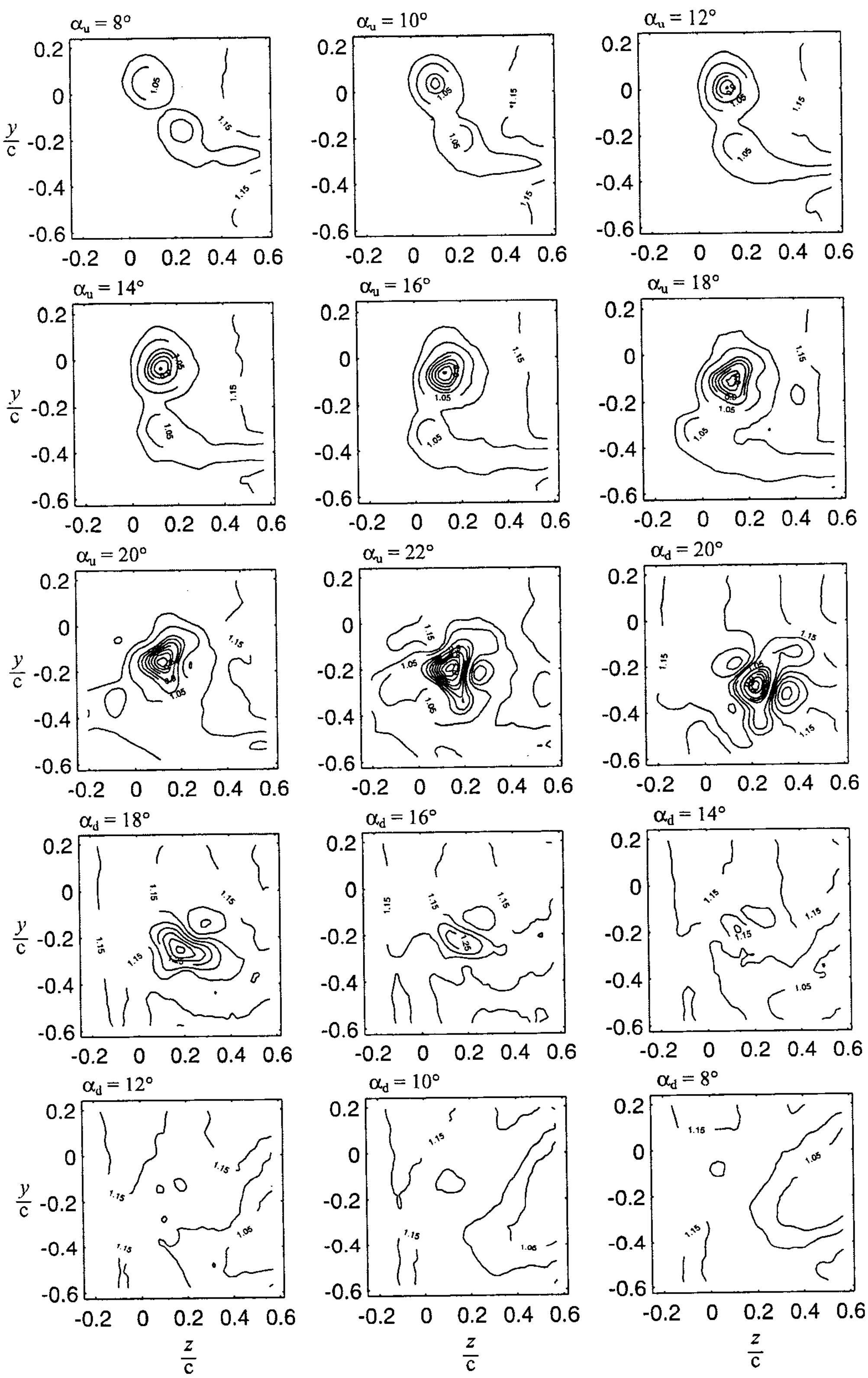

Figure E24 (a) Cross-flow velocity vectors, and contours of constant (b) $\zeta c/u_\infty$, (c) u/u_∞, and (d) u'/u_∞ (%) for the case of δ = -5.3°.

d)

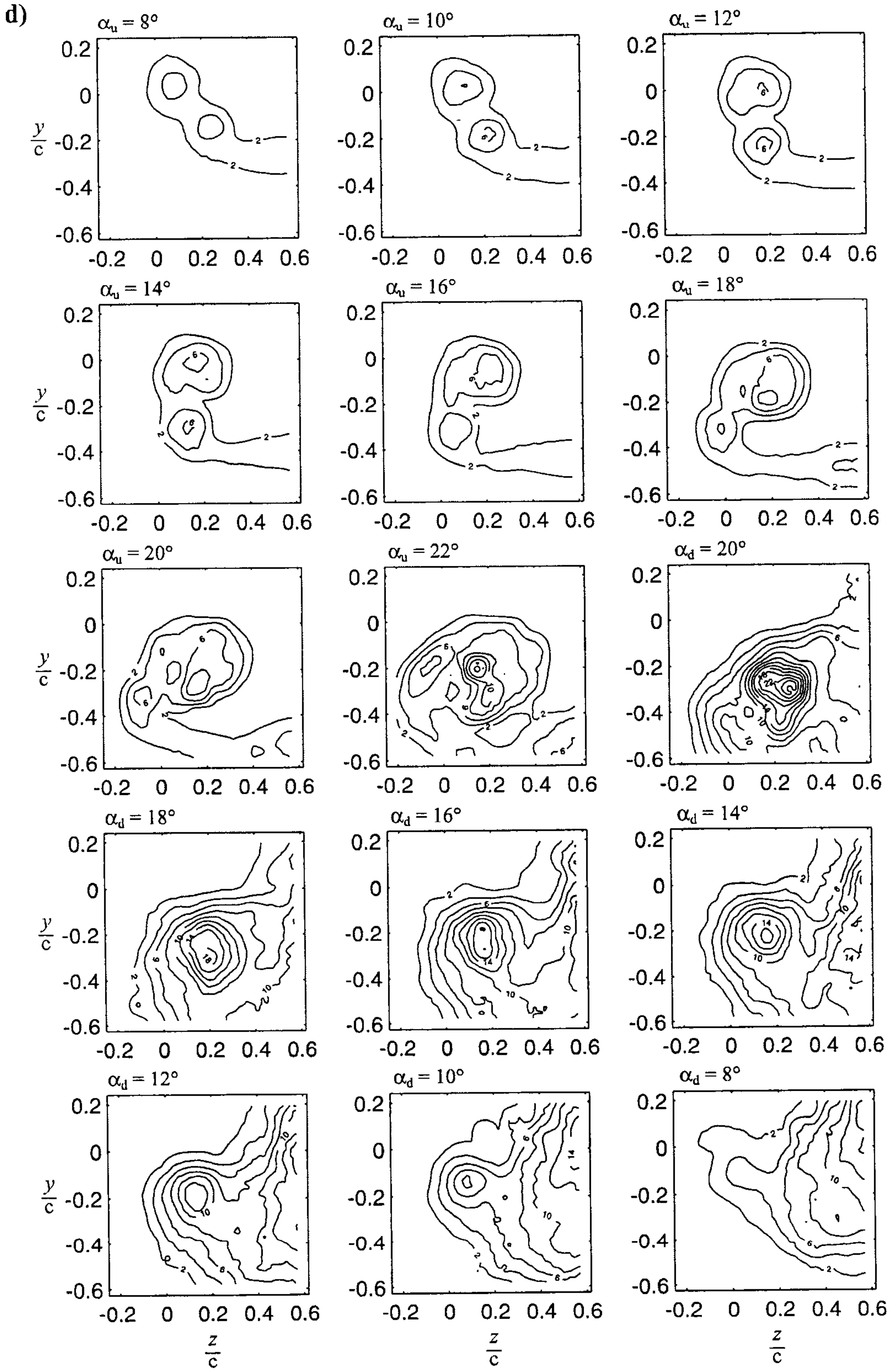

Figure E24 (a) Cross-flow velocity vectors, and contours of constant (b) $\zeta c/u_\infty$, (c) u/u_∞, and (d) u'/u_∞ (%) for the case of δ = -5.3°.

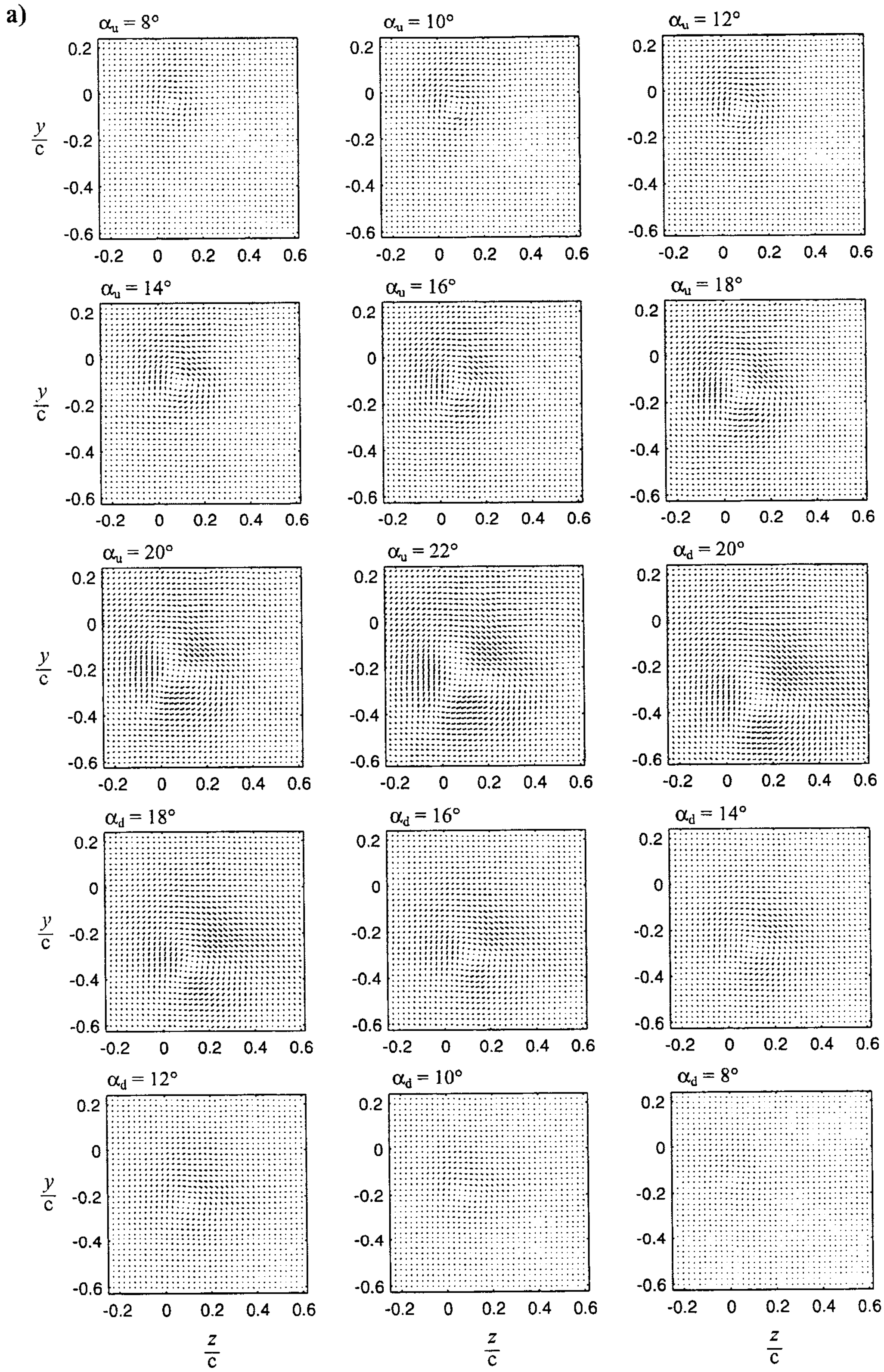

Figure E25 (a) Cross-flow velocity vectors, and contours of constant (b) $\zeta c/u_\infty$, (c) u/u_∞, and (d) u'/u_∞ (%) for case A.

b)

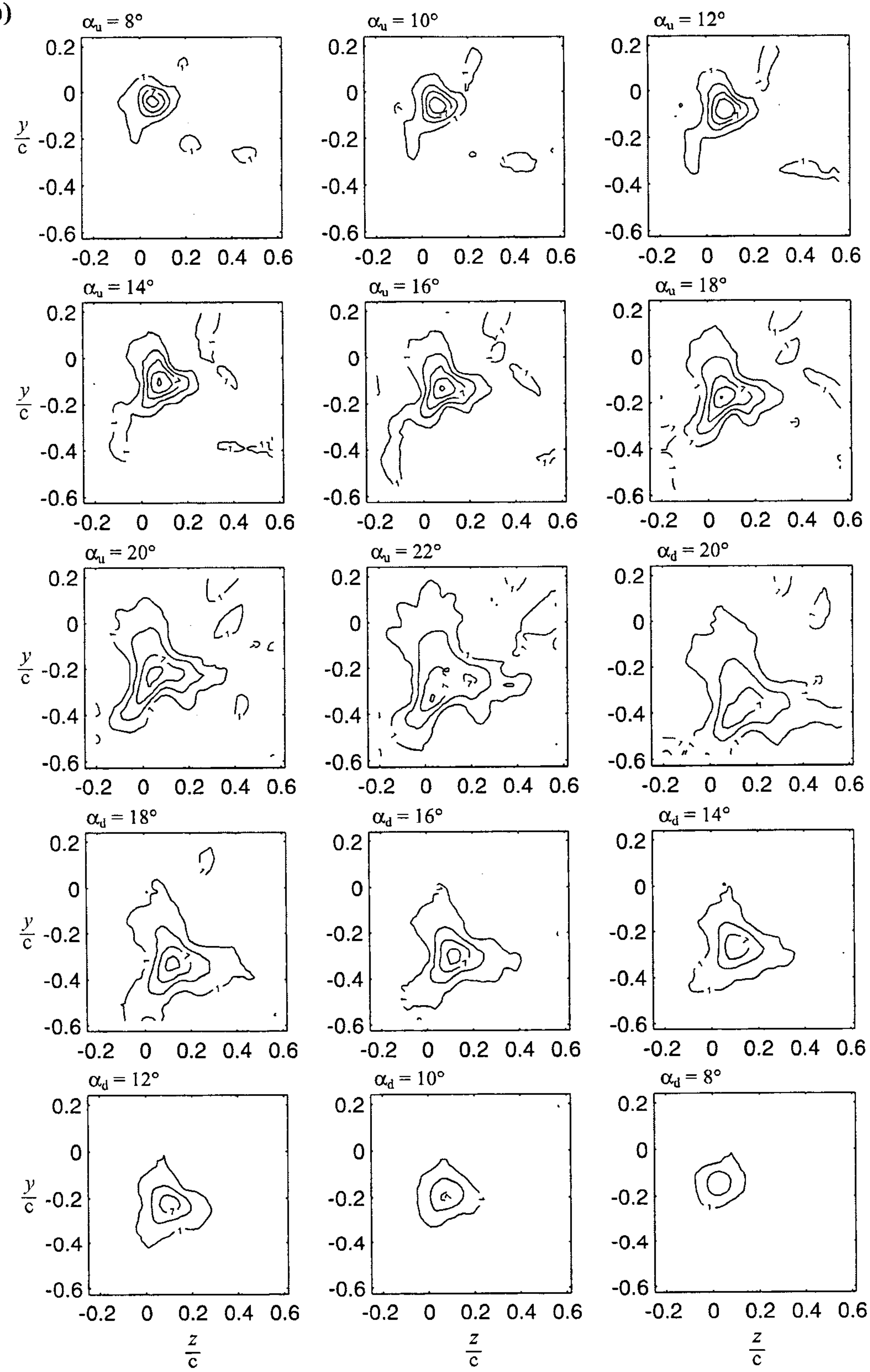

Figure E25 (a) Cross-flow velocity vectors, and contours of constant (b) $\zeta c/u_\infty$, (c) u/u_∞, and (d) u'/u_∞ (%) for case A.

c)

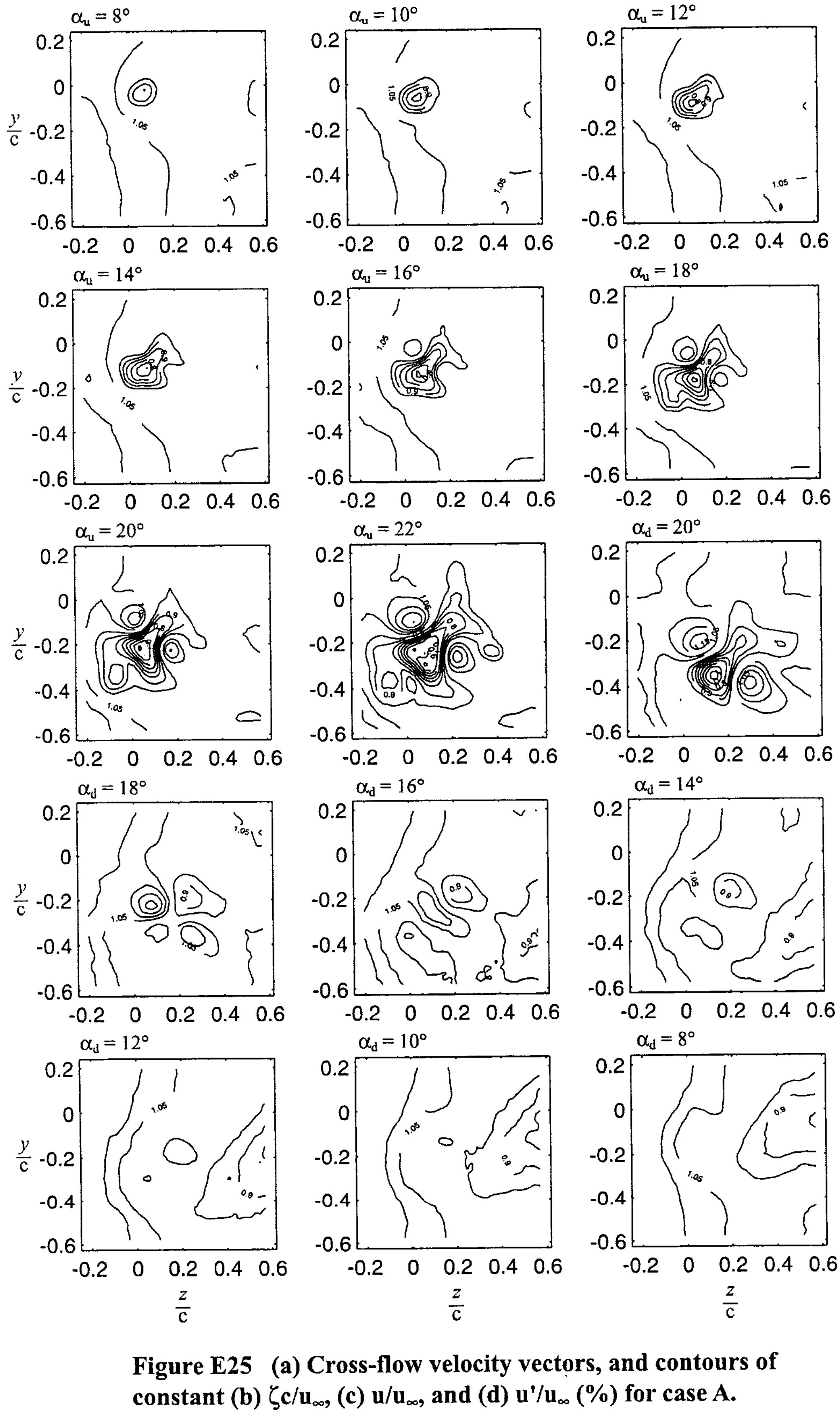

Figure E25 (a) Cross-flow velocity vectors, and contours of constant (b) $\zeta c/u_\infty$, (c) u/u_∞, and (d) u'/u_∞ (%) for case A.

d)

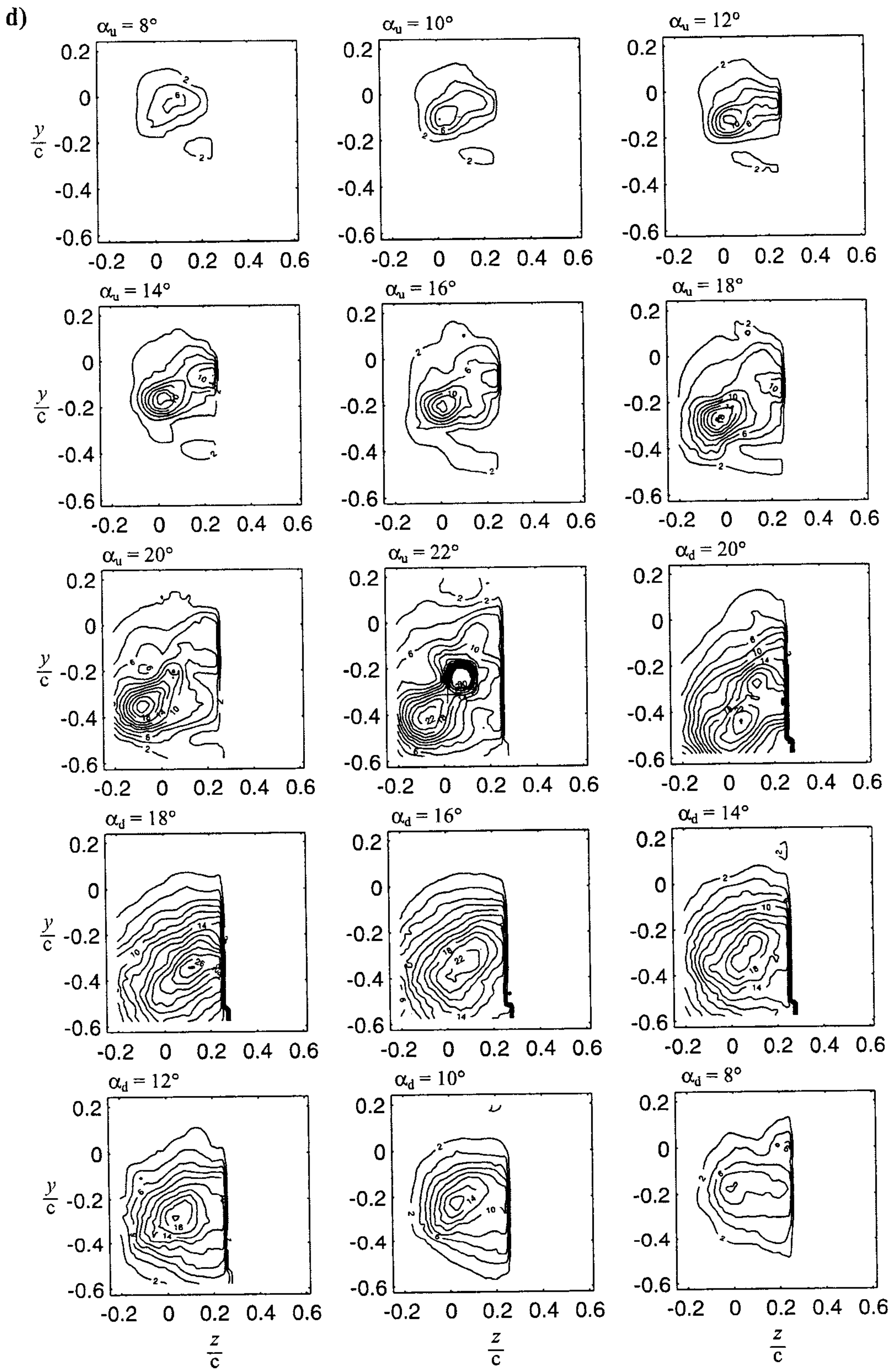

Figure E25 (a) Cross-flow velocity vectors, and contours of constant (b) $\zeta c/u_\infty$, (c) u/u_∞, and (d) u'/u_∞ (%) for case A.

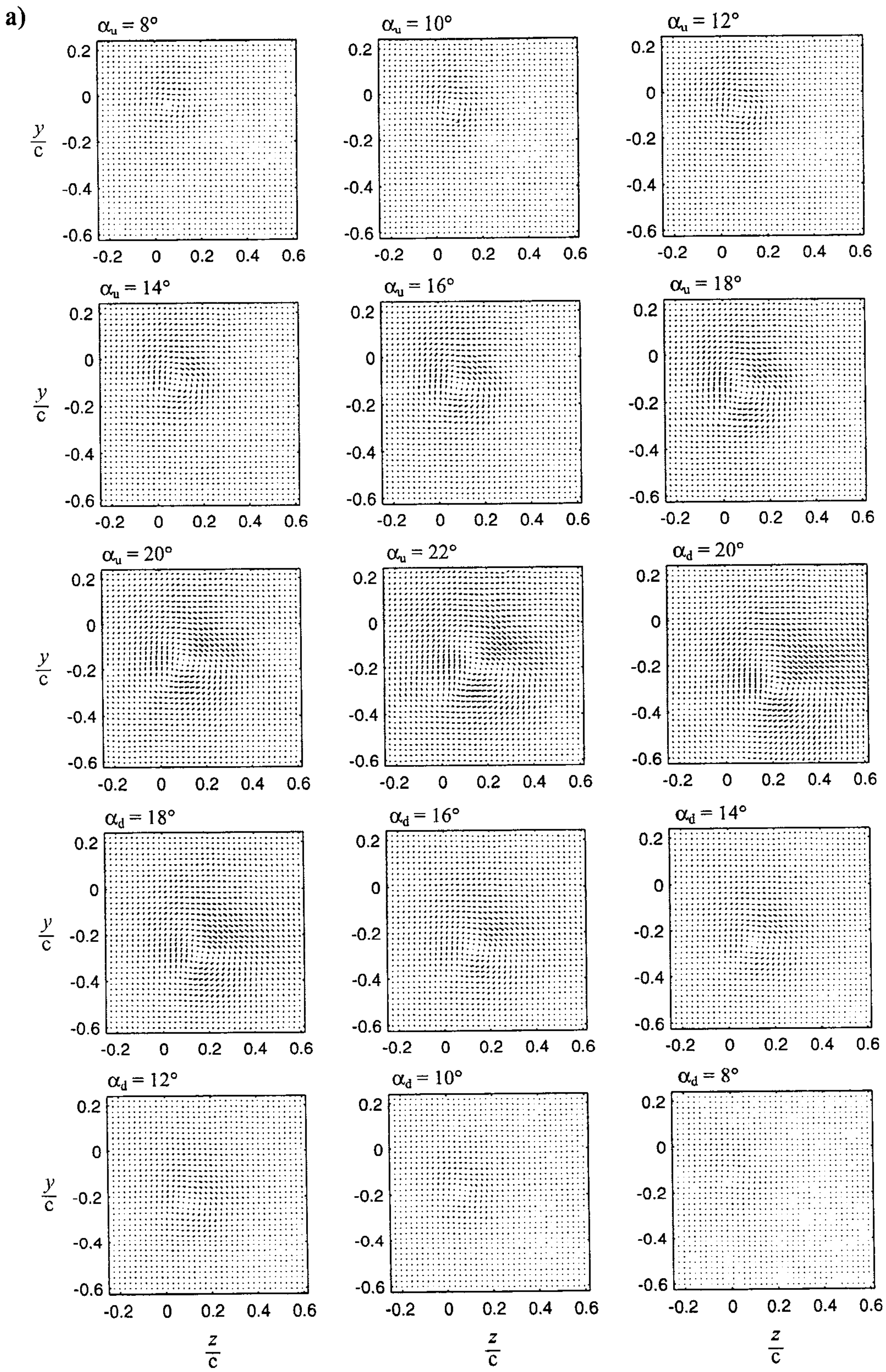

Figure E26 (a) Cross-flow velocity vectors, and contours of constant (b) $\zeta c/u_\infty$, (c) u/u_∞, and (d) u'/u_∞ (%) for case B.

b)

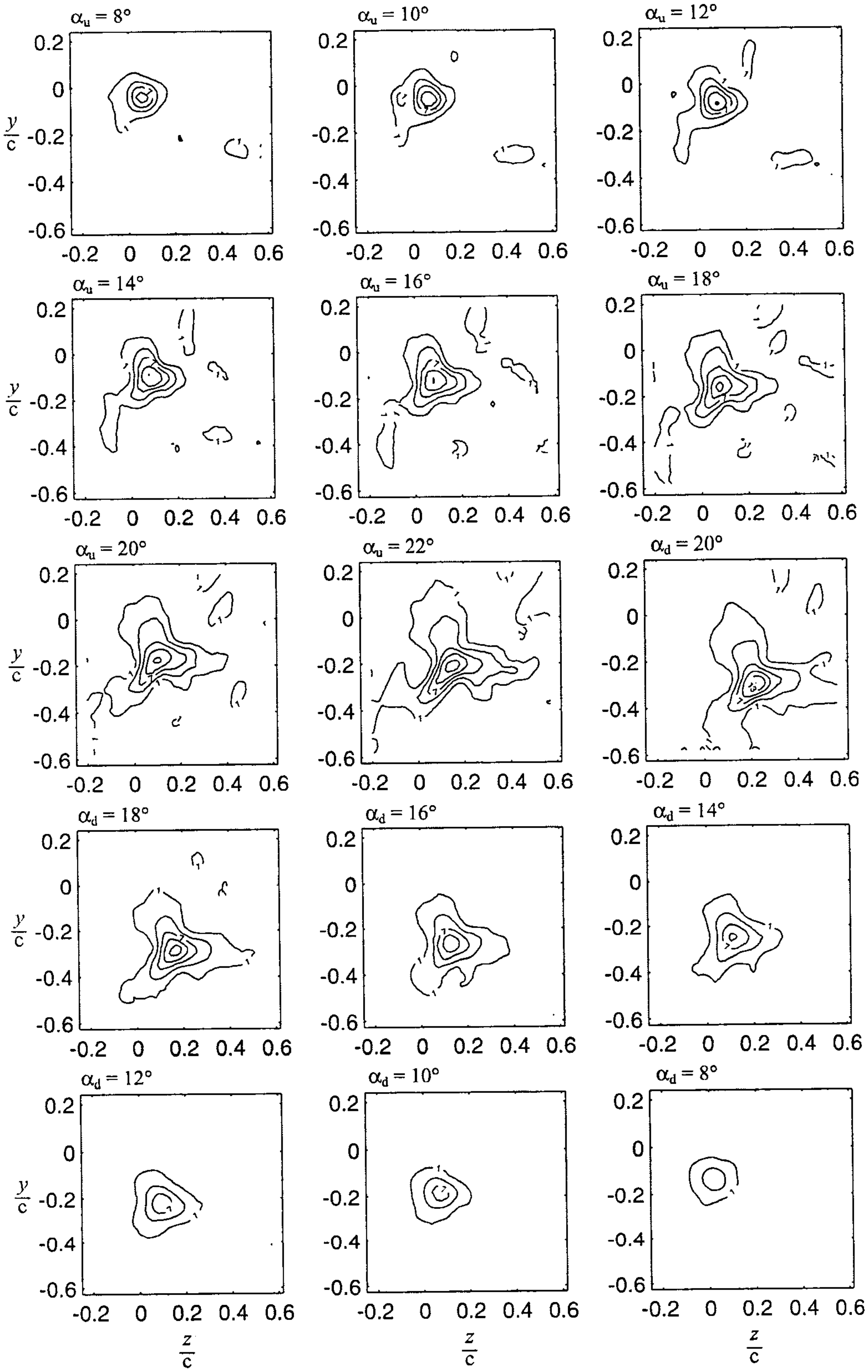

Figure E26 (a) Cross-flow velocity vectors, and contours of constant (b) $\zeta c/u_\infty$, (c) u/u_∞, and (d) u'/u_∞ (%) for case B.

c)

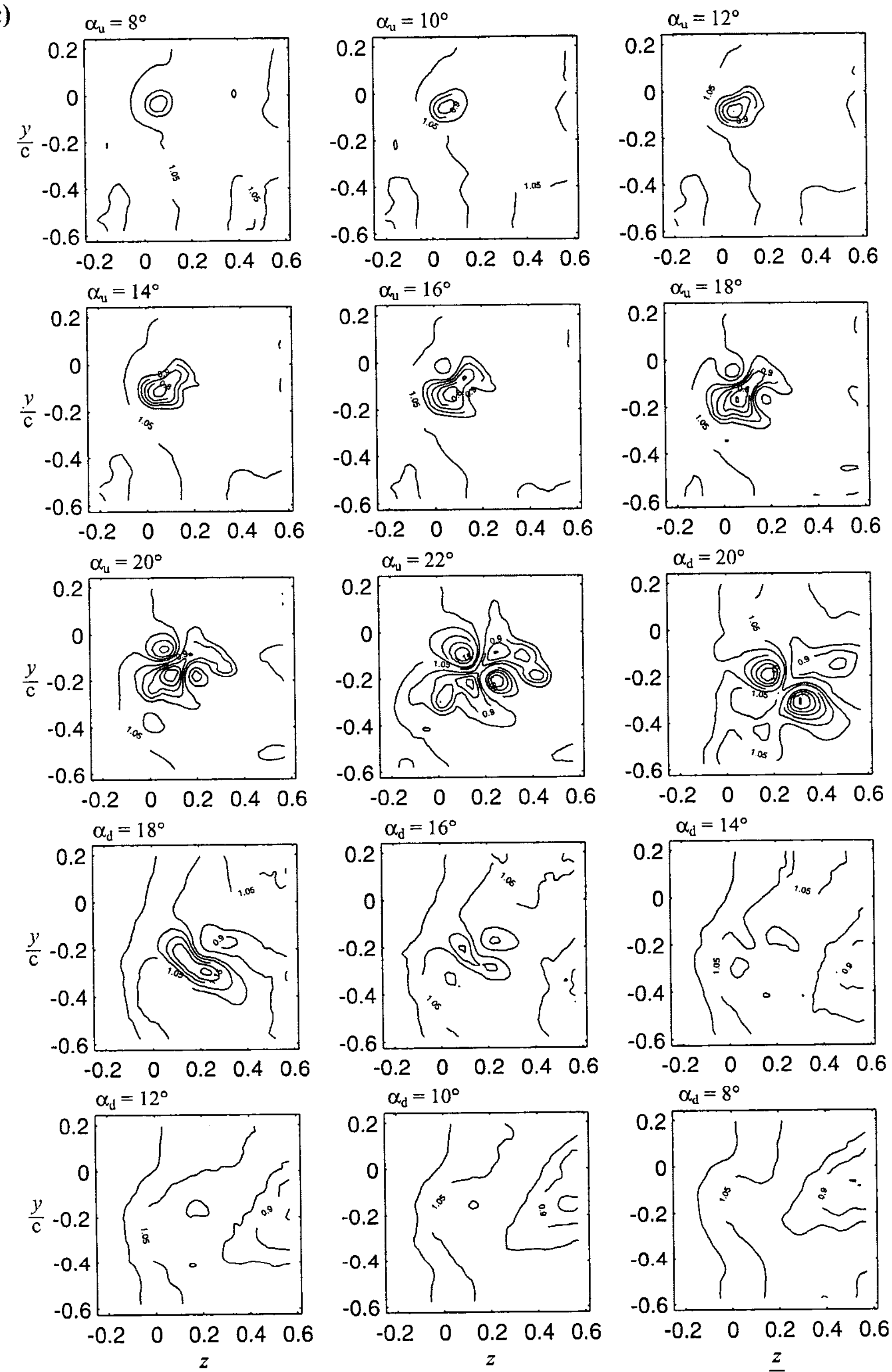

Figure E26 (a) Cross-flow velocity vectors, and contours of constant (b) $\zeta c/u_\infty$, (c) u/u_∞, and (d) u'/u_∞ (%) for case B.

d)

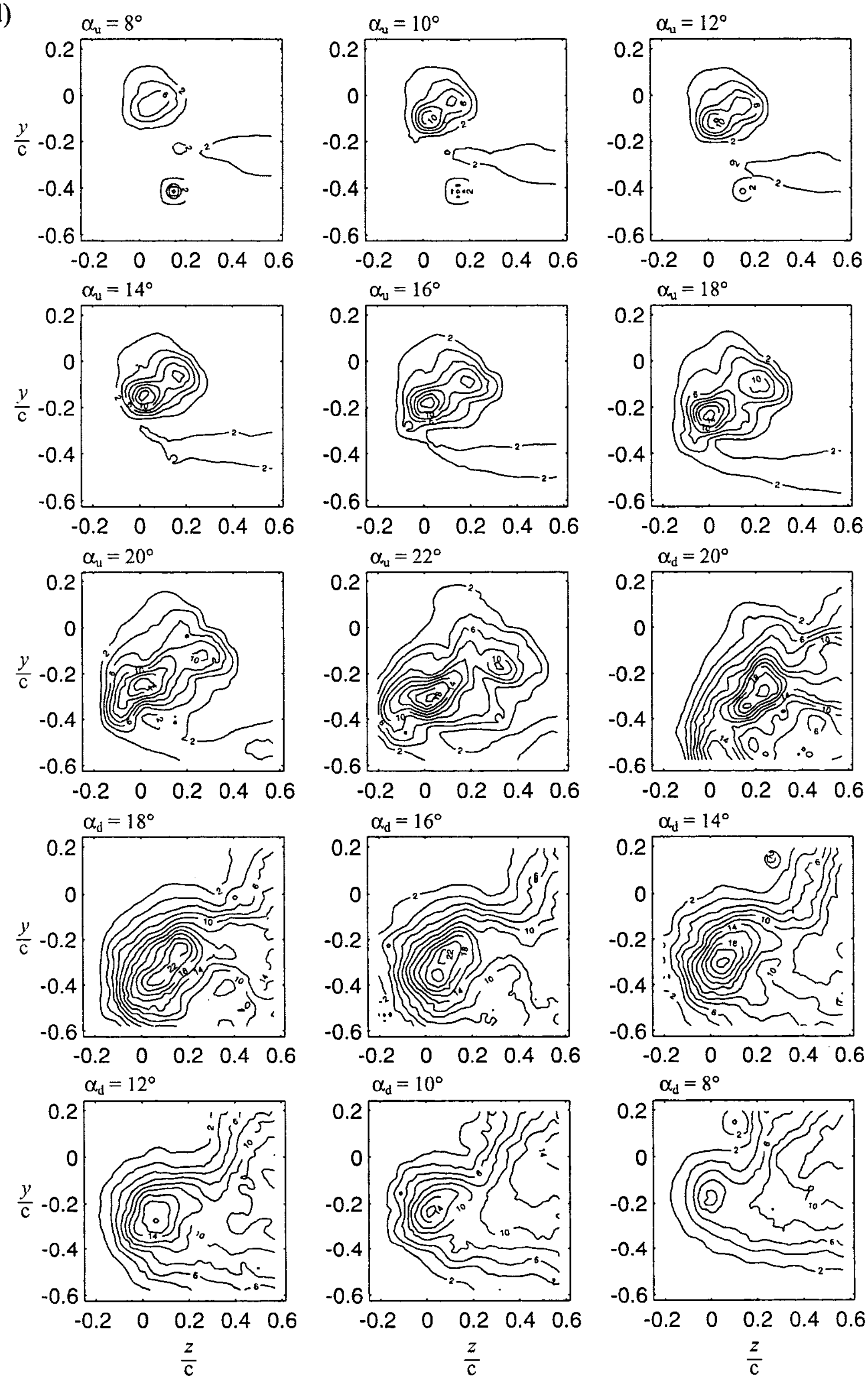

Figure E26 (a) Cross-flow velocity vectors, and contours of constant (b) $\zeta c/u_\infty$, (c) u/u_∞, and (d) u'/u_∞ (%) for case B.

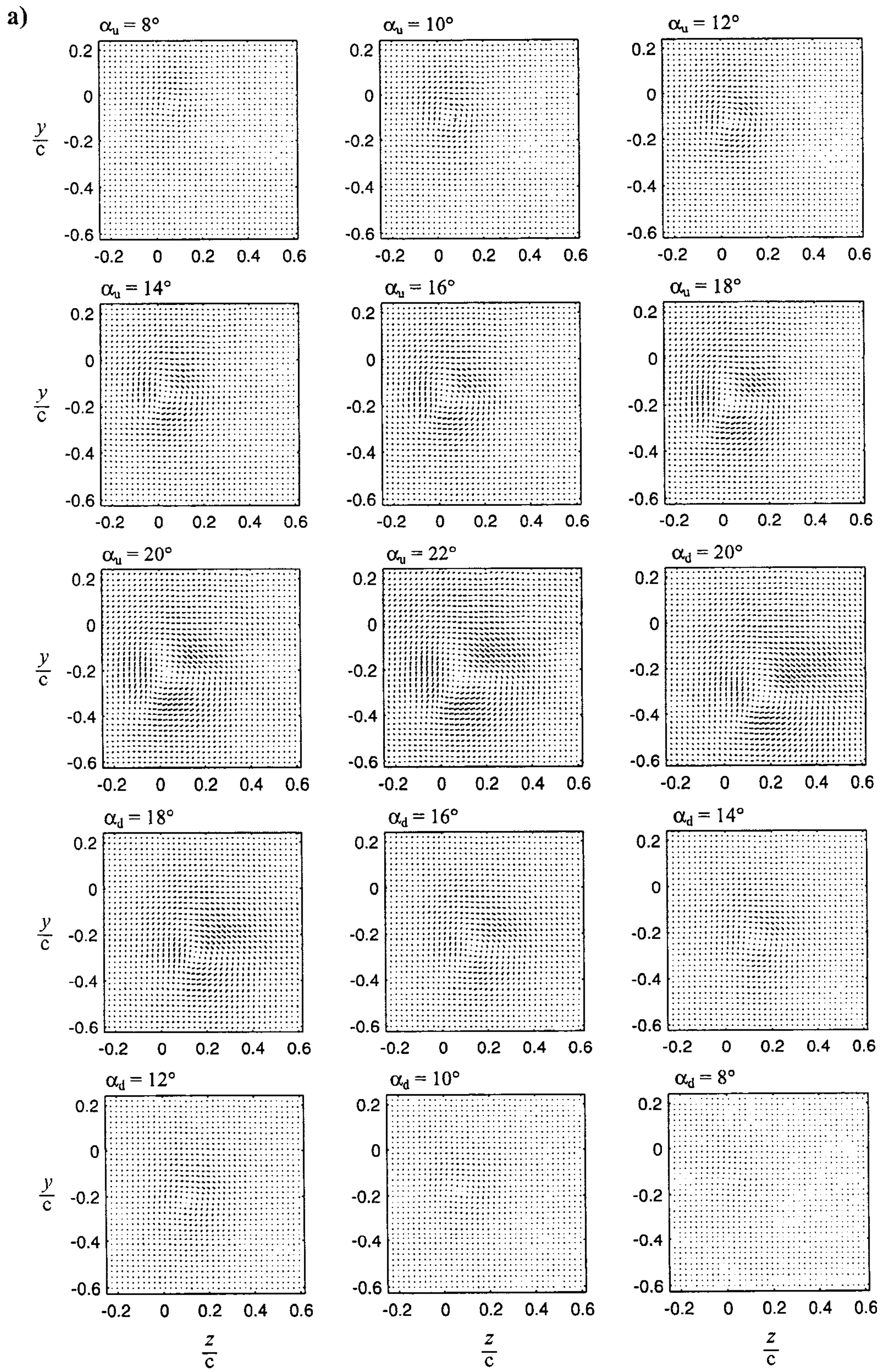

Figure E27 (a) Cross-flow velocity vectors, and contours of constant (b) $\zeta c/u_\infty$, (c) u/u_∞, and (d) u'/u_∞ (%) for case C.

b)

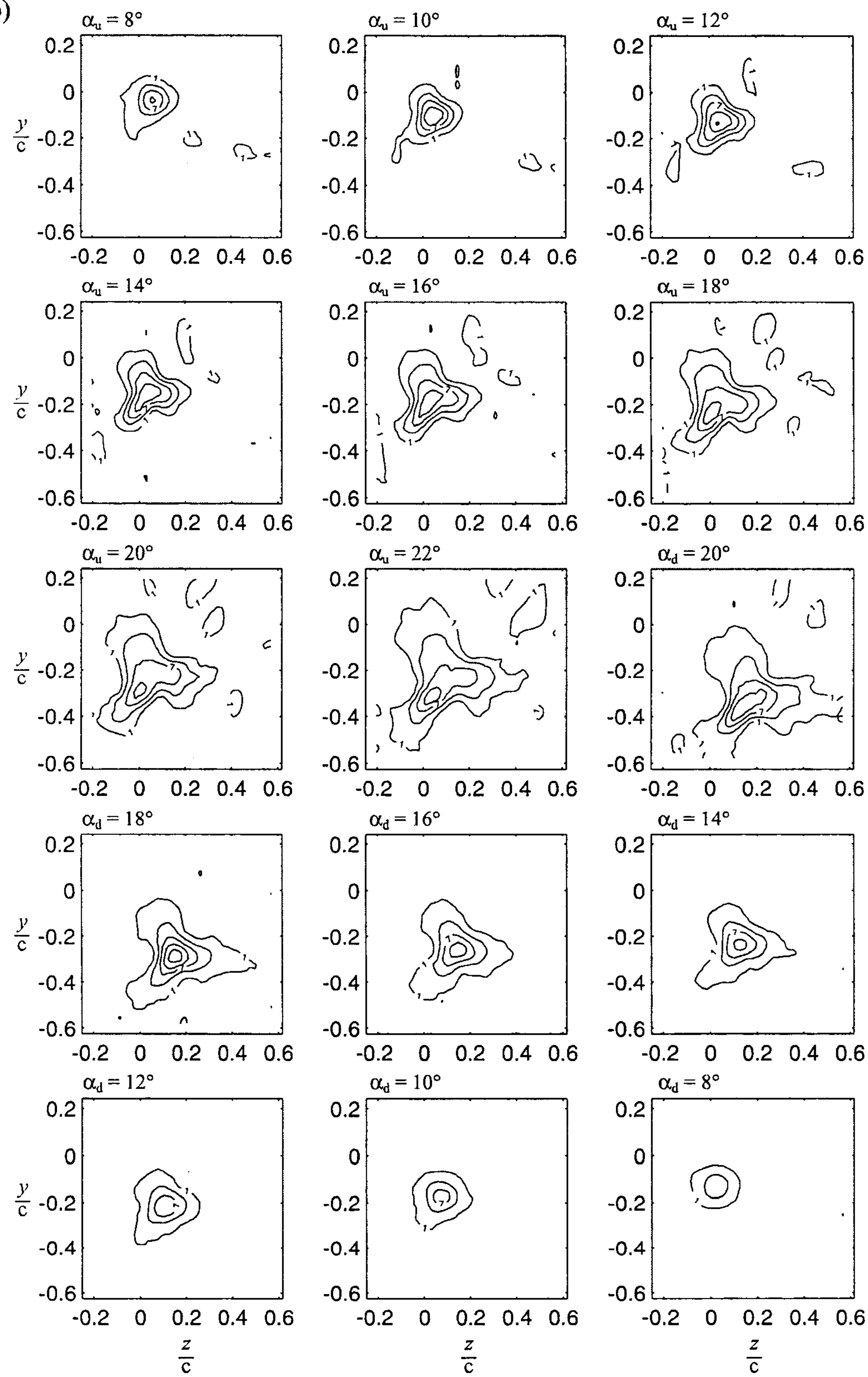

Figure E27 (a) Cross-flow velocity vectors, and contours of constant (b) $\zeta c/u_\infty$, (c) u/u_∞, and (d) u'/u_∞ (%) for case C.

c)

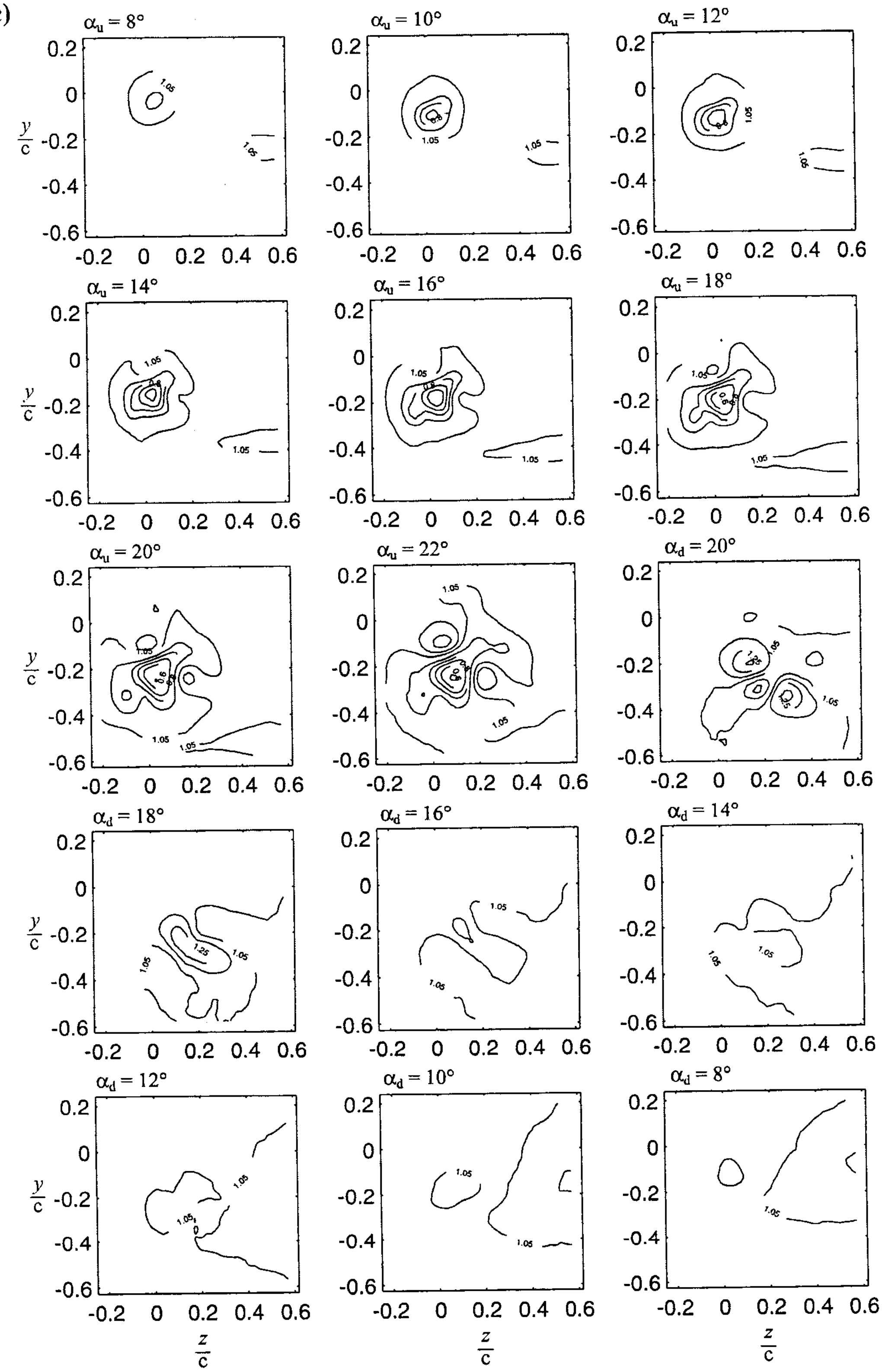

Figure E27 (a) Cross-flow velocity vectors, and contours of constant (b) $\zeta c/u_\infty$, (c) u/u_∞, and (d) u'/u_∞ (%) for case C.

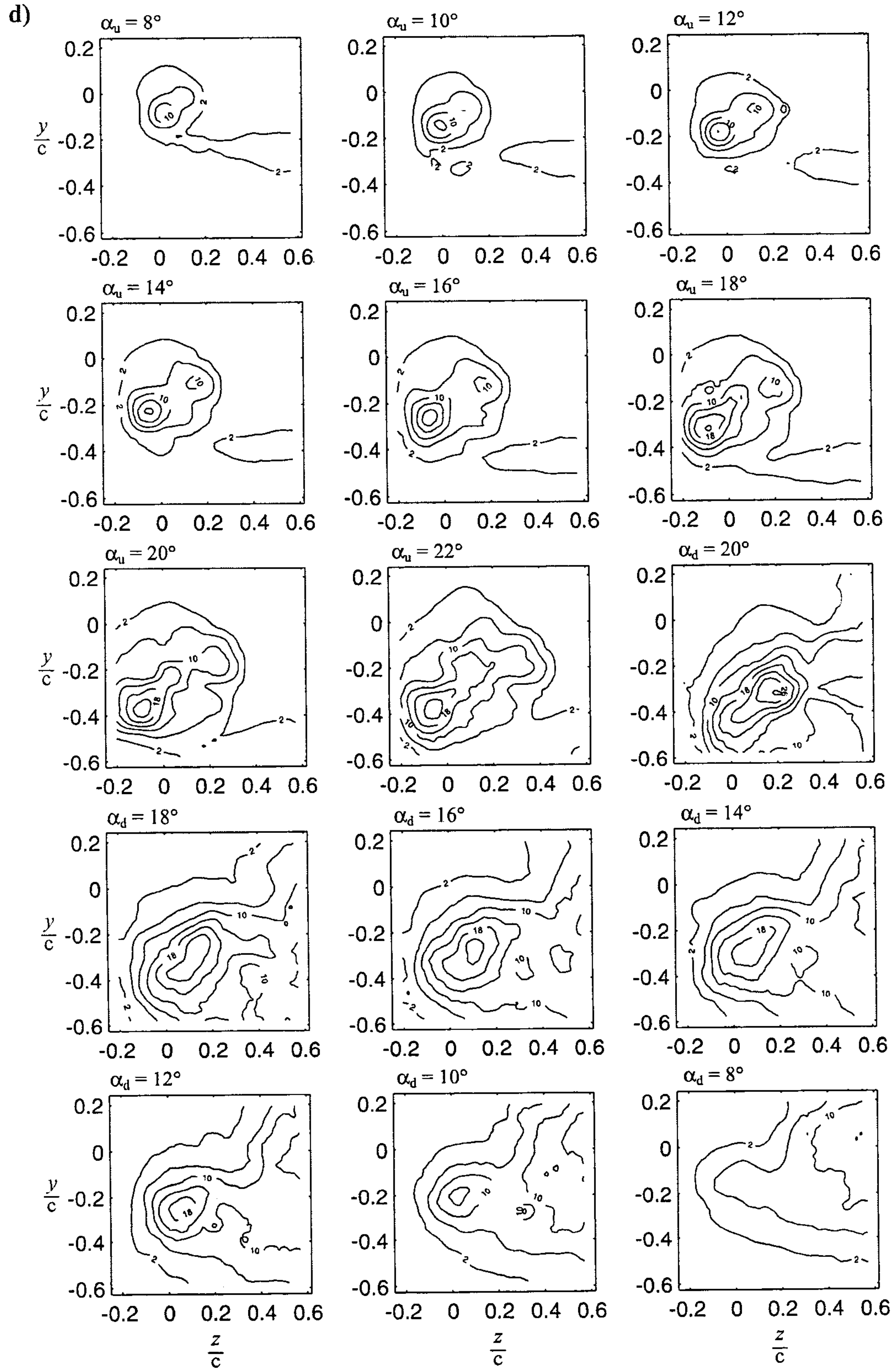

Figure E27 (a) Cross-flow velocity vectors, and contours of constant (b) $\zeta c/u_\infty$, (c) u/u_∞, and (d) u'/u_∞ (%) for case C.

a)

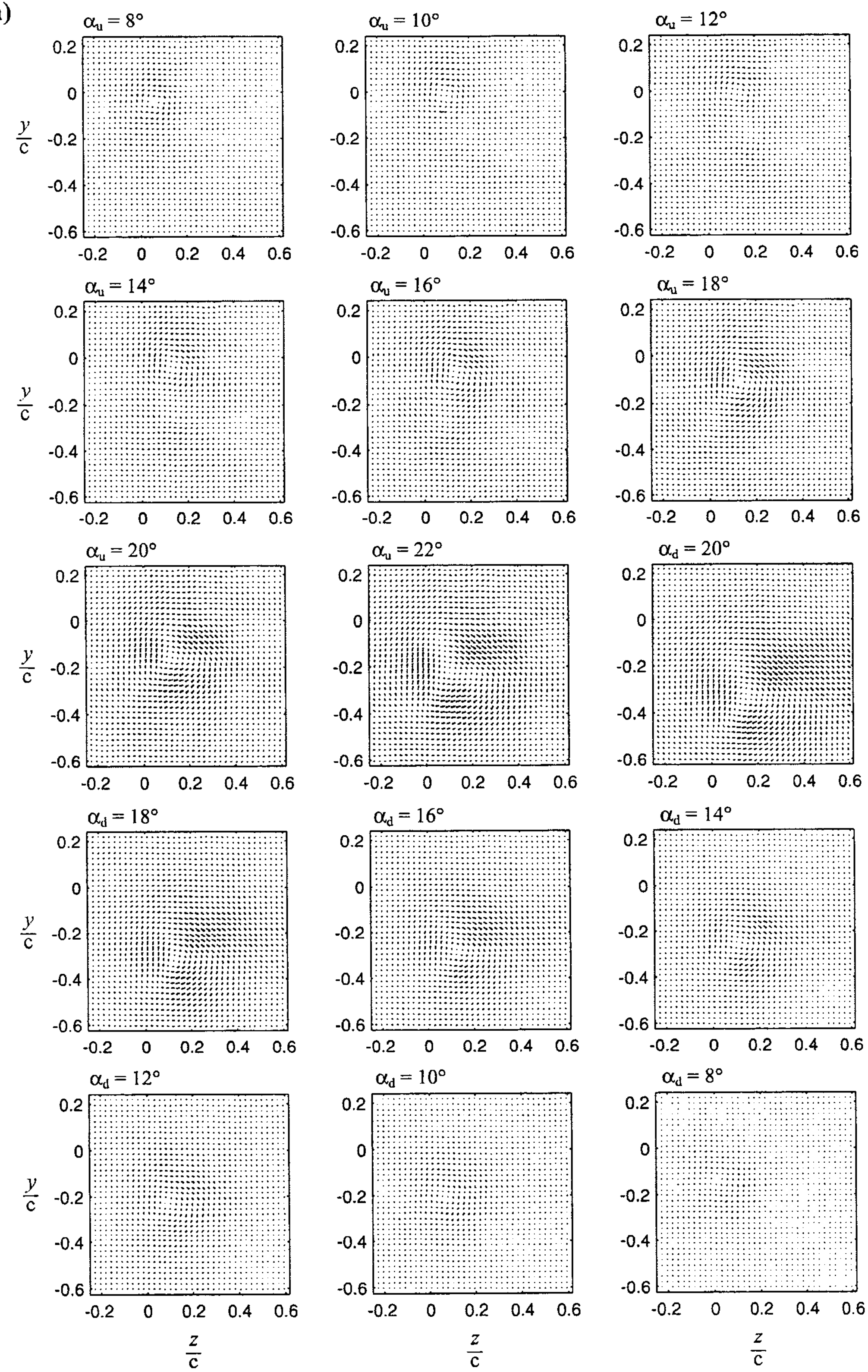

Figure E28 (a) Cross-flow velocity vectors, and contours of constant (b) $\zeta c/u_\infty$, (c) u/u_∞, and (d) u'/u_∞ (%) for case D.

b)

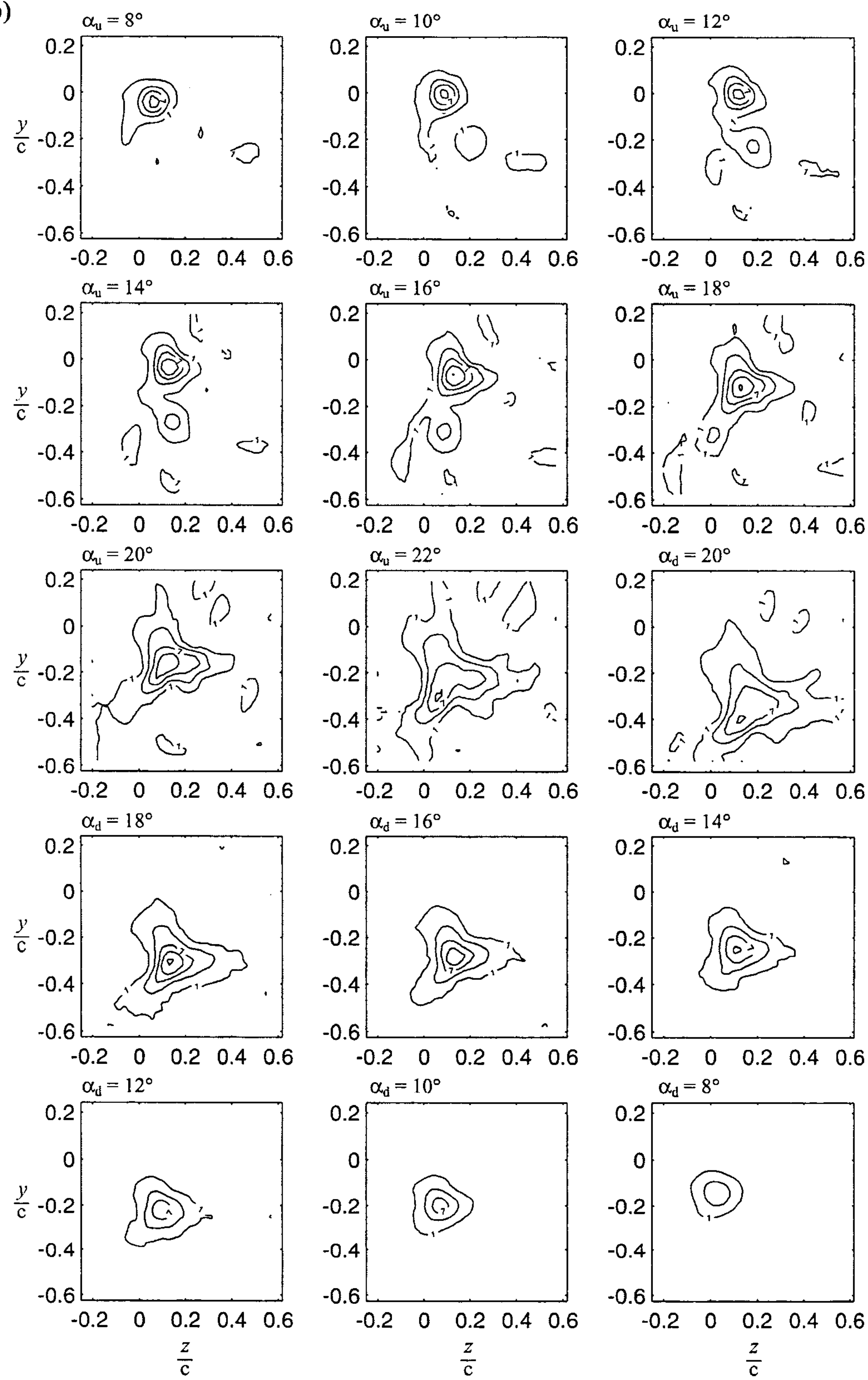

Figure E28 (a) Cross-flow velocity vectors, and contours of constant (b) $\zeta c/u_\infty$, (c) u/u_∞, and (d) u'/u_∞ (%) for case D.

c)

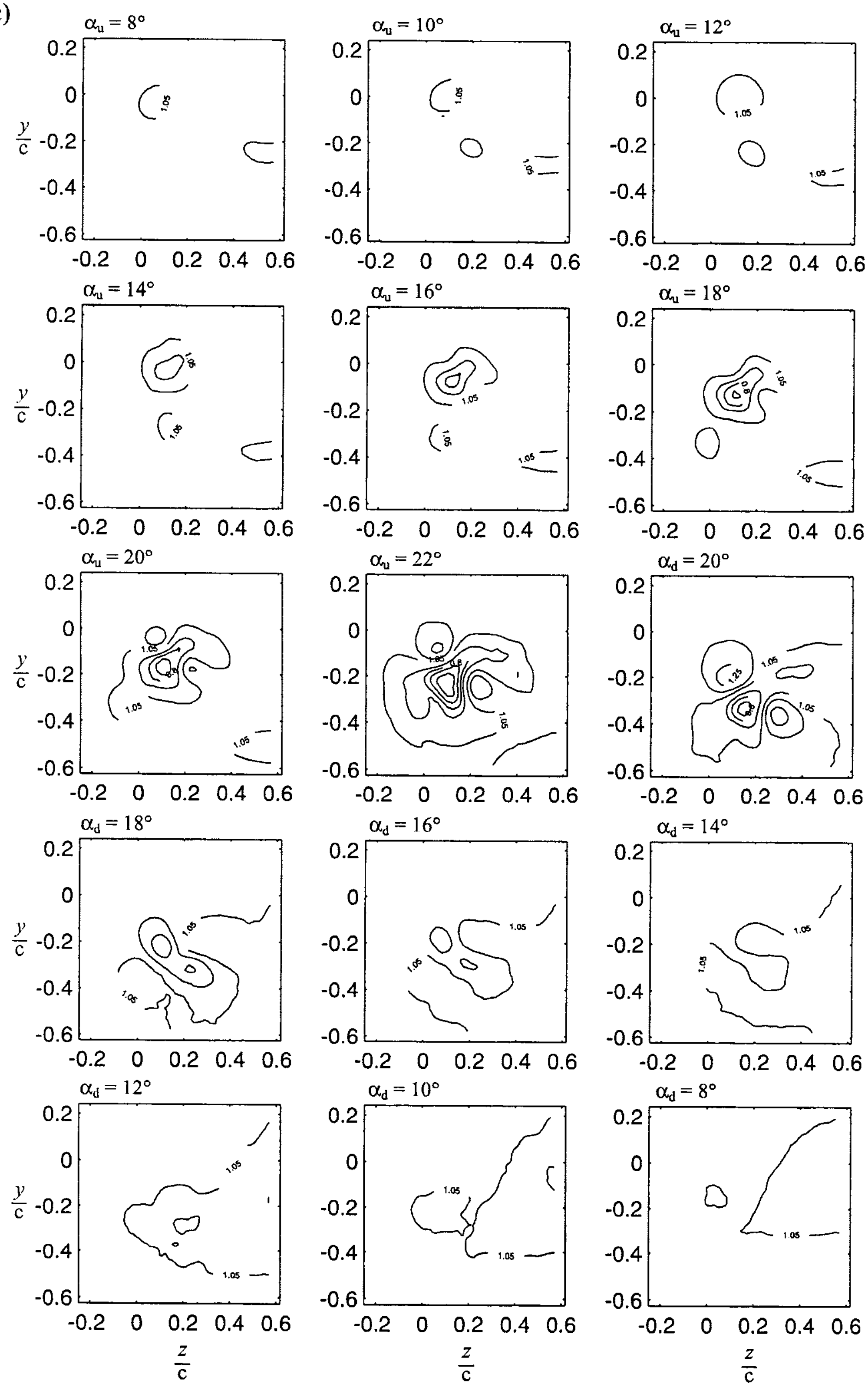

Figure E28 (a) Cross-flow velocity vectors, and contours of constant (b) $\zeta c/u_\infty$, (c) u/u_∞, and (d) u'/u_∞ (%) for case D.

d)

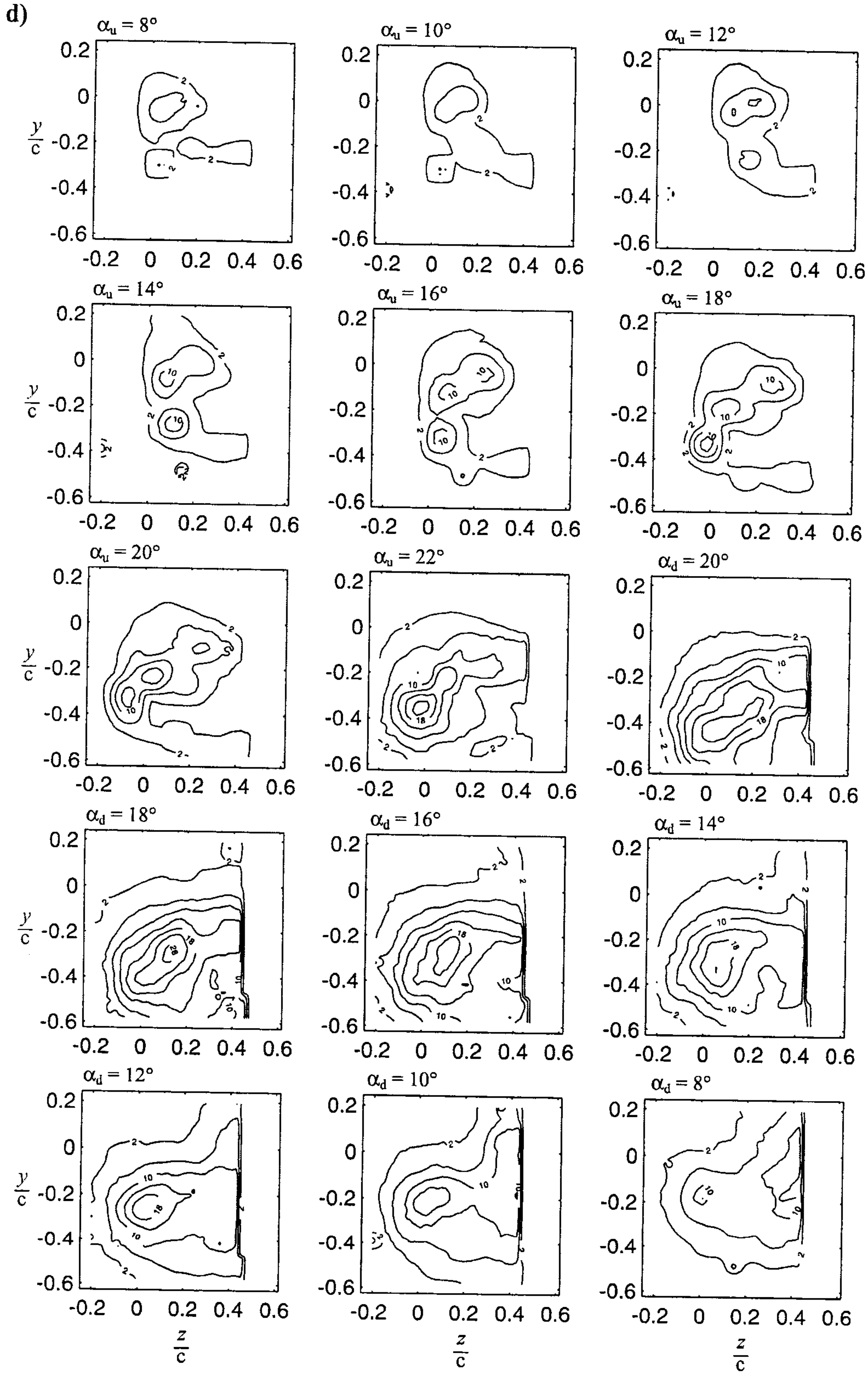

Figure E28 (a) Cross-flow velocity vectors, and contours of constant (b) $\zeta c/u_\infty$, (c) u/u_∞, and (d) u'/u_∞ (%) for case D.